Lecture Notes in Physics

The Lecture Notes in Physics

The series Lecture Notes in Physics (LNP), founded in 1969, reports new developments in physics research and teaching – quickly and informally, but with a high quality and the explicit aim to summarize and communicate current knowledge in an accessible way. Books published in this series are conceived as bridging material between advanced graduate textbooks and the forefront of research to serve the following purposes:

• to be a compact and modern up-to-date source of reference on a well-defined topic;
• to serve as an accessible introduction to the field to postgraduate students and nonspecialist researchers from related areas;
• to be a source of advanced teaching material for specialized seminars, courses and schools.

Both monographs and multi-author volumes will be considered for publication. Edited volumes should, however, consist of a very limited number of contributions only. Proceedings will not be considered for LNP.

Volumes published in LNP are disseminated both in print and in electronic formats, the electronic archive is available at springerlink.com. The series content is indexed, abstracted and referenced by many abstracting and information services, bibliographic networks, subscription agencies, library networks, and consortia.

Proposals should be sent to a member of the Editorial Board, or directly to the managing editor at Springer:

Dr. Christian Caron
Springer Heidelberg
Physics Editorial Department I
Tiergartenstrasse 17
69121 Heidelberg/Germany
christian.caron@springer-sbm.com

Arnab Das Bikas K. Chakrabarti (Eds.)

Quantum Annealing and Related Optimization Methods

Springer

Editors

Arnab Das
Bikas K. Chakrabarti

Saha Institute of Nuclear Physics
Centre for Applied Mathematics
and Computational Science
Bidhannagar 1/AF
700064 Kolkata, India
E-mail: arnab.das@saha.ac.in
bikask.chakrabarti@saha.ac.in

Arnab Das, Bikas K. Chakrabarti, *Quantum Annealing and Related Optimization Methods*, Lect. Notes Phys. 679 (Springer, Berlin Heidelberg 2005), DOI 10.1007/b135699

Library of Congress Control Number: 2005930442

ISSN 0075-8450
ISBN-10 3-540-27987-3 Springer Berlin Heidelberg New York
ISBN-13 978-3-540-27987-7 Springer Berlin Heidelberg New York

Springer is a part of Springer Science+Business Media
springeronline.com

Printed in The Netherlands

Typesetting: by the author using a Springer LaTeX macro package

Printed on acid-free paper SPIN: 11526216 54/TechBooks 5 4 3 2 1 0

Preface

Quantum annealing employs quantum fluctuations in frustrated systems or networks to anneal the system down to its ground state or to its minimum cost state, tuning the quantum fluctuation down to zero eventually. Often this can be more effective in multivariable optimization problems, over classical annealing performed utilizing tunable thermal fluctuations. The effectiveness comes from the fact that unlike in classical annealing, where the system scales the individual barrier heights by utilizing thermal fluctuations, in quantum annealing, fluctuations can help tunneling through these (even infinite but narrow) barriers. Apart from the recent theoretical demonstrations, this has been demonstrated experimentally.

In this book, we discuss the problems and the recent achievements in detail. This book grew out of an international workshop on quantum annealing, held in March 2004 in Kolkata under the auspices of the Centre for Applied Mathematics and Computational Science, Saha Institute of Nuclear Physics, India. With contributions from all the leading scientists/groups involved in its development so far, this first ever book on quantum annealing is expected to become an invaluable primer and also a guidebook for all researchers in this important field.

The book is divided into three parts. In the first part, tutorial materials are introduced. B.K. Chakrabarti and A. Das introduce the transverse Ising model and quantum Monte Carlo techniques, following which most of the theoretical studies on quantum annealing have been made so far. The decomposition of exponential operators used for the Suzuki–Trotter classical mapping in quantum Monte Carlo techniques is discussed in detail by N. Hatano and M. Suzuki. Latest quantum Monte Carlo and other numerical investigations and developments in quantum spin glasses are reviewed by H. Rieger. The question of ergodicity and consequent replica symmetry restoration in quantum spin glasses and ferroelectric glasses, experimental indications included, is reviewed by J.-J. Kim. A. Fisher reviewes the theory of quantum systems coupled to noisy condensed-phase environments and describes how to tailor response functions so as to optimize the coherent evolution of the system.

In the next part, quantum annealing techniques are developed and employed. G. Aeppli and T.F. Rosenbaum describe the experimental realization where the ground state of a glassy sample can be reached faster by tuning the external field (inducing changes in the tunneling field) rather than by tuning the temperature. D. Battaglia, L. Stella, O. Zagordi, G. Santoro, and E. Tosatti discuss the effectiveness of quantum annealing algorithms in solving hard computational problems such as the traveling salesman problem or a satisfiability problem and also in solving some very simple illustrative problems for a basic comparative study with thermal annealing. S. Suzuki and M. Okada investigate the prospect of adiabatic quantum annealing using real-time quantum evolution. A. Das and B.K. Chakrabarti discuss the application of quantum annealing in a kinetically constrained system and in an infinite range quantum spin glass. J.-I. Inoue reviewes the applicability of quantum annealing techniques in restoring informations and images after transportation through corrupted channels.

In the last part some of the classical optimization studies are reviewed and discussed. H. Rieger reviewes the classical algorithms for solving various combinatorial optimization problems. P. Sen and P.K. Das discuss classical annealing in the context of the ANNNI model and make a comparative study with quantum annealing in the same system. V. Martin-Mayor reviewes the problem of annealing and relaxation in the context of classical glasses and supercooled liquids.

With these firsthand and detailed reviews by the poineers in this field, this book on an analog version of quantum computation, we hope, will immediately inspire further research and development.

We are extremely grateful to all the contributors for excellent support and cooperation. We are also grateful to J. Zittartz for his encouragement regarding the publication of this lecture note volume.

Kolkata *Arnab Das*
May, 2005 *Bikas K. Chakrabarti*

Contents

List of Contributors

Bikas K. Chakrabarti
Theoretical Condensed Matter
Physics Division and Center
for Applied Mathematics
and Computational Sciences
Saha Institute of Nuclear Physics
1/AF Bidhannagar, Kolkata, India
bikask.chakrabarti@saha.ac.in

Arnab Das
Theoretical Condensed Matter
Physics Division and Center for
Applied Mathematics
and Computational Sciences
Saha Institute of Nuclear Physics
1/AF, Bidhannagar, Kolkata, India
arnab.das@saha.ac.in

Naomichi Hatano
Institute of Industrial Science
University of Tokyo
4–6–1 Meguro Komaba, Tokyo
153-8505, Japan
hatano@iis.u-tokyo.ac.jp

Masuo Suzuki
Department of Applied Physics
Tokyo University of Science
1–3 Kagurazaka, Shinjuku, Tokyo
162-8601, Japan
msuzuki@ap.kagu.sut.ac.jp

Heiko Rieger
Theoretische Physik
Universität des Saarlandes
66041 Saarbrücken, Germany
h.rieger@mx.uni-saarland.de

Jong-Jean Kim
Physics Department, KAIST
Daejeon 305-701, Korea
jjkim@kaist.ac.kr

Andrew Fisher
Department of Physics and
Astronomy, University College
London, Gower St
London WC1E 6BT
andrew.fisher@ucl.ac.uk

Gabriel Aeppli
London Centre for Nanotechnology
and Dept. of Physics and Astronomy
University College London
London WC1E 6BT UK
gabriel.aeppli@ucl.ac.uk

Thomas F. Rosenbaum
James Franck Institute
and Dept. of Physics
University of Chicago Chicago
Illinois 60637 USA

Demian Battaglia
SISSA INFM Democritos, Via Beirut 2-4, Trieste, Italy
battagli@sissa.it

Lorenzo Stella
SISSA INFM Democritos
Via Beirut 2-4, Trieste, Italy
battagli@sissa.it

Osvaldo Zagordi
SISSA INFM Democritos
Via Beirut 2-4, Trieste, Italyxs
battagli@sissa.it

Giuseppe E. Santoro
SISSA INFM Democritos
Via Beirut 2-4, Trieste
Italy
and
ICTP, Trieste, Italy
battagli@sissa.it

Erio Tosatti
SISSA INFM Democritos
Via Beirut 2-4, Trieste
Italy
and
ICTP, Trieste, Italy.
battagli@sissa.it

Sei Suzuki
Graduate School of Frontier Sciences, University of Tokyo
Kashiwa 277-8561
Japan
and
Brain Science Institute RIKEN
Wako 351-0198, Japan
sei@mns.k.u-tokyo.ac.jp

Masato Okada
Graduate School of Frontier Sciences, University of Tokyo
Kashiwa 277-8561
Japan
and
Brain Science Institute
RIKEN, Wako 351-0198, Japan
sei@mns.k.u-tokyo.ac.jp

Jun-Ichi Inoue
Graduate School of Information Science and Technology
Hokkaido University, N13-W8
Kita-ku, Sapporo 060-8628, Japan
jinoue@cb4.so-net.ne.jp

Parongama Sen
Department of Physics
University of Calcutta
92 Acharya Prafulla Chandra Road
Kolkata 700009, India
psphy@caluniv.ac.in

Pratap K. Das
Department of Physics
University of Calcutta
92 Acharya Prafulla Chandra Road
Kolkata 700009, India
psphy@caluniv.ac.in

Victor Martín-Mayor
Departamento de Física Teórica I
Facultad de Ciencias Físicas
Universidad Complutense
28040 Madrid, Spain
and
Instituto de Biocomputación y Física de
Sistemas Complejos (BIFI)
Corona de Aragón 42
Zaragoza 50009, Spain
victor@lattice.fis.ucm.es

Part I

Tutorial: Introductory Material

Transverse Ising Model, Glass and Quantum Annealing

Bikas K. Chakrabarti and Arnab Das

Theoretical Condensed Matter Physics Division and Center for Applied Mathematics and Computational Sciences, Saha Institute of Nuclear Physics, 1/AF, Bidhannagar, Kolkata, India
bikask.chakrabarti@saha.ac.in
arnab.das@saha.ac.in

1 Introduction

In many physical systems, cooperative interactions between spin-like (two-state) degrees of freedom tend to establish some kind of order in the system, while the presence of some noise effect (due to temperature, external transverse field etc.) tends to destroy it. Tranverse Ising model can quite succeessfully be employed to study the order-disorder transitions in many of such systems.

An example of the above is the study of ferro-electric ordering in Pottasium Dihydrogen Phosphate (KDP) type systems (see, e.g., [1]). To understand such ordering, the basic structure can be viewed as a lattice, where in each lattice point there is a double-well potential created by an oxyzen atom and the hydrogen or proton resides within it in any of the two wells. In the corrosponding Ising (or pseudo-spin) picture the state of a double-well with a proton at the left-well and that with one at the right-well are represented by, say, $|\uparrow\rangle$ and $|\downarrow\rangle$ respectively (see, for a portion of the lattice, Fig. 1). The protons at neighbouring sites have mutual dipolar repulsions. Hence had proton been a classical particle, the zero-temperature configuration of the system would be one with either all the protons residing at their respective left-well or all residing at the right-well (corrosponding to the all-up or all-down configuration of the spin system in presence of cooperative interaction alone, at zero-temperature). Considering no fluctuation at zero temperature, the Hamiltonian for the system in the corrosponding pseudo-spin picture will just be identical to the classical Ising Hamiltonian (without any transverse term). However, proton being a quantum particle, there is always a finite probability for it to tunnel through the finite barrier between two wells even at zero-temperature due to quantum fluctuations. To formulate the term for the tunnelling in the corrosponding spin-picture, we notice that σ^x is the right operater. This is because

B.K. Chakrabarti and A. Das: *Transverse Ising Model, Glass and Quantum Annealing*, Lect. Notes Phys. **679**, 3–36 (2005)
www.springerlink.com

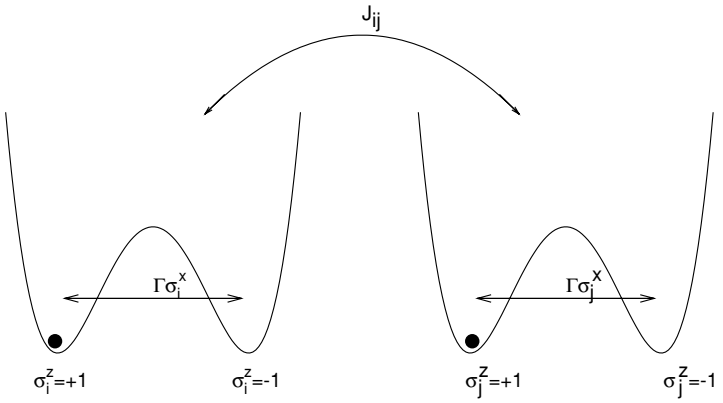

Fig. 1. The double wells at each site (e.g., provided by oxygen in KDP) provide two (low-lying) states of the proton (shown by each double well) indicated by the Ising states $|\uparrow\rangle$ and $|\downarrow\rangle$ at each site. The tunnelling between the states are induced by the transverse field term ($\Gamma\sigma^x$). The dipole-dipole interaction J_{ij} here for the (asymmetric) choice of one or the other well at each site induces the 'exchange' interaction as shown

$$\sigma^x|\uparrow\rangle = |\downarrow\rangle \quad \text{and} \quad \sigma^x|\downarrow\rangle = |\uparrow\rangle\ , \tag{1}$$

where $|\uparrow\rangle$ represents the state where the proton is in the left well, while $|\downarrow\rangle$ represents that with the proton in the right well. Hence the tunelling term will exactly be represented by the tranvere field term in the transverse Ising Hamiltonian. Here the transverse field coefficient Γ will represent the tunnelling integral, which depends on the width and height of the barrier, mass of the particle, etc.

2 Transverse Ising Model (TIM)

Such a system as discussed above, can be represented by a quantum Ising system, having Hamiltonian

$$\mathcal{H} = -\sum_{\langle i,j\rangle} J_{ij}\sigma_i^z\sigma_j^z - \Gamma\sum_i \sigma_i^x\ . \tag{2}$$

Here, J_{ij} is the coupling between the spins at sites i and j, where σ^α's ($\alpha = x, y, z$) are the Pauli spins satisfying the commutation relations

$$[\sigma_i^\alpha, \sigma_j^\beta] = 2i\delta_{ij}\epsilon_{\alpha\beta\gamma}\sigma_i^\gamma \tag{3}$$

Here, δ_{ij} is the Krönecker's δ, and $\epsilon_{\alpha\beta\gamma}$ is the Levi-Civita symbol, and $\langle i,j\rangle$ in (1) represents neighbouring pairs.

The Pauli spin martices being representatives of spin-1/2, σ^z has got two eigenvalues (± 1) corrosponding to spins aligned either along z-direction or along the opposite direction respectively. The eigenstate corrosponding to eigenvalue ($+1$) is symolically denoted by $|\uparrow\rangle$, while that corrosponding to (-1) is denoted by $|\downarrow\rangle$.

If we represent

$$|\uparrow\rangle \Leftrightarrow \begin{pmatrix} 1 \\ 0 \end{pmatrix}$$

and

$$|\downarrow\rangle \Leftrightarrow \begin{pmatrix} 0 \\ 1 \end{pmatrix} , \tag{4}$$

then taking these two eigen-vectors as basis, Pauli spins have following matrix representations

$$\sigma^x = \begin{pmatrix} 0 & 1 \\ 1 & 0 \end{pmatrix}, \ \sigma^y = \begin{pmatrix} 0 & -i \\ i & 0 \end{pmatrix}, \ \sigma^z = \begin{pmatrix} 1 & 0 \\ 0 & -1 \end{pmatrix} . \tag{5}$$

With these, one can see that relations in (3) are easily satisfied and the tunnelling required in (1) can be easily accommodated. The order parameter for such a system is generally taken to be the expeectation value of z-component of the spin, i.e. $\langle\sigma^z\rangle$. Needless to say that in such a system absolute ordering (complete alinement along z-direction) is not possible even at zero-temperature, i.e., $\langle\sigma^z\rangle_{T=0} \neq 1$, when $\Gamma \neq 0$. In general, therefore, the order ($\langle\sigma^z\rangle \neq 0$) to disorder $\langle\sigma^z\rangle = 0$ transition can be brought about by tuning either of, or both of the tunnelling field Γ and the temperature T (see Fig. 2).

3 Mean Field Theory (MFT)

(a) For T = 0

Let,

$$\sigma_i^z = |\boldsymbol{\sigma}| \cos\theta, \quad \text{and} \quad \sigma_i^x = |\boldsymbol{\sigma}| \sin\theta \, , \tag{6}$$

where θ is the angle between $\boldsymbol{\sigma}$ and z-axis. This renders the two mutually non-commuting part of the Hamiltonian (2) commuting, since both are expressed in terms of $|\boldsymbol{\sigma}|$ operator only. If σ is the eigen-value of $|\boldsymbol{\sigma}|$ ($\sigma = 1$ for Pauli spin), then the energy per site of the semi-classical system is given by [2]

$$E = -\sigma\Gamma \sin\theta - \sigma^2 J(0) \cos^2\theta \, , \tag{7}$$

$J(0) = J_i(0) = \sum_{\langle i,j\rangle} J_{ij}$, where j indicates the j-th nearest neighbour of the i-th site. And the average of the spin-components are given by

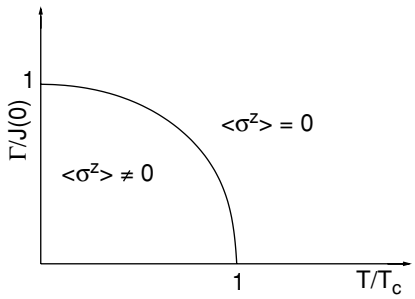

Fig. 2. Schematic phase diagram of the model represented by Hamiltonian (2)

$$\langle \sigma^z \rangle = \cos\theta$$
$$\langle \sigma^x \rangle = \sin\theta \ .$$

The energy (7) is minimized for

$$\sin\theta = \Gamma/J(0) \qquad \text{or,} \qquad \cos\theta = 0 \ . \tag{8}$$

Thus we see that if $\Gamma = 0$, $\langle \sigma^x \rangle = 0$ and the order parameter $\langle \sigma^z \rangle = 1$, indicating perfect order.

On the other hand, if $\Gamma < J(0)$, then the ground state is partially polarized, since none of $\langle \sigma^z \rangle$ or $\langle \sigma^x \rangle$ is zero. However, if $\Gamma \geq J(0)$, then we must have $\cos\theta = 0$ for the ground state energy, which means $\langle \sigma^z \rangle = 0$, i.e., the state is a completely disordered one. Thus, as Γ increases from 0 to J(0), the system undergoes a transition from ordered (ferro)- phase with order parameter $\langle \sigma^z \rangle = 1$ to disordered (para)-phase with order parameter $\langle \sigma^z \rangle = 0$ (see Fig. 2).

(b) For T $\neq$ 0

The mean field method can also be extended to[3, 4] obtain the behaviour of this model at non-zero temperature. In this case we define a mean field $\boldsymbol{h}_i$ at each site i, which is, in some sense, a resultant of the average cooperative enforcement in z-direction and the applied transverse field in x-direction. Precisely, we take, for general random case,

$$\boldsymbol{h}_i = \Gamma\hat{x} + \left(\frac{1}{2}\sum_j J_{ij}\langle\sigma_j^z\rangle\right)\hat{z} \ , \tag{9}$$

and the spin-vector at the i-th site follows $\boldsymbol{h}_i$. The spin-vector at i-th site is given by

$$\boldsymbol{\sigma}_i = \sigma_i^x\hat{x} + \sigma_i^z\hat{z} \ ,$$

and Hamiltonian thus reads

$$\mathcal{H} = -\sum_i \boldsymbol{h}_i.\boldsymbol{\sigma}_i \ . \tag{10}$$

For non-random case, all the sites have identical ambience, hence $\boldsymbol{h_i}$ is replaced by $\boldsymbol{h} = \Gamma\hat{x} + \langle\sigma^z\rangle J(0)$. And the resulting Hamiltonian takes the form

$$\mathcal{H} = -\boldsymbol{h}.\sum_i \boldsymbol{\sigma}_i \ .$$

The spontaneous magnetization can readily be written down as

$$\boldsymbol{\sigma} = \tanh(\beta|\boldsymbol{h}|).\frac{\boldsymbol{h}}{|\boldsymbol{h}|}$$

$$|\boldsymbol{h}| = \sqrt{\Gamma^2 + (J(0)\langle\sigma^z\rangle)^2} \ . \tag{11}$$

Now if $\boldsymbol{h}$ makes an angle θ with z-axis, then $\cos\theta = J(0)\langle\sigma^z\rangle/|\boldsymbol{h}|$ and $\sin\theta = \Gamma|\boldsymbol{h}|$, and hence we have

$$\langle\sigma^z\rangle = |\boldsymbol{h}|\cos\theta = [\tanh(\beta|\boldsymbol{h}|)]\left(\frac{J(0)\langle\sigma^z\rangle}{|\boldsymbol{h}|}\right),$$

and

$$\langle\sigma^x\rangle = [\tanh(\beta|\boldsymbol{h}|)]\frac{\Gamma}{|\boldsymbol{h}|} \ . \tag{12}$$

Here, $\beta = (1/k_BT)$. Equation (12) is the self-consistency equation which can be solved or graphically or otherwise, to obtain the order parameter $\langle\sigma^z\rangle$ at any temperature T and transverse field Γxs. Clearly, the order-disorder transition is tuned both by Γ and T (see Fig. 2).

$\Gamma = 0$ **(Transition driven by T):**

Here,

$$\langle\sigma^z\rangle = \tanh\left(\frac{J(0)\langle\sigma^z\rangle}{k_BT}\right)$$

and

$$\langle\sigma^x\rangle = 0$$

One can easily see graphically, that the above equations has a nontrivial solution only if $k_BT < J(0)$, i.e.,

$$\langle\sigma^z\rangle \neq 0 \qquad \text{for} \quad k_BT < J(0)$$

$$\langle\sigma^z\rangle = 0 \qquad \text{for} \quad k_BT > J(0) \ .$$

This shows that there is a critical temperature $T_c = J(0)$ above which, there is no order.

For $k_BT \to 0$ (Transition driven by Γ):

Here,

$$\langle\sigma^z\rangle = \frac{J(0)\langle\sigma^z\rangle}{\sqrt{(\Gamma)^2 + (J(0)\langle\sigma^z\rangle)^2}} \qquad \left(\text{since,} \quad \tanh x\Big|_{x\to\infty} = 1\right) .$$

From this equation we easily see that in the limit $\Gamma/J(0) \to 1$, the only real nontrivial solution is

$$\langle\sigma^z\rangle \to 0$$

and

$$\langle\sigma^x\rangle = \frac{\Gamma}{\sqrt{(\Gamma)^2 + (J(0)\langle\sigma^z\rangle)^2}} \to 1, \qquad \text{as} \quad \frac{\Gamma}{J(0)} \to 1 .$$

Thus we see that their is a critical transverse field $\Gamma_c = J(0)$ such that for any $\Gamma > \Gamma_c$ there is no order even at zero temperature. In general one sees that at any temperature $T < T_c$, there exist some transverse field Γ_c at which the transition from the ordered state ($\langle\sigma^z\rangle \neq 0$) to the disordered state ($\langle\sigma^z\rangle = 0$) occurs. The equation for the phase boundary in the ($\Gamma - T$) – plane is obtained by putting $\langle\sigma^z\rangle \to 0$ in equation (12). The equation gives the relation between Γ_c and T_c as follows

$$\tanh\left(\frac{\Gamma_c}{k_BT}\right) = \frac{\Gamma_c}{J(0)} . \tag{13}$$

One may note that for ordered phase, since $\langle\sigma^z\rangle \neq 0$,

$$\frac{1}{|\boldsymbol{h}|}\tanh(\beta|\boldsymbol{h}|) = \frac{1}{J(0)} = \text{Constant} .$$

Hence, $\langle\sigma^x\rangle = (\Gamma/|\boldsymbol{h}|)\tanh(\beta|\boldsymbol{h}|) = \Gamma/J(0)$; independent of temperature in the ordered phase. While for the disordered phase, since $\langle\sigma^z\rangle = 0$,

$$\langle\sigma^x\rangle = \tanh(\beta\Gamma) .$$

Using magnetic mapping, mean field theory of this type was indeed applied to (the BCS theory of) superconductivity [5], as shown in appendix A.

4 Dynamic Mode-Softening Picture

The elementary excitations in such a system as described above are known as spin waves, and they can be studied using Heisenberg equation of motion for σ^z using the Hamiltonian. The equation of motion is then given by

$$\dot{\sigma}_i^z = (i\hbar)^{-1}[\sigma_i^z, \mathcal{H}] \tag{14}$$

or,

$$\dot{\sigma}_i^z = 2\Gamma\sigma_i^y \qquad (\text{with} \quad \hbar = 1)$$

Hence,

$$\ddot{\sigma}_i^z = 2\Gamma\dot{\sigma}_i^y = 4\Gamma\sum_j J_{ij}\sigma_i^z\sigma_i^x - 4\Gamma^2\sigma_i^z \ . \tag{15}$$

With Fourier transforms and random phase approximation ($\sigma_i^x\sigma_j^z = \sigma_i^x\langle\sigma_j^z\rangle + \langle\sigma_i^x\rangle\sigma_j^z$, with $\langle\sigma^z\rangle = 0$ in para phase), we get

$$\omega_q^2 = 4\Gamma(\Gamma - J(q)\langle\sigma^x\rangle) \ , \tag{16}$$

for the elementary excitations (where $J(q)$ is the Fourier transform of J_{ij}). The mode corrosponding to ($q = 0$) softens, i.e., ω_0 vanishes at the same phase boundary given by equation (13).

5 Suzuki-Trotter Formalism

Exact analysis for the quantum fluctuation can indeed be tackled by using renormalization group theory; see appendix B for real space quantum RG theory for one dimensional chain (cf [6]). However, such formalisms have serious limitations in applicability and the Suzuki-Trotter formalism to map the quantum problem to a classical one has been of enormous practical importance (e.g. in simulations).

Suzuki-Trotter formalism [7] is essentially a method to transform a d-dimensional quantum Hamiltonian into a $(d+1)$-dimensional effective classical Hamiltonian giving the same canonical partition function. Let us illustrate this by applying it to transverse Ising system. We start with Transverse Ising Hamiltonian

$$\begin{aligned}\mathcal{H} &= -\Gamma\sum_{i=1}^{N}\sigma_i^x - \sum_{(i,j)} J_{ij}\sigma_i^z\sigma_j^z \\ &= \mathcal{H}_0 + \mathcal{V}\end{aligned} \tag{17}$$

The canonical partition function of $\mathcal{H}$ reads

$$Z = Tre^{-\beta(\mathcal{H}_0+\mathcal{V})} \ .$$

Now we apply the Trotter formula

$$\exp(A_1 + A_2) = \lim_{M\to\infty}\left[\exp A_1/M \exp A_2/M\right]^M \ ,$$

even when $[A_1, A_2] \neq 0$. On application of this, Z reads

$$Z = \sum_i \lim_{M\to\infty}\langle s_i|\left[\exp(-\beta\mathcal{H}_0/M)\exp(-\beta\mathcal{V}/M)\right]^M|s_i\rangle \ . \tag{18}$$

Here s_i represent the i-th spin configuration of the whole system, and the above summation runs over all such possible configurations denoted by i. Now we introduce M number of identity operators

$$\mathcal{I} = \sum_{i}^{2^N} |s_{i,k}\rangle\langle s_{i,k}|, \qquad k = 1, 2, \cdots M \ .$$

in between the product of M exponentials in Z, and have

$$Z = \lim_{M\to\infty} Tr \prod_{k=1}^{M} \left\langle \sigma_{1,k}\cdots\sigma_{N,k}| \exp\left(\frac{-\beta\mathcal{H}_0}{M}\right) \exp\left(\frac{-\beta\mathcal{V}}{M}\right)|\sigma_{1,k+1}\cdots\sigma_{N,k+1}\right\rangle \ ,$$

and periodic boundary condition would imply $\sigma_{N+1,p} = \sigma_{1,p}$. Now,

$$\prod_{k=1}^{M} \left\langle \sigma_{1,k}\cdots\sigma_{N,k}| \exp\left(\frac{\beta}{M}\sum_{i,j}\sigma_i^z\sigma_j^z\right)|\sigma_{1,k+1}\cdots\sigma_{N,k+1}\right\rangle$$

$$= \exp\left[\sum_{i,j=1}^{N}\sum_{k=1}^{M}\frac{\beta J_{ij}}{M}\sigma_{i,k}\sigma_{j,k}\right] \ , \tag{19}$$

where $\sigma_{i,k} = \pm 1$ are the eigenvalues of σ^z operator. Also,

$$\prod_{k=1}^{M} \left\langle \sigma_{1,k}\cdots\sigma_{N,k}| \exp\left[\frac{\beta\Gamma}{M}\sum_{i}\sigma_i^x\right]|\sigma_{1,k+1}\cdots\sigma_{N,k+1}\right\rangle$$

$$= \left(\frac{1}{2}\sinh\left[\frac{2\beta\Gamma}{M}\right]\right)^{\frac{NM}{2}} \exp\left[\frac{1}{2}\ln\coth\left(\frac{\beta\Gamma}{M}\right)\sum_{i=1}^{N}\sum_{k=1}^{M}\sigma_{i,k}\sigma_{i,k+1}\right] . \tag{20}$$

The last step follows because

$$e^{a\sigma^x} = e^{-i(ia\sigma^x)} = \cos(ia\sigma^x) - i\sin(ia\sigma^x) = \cosh(a) + \sigma^x\sinh(a) \ ,$$

and therefore

$$\langle\sigma|e^{a\sigma^x}|\sigma'\rangle = \left[\frac{1}{2}\sinh(2a)\right]^{1/2} \exp\left[(\sigma\sigma'/2)\ln\coth(a)\right] \ ,$$

since

$$\langle\uparrow|e^{a\sigma^x}|\uparrow\rangle = \langle\downarrow|e^{a\sigma^x}|\downarrow\rangle = \cosh(a) = \left[\frac{1}{2}\sinh(2a).\coth(a)\right]^{1/2}$$

and

$$\langle\uparrow|e^{a\sigma^x}|\downarrow\rangle = \langle\downarrow|e^{a\sigma^x}|\uparrow\rangle = \sinh(a) = \left[\frac{1}{2}\sinh(2a)/\coth(a)\right]^{1/2} \ .$$

Thus the partition function reads

$$Z = C^{\frac{NM}{2}} Tr_{\sigma}(-\beta \mathcal{H}_{eff}[\sigma]) \;\; C \quad = \frac{1}{2}\sinh\frac{2\beta\Gamma}{M}$$

where the effective classical Hamiltonian is

$$\mathcal{H}_{eff}(\sigma) = \sum_{(i,j)}^{N}\sum_{k=1}^{M}\left[-\frac{J_{ij}}{M}\sigma_{ik}\sigma_{jk} - \frac{\delta_{ij}}{2\beta}\ln\coth\left(\frac{\beta\Gamma}{M}\right)\sigma_{ik}\sigma_{ik+1}\right] . \qquad (21)$$

The Hamiltonian $\mathcal{H}_{eff}$ is a classical one, since the variables $\sigma_{i,k}$'s involved are merely the eigen-values of σ^z, and hence there is no non-commuting part in $\mathcal{H}_{eff}$. It may be noted from (21) that M should be at the order of $\hbar\beta$ (we have taken $\hbar = 1$ in the calculation) for a meaningful comparison of the interaction in the Trotter direction with that in the original Hamiltonian (see Fig. 3). For $T \to 0$, $M \to \infty$, and the Hamiltonian represents a system of spins in a $(d{+}1)$-dimensional lattice, which is one dimension higher than the original d-dimensional Hamiltonian, as is evident from the appearence of one extra label k for each spin variable (see Fig. 3). Thus corrosponding to each single quantum spin varible σ_i in the original Hamiltonian we have an array of M number of classical replica spins σ_{ik}. This new (time-like) dimension along which these classical spins are spaced is known as Trotter dimension. From the explicit form of $\mathcal{H}_{eff}$, we see that in addition to the previous interaction (J) term ($-\sum_{i,j}^{N} J_{ij}\sigma_i\sigma_j$), there is an additional near-est neighbour interaction (J') between the Trotter replicas corrosponding

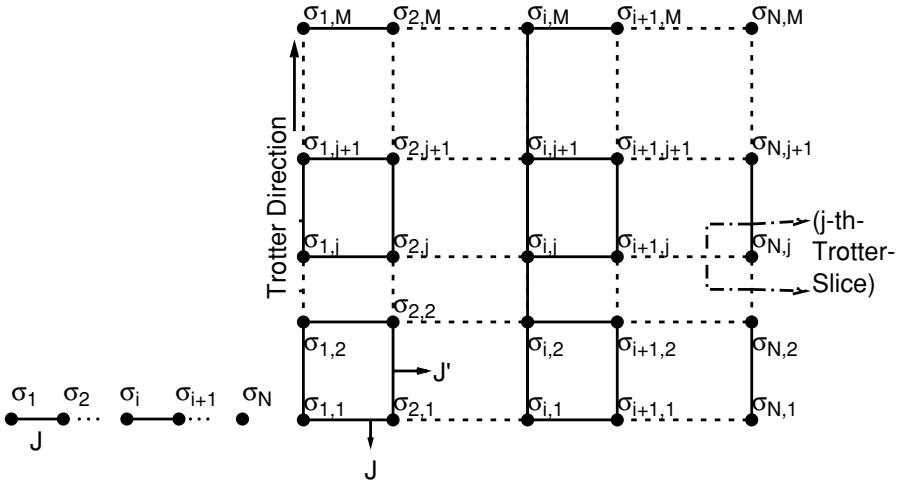

Fig. 3. The Suzuki-Trotter equivalence of quantum one dimensional chain and a (1+1) dimensional classical system. J' indicates the additional interaction in the Trotter direction

to the same original spin, along the Trotter direction, given by the term $(\sum_{i,j}^{N}\sum_{k=1}^{M} -(\delta_{ij}/2\beta)\ln\coth(\beta\Gamma/M)\sigma_{ik}\sigma_{iK+1})$ (as shown in Fig. 3). For finite temperature, the optimal width of the lattice in the Trotter direction is finite and the critical behaviour remains d-dimensional.

The calculations, and consequently the effective Hamiltonian (21), is valid for any general interaction J_{ij}; of course, Γ has been taken to be nonrandom. Figure 4 describes a situation where J_{ij} were nonrandom (we had $J_{ij} = J$). For random J_{ij}, where J_{ij} were nonrandom (we had $J_{ij} = J$). For random J_{ij}, remain identical (J') wheras the spatial randomness in interactions for various Trotter slices get correlated as indicated in Fig. 4. Such equivalence of d-dimensional quantum system with a $(d+1)$-dimensional classical model can also be seen from the renormalization group study of the quantum models (say, one-dimensional transverse Ising model and its equivalent critical behaviour of two-dimensional classical Ising system) as shown in Appendix B.

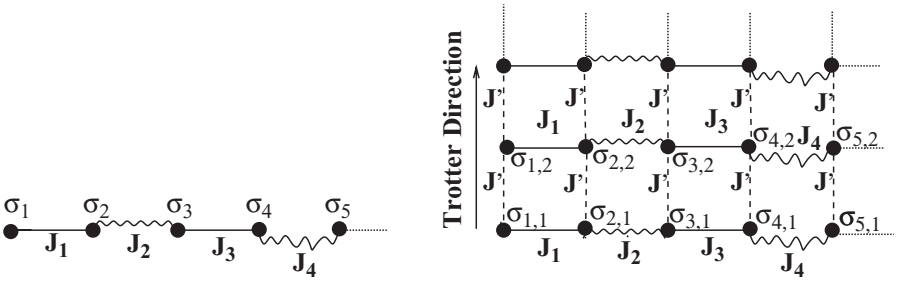

Fig. 4. At the left is a portion of a one dimensional quantum Ising chain with random exchange interactions and at the right is a part of its Suzuki-Trotter equivalent classical lattice with randomness correlated in Trotter direction

6 Classical Spin Glasses: A Summary

Spin glasses are magnetic systems with randomly competing (frustrated) interactions [8]. Frustration is a situation where all of the spins present in the system cannot energetically satisfy every bond associated to them. Here the frustration arises due to competing (ferromagnetic and anti- ferromagnetic) quenched random interactions between the spins. As a result there arise huge barriers ($O(N)$, N = system size) in the free-energy landscape of the system. In thermodynamic limit, height of such barriers occassionally go to infinity. These barrieres strongly separate different configurations of the system, so that once the system gets stuck in a deep valley in between two barriers, it practically gets trapped around that configuration for a macroscopically large time. Because of frustration, the ground state is largely degenerate; degeneracy being of the order of $\exp(N)$. As discussed above, these different ground state

configurations are often separated by $O(N)$ barriers, so that once the system settles down in one of them, it cannot visit the others equally often in course of time, as predicted by the Boltzmann probability factor. The system thus becomes 'nonergodic' and may be described by a nontrivial order parameter distribution [8] in the thermodynamic limit (unlike the unfrustrated cooperative systems, where the the distribution becomes trivially delta function-like). The spins in such a system thus get frozen in random orientations below a certain transition temperature. Although there is no long range magnetic order, i.e., the space average of spin moments vanishes, the time average of any spin is nonzero below the transition (spin-glass) temperature. This time average is treated as a measure of spin freezing or spin glass order parameter.

Several spin glass models have been studied extensively using both analytic and computer simulation techniques. The Hamiltonian for such models can be written as

$$\mathcal{H} = -\sum_{i<j} J_{ij}\sigma_i^z\sigma_j^z \tag{22}$$

where $S_i^z = \pm 1, 2, \ldots, N$, denote the Ising spins, interacting with random quenched interactions J_{ij}, which differs in various models. We will specifically consider three extensively studied models.

(a) In Sherrington-Kirkpatrick (S-K) model J_{ij} are long-ranged and are distributed with a Gaussian probability (centered around zero), as given by

$$P(J_{ij}) = \left(\frac{N}{2\pi J^2}\right)^{1/2} \exp\left(\frac{-NJ_{ij}^2}{2J^2}\right) \tag{23}$$

(b) In Edward-Anderson (EA) model, the J_{ij}'s are short-ranged (say, between the nearest neighbours only), but similarly distributed with Gaussian probability (23)

(c) In another kind of model, the J_{ij}'s are again short-ranged, but having a binary ($\pm J$) distribution with probability p:

$$P(J_{ij}) = p\delta(J_{ij} - J) + (1-p)\delta(J_{ij} - J)\ . \tag{24}$$

The disorder in the spin system being quenched, one has to perform configurational averaging (denoted by overhead bar) over $\ln Z$, where $Z(= Tr \exp -\beta\mathcal{H})$ is the partitation function of the system. To evaluate $\overline{\langle \ln Z \rangle}$, one usually employs replica trick based on the representation $\ln Z = \lim_{n\to 0}[(Z^n - 1)/n]$. Now for classical Hamiltonian (with all commuting spin components), $Z^n = \prod_{\alpha=1}^n Z_\alpha = Z(\sum_{\alpha=1}^n H_\alpha)$, where H_α is the α-th replica of the Hamiltonian $\mathcal{H}$ in equation (22) and Z_α is the corrosponding partition function. The spin freezing can then be measured in terms of replica overlaps, and Edward-Anderson order parameter takes the form

$$q = \frac{1}{N}\sum_{i=1}^{N} \overline{\langle S_i^z(t) S_i^z(0)\rangle}|_{t\to\infty} \simeq \frac{1}{N}\sum_{i=1}^{N} \overline{\langle S_{i\alpha}^z S_{i\beta}^z\rangle}\ ,$$

where α and β corrosponds to different replicas.

Extensive Monte Carlo studies, together with the analytical solutions for the mean field of S-K and EA models, have revealed the nature of spin glass transition. It appears that the lower critical dimension d_l^c for EA model, below which transition ceases to occur (with transition temperature T_c becoming zero), is between 2 and 3: $2 < d_l^c < 3$. Thu upper critical dimension d_u^c, at and above which mean field results (e.g., those of S-K model) apply, appears to be 6: $d_u^c = 6$. Within these dimensions ($d_l^c < d < d_u^c$), the spin glass transitions occur (for Hamiltonians with short-ranged interactions) and the transition behaviour can be characterized by various exponents. Although the linear susceptibility shows a cusp at the transition point, the nonlinear susceptibility $\chi_{SG} = (1/N)\sum_r g(r)$, where $g(r) = (1/N)\sum_i \overline{(\langle S_i^z S_{i+r}^z\rangle)^2}$, diverges at the spin glass transition point :

$$\chi_{SG} \sim (T - T_c)^{-\gamma_c}, \quad g(r) \sim r^{-(d-2+\eta_c)} f\left(\frac{r}{\xi}\right); \quad \xi \sim |T - T_c|^{-\nu_c} \qquad (25)$$

Here ξ denotes the correlation length which determines the length scaling in the spin correlation function $g(r)$ (f in $g(r)$ denotes the scaling function). Numerical simulation gives $\nu_c = 1.3 \pm 0.1$, 0.80 ± 0.15, $1/2$ and $\gamma_c = 2.9 \pm 0.5$, 1.8 ± 0.4, 1 for $d = 2, 3$ and 6 respectively for the values of exponents. One can define the characteristic relaxation time τ through the time dependence of spin auto-correlation

$$q(t) = \overline{\langle S_i^z(t) S_i^z(0)\rangle} \sim t^{-x}\tilde{q}\left(\frac{t}{\tau}\right); \quad \tau \sim \xi^z \sim |T - T_c|^{-\nu_c/z_c} \qquad (26)$$

where $x = (d - 2 + \eta_c)/2z_c$, and z_c denotes the classical dynamical exponent. Numerical simulations give $z_c = 6.1 \pm 0.3$ and 4.8 ± 0.4 in $d = 3$ and 4 dimensions respectively. Of course, such large values of z_c (particularly in lower dimensions) also indicates the possibility of the failure of power law variation (26) of τ with $T - T_c$ and rather suggests a Vogel-Fulcher like variation: $\tau \sim \exp[A/(T - T_c)]$. In the $\pm J$ spin glasses (type (c) above), some exact results are known along the 'Nishimori Line' [8], and the nature of the phase transition there is precisely known.

7 Quantum Spin Glasses

Quantum spin glasses [9, 10, 11, 12, 13] have the interesting feature that the transition in randomly frustrated (competing) cooperatively interactimg systems can be driven both by thermal fluctuations or by quantum fluctuations. Quantum spin glasses can be of two types: vector spin glasses introduced by

Bray and Moore (see [4]), where of course quantum fluctuation cannot be tuned, or a classical spin glass perturbed by some tunable quantum fluctuations e.g., as induced by a non commutative transverse field [4, 9]. The amount of quantum fluctuation being tunable, this Transverse Ising Spin Glass (TISG) model is perhaps the simplest model in which the quantum effects in a random system can be and has been studied extensively and systematically [4, 13]. Precise realization of TISG in $LiHo_xY_{1-x}F_4$, with magnetic Holonium ion concentration around $x = 0.167$ [12], has led to several important developments.

The interesting in such quantum spin glass models is about the possibility of tunnelling through the (infinitely high) barriers of the free energy landscape in the classical spin glass models (e.g., S-K model) due to the quantum fluctuations induced by the transverse field. In classcal system, the overriding of an infinitely high barrier is infinitely hard for thermal fluctuations at any finite temperature. But quantum fluctuation can make a system tunnel through such a barrier, if its width is infinitessimally small. The barrier widths are actually seen to decrease with system size indicating to an ergodic (replica symmetric) picture for the free-energy landscape.

7.1 Models

Sherrington-Kirkpatrick Model in a Transverse Field

The sherrington-Kirkpatrick (S-K) model in presence of a non-commutating tunnelling field, given by the Hamiltonian

$$\mathcal{H} = -\sum_{ij} J_{ij}\sigma_i^z\sigma_j^z - \Gamma\sum_i \sigma_i^x \,, \tag{27}$$

where the follows the Gaussian distribution

$$P(J_{ij}) = \left(\frac{N}{2\pi\Delta^2}\right)^{1/2} \exp\left(\frac{-NJ_{ij}^2}{a\Delta^2}\right) \tag{28}$$

was first studied by Ishi and Yamamoto [9].

Phase Diagram

Several analytical studies have been made to obtain the phase diagram of the transverse Ising S-K model (giving in particular the zero-temperature critical field). The problem of S-K glass in transverse field becomes a nontrivial one due to the presence of noncommuting spin operators in the Hamiltonian. This leads to a dynamical frequency dependent (spin) self-interaction.

(i) Mean Field Estimates

One can study an effective spin Hamiltonian for the above quantum many body system within the mean field framework. A systematic mean field theory for the above model was first carried out by Kopec (see e.g., [4]), using the thermofield dynamical approach and the short time approximation for the dynamical spin self-interaction. Before going into the discussion of this approach, we shall briefly review the replica-symmetric solution of the classical S-K model ($\Gamma = 0$) in a longitudinal field given by the Hamiltonian

$$\mathcal{H} = -\sum_{\langle ij \rangle} J_{ij}\sigma_i^z\sigma_j^z - h\sum \sigma_i^z \tag{29}$$

where J_{ij} follows the Gaussian distribution given by (56). Using the replica trick, one obtains for configuration averaged n-replicated partition function $\bar{Z}^n$, given by

$$\bar{Z}^n = \sum_{(\sigma_{i\alpha}=\pm 1)} \int_{-\infty}^{\infty} P(J_{ij}) dJ_{ij} \exp\left[\beta \sum J_{ij} \sum \sigma_{i\alpha}^z \sigma_{j\alpha}^z + \beta h \sum \sigma_{i\alpha}^z .\right]$$

Performing the Gaussian integral, using Hubbard-Stratonovich transformation and finally using the method of steepest descent to evaluate integrals for thermodynamically large system, one obtains free energy per site f, given by

$$-\beta f = \lim_{n\to 0}\left[\frac{\beta\Delta^2}{4}\left(1 - \frac{1}{n}\sum_{\alpha,\beta} q_{\alpha,\beta}^2 + \frac{1}{n}\ln Tr(\exp L)\right)\right] ,$$

where $L = (\beta J)^2 \sum_{\alpha,\beta} q_{\alpha\beta}\sigma_\alpha^z\sigma_\beta^z + \beta\sum_{\alpha=1}^n \sigma_\alpha^z$ and $q_{\alpha\beta}$ is self-consistently given by the saddle point condition $(\partial f/\partial q_{\alpha\beta}) = 0$. Cosidering the replica symmetric case ($q_{\alpha\beta} = q$), one finds

$$-\beta f = \frac{(\beta\Delta)^2}{2}(1-q) + \frac{1}{\sqrt{2\pi}}\int_{-\infty}^{\infty} dr \quad e^{-\frac{r^2}{2}} \ln\left[2\cosh\left\{\beta h(r)\right\}\right]$$

where r is the excess static noise arising from the random interaction J_{ij} and the spin glass order parameter q is self-consistently given by

$$q = \frac{1}{\sqrt{2\pi}}\int_{-\infty}^{\infty} dr \quad e^{-\frac{r^2}{2}} \tanh^2\left\{\beta h(r)\right\}$$

and $h(r) = \Delta\sqrt{qr} + h$ can be interpreted as a local molecular field acting on a site. Different sites have different fields because of disorder, and the effective distribution of $h(r)$ is Gaussian with mean 0 and varience $\Delta^2 q$.

At this point we can introduce quantum effect through transverse field term $-\Gamma\sum_i \sigma_i^x$ (with longitudinal field $h = 0$). The effective single particle Hamiltonian in the transverse Ising quantum glass can be written as

$$\mathcal{H}_s = -h^z(r)\sigma^z - \Gamma\sigma^x \ ,$$

where $h_z(r)$, as mentioned earlier, is the effective field acting along the z direction arising due to nonzero value of the the spin glass order parameter. Treating $h^z(r)$ and σ as classical vectors in pseudo-spin space, one can write the net effective field acting on each spin as

$$h_0(r) = h^z(r)\hat{z} - \Gamma\hat{x}; \quad |h_0(r)| = \sqrt{h^z(r)^2 + \Gamma^2} \ .$$

One can now arrive at the mean field equation for the local magnetisation, given by

$$m(r) = p(r)\tanh\left[\beta h_0(r)\right]; \quad p(r) = \frac{|h^z(r)|}{|h_0(r)|} \ ,$$

and consequently, the spin glass order parameter can be written as

$$q = \frac{1}{\sqrt{2\pi}}\int_{-\infty}^{\infty} dr \quad e^{-r^2/2}\tanh^2\left\{\beta h_0(r)\right\}p^2(r) \ .$$

The phase boundary can be found from the above expression by putting $q \rightarrow 0 (h^z(r) = J\sqrt{q}r$ and $h_0 = \Gamma)$, when it gives

$$\frac{\Gamma}{\Delta} = \tanh\left(\frac{\Gamma}{k_B T}\right) \ . \tag{30}$$

From above we get $\Gamma_c = J$. Ishi and Yamamoto used the 'reaction field' technique to construct 'TAP' like equation for free energy of the Hamiltonian (27) and perturbatively expanded the free energy in powers of Γ upto the order Γ^2 to obtain

$$k_B T_c = \Delta[1 - 0.23(\Gamma/\Delta)^2] \ .$$

(ii) Monte Carlo Studies

Several Monte Carlo studies have been performed [9, 13] for S-K spin glass in transverse field. Applying Suzuki-Trotter formulation (as discusseed earlier) of effective partition function, one can obtain the effective classical Hamiltonian in Mth Trotter approximation as

$$\mathcal{H}_{eff} = -\frac{1}{M}\sum_{i,j=1}^{N}\sum_{k=1}^{M} J_{ij}\sigma_{ik}\sigma_{jk} - \frac{1}{2\beta}\ln\coth\left(\frac{\beta\Gamma}{M}\right)\sum_{i=1}^{N}\sum_{k=1}^{M}\sigma_{ik}\sigma_{ik+1}$$

$$-\frac{NM}{2}\ln\left[\frac{1}{2}\sinh\frac{2\beta\Gamma}{M}\right] \ , \tag{31}$$

where σ_{ik} denotes the Ising spin defined on the lattice $(i,\ k)$, i being the position in the in the original S-K model and k denoting the position in the additional Trotter dimension.

Ray et al. [10] took $\Gamma \ll J$ and their results indeed indicate a sharp lowering of $T_C(\Gamma)$. Such sharp fall of $T_c(\Gamma)$ with large Γ is obtained in almost all theoretical studies of the phase diagram of the model.

Edward-Anderson Model in a Transverse Field

The Hamiltonian for the Edward-Anderson spin glass in presence of transverse field is that given by (27), where the random interaction this time is restricted among the nearest neighbours and satisfies a Gaussian distribution with zero mean and variance J, as given by

$$P(J_{ij}) = \frac{1}{\sqrt{2\pi}} \exp\left(-\frac{J_{ij}^2}{2J^2}\right).$$

With $\Gamma = 0$, the above model represents the E-A model with order parameter $q = \overline{\langle\sigma_i^z\rangle^2} = 1$ (at $T = 0$). When the transverse field is introduced, q decreases, and at a critical value of the transverse field the order parameter vanishes. To study this quantum phase transition using quantum Monte Carlo techniques, one must remember that the ground state of a d-dimensional quantum model is equivalent to the free enery of a classical model with one added dimension which is the imaginary time (Trotter) dimension. The effective classical Hamiltonian can be written as

$$\mathcal{H} = \sum_k \sum_{ij} K_{ij}\sigma_{ik}\sigma_{jk} - \sum_k \sum_i K\sigma_{ik}\sigma_{ik+1} \ , \tag{32}$$

with

$$K_{ij} = \frac{\beta J_{ij}}{M}; \qquad K = \frac{1}{2}\ln\coth\left(\frac{\beta\Gamma}{M}\right),$$

where σ_{ik} are classical Ising spins and (i, j) denotes the original d-dimensional lattice sites and $k = 1, 2, \ldots, M$ denotes a time slice. Although the equivalence between classical and the quantum model holds exactly in the limit $M \to \infty$, one can always make an optimum choice for M. The equivalent classical Hamiltonian has been studied using standard Monte Carlo technique. The numerical estimates of the phase diagram etc. are reviewed in details in [13]

7.2 Replica Symmetry in Quantum Spin Glasses

The question of existence of replica-symmetric ground states in quantum spin glasses has been studied extensively in recent years. Replica symmetry restoration is a quantum phenomena arising due to the quantum tunnelling between the classically 'traped' states seperated by infinitely high (but infinitessimally narrow) barriers in the free energy surface, which is possible as the tunnelling probability is proportional to the barrier area, which remains finite. To investigate this aspect of quantum glasses, one has to study the overlap distribution function $P(q)$ given by

$$P(q) = \overline{\sum_{l,l'} P_l P_{l'} \delta(q - q^{(ll')})} \ , \tag{33}$$

where P_l is the Boltzman weight associated with the state l and $q^{ll'}$ is the overlap between the sates l and l'

$$q^{(ll')} = \frac{1}{N}\sum_{i=1}^{N}\langle\sigma_i\rangle^{(l)}\langle\sigma_i\rangle^{(l')} \ . \tag{34}$$

One can also define the overlap distribution in the following form (for a finite system of size N)

$$P_N(q) = \overline{\langle\delta(q - q^{(12)})\rangle} \ , \tag{35}$$

where $q^{(12)}$ is the overlap between two sets of spins $\sigma_i^{(1)}$ and $\sigma_i^{(2)}$, with identical bond distribution but evolved with different dynamics,

$$q^{(12)} = \frac{1}{N}\sum_{i}\sigma_i^{(1)}\sigma_i^{(2)} \ . \tag{36}$$

$P_N(q) \to P(q)$ in the thermodynamic limit. In quantum glass problem one can study similarly this overlap distridution $P_N(q)$; and if the replica symmetric ground states exists, the above function must tend to a delta function in thermodynamic limit. In para-phase, the the distribution will approach a delta function at $q = 0$ for the infinite system.

Ray, Chakrabarti and Chakrabarti [10], performed Monte Carlo simulations, mapping the d-dimensional transverse S-K spin glass Hamiltonian to an equivalent $(d + 1)$-dimensional classical Hamiltonian and addressed the question of stability of the replica symmetric solution, with the choice of order parameter distribution function given by

$$P_N(q) = \overline{\left\langle \delta\left(q - \frac{1}{NM}\sum_{i=1}^{N}\sum_{k=1}^{M}\sigma_{ik}^{(1)}\sigma_{ik}^{(2)}\right)\right\rangle} \ , \tag{37}$$

where, as mentioned earlier, subscripts (1) and (2) refer to the two identical samples but evolved through different Monte Carlo dynamics. It may be noted that a similar definition for q (involving overlaps in identical Trotter indices) was used by Guo et al. [11]. Lai and Goldschmidt performed Monte Carlo studies with larger system size ($N \leq 100$) and studied the order parameter distribution function

$$P_N(q) = \overline{\left\langle \delta\left(q - \frac{1}{N}\sum_{i=1}^{N}\sigma_{ik}^{(1)}\sigma_{ik'}^{(2)}\right)\right\rangle} \ , \tag{38}$$

where the overlap is taken between different (arbitrarily chosen) Trotter indices k and k'; $k \neq k'$. Their studies indicate that $P_N(q)$ does not depend upon the choice of k and k' (Trotter symmetry). Rieger and Young (see [4]) also defined $q^{(12)}$ in similar way ($q^{(12)} = (1/NM)\sum_N^i\sum_{kk'}^M)\sigma_{ik}^{(1)}\sigma_{ik'}^{(2)}$. There are striking differences between the results Lai and Goldschmidt obtained with

the results of Ray et al. [10]. For $\Gamma \ll \Gamma_c$, $P(q)$ is found to have (in [10]) an oscillatory dependence on q with a frequency linear in N (which is probably due to the formation of standing waves for identical Trotter overlaps). However, with increase in N, the amplitude of oscillation decreases and the magnitude of $P(q = 0)$ decreases, indicating that $P(q)$ might go over to a delta function in thermodynamic limit. The envelope of this distribution function appears to have an increasing $P(q = 0)$ value as the system size is increased. Ray et al. [10] argued that the whole spin glass phase is replica symmetric due to quantum tunnelling between the classical trap states. Lai and Goldschmidt on the other hand, do not find any oscillatory behaviour in $P(q)$. In contrary they get a replica symmetry breaking (RSB) in the whole spin glass phase from the nature of $P(q)$, which in this case, has a tail down to $q = 0$ even as N increases. According to them their results are different from Ray et al. [10] because of different choices of the overlap function. Goldschmidt and Lai have also obtained replica symmetry breaking solution at first step RSB, and hence the phase diagram.

Büttner and Usadel (see e.g., Chakrabarti et al. [4]), have shown that the replica symmetric solution is unstable for the effective classical Hamiltonian (58) and also estimated the order parameter and other thermodynamic quantities like susceptibility, internal energy and entropy by applying Parisi's replica symmetry breaking scheme to the above effetive Hamiltonian. Using static approximation, Thirumalai et al. (see [4]), found stable replica symmetric solution in a small region close to the spin glass freezing temperature near the phase boundary. But as mentioned earlier, in the region close to the critical line, quantum fluctuations are subdued by the thermal fluctuations. Thus the restoration of replica symmetry breaking, which is essentially a quantum effect, perhaps connot be prominent there.

All these numerical studies are for equivalent classical Hamiltonian, obtained by applying the Suzuki-Trotter formalism to the original quantum Hamiltonian, where the interactions are anisotropic in the spatial and Trotter direction and the interaction in the Trotter direction becomes singular in the limit $T \to 0$. Obviously one cannot extrapolate the finite temperature results in zero temperature limit. The results of exact diagonalization of finite systems ($N \leq 10$) at $T = 0$ itself do not indicate any qualitative difference in the behaviour of the (configuration average) mass gap Δ and the internal energy E_g from that of a ferromagnetic transverse Ising case, indicating the possibility that the system might become 'ergodic'. On the other hand, the zero temperature distribution for the order parameter does not appear to go to delta function with increasing N as is clearly found for the corrosponding ferromagnet (random long range interaction without competition). In this case the order parameter distribution $P(q)$ is simply the number of ground state configuratons having the order parameter value as q. This perhaps indicate broken ergodicity for small values of Γ. The order parameter distribution also shows oscillations similar to that obtained by Ray et al. [10].

Kim and Kim [14] have very recently investigated the S-K model in transverse field using imaginary time replica formalism, under static approximation. They have shown that the replica-symmetric quantum spin glass phase is stable in most of the area of the spin glass phase, as have been argued by Ray et al., in contrary to the results of Lai et al. and Thirumalai et al. (see e.g., Chakrabarti et al. [4]).

8 Quantum Annealing

8.1 Multivariable Optimization and Simulated Annealing

Multivarable optimization problems consists of finding the maximum or minimum values of a function (known as cost function) of very many independent variables. A given set of values for the whole set of independent variables defines a configuration. The value of the cost function depends on the configurations, and one has to find the optimum configuration that minimizes or maximizes the cost function. The explicit evaluation of the cost function for all possible configurations in this context, generally turns out to be absolutely impracticable for most systems.

One can therefore start from an arbitrary state and go on changing the configuration following some stochastic rule, unless an extremum is reached. For example, in a minimization problem, one may start from an arbitrary configuration, change the configuration according to some stochastic rule, evaluate the cost function of the changed configuration, and then compare its value with that of the original configuration. If the new cost function is lower, the change is retained, i.e.,the new configuration is accepted. Otherwise the change is not accepted. Such steps may be repeated for times unless a minimum is reached. But in most cases of multivariable optimisation problem, there are many local extrema in the cost function landscape, and one cannot be sure that the extremum that has been reached is the global one. Kirkpatrick et al. [15] proposed a very ingenious physical solution to this mathematical problem, now known by the name simulated annealing. The basic underlying principle of simulated annealing as follows. It is known that an ergodic physical system, at any finite temperature resides in the global minimum of its free energy. The minimum of the free energy is a thermodynamic macro-state corrosponding to a maximum number of accessible microcsopic configuration. Hence at thermal equilibrium an ergodic system explores its configuration space randomly with equal apriori probability of visiting any configuration, and consequently is found most of the time at one or other of the configurations that corrosponds to the free energy minimum (since the number of configurations corrosponding to such minimum is overwhelmingly large compared to that of any other macro-state). Now if the system starts from an arbitrary macrostate (not the minimum of free energy) then due to thermal fluctuation it reaches the free energy minimum within some time τ known as the thermal relaxation time of the system.

For an ergodic system (away from critical point) this relaxation time increases linearly with system size (which is logerithmically smaller a number compared to the corrosponding number of all possible configurations). Hence if one follows the random dynamics of the thermal relaxation of a system, then he will be able to reach the minimum of cost function (zero temperatur free energy) in a substancially smaller time. What one needs to do is to view the cost function E as the internal energy of some system and start from an arbitrary configuration. Then one changes the configuration according to somestochastic rule, just as before. Now if the energy is lowered by the change, the change is accepted, but if it is not, the change is not thrown away with certainity. Instead it is accepted with a probability equal to the Boltzmann factor $e^{-\Delta E/k_B T}$, where $\Delta E = E_{(\text{after change})} - E_{(\text{before change})}$ (since this is the way how systems relax thermally to their free energy minimum). Temperature T here is an artifically introduced parameter which has a high value initially, and is reduced slowly as time goes on, finally tending towards zero. At zero temperature the free energy is nothing but the internal energy of the system, and thus at the end of the final stage of annealing the system can be expected to be found, with a very high probability, in a configuration that minimizes the internal energy (cost function).

However this simulated annealing technique can suffer severe set back when the system is 'nonergodic', like the spin glasses we discussed earlier. In such cases configurations corrosponding to minimum of the cost function are separated by $O(N)$ sized barriers, and at any finite temperature thermal fluctuations will take practically infinite time to relax the system to the global minimum crossing these barriers in thermodynamic limit $N \to \infty$.

8.2 Ergodicity of Quantum Spin Glasses and Quantum Annealing

The non-ergodicity problem makes the search of the ground state of a classical spin glass a computationally hard problem (no algorithm bounded by some polynomial in system size exists for such NP-hard problems). The problems of simulated annealing of spin glass-like systems can be overridden (atleast partially) by employing the method of quantum annealing [16, 17]. The basic idea is as follows: First the problem has to be mapped to a corrosponding physical problem, where the cost function is represented by some classical Hamiltonian (say $\mathcal{H}_0$) of the form (22). Then a suitably chosen noncommuting quantum tunnelling term (say $\mathcal{H}'(t)$) is to be added so that the Hamiltonian takes the form of (27). One can then solve the time dependent Schrodinger equation

$$i\hbar \frac{\partial \psi}{\partial t} = [\mathcal{H}_0 + \mathcal{H}'(t)]\psi \tag{39}$$

for the wave-function $\psi(t)$ of the entire system $\mathcal{H}_0 + \mathcal{H}'(t)$. The solution of the time dependent schrodinger equation approximately describes a tunnelling dynamics of the system between different eigenstates of $\mathcal{H}_0$. Like thermal fluctuations in (classical) simulated annealing, the quantum (tunnelling) fluctuations

owing to $\mathcal{H}'$ in (39) help the system to come out of the local 'trap' states. If $\mathcal{H}'(t) \to 0$ for $t \to \infty$, the system eventually settles in one of the eigenstates of $\mathcal{H}_0$; hopefully the ground state. The introduction of such a quantum tunnelling is supposed to make the infinitely high (but infinitessimally thin) barriers transparent to the system (see, e.g., Appendix C), and it can make transitions to different configurations trapped between such barriers, in course of annealing. In other words, it is expected that application of a quantum tunnelling term will make the free energy landscape ergodic, and the system will consequently be able to visit any configuration with finite probability. Finally the quantum tunnelling term is tuned to zero ($\mathcal{H}'(t) \to 0$) to get back the classical Hamiltonian. It may be noted that the success of quantum annealing is directely connected to the replica symmetry restoration in quantum spin glass [10, 14] due to tunnelling through barriers (see Fig. 5 and the discussion in the preceeding section).

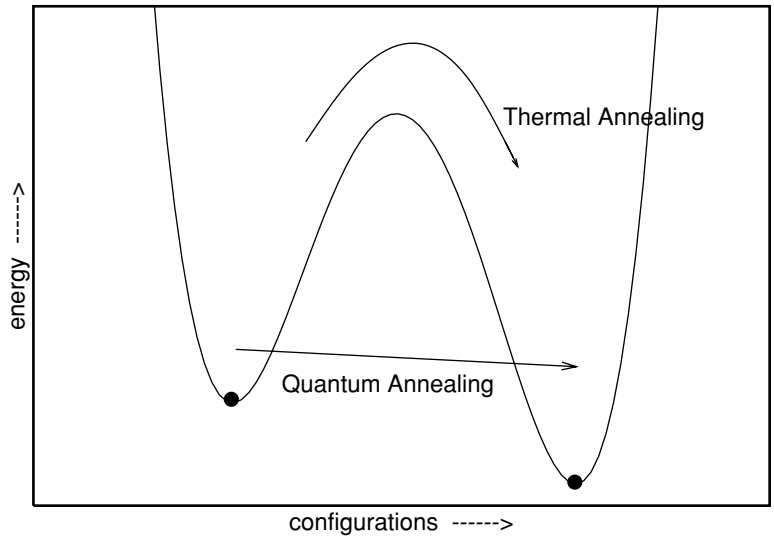

Fig. 5. Schematic indication of the advantage of quantum annealing over classical annealing

Here, the d-dimensional quantum Hamiltonian (27) (to be annealed) is mapped to the $(d+1)$-dimensional effective Hamiltonian

$$\mathcal{H}_{d+1} = -\sum_{k+1}^{M} \left(\sum_{i,j}^{N} J_{ij} \sigma_i^k \sigma_j^k + J' \sum_{i=1}^{N} \sigma_i^k \sigma_i^{k+1} \right) ,$$

where

$$J' = -\frac{MT}{2} \ln \tanh \left(\frac{\Gamma}{MT} \right) > 0$$

is the nearest neighbour ferromagnetic coupling in Trotter direction, between the Trotter replicas of the same spin. In course of annealing, the temperature is kept constant at a low but nonzero value, and the tunnelling field Γ is tuned slowly from a high initial value to zero. The decrease in Γ amounts to the increase in J' (as casn be seen from above expression of J'). Initially at high Γ, J' is low, and each Trotter replica behaves almost like an independent classical spin system. The tunnelling field is then lowered in small steps. In each such step, the system is annealed in presence of the small temperature. Finally as $\Gamma \to 0$, $J' \to \infty$, forcing all replicas to coinside at the end. As mentioned already, quantum annealing possibility directly rests on the replica symmetry restoration feature of quantum spin glasses, discussed in earlier section. In fact ergodicity in quantum spin glasses, as suggested in Fig. 5 was attributed by Ray et al. to the "quantum fluctuations due to transverse field. Quantum tunnelling between the classical 'trap' states, separated by infinite (but narrow) barriers in the free-energy surface, is possible as quantum tunnelling probability is proportional to the barrier area which is finite." (Sect. V, [10]).

8.3 Quantum Annealing in Kinetically Constrained Systems

It is largely believed that apart from the complexity associated to the nontrivial ground state structure of a glassy system, the occurance of certain kinetic constraints (blockings) during relaxation also contributes substancially to the slowness of its low temperature dynamics. The Kinetic constraints or blockings can be viewed as infinitely high energy barriers appearing in the relaxation path of the system. In order to relax to the minimum of the free energy, the system has to jump over these high barriers thermally, which they fail to do at any finte temperature. However if such barriers are infinitessimally narrow, then the system might be able to tunnel through them quantum mechanically if sufficient quantum fluctuation Γ is present in the system. Thus if one tries to anneal such a system down to its ground state starting from an arbitrary state, then quantum annealing might turn out to be much superior to the thermal annealing (see e.g., [18, 19]).

We have studied [20] the annealing of a kinetically constrained Ising spin chain of N spins, starting from a disordered state (with negligible initial magnetization), to its (external field induced) fully ordered ground state. At any finite temperature T (in the classical model) the system takes an exponentially long time to relax to the ordered state because of the kinetic constraints, which act like an infinite potential barrier, depending on the neighbouring spin configurations. Quantum mechanically, this infinite barrier is taken to be penetrable, i.e. with finite tunnelling probability, depending on the barrier height χ and width a ($a \to 0$ faster than χ^{-2}). The introduced noise, required for the annealing, is reduced following an exponential schedule in both the cases: $T = T_0 e^{-t/\tau_C}$, $\Gamma = \Gamma_0 e^{-t/\tau_Q}$, with $T_0 \approx \Gamma_0$. For our simulation for the quantum case, we have taken the tunnelling probabilities P (for cases I–IV) and employed them in a semi-classical fashion for the one dimensional spin chain

considered. We observe that for similar achievement in final order ($m_f \simeq 0.92$ starting from $m_i = 10^{-3}$), $\tau_C \sim 10^3 \tau_Q$ for $N = 5 \times 10^4$. For even larger order ($m_f \sim 1$), quantum annealing works even better ($\tau_C \sim 10^3 \tau_Q$, for the same value of N). These comparison are for $g = 10^2$ and $\chi = 10^3$ for the constraint barriers [20].

In this picture, we considered the collective dynamics of a many particle system, where each one is confined in a (field) induced asymmetric double well potential for which we considered only the low lying two states (the wave packet localized in one well or the other), representing the two states (up and down) of an Ising spin discussed above. The tunnelling of the wave packet from one well to the other was taken into account by employing a scattering picture and we used the tunnelling probabilities as the flip probabilities for the quantum Ising spins. As such, the reported simulation for the one dimensional quantum East model is a semiclassical one. It may be noted however that, because of the absence of inter-spin interaction, the dimensionality actually plays no role in this model except for the fact that the kinetic constraints on any spin depend only on the left nearest neighbour (directedness in one dimension). Hence the semiclassical one dimensional simulation, instead of a proper quantum Monte Carlo simulation (equivalent to a higher dimensional classical one [4]), is quite appropriate here.

9 Summary and Discussions

We have introduced the transverse Ising model for discussing the order-disorder transition (at zero temperature) driven by quantum fluctuations. Mean field theories are discussed next in Sects. 3 and 4. Application to BCS superconductivity theory is discussed in appendix A. Renormalization group technique for study of critical behaviour in such quantum systems is discussed in appendix B (for a chain). Next we have discussed the Suzuki-Trotter mapping of the d-dimensional quantum system to $d+1$ dimensional classical system (in Sect. 6). We introduce then the transverse Ising spin glass models, namely, the S-K model in transverse field and the E-A model in transverse field (Sect. 8.2). The existing studies on their phase diagrams are discussed briefly. We then discuss about the problem of replica symmetry restoration in quantum spin glasses (in Sect. 8.3). The application of the quantum annealing technique to capture the near-global minima of NP-hard problems is then discussed, and the effectiveness of quantum tunnelling over the thermal barrier hopping is discussed (Sect. 9).

It may be noted in this connection that some recent attempts have been made to apply similar annealing, induced by quantum fluctuations, to the optimization problems like the travelling salesman problem, image restoration, etc. [18, 19]. Like the near-global minima in free energy landscape of such spin glasses, the barriers are often globally contributed and these barrier heights grow as the system size grows (unlike the locally optimized configurations and

the barriers between them). Classically, the system becomes nonergodic due to these macroscopically high barriers (NP-hard to reach the ground state), as thermal fluctuations have to wait until they can scale such macroscopically high barriers. Quantum tunnelling does not necessarily look for barrier height [10] to overcome them (by tunnelling through; see appendix C, see Fig. 5) and helps restoring replica symmetry as well as annealing [16, 17].

Acknowledgement

We are grateful to Amit Dutta, Jun-ichi Inoue and Robin Stincombe for many useful discussions and comments.

10 Appendix

Appendix A

MFT of TIM and BCS Theory of Superconductivity

The phonon mediated effective attractive interaction between electrons give rise to a cooperative quantum Hamiltonian. Although the quantum phase transition in such a system is not physical or meaningful, the finite temperature superconducting phase transition can be studied easily following the mean field theory discussed here (using a pseudo-spin mapping [5]). The relevant part of the Hamiltonian of electrons that take part in superconductivity has the following form

$$\mathcal{H} = \sum_k \epsilon_k (c_k^\dagger c_k + c_{-k}^\dagger c_{-k}) - V \sum_{kk'} c_{k'}^\dagger c_{-k'}^\dagger c_{-k} c_k \qquad (A1)$$

Here the suffix k indicates a state with momentum $\boldsymbol{k}$ and spin up, while $(-k)$ indicates a state with momentum $-\boldsymbol{k}$ and spin down and V is a positive constant that models the attractive coupling between electrons through phonons. We will solve this equation following spin-analog method [4]. Here we are considering low-lying states containing pair of electrons $(k, -k)$. For a given k, there are two possible states that come into consideration: either the pair exists, or it does not. Thus we enter into a spin-like two-state picture as follows.

Let us introduce the number operator $\hat{n}_k = c_k^\dagger c_k$. This reduces the Hamiltonian (A1) to

$$\mathcal{H}_{red} = -\sum_k \epsilon_k (1 - \hat{n}_k - \hat{n}_{-k}) - V \sum_{kk'} c_{k'}^\dagger c_{-k'}^\dagger c_{-k} c_k \; . \qquad (A2)$$

Here we have introduced a term $-\sum_k \epsilon_k$ with the choice $\sum_k \epsilon_k = 0$ in mind, for all k's (basically these sums are over the states within energy $\pm\omega_D$ about

the fermi level, where ω_D is the Debye energy) that partictpates in pair formation. As stated earlier, if n_k denotes the number of electrons in k-state, then we are considering only a subspace of states defined by $n_k = n_{-k}$, where either the both of the states in the pair $(k,-k)$ are occupied, or both are empyt. Now if we denote by $|1_k 1_{-k}\rangle$ a $(k,-k)$ pair-occupied state and by $|0_k 0_{-k}\rangle$ an unoccupied one, then

$$(1 - \hat{n}_k - \hat{n}_{-k})|1_k 1_{-k}\rangle = (1 - 1 - 1)|1_k 1_{-k}\rangle = -|1_k 1_{-k}\rangle \ ,$$

and

$$(1 - \hat{n}_k - \hat{n}_{-k})|0_k 0_{-k}\rangle = (1 - 0 - 0)|0_k 0_{-k}\rangle = |0_k 0_{-k}\rangle$$

Thus we switch over to our good old pseudo-spin picture through the following corrospondences

$$|1_k 1_{-k}\rangle \Leftrightarrow |\downarrow\rangle_k \ ,$$
$$|0_k 0_{-k}\rangle \Leftrightarrow |\uparrow\rangle_k \ ,$$
$$\text{and} \qquad (1 - n_k - n_{-k}) \Leftrightarrow \sigma_k^z \ . \tag{A3}$$

Since

$$c_k^\dagger c_{-k}^\dagger|\uparrow\rangle_k = |\downarrow\rangle_k, \quad c_k^\dagger c_{-k}^\dagger|\downarrow\rangle_k = 0 \quad \& \quad c_{-k}c_k|\downarrow\rangle_k = |\uparrow\rangle_k, \quad c_{-k}c_k|\uparrow\rangle_k = 0 \ ,$$

we immediately identify its corrospondence with raising and lowering operator σ^+/σ^- :

$$\sigma^- = \sigma^x - i\sigma^y = \begin{pmatrix} 0 & 0 \\ 2 & 0 \end{pmatrix}$$

and

$$\sigma^+ = \begin{pmatrix} 0 & 2 \\ 0 & 0 \end{pmatrix}$$

and therefore

$$c_k^\dagger c_{-k}^\dagger = \frac{1}{2}\sigma_k^- , \quad c_{-k}c_k = \frac{1}{2}\sigma_k^\dagger \ . \tag{A4}$$

Hence in terms of these spin operators, Hamiltonian (A2) takes the form

$$\mathcal{H} = -\sum_k \epsilon_k \sigma_k^z - \frac{1}{4}V\sum_{kk'} \sigma_{k'}^- \sigma_k^+ \ . \tag{A5}$$

Since the term $\sum_{kk'}(\sigma_{k'}^x\sigma_k^y - \sigma_{k'}^y\sigma_k^x)$ vanishes due to symmetric summing done over k and k', the Hamiltonian finally reduces to

$$\mathcal{H} = -\sum_k \epsilon_k \sigma_k^z - \frac{1}{4}V\sum_{kk'}(\sigma_{k'}^x\sigma_k^x + \sigma_{k'}^y\sigma_k^y) \ . \tag{A6}$$

To obtain the energy spectrum of the pseudo-spin BCS Hamiltonian (A6) we apply now the mean field theory developed in earlier section.

Weiss' Mean Field Solution

Just as we did in case of TIM (see Sect. 3), here also we introduce an average effective field $\boldsymbol{h}_k$ for each pseudo-spin σ_k as

$$\boldsymbol{h}_k = \epsilon_k \hat{z} + \frac{1}{2} V \sum_{k'} (\langle \sigma_{k'}^x \rangle \hat{x} + \langle \sigma_{k'}^y \rangle \hat{y})$$

and conseqently the Hamiltonian (A6) takes the form

$$\mathcal{H} = -\sum_k \boldsymbol{h}_k . \boldsymbol{\sigma}_k \ .$$

Here for each k there is an independent spin $\boldsymbol{\sigma}_k$ which interacts only with some effective field $\boldsymbol{h}_k$, and our system is a collection of such mutually non-interacting spins under a field $\boldsymbol{h}_k$.

Now if redefine our x-axis along the projection of $\boldsymbol{h_k}$ on the x-y plane for each k, then with all $\langle \sigma_{k'}^y \rangle = 0$ we get

$$\tan\theta_k = \frac{h_k^x}{h_k^z} = \frac{\frac{1}{2} V \sum_{k'} \langle \sigma_{k'}^x \rangle}{\epsilon_k} \ , \qquad (A7)$$

where θ_k is the angle between z-axis and $\boldsymbol{h}_k$.

Excitation Spectra at T = 0

Since at $T = 0$ $\langle \sigma^x \rangle = 1$,

$$\langle \sigma_{k'}^x \rangle = |\boldsymbol{\sigma}| \sin\theta_{k'} = \sin\theta_{k'} \qquad (A8)$$

Thus from (A7) we get

$$\tan\theta_k = (v/2\epsilon_k) \sum_{k'} \sin\theta_{k'}$$

Now let us define

$$\Delta \equiv \frac{1}{2} V \sum_{k'} \sin\theta_{k'} \ ,$$

so that $\tan\theta_k = \Delta/\epsilon_k$. Then simple trigonometry gives –

$$\sin\theta_k = \frac{\Delta}{\sqrt{\Delta^2 + \epsilon_k^2}} \ ; \qquad \cos\theta_k = \frac{\epsilon_k}{\sqrt{\Delta^2 + \epsilon_k^2}} \ . \qquad (A9)$$

Substituting for $\sin\theta_{k'}$ into the above equation we get

$$\Delta = \frac{1}{2} V \sum_{k'} \frac{\Delta}{\sqrt{\Delta^2 + \epsilon_{k'}^2}} \ .$$

Assuming the spectrum to be nearly continuous, we replace the summation by an integral and note that V is attractive for energy within $\pm\omega_D$ on both sides of fermi level; ω_D being of the order of Debye energy. Then the last equation becomes

$$1 = \frac{1}{2} V \rho_F \int_{-\omega_D}^{\omega_D} \frac{d\epsilon}{\sqrt{\Delta^2 + \epsilon^2}} = V \rho_F \sinh^{-1}(\omega_D/\Delta) \ .$$

Here ρ_F is the density of states at fermi level. Thus

$$\Delta = \frac{\omega_D}{\sinh(1/V\rho_F)} \cong 2\omega_D e^{-1/V\rho_F}, \qquad (\text{if} \quad \rho_F V \ll 1) \tag{A10}$$

We see that Δ is positive if V is positive. To interprate the parameter Δ, one may notice that at first approximation, the excitation spectrum is obtained as the energy $\mathcal{E}_k$ to reverse a pseudo-spin in the field $\boldsymbol{h}_k$, i.e.,

$$\mathcal{E}_k = 2|\boldsymbol{h}_k| = 2\left(\epsilon_k^2 + \Delta^2\right)^{1/2} \ . \tag{A11}$$

From this expression we clearly see that the minimum excitation energy is 2Δ, i.e. Δ gives the energy gap in the excitation spectrum.

Estimating Transition Temperature T_c

To find the critical temperature for BCS transition, we just extend here the non-zero temperature version of mean field theory done for Ising case. We should have (unlike that in (A11), where $\langle\sigma_k\rangle = 1$) for $T = 0$:

$$\langle\sigma_k^z\rangle = \tanh\left(\beta|\boldsymbol{h}_k|\right) \ . \tag{A12}$$

Equation (23) accordingly modifies to

$$\tan\theta_k = \left(\frac{V}{2\epsilon_k}\right) \sum_{k'} \tanh\left(\beta|\boldsymbol{h}_{k'}|\right) \sin\theta_{k'} \equiv \frac{\Delta(T)}{\epsilon_k} \ , \tag{A13}$$

where $\Delta(T) = \frac{V}{2}\sum_{k'} \tanh\left(\frac{|\boldsymbol{h}_{k'}|}{T}\right) \sin\theta_{k'}$. From equation (A11) we have

$$|\boldsymbol{h}_k| = \left[\epsilon_k^2 + \Delta^2(T)\right] \ .$$

The BCS transition is characterized by the vanishing of the gap Δ, since without such a gap in the spectrum, infinite conductance would not be possible except at $T = 0$. Hence, as $T \to T_c, \quad \Delta \to 0$, i.e., using (A11), $|\boldsymbol{h}_k| = \epsilon_k$ and putting this and relations like (A9) in (A13), we get

$$1 = V \sum_{k'} \frac{1}{2\epsilon_{k'}} \tanh\left(\frac{\epsilon_{k'}}{T_c}\right) \ . \tag{A14}$$

Above relation is correct if we consider an excited pair as a single entity. However, if we extend our picture to incorporate single particles excited symmetrically in momentum space, then we double the number of possible excitations,

thereby doubling the overall entropy. This is exactly equivalent to a doubling of the temperature in free energy. The energy contribution to the free energy, however, remains unaltered, since two single particle excitations of same $|\boldsymbol{k}|$ have same energy as that of a pair of equal $|\boldsymbol{k}|$. Hence we replace T_c by $2T_c$, and in the continuum limit, get

$$\frac{2}{V\rho_F} = \int_{-\omega_D}^{\omega_D} \frac{d\epsilon}{\epsilon} \tanh\left(\frac{\epsilon}{2T_c}\right) = 2\int_0^{\omega_D/2T_c} \frac{\tanh x}{x} dx \ ,$$

with $(x = \epsilon/2T_c)$ This is the equation from which we obtain T_c on integration. If $T_c \ll \omega_D$, then we may approximate $\tanh x \approx 1$, for $x \geq 1$, and for $x \ll 1$, we set $\tanh x \approx x$. This readily reduces the integral to the value $1 + \log(\omega_D/2T_c)$, from which we have

$$T_c = (e/2)\omega_D e^{-1/V\rho_F} \ .$$

Grphical integration gives a closer result

$$T_c = 1.14\omega_D e^{-1/V\rho_F} \ . \qquad (A15)$$

Comparing (A10) and (A15) we get the approximate relationship

$$2\Delta \simeq 3.5T_c \ . \qquad (A16)$$

This result is quite consistent with the exprimental values for a number of materials. For example, the value of $2\Delta/T_c$ are 3.5, 3.4, 4.1, 3.3 for Sn, Al, Pb, and Cd superconductors respectively.

Appendix B

Real Space Renormalization for Transverse Ising Chain

Here the basic idea of real space block renormalization [4, 6] is illustrated by applying it on an Ising chain in transverse field. Taking the cooperative interaction along x-axis, and the transverse field along z-axis, the Hamiltonian reads

$$\begin{aligned} \mathcal{H} &= -\Gamma \sum_{i=1}^{N} \sigma_i^z - J \sum_{i=1}^{N-1} \sigma_i^x \sigma_{i+1}^x \\ &= \mathcal{H}_B + \mathcal{H}_{IB} \quad \text{(say)} \ . \end{aligned} \qquad (B1)$$

Here

$$\mathcal{H}_B = \sum_{p=1}^{N/b} \mathcal{H}_p \ ; \qquad \mathcal{H}_p = -\sum_{i=1}^{b} \Gamma \sigma_{i,p}^z - \sum_{i-1}^{b-1} J\sigma_{i,p}^x \sigma_{i+1,p}^x \qquad (B2)$$

and

$$\mathcal{H}_{IB} = \sum_{p=1}^{N/(b-1)} \mathcal{H}_{p,p+1} \; ; \qquad \mathcal{H}_{p,p+1} = -J\sigma^x_{b,p}\sigma^x_{1,p+1} \; . \tag{B3}$$

The above rearrangement of the Hamiltonian recasts the picture of N spins with nearest-neighbour interaction into one in which there are $N/(b-1)$ blocks, each consisting of b number of spins. The part $\mathcal{H}_B$ represents the interaction between the spins within the blocks, while $\mathcal{H}_{IB}$ represents the interactions between the blocks through their terminal spins(see Fig. 6).

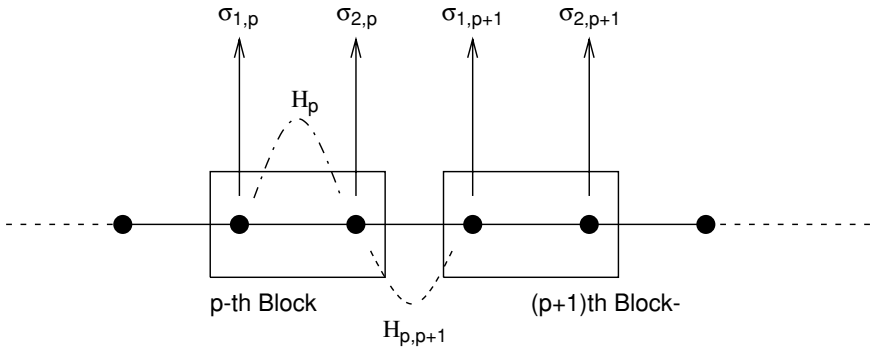

Fig. 6. The linear chain is broken up into blocks of size b (= 2 here) and the Hamiltonian (B1) can be written as the sum of block Hamiltonians $\mathcal{H}_p$ and inter-block Hamiltonians $\mathcal{H}_{p,p+1}$. The Hamiltonian $\mathcal{H}_p$ is diagonalized exactly and the lowest lying two states are identified as the renormalized spin states in terms of which the inter-block Hamiltonian is rewritten to get the RG recursion relation

Here we will consider $b = 2$, as shown in the figure. Now $\mathcal{H}_p$ has got 4 eigen-states, and one can express them in terms of the linear superposition of the eigen-states of $\sigma^z_{1,p} \otimes \sigma^z_{2,p}$; namely,

$$|\uparrow\uparrow\rangle, \quad |\downarrow\downarrow\rangle, \quad |\uparrow\downarrow\rangle, \quad \text{and} \quad |\downarrow\uparrow\rangle \; .$$

Considering the orthonormality of the eigen-states, one may easily see that the eigenstates of $\mathcal{H}_p$ can be expressed as

$$\begin{aligned}
|0\rangle &= \frac{1}{\sqrt{1+a^2}}(|\uparrow\uparrow\rangle + a|\downarrow\downarrow\rangle) \\
|1\rangle &= \frac{1}{\sqrt{2}}(|\uparrow\downarrow\rangle + |\downarrow\uparrow\rangle) \\
|2\rangle &= \frac{1}{\sqrt{2}}(|\uparrow\downarrow\rangle - |\downarrow\uparrow\rangle) \\
|3\rangle &= \frac{1}{\sqrt{1+a^2}}(a|\uparrow\uparrow\rangle - |\downarrow\downarrow\rangle) \; .
\end{aligned} \tag{B4}$$

Here a is a coefficient required to be chosen properly, so that $|0\rangle$ and $|3\rangle$ are eigenstates of $\mathcal{H}_p$. One gets,

$$\begin{aligned}
\mathcal{H}_P|0\rangle &= \mathcal{H}_p\left[\frac{1}{\sqrt{1+a^2}}|\uparrow\uparrow\rangle + a|\downarrow\downarrow\rangle\right] \\
&= [-\Gamma(\sigma_1^z+\sigma_2^z) - J(\sigma_1^x\sigma_2^x)]\frac{1}{\sqrt{1+a^2}}(|\uparrow\uparrow\rangle + a|\downarrow\downarrow\rangle) \\
&= \frac{1}{\sqrt{1+a^2}}[-\Gamma(2|\uparrow\uparrow\rangle - 2a|\downarrow\downarrow\rangle) - J(|\downarrow\downarrow\rangle) + a|\uparrow\uparrow\rangle] \\
&= -(2\Gamma+Ja)\frac{1}{\sqrt{1+a^2}}\left[|\uparrow\uparrow\rangle + \left(-\frac{2\Gamma - J/a}{2\Gamma+Ja}\right)a|\downarrow\downarrow\rangle\right]
\end{aligned}$$

Thus $|0\rangle$ to be an eigenstate of $\mathcal{H}_p$, one must have

$$\begin{aligned}
-\frac{2\Gamma - J/a}{2\Gamma+Ja} &= 1 \\
\Rightarrow \qquad Ja^2 - 4\Gamma a - J &= 0 \\
\text{or,} \qquad a &= \frac{\pm\sqrt{4\Gamma^2+J^2} - 2\Gamma}{J}\,. \qquad (B5)
\end{aligned}$$

To minimize the energy, we have to choose,

$$a = \frac{\sqrt{4\Gamma^2+J^2} - 2\Gamma}{J}\,.$$

One can now see, applying $\mathcal{H}_p$ on its eigen-states,

$$\begin{aligned}
\mathcal{H}_p|0\rangle &= E_0|0\rangle, \quad E_0 = -\sqrt{4\Gamma^2+J^2} \\
\mathcal{H}_p|1\rangle &= E_1|1\rangle, \quad E_1 = -J \\
\mathcal{H}_p|2\rangle &= E_2|2\rangle, \quad E_2 = +J \\
\mathcal{H}_p|3\rangle &= E_3|3\rangle, \quad E_3 = +\sqrt{4\Gamma^2+J^2}\,. \qquad (B6)
\end{aligned}$$

Now we define our new renormalized spin variables σ''s, each replacing a block in the original Hamiltonian. We retain only the two lowest lying states $|0\rangle$ and $|1\rangle$ of a block and define corrosponding $\sigma_p'^Z$ to have them as its two eigenstates, $|\uparrow\rangle = |0\rangle$ and $|\downarrow\rangle = |1\rangle$. We also define

$$\sigma'^x = \frac{\sigma_1^x \otimes \mathcal{I} + \mathcal{I}\otimes\sigma_2^x}{2}\,,$$

where $\mathcal{I}$ is the 2×2 identity matrix. Now since

$$\langle 0|\sigma'^x|1\rangle = \frac{1+a}{\sqrt{2(1+a^2)}}\,,$$

we take our renormalized J to be

$$J' = J\frac{(1+a)^2}{2(1+a^2)}\ , \tag{B7}$$

and since the energy gap between $|0\rangle$ and $|1\rangle$ must be equal to $2\Gamma'$ (This gap was 2Γ in the unrenormalized states), we set

$$\Gamma' = \frac{E_1 - E_0}{2} = \frac{\sqrt{4\Gamma^2 + J^2} + J}{2} = \frac{J}{2}[\sqrt{4\lambda^2 + 1} + 1]\ , \tag{B8}$$

where $a = \sqrt{4\lambda^2 + 1} - 2\lambda$, defining the relevant variable $\lambda = \Gamma/J$.

The fixed points of the recurrence relation (rewritten in terms of λ) are

$$\begin{aligned} &\lambda^\star = 0 \\ &\lambda^\star \to \infty \\ \text{and}\quad &\lambda^\star \simeq 1.277\ . \end{aligned} \tag{B9}$$

Now if correlation length goes as

$$\xi \sim (\lambda - \lambda_c)^\nu\ ,$$

in the original system, then in the renormalized system we should have

$$\xi' \sim (\lambda' - \lambda_c)^\nu$$

$$\Rightarrow \qquad \frac{\xi'}{\xi} = \left(\frac{\lambda' - \lambda_c}{\lambda - \lambda_c}\right)^{-\nu} \Rightarrow \left(\frac{\xi'}{\xi}\right)^{-1/\nu} = \frac{d\lambda'}{d\lambda}\Big|_{\lambda=\lambda_c\equiv\lambda^\star}\ . \tag{B10}$$

Now since the actual physical correlation length should remain same as we renormalize, ξ' (correlation length in the renormalized length scale) must be smaller by the factor b (that scales the length), than ξ (correlation length in original scale). i.e., $\xi'/\xi = b$, or,

$$b^{-1/\nu} = \left(\frac{d\lambda'}{d\lambda}\right)_{\lambda=\lambda_c=\lambda^\star} \equiv \Omega \qquad (\text{say})\ ,$$

$$\text{hence,} \qquad \nu = \left(\frac{\ln \Omega}{\ln b}\right)_{\lambda=\lambda^\star} = \frac{\ln \Omega}{\ln 2} \simeq 1.47, \qquad (\text{for} \quad b = 2)\ , \tag{B11}$$

compared to the exact value $\nu = 1$ for $(d + 1 =)$ 2 dimensional classical Ising system. Similarly $E_g \sim \omega \sim (\text{time})^{-1} \sim \xi^{-z}$; $\quad z = 1$. But for $b = 2$, we donot get $z = 1$. Instead, $\lambda'/\lambda \sim b^{-z}$ gives $z \simeq 0.55$. Energy gap

$$\Delta(\lambda) \sim |\lambda_c - \lambda|^s \sim \xi^{-z} \sim |\lambda^c - \lambda|^{\nu z} \tag{B12}$$

Hence $s = \nu z = 0.55 \times 1.47 \simeq 0.81$ (compared to the exact result $s = 1$). Results improve rapidly for large b values [6].

Appendix C

Tunnelling Through Asymmetric Barrier

Let us consider an asymmetric potential energy barrier in one dimension, (as shown in Fig. 7). It is essentially a rectangular barrier of height χ and width a between two different energy levels with a potential difference h between them. The potential energy V is zero at the left of the barrier ($x < 0$),

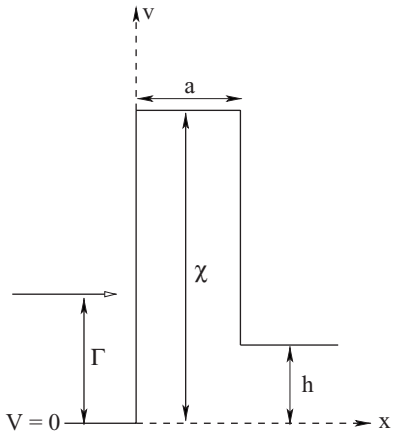

Fig. 7. Quantum tunnelling thruogh asymmetric barrier

and it is h (h may be negative as well) at the right of the barrier ($x > a$). If a beam of free particles of mass m with kinetic energy Γ incidents on the barrier from the left, then one can calculate the probability for a particle in the beam to get transmitted through (or reflected by) the barrier by solving the time-independent Schrödinger equation (with a time-independent V). The transmission coefficient T (defined below) describes the probability of transmission for a single particle, as well as the average transmission of the incident beam.

The incident wave function $\psi_1(x)$, the intermediate wave function $\psi_2(x)$ and the transmitted wave function $\psi_3(x)$ then takes the form

$$\begin{aligned}
\psi_1(x) &= Ae^{-ik_1x}, \qquad x < 0, \\
\psi_2(x) &= Be^{k_2x} + Ce^{-k_2x}, \qquad 0 \le x \le a \\
\psi_3(x) &= De^{ik_3x}, \qquad x > a
\end{aligned}$$

where,

$$k_1^2 = \Gamma; \qquad k_2^2 = \Gamma - \chi \quad \text{and} \qquad k_3^2 = \Gamma - h \ ,$$

setting $2m/\hbar^2 = 1$. Here A and D are the amplitudes of the incident and the transmitted wave respectively. At this point one may note that for $\Gamma < h$

transmission is trivially zero. Hence we consider the case for $\Gamma > h$ i.e., for real k_3. In that case, applying the condition of continuiety of the wave function and its space derivatives at the boundaries, one obtains the relation (cf. [21])

$$A = \frac{1}{2} D e^{ik_3 a}[(1 + k_3/k_1)\cosh \kappa a + i(\kappa/k_1 - k_3/\kappa)\sinh \kappa a] \ ,$$

where $\kappa^2 = -k_2^2 = \chi - \Gamma$. We now consider the limit of very high but narrow barrier, such that $\chi \to \infty$, $a \to 0$, with $g = \chi a$ finite. We also assume that $\chi \gg \Gamma$, so that $\kappa^2 \approx \chi$, and of course κ is real. Since $\Gamma \geq 0$, k_1 is also real. Hence under this condition the transmission coefficient defined as $T = |D|^2 k_3/|A|^2 k_1$ is given by (cf. [21])

$$T = \frac{4k_3/k_1}{\left(1 + \frac{k_3}{k_1}\right)^2 \cosh^2(\kappa a) + \left(\frac{\kappa}{k_1} - \frac{k_3}{\kappa}\right)^2 \sinh^2(\kappa a)} \ .$$

In the limit of high but narrow barrier specified above, one has $\kappa a \ll 1$. Hence neglecting terms quadratic or of higher order in κa and linear in $1/\kappa$, one gets

$$\begin{aligned} T &\approx \frac{4k_3/k_1}{\left(1 + \frac{k_3}{k_1}\right)^2 + \left(\frac{\kappa}{k_1}\right)^2 (\kappa a)^2} \\ &= \frac{4\sqrt{\Gamma(\Gamma - h)}}{(\sqrt{\Gamma} + \sqrt{\Gamma - h})^2 + g^2} \ , \end{aligned}$$

putting $k_1 = \sqrt{\Gamma}$, $k_3 = \sqrt{\Gamma - h}$ and $\kappa^2 a \approx \chi a = g$. The transmission coefficient T is thus finite even when the barrier height χ diverges keeping $g = \chi a$ finite.

References

1. R. Blinc, J. Phys. Chem. Solids **13** 204 (1960); S. Katsura, Phys. Rev. **127** 1508 (1962) 3
2. P. G. de Gennes, Solid State Comm. **1** 132 (1963) 5
3. R. Brout, K. A. Müller and H. Thomas, Solid State Comm. **4** 507 (1996); R. B. Stinchcombe, J. Phys. **C6** 2459 (1973) 6
4. B. K. Chakrabarti, A. Dutta and P. Sen, *Quantum Ising Phases and Transitions in Transverse Ising Models*, Lect. Notes Phys. **m41** (1996); see also S. Sachdev, *Quantum Phase Transitions*, Cambridge Univ. Press, Cambridge (1999) 6, 15, 16, 19, 20, 21, 25, 26, 30
5. P. W. Anderson, Phys. Rev. **112** 900 (1985); see also C. Kittel, *Quantum theory of Solids*, John Wiley, New York (1987) 8, 26
6. R. Jullien, P. Pfeuty, J. N. Fields and S. Doniach, Phys. Rev. B **18** 3568 (1978); R. Jullien, P. Pfeuty, J. N. Fields and K. A. Penson, in *Real Space Renormalization,* Ed. T. W. Brukhardt and J. M. J van Leeuween, Springer-Verlag, p. 119 (1982) 9, 30, 33

7. M. Suzuki, Prog. Theor. Phys. **46** 1337 (1971); *Quantum Monte Carlo Methods*, Ed. M. Suzuki, Springer-Verlag, Heidelberg (1987); R. J. Elloitt, P. Pfeuty and C. Wood, Phys. Rev. Lett. **25** 443 (1970); see also N. Hakano and M. Suzuki, *Finding Exponential Product Formulas of Higher Orders*. In: Lect. Notes Phys. **679** (2005) 9
8. D. Chowdhury, *Spin Glass and Other Frustrated Systems,* World Scientific, Singapore (1986); H. Nishimori, *Statistical Physics of Spin Glasses and Information Processing: an Introduction,* Oxford University Press, Oxford (2001) 12, 13, 14
9. B. K. Chakrabarti, Phys. Rev. B **24** 4062 (1981); H. Ishii and T. Yamamoto, J. Phys. C **18** 6225 (1985) 14, 15, 17
10. P. Ray, B. K. Chakrabarti and A. Chakrabarti Phys. Rev. B **39** 11828 (1989) 14, 17, 19, 20, 23, 24, 26
11. M. Guo, R. N. Bhatt and D. A. Huse, Phys. Rev. Lett. **72** 4137 (1994); D. Fisher, Phys. Rev. B **50** 3799 (1994) 14, 19
12. W. Wu, B. Ellman, T. F. Rosenbaum, G. Aeppli and D. H. Reich, Phys. Rev. Lett. **67** 2076 (1991); W. Wu, D. Bitko, T. F. Rosenbaum and G. Aeppli, Phys. Rev. Lett. **74** 3041 (1993) 14, 15
13. Heiko Rieger, *Qunatum Spin Classes*. In: Lect. Notes Phys. **679** (2005). See also R. N. Bhatt in *Spin Glasses and Random Fields*, Ed. A. P, Young, World Scientific, Singapore, pp. 225–249 (1998) 14, 15, 17, 18
14. D.-H. Kim and J.-J. Kim, Phys. Rev. B **66** 054432 (2002); see however, D. Thirumalai, Q. Li and T. R. Kirkpatrick, J. Phys. A **22** 3339 (1989); J.-J. Kim, *Ergodicity, Replica Symmetry, Spin Glass and Quantum Phase Transition*. In: Lect. Notes Phys. **679** (2005) 21, 23
15. S. Kirkpatrick, C. D. Gelatt and M. P. Vecchi, Science, **220**, 671 (1983) 21
16. T. Kadowaki and H. Nishimori, Phys. Rev. E **58** 5355 (1998) 22, 26
17. J. Brook, D. Bitko, T. F. Rosenbaum and G. Aeppli, Science **284** 779 (1999); G. Aeppli and T. F. Rosenbaum, *Experiments on Quantum Annealing*. In: Lect. Notes Phys. **679** (2005), pp. 159–169 22, 26
18. G. E. Santoro, R. Martonak, E. Tosatti and R. Car, Science 295, 2427 (2002) 24, 25
19. D. A. Battaglia, G. E. Santoro, and E. Tosatti, cond-mat/0502468, (2005), L. Stella, G. E. Santoro, E. Tosatti, cond-mat/0502129, (2005), H. Nishimori and K.Y.M. Wong, Phys. Rev. E **60** 132 (1999); J. Inoue, Phys. Rev. E **63** 046114 (2001); K. Tanaka, J. Phys. A **35** R81 (2002); J. Inoue, Physica Scr. T **106** 70 (2003); S. Suzuki, cond-mat/0502203, (2005); S. Suzuki, *Simulated Quantum Annealing by the Real-time Evolution*. In: Lect. Notes Phys. **679** (2005), pp. 207–238 24, 25
20. A. Das, B. K. Chakrabarti and R. B. Stinchcombe, Phys. Rev. E **72**, 026701 (2005); A. Das and B. K. Chakrabarti, *Quantum Annealing of a $\pm J$ Spin Glass and a Kinetically Constrained System*. In: Lect. Notes Phys. **679** (2005), pp. 239–257 24
21. H. Margenau and G. M. Murphy, *Mathematics of Physics and Chemistry* (2nd Ed.), Van Nostrand, New Jersey (1956), pp. 356–358; E. Merzbacher,*Quantum Mecahnics* (3rd Ed.), John Wiley & Sons Inc., USA (1998), pp. 93–96 35

Finding Exponential Product Formulas of Higher Orders

Naomichi Hatano[1] and Masuo Suzuki[2]

[1] Institute of Industrial Science, University of Tokyo, 4–6–1 Meguro, Komaba, Tokyo 153-8505, Japan
hatano@iis.u-tokyo.ac.jp
[2] Department of Applied Physics, Tokyo University of Science, 1–3 Kagurazaka, Shinjuku, Tokyo 162-8601, Japan
msuzuki@ap.kagu.sut.ac.jp

1 Introduction

In the present article, we review the progress in the last two decades of the work on the Suzuki-Trotter decomposition, or the exponential product formula. The simplest Suzuki-Trotter decomposition, or the well-known Trotter decomposition [1, 2, 3, 4] is given by

$$\mathrm{e}^{x(A+B)} = \mathrm{e}^{xA}\mathrm{e}^{xB} + \mathrm{O}(x^2) \,, \tag{1}$$

where x is a parameter and A and B are arbitrary operators with some commutation relation $[A, B] \neq 0$. Here the product of the exponential operators on the right-hand side is regarded as an approximate decomposition of the exponential operator on the left-hand side with correction terms of the second order of x. Mathematicians put (1) in the form

$$\mathrm{e}^{xA}\mathrm{e}^{xB} = \mathrm{e}^{x(A+B)+\mathrm{O}(x^2)} \tag{2}$$

and ask what correction terms appear in the exponent of the right-hand side owing to the product in the left-hand side. They hence refer to it as an exponential product formula. (The readers should convince themselves by the Taylor expansion that the second-order correction in (1) is the same as that in (2). The higher-order corrections take different forms.)

We here ask how we can generalize the Trotter formula (1) to decompositions with higher-order correction terms. We concentrate on the form

$$\mathrm{e}^{x(A+B)} = \mathrm{e}^{p_1 xA}\mathrm{e}^{p_2 xB}\mathrm{e}^{p_3 xA}\mathrm{e}^{p_4 xB}\cdots\mathrm{e}^{p_M xB} + \mathrm{O}(x^{m+1}) \,, \tag{3}$$

or equivalently

$$\mathrm{e}^{p_1 xA}\mathrm{e}^{p_2 xB}\mathrm{e}^{p_3 xA}\mathrm{e}^{p_4 xB}\cdots\mathrm{e}^{p_M xB} = \mathrm{e}^{x(A+B)+\mathrm{O}(x^{m+1})} \,. \tag{4}$$

N. Hatano and M. Suzuki: *Finding Exponential Product Formulas of Higher Orders*, Lect. Notes Phys. **679**, 37–68 (2005)
www.springerlink.com

We adjust the set of the parameters $\{p_1, p_2, \ldots, p_M\}$ so that the correction term may be of the order of x^{m+1}. We refer to the right-hand side of (3) as an mth-order approximant in the sense that it is correct up to the mth order of x. (See Appendix A for another type of the exponential product formula.)

One of the present authors (M.S.) has studied on the higher-order approximant continually [4, 5, 6, 7, 8, 9, 10, 11, 12, 13, 14, 15, 16, 17, 18, 19, 20, 21, 22, 23, 24, 25, 26, 27, 28, 29, 30, 31, 32, 33, 34, 35, 36, 37]. The present article mostly reviews his work on the subject. We first show the importance of the exponential operator in Sect. 2 and the effectiveness of the exponential product formula in Sect. 3. We demonstrate the effectiveness in examples of the time-evolution operator in quantum dynamics and the symplectic integrator in Hamilton dynamics. Section 4 explains a recursive way of constructing higher-order approximants, namely the fractal decomposition. We present in Sect. 5 an application of the fractal decomposition to the time-ordered exponential. We finally review in Sect. 6 the quantum analysis, an efficient way of computing correction terms of general orders algebraically. We can use the quantum analysis for the purpose of finding approximants of an arbitrarily high order by solving a set of simultaneous equations where the higher-order correction terms are put to zero. We demonstrate the prescription in three examples. We mention in Appendix A, a type of the exponential product formula different from the form (3); it contains exponentials of commutation relations. We give in Appendix B, a short review on the world-line quantum Monte Carlo method with the use of the Trotter approximation (1).

2 Why Do We Need the Exponential Product Formula?

First of all, we discuss as to why we have to treat the exponential operator and why we need an approximant in order to treat the exponential operator. The exponential operator appears in various fields of physics as a formal solution of the differential equation of the form

$$\frac{\partial}{\partial t} f(t) = \mathcal{M} f(t) \,, \tag{5}$$

where f is a function or a vector and $\mathcal{M}$ is an operator or a matrix. Typical examples are the Schrödinger equation

$$\mathrm{i}\frac{\partial}{\partial t}\psi(x,t) = \mathcal{H}\psi(x,t) \tag{6}$$

(we put $\hbar = 1$ here and hereafter), the Hamilton equation

$$\frac{\mathrm{d}}{\mathrm{d}t}\begin{pmatrix} \boldsymbol{p}(t) \\ \boldsymbol{q}(t) \end{pmatrix} = \mathcal{H}\begin{pmatrix} \boldsymbol{p}(t) \\ \boldsymbol{q}(t) \end{pmatrix} \,, \tag{7}$$

(see (14) below) and the diffusion equation with a potential

$$\frac{\mathrm{d}}{\mathrm{d}t}P(x,t) = \mathcal{L}P(x,t) \ . \tag{8}$$

A solution of (5) is given in the form of the Green's function as

$$f(t) = G(t;0)f(0) = \mathrm{e}^{t\mathcal{M}}f(0) \ , \tag{9}$$

although it is only a formal solution; obtaining the Green's function $G(t;0) \equiv \mathrm{e}^{t\mathcal{M}}$ is just as difficult as solving the equation (5) in any other way. Another important incident of the exponential operator is the partition function in equilibrium quantum statistical physics:

$$Z = \mathrm{Tr}\,\mathrm{e}^{-\beta\mathcal{H}} \ , \tag{10}$$

where $\mathcal{H}$ is a quantum Hamiltonian.

The exponential operator, however, is hard to compute in many interesting cases. The most straightforward way of computing the exponential operator $\mathrm{e}^{x\mathcal{M}}$ is to diagonalize the operator $\mathcal{M}$. In quantum many-body problems, however, the basis of the diagonalized representation is often nontrivial, because we are typically interested in the Hamiltonian with two terms or more that are mutually non-commutative; for example, the Ising model in a transverse field,

$$\mathcal{H} = -\sum_{\langle i,j\rangle} J_{ij}\sigma_i^z\sigma_j^z - \Gamma\sum_i \sigma_i^x \ , \tag{11}$$

and the Hubbard model,

$$\mathcal{H} = -t\sum_{\sigma=\uparrow,\downarrow}\sum_{\langle i,j\rangle}\left(c_{i\sigma}^\dagger c_{j\sigma} + c_{j\sigma}^\dagger c_{i\sigma}\right) + U\sum_i n_{i\uparrow}n_{i\downarrow} \ . \tag{12}$$

In the first example (11), the quantization axis of the first term is the spin z axis, while that of the second term is the spin x axis. The two terms are therefore mutually non-commutative. In the second example (12), the first term is diagonalizable in the momentum space, whereas the second term is diagonalizable in the coordinate space. In both examples, each term is easily diagonalizable. Since one quantization axis is different from the other, the diagonalization of the sum of the terms becomes suddenly difficult.

The same situation arises in chaotic Hamilton dynamics. Consider a classical Hamiltonian

$$H(\boldsymbol{p},\boldsymbol{q}) = K(\boldsymbol{p}) + V(\boldsymbol{q}) \ , \tag{13}$$

where $K(\boldsymbol{p})$ is the kinetic term and $V(\boldsymbol{q})$ is the potential term. The Hamilton equation is expressed in the form

$$\frac{\mathrm{d}}{\mathrm{d}t}\begin{pmatrix}\boldsymbol{p}(t)\\ \boldsymbol{q}(t)\end{pmatrix} = \begin{pmatrix}-\frac{\mathrm{d}}{\mathrm{d}\boldsymbol{q}}V(\boldsymbol{q})\\ \frac{\mathrm{d}}{\mathrm{d}\boldsymbol{p}}K(\boldsymbol{p})\end{pmatrix} \equiv \begin{pmatrix}0 & -\hat{V}\cdot\\ \hat{K}\cdot & 0\end{pmatrix}\begin{pmatrix}\boldsymbol{p}\\ \boldsymbol{q}\end{pmatrix} \ , \tag{14}$$

where the operators $\hat{K}\cdot$ and $\hat{V}\cdot$ are symbolic ones standing for the operations

$$\hat{K}\cdot\boldsymbol{p} \equiv \frac{\mathrm{d}}{\mathrm{d}\boldsymbol{p}}K(\boldsymbol{p}) \qquad \text{and} \qquad \hat{V}\cdot\boldsymbol{q} \equiv \frac{\mathrm{d}}{\mathrm{d}\boldsymbol{q}}V(\boldsymbol{q})\ . \tag{15}$$

Although each operation of $\hat{K}\cdot$ and $\hat{V}\cdot$ is simple enough, the "Hamiltonian" operator

$$\mathcal{H} \equiv \begin{pmatrix} & -\hat{V}\cdot \\ \hat{K}\cdot & \end{pmatrix} \tag{16}$$

is not easily tractable. This is because the kinetic part and the potential part,

$$\mathcal{K} \equiv \begin{pmatrix} & \\ \hat{K}\cdot & \end{pmatrix} \qquad \text{and} \qquad \mathcal{V} \equiv \begin{pmatrix} & -\hat{V}\cdot \\ & \end{pmatrix}\ , \tag{17}$$

do not commute with each other; see an example in Sect. 3.2 below.

To summarize this section, we frequently encounter the situation where the exponential operator of each term, e^{xA} and e^{xB}, is easily obtained and yet the desired exponential operator $\mathrm{e}^{x(A+B)}$ is hard to come. This is the situation where the Trotter decomposition (1) becomes useful.

3 Why is the Exponential Product Formula a Good Approximant?

We discussed in the previous section the importance of the exponential operator and the necessity of a way of treating it. We here discuss a remarkable advantage of the Trotter approximant to the exponential operator.

Let us first confirm that the Trotter approximant (1) is indeed a first-order approximant. By expanding the both sides of (1), we have

$$\begin{aligned} \mathrm{e}^{x(A+B)} &= I + x(A+B) + \frac{1}{2}x^2(A+B)^2 + \mathrm{O}(x^3) \\ &= I + x(A+B) + \frac{1}{2}x^2\left(A^2 + AB + BA + B^2\right) + \mathrm{O}(x^3)\ , \qquad (18) \\ \mathrm{e}^{xA}\mathrm{e}^{xB} &= \left(I + xA + \frac{1}{2}x^2A^2 + \mathrm{O}(x^3)\right)\left(I + xB + \frac{1}{2}x^2B^2 + \mathrm{O}(x^3)\right) \\ &= I + x(A+B) + \frac{1}{2}x^2\left(A^2 + 2AB + B^2\right) + \mathrm{O}(x^3)\ , \qquad (19) \end{aligned}$$

where I is the identity operator. The difference between the two comes from the fact that in the approximant (19), the operator A always comes on the left of the operator B. Hence we obtain

$$\mathrm{e}^{xA}\mathrm{e}^{xB} = \mathrm{e}^{x(A+B)+\frac{1}{2}x^2[A,B]+\mathrm{O}(x^3)}\ . \tag{20}$$

In the actual application of the approximant, we divide the parameter x into n slices in the form

$$\left(\mathrm{e}^{\frac{x}{n}A}\mathrm{e}^{\frac{x}{n}B}\right)^n = \left[\mathrm{e}^{\frac{x}{n}(A+B)+\frac{1}{2}\left(\frac{x}{n}\right)^2[A,B]+\mathrm{O}\left(\left(\frac{x}{n}\right)^3\right)}\right]^n = \mathrm{e}^{x(A+B)+\frac{1}{2}\frac{x^2}{n}[A,B]+\mathrm{O}\left(\frac{x^3}{n^2}\right)} . \tag{21}$$

Thus the correction term vanishes in the limit $n \to \infty$. We refer to the integer n as the Trotter number.

Now we discuss as to why we should be interested in generalizing the Trotter approximation. The Trotter approximant (1) and the generalized one (3), in fact, have a remarkable advantage over other approximants such as the frequently used one

$$\mathrm{e}^{x(A+B)} = I + x(A+B) + \mathrm{O}(x^2) . \tag{22}$$

The approximant of the form (3) conserves an important symmetry of the system in problems of quantum dynamics and Hamilton dynamics.

In problems of quantum dynamics, the exponential operator, or the Green's function $\mathrm{e}^{-\mathrm{i}t\mathcal{H}}$ is a unitary operator; hence the norm of the wave function does not change, which corresponds to the charge conservation. We here emphasize that the exponential product

$$\mathrm{e}^{-\mathrm{i}tp_1A}\mathrm{e}^{-\mathrm{i}tp_2B}\mathrm{e}^{-\mathrm{i}tp_3A}\cdots\mathrm{e}^{-\mathrm{i}tp_MB} \tag{23}$$

is also a unitary operator. The perturbational approximant (22), on the other hand, does not conserve the norm of the wave function; in fact, the norm typically increases monotonically as the time passes as we demonstrate in Sect. 3.1 below.

In problems of Hamilton dynamics, the time evolution of the Hamilton system conserves the volume in the phase space $\{\boldsymbol{p}, \boldsymbol{q}\}$, which is called the symplecticity in mathematics. The exponential product formula, in general, also has the symplecticity.

The time evolution of the Hamilton equation (14) is described by the exponential operator

$$\begin{pmatrix} \boldsymbol{p}(t) \\ \boldsymbol{q}(t) \end{pmatrix} = \mathrm{e}^{t\mathcal{H}} \begin{pmatrix} \boldsymbol{p}(0) \\ \boldsymbol{q}(0) \end{pmatrix} , \tag{24}$$

where $\mathcal{H}$ is the "Hamiltonian" operator (16). The Trotter decomposition approximates the time evolution with the operator

$$\mathrm{e}^{t\mathcal{H}} \simeq \left(\mathrm{e}^{\frac{t}{n}\mathcal{K}}\mathrm{e}^{\frac{t}{n}\mathcal{V}}\right)^n \tag{25}$$

with $\mathcal{K}$ and $\mathcal{V}$ given by (17). The operator $\mathrm{e}^{\frac{t}{n}\mathcal{K}}$ describes the time evolution over the time slice t/n of a Hamilton system with only the kinetic energy $K(p)$. It thereby conserves the phase-space volume, so does the operator $\mathrm{e}^{\frac{t}{n}\mathcal{V}}$. The whole Trotter approximant therefore conserves the phase-space volume. This holds for any exponential product formula in the form (3) as well. Hence the exponential product formula, when used in the Hamilton dynamics, is sometimes called a symplectic integrator.

In equilibrium quantum statistical physics, the operator $\mathrm{e}^{-\beta\mathcal{H}}$ does not have a particular symmetry except the symmetries of the Hamiltonian itself. The above advantage of the exponential product formula is hence lost when applied to numerical calculations of the partition function $Z = \mathrm{Tr}\,\mathrm{e}^{-\beta\mathcal{H}}$. In fact, in applying the higher-order decomposition (3) to the world-line quantum Monte Carlo simulation, some of the parameters $\{p_1, p_2, \ldots, p_M\}$ are negative, which causes the negative-sign problem in systems that usually do not have the negative-sign problem [38]. The negative-sign problem is the problem that the Boltzmann weight of the system to be simulated becomes negative for some configurations.

Thanks to a recent development of the world-line quantum Monte Carlo simulation [39], the higher-order decomposition is not necessary anymore in some cases; the simulation is carried out in the limit $n \to \infty$ from the very beginning and hence the order of the correction term does not matter in such cases. See Appendix B for a brief review over the recent development.

3.1 Example: Spin Precession

The fact that the exponential product formula keeps the symmetry of the system is one of its remarkable advantages. In the present and next subsections, we demonstrate that this indeed affects numerical accuracy strongly. In the present subsection, we use a simple example of quantum dynamics, namely the spin precession.

Consider the simple Hamiltonian

$$\mathcal{H} = \sigma_z + \Gamma\sigma_x = \begin{pmatrix} 1 & \Gamma \\ \Gamma & -1 \end{pmatrix} . \tag{26}$$

If we start the dynamics from the up-spin state

$$\psi(0) = \begin{pmatrix} 1 \\ 0 \end{pmatrix} , \tag{27}$$

the spin precesses around the axis of the magnetic field $\boldsymbol{H} = (\Gamma, 0, 1)$ with the period

$$T = \frac{\pi}{\sqrt{1+\Gamma^2}} . \tag{28}$$

Although it is easy to compute the dynamics exactly, we here use the Trotter approximant

$$G(t+\Delta t; t) \simeq \mathrm{e}^{-\mathrm{i}\Delta t\sigma_z}\mathrm{e}^{-\mathrm{i}\Delta t\Gamma\sigma_x} \tag{29}$$

and the perturbational approximant

$$G(t+\Delta t; t) \simeq I - \mathrm{i}\Delta t\mathcal{H} = I - \mathrm{i}\Delta t(\sigma_z + \Gamma\sigma_x) . \tag{30}$$

The exact dynamics should conserve the energy expectation $\langle\mathcal{H}\rangle$. Figure 1 shows the energy deviation due to the approximations. The error in the energy

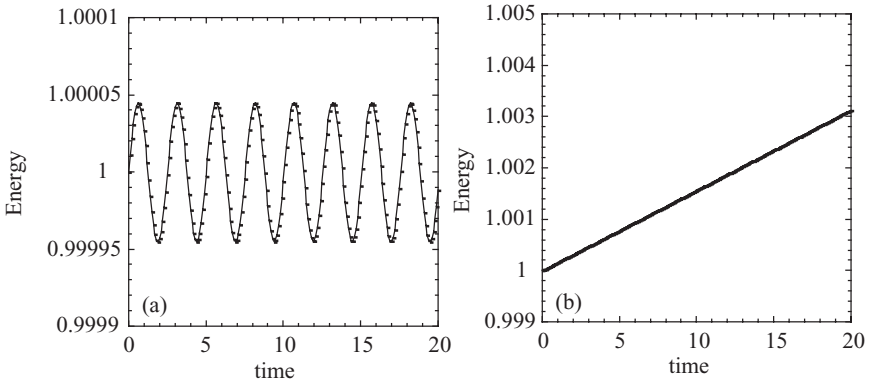

Fig. 1. The energy deviation due to the approximations given by (**a**) the Trotter approximant (29) and (**b**) the perturbational approximant (30). In both calculations, we put $\Gamma = 3/4$ and $\Delta t = 0.0001$. The initial state is the one in (27) with the energy expectation $\langle \mathcal{H} \rangle = 1$

of the Trotter approximation (29) oscillates periodically and never increases beyond the oscillation amplitude. The period of the oscillation in Fig. 1(a) is equal to that of the spin precession. We can understand this as follows: when the spin comes back to the original position after one cycle of the precession, it comes back accurately to the initial state (27) because of the unitarity of the Trotter approximation, and hence the oscillation.

In contrast, the error in the energy monotonically grows in the case of the perturbational approximant as is shown in Fig. 1(b). This is because the norm of the wave vector increases by the factor

$$\| \, 1 - \mathrm{i}\Delta t \mathcal{H} \, \| \simeq 1 + \Delta t \, \| \, \mathcal{H} \, \| > 1 \, . \tag{31}$$

The remarkable difference between Fig. 1(a) and Fig. 1(b) thus comes from the fact that the Trotter approximant is unitary.

3.2 Example: Symplectic Integrator

We next demonstrate the Trotter decomposition (25) in an interesting example of chaotic dynamics. We again emphasize that keeping the symplecticity of the Hamilton dynamics has an important effect on numerical accuracy.

Let us first notice that the operators in (17) satisfy

$$\mathcal{K}^2 = \mathcal{V}^2 = 0 \, . \tag{32}$$

We therefore have

$$\mathrm{e}^{\mathcal{K}\Delta t} \begin{pmatrix} \boldsymbol{p} \\ \boldsymbol{q} \end{pmatrix} = (I + \mathcal{K}\Delta t) \begin{pmatrix} \boldsymbol{p} \\ \boldsymbol{q} \end{pmatrix} = \begin{pmatrix} \boldsymbol{p} \\ \boldsymbol{q} + \Delta t \frac{\mathrm{d}}{\mathrm{d}\boldsymbol{p}} K(\boldsymbol{p}) \end{pmatrix} , \tag{33}$$

$$\mathrm{e}^{\mathcal{V}\Delta t} \begin{pmatrix} \boldsymbol{p} \\ \boldsymbol{q} \end{pmatrix} = (I + \mathcal{V}\Delta t) \begin{pmatrix} \boldsymbol{p} \\ \boldsymbol{q} \end{pmatrix} = \begin{pmatrix} \boldsymbol{p} - \Delta t \frac{\mathrm{d}}{\mathrm{d}\boldsymbol{q}} V(\boldsymbol{q}) \\ \boldsymbol{q} \end{pmatrix} \, . \tag{34}$$

Note that applying the two operators in the order $e^{\mathcal{K}\Delta t}e^{\mathcal{V}\Delta t}$ is different from applying them in the order $e^{\mathcal{V}\Delta t}e^{\mathcal{K}\Delta t}$; in the former, the update of $\boldsymbol{q}$ in the application of $e^{\mathcal{K}\Delta t}$ is done under the updated $\boldsymbol{p}$, whereas in the latter, it is done under $\boldsymbol{p}$ before the update.

Umeno and Suzuki [11, 12] demonstrated the use of symplectic integrators for chaotic dynamics of the system

$$K(\boldsymbol{p}) = \frac{1}{2}\left({p_1}^2 + {p_2}^2\right) \qquad \text{and} \qquad V(\boldsymbol{q}) = \frac{1}{2}{q_1}^2{q_2}^2 \,. \tag{35}$$

The equipotential contour is given by $|q_1 q_2|$ =constant; hence the system is confined in the area surrounded by four hyperbolas as exemplified in Fig. 2(a). The exact dynamics should conserve the energy. The Trotter approximation of the dynamics, (25), gives the energy fluctuation shown in Fig. 2(b). The energy, though deviates from the correct value sometimes, comes back after the deviation. In fact, the deviation occurs when the system goes into one of

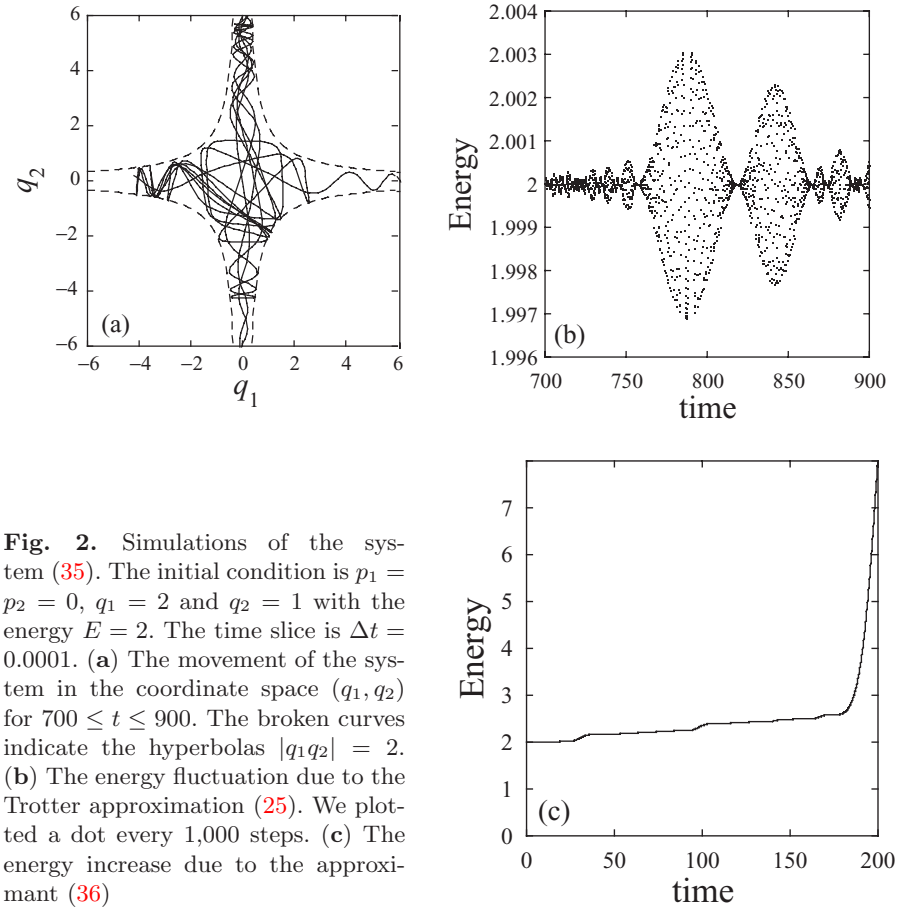

Fig. 2. Simulations of the system (35). The initial condition is $p_1 = p_2 = 0$, $q_1 = 2$ and $q_2 = 1$ with the energy $E = 2$. The time slice is $\Delta t = 0.0001$. (**a**) The movement of the system in the coordinate space (q_1, q_2) for $700 \le t \le 900$. The broken curves indicate the hyperbolas $|q_1 q_2| = 2$. (**b**) The energy fluctuation due to the Trotter approximation (25). We plotted a dot every 1,000 steps. (**c**) The energy increase due to the approximant (36)

the four narrow valleys of the potential; it is suppressed again and again when the system comes back to the central area.

This is in striking contrast to the update due to the perturbational approximant

$$\begin{pmatrix} \boldsymbol{p} \\ \boldsymbol{q} \end{pmatrix} \longrightarrow (I + \Delta t \mathcal{H}) \begin{pmatrix} \boldsymbol{p} \\ \boldsymbol{q} \end{pmatrix} = \begin{pmatrix} \boldsymbol{p} - \Delta t \frac{\mathrm{d}}{\mathrm{d}\boldsymbol{q}} V(\boldsymbol{q}) \\ \boldsymbol{q} + \Delta t \frac{\mathrm{d}}{\mathrm{d}\boldsymbol{p}} K(\boldsymbol{p}) \end{pmatrix} , \tag{36}$$

which yields the monotonic energy increase shown in Fig. 2(c). The reason of the difference between the approximants, though less apparent than in the case of the previous subsection, must be keeping the symplecticity, or the conservation of the phase-space volume.

4 Fractal Decomposition

We emphasized in the previous section the importance of the exponential product formula. In the present section, we describe a way of constructing higher-order exponential product formulas *recursively* [5, 6, 7, 8, 9, 10, 11, 12, 13, 14].

The easiest improvement of the Trotter formula (2) is the symmetrization:

$$S_2(x) \equiv \mathrm{e}^{\frac{x}{2}A} \mathrm{e}^{xB} \mathrm{e}^{\frac{x}{2}A} = \mathrm{e}^{x(A+B)+x^3 R_3 + x^5 R_5 + \cdots} . \tag{37}$$

The symmetrized approximant has the property

$$S_2(x) S_2(-x) = \mathrm{e}^{\frac{x}{2}A} \mathrm{e}^{xB} \mathrm{e}^{\frac{x}{2}A} \mathrm{e}^{-\frac{x}{2}A} \mathrm{e}^{-xB} \mathrm{e}^{-\frac{x}{2}A} = I , \tag{38}$$

because of which the even-order terms vanish in the exponent of the right-hand side of (37). We can thereby promote the approximant (37) to a second-order approximant.

Now we introduce a way of constructing a symmetrized fourth-order approximant from the symmetrized second-order approximant (37). Consider a product

$$S(x) \equiv S_2(sx) S_2((1-2s)x) S_2(sx) \tag{39}$$

$$= \mathrm{e}^{\frac{s}{2}xA} \mathrm{e}^{sxB} \mathrm{e}^{\frac{1-s}{2}xA} \mathrm{e}^{(1-2s)xB} \mathrm{e}^{\frac{1-s}{2}xA} \mathrm{e}^{sxB} \mathrm{e}^{\frac{s}{2}xA} , \tag{40}$$

where s is an arbitrary real number for the moment. The expression (37) is followed by

$$\begin{aligned} S(x) &= S_2(sx) S_2((1-2s)x) S_2(sx) \\ &= \mathrm{e}^{sx(A+B)+s^3x^3R_3+\mathrm{O}(x^5)} \mathrm{e}^{(1-2s)x(A+B)+(1-2s)^3x^3R_3+\mathrm{O}(x^5)} \\ &\quad \times \mathrm{e}^{sx(A+B)+s^3x^3R_3+\mathrm{O}(x^5)} \\ &= \mathrm{e}^{x(A+B)+\left[2s^3+(1-2s)^3\right]R_3+\mathrm{O}(x^5)} . \end{aligned} \tag{41}$$

(The readers should convince themselves by the Taylor expansion that the third-order correction in the exponent of the last line is just the sum of the third-order corrections in the exponents of the second line. This is not true for higher-order corrections.) Note that we arranged the parameters in the form $\{s, 1-2s, s\}$ in (39) so that (i) the first-order term in the exponent of the last line of (41) should become $x(A+B)$ and (ii) the whole product $S(x)$ should be symmetrized, or should satisfy $S(x)S(-x) = I$. Because of the second property, the even-order corrections vanish in the exponent of the last line of (41). Making the parameter s a solution of the equation

$$2s^3 + (1-2s)^3 = 0, \quad \text{or} \quad s = \frac{1}{2 - \sqrt[3]{2}} = 1.351207191959657\cdots , \tag{42}$$

we promote the product (39) to a fourth-order approximant [5].

Following the same line of thought, we come up with another fourth-order approximant [5] in the form

$$\begin{aligned} S_4(x) &\equiv S_2(s_2x)^2 S_2((1-4s_2)x) S_2(s_2x)^2 \qquad (43)\\ &= \mathrm{e}^{\frac{s_2}{2}xA}\mathrm{e}^{s_2xB}\mathrm{e}^{s_2xA}\mathrm{e}^{s_2xB}\mathrm{e}^{\frac{1-3s_2}{2}xA}\mathrm{e}^{(1-4s_2)xB}\mathrm{e}^{\frac{1-3s_2}{2}xA} \\ &\quad \times \mathrm{e}^{s_2xB}\mathrm{e}^{s_2xA}\mathrm{e}^{s_2xB}\mathrm{e}^{\frac{s_2}{2}xA} , \qquad (44) \end{aligned}$$

where the parameter s_2 is a solution of the equation

$$4{s_2}^3 + (1-4s_2)^3 = 0, \quad \text{or} \quad s_2 = \frac{1}{4 - \sqrt[3]{4}} = 0.414490771794375\cdots . \tag{45}$$

We can compare the fourth-order approximants (39) and (43) using the following diagram. Suppose that the exponential operator $\mathrm{e}^{x(A+B)}$ is a time-evolution operator from the time $t = 0$ to the time $t = x$. In the product (39), the term $S_2(sx)$ on the right approximates the time evolution from $t = 0$ to $t = sx \simeq 1.35x$, the term $S_2((1-2s)x)$ in the middle approximates the time evolution from $t = sx$ to $t = sx + (1-2s)x = (1-s)x \simeq -0.35x$, and the term $S_2(sx)$ on the left approximates the time evolution from $t = (1-s)x$ to $t = (1-s)x + sx = x$. Let us express this time evolution as in Fig. 3(a). The product (43) is similarly represented as in Fig. 3(b).

As is evident, the first product (39) has a part that goes into the "past," or $t < 0$. This can be problematic in some situations; in the diffusion from a delta-peak distribution, for example, there exists no "past" of the initial delta peak. The second product (43) does not have the problem and hence is recommended for general use.

Once we know how to construct the fourth-order approximant from the second-order approximant, the rest is quite straightforward [5]. Following the construction (43), we construct the sixth-order approximant in the form

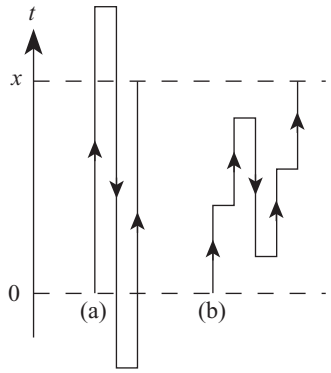

Fig. 3. Diagrams that represent the time evolution of (**a**) the fourth-order approximant (39) and (**b**) the fourth-order approximant (43)

$$\begin{aligned} S_6(x) &\equiv S_4(s_4x)^2 S_4((1-4s_4)x) S_4(s_4x)^2 \\ &= \left(S_2(s_4s_2x)^2 S_2(s_4(1-4s_2)x) S_2(s_4s_2x)^2\right)^2 \\ &\quad \times S_2((1-4s_4)s_2x)^2 S_2((1-4s_4)(1-4s_2)x) S_2((1-4s_4)s_2x)^2 \\ &\quad \times \left(S_2(s_4s_2x)^2 S_2(s_4(1-4s_2)x) S_2(s_4s_2x)^2\right)^2 \end{aligned} \tag{46}$$

with

$$4s_4^5 + (1-4s_4)^5 = 0, \quad \text{or} \quad s_4 = \frac{1}{4-\sqrt[5]{4}} = 0.373065827733272\cdots, \tag{47}$$

and further construct the eighth-order approximant in the form

$$S_8(x) \equiv S_6(s_6x)^2 S_6((1-4s_6)x) S_6(s_6x)^2 \tag{48}$$

with

$$4s_6^7 + (1-4s_6)^7 = 0, \quad \text{or} \quad s_6 = \frac{1}{4-\sqrt[7]{4}} = 0.359584649349992\cdots. \tag{49}$$

These approximants are represented by the diagrams in Fig. 4. We can continue this recursive procedure, ending up with the exact time evolution, where the diagram ultimately becomes a fractal object. This is why the series of the approximants is called the fractal decomposition. It is an interesting thought that the back-and-forth time evolution in a fractal way reproduces the exact time evolution.

5 Time-Ordered Exponential

Before going into another way of constructing higher-order exponential product formulas, let us introduce, as an interlude, an important application of the

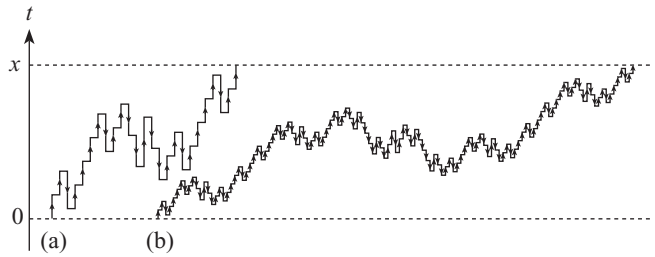

Fig. 4. Diagrams that represent the time evolution of (**a**) the six-order approximant (46) and (**b**) the eighth-order approximant (48)

exponential product formula. We show how to approximate the time-ordered exponential [10].

We have considered until now only the case where the operators A and B do not depend on x, or in other words, only the time evolution of a time-independent Hamiltonian. The fractal decomposition introduced in the previous section needs modification when applied to problems such as the quantum dynamics of a time-dependent Hamiltonian; in quantum annealing [40, 41, 42], for example, the transverse field Γ in the Hamiltonian (11) is changed in time.

The time-evolution operator of the quantum Hamiltonian

$$\mathcal{H}(t) = A(t) + B(t) \tag{50}$$

is not simply $\mathrm{e}^{-\mathrm{i}\mathcal{H}t}$ but a time-ordered exponential in the form

$$G(t_2; t_1) = \mathrm{T}\left[\exp\left(-\mathrm{i}\int_{t_1}^{t_2} \mathcal{H}(s)ds\right)\right] . \tag{51}$$

It is quite well-known that

$$G_1(t + \Delta t; t) \equiv \mathrm{e}^{-\mathrm{i}\Delta t A(t+\Delta t)}\mathrm{e}^{-\mathrm{i}\Delta t B(t+\Delta t)} \tag{52}$$

is an approximant of the first order of Δt and

$$G_2(t + \Delta t; t) \equiv \mathrm{e}^{-\frac{\mathrm{i}}{2}\Delta t A\left(t+\frac{1}{2}\Delta t\right)}\mathrm{e}^{-\mathrm{i}\Delta t B\left(t+\frac{1}{2}\Delta t\right)}\mathrm{e}^{-\frac{\mathrm{i}}{2}\Delta t A\left(t+\frac{1}{2}\Delta t\right)} \tag{53}$$

is an approximant of the second order. How do we construct higher-order approximants? We here show that a slight modification of the fractal decomposition gives the answer.

The key is to introduce a shift-time operator [10] defined in

$$F(t)\mathrm{e}^{-\mathrm{i}\Delta t\mathcal{T}}G(t) = F(t + \Delta t)G(t) . \tag{54}$$

Note that the operator acts on the function on the left. The shift-time operator is expressed in the form

$$\mathcal{T} = \mathrm{i}\,\frac{\overleftarrow{\partial}}{\partial t} \tag{55}$$

in the case where $F(t)$ is an analytic function, but the definition (54) does not limit its use to the analytic case. If we have two shift-time operators, the result is

$$\begin{aligned} F(t)\mathrm{e}^{-\mathrm{i}\Delta t\mathcal{T}}G(t)\mathrm{e}^{-\mathrm{i}\Delta t\mathcal{T}}H(t) &= F(t+\Delta t)G(t)\mathrm{e}^{-\mathrm{i}\Delta t\mathcal{T}}H(t) \\ &= F(t+2\Delta t)G(t+\Delta t)H(t)\,. \end{aligned} \tag{56}$$

With the use of the shift-time operator, the time-ordered exponential (51) is transformed [10] as

$$\mathrm{T}\left[\exp\left(-\mathrm{i}\int_t^{t+\Delta t}\mathcal{H}(s)ds\right)\right] = \mathrm{e}^{-\mathrm{i}\Delta t(\mathcal{H}(t)+\mathcal{T})}\,. \tag{57}$$

We can prove this by using the Trotter approximation as follows:

$$\begin{aligned} \mathrm{e}^{-\mathrm{i}\Delta t(\mathcal{H}(t)+\mathcal{T})} &= \lim_{n\to\infty}\left(\mathrm{e}^{-\mathrm{i}\frac{\Delta t}{n}\mathcal{H}(t)}\mathrm{e}^{-\mathrm{i}\frac{\Delta t}{n}\mathcal{T}}\right)^n \\ &= \lim_{n\to\infty}\mathrm{e}^{-\mathrm{i}\frac{\Delta t}{n}\mathcal{H}(t)}\mathrm{e}^{-\mathrm{i}\frac{\Delta t}{n}\mathcal{T}}\mathrm{e}^{-\mathrm{i}\frac{\Delta t}{n}\mathcal{H}(t)}\mathrm{e}^{-\mathrm{i}\frac{\Delta t}{n}\mathcal{T}}\cdots\mathrm{e}^{-\mathrm{i}\frac{\Delta t}{n}\mathcal{H}(t)}\mathrm{e}^{-\mathrm{i}\frac{\Delta t}{n}\mathcal{T}} \\ &= \lim_{n\to\infty}\mathrm{e}^{-\mathrm{i}\frac{\Delta t}{n}\mathcal{H}(t+\Delta t)}\mathrm{e}^{-\mathrm{i}\frac{\Delta t}{n}\mathcal{H}\left(t+\frac{n-1}{n}\Delta t\right)}\cdots\mathrm{e}^{-\mathrm{i}\frac{\Delta t}{n}\mathcal{H}\left(t+\frac{1}{n}\Delta t\right)} \\ &= \mathrm{T}\left[\exp\left(-\mathrm{i}\int_t^{t+\Delta t}\mathcal{H}(s)ds\right)\right]\,. \end{aligned} \tag{58}$$

Decomposing the Hamiltonian into two parts as in (50), we have now three parts in the exponent of the time-evolution operator as in

$$\mathrm{T}\left[\exp\left(-\mathrm{i}\int_t^{t+\Delta t}\mathcal{H}(s)ds\right)\right] = \mathrm{e}^{-\mathrm{i}\Delta t(A(t)+B(t)+\mathcal{T})}\,. \tag{59}$$

We then approximate the exponential in the right-hand side of (59). The first-order approximant is given by

$$\begin{aligned} G_1(t+\Delta t;t) &= \mathrm{e}^{-\mathrm{i}\Delta tA(t)}\mathrm{e}^{-\mathrm{i}\Delta tB(t)}\mathrm{e}^{-\mathrm{i}\Delta t\mathcal{T}} \\ &= \mathrm{e}^{-\mathrm{i}\Delta tA(t+\Delta t)}\mathrm{e}^{-\mathrm{i}\Delta tB(t+\Delta t)} \end{aligned} \tag{60}$$

and the second-order approximant is given by

$$\begin{aligned} G_2(t+\Delta t;t) &= \mathrm{e}^{-\frac{\mathrm{i}}{2}\Delta t\mathcal{T}}\mathrm{e}^{-\frac{\mathrm{i}}{2}\Delta tA(t)}\mathrm{e}^{-\mathrm{i}\Delta tB(t)}\mathrm{e}^{-\frac{\mathrm{i}}{2}\Delta tA(t)}\mathrm{e}^{-\frac{\mathrm{i}}{2}\Delta t\mathcal{T}} \\ &= \mathrm{e}^{-\frac{\mathrm{i}}{2}\Delta tA\left(t+\frac{1}{2}\Delta t\right)}\mathrm{e}^{-\mathrm{i}\Delta tB\left(t+\frac{1}{2}\Delta t\right)}\mathrm{e}^{-\frac{\mathrm{i}}{2}\Delta tA\left(t+\frac{1}{2}\Delta t\right)}\,. \end{aligned} \tag{61}$$

Higher-order approximants are given by the fractal decomposition of the three parts, A, B, and $\mathcal{T}$. The fractal decomposition of three parts is easily obtained by substituting

$$S_2(x) \equiv \mathrm{e}^{\frac{x}{2}A}\mathrm{e}^{\frac{x}{2}B}\mathrm{e}^{xC}\mathrm{e}^{\frac{x}{2}B}\mathrm{e}^{\frac{x}{2}A} = \mathrm{e}^{x(A+B+C)+\mathrm{O}(x^3)} \tag{62}$$

for (37). The fourth-order approximant is thereby obtained [10] as

$$\begin{aligned}
&G_4(t+\Delta t;t)\\
&\equiv \left(\mathrm{e}^{-\frac{\mathrm{i}}{2}s_2\Delta t\mathcal{T}}\mathrm{e}^{-\frac{\mathrm{i}}{2}s_2\Delta tA(t)}\mathrm{e}^{-\mathrm{i}s_2\Delta tB(t)}\mathrm{e}^{-\frac{\mathrm{i}}{2}s_2\Delta tA(t)}\mathrm{e}^{-\frac{\mathrm{i}}{2}s_2\Delta t\mathcal{T}}\right)^2\\
&\quad\times \mathrm{e}^{-\frac{\mathrm{i}}{2}(1-4s_2)\Delta t\mathcal{T}}\mathrm{e}^{-\frac{\mathrm{i}}{2}(1-4s_2)\Delta tA(t)}\\
&\quad\times \mathrm{e}^{-\mathrm{i}(1-4s_2)\Delta tB(t)}\mathrm{e}^{-\frac{\mathrm{i}}{2}(1-4s_2)\Delta tA(t)}\mathrm{e}^{-\frac{\mathrm{i}}{2}(1-4s_2)\Delta t\mathcal{T}}\\
&\quad\times \left(\mathrm{e}^{-\frac{\mathrm{i}}{2}s_2\Delta t\mathcal{T}}\mathrm{e}^{-\frac{\mathrm{i}}{2}s_2\Delta tA(t)}\mathrm{e}^{-\mathrm{i}s_2\Delta tB(t)}\mathrm{e}^{-\frac{\mathrm{i}}{2}s_2\Delta tA(t)}\mathrm{e}^{-\frac{\mathrm{i}}{2}s_2\Delta t\mathcal{T}}\right)^2\\
&= \mathrm{e}^{-\frac{\mathrm{i}}{2}s_2\Delta tA\left(t+\frac{2-s_2}{2}\Delta t\right)}\mathrm{e}^{-\mathrm{i}s_2\Delta tB\left(t+\frac{2-s_2}{2}\Delta t\right)}\mathrm{e}^{-\frac{\mathrm{i}}{2}s_2\Delta tA\left(t+\frac{2-s_2}{2}\Delta t\right)}\\
&\quad\times \mathrm{e}^{-\frac{\mathrm{i}}{2}s_2\Delta tA\left(t+\frac{2-3s_2}{2}\Delta t\right)}\mathrm{e}^{-\mathrm{i}s_2\Delta tB\left(t+\frac{2-3s_2}{2}\Delta t\right)}\mathrm{e}^{-\frac{\mathrm{i}}{2}s_2\Delta tA\left(t+\frac{2-3s_2}{2}\Delta t\right)}\\
&\quad\times \mathrm{e}^{-\frac{\mathrm{i}}{2}s_2\Delta tA\left(t+\frac{1}{2}\Delta t\right)}\mathrm{e}^{-\mathrm{i}s_2\Delta tB\left(t+\frac{1}{2}\Delta t\right)}\mathrm{e}^{-\frac{\mathrm{i}}{2}s_2\Delta tA\left(t+\frac{1}{2}\Delta t\right)}\\
&\quad\times \mathrm{e}^{-\frac{\mathrm{i}}{2}s_2\Delta tA\left(t+\frac{3s_2}{2}\Delta t\right)}\mathrm{e}^{-\mathrm{i}s_2\Delta tB\left(t+\frac{3s_2}{2}\Delta t\right)}\mathrm{e}^{-\frac{\mathrm{i}}{2}s_2\Delta tA\left(t+\frac{3s_2}{2}\Delta t\right)}\\
&\quad\times \mathrm{e}^{-\frac{\mathrm{i}}{2}s_2\Delta tA\left(t+\frac{s_2}{2}\Delta t\right)}\mathrm{e}^{-\mathrm{i}s_2\Delta tB\left(t+\frac{s_2}{2}\Delta t\right)}\mathrm{e}^{-\frac{\mathrm{i}}{2}s_2\Delta tA\left(t+\frac{s_2}{2}\Delta t\right)}
\end{aligned} \tag{63}$$

with the coefficient s_2 given by (45).

6 Quantum Analysis – Towards the Construction of General Decompositions

In the last section before the summary, we discuss the calculus of the correction terms. In the fractal decomposition, we construct higher-order approximants recursively. Is it possible to construct higher-order approximants *directly*, not recursively? In fact, Ruth [43] found (not systematically) a third-order formula

$$\mathrm{e}^{\frac{7}{24}xA}\mathrm{e}^{\frac{2}{3}xB}\mathrm{e}^{\frac{3}{4}xA}\mathrm{e}^{-\frac{2}{3}xB}\mathrm{e}^{-\frac{1}{24}xA}\mathrm{e}^{xB} = \mathrm{e}^{x(A+B)+\mathrm{O}(x^4)}\ , \tag{64}$$

which would not be found within the framework of the fractal decomposition.

For the purpose of finding higher-order formulas directly, we need to compute the correction terms in the exponent as

$$\mathrm{e}^{p_1xA}\mathrm{e}^{p_2xB}\mathrm{e}^{p_3xA}\mathrm{e}^{p_4xB}\cdots\mathrm{e}^{p_MxB} = \mathrm{e}^{x(A+B)+x^2R_2+x^3R_3+\cdots}\ . \tag{65}$$

This is one of the aims of the quantum analysis developed by one of the present authors (M.S.) [29, 30, 31, 32, 33, 34, 35]. Then we can put the correction terms to zero up to a desired order and solve the set of non-linear simultaneous equations

$$R_2 = 0, \qquad R_3 = 0, \ldots, R_m = 0\ , \tag{66}$$

thereby obtaining the parameters $\{p_i\}$.

6.1 Operator Differential

The main feature of the quantum analysis is to introduce operator differential. In order to motivate the readers, suppose that we can write down an identity

$$\frac{\mathrm{d}}{\mathrm{d}x} f(A(x)) = \frac{\mathrm{d}f(A)}{\mathrm{d}A} \cdot \frac{\mathrm{d}A(x)}{\mathrm{d}x} \ , \tag{67}$$

where $f(A)$ is an operator functional. The derivative with respect to x on the right-hand side is well-defined; for example, $\mathrm{d}A(x)/\mathrm{d}x = B + 2xC$ for $A(x) = xB + x^2C$. Now, is it possible to define the differentiation $\mathrm{d}f(A)/\mathrm{d}A$?

Let us discuss as to what should be the definition of the operator differential in order for the identity (67) to hold. The definition of the x derivative is expressed as

$$A(x+h) = A(x) + h\frac{\mathrm{d}A(x)}{\mathrm{d}x} + \mathrm{O}(h^2) \ . \tag{68}$$

The left-hand side of the identity (67) is given by the definition of the derivative as

$$\begin{aligned} \frac{\mathrm{d}}{\mathrm{d}x} f(A(x)) &= \lim_{h\to 0} \frac{f(A(x+h)) - f(A(x))}{h} \\ &= \lim_{h\to 0} \frac{f\left(A(x) + h\frac{\mathrm{d}A(x)}{\mathrm{d}x}\right) - f(A(x))}{h} \ . \end{aligned} \tag{69}$$

The identity (67) suggests that the operator differential $\mathrm{d}f(A)/\mathrm{d}A$ must be a hyperoperator that maps the operator $\mathrm{d}A(x)/\mathrm{d}x$ to the operator given by (69).

Thus we arrive at the definition of the operator differential within the framework of the quantum analysis [29]: if we can express the operator given by

$$\mathrm{d}f(A) \equiv \lim_{h\to 0} \frac{f(A + h\mathrm{d}A) - f(A)}{h} \tag{70}$$

in terms of a hyperoperator mapping from an arbitrary operator $\mathrm{d}A$ as in $\mathrm{d}A \longrightarrow \mathrm{d}f(A)$, then we refer to the hyperoperator as an operator differential $\mathrm{d}f(A)/\mathrm{d}A$ and denote it in the form

$$\mathrm{d}f(A) = \frac{\mathrm{d}f(A)}{\mathrm{d}A} \cdot \mathrm{d}A \ . \tag{71}$$

We stress here that the operator differential $\mathrm{d}f(A)/\mathrm{d}A$ must be expressed in terms of A and the commutation relation of A, or the "inner derivation"

$$\delta_A \equiv [A, \quad] \ , \tag{72}$$

but *not* in terms of the arbitrary operator $\mathrm{d}A$. The convergence of (70) is in the sense of the norm convergence which is uniform with respect to the arbitrary operator $\mathrm{d}A$.

Let us consider the application of the above in a simple example $f(A) = A^2$. The definition (70) is followed by

$$\begin{aligned} \mathrm{d}f(A) &= \lim_{h\to 0} \frac{(A+h\mathrm{d}A)^2 - A^2}{h} = \lim_{h\to 0} \frac{hA\,\mathrm{d}A + h\mathrm{d}A\,A + h^2(\mathrm{d}A)^2}{h} \\ &= A\,\mathrm{d}A + \mathrm{d}A\,A = 2A\,\mathrm{d}A - (A\,\mathrm{d}A - \mathrm{d}A\,A) \\ &= (2A - \delta_A)\,\mathrm{d}A\ . \end{aligned} \tag{73}$$

Thus we have [29]

$$\frac{\mathrm{d}(A^2)}{\mathrm{d}A} = 2A - \delta_A\ . \tag{74}$$

If $A = xB + x^2C$, we use the result (74) for (67) and have

$$\begin{aligned} \frac{\mathrm{d}}{\mathrm{d}x}(xB + x^2C)^2 &= \left(2xB + 2x^2C - \delta_{xB+x^2C}\right)(B + 2xC) \\ &= (2xB + 2x^2C)(B + 2xC) - \left[xB + x^2C, B + 2xC\right] \\ &= 2xB^2 + 4x^2BC + 2x^2CB + 4x^3C^2 \\ &\quad -2x^2(BC - CB) - x^2(CB - BC) \\ &= 2xB^2 + 3x^2BC + 3x^2CB + 4x^3C^2\ , \end{aligned} \tag{75}$$

which is indeed identical to the result of straightforward algebra.

We cannot see in this simple example any merit of the use of the quantum analysis. The readers should wait for more complicated examples given later in Sect. 6.3, where we show that the differential of exponential operators is given in terms of the inner derivation. The Lie algebra is defined by commutation relations, or the inner derivation; it is hence essential to obtain results in terms of the inner derivation, not in terms of naive expansions such as the right-hand side of (75).

6.2 Inner Derivation

We here provide some of the important formulas of the inner derivation (72) as preparation for the next subsection, where we give the differential of exponential operators.

First, we have linearity: for any c-numbers a and b, the inner derivation of the operators A and B satisfies

$$\delta_{aA+bB} = [aA + bB,\quad] = a\,[A,\quad] + b\,[B,\quad] = a\delta_A + b\delta_B\ . \tag{76}$$

Any powers of the operator A are commutable with the inner derivation of any powers of the same operator:

$$[A^m, \delta_{A^n}] = 0\ , \tag{77}$$

because

$$A^m \delta_{A^n} B = A^m \left[A^n, B\right] = \left[A^n, A^m B\right] = \delta_{A^n} A^m B \tag{78}$$

for an arbitrary operator B and any integers m and n. We can generalize the identity (77) to the case of any analytic functions of the operator A:

$$\left[f(A), \delta_{g(A)}\right] = 0 \,, \tag{79}$$

where $f(A)$ and $g(A)$ are defined by the Taylor expansion as

$$f(A) = \sum_{n=0}^{\infty} a_n A^n \qquad \text{and} \qquad g(A) = \sum_{n=0}^{\infty} b_n A^n \,. \tag{80}$$

Next, we prove the identity [29]

$$\delta_{f(A)g(A)} = f(A)\delta_{g(A)} + g(A)\delta_{f(A)} - \delta_{g(A)}\delta_{f(A)} \,. \tag{81}$$

The proof is as follows: for an arbitrary operator B, we have

$$\begin{aligned} & f(A)\delta_{g(A)}B + g(A)\delta_{f(A)}B - \delta_{g(A)}\delta_{f(A)}B \\ & = f(A)\left[g(A), B\right] + g(A)\left[f(A), B\right] - \left[g(A), \left[f(A), B\right]\right] \\ & = f(A)\left[g(A), B\right] + \left[f(A), B\right] g(A) = \left[f(A)g(A), B\right] \\ & = \delta_{f(A)g(A)}B \,. \end{aligned} \tag{82}$$

Note that we can rewrite the identity (81) as

$$\begin{aligned} \delta_{f(A)g(A)} &= \delta_{g(A)} f(A) + g(A)\delta_{f(A)} - \delta_{g(A)}\delta_{f(A)} \\ &= \delta_{g(A)}\left(f(A) - \delta_{f(A)}\right) + g(A)\delta_{f(A)} \end{aligned} \tag{83}$$

because of the identity (79). In the special case $f(A) = A$, we have

$$\delta_{Ag(A)} = \delta_{g(A)}\left(A - \delta_A\right) + g(A)\delta_A \,. \tag{84}$$

With the repeated use of the identity (84), we then prove the identity [29]

$$\delta_{A^n} = A^n - \left(A - \delta_A\right)^n \tag{85}$$

for any integer n. This is proved by means of mathematical induction. The identity (85) indeed holds for $n = 1$. Assume now that

$$\delta_{A^{n-1}} = A^{n-1} - \left(A - \delta_A\right)^{n-1} \,. \tag{86}$$

Then the identity (84) yields

$$\begin{aligned} \delta_{A^n} &= \delta_{AA^{n-1}} = \delta_{A^{n-1}}\left(A - \delta_A\right) + A^{n-1}\delta_A \\ &= \left[A^{n-1} - \left(A - \delta_A\right)^{n-1}\right]\left(A - \delta_A\right) + A^{n-1}\delta_A \\ &= A^n - \left(A - \delta_A\right)^n \,. \end{aligned} \tag{87}$$

An interesting and quite well-known identity is

$$\mathrm{e}^{xA}B\mathrm{e}^{-xA} = \mathrm{e}^{x\delta_A}B\,. \tag{88}$$

We can prove this by differentiating the left-hand side by x. First, note that

$$\frac{\mathrm{d}}{\mathrm{d}x}\mathrm{e}^{xA}B\mathrm{e}^{-xA} = \mathrm{e}^{xA}AB\mathrm{e}^{-xA} - \mathrm{e}^{xA}BA\mathrm{e}^{-xA} = \mathrm{e}^{xA}\,[A,B]\,\mathrm{e}^{-xA}\,. \tag{89}$$

We thereby have the following in each order of x:

$$\left.\frac{\mathrm{d}}{\mathrm{d}x}\mathrm{e}^{xA}B\mathrm{e}^{-xA}\right|_{x=0} = \left.\mathrm{e}^{xA}\,[A,B]\,\mathrm{e}^{-xA}\right|_{x=0} = \delta_A B\,, \tag{90}$$

$$\left.\frac{\mathrm{d}^2}{\mathrm{d}x^2}\mathrm{e}^{xA}B\mathrm{e}^{-xA}\right|_{x=0} = \left.\mathrm{e}^{xA}\,[A,[A,B]]\,\mathrm{e}^{-xA}\right|_{x=0} = {\delta_A}^2 B\,, \tag{91}$$

$$\cdots,$$

which proves the identity (88). As a corollary, we obtain the following identity:

$$\mathrm{e}^{\delta_A}\mathrm{e}^{\delta_B} = \mathrm{e}^{\delta_\Phi} \qquad \text{if} \qquad \mathrm{e}^{A}\mathrm{e}^{B} = \mathrm{e}^{\Phi}\,. \tag{92}$$

The proof is straightforward; for an arbitrary operator C, we have

$$\mathrm{e}^{\delta_A}\mathrm{e}^{\delta_B}C = \mathrm{e}^{A}\mathrm{e}^{B}C\mathrm{e}^{-B}\mathrm{e}^{-A} = \mathrm{e}^{\Phi}C\mathrm{e}^{-\Phi} = \mathrm{e}^{\delta_\Phi}C\,. \tag{93}$$

6.3 Differential of Exponential Operators

We are now in a position to discuss the differential of exponential operators. We begin with the differential of the power of an operator, $f(A) = A^n$, a generalization of the identity (74). The result is [29]

$$\frac{\mathrm{d}\,(A^n)}{\mathrm{d}A} = \frac{A^n - (A-\delta_A)^n}{\delta_A} = \frac{\delta_{A^n}}{\delta_A}\,. \tag{94}$$

An important comment is in order. The identity (94) does not claim that the inverse of δ_A is well-defined. In fact, the inner derivation δ_A in the denominator is canceled when we expand the numerator of the second expression. The denominator is well-defined only in such cases.

We use the identity (85) in the derivation of the identity (94). The definition (70) is followed by

$$\begin{aligned}\mathrm{d}f(A) &= \lim_{h\to 0}\frac{(A+h\mathrm{d}A)^n - A^n}{h} = \sum_{j=1}^{n} A^{j-1}(\mathrm{d}A)A^{n-j} \\ &= \left(nA^{n-1} - \sum_{j=1}^{n} A^{j-1}\delta_{A^{n-j}}\right)\mathrm{d}A\end{aligned}$$

$$= \left\{ nA^{n-1} - \sum_{j=1}^{n} A^{j-1} \left[A^{n-j} - (A - \delta_A)^{n-j} \right] \right\} \mathrm{d}A$$
$$= \sum_{j=1}^{n} A^{j-1} (A - \delta_A)^{n-j} \, \mathrm{d}A = \frac{A^n - (A - \delta_A)^n}{A - (A - \delta_A)} \mathrm{d}A$$
$$= \frac{A^n - (A - \delta_A)^n}{\delta_A} \mathrm{d}A = \frac{\delta_{A^n}}{\delta_A} \mathrm{d}A \, . \tag{95}$$

Note again that the transformation in the fourth line is well-defined only because the expansion of the numerator cancels the denominator.

We can generalize the identity (94) to any analytic functions defined by the Taylor expansion (80). The result is

$$\frac{\mathrm{d}f(A)}{\mathrm{d}A} = \frac{f(A) - f(A - \delta_A)}{\delta_A} = \frac{\delta_{f(A)}}{\delta_A} \, . \tag{96}$$

It is interesting to note that the operator differential or the quantum derivative [10] is expressed by a difference form of hyperoperators. As a special case, we arrive at the identity [29]

$$\frac{\mathrm{d}\mathrm{e}^A}{\mathrm{d}A} = \frac{\mathrm{e}^A - \mathrm{e}^{A - \delta_A}}{\delta_A} = \mathrm{e}^A \frac{1 - \mathrm{e}^{-\delta_A}}{\delta_A} \, . \tag{97}$$

6.4 Example: Baker-Campbell-Hausdorff Formula

We now use the formula (97) for the derivation of the Baker-Campbell-Hausdorff formula, or the derivation of higher-order terms of the exponent $\Phi(x)$ given in

$$\mathrm{e}^{\Phi(x)} = \mathrm{e}^{xA} \mathrm{e}^{xB} \, . \tag{98}$$

The differential of the left-hand side of (98) gives

$$\frac{\mathrm{d}}{\mathrm{d}x} \mathrm{e}^{\Phi(x)} = \frac{\mathrm{d}\mathrm{e}^{\Phi}}{\mathrm{d}\Phi} \cdot \frac{\mathrm{d}\Phi(x)}{\mathrm{d}x} = \mathrm{e}^{\Phi(x)} \frac{1 - \mathrm{e}^{-\delta_{\Phi(x)}}}{\delta_{\Phi(x)}} \frac{\mathrm{d}\Phi(x)}{\mathrm{d}x} \tag{99}$$

owing to (97), while the differential of the right-hand side of (98) gives

$$\frac{\mathrm{d}}{\mathrm{d}x} \mathrm{e}^{xA} \mathrm{e}^{xB} = \mathrm{e}^{xA} A \mathrm{e}^{xB} + \mathrm{e}^{xA} \mathrm{e}^{xB} B = \mathrm{e}^{xA} \mathrm{e}^{xB} \left(\mathrm{e}^{-xB} A \mathrm{e}^{xB} + B \right)$$
$$= \mathrm{e}^{\Phi(x)} \left(\mathrm{e}^{-x\delta_B} A + B \right) \, , \tag{100}$$

where we have used the identity (88). Equating the both sides, we have

$$\frac{\mathrm{d}\Phi(x)}{\mathrm{d}x} = \frac{\delta_{\Phi(x)}}{1 - \mathrm{e}^{-\delta_{\Phi(x)}}} \left(\mathrm{e}^{-x\delta_B} A + B \right) = \frac{\delta_{\Phi(x)}}{\mathrm{e}^{\delta_{\Phi(x)}} - 1} \left(A + \mathrm{e}^{x\delta_A} B \right) \, . \tag{101}$$

The second equality is due to the identity (92).

We can expand the right-hand side of (101) as follows. Note here that

$$\mathrm{e}^{\delta_{\Phi(x)}} = \mathrm{e}^{x\delta_A}\mathrm{e}^{x\delta_B} \qquad \text{yields} \qquad \delta_{\Phi(x)} = \log\left(\mathrm{e}^{x\delta_A}\mathrm{e}^{x\delta_B}\right) . \tag{102}$$

Thus we transform (101) as

$$\begin{aligned}\frac{\mathrm{d}\Phi(x)}{\mathrm{d}x} &= \frac{\log\left(\mathrm{e}^{x\delta_A}\mathrm{e}^{x\delta_B}\right)}{\mathrm{e}^{x\delta_A}\mathrm{e}^{x\delta_B}-1}\left(A+\mathrm{e}^{x\delta_A}B\right) \\ &= \sum_{k=0}^{\infty}\frac{(-1)^k}{k+1}\left(\mathrm{e}^{x\delta_A}\mathrm{e}^{x\delta_B}-1\right)^k\left(A+\mathrm{e}^{x\delta_A}B\right) .\end{aligned} \tag{103}$$

We finally arrive [30] at

$$\Phi(x) = \sum_{k=0}^{\infty}\frac{(-1)^k}{k+1}\int_0^x\left(\mathrm{e}^{t\delta_A}\mathrm{e}^{t\delta_B}-1\right)^k\left(A+\mathrm{e}^{t\delta_A}B\right)dt . \tag{104}$$

It is very important to notice here that all the expansion terms are given by commutation relations. One of the merits of the quantum analysis is to be able to express the expansion in terms of commutation relations.

Let us derive, for example, the term of the third order of x, or the second order of t of (104). Up to the second order, we have

$$\begin{aligned}\mathrm{e}^{t\delta_A}\mathrm{e}^{t\delta_B}-1 &\simeq t\left(\delta_A+\delta_B\right)+\frac{t^2}{2}\left({\delta_A}^2+2\delta_A\delta_B+{\delta_B}^2\right) \\ &= t\delta_{A+B}+\frac{t^2}{2}\left({\delta_{A+B}}^2+\delta_A\delta_B-\delta_B\delta_A\right),\end{aligned} \tag{105}$$

$$\left(\mathrm{e}^{t\delta_A}\mathrm{e}^{t\delta_B}-1\right)^2 \simeq t^2{\delta_{A+B}}^2, \tag{106}$$

and hence

$$\left(\mathrm{e}^{t\delta_A}\mathrm{e}^{t\delta_B}-1\right)^0\left(A+\mathrm{e}^{t\delta_A}B\right) \simeq (A+B)+t\delta_A B+\frac{t^2}{2}{\delta_A}^2B, \tag{107}$$

$$\begin{aligned}\left(\mathrm{e}^{t\delta_A}\mathrm{e}^{t\delta_B}-1\right)^1\left(A+\mathrm{e}^{t\delta_A}B\right) &\simeq t\delta_{A+B}\left(A+B\right) \\ &+\frac{t^2}{2}\left({\delta_{A+B}}^2+\delta_A\delta_B-\delta_B\delta_A\right)(A+B)+t^2\left(\delta_A+\delta_B\right)\delta_A B \\ &= \frac{t^2}{2}\left(\delta_A\delta_B A-\delta_B\delta_A B\right)+t^2\left(\delta_A+\delta_B\right)\delta_A B,\end{aligned} \tag{108}$$

$$\left(\mathrm{e}^{t\delta_A}\mathrm{e}^{t\delta_B}-1\right)^2\left(A+\mathrm{e}^{t\delta_A}B\right) \simeq t^2{\delta_{A+B}}^2(A+B)=0. \tag{109}$$

Summing up the second-order terms with the coefficient $(-1)^k/(k+1)$, we have

$$\frac{t^2}{2}{\delta_A}^2B-\frac{t^2}{4}\left(\delta_A\delta_B A-\delta_B\delta_A B\right)-\frac{t^2}{2}\left(\delta_A+\delta_B\right)\delta_A B=\frac{t^2}{4}\left({\delta_A}^2B+{\delta_B}^2A\right) , \tag{110}$$

which we integrate to obtain

$$\frac{x^3}{12}\left({\delta_A}^2B+{\delta_B}^2A\right)=\frac{x^3}{12}\left([A,[A,B]]+[[A,B],B]\right) . \tag{111}$$

6.5 Example: Ruth's Formula

We now extend the above computation to the exponential product

$$\mathrm{e}^{p_1 x A}\mathrm{e}^{p_2 x B}\mathrm{e}^{p_3 x A}\mathrm{e}^{p_4 x B}\mathrm{e}^{p_5 x A}\mathrm{e}^{p_6 x B} = \mathrm{e}^{\Phi(x)} \tag{112}$$

and seek Ruth's formula (64) as a specific solution of the general formula. We compute the second-order and third-order correction terms of $\Phi(x)$, defined in

$$\Phi(x) = x(A+B) + x^2 R_2 + x^3 R_3 + \mathrm{O}(x^4)\ , \tag{113}$$

and put $R_2 = R_3 = 0$.

The same computation as from (99) through (104) produces

$$\begin{aligned}\Phi(x) = \sum_{k=0}^{\infty} \frac{(-1)^k}{k+1} \int_0^x \left(\mathrm{e}^{p_1 t\delta_A}\mathrm{e}^{p_2 t\delta_B}\mathrm{e}^{p_3 t\delta_A}\mathrm{e}^{p_4 t\delta_B}\mathrm{e}^{p_5 t\delta_A}\mathrm{e}^{p_6 t\delta_B} - 1\right)^k \\ \times \left(p_1 A + \mathrm{e}^{p_1 t\delta_A} p_2 B + \mathrm{e}^{p_1 t\delta_A}\mathrm{e}^{p_2 t\delta_B} p_3 A \cdots\right) dt\ .\end{aligned} \tag{114}$$

Note again that all the terms are given by commutation relations.

For the term $k = 0$, we have up to the second order of x,

$$\begin{aligned}
&p_1 A + \mathrm{e}^{p_1 t\delta_A} p_2 B + \mathrm{e}^{p_1 t\delta_A}\mathrm{e}^{p_2 t\delta_B} p_3 A \cdots \\
&\simeq p_1 A + \left(1 + t p_1\delta_A + \frac{t^2}{2} {p_1}^2 {\delta_A}^2\right) p_2 B \\
&\quad + \left[1 + t\left(p_1\delta_A + p_2\delta_B\right) + \frac{t^2}{2}\left({p_1}^2{\delta_A}^2 + 2p_1p_2\delta_A\delta_B + {p_2}^2{\delta_B}^2\right)\right] p_3 A + \cdots \\
&= \left(p_1 + p_3 + p_5\right) A + \left(p_2 + p_4 + p_6\right) B \\
&\quad + t\left[p_1p_2\delta_A B + p_2p_3\delta_B A + \left(p_1 + p_3\right) p_4\delta_A B\right. \\
&\quad \left. +\ \left(p_2 + p_4\right) p_5\delta_B A + \left(p_1 + p_3 + p_5\right) p_6\delta_A B\right] \\
&\quad + \frac{t^2}{2}\left[p_1^2 p_2 {\delta_A}^2 B + p_2^2 p_3 {\delta_B}^2 A + 2p_1p_2p_3\delta_A\delta_B A + \left(p_1 + p_3\right)^2 p_4 {\delta_A}^2 B\right. \\
&\quad + 2p_2p_3p_4\delta_B\delta_A B + \left(p_2 + p_4\right)^2 p_5 {\delta_B}^2 A \\
&\quad + 2\left(p_1p_2 + p_1p_4 + p_3p_4\right) p_5\delta_A\delta_B A + \left(p_1 + p_3 + p_5\right)^2 p_6 {\delta_A}^2 B \\
&\quad \left. +2\left(p_2p_3 + p_2p_5 + p_4p_5\right) p_6\delta_B\delta_A B\right]\ .
\end{aligned} \tag{115}$$

The zeroth-order term with respect to t appears only here and hence we have the conditions

$$p_1 + p_3 + p_5 = 1 \qquad \text{and} \qquad p_2 + p_4 + p_6 = 1\ . \tag{116}$$

Using (116) and the identity $\delta_B A = -\delta_A B$, we can reduce the right-hand side of (115) as

$$A + B + t(1-2q)\delta_A B + \frac{t^2}{2}\left[(1-q-3r){\delta_A}^2 B + (q-3s){\delta_B}^2 A\right] \tag{117}$$

with

$$q \equiv p_2p_3 + p_2p_5 + p_4p_5 \ , \tag{118}$$
$$r \equiv p_1p_2p_3 + p_1p_2p_5 + p_1p_4p_5 + p_3p_4p_5 \ , \tag{119}$$
$$s \equiv p_2p_3p_4 + p_2p_3p_6 + p_2p_5p_6 + p_4p_5p_6 \ . \tag{120}$$

For $k = 1$, we first have

$$\begin{aligned} &\mathrm{e}^{p_1 t\delta_A}\mathrm{e}^{p_2 t\delta_B}\mathrm{e}^{p_3 t\delta_A}\mathrm{e}^{p_4 t\delta_B}\mathrm{e}^{p_5 t\delta_A}\mathrm{e}^{p_6 t\delta_B} - 1 \\ &\simeq t\delta_{A+B} + \frac{t^2}{2}\left[{\delta_A}^2 + {\delta_B}^2 + 2(1-q)\delta_A\delta_B + 2q\delta_B\delta_A\right] \ , \end{aligned} \tag{121}$$

where we already used the conditions in (116). Applying (121) to (117) and dropping higher-order terms, we note that the first-order term vanishes and have

$$\begin{aligned} &\left(\mathrm{e}^{p_1 t\delta_A}\mathrm{e}^{p_2 t\delta_B}\mathrm{e}^{p_3 t\delta_A}\mathrm{e}^{p_4 t\delta_B}\mathrm{e}^{p_5 t\delta_A}\mathrm{e}^{p_6 t\delta_B} - 1\right) \\ &\quad \times \left(p_1 A + \mathrm{e}^{p_1 t\delta_A}p_2 B + \mathrm{e}^{p_1 t\delta_A}\mathrm{e}^{p_2 t\delta_B}p_3 A \cdots\right) \\ &\simeq t^2(1-2q)\delta_{A+B}\delta_A B + \frac{t^2}{2}\left[{\delta_A}^2 + {\delta_B}^2 + 2(1-q)\delta_A\delta_B + 2q\delta_B\delta_A\right](A+B) \\ &= t^2(1-2q)\left({\delta_A}^2 B - {\delta_B}^2 A\right) \\ &\quad + \frac{t^2}{2}\left[{\delta_A}^2 B + {\delta_B}^2 A - 2(1-q){\delta_A}^2 B - 2q{\delta_B}^2 A\right] \\ &= t^2\left(\frac{1}{2} - q\right)\left({\delta_A}^2 B - {\delta_B}^2 A\right) \ . \end{aligned} \tag{122}$$

The second-order term of t in the term $k = 2$ vanishes just as in (109). Thus we arrive at

$$\begin{aligned} \Phi(x) = x(A+B) &+ \frac{x^2}{2}(1-2q)\delta_A B \\ &+ \frac{x^3}{3!}\left[\left(\frac{1}{2} - 3r\right){\delta_A}^2 B + \left(\frac{1}{2} - 3s\right){\delta_B}^2 A\right] + \mathrm{O}(x^4) \ . \end{aligned} \tag{123}$$

Putting the second-order and third-order terms to zero, we have a set of simultaneous equations of the parameters as

$$p_1 + p_3 + p_5 = 1 \ , \tag{124}$$
$$p_2 + p_4 + p_6 = 1 \ , \tag{125}$$
$$2q = 2\left(p_2p_3 + p_2p_5 + p_4p_5\right) = 1 \ , \tag{126}$$
$$6r \overset{()}{=} 3\left(p_1 + 2p_3p_4p_5\right) = 1 \ , \tag{127}$$
$$6s \overset{()}{=} 3\left(2p_2p_3p_4 + p_6\right) = 1 \ . \tag{128}$$

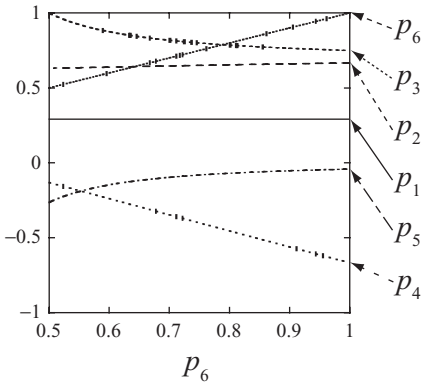

Fig. 5. The solution line of the set of simultaneous equations (124)–(128)

We can confirm that Ruth's formula (64), or

$$p_1 = \frac{7}{24}, \quad p_2 = \frac{2}{3}, \quad p_3 = \frac{3}{4}, \quad p_4 = -\frac{2}{3}, \quad p_5 = -\frac{1}{24}, \quad \text{and} \quad p_6 = 1 \tag{129}$$

is indeed a solution of the above set of simultaneous equations. With six variables for five equations, the solution is in fact a continuous line; Ruth's solution (129) is just a point on the line. By adjusting the last variable p_6, we have the continuous solution shown in Fig. 5.

(We can solve the set of equations with five parameters by putting $p_6 = 0$, but the solution is complex.)

6.6 Example: Perturbational Composition

We finally present an interesting exercise, motivated by the "perturbational composition" [44]. Suppose that we apply a weak transverse field to an Ising spin. We ask what is the correction term in the exponent of the right-hand side of

$$\mathrm{e}^{\frac{x}{2}\gamma\sigma_x}\mathrm{e}^{x\sigma_z}\mathrm{e}^{\frac{x}{2}\gamma\sigma_x} = \mathrm{e}^{\Phi(x,\gamma)} = \mathrm{e}^{x\left(\sigma_z+\gamma C_1(x)+\mathrm{O}(\gamma^2)\right)} \,. \tag{130}$$

Notice that we expand the exponent with respect to the perturbation parameter γ, not with respect to x as in the preceding sections The first-order perturbation term $C_1(x)$ in turn contains higher orders of x. We could explicitly compute the 2×2 matrices on both sides of (130), expand them with respect to γ and compare them term by term, but the quantum analysis provides a more elegant way of computation.

We differentiate the both sides of (130) with respect to γ:

$$\frac{\mathrm{d}}{\mathrm{d}\gamma}\mathrm{e}^{x\left(\sigma_z+\gamma C_1(x)+\mathrm{O}(\gamma^2)\right)} = \frac{\mathrm{d}\mathrm{e}^{\Phi}}{\mathrm{d}\Phi}\cdot\frac{\partial\Phi(x,\gamma)}{\partial\gamma} = \mathrm{e}^{\Phi}\frac{1-\mathrm{e}^{-\delta_\Phi}}{\delta_\Phi}\frac{\partial\Phi}{\partial\gamma} \,, \tag{131}$$

$$\begin{aligned}\frac{\mathrm{d}}{\mathrm{d}\gamma}\mathrm{e}^{\frac{x}{2}\gamma\sigma_x}\mathrm{e}^{x\sigma_z}\mathrm{e}^{\frac{x}{2}\gamma\sigma_x} &= \frac{x}{2}\left(\sigma_x\mathrm{e}^{\frac{x}{2}\gamma\sigma_x}\mathrm{e}^{x\sigma_z}\mathrm{e}^{\frac{x}{2}\gamma\sigma_x} + \mathrm{e}^{\frac{x}{2}\gamma\sigma_x}\mathrm{e}^{x\sigma_z}\mathrm{e}^{\frac{x}{2}\gamma\sigma_x}\sigma_x\right) \\ &= \frac{x}{2}\mathrm{e}^{\Phi}\left(\mathrm{e}^{-\Phi}\sigma_x\mathrm{e}^{\Phi} + \sigma_x\right) \\ &= \frac{x}{2}\mathrm{e}^{\Phi}\left(\mathrm{e}^{-\delta_\Phi} + 1\right)\sigma_x\ . \end{aligned} \tag{132}$$

Equating the both sides, we have

$$\begin{aligned}\frac{\partial\Phi}{\partial\gamma} &= xC_1(x) + \mathrm{O}(\gamma) \\ &= \frac{x}{2}\frac{\delta_\Phi}{1-\mathrm{e}^{-\delta_\Phi}}\left(1+\mathrm{e}^{-\delta_\Phi}\right)\sigma_x \\ &= \frac{x}{2}\left(x\delta_{\sigma_z} + \mathrm{O}(\gamma)\right)\frac{1+\mathrm{e}^{-\delta_\Phi}}{1-\mathrm{e}^{-\delta_\Phi}}\sigma_x\ . \end{aligned} \tag{133}$$

Putting $\gamma = 0$, we have

$$C_1(x) = \frac{1}{2}x\delta_{\sigma_z}\frac{1+\exp\left(-x\delta_{\sigma_z}\right)}{1-\exp\left(-x\delta_{\sigma_z}\right)}\sigma_x = \frac{1}{2}\sum_{n=0}^{\infty}a_n x^n {\delta_{\sigma_z}}^n\sigma_x \tag{134}$$

owing to the fact $\delta_\Phi = x\delta_{\sigma_z} + \mathrm{O}(\gamma)$, where we have made the Taylor expansion

$$x\frac{1+\mathrm{e}^{-x}}{1-\mathrm{e}^{-x}} = \sum_{n=0}^{\infty}a_n x^n \tag{135}$$

with $a_0 = 1$. We also note that the function (135) is even with respect to x and hence $a_n = 0$ for odd integers n.

The right-hand side of (134) is explicitly calculated as follows. In each order, we have

$$\delta_{\sigma_z}\sigma_x = [\sigma_z, \sigma_x] = 2\mathrm{i}\sigma_y\ , \tag{136}$$

$${\delta_{\sigma_z}}^2\sigma_x = 2\mathrm{i}\left[\sigma_z, \sigma_y\right] = 4\sigma_x\ , \tag{137}$$

$${\delta_{\sigma_z}}^3\sigma_x = 4\left[\sigma_z, \sigma_x\right] = 8\mathrm{i}\sigma_y\ , \tag{138}$$

$$\cdots,$$

or in general,

$${\delta_{\sigma_z}}^n\sigma_x = \begin{cases} 2^n\mathrm{i}\sigma_y & \text{for odd } n\ , \\ 2^n\sigma_x & \text{for even } n\ . \end{cases} \tag{139}$$

We substitute (139) for each even-order term of the right-hand side of (134) and arrive at

$$C_1(x) = \frac{1}{2}\sum_{n=0}^{\infty}a_n(2x)^n\sigma_x = x\frac{1+\mathrm{e}^{-2x}}{1-\mathrm{e}^{-2x}}\sigma_x = \left(x\coth x\right)\sigma_x\ . \tag{140}$$

(In the second equality, we used the Taylor expansion (135) in the reverse direction.)

In summary, we have

$$\mathrm{e}^{\frac{x}{2}\gamma\sigma_x}\mathrm{e}^{x\sigma_z}\mathrm{e}^{\frac{x}{2}\gamma\sigma_x} = \mathrm{e}^{x\left[\sigma_z+\gamma(x\coth x)\sigma_x+\mathrm{O}(\gamma^2)\right]}\,. \tag{141}$$

The coefficient $x\coth x$ behaves as shown in Fig. 6. We have $x\coth x \simeq 1$ for small x as is expected, but $x\coth x \simeq x$ for large x, and hence the first-order perturbation term grows as x^2.

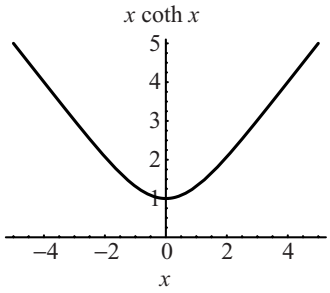

Fig. 6. The coefficient of the first-order perturbation of (141)

7 Summary

In the present article, we have reviewed a continual effort on generalization of the Trotter formula to higher-order exponential product formulas. As was emphasized in Sect. 3, the exponential product formula is a good and useful approximant, particularly because it conserves important symmetries of the system dynamics.

We focused on two algorithms of constructing higher-order exponential product formulas. The first is the fractal decomposition, where we construct higher-order formulas recursively. The second is to make use of the quantum analysis, where we compute higher-order correction terms directly. As interludes, we also have described the decomposition of symplectic integrators, the approximation of time-ordered exponentials, and the perturbational composition. It is our hope that the readers find the present article a useful and tutorial "manual" when they numerically investigate dynamical systems. For more practical applications of the exponential product formulas, we refer the readers to the review articles found in [45, 46, 47, 48].

8 Appendix

Appendix A

Hybrid Exponential Product Formula

We mention here another kind of the exponential product formula [20, 21, 22]. Consider the Trotter approximant

$$\mathrm{e}^{xA}\mathrm{e}^{xB} = \mathrm{e}^{x(A+B)+\frac{1}{2}x^2[A,B]+\mathrm{O}(x^3)} \ . \tag{142}$$

We can cancel out the second-order correction term in the form

$$\mathrm{e}^{xA}\mathrm{e}^{xB}\mathrm{e}^{-\frac{1}{2}x^2[A,B]} = \mathrm{e}^{x(A+B)+\mathrm{O}(x^3)} \ . \tag{143}$$

If, in some problems, the commutation relation $[A, B]$ is easily diagonalized, (143) may be a useful approximant.

A more complicated one is the fourth-order approximant [20, 21, 22]

$$\mathrm{e}^{\frac{x^3}{432}[B,[A,B]]}S_a\left(\frac{x}{3}\right)S_b\left(\frac{x}{3}\right)S_a\left(\frac{x}{3}\right)\mathrm{e}^{\frac{x^3}{432}[B,[A,B]]} = \mathrm{e}^{x(A+B)+\mathrm{O}(x^5)} \ , \tag{144}$$

where

$$S_a(x) \equiv \mathrm{e}^{\frac{1}{2}xA}\mathrm{e}^{xB}\mathrm{e}^{\frac{1}{2}xA} \qquad \text{and} \qquad S_b(x) \equiv \mathrm{e}^{\frac{1}{2}xB}\mathrm{e}^{xA}\mathrm{e}^{\frac{1}{2}xB} \ . \tag{145}$$

In fact, the diffusion equation is described by

$$A = -\frac{1}{2}\Delta \qquad \text{and} \qquad B = V(\boldsymbol{q}) \tag{146}$$

and we have

$$[B,[A,B]] = (\nabla V(\boldsymbol{q}))^2 \ . \tag{147}$$

The above type of the exponential product formula was referred to as the hybrid exponential product formula. We do not give its details in this article, since commutation relations are not easily diagonalized except for a few specific problems.

Appendix B

World-Line Quantum Monte Carlo Method

In the present appendix, we give a short review of the world-line quantum Monte Carlo method. The world-line quantum Monte Carlo method is to transform the partition function (10) of a quantum system $\mathcal{H}$ into the partition function of a classical system by means of the path-integral representation and

simulate the latter system. We explain the method using the transverse Ising model (11), or $\mathcal{H} = A + B$ with

$$A = -\sum_{\langle i,j \rangle} J_{ij} \sigma_i^z \sigma_j^z \qquad \text{and} \qquad B = -\Gamma \sum_i \sigma_i^x \ . \tag{148}$$

The starting point is the Trotter decomposition (21) of the partition function, namely the Suzuki-Trotter transformation [3], of the form:

$$\begin{aligned} Z &= \mathrm{Tr}\, \mathrm{e}^{-\beta \mathcal{H}} = \lim_{n \to \infty} \mathrm{Tr} \left(\mathrm{e}^{-\frac{\beta}{n} A} \mathrm{e}^{-\frac{\beta}{n} B} \right)^n \\ &= \lim_{n \to \infty} \sum_{\{\sigma_i\}} \left\langle \left\{ \sigma_i^{(0)} \right\} \middle| \left(\mathrm{e}^{-\frac{\beta}{n} A} \mathrm{e}^{-\frac{\beta}{n} B} \right)^n \middle| \left\{ \sigma_i^{(0)} \right\} \right\rangle \\ &= \lim_{n \to \infty} \sum_{\left\{ \sigma_i^{(0)} \right\}} \left\langle \left\{ \sigma_i^{(0)} \right\} \middle| \mathrm{e}^{-\frac{\beta}{n} A} \mathrm{e}^{-\frac{\beta}{n} B} \mathrm{e}^{-\frac{\beta}{n} A} \mathrm{e}^{-\frac{\beta}{n} B} \cdots \mathrm{e}^{-\frac{\beta}{n} B} \middle| \left\{ \sigma_i^{(0)} \right\} \right\rangle \ . \end{aligned} \tag{149}$$

In the second line, we have taken the trace with respect to a complete basis set by using the spin z axis as the quantization axis:

$$\sigma_k^z \left| \left\{ \sigma_i^{(0)} \right\} \right\rangle = \sigma_k^{(0)} \left| \left\{ \sigma_i^{(0)} \right\} \right\rangle \ , \tag{150}$$

where the eigenvalue is $\sigma_k^{(0)} = \pm 1$. The meaning of the superscript (0) becomes self-evident just below. We further insert the resolution of unity in between each pair of the exponential operators in the last line of (149), obtaining

$$\begin{aligned} Z = \lim_{n \to \infty} & \sum_{\left\{ \sigma_i^{(0)} \right\}} \sum_{\left\{ \sigma_i^{(1)} \right\}} \sum_{\left\{ \sigma_i^{(2)} \right\}} \cdots \sum_{\left\{ \sigma_i^{(n-1)} \right\}} \\ & \left\langle \left\{ \sigma_i^{(0)} \right\} \middle| \mathrm{e}^{-\frac{\beta}{n} A} \middle| \left\{ \sigma_i^{(0)} \right\} \right\rangle \left\langle \left\{ \sigma_i^{(0)} \right\} \middle| \mathrm{e}^{-\frac{\beta}{n} B} \middle| \left\{ \sigma_i^{(1)} \right\} \right\rangle \\ & \times \left\langle \left\{ \sigma_i^{(1)} \right\} \middle| \mathrm{e}^{-\frac{\beta}{n} A} \middle| \left\{ \sigma_i^{(1)} \right\} \right\rangle \left\langle \left\{ \sigma_i^{(1)} \right\} \middle| \mathrm{e}^{-\frac{\beta}{n} B} \middle| \left\{ \sigma_i^{(2)} \right\} \right\rangle \\ & \cdots \times \left\langle \left\{ \sigma_i^{(n-1)} \right\} \middle| \mathrm{e}^{-\frac{\beta}{n} B} \middle| \left\{ \sigma_i^{(0)} \right\} \right\rangle \ . \end{aligned} \tag{151}$$

In the above expression, we used the fact that the operator A is diagonal in the representation of $\{\sigma_i^{(m)}\}$ and hence made the complete set on the both sides of each operator $\mathrm{e}^{-\frac{\beta}{n} A}$ identical. In contrast, the operator $\mathrm{e}^{-\frac{\beta}{n} B}$ has off-diagonal elements.

Let us calculate the matrix elements in (151). The matrix element of the operator $\mathrm{e}^{-\frac{\beta}{n} A}$ is easy:

$$\left\langle \left\{ \sigma_i^{(m)} \right\} \middle| \mathrm{e}^{-\frac{\beta}{n} A} \middle| \left\{ \sigma_i^{(m)} \right\} \right\rangle = \exp \left(\frac{\beta}{n} \sum_{\langle i,j \rangle} J_{ij} \sigma_i^{(m)} \sigma_j^{(m)} \right) \ . \tag{152}$$

This is because the operators $\{\sigma_i^z\}$ are all diagonal in the present representation as in (150). On the other hand, the operator $\mathrm{e}^{-\frac{\beta}{n}B}$ has off-diagonal elements as well as diagonal ones in the following form:

$$\left\langle \left\{\sigma_i^{(m)}\right\} \left| \mathrm{e}^{-\frac{\beta}{n}B} \right| \left\{\sigma_i^{(m+1)}\right\} \right\rangle = \prod_i \left\langle \sigma_i^{(m)} \left| \mathrm{e}^{\frac{\beta\Gamma}{n}\sigma_i^x} \right| \sigma_i^{(m+1)} \right\rangle \tag{153}$$

with each matrix element given by

$$\begin{aligned} &\left\langle \sigma_i^{(m)} \left| \mathrm{e}^{\frac{\beta\Gamma}{n}\sigma_i^x} \right| \sigma_i^{(m+1)} \right\rangle \\ &= \begin{array}{c} \\ \left\langle \sigma_i^{(m)} = +1 \right| \\ \left\langle \sigma_i^{(m)} = -1 \right| \end{array} \begin{array}{c} \begin{array}{cc} \left| \sigma_i^{(m+1)} = +1 \right\rangle & \left| \sigma_i^{(m+1)} = -1 \right\rangle \end{array} \\ \begin{pmatrix} \cosh\dfrac{\beta\Gamma}{n} & \sinh\dfrac{\beta\Gamma}{n} \\ \sinh\dfrac{\beta\Gamma}{n} & \cosh\dfrac{\beta\Gamma}{n} \end{pmatrix} \end{array} . \end{aligned} \tag{154}$$

These matrix elements are expressed in a single equation

$$\left\langle \sigma_i^{(m)} \left| \mathrm{e}^{\frac{\beta\Gamma}{n}\sigma_i^x} \right| \sigma_i^{(m+1)} \right\rangle = \exp\left(\gamma_n \sigma_i^{(m)} \sigma_i^{(m+1)} + \delta_n\right) , \tag{155}$$

where the parameters γ_n and δ_n are defined in

$$\mathrm{e}^{\gamma_n+\delta_n} = \cosh\frac{\beta\Gamma}{n} \qquad \text{and} \qquad \mathrm{e}^{-\gamma_n+\delta_n} = \sinh\frac{\beta\Gamma}{n} , \tag{156}$$

or more explicitly defined by

$$\gamma_n = -\frac{1}{2}\log\tanh\frac{\beta\Gamma}{n} \qquad \text{and} \qquad \delta_n = \frac{1}{2}\log\frac{1}{2}\sinh\frac{2\beta\Gamma}{n} . \tag{157}$$

The expressions (152) and (155) give the partition function (151) in the form [3]

$$Z = \lim_{n\to\infty} \sum_{\left\{\sigma_i^{(m)}\right\}} \mathrm{e}^{-\beta\mathcal{H}_n} \tag{158}$$

with the resulting classical Hamiltonian [3]

$$-\beta\mathcal{H}_n \equiv \frac{\beta}{n}\sum_{m=0}^{n-1}\sum_{\langle i,j\rangle} J_{ij}\sigma_i^{(m)}\sigma_j^{(m)} + \gamma_n \sum_{m=0}^{n-1}\sum_i \sigma_i^{(m)}\sigma_i^{(m+1)} , \tag{159}$$

where we dropped a constant term due to δ_n. Note that the periodic boundary conditions, $\sigma_i^{(n)} \equiv \sigma_i^{(0)}$, must be required in the second term of (159) because the trace operation in (149) demands it.

The classical Hamiltonian (159) is interpreted as follows (Fig. 7). Suppose that the original quantum system (148) is defined on a square lattice. The

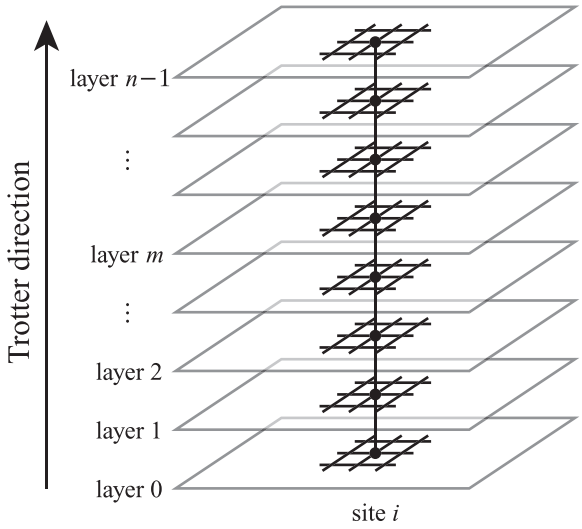

Fig. 7. The three-dimensional classical system (159) mapped from the two-dimensional quantum system (148)

first term of (159) indicates that the two-dimensional system is replicated into n layers with the intra-layer interaction reduced by n times. The second term of (159) represents the inter-layer interactions. The coupling is $-\gamma_n/\beta$ as defined in (159). Thus the quantum system on a square lattice is mapped to an Ising model on a cubic lattice. In general, a d-dimensional quantum system is mapped to a $(d+1)$-dimensional classical system. The additional axis is called the Trotter direction. The physical quantities of the quantum system can be estimated by Monte Carlo simulation of the mapped classical system. This is the basic idea of the world-line quantum Monte Carlo method [3].

We can use this mapping in order to study the quantum annealing [40, 41, 42]. Suppose that we look for the ground state of the diagonal part A of the system (148). Random exchange interactions $\{J_{ij}\}$ may produce many local minima that are only slightly above the ground state in energy but far apart from the ground state in the phase space. The simulated annealing, a well-known method of ground-state search, is often trapped in a local minima and does not reach the ground state. In quantum annealing, we use the transverse field Γ in order to induce tunneling from local minima to the ground state. We first apply the off-diagonal part B of (148) strongly and turn it off gradually, hoping to end up with the ground state of the diagonal part A. This corresponds to a Monte Carlo simulation of the mapped classical system (159) with the intra-layer coupling γ_n being infinitesimally weak at the beginning and infinitely strong at the end. Each layer of the system (159) is first independent of each other and is gradually frozen into an identical configuration, which we hope is the ground state.

An annoying problem inherent in the algorithm of the quantum Monte Carlo method is the systematic error due to the finite Trotter number n. It used to be that simulations were carried out for various finite values of n, quantities were estimated in each simulation, and then the limit $n \to \infty$ was taken in the process of the data analysis, which was called the Trotter extrapolation. A recent development of the quantum Monte Carlo method dramatically changed the situation. We here mention the development briefly; see [39] for a tutorial and exhaustive review of the topic.

In the most recent quantum Monte Carlo algorithm, it is possible for some systems to take the Trotter limit *before* we set up the classical system for simulation. Taking the Trotter limit $n \to \infty$, we have a continuum Trotter axis (Fig. 8). (Note again that the boundary conditions are required in the Trotter direction.) The interaction is described as follows (Fig. 9). Instead of Ising spins on lattice points of a Trotter axis, we have up-spin domains and down-spin domains on the axis. Instead of intra-layer interactions between a pair of nearest-neighbor spins, we have parallel-spin areas and anti-parallel-spin areas. In Monte Carlo simulation, we update the up-spin domains and down-spin domains on the basis of the energy of the parallel-spin areas and anti-parallel-spin areas.

It is thus possible in such situations to carry out a simulation in the Trotter limit $n \to \infty$. Monte Carlo estimates of such a simulation are free of the systematic error of the order β^2/n in (21), and hence do not need the higher-order exponential product formula for such systems.

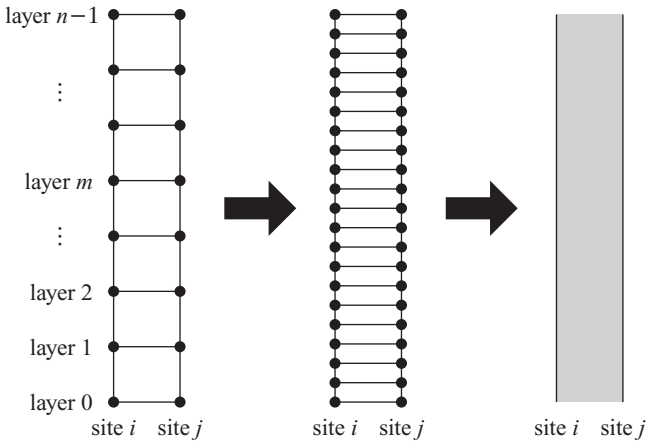

Fig. 8. In the Trotter limit $n \to \infty$, the Trotter axis becomes a continuum. The intra-layer interaction becomes an interaction between two continuum axes

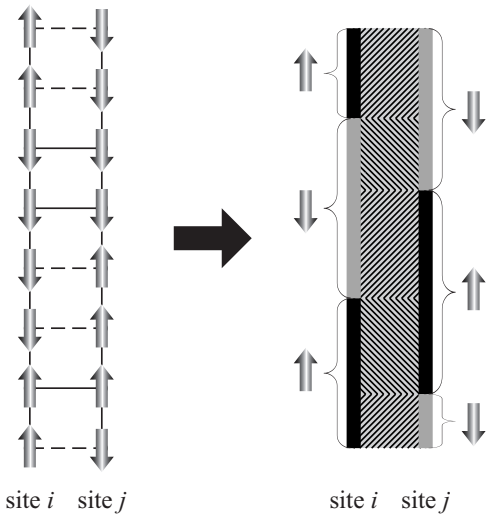

Fig. 9. Spins on lattice points become domains on Trotter axes in the Trotter limit $n \to \infty$

References

1. M. Suzuki: Commun. Math. Phys. **51**, 183 (1976) 37
2. M. Suzuki: Commun. Math. Phys. **57**, 193 (1977) 37
3. M. Suzuki: Prog. Theor. Phys. **56**, 1454 (1976) 37, 63, 64, 65
4. M. Suzuki: J. Math. Phys. **26**, 601 (1985) 37, 38
5. M. Suzuki: Phys. Lett. A **146**, 319 (1990) 38, 45, 46
6. M. Suzuki: J. Math. Phys. **32**, 400 (1991) 38, 45
7. M. Suzuki: Phys. Lett. A **165**, 387 (1992) 38, 45
8. M. Suzuki: J. Phys. Soc. Jpn. **61**, 3015 (1992) 38, 45
9. M. Suzuki: Physica A **191**, 501 (1992) 38, 45
10. M. Suzuki: Proc. Jpn. Acad. **69** B, 161 (1993) 38, 45, 48, 49, 50, 55
11. K. Umeno, M. Suzuki: Phys. Lett. A **181**, 387 (1993) 38, 44, 45
12. M. Suzuki, K. Umeno: Higher-order decomposition theory of exponential operators and its applications to QMC and nonlinear dynamics. In: *Computer Simulation Studies in Condensed-Matter Physics VI*, ed by D.P. Landau, K.K. Mon, H.-B. Schüttler (Springer, Berlin Heidelberg, 1993) pp 74–86 38, 44, 45
13. M. Suzuki: Physica A **194**, 432 (1993) 38, 45
14. M. Suzuki: Physica A **205**, 65 (1994) 38, 45
15. M. Suzuki: Commun. Math. Phys. **163**, 491 (1994) 38
16. H. Kobayashi, N. Hatano, M. Suzuki: Physica A **211**, 234 (1994) 38
17. M. Suzuki: Phys. Lett. A **180**, 232 (1993) 38
18. M. Suzuki: Convergence of exponential product formula and its applications to Hamiltonian systems. In: *Dynamical Systems and Chaos*, vol 2, ed by Y. Aizawa, S. Saito, K. Shiraiwa (World Scientific, Singapore, 1994) pp 450–453 38
19. M. Suzuki: Exponential product formula and Lie algebra. In: *Group Theoretical Methods in Physics*, ed by A. Arima, T. Eguchi, N. Nakanishi (World Scientific, Singapore, 1995) pp 459–464 38

20. M. Suzuki: Phys. Lett. A **201**, 425 (1995) 38, 62
21. M. Suzuki: New scheme of hybrid exponential product formulas with applications to quantum Monte Carlo simulations. In: *Computer Simulation Studies in Condensed-Matter Physics VIII*, ed by D.P. Landau, K.K. Mon, H.-B. Schüttler (Springer, Berlin Heidelberg New York, 1995) pp 169–174 38, 62
22. M. Suzuki: General theory of exponential product formulas. In: *Computational Physics as a New Frontier in Condensed Matter Research*, ed by H. Takayama, M. Tsukada, H. Shiba, F. Yonezawa, M. Imada, Y. Okabe (Physical Society of Japan, Tokyo, 1995) pp 51–56 38, 62
23. M. Suzuki: Systematics and numerics in many-body systems. In: *Recent Progress in Many-Body Theories*, vol 4, ed by E. Schachinger, H. Mitter, H. Sormann (Plenum Press, New York, 1995) pp 65–70 38
24. M. Suzuki: General theory of exponential product formulas and its applications to quantum fluctuation. In: *Coherent Approaches to Fluctuations*, ed by M. Suzuki, N. Kawashima (World Scientific, Singapore, 1996) pp 95-100 38
25. Z. Tsuboi, M. Suzuki: Int. J. Mod. Phys. B **9**, 3241 (1995) 38
26. M. Suzuki: Rev. Math. Phys. **8**, 487 (1996) 38
27. M. Suzuki: Int. J. Mod. Phys. B **10**, 1637 (1996) 38
28. M. Suzuki: Int. J. Mod. Phys. C **7**, 355 (1996) 38
29. M. Suzuki: Commun. Math. Phys. **183**, 339 (1997) 38, 50, 51, 52, 53, 54, 55
30. M. Suzuki: J. Math. Phys. **38**, 1183 (1997) 38, 50, 56
31. M. Suzuki: Phys. Lett. A **224**, 337 (1997) 38, 50
32. M. Suzuki: Prog. Theor. Phys. **100**, 475 (1998) 38, 50
33. M. Suzuki: Int. J. Mod. Phys. C **10**, 1385 (1999) 38, 50
34. M. Suzuki: Rev. Math. Phys. **11**, 243 (1999) 38, 50
35. M. Suzuki: Comp. Phys. Commun. **127**, 32 (2000) 38, 50
36. M. Suzuki: J. Stat. Phys. **110**, 945 (2003) 38
37. M. Suzuki: Physica A **321**, 334 (2003) 38
38. N. Hatano, M. Suzuki: Prog. Theor. Phys. **85**, 481 (1991) 42
39. N. Kawashima, K. Harada: J. Phys. Soc. Jpn. **73**, 1379 (2004) 42, 66
40. T. Sato: Simulated annealing using quantum fluctuation. Master Thesis, University of Tokyo, Tokyo (1995); T. Sato, N. Hatano, M. Suzuki, H. Takayama: unpublished 48, 65
41. T. Kadowaki, H. Nishimori: Phys. Rev. E **58**, 5355 (1998) 48, 65
42. B.K. Chakrabarti: *Transverse Ising Model, Glass and Quantum Annealing*. In: Lect. Notes Phys. **679** (2005) 48, 65
43. R.D. Ruth: IEEE Trans. Nucl. Sci. **30**, 2669 (1983) 50
44. R.I. McLachlan: BIT **35**, 258 (1995) 59
45. H. De Raedt, A. Lagendijk: Phys. Rep. **127**, 233 (1985) 61
46. M. Suzuki (ed): *Quantum Monte Carlo Methods in Equilibrium and Nonequilibrium Systems* (Springer, Berlin, 1987) 61
47. M. Suzuki (ed): *Quantum Monte Carlo Methods in Condensed-Matter Physics* (World Scientific, Singapore, 1993) 61
48. B.K. Chakrabarti, A. Dutta, P. Sen: *Quantum Ising Phases and Transitions in Transverse Ising Models*. In: Lect. Notes Phys. **m41** (1996) 61

Quantum Spin Glasses

Heiko Rieger

Theoretische Physik, Universität des Saarlandes, 66041 Saarbrücken, Germany
h.rieger@mx.uni-saarland.de

1 Introduction

In this chapter of this monograph we want to provide an overview on the current status of our knowledge on the theory of quantum spin glasses. Spin glasses are frustrated magnetic systems and a hallmark of their "glassiness" is the presence of a rugged energy landscape with many local minima. It appears obvious that in such an environment quantum effects might play an important role by opening new routes for relaxation due to quantum mechanical tunneling and indeed one observes experimentally a significant acceleration of the dynamics at low temperatures if quantum fluctuations are enhanced. Here we will first focus more on the equilibrium properties of disordered quantum magnets, with and without frustration, in particular to what is expected (theoretically) to happen at and close to a quantum critical point.

A quantum spin glass is a magnetic system that can be described by a quantum mechanical Hamiltonian with spin-glass like features (randomness and frustration). In such a system, a spin glass phase may exist while at the same time quantum fluctuations play an important role, possibly a dominant role, in particular, in the absence of thermal fluctuations at zero temperature. Such a Hamiltonian is, for instance, the spin-1/2 Heisenberg spin glass

$$H = \sum_{(ij)} J_{ij}(\sigma_i^x \sigma_j^x + \sigma_i^y \sigma_j^y + \sigma_i^z \sigma_j^z) \;, \tag{1}$$

where $\sigma^{x,y,z}$ are Pauli spin-1/2 operators, J_{ij} random exchange interactions (e.g., Gaussian), and the sum runs over all nearest neighbors on some d-dimensional lattice. Another example is the Ising spin glass in a transverse field

$$H = -\sum_{(ij)} J_{ij}\sigma_i^z \sigma_j^z + \Gamma \sum \sigma_i^x \;, \tag{2}$$

where Γ denotes the transverse field strength. This Hamiltonian becomes diagonal if Γ is zero, in which case it reduces simply to the classical Ising spin

H. Rieger: *Quantum Spin Glasses*, Lect. Notes Phys. **679**, 69–99 (2005)
www.springerlink.com

glass that we have discussed in the previous sections. Thus the role of the parameter Γ is to tune the strength of quantum fluctuations, they do not play a role in the equilibrium statistical physics of a diagonal Hamiltonian. An important experimental realization of this model Hamiltonian is the system $LiHo_xY_{1-x}F_4$,[5] an insulating magnetic material in which the magnetic ions (Ho) are in a doublet state due to crystal field splitting. The interactions between Ho ions can be described by an Ising model with dipolar couplings. For $x = 1$ the system is a ferromagnet with a critical temperature of $T_c = 1.53\,\mathrm{K}$ at $\Gamma = 0$ and as x is reduced the critical temperature decreases. For concentrations below 25% Ho and above 10% Ho a thermal phase transition to a spin glass phase occurs indicated by a diverging nonlinear susceptibility (for instance at $x = 0.167$ the spin glass transition temperature is $T_g = 0.13\,\mathrm{K}$ at $\Gamma = 0$). If a transverse field is applied ($\Gamma > 0$) the spin glass transition temperature decreases monotonically to zero (see Fig. 1). This particular point, at zero temperature and at a critical field strength is what we denote as a quantum-phase-transition point [1].

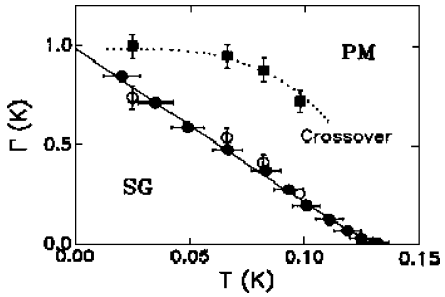

Fig. 1. Phase diagram of $LiHo_{0.167}Y_{0.833}F_4$ according to the measurement of the nonlinear susceptibility. From [5]

Earlier reviews on quantum spin glasses and in particular the Ising spin glass in a transverse field can be found in [2, 3, 4]. Here we try to focus on a number of new developments that have been made since then.

2 Random Transverse Ising Models in Finite Dimensions

The generic phase diagram for the EA Ising spin glass model in a transverse field Γ is shown in Fig. 2 for two dimensions and for three dimensions. In the three-dimensional case, starting from the classical spin glass transition temperature T_c for $\Gamma = 0$ the critical temperature decreases monotonically with increasing transverse field strength Γ until it reaches $T = 0$. One expects that the universality class of the transition at any non-vanishing temperature is the same as the one of the classical Ising spin glass transition at T_c. The

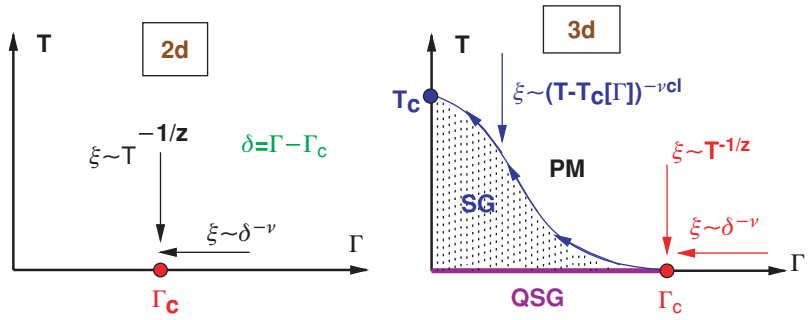

Fig. 2. *Left*: Generic phase diagram for the two-dimensional Ising spin glass in a transverse field Γ. Since no spin glass phase is present in $d = 2$ for $T > 0$, only a quantum spin glass phase and a quantum phase transition at $T = 0$ exists. Approaching the quantum critical point at Γ_c by decreasing the temperature T, the correlation length diverges like $T^{-1/z}$, where z is the dynamical critical exponent (if z is formally infinite, it increases logarithmically). *Right*: Generic phase diagram of a three-dimensional Ising spin glass in a transverse filed. The classical transition temperature (at $\Gamma = 0$) is T_c and the corresponding classical correlation length exponent is ν_{cl}

zero-temperature quantum phase transition, however, establishes a new universality class. This transition exists in any dimension, including one and two dimensions. A critical value Γ_c for the transverse field strength separates a disordered or paramagnetic phase for $\Gamma > \Gamma_c$ from an ordered phase for $\Gamma < \Gamma_c$. This transition is characterized by a diverging length scale $\xi \sim |\Gamma - \Gamma_c|^{-\nu}$ and a vanishing characteristic frequency $\omega \sim \Delta E \sim \xi^{-z}$. The latter is the quantum analog of "critical slowing-down" in the critical dynamics of classical, thermally driven transitions. The new and most important property occurring at zero temperature in the random transverse Ising model is the *infinite randomness fixed point* (IRFP) that governs the quantum critical behavior at the critical value Γ_c of the transverse field [13]. One feature of the IRFP is that the dynamical exponent z is formally infinite, the relation between length and energy scales is not algebraic but exponential: $\Delta E \sim \exp(-A\xi^{\psi})$.

To describe this scenario we generalize the discussion of the transverse Ising spin glass by including also random *ferromagnetic* interactions $J_{ij} > 0$, because many more analytical and numerical results are available for the ferromagnetic rather than the spin glass case and the same main features are expected to hold in both cases.

2.1 Random Transverse Ising Chain and the Infinite Randomness Fixed Point

Let us start with a review of the one-dimensional case, in which the sign (if it can be negative) of the nearest neighbor couplings can be gauged away so that

all interactions are ferromagnetic and the resulting model is the random Ising chain in a transverse field or a random transverse-field Ising model (RTIM) in one dimension:

$$\mathcal{H} = -\sum_i J_i \sigma_i^z \sigma_{i+1}^z + \sum_i h_i \sigma_i^x \ . \qquad (J_i > 0) \tag{3}$$

A uniform transverse field is represented by $h_i = \Gamma$ for all sites. Since this case and the case of random transverse fields turn out to belong to the same universality class, we also consider random transverse field here. The couplings J_i and the transverse fields h_i are random variables with distributions $\pi(J)$ and $\rho(h)$, respectively. The Hamiltonian in (3) is closely related to the transfer matrix of a classical two-dimensional layered Ising model, which was first introduced and studied by McCoy and Wu [9]. Extensive researches on this model were initiated by D. Fisher[10] with an application of the Ma-Dasgupta-Hu renormalization group scheme,[14] followed by numerical and analytical work [15, 16, 17, 18, 19, 20, 21, 22]. We briefly summarize the results. The quantum control-parameter of the model is given by

$$\delta = \frac{[\ln h]_{av} - [\ln J]_{av}}{\mathrm{var[ln\,h]} + \mathrm{var[ln\,J]}} \ . \tag{4}$$

For $\delta < 0$ the system is in the ordered phase with a non-vanishing average magnetization, whereas the region $\delta > 0$ corresponds to the disordered phase. There is a phase transition in the system at $\delta = 0$ with rather special properties, which differs in several respects from the usual second-order phase transitions of pure systems. One of the most striking phenomena is that some physical quantities are not self-averaging, which is due to very broad, logarithmic probability distributions. As a consequence the *typical value* (which is the value in an frequent event) and the *average value* of such quantities can be drastically different. Thus the critical behavior of the system is primarily determined by rare events that give dominating contributions to the averaged values of various observables.

The average bulk magnetization is characterized by an exponent β, which is $\beta = 2 - \tau$ where $\tau = (1 + \sqrt{5})/2$ is the golden-mean. The average spin-spin correlation function $C(r) = [\langle \sigma_i^z \sigma_{i+r}^z \rangle]_{av}$ involves the average correlation length ξ, which diverges at the critical point as $\xi \sim |\delta|^{-\nu_{\mathrm{av}}}$, and $\nu_{\mathrm{av}} = 2$. On the other hand, the typical correlations have a faster decay, since $\xi_{\mathrm{typ}} \sim |\delta|^{-\nu_{\mathrm{typ}}}$ with $\nu_{\mathrm{typ}} = 1$.

Close to the critical point the relaxation time t_r is related to the correlation length as $t_r \sim \xi^z$, where z is the dynamical exponent. The random transverse-field Ising spin chain is strongly anisotropic at the critical point, since according to the RG-picture[10] and to numerical results[23]

$$\ln t_r \sim \xi^{1/2} \ , \tag{5}$$

which corresponds to $z = \infty$. On the other hand the relaxation time is related to the inverse of the energy-level spacing at the bottom of the spectrum $t_r \sim$

$(\Delta E)^{-1}$. Then, as a consequence of (5), some quantities (such as specific heat, bulk and surface susceptibilities, etc.) have an essential singularity at the critical point, and the correlation function of the critical energy-density has a stretched exponential decay, in contrast to the usual power law behavior.

Away from the critical point in the disordered phase the rare events with strong correlations still play an important role, up to the point, $\delta = \delta_G$. Above this point, all transverse-fields are bigger than the interactions. In the region $0 < \delta < \delta_G$, which is called the Griffiths-McCoy phase [9, 8], the magnetization is a singular function of the uniform longitudinal field H_z as $m_{\text{sing}} \sim |H_z|^{1/z}$, where the dynamical exponent z varies with δ. At the two borders of the Griffiths-McCoy phase it behaves as $z \approx 1/2\delta \times (1 + \mathcal{O}(\delta))$ [10] as $\delta \searrow 0$ and $z = 1$ as $\delta \nearrow \delta_G$, respectively.

All these results could be obtained and understood by the application of a Ma-Dasgupta-Hu renormalization group scheme [10], in which strong bonds or fields are successively decimated either by elimination of spins (in case of large transverse fields) or formation of strongly coupled clusters (in case of large ferromagnetic bonds). With decreasing energy scale Δ of the bonds and fields to be decimated the typical size L of these strongly coupled clusters increases as

$$L \sim |\ln \Delta|^{1/\psi} \tag{6}$$

defining an exponent ψ that is 1/2 in the random transverse-field Ising chain. Such a cluster typically contains

$$\mu \sim L^{\phi\psi} (= |\ln \Delta|^{\phi}) \tag{7}$$

spins that essentially behave collectively (for instance in response to the application of a longitudinal magnetic field H – and thus generating a huge contribution to the spin susceptibility). This defines another exponent ϕ, which is $(1 + \sqrt{5})/2$ in the RTIM. Finally there is the correlation length exponent ν that defines the characteristic length scale of spin-spin correlations away from the critical point.

The RG runs into a fixed point that is fully determined by the geometrical features of the clusters that are generated asymptotically – very much in reminiscence of the percolationndexpercolation fixed point inconventional percolation. This picture is expected to hold also for higher-dimensional RTIMs, and even for the spin glass case. Therefore we summarize its essence here. The distribution of the random bonds and fields not yet decimated during the RG procedure becomes broader and broader. Hence the name, *infinite randomness fixed point* (IRFP). It is characterized by the three exponents ψ, ϕ and ν and the critical behavior of the physical observables is determined by them. For instance the correlation function (at criticality) for two spins at site i and j with a distance r from each other is simply given by their probability to belong to the same cluster of size r: $[C_{ij}]_{\text{av}} \sim |\mathbf{r}_i - \mathbf{r}_j|^{-2(d-\phi\psi)}$. Other relations follow straightforwardly from this scheme[13]:

lowest energy scale:	$-\ln \Delta$	$\sim L^{\psi}$
magnetic moment:	μ	$\sim (-\ln \Delta)^{\phi}$
average correlations:	$[C_{ij}]_{\rm av}$	$\sim \lvert\mathbf{r}_i - \mathbf{r}_j\rvert^{-2(d-\phi\psi)}$
typical correlations:	$-[\ln C_{ij}]_{\rm av}$	$\sim \kappa_{ij}\lvert\mathbf{r}_i - \mathbf{r}_j\rvert^{\psi}$
finite T-susceptibility:	χ	$\sim T^{-1}(-\ln T)^{2\phi-d/\psi}$
finite H-magnetization:	M	$\sim (-\ln H)^{-\phi+d/\psi}$

Away from the critical point ($\delta \neq 0$) the correlation length is finite and its average and typical value scale differently:

average correlation length:	$\xi_{\rm av}$	$\sim \delta^{-\nu}$
typical correlation length:	$\xi_{\rm typ}$	$\sim \xi_{\rm av}^{1-\psi}$
spontaneous magnetization:	M_0	$\sim (-\delta)^{\nu(d-\phi\psi)}$

In spite of the finiteness of the average correlation length away from the critical point still arbitrarily large strongly-coupled clusters exist – though with an exponentially small probability – leading to algebraically decaying correlations in imaginary time. Phenomenologically, one can understand that as a consequence of the appearence of Griffiths singularities [8] close to a quantum critical point [7, 11]: Let L be the size of a region of *strongly coupled* spins. In a random system in the paramagnetic phase they occur with an exponentially small probability $P(L) \propto \exp(-\lambda L^d)$. For instance in the diluted ferromagnet strongly coupled regions are connected clusters and their probability is p^V, where V is the region's volume and p is the site occupation probability ($0 < p < 1$). Then, λ is given by $\lambda = |\ln p| > 0$. The special feature of transverse-field Ising systems is that in first order perturbation theory the gap of a finite system containing L^d spins is exponentially small: $\Delta_0 \sim \exp(-sL^d)$. An exponentially small gap means an exponentially large tunneling time, and combining the two observations on cluster probability and relaxation time one obtains an algebraical decay for the spin-spin correlation function: $C(\tau) = [\langle\sigma_i(\tau)\sigma_i(0)\rangle]_{\rm av} \sim \tau^{-\lambda/s} = \tau^{-d/z(\delta)}$. The parameter $z(\delta) = s/d\lambda$ is called the *dynamical exponent* in the Griffiths phase and it varies continuously with the distance from the critical point. The consequences, e.g., for the susceptibility are dramatic: $\chi(\omega = 0) = \int_0^{1/T} d\tau\, C(\tau) \propto T^{-1+d/z(\delta)}$ which implies that for $z > d$ the susceptibility diverges for $T \to 0$ even away from the critical point. Since in random transverse-field Ising system $z(\delta)$ grows without bounds for $\delta \to 0$ (and thus merging with the critical dynamical exponent at $\delta = 0$, which is infinite), there is always a region around the critical point, where the susceptibility diverges.

In general the dynamical exponent $z(\delta)$ introduced above is expected to determine all singularities occurring in the Griffiths-McCoy phase close to an IRFP[13]:

dynamical exponent:	$z(\delta)$	$\propto \delta^{-\psi\nu}$
lowest energy scale:	Δ	$\sim L^{-z(\delta)}$
finite H-magnetization:	M	$\sim H^{1/z(\delta)}$
susceptibility:	$\chi(\omega = 0)$	$\sim T^{-1+d/z(\delta)}$
nonlinear susceptibility:	$\chi_{nl}(\omega = 0)$	$\sim T^{-1+d/3z(\delta)}$
specific heat:	c	$\sim T^{d/z(\delta)}$

The last three tables summarize the scaling predictions at and close to a IRFP and in $1d$ they have been confirmed many times, analytically and numerically [15, 16, 17, 18, 19, 20, 21, 22].

2.2 Diluted Ising Ferromagnet in a Transverse Field

In higher dimensions $d \geq 2$ the randomly diluted Ising-ferromagnet in a transverse field is a show-case for a quantum phase transition governed by an IRFP. The site diluted model is defined by the Hamiltonian

$$H = -J \sum_{(ij)} \varepsilon_i \varepsilon_j \sigma_i^z \sigma_j^z - \Gamma \sum_i \varepsilon_i \sigma_i^x \tag{8}$$

and the bond diluted model by

$$H = -J \sum_{(ij)} \varepsilon_{ij} \sigma_i^z \sigma_j^z - \Gamma \sum_i \sigma_i^x \tag{9}$$

where ε_i and ε_{ij} are random variables that take on the values 1 with probability p and 0 with probability $1 - p$. Its phase diagram is depicted in Fig. 3

Along the vertical line starting from the point $(p, \Gamma) = (p_c, 0)$ up to the multi-critical point the transition from the paramagnetic to the ferromagnetic phase is a *classical percolation transition* [24, 25]. Denoting the distance from the critical point with $\delta = p_c - p$ the connectivity correlation length diverges

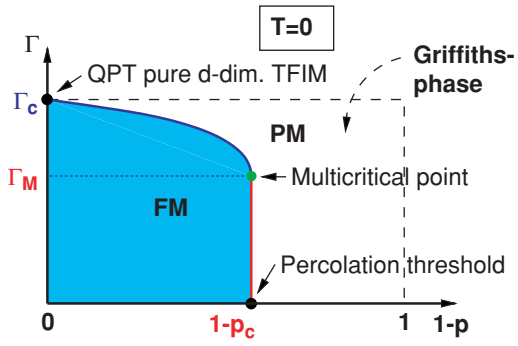

Fig. 3. Phase diagram of the diluted Ising ferromagnet in an transverse field Γ at zero temperature $T = 0$

upon approaching the percolation point $1-p_c$ as $\xi \sim |\delta|^{-\nu_{\rm perc}}$. The number of spins M in the percolating cluster at $p = p_c$ scales with the linear system-size L as $M \sim L^{D_{perc}}$, where D_{perc} is the fractal dimension of the percolating clusters. For small values of the transverse field Γ one expects the percolating cluster to be fully magnetized, which implies that the gap scales as $\Delta \sim \exp(-L^{D_{perc}})$. This means that $\psi = D_{perc}$ in the IRFP scenario described above. Moreover, the connectivity correlation function at the percolation threshold p_c decays as $C(r) \sim r^{-(d-2+\eta_{\rm perc})}$, which means that the exponent ϕ is given by the relation $2(d-\psi\phi) = (d-2+\eta_{\rm perc})$. To summarize the exponents characterizing the IRFP in the randomly diluted ferromagnet in a transverse field are related to the classical percolation exponents (which are exactly known in dimensions $d = 2$ and in $d > 6$) via:

$$\nu = \nu_{\rm perc}\,, \quad \psi = D_{\rm perc}\,, \quad \phi = (d+2-\eta_{perc}))/D_{\rm perc}\ . \tag{10}$$

2.3 Higher Dimensional Random Bond Ferromagnets in a Transverse Field

Let us consider now to the random bond ferromagnet in a transverse field in dimensions $d \geq 2$

$$H = -\sum_{(ij)} J_{ij}\sigma_i^z\sigma_j^z - \sum_i h_i\sigma_i^x\ , \tag{11}$$

where the sum runs over all nearest neighbor pairs (ij) of a d-dimensional lattice, the random couplings J_{ij} and transverse fields h_i are all positive and obey some distribution. Here one has to rely on numerical calculations. In quantum Monte-Carlo simulations the IFRP-scenario manifests itself in a non-conventional finite size scaling behavior with $\ln\beta/L^{\psi}$ as one scaling varibale (instead of β/L^z in conventional scaling scenarios) and a different scaling of average and typical correlation functions. For instance for the Binder cumulant $g_{\rm av}$ one would expect the following scaling form

$$g_{\rm av} = 0.5[3 - \langle M^4\rangle/\langle M^2\rangle^2]_{\rm av} = g(\delta L^{-1/\nu}, \ln\beta/L^{\psi})\ , \tag{12}$$

where M is the magnetization and δ is the distance from the critical point. In Fig. 4 we show numerical data for $g_{\rm av}$ at the critical point ($h_0 = 7.5$ for h_i uniform over $[0, h_0]$ and J_{ij} uniform over $[0, 1]$) of the 2d random bond ferromagnet in a transverse field, and we observe that they scale accordingly with $\psi \approx 0.6$.

In Fig. 5 we show numerical data for the average and typical correlation functions $C_{\rm av}(r) = [\langle\sigma_i^z\sigma_{i+r}^z\rangle]_{\rm av}$ and $C_{\rm av}(r) = \exp(\ln[\langle\sigma_i^z\sigma_{i+r}^z\rangle]_{\rm av})$, respectively. On one hand $C_{\rm av}(r)$ decays algebraically with an exponent -2.3, implying $2(d-\phi\psi) = 2.3$, i.e $\phi \approx 1.41$ when we use the estimate $\psi = 0.6$ obtained from scaling of the Binder cumulant. On the other hand $C_{\rm typ}(r)$ decays with a strechted exponential, i.e $\propto \exp(-cr^{\psi})$, with $\psi \approx 0.58$, compatibel with the

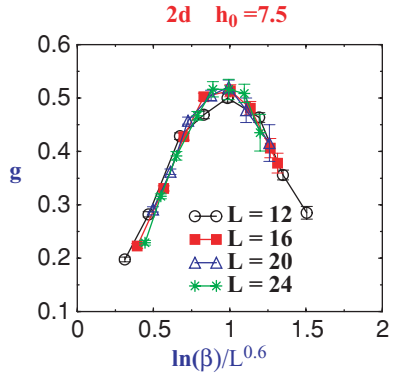

Fig. 4. 2d random bond Ising ferromagnet: Scaling plot of the Binder cumulant at the critical point using activated dynamics scaling wth $\psi = 0.6$. Data obtained by quantum Monte Carlo simulations using a continuous time cluster algorithm [26, 27]

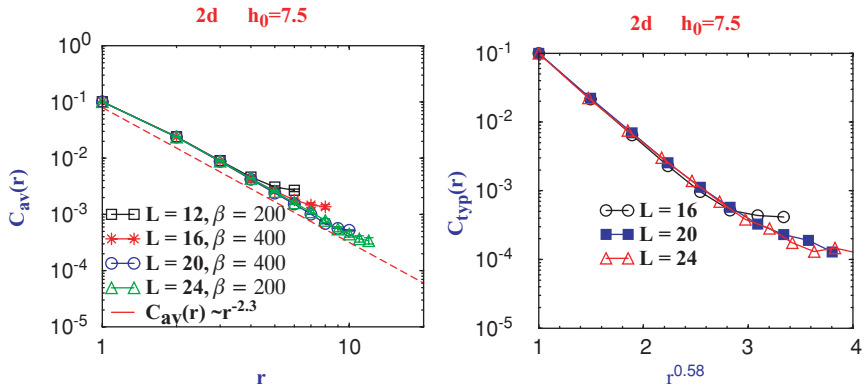

Fig. 5. 2d random bond Ising ferromagnet: *Left*: Average correlation function $C_{\rm av}$ in a log-log plot. The straight line has slop -2.3. *Right*: Typical correlation function $C_{\rm typ}$ as a function of $r^{0.58}$. The data tend to approach a straight line for $L \to \infty$. Data obtained by quantum Monte Carlo simulations using a continuous time cluster algorithm [26, 27]

estimated for ψ obtained before. Both results, the activated dynamics scaling for $g_{\rm av}$ as well as the different scaling of $C_{\rm av}(r)$ and $C_{\rm typ}(r)$, the latter compatible with the exponent ψ estimated from the activated dynamics scaling, indicate strongly that the quantum critical point in the 2d random bond ferromagnet in a transverse field is an IRFP.

A numerical implementation of the Ma-Dasgupta-Hu RG scheme indeed provided another evidence for an infinite randomness fixed point[28, 29] with estimate for ϕ and ψ that are compatibel with those mentioned above obtained in quantum Monte Carlo simulations. For random Ising ferromagnets in a

transverse field the existence of the IRFP dominating the quantum critical behavior thus appears to be confirmed for finite dimensions. Strictly speaking detailed numerical studies have only be performed for $d = 1$ and $d = 2$ up to now, but there seems to be no strong argument against the existence of the IRFP also in higher, finite, dimensions although one expects the numerical and experimental visibility of the IRFP to diminish for increasing dimension d. In the mean field limit ($d \to \infty$) the quantum phase transition is *not* described by an IRFP and obeys conventional scaling laws. In particular z is finite and Griffiths-McCoy singularities are absent.

2.4 Quantum Ising Spin Glass in a Transverse Field

What about the spin glass case? Within the SDRG picture of the quantum phase transition in disordered systems with a discrete symmetry, as for instance Ising systems, one would also expect an IRFP in quantum spin glasses [13]. Quantum Monte Carlo simulations of the Ising spin glass with a transverse-field have been performed for the cases $d = 2$[6, 7] and $d = 3$,[31, 32] they are reviewed in [3, 4]. The main result is that the numerical data appeared to be compatible with a finite value for the dynamical exponent in $d = 2$ and 3 and that the critical behavior can be described by conventional scaling laws. However, the existence of a Griffiths-McCoy phase away from the critical point has been uncovered, with a continuously varying dynamical exponent describing the singularities of the susceptibility and non-linear susceptibility. In contrast to the quantum Monte-Carlo simulations of the random bond ferromagnets no cluster-algorithm could be used in the quantum spin glass case, which restricted the system sizes and in particular the temperatures to rather small values (note that anisotropic finite size scaling demands that the temperature has to decrease exponentially with the system size at a quantum critical point described by an IRFP). In addition a homogeneous rather than a random transverse field has been used, which causes strong cross-over effects and the true asymptotic scaling behavior might be more difficult to extract. Therefore it might very well be that the indications found for the absence of a IRFP in the $2d$ and $3d$ quantum spin glass are still pre-asymptotic and that studies using larger system sizes and more sophisticated simulation methods could detect evidence for the IRFP also here.

Finally a word about the consequences of the aforementioned theoretical developments for the experiments. There it was observed that upon approaching the quantum critical point the divergence of the non-linear susceptibility was drastically suppressed indicating even the absence of a divergence at zero temperature. The numerical results, on the other hand, hint at a strong divergence of the non-linear susceptibility at the quantum critical point – even more than the IRFP scenario. Up to now no clear reason for the discrepancy has been pinned down. The possibility of a second-order transition turning a first-order one at low temperatures has been raised,[42] but this possibility can definitely be ruled out for a system that can be described by the

Hamiltonian (3) that we discussed here. We do not think that dipolar interactions of a magnetically diluted system cause substantial modifications of the picture that emerged for short range interactions. At this point one cannot rule out the possibility that the transverse field Ising Hamiltonian with quenched disorder is simply not a sufficiently detailed description of $LiHo_{0.167}Y_{0.833}F_4$.

3 Mean-Field Theory for Quantum Ising Spin Glasses

As a mean-field model of quantum Ising spin glass, we consider the Sherrington-Kirkpatrick model in a transverse field

$$H = -\sum_{(i,j)} J_{ij}\sigma_i^z\sigma_j^z - \Gamma\sum_i \sigma_i^x \ . \tag{13}$$

The first sum is over all pairs of spins and the couplings J_{ij} are quenched random variables that obey the Gaussian distribution with zero mean and variance J^2/N, where N is the number of spins. Γ is the strength of the transverse field. Although no exact solution has been found for finite Γ, the phase diagram of this model has been well delineated. At zero transverse field the transition is the well-known classical transition of the SK model at $T_c(\Gamma = 0) = J$. For sufficiently high temperature and/or sufficiently large Γ, thermal and/or quantum fluctuations destroy the spin glass order, yielding a paramagnet [30]. For low T and small Γ one finds a SG ordered phase, apparently with broken replica symmetry [33]. Monte Carlo calculation, numerical spin summation[34] and perturbation expansion[35] in $1/\Gamma$ have determined the phase boundary to some precision. As in the classical model, the infinite range interactions apparently wipe out the Griffiths singularities discussed in the last subsection. The critical behavior along the line $T_c(\Gamma)$ is expected to be the same as the classical critical behavior, i.e., the non-linear susceptibility diverges as $\chi_{nl} \sim (T - T_c(\Gamma))^{-\gamma}$ with $\gamma = 1$, the specific heat exponent is $\alpha = 0$, etc.

3.1 Quantum Phase Transition

The zero temperature quantum critical point $\Gamma_c(T = 0)$ is in a different universality class and has been studied in [37, 38, 39]. The static approximation – the approximation usually applied to small field values in which the imaginary time correlation function $C(\tau) = \langle\sigma_i(\tau)\sigma_i(0)\rangle$ is assumed to be time independent – is not valid at $T = 0$ (large fields) and the full functional form of $C(\tau)$ has to be explored. The dynamical self-consistency equations obtained via standard manipulations[30, 36] was analyzed at $T = 0$ at the quantum critical point in [37, 38, 39], and it turned out that the quantum critical point is located at $\Gamma_c \approx 0.7J$. At $\Gamma > \Gamma_c$ (and zero temperature) $C(\tau)$ decays exponentially with τ as $\tau \to \infty$, indicating a gap Δ in the corresponding spectral density;

at $\Gamma = \Gamma_c$, $C(\tau)$ decays as $1/\tau^2$, and in the ordered phase, $C(\tau) \to q_{\rm EA}$. The Fourier transform of $C(\tau)$ has the form $C(\omega) \sim$ const. $- \sqrt{\omega^2 - \Delta^2}$ for $\Gamma \geq \Gamma_c$, which is responsible for the $1/\tau^2$ behavior at Γ_c and it turned out that the correlation time diverges as $\xi_\tau \sim 1/\Delta \sim [(\Gamma - \Gamma_c)^{-1} \ln(\Gamma - \Gamma_c)]^{1/2}$. Thus we can define an exponent $z\nu$, anticipating anisotropic scaling in space and time in the short range model, which takes the value $z\nu = 1/2$ in the infinite-range model. Since $C(\tau \to \infty) = q_{\rm EA}$ is the Edwards-Anderson order parameter, we may also define $q_{\rm EA} = (\Gamma_c - \Gamma)^\beta$ and it was found that $\beta = 1$. At $\Gamma = \Gamma_c$ one expects $C(\tau) \sim \tau^{-\beta/z\nu}$, which is satisfied with the values obtained. The non-linear susceptibility diverges as $1/\Delta$, which implies with $\chi_{nl} \sim (\Gamma - \Gamma_c)^{-\gamma}$ that $\gamma = 1/2$. Studying Gaussian fluctuations around the saddle-point solution valid for infinite range one finds[39] for the correlation length exponent above the upper critical dimension (i.e. $d \geq 8$) that $\nu = 1/4$ and therefore $z = 2$. Moreover $\eta = 0$ in mean field theory. The complete collection of critical exponents obtained so far in comparison with the classical model ($T > 0$, where we assume to cross the phase boundary under a non-vanishing angle) are as follows:

	β	γ	ν	z
quantum ($T = 0$)	1/2	1/2	1/4	2
classical ($T = 0$)	1	1	1/2	–

(14)

Note that as a consequence of the absence of Griffiths-singularities in mean-field models the dynamical exponent z is finite in contrast to the IRFP scenario that is supposedly valid for the finite-dimensional models. In a longitudinal field one obtains, in analogy to the classical case, an AT manifold in the T, Γ, h phase diagram below which replica symmetry is broken and the system is in the SG phase.

The dynamics of the model (13) in the paramagnetic phase has been studied in [40], where the dynamical single-site self-consistency equations have been iteratively solved using a quantum Monte Carlo scheme developed in [41]. They mapped the spin-glass transition line in the Γ-T plane using the stability criterion $1 = J\chi_{\rm loc}$, where $\chi_{\rm loc} = \int_0^\beta d\tau\, C(\tau)$ is the local susceptibility. They found a second-order transition line ending at a quantum critical point at $T = 0$ in agreement with the argument presented above. Going down in temperature to $T \sim 0.01J$ and extrapolating the results to $T = 0$ they determined a precise value for the critical field $\Gamma_c = 0.76 \pm 0.01$, which lies between previous estimates [33, 37]. The asymptotic form of $C(\tau) \sim \tau^{-2}$ found in [37] was also confirmed. A comparison of the results for the low-frequency susceptibility with the experimental curves obtained for $LiHo_{0.167}Y_{0.833}F_4$ in [5] yields a good agreement.

A different class of mean-field spin-glass models has been studied in [42] – simplified in so far as spherical spins rather than Ising spins were considered and more general in so far as p-spin interactions were considered. The quantum fluctuations are introduced via a kinetic energy rather than the transverse field. The corresponding quantum spherical p-spin-glass Hamiltonian is

defined by

$$H = \frac{1}{2M}\sum_{i=1}^{N}\hat{p}_i^2 - \sum_{i_1,\ldots,i_p} J_{i_1,\ldots,i_p} s_{i_1}\cdots s_{i_p} \tag{15}$$

where s_i are "soft-spins" fulfilling the spherical constraint $\sum_{i=1}^{N} s_i(t)^2 = N$ for all times t. Quantum mechanics is introduced into the classical p-spin glass via the canonical momenta $\hat{p}_i$ that fulfill the commutation relation $[\hat{p}_i, s_j] = -i\hbar\delta_{ij}$. The multi-spin coupling constants are taken from a Gaussian distribution with zero mean and variance $\tilde{J}p!/(2N^{p-1})$ with $\tilde{J}$ being a constant of $\mathcal{O}(1)$.

Before we discuss this model we want to clarify the connection to the SK model in a transverse field discussed above. The replacement of Ising spins $S_i = \pm 1$ by continuous spins $s_i \in [-\infty, +\infty]$ is often performed in the theory of critical phenomena – the discrete symmetry is then enforced by a quartic term $\sum_i s_i^4$ in the Hamiltonian (this is just the usual Φ^4 Ginzburg-Landau theory for critical phenomena with a discrete symmetry), which also restricts automatically the spin length. Analytically the quartic term causes extra complications in all computations, saddle point evaluations, RG calculations, dynamical formalism etc. – for which reason one often skips it and replaces it by a spherical constraint (either strictly or via a Lagrangian parameter having the same effect as a chemical potential). Unfortunately the classical spherical mean-field spin-glass model with the usual 2-spin interactions does not have a non-trivial spin glass phase. Therefore, generalizations to p-spin interactions are sometimes considered. [56] At this point a clear connection to the original magnetic system of interest is already lost. Nevertheless, one might expect that one can learn something about possible scenarios.

Finally spherical spins cannot be quantized in the same way as Ising spins via the application of a transverse field. Therefore they are usually quantized via the introduction of a kinetic energy term as in (15). In addition, various analytical techniques available for interacting soft spins with kinetic energy, such as the Schwinger-Keldysh formalism [54], are not available for spin operators. The microscopic details of the quantum dynamics described by either a transverse field or a kinetic energy term might be very different, on large timescales, however, one expects a similar behavior for the following reason. To see this, let us consider a model that consists of two terms; an arbitrary classical Hamiltonian, $H_{\rm cl}$, that is diagonal in the z-representation of the spins, and the transverse-field term. Performing a Trotter decomposition of the partition function of this model, one obtains

$$\begin{aligned}
\mathrm{Tr} e^{-\beta(\Gamma\sigma^x + H_{\rm cl}(\sigma^z))} &= \lim_{\Delta\tau\to 0}\prod_{\tau=1}^{L_\tau}\left\langle S_\tau \left| e^{-\Delta\tau[\Gamma\sigma^x + H_{\rm cl}(\sigma^z)]}\right| S_{\tau+1}\right\rangle \\
&\propto \lim_{\Delta\tau\to 0}\sum_{S_1,\ldots,S_{L_\tau}} \exp\left(-\Delta\tau\Big[\sum_{\tau=1}^{L_\tau} K(S_\tau - S_{\tau+1})^2 + H_{\rm cl}(S_\tau)\Big]\right)
\end{aligned} \tag{16}$$

where L_τ is the number of Trotter slices in the imaginary time direction, $\Delta\tau = \beta/L_\tau$ and K given by $e^{-2K} = \tanh(\Delta\Gamma)$. For $\Delta\tau \ll 1$ it is $K = |\ln(\Delta\tau\Gamma)|/2$. In the last step we neglected a constant factor $\cosh(\Delta\tau\Gamma)^{L_\tau}$. If we choose $\Delta\tau$ as a small time cut-off (representing the typical spin flip time) we can approximate the last Trotter sum as the imaginary time path integral

$$Z \approx \int \mathcal{D}S(\tau) \exp\left(\int_0^\beta d\tau \left[\frac{M}{2}\left(\frac{\partial S}{\partial \tau}\right)^2 + H_{\rm cl}(S(\tau))\right]\right) \tag{17}$$

where $M = 2K\Delta\tau = \Delta\tau|\ln(\Gamma\Delta\tau)|$. The first term in the integral of the action is identical to what one would obtain for the kinetic energy if one writes down the imaginary time path integral for the partition sum of the Hamiltonian (15). In this way, the transverse-field term and the kinetic-energy term are related.

In [42] the equilibrium properties of the model were obtained using a replicated imaginary-time path integral formalism[36] and analyzing the dynamical self-consistency equations for the spin auto-correlation function $C(\tau)$ arising in the limit $N \to \infty$ from a saddle point integration. The result for the phase diagram, EA order-parameter and linear susceptibility in the case $p = 3$ are depicted in Fig. 6, where the parameter $\Gamma = \hbar^2/(JM)$ has been used – resembling the transverse field strength (since for $\Gamma \to 0$ one recovers the classical case). Above a temperature T^* one has a continuous transition at a critical point $\Gamma = \Gamma_c(T)$ from a paramagnetic phase with vanishing EA order parameter to a spin glass phase with $q_{EA} \neq 0$ and one-step replica-symmetry-breaking (1RSB). Although the EA order-parameter jumps discontinuously the transition is second order: there is no latent heat (as in the classical case

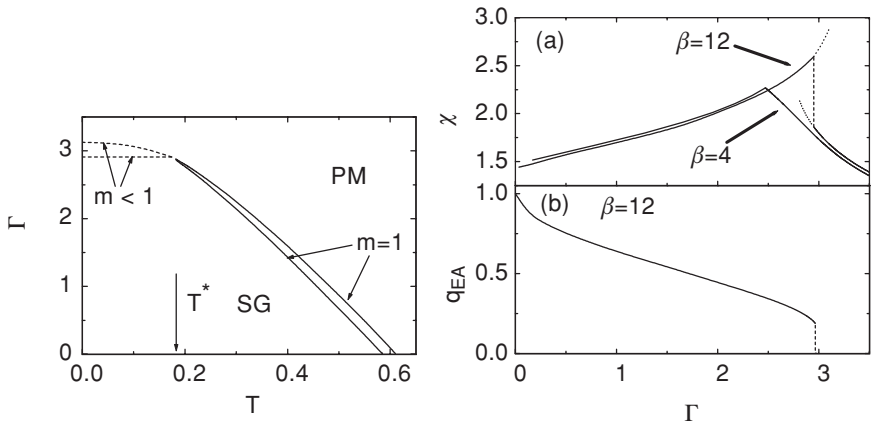

Fig. 6. *Left*: Static (*thin lines*) and dynamic (*thick lines*) phase diagrams of the p-spin model for $p = 3$. *Solid* and *dashed* lines represent second and first order transitions, respectively. *Right*: Magnetic susceptibility (**a**) and Edwards-Anderson order parameter (**b**) of the $p = 3$ model. (From [42])

$\Gamma = 0$) and the susceptibility has only a cusp. This is due to the fact that the parameter m characterizing the Parisi order parameter function $q(x)$ (which is a step function with a single step at $x = m$) is unity at the transition. However, for temperatures below T^* this parameter jumps at the transition, too, and the transition becomes discontinuous; for $T < T^*$ the transition is of the first order with latent heat and a discontinuous susceptibility (see Fig. 6).

3.2 Dissipative Effects

An important question that arises for interacting quantum spins at low temperatures are the effects of a dissipative environment [44, 45]. This is usually described in terms of its collective excitations, lattice vibrations, spin or charge fluctuations, etc., which may be thought of as an ensemble of independent quantum harmonic oscillators [46, 47, 48, 49, 50]. A concrete example of a single quantum degree of freedom, a spin-1/2 or a so-called two-level-system (TLS), coupled to a bath of bosons is the well-known spin-boson-model [44, 45]:

$$H = H_S + H_B + H_{SB} \tag{18}$$

where H_S, H_B and H_{SB} denote the Hamiltonian of the system, the bath and their coupling, respectively. These are given by

$$\begin{aligned} H_S &= -\Gamma\sigma^x \\ H_B &= \frac{1}{2}\sum_n (p_n^2/m_n + m_n\omega_n^2 x_n^2) \\ H_{SB} &= -\sum_n c_n x_n \sigma^z \end{aligned} \tag{19}$$

where Γ is the transverse field (or tunneling matrix element in the context of TLSs), n the index enumerating an infinite number of harmonic oscillators with coordinates and momenta, x_n and p_n, and mass and frequency, m_n and ω_n, respectively. The constant c_n is the coupling between oscillator n and the spin. The spectral density of the environment, $I(\omega) = \pi\sum_n(|c_n|^2/(m_n\omega_n)\delta(\omega - \omega_n))$, is commonly assumed to take the standard form[45]

$$I(\omega) = 2\alpha\hbar(\omega/\omega_{\rm ph})^{s-1}\omega e^{-\omega/\omega_c} \ , \tag{20}$$

where α is a dimensionless coupling constant, ω_c a high frequency cut-off (which can be set to $\omega_c = \infty$ if $0 < s < 2$), and $\omega_{\rm ph}$ a phonon frequency necessary in the non-ohmic ($s \neq 1$) case to keeps α dimensionless.

With standard techniques[51, 44] one can integrate out the oscillator degrees of freedom to express the partition function of the system solely in terms of the spin variables

$$Z = {\rm Tr}\, e^{-\beta H} = \int \mathcal{D}\sigma(\tau)\, \mathcal{T} \exp(-S/\hbar) \ , \tag{21}$$

where $\int \mathcal{D}\sigma(\tau)$ denotes a path integral over all spin configurations (in time), $\mathcal{T}$ is the imaginary time ordering operator and the action is

$$S = -\int_0^{\beta\hbar} d\tau\, \Gamma\sigma^x(\tau) - \frac{1}{2}\int_0^{\beta\hbar} d\tau \int_0^{\beta\hbar} d\tau'\, K(\tau-\tau')\sigma^z(\tau)\sigma^z(\tau')\ . \qquad (22)$$

The kernel $K(\tau)$ is related to the spectral density $I(\omega)$ and is for the ohmic case ($s = 1$) essentially an inverse square $K(\tau-\tau') \propto \alpha/(\tau-\tau')^2$. The effect of the dissipative environment is therefore a long range interaction of the quantum spin in imaginary time. In analogy to the Ising model with inverse square interactions[53] depending on the strength of the coupling constant α, the system is ferromagnetically ordered or paramagnetic in the imaginary time direction; for large α the spin is frozen and for small α the spin will tunnel.

Indeed, for the ohmic case, at zero temperature, there is a phase transition at $\alpha = 1$ [47, 48]. For $\alpha < 1$ there is tunneling and two distinct regimes develop. If $\alpha < 1/2$, the system relaxes with damped coherent oscillations; in the intermediate region $1/2 < \alpha < 1$ the system relaxes incoherently. For $\alpha > 1$ quantum tunneling is suppressed and $\langle\sigma^z\rangle \neq 0$, signaling that the system remains localized in the state in which it was prepared. These results also hold for sub-Ohmic baths while weakly damped oscillations persist for super-Ohmic baths [44]. At finite temperatures (but low enough such that thermal activation can be neglected) there is no localization but the probability of finding the system in the state it was prepared decreases slowly with time for $\alpha > \alpha_c$.

These conclusions hold for a single spin interacting with a bath. The question then arises as to which are the effects of the interplay between the spin-spin interactions and the spin-noise coupling in the physics of the interacting system. In [54] the effect of a dissipative bath on a mean-field spin glass model with p-spin interactions has been investigated. They studied the dissipative spin-boson system (19) for N interacting spins $H = H_S + H_B + H_{SB}$, where the bath Hamiltonian is the same, the coupling Hamiltonian gets an additional sum over the spin index i and H_S is now the p-spin Hamiltonian with transverse field

$$H_S = -\Gamma\sum_{i=1}^{N}\sigma_i^x - \sum_{i_1,\ldots,i_p} J_{i_1,\ldots,i_p}\sigma_{i_1}^z\cdots\sigma_{i_p}^z\ . \qquad (23)$$

The second term, namely, the multi-spin interaction term is the same as the one in (15). For the reason explained in the last section it is analytically easier to study spherical spins instead of quantum spin-1/2 degrees of freedom and the quantization of the spherical spins is done via the introduction of a kinetic energy term. The partition function then reads

$$Z = \int \mathcal{D}\sigma(\tau)\, \exp(-S/\hbar)\ , \qquad (24)$$

with the action

$$S = \int_0^{\hbar\beta} d\tau \left[\frac{M}{2} \sum_i \left(\frac{\partial s_i(\tau)}{\partial \tau} \right)^2 - \sum_{i_1 < \ldots < i_p} J_{i_1,\ldots,i_p} s_{i_1}(\tau) \cdots s_{i_p}(\tau) \right.$$
$$\left. + z \sum_i [s_i^2(\tau) - 1] \right] - \int_0^{\hbar\beta} d\tau \int_0^{\hbar\beta} d\tau' \, K(\tau - \tau') s_i(\tau) s_i(\tau') \,, \quad (25)$$

where the first term is the kinetic-energy term already motivated in (16–17) replacing the transverse-field term, the second is the p-spin interaction term, the third a term with the Lagrangian multiplier z enforcing the spherical constraint and the last term is the long range interaction imaginary time (22) that is generated by the integration over the bath variables.

Starting from (25) the saddle point equations for the self-consistent single-spin dynamics were derived[54] and the phase diagram computed. Analogous to the non-dissipative case discussed in the previous subsection a critical line with a second-order section (close to the classical critical point $(T_d, \Gamma = 0)$) and a first-order section (close to the quantum critical point $(T = 0, \Gamma_d)$) was obtained in the presence of a dissipative environment. The second order critical line is determined by the condition $m = 1$, the first order critical line is defined as the locus of the points where a marginally stable solution first appears with decreasing Γ for T fixed. For each Γ and α this defines a *dynamic* transition temperature $T_d(\Gamma, \alpha)$. The qualitative features of the phase diagram, similar to those found for the isolated system, see the discussion in the previous section. Notice that the line $T_d(\Gamma, \alpha)$ lies always *above* $T_s(\Gamma, \alpha)$, the static critical line that we shall discuss below.

On the right side of Fig. 7 the dynamic phase diagrams obtained for $p = 3$ and three values of the coupling to an Ohmic bath, $\alpha = 0, 0.25, 0.5$ is shown. The full line and the line-points represent second and first order transition, respectively.

The first observation that can be made is that in the limit $\Gamma \to 0$ the transition temperature is independent of the strength of the coupling to the bath. This is a consequence of the fact that in the limit $\Gamma \to 0$ the partition function is essentially determined by the zero-frequency components of the pseudo-spin which are decoupled from the bath. This result is however non-trivial from a dynamical point of view, since it implies that the dynamic transition of a classical system coupled to a colored classical bath is not modified by the latter.

The second observation is that the size of the region in the phase space where the system is in the ordered state increases with α. Coupling to the dissipative environment thus stabilizes this state. This follows from simple physical considerations. The interaction term in the action favors spin-glass order. Coupling to the bath favors localization and its effect is to reduce the effective tunneling frequency. Therefore, in the presence of the bath, the value of the bare tunneling frequency needed to destroy the ordered state

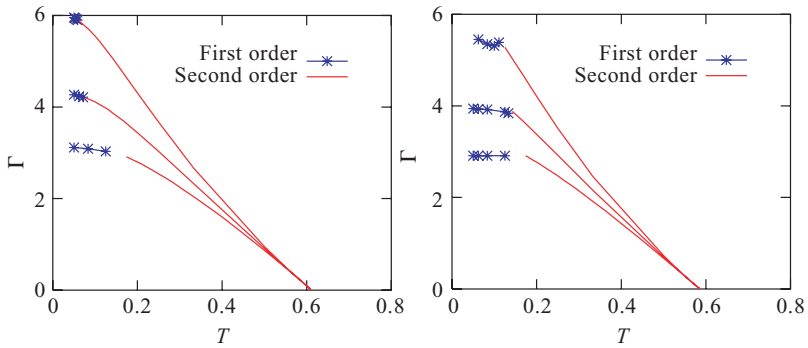

Fig. 7. Static (*left*) and dynamic (*right*) phase diagrams for the $p = 3$ spin model coupled to an Ohmic bath ($s = 1$). The couplings to the bath are $\alpha = 0$, 0.25, and 0.5 from bottom to top. The solid line and line-points represent second and first order transitions, respectively. (From [54])

must increase with α. Even if the localized state and the glassy state may seem superficially similar, they are indeed very different. In the former, the correlation function $C(t + t_w, t_w)$ approaches a plateau as a function of t and never decays toward zero while in the latter the relaxation first approaches a plateau but it eventually leaves it to reach zero for $t \gg t_w$. The fact that the coupling to the environment favors the ordered state also reflects itself in the value taken by the order parameters $C(\tau)$ and q_{EA}. As α increases, $q_d(\tau)$ reaches a higher plateau level at long imaginary times.

3.3 Off Equilibrium Dynamics

The out-of-equilibrium dynamics in real time of the quantum spherical p-spin glass model coupled to a dissipative environment, which was discussed in the last subsection, was actually studied earlier[55] than the equilibrium properties. The response and correlation function are defined in analogy to the classical case; $C(t + t_w, t_w) = N^{-1} \sum_i (s_i(t + t_w)s_i(t_w) + s_i(t_w)s_i(t + t_w))$ (note that the time evolution is now governed by the quantum dynamics and C has to be symmetrized in the operators $s_i(t + t_w)$ and $s_i(t_w)$) and $R(t + t_w, t_w) = N^{-1} \sum_i \delta s_i(t + t_w)/\delta h_i(t_w)$.

In equilibrium the quantum FDT relates $R(t)$ and $C(t)$:

$$R(t) = \frac{2i}{\hbar}\theta(t) \int \frac{d\omega}{2\pi} e^{-i\omega t} \tanh(\beta\hbar\omega/2) C(\omega) \tag{26}$$

Away from the critical line, C and R decay to zero very fast with oscillations. Approaching the critical line $T_d(\alpha)$, the decay slows down and if $T_d > 0$ a plateau develops in C. At the critical line the length of the plateau tends to infinity.

In the glassy phase (below the transition) the system does not reach equilibrium. For small time differences the dynamics is stationary and time translational invariance as well as the QFDT holds: $\lim_{t_w\to\infty} C(t+t_w,t_w) = q + C_{\rm eq}(t)$. For large times the dynamics is non-stationary, time translational invariance nor the QFDT does not hold, and the correlations decay from q to 0. The decay of C becomes monotonic in the aging regime, which implies $C_{\rm aging}(t+t_w,t_w) = c(h(t_w)/h(t+t_w))$. One can generalize the QFDT in the same spirit as the classical FDT was generalized [56]:

$$R(t+t_w,t_w) = \frac{2i}{\hbar}\theta(t)\int \frac{d\omega}{2\pi} e^{-i\omega t}\tanh(X(t+t_w,t_w)\beta\hbar\omega/2)C(t+t_w,\omega) \quad (27)$$

with $C(t,\omega) = 2{\rm Re}\int_0^t ds\, \exp[i\omega(t-s)]C(t,s)$. Again, as in the classical case, $T_{\rm eff} \equiv T/X(t+t_w,t_w)$ acts as an effective temperature in the system. For a model with two time-sectors it is proposed

$$X(t+t_w,t_w) = \begin{cases} X_{\rm st} = 1 & \text{if} \quad t \le \mathcal{T}(t_w) \\ X_{\rm age}(\hbar,T) & \text{if} \quad t > \mathcal{T}(t_w) \end{cases}.$$

with $X_{\rm age}$ a non-trivial function of $\hbar$ and T and $\mathcal{T}(t_w)$ is a certain time-scale that separates the stationary and aging time-regimes. When t and t_w are widely separated, the integration over ω in (27) is dominated by $\omega \sim 0$. Therefore, the factor $\tanh(X_{\rm age}(t+t_w,t_w)\beta\hbar\omega/2)$ can be substituted by $X_{\rm age}\beta\hbar\omega/2$ (*even at* $T=0$ if $X_{\rm age}(\hbar,T) = x(\hbar)T$ when $T\sim 0$). Hence,

$$R_{\rm age}(t+t_w,t_w) \sim \theta(t)X_{\rm age}\beta\partial_{t_w}C_{\rm age}(t+t_w,t_w) \quad (28)$$

and one recovers, in the aging regime, the *classical* modified FDT [56, 58].

The self-consistency equations for $C(t+t_w,t_w)$ and $R(t+t_w,t_w)$ were evaluated numerically in [55]. An example of the solution is shown in Fig. 8 for $p=3$. In all figures the following parameters have been chosen: zero temperature $T=0$, the width of the coupling distribution $J=1$, the frequency cut-off for the oscillator bath set to $\omega_c = 5$, the mass in the kinetic energy term $M=1$, and the strength of the quantum fluctuations $\tilde{\hbar} = \alpha\hbar$ (where α is the spin-bath coupling strength) is $\tilde{\hbar} = 0.1$.

These plots demonstrate the existence of the stationary and aging regimes. For $t < \mathcal{T}(t_w)$ (e.g. $\mathcal{T}(40)\sim 5$) time translational invariance and fluctuation dissipation theorem are established while beyond $\mathcal{T}(t_w)$ they break down. For $\tilde{\hbar} = 0.1$ the plateau in C is at $q\sim 0.97$. C oscillates around q but is monotonous when it goes below it. In the inset the dependence of q_{EA} on $\tilde{\hbar}$ for $T=0$ is presented. Quantum fluctuations generate a $q_{EA} < 1$ such that the larger $\tilde{\hbar}$ the smaller q_{EA}. The addition of thermal fluctuations has a similar effect, the larger T, the smaller q_{EA}. In order to check the FDT in the stationary regime, in the inset of the right part of Fig. 8 a comparison is shown of $R(t+t_w,t_w)$ from the numerical algorithm for $t+t_w = 40$ fixed and $t_w \in [0,40]$ (full line) with $R(t+t_w,t_w)$ from (27) with $X=1$ using

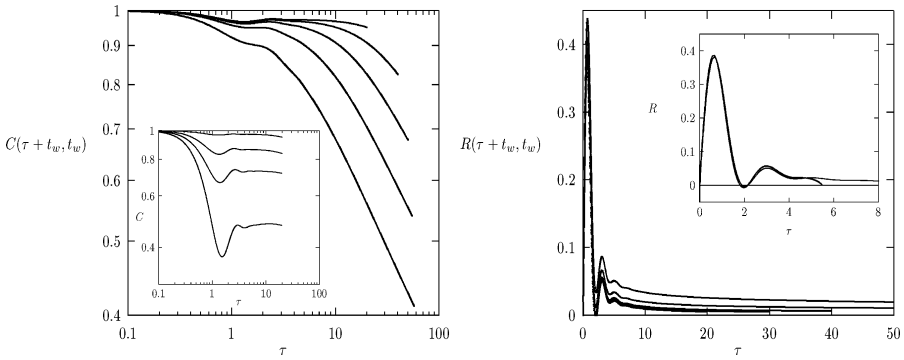

Fig. 8. *Left*: The correlation function $C(\tau + t_w, t_w)$ vs τ for the $p = 3$ quantum spherical p-spin SG model. The waiting times are, from bottom to top, $t_w = 2.5, 5, 10, 20, 40$. $q_{EA} \sim 0.97$. In the inset, the same curves for $t_w = 40$ and, from top to bottom, $\tilde{\hbar} = 0.1, 0.5, 1, 2$. *Right*: The response function for the same model as in the left part. The waiting-times increase from top to bottom. In the inset, check of FDT in the stationary regime. The full line is $R(t + t_w, t_w)$ for $t + t_w = 40$ fixed and $t_w \in [0, 40]$. The dots are obtained from (27) with $X_{\rm st} = 1$, using the numerical data for $C_{\rm stat}(t) = C(t + t_w, t_w) - q$ ($q_{EA} \sim 0.97$, see left part). In both cases the response is plotted against t. (From [55])

$C_{\rm stat}(t) = C(t+t_w, t_w) - q$, $q \sim 0.97$ obtained from the algorithm (dots). The accord is very good if $t \leq \mathcal{T}(t_w) \sim 5$. Finally, when one plots parametrically the integrated response χ vs. C one finds that for $C < q \sim 0.97$ the χ vs C curve approaches a straight line of *finite* slope $1/T_{\rm eff} = X_{\rm age}/T \sim 0.60$.

4 Heisenberg Quantum Spin Glasses

The spin-1/2 Heisenberg quantum spin glass is defined by the Hamiltonian (1) where the random exchange interactions J_{ij} can be ferromagnetic and anti-ferromagnetic. The system cannot be studied efficiently with quantum Monte-Carlo methods, due to the sign problem arising from the frustration. Therefore, not much is known about these models in finite dimensions, and also the mean field theory becomes tractable only in certain limits and approximations.

4.1 Finite Dimensions

In [61] and later in [62] small clusters of the two-dimensional Heisenberg quantum spin glass were studied using exact diagonalization. The average total spin in the ground state turned out to scale as $S \propto \sqrt{N}$, where N is the number of sites. The spin glass order parameter in the ground state extrapolates to a small but non-vanishing value in the thermodynamic limit and

the spin stiffness does not scale to zero either in the thermodynamic limit. Ma-Dasgupta-Hu renormalization group studies[14, 66] were performed for randomly frustrated spin-ladders[64] and in $d = 2$ and 3[65] for various lattices and spin-values. The general idea of this RG procedure was already described in Subsect. 2; large energies (in the form of exchange interactions) are successively decimated, ferromagnetic bonds lead to large spin formation and anti-ferromagnetic bonds to a spin reduction or even elimination in case of equal effective spins connected by the bond to be decimated.

The basic ingredient of the SDRG method in Heisenberg models is a successive decrease of the energy scale of excitations via a successive decimation of couplings. We start with a $S = 1/2$ HAF model in which the strongest coupling is, say J_{23}, the one between lattice sites 2 and 3 (c.f. Fig. 9). If J_{23} is much larger than its neighboring couplings J_{12}, J_{13}, J_{24} and J_{34}, the spins at 2 and 3 form an effective singlet and are decimated. The effective coupling between the remaining sites, 1 and 4 in second order perturbation theory is given by:

$$\tilde{J}_{14}^{\text{eff}} = \lambda \frac{(J_{12} - J_{13})(J_{34} - J_{24})}{J_{23}}, \quad \lambda(S = 1/2) = 1/2 \,. \tag{29}$$

In a chain geometry the couplings J_{13} and J_{24} would not be present and the resulting RG flow always generates AF couplings. However, for extended, not strictly $1d$ objects, some of the generated new couplings can be ferromagnetic (e.g. if $J_{12} < J_{13}$ and $J_{34} > J_{24}$ or vice versa) and therefore the decimation rules have to be extended. If at one RG step an F bond turns out to be the strongest one, its decimation will lead to an effective spin $\tilde{S} = 1$. In the following steps, the system will renormalize to a set of effective spins of different magnitude interacting via F *and/or* AF couplings.

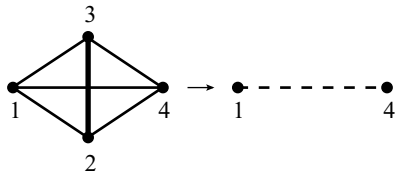

Fig. 9. Singlet formation and decimation for a spin configuration that does not have a chain topology and typically occurs in higher dimensional systems

For higher dimensional systems, the basic decimation processes are the singlet formation in (29) and the effective spin (cluster) formation. To specify the latter, let us consider three spins S_1, S_2 and S_3 with interactions fulfilling $|J_{23}| \gg |J_{12}|, |J_{13}|$. In the action of the RG, the two original spins S_2 and S_3 form a new effective spin of magnitude $\tilde{S} = |S_2 \pm S_3|$ representing the total spin of the ground state in the two-spin Hamiltonian $H_{23} = J_{23}\mathbf{S}_2\mathbf{S}_2$, where

the positive (negative) sign refers to an F (AF) coupling. The corresponding energy gap, Δ, between the ground state and the first excited state in the Hamiltonian H_{23} is given by $\Delta = |J_{23}|(S_2 + S_3)$ and $\Delta = J_{23}(|S_2 - S_3| + 1)$, for an F and AF coupling, respectively. If $J_{23} > 0$ (AF) and $S_2 = S_3$, it follows an effective singlet formation as described above. If $\tilde{S} \neq 0$, within first order perturbation theory the new coupling between S_1 and $\tilde{S}_{23}$ is given by

$$\tilde{J}^{\text{eff}} = c_{12}J_{12} + c_{13}J_{13} \ , \tag{30}$$

with

$$c_{12} = \frac{\tilde{S}(\tilde{S}+1) + S_2(S_2+1) - S_3(S_3+1)}{2\tilde{S}(\tilde{S}+1)}$$

and

$$c_{13} = \frac{\tilde{S}(\tilde{S}+1) + S_3(S_3+1) - S_2(S_2+1)}{2\tilde{S}(\tilde{S}+1)} \ .$$

At each RG step, we find the pair of the spins with the largest energy gap Δ that sets the energy scale, Ω, and decimate them according to renormalization rules described in (29) or (30). A detailed derivation of these renormalization rules can be found in [67].

The fixed point of the RG transformation for lattices that do *not* have a chain geometry may depend on their topology, the original distribution of bonds, the strength of the disorder, etc. We briefly summarize the existing results for spin chains and ladders since it might be helpful for analyzing the RG results in higher dimensional systems.

In the case of the random AF chain (which does neither have F bonds nor frustration), the RG procedure described above runs into an infinite randomness fixed point (IRFP) corresponding to a random singlet phase. In this phase the renormalized clusters are singlets, thus the total magnetic moment is zero, and the energy and length scales are related via

$$-\ln \Omega \sim L^{1/2} \ , \tag{31}$$

which means that the dynamical exponent is formally infinite.

A dimerized $S = 1/2$ chain with random AF even (J_{e}) and odd (J_{o}) couplings shows dimer order and the low-energy behavior is controlled by a *random dimer fixed point* at which the dynamical exponent, z, is finite and a continuously varying function of the strength of the dimerization measured by $\delta_{\text{dim}} = [\ln J_{\text{e}}]_{\text{av}} - [\ln J_{\text{o}}]_{\text{av}}$[22]. At this fixed point, the low-energy-tail of the distribution of the effective couplings, J_e, is given by:

$$P(J_{\text{e}}, \Omega)\mathrm{d}J_{\text{e}} \simeq \frac{1}{z}\left(\frac{J_{\text{e}}}{\Omega}\right)^{-1+1/z} \frac{\mathrm{d}J_{\text{e}}}{\Omega} \ , \tag{32}$$

for $\delta_{\text{dim}} > 0$. This random dimer phase is a Griffiths phase [8] and we refer to it as a Griffiths fixed point (GFP). At this GFP, the gap of finite chains of length L obey a distribution similar to (32):

$$P_L(\Delta) = L^z \tilde{P}(L^z \Delta) \sim L^{z(1+\omega)} \Delta^{\omega} \,, \tag{33}$$

which is characterized by the gap exponent, ω. As a consequence of (33), which holds in any dimension, several dynamical quantities at a GFP are singular and the characteristic exponents can all expressed via ω. For example the susceptibility χ, the specific heat C_v (at a small temperatures T), and the magnetization m (in a small field h), behave as:

$$\chi(T) \sim T^{-\omega}, \quad C_v(T) \sim T^{\omega+1}, \quad m(h) \sim h^{\omega+1} \,. \tag{34}$$

In the Griffiths phase there is a simple relation between the dynamical exponent, z, and the gap exponent, ω, which can be obtained by the following phenomenological consideration [11, 7, 20]: If the Griffiths singularities are due to rare events (produced by the couplings) that give rise to *localized* low-energy excitations, the gap distribution should be proportional to the volume, $P_L(\Delta) \sim L^d$. From (33) then follows:

$$z = \frac{d}{1+\omega} \quad \text{or} \quad \omega = -1 + \frac{d}{z} \,, \tag{35}$$

which is consistent with the exact result in the random dimer phase in (32). However, if the low-energy excitations are *extended* the relation (35) might not hold.

In a spin chain with mixed F and AF couplings [68], large effective spins, S_{eff}, are formed at the fixed point of the transformation. The size of these spin clusters scales with the fraction of surviving sites during decimation, $1/N$, as:

$$S_{\text{eff}} \sim N^{\zeta} \,. \tag{36}$$

The following random walk argument [68] gives $\zeta = 1/2$: The total moment of a typical cluster of size N can be expressed as $S_{\text{eff}} = |\sum_{1=1}^{N} \pm S_i|$, where neighboring spins with F (AF) couplings enter the sum with the same (different) sign. If the position of the F and AF bonds are uncorrelated and if their distribution is symmetrical, one has $S_{\text{eff}} \propto N^{1/2}$, i.e. (36) with $\zeta = 1/2$.

A non-trivial relation constitutes the connection between the energy scale Ω and the size of the effective spin:

$$S_{\text{eff}} \sim \Omega^{-\kappa} \,, \tag{37}$$

where a numerical estimate of the exponent is $\kappa = 0.22(1)$[68]. Comparing (36) with (37), the relation between the length scale $L \sim N^{1/d}$ ($d = 1$) and the energy scale is:

$$\Omega \sim L^{-z}, \quad z = \frac{d\zeta}{\kappa} = \frac{1}{2\kappa} \,, \tag{38}$$

where z is the dynamical exponent. The distribution of low-energy gaps, $P_L(\Delta)$, has the same power-law form as in (33). Therefore from the scaling behavior of $P_L(\Delta)$ the gap exponent, ω, and the dynamical exponent, z, can

be obtained. Due to the large moment formation the singularities of the dynamical quantities are different from those in the random dimer phase in (34), i.e. at a GFP. Generalizing the reasoning in [68], one obtains in d-dimensions:

$$\chi(T) \sim T^{-1},\ C_v(T) \sim T^{2\zeta(\omega+1)} |\ln T|,\ m(h) \sim h^{\frac{\zeta(1+\omega)}{1+\zeta(1+\omega)}}\ , \tag{39}$$

thus the singularities involve both exponents ζ and ω. In the following, we refer to this type of fixed point as large spin fixed point (LSFP).

AF spin ladders, although being quasi-one-dimensional, have a non-trivial, non-chain-like topology and during renormalization also F bonds can be generated according to (29). Different random AF two-leg ladders were studied in [64] with the following results: If the disorder is strong enough the gapped phases of the non-random systems become gapless. The low energy behavior is generally controlled by a GFP, where the dynamical exponent is finite and depends on the strength of the disorder. However, at random quantum critical points, separating phases with different topological or dimer order, the low-energy behavior is controlled by an IRFP. In diluted AF spin ladders also LSFP-s have been identified [69]. Thus in one-dimensional and in quasi-one-dimensional random Heisenberg systems there are two different types of low-energy fixed points, which are expected to be present in higher dimensional systems, too. Both for a GFP and for a LSFP, the low-energy excitations follow the same power-law form in (33) from which the exponents, ω and z can be deduced. At a GFP these two exponents are expected to be related through $z = \frac{d}{1+\omega}$ (35). On the other hand, for a LSFP, where the excitations are not localized, this relation probably does not hold. At such a LSFP there is a third independent exponent, ζ involved in the dynamical singularities partially listed in (39).

Various two- and three-dimensional Heisenberg antiferromagnets with random couplings were studied by the application of the SDRG described above [65]. Here we discuss the results for the Heisenberg model on the square lattice with a random mixture of F and AF couplings. This is a model for a Heisenberg quantum spin glass [61, 62] and the corresponding fixed point is denoted as a *spin glass fixed point* (SGFP) since it differs from the other fixed points one finds for non-frustrated models. In particular we one finds a large spin formation proportional to L during RG procedure implying a ground state spin $S \propto \sqrt{N}$, which is reminiscent of the spin glass behavior found in [61, 62] for this model with alternative methods.

For Gaussian randomness (i.e $P(J_{ij})$ a Gaussian with mean zero an variance one) the distributions of the gaps and of the effective spin moments are shown in Fig. 10. The gap-distributions for different finite sizes have a very similar structure: they are merely shifted to each other by a constant proportional to $\ln L$. The slope of the low-energy tail of the distributions is practically independent of the strength of disorder and in all cases the gap exponent is equal to:

$$\omega_{SG} = 0, \quad d = 2\ , \tag{40}$$

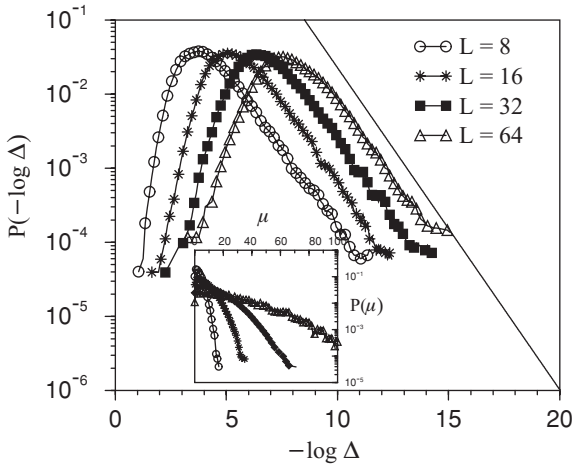

Fig. 10. Heisenberg spin glass in 2d: Probability distribution of the energy gap for a 2d Heisenberg antiferromagnet on a square lattice with J_{ij} distributed according to a Gaussian with mean zero and variance one. Inset: Distribution of the spin moments

within an accuracy of a few percent. From the finite-size scaling of the gap distribution, we infer that the relation in (35) is satisfied and therfore the excitations are localized, implying

$$z_{SG} = 2, \quad d = 2\,, \tag{41}$$

within an accuracy of a few percent.

On the other hand, the distribution of the effective spin moments in the inset to Fig. 10 shows a tendency to broaden with increasing system size and its average value has a linear L dependence, $[\mu_L]_{\rm av} \approx .42L$. Therefore the moment exponent in (36) is

$$\zeta_{SG} = 1/2, \quad d = 2\,, \tag{42}$$

Other coupling distributions, like a uniform distribution of J_{ij} between -1 and $+1$, other spin values ($S = 1$ in addition to $S = 1/2$) yield the same critical exponents as in the Gaussian case. Thus one can conclude that the low-energy behavior in randomly frustrated $2d$ models is controlled by the same SGFP, independent of the type of randomness and the size of the spin. Even more, also geometrically frustrated Heisenberg models with random antiferromegnetic couplings are described by the same SGFP in 2d [65].

In 3d SDRG computations for models with mixed F and AF couplings for different form of initial randomness (Gaussian, symmetric and asymmetric rectangular) and different spin values have been performed [65]. Figure 11 shows the resulting gap distributions. One observes that the slopes of the low-energy tail of the gap-distributions are approximately constant, and for our finite systems they are consistent with a vanishing gap exponent:

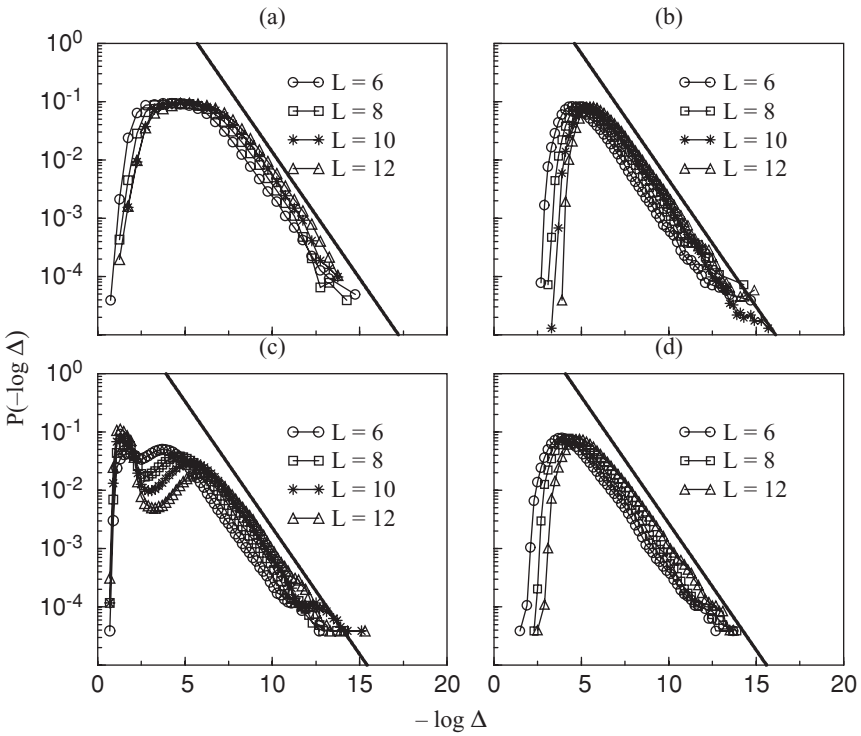

Fig. 11. Probability distribution of the energy gap on the cubic lattice with mixed F and AF bonds. (**a**) Gaussian distribution, $\sigma = 1$; (**b**) symmetric rectangular distribution ($r = 0$); (**c**) asymmetric rectangular distribution ($r = 0.25$); (**d**) $S = 1$ symmetric rectangular distribution. The low-energy tails of the gap distributions for all cases, indicated by straight lines, have a slope -1, corresponding to $\omega = 0$

$$\omega \approx 0 \quad (d = 3)\ . \tag{43}$$

During renormalization, as in $2d$, there is a large spin formation and the corresponding moment exponent is $\zeta = 0.55$, for symmetric distributions (Gaussian and rectangular) and $\zeta = 0.58$ for the asymmetric rectangular distribution. Thus ζ appears to be close to $1/2$ in both cases. The scaling behavior of the reduced gap distribution, $\tilde{P}(L^z\Delta) = L^{-z}P_L(\Delta)$ is shown in Fig. 12, and yields $z \approx 1.5$ independently of the disorder distribution. The scaling curves seem to tend to a finite limiting value at $\Delta = 0$, implying a gap exponent $\omega \approx 0$. One can thus conclude that – within the range of validity of the SDRG method – the relation in (35) is not valid for frustrated 3d models.

To summerize the picture that emerges from the application of the SDRG to Heisenberg quantum spin glasses in 2 and 3 dimensions: The ground state magnetization increases with system size as $\sqrt{N}$, the probability distribution of the low energy excitations scales as $P(\Delta) \sim \Delta^{\omega}$ with $\omega = 0$, i.e. $P(\Delta)$ does

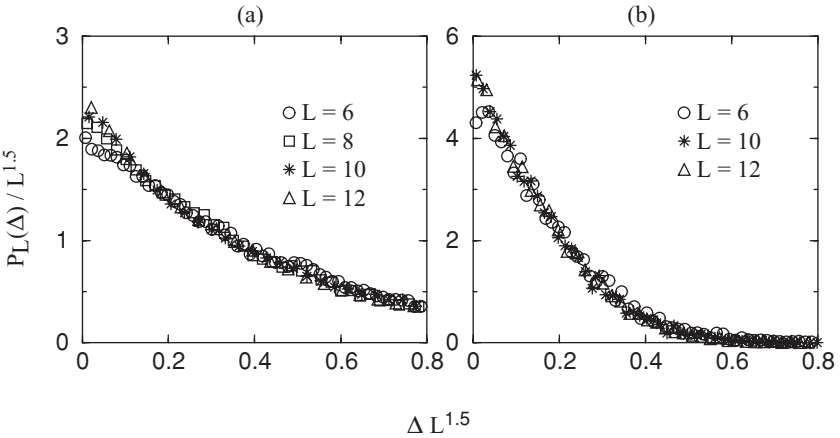

Fig. 12. Scaling of the reduced gap distribution, $\tilde{P}(L^z\Delta) = L^{-z}P_L(\Delta)$, for randomly frustrated 3d systems: **a**) Gaussian randomness, $\sigma = 1$, **b**) uniform randomness. In both cases it is $z = 1.5$

not diverge (or only weakly) at $\delta = 0$ in $2d$ as well as in $3d$ and the dynamical critical exponent is $z = 2$ in $d = 2$ and $z = 3/2$ in $d = 3$.

4.2 Mean-Field Model

The first analytical treatment of the mean-field model of the Heisenberg quantum spin glass was performed in [36] applying the replica theory. Although the solution was confined to the paramagnetic state, the arguments for the existence of a low-temperature spin-glass phase were given and the critical temperature was estimated.

Later a Landau theory for quantum rotors on a regular d-dimensional lattice was studied in [39], which is defined by the Hamiltonian

$$H = \frac{g}{2}\sum_i \hat{\mathbf{L}}_i^2 - \sum_{\langle ij\rangle} J_{ij}\hat{\mathbf{n}}_i\hat{\mathbf{n}}_j \quad , \tag{44}$$

where $\hat{\mathbf{n}}_i$ are M-component vectors of unit length ($\hat{\mathbf{n}}_i^2 = 1$) and represent the orientation of the rotors on the surface of a sphere in M-dimensional rotor space. The operators $\hat{\mathbf{L}}_{i\mu\nu}$ ($\mu < \nu$, $\mu, \nu = 1, \ldots, M$) are the $M(M-1)/2$ components of the angular momentum $\hat{\mathbf{L}}_i$ of the rotor: the first term in H is the kinetic energy of the rotor with $1/g$ the moment of inertia. The different components of $\hat{\mathbf{n}}_i$ constitute a complete set of commuting observables and the state of the system can be described by a wave function $\Psi(n_i)$. The action of $\hat{\mathbf{L}}_i$ on Ψ is given by the usual differential form of the angular momentum $\hat{\mathbf{L}}_{i\mu\nu} = -i(n_{i\mu}\partial/\partial_{i\nu} - n_{i\nu}\partial/\partial_{i\mu})$. The difference between rotors and Heisenberg-Dirac quantum spins is that the components of the latter at the same site do not commute, whereas the components of the $\hat{\mathbf{n}}_i$ do.

In [39] a Landau theory for this model is derived and it is shown that for a suitable distribution of exchange constants J_{ij} this model displays spin-glass and quantum paramagnetic phases and a zero-temperature quantum phase transition between them. The mean-field phase diagram near the $T = 0$ critical point is mapped out as a function of T, the strength of the quantum coupling g and applied fields. The spin glass phase has replica symmetry breaking. Moreover, the consequences of fluctuations in finite dimensions are considered and above $d = 8$ the transition turned out to be controlled by a Gaussian fixed point with mean-field exponents. Below $d = 8$ a runaway RG flow to strong coupling was found.

Recently the mean-field Heisenberg quantum spin glass model was generalized from the $SU(2)$ spin algebra to an $SU(N)$ symmetry and solved in the limit $N \to \infty$ [70]. Certain universal critical properties are shown to hold to all orders in $1/N$. A spin-glass transition was found for all values of the spin S and the phase diagram as a function of the spin S and temperature T was described. The quantum critical regime associated with the quantum transition at spin value $S = 0$ and the various regimes in the spin-glass phase at high spin are analyzed. The specific heat is shown to vanish linearly with temperature.

The out-of-equilibrium dynamics of the the same model in the same limit $N \to \infty$, but coupled to a thermal bath, was studied in [71]. It was found that the model displays a dynamical phase transition between a paramagnetic and a glassy phase. In the latter, the system remains out-of-equilibrium and displays an aging phenomenon, which we characterize using both analytical and numerical methods. In the aging regime, the quantum fluctuation-dissipation relation is violated and replaced over a very long time-range by its classical generalization, as in models involving simple spin algebras studied previously.

In the context of Heisenberg spin glasses also the work on metallic spin glasses should be mentioned, which were first considered in [57] and later more extensively in [59], [72] and [73]. The main ingredient of a metallic spin glass is an itinerant electron systems with random (and frustrated) exchange interactions between the electron spins. Thus in contrast to the spin glass systems discussed so far the spins are not fixed to particular sites but can diffuse (quantum mechanically) from site to site. These systems are motivated by experiments on heavy-fermion compounds such as $Y_{1-x}U_xPd_3$,[60] which appear to show a paramagnetic to spin-glass transition with increasing doping, x, in a metallic regime. To be concrete the Hamiltonian studied in [72] is

$$H = -\sum_{i<j,\alpha} t_{ij} c_{i\alpha} c_{j\alpha} - \sum_{i<j,\mu} J_{ij} S_{i\mu} S_{j\mu} + H_{\rm int} \ , \tag{45}$$

where $c_{i\alpha}$ annihilates an electron on site i with spin $\alpha = \uparrow, \downarrow$, and the spin operator is given by $S_{i\mu} = \sum_{\alpha\beta} c^+_{i\alpha} \sigma^\mu_{\alpha\beta} c_{i\beta}/2$, with σ^μ the Pauli spin matrices. The sites i, j lie on a d-dimensional lattice, the hopping matrix elements t_{ij} are short-ranged and possibly random, and the J^μ_{ij} are Gaussian random

exchange interactions, possibly with spin-anisotropies. The remainder $H_{\rm int}$ includes other possible short-range interactions between the electrons, and the resulting total Hamiltonian H has a metallic ground state.

Starting from this Hamiltonian, in [72], an effective field theory for the vicinity of a zero temperature quantum transition between a metallic spin glass ("spin density glass") and a metallic quantum paramagnet was introduced. Following a mean-field analysis, a perturbative renormalization-group study was performed and it was found that critical properties are dominated by static disorder-induced fluctuations, and that dynamic quantum-mechanical effects are dangerously irrelevant. A Gaussian fixed point was found to be stable for a finite range of couplings for spatial dimensionality $d > 8$, but disorder effects always lead to runaway flows to strong coupling for $d \leq 8$. Moreover, scaling hypotheses for a *static* strong-coupling critical field theory were proposed. The non-linear susceptibility has an anomalously weak singularity at such a critical point.

In [73] the competition between the Kondo effect and RKKY interactions near the zero-temperature quantum critical point of an Ising-like metallic spin-glass was studied. In the 'quantum-critical regime,' non-analytic corrections to the Fermi liquid behavior were found for the specific heat and uniform static susceptibility, while the resistivity and NMR relaxation rate have a non-Fermi liquid dependence on temperature.

References

1. S. Sachdev: *Quantum Phase Transitions* (Cambridge University Press, 1999). 70
2. B. K. Chakrabarti, A. Dutta, and P. Sen, *Quantum Ising Phases and Transitions in Transverse Ising Models*. In: Lect. Notes Phys. **m41** (1996) 70
3. H. Rieger and A. P. Young: *Quantum Spin Glasses*, Lect. Notes Phys. **492** "Complex Behaviour of Glassy Systems", p. 254, ed. J.M. Rubi and C. Perez-Vicente (Springer Verlag, Berlin-Heidelberg-New York, 1997). 70, 78
4. R. N. Bhatt in *Spin Glasses and Random Fields*, ed. A. P. Young (World Scientific, Singapore, 1998). 70, 78
5. W. Wu, D. Bitko, T. F. Rosenbaum, and G. Aeppli, Phys. Rev. Lett. **71**, 1919 (1993). 70, 80
6. H. Rieger and A. P. Young, Phys. Rev. Lett. **72**, 4141 (1994). 78
7. H. Rieger and A. P. Young, Phys. Rev. B **54**, 3328 (1996). 74, 78, 91
8. R.B. Griffiths, Phys. Rev. Lett. **23**, 17 (1969). 73, 74, 90
9. B.M. McCoy and T.T. Wu, Phys. Rev. **176** (1968) 631; **188** (1969) 982; B.M. McCoy, Phys. Rev. **188** (1969) 1014. 72, 73
10. D.S. Fisher, Phys. Rev. Lett. **69** (1992) 534; Phys. Rev. B **51** (1995) 6411. 72, 73
11. M. J. Thill and D. A. Huse, Physica A **214**, (1995) 321. 74, 91
12. F. Iglói and H. Rieger, Phys. Rev. B **57**, 11404 (1998).
13. D. S. Fisher, Physica A **263** (1999) 222. 71, 73, 74, 78
14. S. K. Ma, C. Dasgupta, and C.-K. Hu, Phys. Rev. Lett. **43** (1979) 1434; C. Dasgupta and S. K. Ma, Phys. Rev. B **22** (1980) 1305. 72, 89
15. F. Iglói and H. Rieger, Phys, Rev. Lett. **78** (1997) 2473. 72, 75

16. F. Iglói and H. Rieger, Phys. Rev. B **57** (1998) 11404. 72, 75
17. H. Rieger and F. Iglói, Europhys. Lett. **39** (1997) 135. 72, 75
18. F. Iglói, D. Karevski and H. Rieger, Eur. Phys. J. B **1** (1998) 513; **5** (1998) 613. 72, 75
19. F. Iglói and H. Rieger, Phys. Rev. E **58** (1998) 4238. 72, 75
20. F. Iglói, R. Juhász and H. Rieger, Phys. Rev. B **59** (1999) 11308. 72, 75, 91
21. H. Rieger and F. Iglói, Phys. Rev. Lett. **83** (1999) 3741. 72, 75
22. F. Iglói, R. Juhász und H. Rieger, Phys. Rev. B **61** (2000) 11552. 72, 75, 90
23. A. P. Young and H. Rieger, Phys. Rev. B **53** (1996) 8486. 72
24. T. Senthil and S. Sachdev, Phys. Rev. Lett. **77**, (1996) 5292. 75
25. T. Ikegami, S. Miyashita and H. Rieger, J. Phys. Soc. Jap. **67** (1998) 2761. 75
26. C. Pich, A. P. Young, H. Rieger and N. Kawashima, Phys. Rev. Lett. **81** (1998) 5916. 77
27. H. Rieger and N. Kawashima, Eur. Phys. J. B **9** (1999) 233. 77
28. O. Motrunich, S.-C. Mau, D. A. Huse, D. S. Fisher, Phys. Rev. B **61** (2000) 1160. 77
29. Y.-C. Lin, N. Kawashima, F. Iglói, and H. Rieger, Prog. Theor. Phys. Suppl. **138**, 479 (2000). 77
30. Y. V. Fedorov and E. F. Shender, Zh. Eksp. Teor. Fiz. **43**, 526 (1986) [JETP Lett. **43**, 681 (1986)]. 79
31. M. Guo, R. N. Bhatt, and D. A. Huse, Phys. Rev. Lett. **72** (1994) 4137. 78
32. M. Guo, R. N. Bhatt, and D. A. Huse, Phys. Rev. B **54** (1996) 3336. 78
33. Y. Y. Goldschmidt and P. Y. Lai, Phys. Rev. Lett. **64**, 2467 (1990). 79, 80
34. K. D. Usadel and B. Schmidt, Solid State Comm. **64**, 975 (1987). 79
35. T. Yamamoto and H. Ishii, J. Phys. C. **20**, 6053 (1987). 79
36. A. J. Bray and M. A. Moore, J. Phys. C **13**, 655 (1980). 79, 82, 95
37. J. Miller and D. A. Huse, Phys. Rev. Lett. **70**, 3147 (1993). 79, 80
38. J. Ye, S. Sachdev, and N. Read, Phys. Rev. Lett. **70**, 4011 (1993). 79
39. N. Read, S. Sachdev, and J. Ye, Phys. Rev. B **52**, 384 (1995). 79, 80, 95, 96
40. M. J. Rozenberg and D. R. Grempel, Phys. Rev. Lett. **81**, 2550 (1998). 80
41. D. R. Grempel and M. J. Rozenberg, Phys. Rev. Lett. **80**, 389 (1998). 80
42. L. F. Cugliandolo, D. R. Grempel, and C. A. da Silva Santos, Phys. Rev. Lett. **85**, 2589 (2000); Phys. Rev. B **64**, 014403 (2001). 78, 80, 82
43. M. Suzuki, Prog. Theor. Phys. **56**, 1454 (1976).
44. A. J. Leggett et al., Rev. Mod. Phys. **59**,1 (1987); **67**, 725 (1995). 83, 84
45. U. Weiss, in Series Modern Condensed Matter Physics Vol. 2. (World Scientific, Singapore, 1993). 83
46. A. O. Caldeira and A. J. Leggett, Phys. Rev. Lett. **46**, 211 (1981); Ann. Phys. N.Y. **149**, 374 (1983). 83
47. A. J. Bray and M. A. Moore, Phys. Rev. Lett. **49**, 1545 (1982). 83, 84
48. S. Chakravarty, Phys. Rev. Lett. **49**, 681 (1982); S. Chakravarty and A. J. Leggett, ibid. **52**, 5 (1984). 83, 84
49. R. P. Feynman and F. L. Vernon, Jr., Ann. Phys. N.Y. **24**, 118 (1963). 83
50. N. V. Prokofev and P. C. E. Stamp, Phys. Rev. Lett. **80**, 5794 (1998). 83
51. H. Grabert, P. Schramm, and G-L. Ingold, Phys. Rep. **168**, 115 (1988). 83
52. A. Caldeira and A. Legget, Phys. Rev. A **31**, 1059 (1985).
53. W. Anderson and G. Yuval, Phys. Rev. Lett. **32**, 89 (1969); J. Phys. C **4**, 607 (1971); P. W. Anderson, G. Yuval, and D. R. Hammann, Phys. Rev. B **1**, 4464 (1970). 84
54. L. F. Cugliandolo, D. R. Grempel, G. Lozano, H. Lozza, and C. A. da Silva Santos, Phys. Rev. B **66**, 014444 (2002). 81, 84, 85, 86

55. L. F. Cugliandolo and G. Lozano, Phys. Rev. Lett. **80**, 4979 (1998). 86, 87, 88
56. L. F. Cugliandolo and J. Kurchan, J. Phys. A **27** (1994) 5749. 81, 87
57. J. A. Hertz, Phys. Rev. B **19** (1979) 4796. 96
58. T. Giamarchi and P. Le Doussal, Phys. Rev. **B53** (1996) 15206. 87
59. R. Oppermann and M. Binderberger, Ann. Phys. (N.Y.) **3** (1994) 494. 96
60. W. D. Wu et al., Phys. Rev. Lett. **72** (1994) 3722. 96
61. Y. Nonomura and Y. Ozeki, J. Phys. Soc. Jpn., **64**, 2710 (1995). 88, 92
62. J. Oitmaa and O. P. Sushkov, Phys. Rev. Lett. **87**, 167206 (2001). 88, 92
63. L. Arrachea and M. J. Rozenberg, Phys. Rev. Lett. **86**, 5172 (2001).
64. R. Mélin, Y.-C. Lin, P. Lajkó, H. Rieger and F. Iglói, Phys. Rev. B **65**, 104415 (2002); 89, 92
65. Y.-C. Lin, R. Mélin, H. Rieger and F. Iglói, Phys. Rev. B **68**, 024424 (2003). 89, 92, 93
66. D. S. Fisher, Phys. Rev. B **50**, 3799 (1994). 89
67. R. Mélin, Eur. Phys. J. B **16**, 261 (2000). 90
68. E. Westerberg, A. Furusaki, M. Sigrist and P.A. Lee, Phys. Rev. Lett. **75**, 4302 (1995); Phys. Rev. B **55**, 12578 (1997). 91, 92
69. E. Yusuf and K. Yang, preprint-cond-mat/0208458. 92
70. A. Georges, O. Parcollet, and S. Sachdev, Phys. Rev. Lett. **85**, 840 (2000); Phys. Rev. B **63**, 134406 (2001). 96
71. G. Biroli and O. Parcollet, Phys. Rev. B **65**, 094414 (2002) 96
72. S. Sachdev, N. Read, and R. Oppermann, Phys. Rev. B **52**, 10286 (1995). 96, 97
73. A. Sengupta and A. Georges, Phys. Rev. B **52**, 10295 (1995). 96, 97

Ergodicity, Replica Symmetry, Spin Glass and Quantum Phase Transition

Jong-Jean Kim

Physics Department, KAIST,
Daejeon 305-701, Korea
jjkim@kaist.ac.kr

1 Introduction

This pedagogical lecture note is aimed at a tutorial introduction to the essential concepts of spin glass with a focus on quantum spin glass in order to make a comfortable contact with spin glass problems in quantum annealing and optimization applications.

Although this subject of spin glass is well known, quantum spin glass has been considered something beyond reality as noted in the book of Fisher and Hertz[1], where we read "$\cdots$ because quantum effects are not very important in the materials which have been studied experimentally, nor have quantum models been a significant part of the conceptual theoretical developments."

They were both frontier pioneers studying quantum effects on spin glass to introduce the Heisenberg quantum spin glass[2] and a quantum phase transition in Fermi liquid metals[3].

I would like to follow also this classics on spin glass by Fisher and Hertz[1] to give an overview of spin glass phenomenology.

Thus this lecture will be presented according to the outlines as follows

(1) Introduction
(2) Overview of spin glass
(3) Ergodicity
(4) Replica symmetry
(5) Glass Transition
(6) Quantum phase transition
(7) Quantum spin glass
(8) Appendix

Indeed, nothing new from my own but more comprehensive introductions of representative works, already so well presented as in many other previous lecutre notes [4, 5, 6, 7, 8, 9, 10] and books [1, 11, 12, 13, 14], are attempted.

J.-J. Kim: *Ergodicity, Replica Symmetry, Spin Glass and Quantum Phase Transition*, Lect. Notes Phys. **679**, 101–129 (2005)
www.springerlink.com

2 Overview of Spin Glass

Spin glass is characterized by a cusp anomaly of magnetic susceptibility at finite temperature and a very slow dynamics of relaxations represented by a power law or a stretched exponential tail. Figures 1 & 2 are intended to show the essential schematics of these spin glass anomalies [1, 11, 15, 16].

Figure 1 represents a typical experimental data of a real part susceptibility measured as a function of temperature at dc static (solid line), very low frequency ac fields (• • •), and high frequency ac fields (○ ○ ○). A sharp cusp discontinuity can be observed at $T = T_g$ only with a small field dc static measurement, and already at mHz ac fields this cusp anomaly is changed to a continuous peak, which becomes more rounded as the ac frequency of the probe field increases to kHz [1, 11, 15].

In Fig. 2 a schematic cartoon of the remanent magnetization decaying after removal of magnetic field is depicted to show the experimental data of

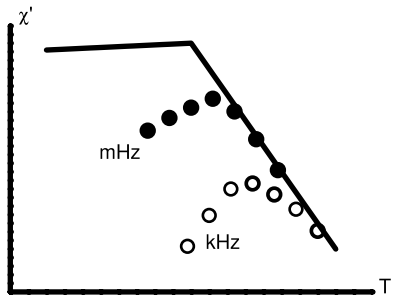

Fig. 1. A schematic drawing of magnetic susceptibility χ' across the spin glass transition probed by χ_{FC}-static (*solid line*), mHz (• • •), and kHz (○ ○ ○) ac fields as a function of temperature (see for details of experimental measurements [1, 11, 15])

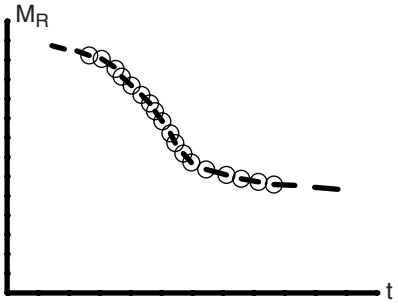

Fig. 2. A schematic cartoon of remanent magnetization observed as a function of time after removal of the applied field in the spin glass phase (see for details of experimental measurements [1, 11, 16]). Experimental data (○ ○ ○) are fitted (− − −) by a power law decay function t^{-x} plus a stretched exponential dacay function $\exp -(t/\tau)^{\beta}$ [16]

measurements ($\circ\ \circ\ \circ$) best fitted ($-\ -\ -$) by a power law plus a stretched exponential decay function.

A power law function is seen to fit the experimental data in the tail part whereas a stretched exponential function better fits the head part of the data, and there is certainly a region where both power law and stretched exponential functions can best fit the experimental data.

A small concentration ($0.1\% \sim 10\%$) of transition metal magnetic impurities (Mn, Cr, Fe, etc.) in noble metals (Cu, Ag, Au, etc.) forms a canonical spin glass.

We have also insulating mixed crystal spin glass systems between ferromagnetic and antiferromagnetic components, and many other spin glass systems including amorphous or diluted magnetic semiconductors [1, 11].

Spin glass is characterized by randomly competing interactions and quenched disorders. A simple model has been known for long [1, 4, 11, 12] to capture essential features of the spin glass transition

$$H = -\frac{1}{2}\sum_{i>j} J_{ij}\,\overrightarrow{S}_i \cdot \overrightarrow{S}_j$$

with the random interaction variables $\{J_{ij}\}$ assumed to have a Gaussian distribution

$$P(J_{ij}) = \frac{1}{\sqrt{2\pi\Delta_{ij}}}\exp(-{J_{ij}}^2/2\Delta_{ij})$$

The short-range Edward-Anderson model [17] can be simplified when the Heisenberg spins are replaced by the Ising spins on a regular lattice of translational symmetry so that we can take

$$\langle {J_{ij}}^2\rangle_C = \Delta_{ij} = \Delta(\overrightarrow{R}_i - \overrightarrow{R}_j)$$

where $\langle\cdots\rangle_C$ represents a configurational average over the Gaussian random distribution of $\{J_{ij}\}$. The difference between annealed-disorder paramagnetic phase and quenched-disorder spin glass phase can be described by the Edwards-Anderson order parameter q_{EA} defined by

$$q_{EA} = \lim_{t\to\infty}\lim_{N\to\infty}\langle\langle S_i(t_0)S_i(t_0+t)\rangle_{t_0}\rangle_C$$

where $\langle\cdots\rangle_{t_0}$ represents an average over an infinite set of initial times t_0. This q_{EA} can be seen to be zero when the system is ergodic as in the paramagnetic phase with $S_i = \pm 1$.

One important ingredient to form a spin glass is frustration [1, 11, 12, 18], and the Mattis disorder system lacking of frustration is known to have no spin glass transition [1, 7, 19, 20].

We show a schematic illustration of frustration in Fig. 3. Figure 3 (a,b) illustrates a possible generation of frustration by a randomly competing interaction between $+J$ and $-J$ in a square lattice.

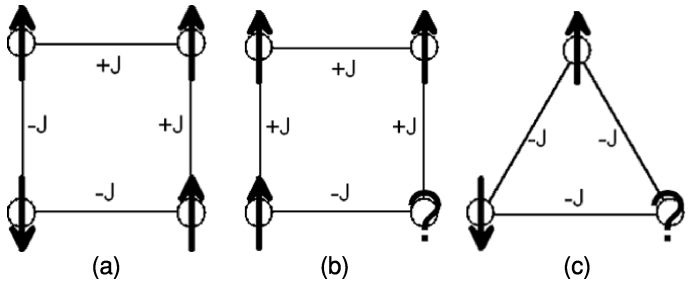

Fig. 3. Origins of frustration. Rectangluar lattice systems with random bond disorder (**a**, **b**), and a triangluar lattice system with all antiferromagnetic bonds and no random bond disorder (**c**). Frustrations are generated in (b) and (c). See [1, 11, 12, 18] and [20] for more details

For a square lattice system a frustration spin site can be produced only when the four random bonds are distributed to give an odd number of $-J$ and $+J$ bonds so that only the (b) system is frustrated but the random disorder system (a) is not frustrated. Fig. 3(c) illustrates a triangular lattice of no random disorder but uniform $-J$ bonds can have frustration generated due to a geometrical constraint [1, 12].

Ising spin version of the Edwards-Anderson model in the infinite-range interaction, mean field approximation was then introduced by Sherrington and Kirkpatrick [21]. The SK solution of this mean field model was found to be unstable in magnetic field in the low temperature region below the Almeida-Thouless line [22].

Parisi then succeeded to find a stable solution of the SK model in the low temperature phase characterized by the replica symmetry breaking and the order parameter function [23].

In more realistic 3D systems of spin glass model it has been shown that there is no Almeida-Thouless line, that is, no phase transition under magnetic field, implying that any finite magnetic field would destroy the equilibrium phase of spin glass state [24].

Susceptibility defined as $\chi = \partial M/\partial H$ in magnetic materials, where magnetization M can be easily measured, need a more general definition from the fluctuation-dissipation theorem to be extended to spin glass :

$$\chi(T, H = 0) = \frac{\mu_0}{k_B T} \frac{1}{V} \sum_{i>j} \left(\langle \langle S_i S_j \rangle - \langle S_i \rangle \langle S_j \rangle \rangle_C \right)$$

In spin glass of no spatial ($i \neq j$) correlations and thus no magnetization, with $\langle \langle {S_i}^2 \rangle \rangle_C = 1$ and $\langle \langle S_i \rangle^2 \rangle_C = q$, we can obtain [1, 15]

$$\begin{aligned} \chi(T) &= \frac{\mu_0}{k_B T} \frac{1}{V} \sum_{i=j} \left(S^2 - \langle \langle S_i \rangle^2 \rangle_C \right) \\ &= \chi_0 - \frac{\mu_0}{k_B T} q(T) \end{aligned}$$

where $S = |S_i|$, $\chi_0 = \mu_0 S^2 N/Vk_BT$, and a Gaussian distribution is assumed for quenched random disorder variables in the configurational average of $\langle\cdots\rangle_C$.

We may thus obtain the order parameter $q(T)$ from the susceptibility measurements. However, the static susceptibility can not be readily measured due to extremely slow responses as $T \to T_g$ [15].

We can also define a nonequilibrium local order parameter $q(t)$ as

$$q(t) = \langle\langle S_i(0)S_i(t)\rangle\rangle_C \ .$$

We can then find [25]

$$\lim_{t\to\infty} q(t) = q_{EA}$$

and true equilibrium order parameter can be seen to be obtained by

$$q = \lim_{N\to\infty}\lim_{t\to\infty} q(t) \ .$$

In terms of the time-dependent local order parameter $q(t)$ we may thus define the time dependent susceptibility as [11]

$$\chi(t) = \frac{1}{k_BT}[1 - q(t)]$$

corresponding to the dynamical susceptibility as defined from the Sompolinsky dynamic formulation [1, 26].

Instead of the cusp anomaly for all these linear response susceptibilities a divergence at T_g is expected in the order parameter random field susceptibility χ_{SG} defined as [15]

$$\begin{aligned}\chi_{SG} &\propto \frac{1}{(k_BT)^2}\Big\langle(\langle\sigma_i\sigma_j\rangle - \langle\sigma_i\rangle\langle\sigma_j\rangle)^2\Big\rangle_C \\ &\propto \epsilon^{-\gamma}\end{aligned}$$

where $\epsilon = (T - T_g)/T_g$.

This divergence is more discernible than the cusp anomaly by experimental measurements. What is more, this χ_{SG} conjugate to random field is found to be proportional to the second order nonlinear susceptibility χ_2 measurable by a laboratory uniform field. Nonlinear susceptibility χ_{nl} is defined by a power series expansion of the magnetization M [1, 11]

$$M = \chi_0 h - \chi_2 h^3 + \cdots$$

that is, $\chi_{nl} = \chi_0 - M/h = \chi_2 h^2 + \chi_4 h^4 + \cdots$.

Scaling analysis can be applied to χ_{SG}, that is, experimental data of χ_2 measurements, to obtain various critical exponents of the spin glass transition at T_g [15].

With applied fields of $h = H + h' \cos \omega t$, where H is a dc field and $h' \ll H$, ac susceptibility χ' at a fundamental frequency ω can be written as [15, 27]

$$\chi' = \chi_0 + 3\chi_2 H^2 + 5\chi_4 H^4 + \cdots$$

to give $\chi_{nl} = \chi_0 - \chi'$ in the static limit where the imaginary part χ'' can be set to be zero.

This ac susceptibility χ' is distinguished from the equilibrium susceptibility represented by the small field field-cooled susceptibility χ_{FC} as measured, for example, by cooling the sample in a field and equilibrating the system for ~ 1000 sec at each temperature with temperature decrements by ~ 0.1K [28].

Temperatures at which χ'' signals (loss part of the dynamic susceptibility) start to appear mark the irreversibility temperatures of starting deviation between χ' and χ_{FC}.

Below the irreversibility temperatures of deviation the χ_{nl} data of experimental measurements often includes additional dynamic effects from the critical slowing down behavior of the spin glass transition.

Application of a dc field H would suppress the dynamic loss part χ'' and lower the appearance temperatures of χ'' signals so that the scaling analysis may be well extended to be applied at lower temperatures, down to $T \simeq 1.05 T_g$ at $\omega = 0.01$Hz for example [15]. Although it is better to use χ_2 measurement rather than ac susceptibility or low field χ_{FC} data for determination of T_g, diversity or discrepancy is reported in the experimental results probably due to still too high fields or too large ϵ values employed in the scaling analysis of the χ_2 data to determine the critical exponents [15]. Especially, metallic spin glass of RKKY interaction may belong to a different universality class of a mean field behavior due to a long range interaction in comparison to the Ising or Heisenberg systems of short range interactions [15].

In the weak field regime we have

$$\begin{aligned} M(t)/h &= \chi_0 - \frac{\mu_0}{k_B T} q(t) \\ &\simeq \chi'(\omega = 1/t) \ , \end{aligned}$$

and obtain from the $\chi'(\omega)$ measurements

$$q(t) = \left(\chi_{FC} - \frac{M(t)}{h} \right) \Big/ \chi_{FC}$$

in the equivalent time domain as wide as from 10^{-6}/sec to 10^{3}/sec, which was found to be best fitted by [15, 29]

$$q(t) = a t^{-\alpha} \exp(-(t/\tau)^{\beta})$$

in the temperature range of $1.04 < T/T_g < 1.10$ for $Fe_{0.5}Mn_{0.5}TiO_3$.

Although dynamic scaling analysis of the susceptibility data has been used to support evidence for universal critical behaviors of the spin glass transition

[15], with respect to 3D spin glass under fields the renormalization group theory suggests disappearance of phase transition in a field [30] whereas a mean field theory predicts a field dependence of the transition temperature [22].

Experimental results of crossing points between the ac susceptibility $\chi'(\omega, T)$ and the field cooled susceptibility $\chi_{FC} = \partial M_{FC}/\partial H$ give the $T_f(\omega, H)$ line, from which an activation dynamics of $\ln(t/\tau) \propto \Delta/T_f$ is suggested rather than a phase transition at a finite temperature T_g for 3D Ising spin glass in magnetic field [31].

Another important characteristics of spin glass is the ageing [1, 8, 9, 10, 11], where the age is defined as the time spent at constant T and H after being quenched. Although the spin glass can be viewed as being in a nonequilibrium state with a continuous and spontaneous reorganization of the spin configuration, the observables may appear as stationary, that is, observations are bound to show equilibrium responses as long as $\ln t \ll \ln t_a$ where $t = 1/\omega$ is a probing time and t_a the age of the quenched system.

Otherwise, nonlinearity effects associated with nonequilibrium dynamics may start to affect the measurements in fields [15].

3 Ergodicity

Glass is a representative system of the ergodic to nonergodic crossover transition. Ergodic state is so defined as returning to equilibrium from any initial state of nonequilibrium ultimately after a sufficiently long time of relaxation.

Equilibrium value of a thermodynamic measurement is given by a long time average as

$$\langle X \rangle = \lim_{t_A \to \infty} \frac{1}{t_A} \int_0^{t_A} X(t) dt$$

where t_A represents the observing period of time.

Fluctuations and correlation functions are then defined as $\Delta X(t) = X(t) - \langle X \rangle$ and $\langle \Delta X(t) \Delta X(0) \rangle = \langle X(t) X(0) \rangle - \langle X \rangle^2$, respectively.

Mean square fluctuations of thermodynamic equilibrium variables are bound to follow the fluctuation-dissipation theorem to be related to the respective linear response functions [32, 33].

For example, fluctuation in number of particles N in the system can be shown to satisfy

$$\begin{aligned} \langle (\Delta N)^2 \rangle &= \langle (N - \langle N \rangle)^2 \rangle \\ &= \langle N \rangle \frac{k_B T}{V/N} K_T \end{aligned}$$

where V represents volume, T temperature, and K_T isothermal compressibility. Similarly for fluctuation of thermal energy E we have

$$\begin{aligned}\langle(\Delta E)^2\rangle &= \langle(E-\langle E\rangle)^2\rangle \\ &= k_B T^2 C_{V,N}\end{aligned}$$

where $C_{V,N}$ represents heat capacity at constant volume V and constant number of particles N.

We can also define the statistical average or the expectation value $\langle X\rangle$ in terms of the probability density ρ of phase points at time t as corresponding to the number density of phase points divided by the total number of phase points to write

$$\langle X\rangle = \int_{\Omega} \rho X d\overrightarrow{p}\, d\overrightarrow{q}\ .$$

This is an ensemble average at a single instant of time t equivalent to the time average for one single system. Since each member of the ensemble corresponds to a point of the phase space Ω, we may well understand the ergodicity hypothesis as equivalent to a statement that ensemble average gives the same result as time average.

Different thermodynamic conditions of a system lead to different ensemble averages. Quantum mechanics is introduced in the statistical averages by use of the probability density operator $\widetilde{\rho}$ as [33]

$$\langle\widetilde{X}\rangle = \mathrm{Tr}(\widetilde{\rho}(t)\widetilde{X}) = \mathrm{Tr}(\widetilde{\rho}\widetilde{X}(t))$$

where $\widetilde{X}$ represents the quantum mechanical operator corresponding to the classical observable X.

Thermodynamic quantities of a macroscopic system are given a time-independent average value

$$\langle\phi\rangle = \lim_{t_\infty\to\infty}\frac{1}{t_\infty}\int_0^{t_\infty}\phi[\overrightarrow{X}^N(t)]dt$$

where $\overrightarrow{X}^N(t)$ represents a state vector of the system at time t in the $6N$-dimensional phase space of the N particle system.

In the above calculation of $\langle\phi\rangle$ we assume the ergodic hypothesis: "during the time interval t_∞ the phase point $\overrightarrow{X}^N(t)$ of the system dynamics will spend equal times at all the phase points accessible to the selected ensemble."

In the microcanonical ensemble where N, V and E are specified in the system so that all systems of the ensemble have the same fixed energy E the ergodic hypothesis can be reworded as, "all the degenerated J states of $E_n = E$ will be equally probable with the same probability $1/J$" where J is the degeneracy. That is,

$$\begin{aligned}P_n &= \langle E_n|\widetilde{\rho}|E_n\rangle \\ &= \delta(E_n - E)/J\end{aligned}$$

where P_n represents the probability of observing the system to be in the state $|E_n\rangle$, $\sum_{n=1}^{J} P_n = 1$, and $\widetilde{\rho}|E_n\rangle = E_n|E_n\rangle$ since $[\widetilde{H},\widetilde{\rho}] = 0$.

In the canonical ensemble specified by N, V and T the probability to find the system in a state $|E_n\rangle$ is given by

$$P_n = \frac{1}{Z}\exp(-E_n/k_BT)$$

where $Z = \sum_n \exp(-E_n/k_BT)$ is the partition function.

In the grand canonical ensemble of open systems characterized by V, T and chemical potential μ we can define

$$F = \widetilde{H} - \mu\widetilde{N} \quad \text{and} \quad F|n\rangle = F_n|n\rangle$$

so that we may generalize the definition as

$$\widetilde{\rho}_G = \frac{1}{Z_G}\exp(-F/k_BT)$$

to obtain [33]

$$\begin{aligned}\langle X\rangle_G &= \mathrm{Tr}(\widetilde{X}\widetilde{\rho}_G)\\ &= \frac{1}{Z_G}\mathrm{Tr}\left(\widetilde{X}\exp(-F/k_BT)\right)\\ &= \frac{1}{Z_G}\sum_n \langle n|\widetilde{X}|n\rangle\exp(-F_n/k_BT)\end{aligned}$$

where

$$\begin{aligned}Z_G &= \mathrm{Tr}\left(-\exp(-F/k_BT)\right)\\ &= \sum_{n,N}\exp\left(\frac{\mu N - E_n}{k_BT}\right)\end{aligned}$$

and

$$\mathrm{Tr}(\widetilde{\rho}_G) = 1$$

All these ensemble averages, equivalent to each other in the thermodynamic limit, assume the system to be ergodic in probabilistic terms.

A quantum mechanical system is found to be ergodic only when the system is nondegenerate, that is, no other observables are commuting with the Hamiltonian [34].

Ergodicity breaking is accompanied also by a phase transition of spontaneous symmetry breaking at T_c. Even at above T_c the crystal, strictly speaking, may not be ergodic because not all the phase space points allowed energetically are sampled in a finite time of observation.

However, we do not have to stick to the ergodic hypothesis of equivalence between time average and ensemble average when the lattice atoms are at well-defined sites of crystallographic equivalence so that different regions of the equipotential configurational energy surface would make essentially the same contribution to the ensemble average.

In glass, however, every site is at specific local environment of a specific ligand and may not be equivalent to each other so that the permutation symmetry is broken. This permutation symmetry is equivalent to the statistical symmetry with respect to the time average in fluids due to the spatial homogeneity.

With freezing into a structural state before internal state of equilibrium is reached, that is, as the system is quenched, the internal equilibrium state will get lost at the glass transition temperature T_g. Above T_g the ergodic hypothesis of statistical mechanics holds so that thermal fluctuations would drive the system at equilibrium to revisit the same state in a finite period of time whereas glass is frozen at one minimum valley, leading to a difference between time average and ensemble average over all the minimun valleys, and becomes nonergodic below T_g.

Glass transition temperature T_g depends on cooling rate when observation is made in the cooling cycle but would depend also on thermal history when observation is made in the heating cycle because ergodicity is broken in the beginning [1, 35].

New excitations of some glassy degrees of freedom are expected to take place as $T \to T_g^+$. Two major relaxations are a strong cooperative dynamics of α-relaxation and a weak faster β-relaxation as a continuation from high temperature relaxations before a full strength cooperative moding. This relaxation occurs from a landscape generality, and rearrangement over the landscape energy barrier is a cooperative action of $3N + 1$ coordinates.

In the ergodic region relaxations are of entropic type given by

$$\tau = \tau_0 \exp(a\Delta F/TS_c)$$

where ΔF represents a free enegy barrier to rearrangement, and $S_c = \Delta C_p \ln T/T_k$ excess configurational entropy with excess specific heat $\Delta C_p = b/T$. When approximation is made of $\Delta S = \Delta C_p(T_k)(T - T_k)/T_k$ we can obtain the Vogel-Fucher equation [35]

$$\tau = \tau_0 \exp(cT_0/(T - T_0)) \; .$$

In the nonergodic region S_c becomes time-dependent with an ultimate relaxation to the Adam-Gibbs value of equilibrium where τ becomes time-independent [36]

Ergodic hypothesis may be generalized to mean that a system at equilibrium can be found in any other accessible configuration corresponding to a macrostate of various microstates with a probability given by Boltzmann distribution $\exp(-E/k_BT)$. The ergodicity breaking is thus not possible at $T = 0$ if the system is prepared strictly at equilibrium. Ergodicity breaking is then put in by hand such as by the way of applying an infinitesimal field h to restrict the trace sum average,

$$\lim_{h\to 0}(\lim_{N\to\infty} M_N) = M \; .$$

However, we get a different result if there is no symmetry-breaking field kept until taking the thermodynamic limit ($N \to \infty$)

$$\lim_{N\to\infty}(\lim_{h\to 0} M_N) = 0$$

since fluctuations in a finite system have a finite lifetime, and lead to the Gibbs average over two possible microstates of the thermodynamic ground state at $T = 0$ as an equal mixture [1].

4 Replica Symmetry

Let's consider a representative exactly solvable model of spin glass, Sherrington-Kirkpatrick(SK) model, which is the infinite range ($R \to \infty$), infinite number of interaction neighbors ($z \to \infty$), and infinite dimensional ($d \to \infty$), randomly disordered Ising spin glass model as described by [21, 37]

$$H = -\sum_{i\neq j}^{N} J_{ij}{\sigma_i}^z{\sigma_j}^z$$

with

$$P(J_{ij}) = \prod_{i\neq j}\left(\sqrt{\frac{N}{2\pi}}\exp(-\frac{N}{2}{J_{ij}}^2)\right)$$

for a Gaussian probability distribution of quenched random variables J_{ij} describing a pairwise interaction between any two spins at the sites i and j. For each spin σ_i all the other spins $\sigma_j (i \neq j)$ form the coordinate neighbors of interaction so that this SK model of infinite range interactions corresponds to the space dimensionality of infinity in the $N \to \infty$ limit.

The SK model of this infinite dimensionality should then have exact solution given by the mean field approximation.

For this randomly quenched disorder system the free energy F is given by

$$F = \langle\langle F_J\rangle\rangle_C = -k_B T\langle\langle \ln Z_J\rangle\rangle_C$$

where partition function Z_J is

$$Z_J = \sum_{\{\sigma\}}\exp\Big(-\frac{H(\{\sigma\}_J)}{k_B T}\Big)$$

with the subscript J representing a fixed set of quenched random variables $\{J_{ij}\}$ supplied from the Gaussian distribution.

Direct calculation of F is not trivial, and we make use of a mathematical identity of replica trick to deal with Z_J instead of $\ln Z_J$

$$\ln Z = \lim_{n\to 0}\left(\frac{1}{n}(Z^n - 1)\right)$$

That is,

$$\begin{aligned} F &= -k_B T \left\langle \left\langle \lim_{n\to 0} \left(\frac{1}{n}(Z_J^n - 1) \right) \right\rangle \right\rangle_C \\ &= \lim_{n\to 0} F_n \end{aligned}$$

where we introduce n-replica free energy

$$F_n = -\frac{1}{n} k_B T (Z_n - 1)$$

by defining the partition function of the n-replica systems [1, 11, 12, 37]

$$\begin{aligned} Z_n &= \langle\langle Z_J^n \rangle\rangle_C \\ &= \int DJP(J) Z_J^n \\ &= \int DJP(J) \prod_{\alpha=1}^{n} \sum_{\{\sigma^{(\alpha)}\}} \exp\left(\frac{1}{k_B T} \sum_{i\neq j}^{N} J_{ij} \sigma_i^{(\alpha)} \sigma_j^{(\alpha)} \right) \\ &= \int DJ \sum_{\{\sigma^{(\alpha)}\}} \exp\left(\frac{1}{k_B T} \sum_{\alpha=1}^{n} \sum_{i\neq j}^{N} J_{ij} \sigma_i^{(\alpha)} \sigma_j^{(\alpha)} - \frac{1}{2} \sum_{i\neq j} N J_{ij}^2 \right) \\ &= \sum_{\{\sigma^{(\alpha)}\}} \exp\left(\frac{1}{2N} \frac{1}{k_B^2 T^2} \sum_{i\neq j}^{N} \left(\sum_{\alpha=1}^{n} \sigma_i^{(\alpha)} \sigma_j^{(\alpha)} \right)^2 \right) \\ &= \sum_{\sigma^{(\alpha)}} \exp\left(\frac{1}{4k_B^2 T^2} Nn + \frac{N}{\frac{1}{2} k_B^2 T^2} \sum_{\alpha\neq\beta}^{n} \left(\frac{1}{N} \sum_{i}^{N} \sigma_i^{(\alpha)} \sigma_i^{(\beta)} \right)^2 \right) \\ &= \prod_{\alpha\neq\beta}^{n} \left(\int dQ_{\alpha\beta} \right) \sum_{\{\sigma_i^{(\alpha)}\}} \\ &\quad \times \exp\left(\frac{1}{4k_B^2 T^2} Nn - \frac{1}{2} \frac{N}{k_B^2 T^2} \sum_{\alpha\neq\beta}^{n} Q_{\alpha\beta}^2 + \frac{1}{k_B^2 T^2} \sum_{\alpha,\beta}^{n} \sum_{i}^{N} Q_{\alpha\beta} \sigma_i^{(\alpha)} \sigma_i^{(\beta)} \right) \end{aligned}$$

where the replica matrix $Q_{\alpha\beta}$ is given by

$$Q_{\alpha\beta} = \frac{1}{N} \sum_{i}^{N} \langle \sigma_i^{(\alpha)} \sigma_i^{(\beta)} \rangle$$

as satisfying $\delta Z_n / \delta Q_{\alpha\beta} = 0$. We can rearrange terms to rewrite [1, 12, 20]

$$Z_n = \prod_{\alpha,\beta}^{n} \left(\int dQ_{\alpha\beta} \right) \exp\left(\frac{1}{4} \frac{1}{k_B^2 T^2} Nn - \frac{N}{2} \frac{1}{k_B^2 T^2} \sum_{\alpha,\beta}^{n} Q_{\alpha\beta}^2 \right)$$

$$
\begin{aligned}
&\times \prod_{i}^{N} \left(\sum_{\{\sigma_i^{(\alpha)}\}} \exp\left(\frac{1}{k_B^2 T^2} \sum_{\alpha,\beta}^{n} Q_{\alpha\beta} \sigma_i^{(\alpha)} \sigma_i^{(\beta)} \right) \right) \\
&= \prod_{\alpha,\beta}^{n} \left(\int dQ_{\alpha\beta} \right) \\
&\quad \times \exp\left(\frac{1}{4} \frac{1}{k_B^2 T^2} Nn - \frac{N}{2} \frac{1}{k_B^2 T^2} \sum_{\alpha,\beta}^{n} Q_{\alpha\beta}^2 \right. \\
&\quad \left. + N \ln \left(\sum_{\{\sigma^{(\alpha)}\}} \exp\left(\frac{1}{k_B^2 T^2} \sum_{\alpha,\beta}^{n} Q_{\alpha\beta} \sigma^{(\alpha)} \sigma^{(\beta)} \right) \right) \right) \\
&= \int d\widetilde{Q} \exp\left(- \frac{1}{k_B T} nN f(\widetilde{Q}) \right)
\end{aligned}
$$

where we have

$$
\begin{aligned}
f(\widetilde{Q}) = &\frac{1}{4} \frac{1}{k_B T} \\
&+ \frac{1}{2n} \frac{1}{k_B T} \sum_{\alpha,\beta}^{n} Q_{\alpha\beta}^2 - \frac{k_B T}{n} \ln \left(\sum_{\{\sigma^{(\alpha)}\}} \exp\left(\frac{1}{k_B^2 T^2} \sum_{\alpha,\beta}^{n} Q_{\alpha\beta} \sigma^{\alpha} \sigma^{\beta} \right) \right)
\end{aligned}
$$

The above integral can be solved from the saddle point method (the steepest descent method) to give, in the thermodynamic limit, in the leading order of N [12]

$$
Z_n \simeq \frac{1}{\sqrt{|\det \delta^2 f / \delta \widetilde{Q}^2|}} \exp\left(- \frac{1}{k_B T} nN f(\widetilde{Q}^*) \right)
$$

where $\widetilde{Q}^*$ is the matrix for minimizing $f(\widetilde{Q})$ and giving the saddle point, that is,

$$
\left. \frac{\delta f(\widetilde{Q})}{\delta Q_{\alpha\beta}} \right|_{\widetilde{Q}=\widetilde{Q}^*} = 0
$$

Replica symmetric solutions are obtained by assuming

$$
Q_{\alpha\beta} = q \quad \text{for all } \alpha \text{ and } \beta
$$

corresponding to one and only one ground state in the system.

In the limit $n \to 0$ we find

$$
\begin{aligned}
f(q) = &-\frac{1}{4} \frac{1}{k_B T} (1-q)^2 - k_B T \int_{-\infty}^{\infty} dz \frac{1}{\sqrt{2\pi}} \exp\left(- \frac{1}{2} z^2 \right) \\
&\ln \left(2 \cosh \left(\frac{1}{k_B T} \sqrt{q} z \right) \right)
\end{aligned}
$$

where we have [11, 20, 37]

$$q = \int_{-\infty}^{\infty} dz \frac{1}{\sqrt{2\pi}} \exp\left(-\frac{1}{2} z^2 \tanh^2\left(\frac{1}{k_B T}\sqrt{q} z \right) \right).$$

We can see that $q = 0$ at $T > 1$ and $q \to 1$ at $T \to 0$. However, this replica symmetric solution can be seen to be unstable at low temperatures of $T < 1$, that is, $\det|\delta^2 f/\delta \widetilde{Q}^2| < 0$, and give a negative entropy at very low temperatures with $S_C = -1/2\pi$ at $T = 0$ [11, 21, 37].

A correct low temperature solution of the replica matrix $\widetilde{Q}$ in the $n \to 0$ limit is obtained by a replica symmetry breaking scheme of Parisi [1, 4, 11, 12, 38].

An infinite sequence of the symmetry breaking scheme improves the results towards the true solution by introducing the continuous stability parameters. By one-step replica symmetry breaking $\widetilde{Q}$ will assume the following new structure [1, 4, 11, 12].

$$\widetilde{Q} = \begin{vmatrix} \begin{matrix} 0 & q_1 & q_1 & q_1 \\ q_1 & 0 & q_1 & q_1 \\ q_1 & q_1 & 0 & q_1 \\ q_1 & q_1 & q_1 & 0 \end{matrix} & ((q_0)) & ((q_0)) & ((q_0)) \\ ((q_0)) & ((\widetilde{q}_1)) & ((q_0)) & ((q_0)) \\ ((q_0)) & ((q_0)) & ((\widetilde{q}_1)) & ((q_0)) \\ ((q_0)) & ((q_0)) & ((q_0)) & ((\widetilde{q}_1)) \end{vmatrix}$$

where

$$((q_0)) = \begin{vmatrix} q_0 & q_0 & q_0 & q_0 \\ q_0 & q_0 & q_0 & q_0 \\ q_0 & q_0 & q_0 & q_0 \\ q_0 & q_0 & q_0 & q_0 \end{vmatrix} \quad \text{and} \quad ((\widetilde{q}_1)) = \begin{vmatrix} 0 & q_1 & q_1 & q_1 \\ q_1 & 0 & q_1 & q_1 \\ q_1 & q_1 & 0 & q_1 \\ q_1 & q_1 & q_1 & 0 \end{vmatrix}$$

Further to the two-step replica symmetry breaking the new structure of the replica matrix $\widetilde{Q}$ is organized in the following form [4, 12]

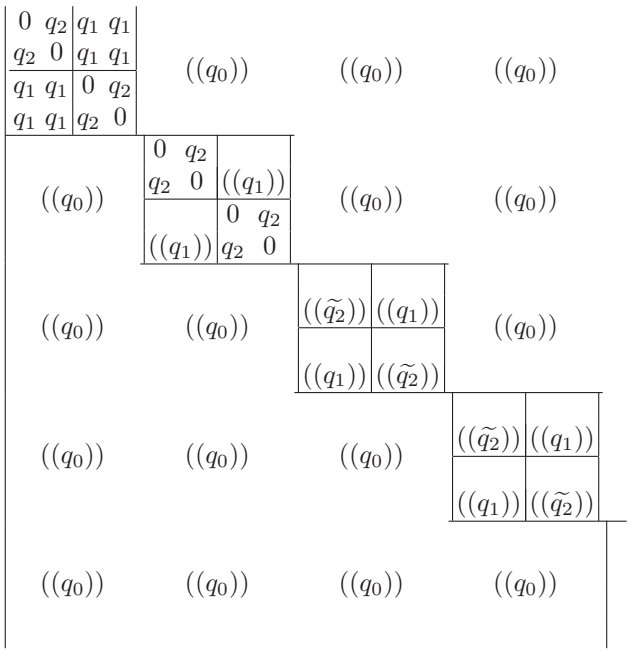

where $((q_1))$ represents $\begin{vmatrix} q_1 & q_1 \\ q_1 & q_1 \end{vmatrix}$ and $((\widetilde{q}_2))$ represents $\begin{vmatrix} 0 & q_2 \\ q_2 & 0 \end{vmatrix}$.

Starting from $(n \times n)$ matrix $\widetilde{Q}$ of n replicas where all the diagonal elements are zero and all the off-diagonal elements are q_0, we divide the matrix into $(m \times m)$ matrix blocks where n/m is a complete integer. In the above illustration of one-step replica symmetry breaking the $(n \times n)$ matrix $\widetilde{Q}$ can be seen to be divided into (4×4) matrix blocks, $((\widetilde{q}_1))$ and $((q_0))$.

In the two-step replica symmetry breaking the $(m \times m)$ matrix blocks are further divided into smaller $(l \times l)$ matrix blocks where m/l is again an integer. In the illustration above we can see $m = 4$ and $l = 2$.

We can observe that the off-diagonal matrix blocks are left without any change and only along the diagonal blocks new q values are introduced in the succeeding steps of replica symmetry breaking as in $(m \times m)$ $((\widetilde{q}_1))$ – and then $(l \times l)$ $((\widetilde{q}_2))$ – block matrices derived from the preceding $(n \times n)$ and $(m \times m)$ parent matrices, respectively.

All the n replicas are supposed to have the same microscopic distribution of randomly competing interactions $\{J\}$ but do not represent the same ground states degenerated from the frustration structures of the spin configurations $\{\sigma\}$ so that they are macroscopically different. That is, replicas do not correspond to valleys by one to one but certainly have nontrivial relations.

Instead of the two equivalent valleys, corresponding to $+M$ and $-M$ in the ferromagnetic systems, separated by an infinite barrier of free energy, in the spin glass systems of replica symmetry breaking solutions so many valleys of

ergodicity breaking are formed with each valley containing many metastable states separated by finite energy barriers [1, 4, 8, 10, 39].

As temperature is lowered phase space is broken into many valleys, that is, different regions separated by energy barriers in free energy landscape.

Although each separated valley of infinite barrier in the $N \to \infty$ limit has the same value of q_{EA} defined by

$$q_{EA} = \frac{1}{N} \sum_{i=1}^{N} |\langle \sigma_i^{(a)} \rangle|^2$$

overlap or closeness between two valleys a and b may well be defined as [1, 4, 12]

$$q_{ab} = \frac{1}{N} \sum_{i=1}^{N} \langle \sigma_i^{(a)} \rangle \langle \sigma_i^{(b)} \rangle \ .$$

The probability distribution function for this overlap parameter q_{ab} defines the order parameter function of spin glass as [1, 4, 40, 41]

$$P(q) = \sum_{a,b} \delta(q - q_{ab}) \ .$$

Edwards-Anderson order parameter q_{EA} then corresponds to a typical overlap between two representative configurations inside the same valley q_{aa}. From the whole distribution of valleys only those valleys of the minimum free energy are dominant to determine thermodynamics, and zero overlap can be assumed for the probability distribution of free energy in a valley [42].

5 Glass Transition

One of the best understood model system for glass transition is the spin glass characterized by a random distribution of quenched disorders and frustration. Glass transition in spin glass system has been understood mostly by the Sherrington-Kirkpatrick(SK) model. Parisi showed from his low temperature solutions of the SK model that glass transition should be an equilibrium phenomenon of replica symmetry breaking. Mezard et al., exploring physics of the replica symmetry breaking, succeeded to give a better understanding of the replica physics in terms of overlaps, ultrametricity and non-self averaging [4, 11, 12, 43].

A new type of ordering of the spin glass transition may be represented by superposition of infinitely many pure states [4, 40, 44] which are not related by simple symmetry transformations, and we may require a continuous order parameter function instead of one single order parameter.

In contrast to this mean field replica symmetry breaking theory assuming infinitely many pairs of pure states we have also the droplet model theory

[1, 11, 45] based on one single pair of pure states where low temperature behavior is described in terms of low energy excitations forming clusters of coherent spin-flips.

At low temperatures a dilute gas of coherent clusters may be considered as a common origin for the two level systems in glass [10, 46], and leading to the asymptotic behavior of two states rather than infinitely many pure states.

A nonequilibrium signature of glassy systems can be verified with the aging phenomena [8, 9, 47, 48]. The glassy response function $R(t, t_w)$ of a very weak and long memory can not easily be measurable, and instead, an integrated response is used to introduce the time-dependent susceptibility $\chi(t, t_w)$

$$\chi(t, t_w) = \int_{t_w}^{t} R(t, t')dt'$$

where t_w represents a waiting time [1, 11, 15].

Fluctuation-dissipation theorem of equilibrium systems does not hold in the aging systems of nonequilibrium, and $\chi(t, t_w)$ can be approximated as a sum of two separate contributions: a stationary part satisfying the fluctuation-dissipation theorem and an aging part violating the fluctuation-dissipation theorem [8, 9].

In the asymptotic limit of $(t - t_w) \gg t_w$ we can approximate [8, 9]

$$C(t, t_w) \simeq C_{age}(t, t_w)$$

so that we may assume [9]

$$\frac{\partial}{\partial t_w} C_{age}(t, t_w) = T_{eff}\left(C_{age}(t, t_w)\right) R_{age}(t, t_w)$$

where T_{eff} represents an effective temperature, $C(t, t_w)$ correlation function, and $R(t, t_w)$ response function.

This definition of effective temperature introduces quasi fluctuation-dissipation theorem in conformity with the fluctuation-dissipation theorem of equilibrium system.

Glassy system, characterized by an extremely slow relaxation, may be regarded as to be in quasi equilibrium over time scales much longer than microscopic fast time scales but shorter than macroscopic slow relaxation times. A more general extension of partial equilibrium in a limited subset of relaxational degrees of freedom may be incorporated to nonequilibrium to define an ensemble sampling of phase space components [49].

Many effective temperatures may be required to cover the whole nonequilibrium regime so that glassy systems can be classified into three hierachical groups according to T_{eff} dependence on $C_{age}(t, t_w)$ [8, 9]. Coarsening systems, for example, are replica symmetric and described by two T_{eff} values with two time scales. Systems of one-step replica symmetry breaking also need two T_{eff} values and two time scales, which include structural glasses and are often referred to two time scale systems.

Full scale replica symmetry breaking systems including spin glass are known to have many time scales with a continuous spectrum of T_{eff} values [8, 9]. A special one-step replica symmetry breaking system of zero temperature glass transition is often referred as one time scale system because of no stationary regime with nonequilibrium dynamics characterized by a T_{eff}.

In the region of $C(t, t_w) > q_{EA}$ corresponding to the stationary regime all the above three classes of glassy systems are found to satisfy the fluctuation-dissipation theorem [8, 9].

In the mean field limit $N \to \infty$ the two-time correlation fuction

$$C(t, t') = \langle S_i(t) S_i(t') \rangle$$

and the linear response function

$$R(t, t') = \left\langle \frac{\delta \langle S_i(t) \rangle}{\delta h_i(t')} \right\rangle$$

vanish for $t < t'$ due to causality, and the correlation function develops a plateau with $C(t - t') \to q_{EA}$ near $T \gtrsim T_c$ before decaying ultimately to zero at very long t [8, 9].

The plateau interval increases toward divergence at $T = T_c$ of the mode-coupling theory in a power law and a dynamic crossover follows in $C(t - t')$ as [8, 9, 47]

$$\begin{aligned} C(t - t') &\sim q_{EA} + A(t - t')^{-a}, \quad C > q_{EA} \\ &\sim q_{EA} - B(t - t')^{b}, \quad C < q_{EA} \end{aligned}$$

This plateau length sets the equilibration time scale so that the correlation function would not decay to the equilibrium zero with a divergence of the plateau length as temperature is lowered to T_c [8, 9, 50].

Further below T_c the spin glass system cannot go equilibrating but the system evolution may go depending on initial states with ergodicity breaking, which brings about the permutation symmetry breaking between replicas [40, 51]. Effective temperature can also be defined in terms of configurational entropy or complexity in analogy with equilibrium temperature of Boltzmann entropy to attempt a thermodynamic formulation of glassy states.

Within the mean field approximations the short-range models and the infinite-range Sherrington-Kirkpatrick model are in qualitative agreements in most of the results, although cooperative slow dynamics of glass was found to involve only a few tens of atoms in nanometer scale cages [35, 52].

Discontinuous spin glass transition was predicted by models including q-state Pott glass ($q \geq 4$) [53] and p-spin glass ($p \geq 3$) [54].

In the limit of $p \to \infty$ and $q \to \infty$ the models correspond to the random energy model [55] which can be solved without replica trick to show a discontinuous jump from $q_{EA} = 0$ ($T > T_g$) to $q_{EA} = 1$ ($T < T_g$) at the transition temperature T_g. Random orthogonal model [56] is another model showing the discontinuous transition where random quenched disorder variables J_{ij}

are matrix elements in a random orthogonal ensemble of matrices satisfying $J_{ij}J_{jk} = \delta_{ik}$. Both continuous and discontinuous spin glass transitions with respect to q_{EA} may be continuous in viewpoints of thermodynamic averages as suggested by a notion that $q(x)$ is a continuous function of $x[0,1]$ and thermodynamic quantity is given by an integral involving various moments of $q(x)$ [57].

The p-spin spherical model, showing a mean field discontinuous spin glass transition, can be solved by one-step replica symmetry breaking to give the spin glass solution. This implies that the phase space may be broken up into all equivalent ergodic components separated by infinite barriers, when three parameters may be sufficient to describe the equilibrium: the overlap between two ergodic components, the overlap inside each ergodic component (equivalent to q_{EA}), and the probability distribution that two different replicas will be found in the same ergodic component [58, 59]. Ising spin p-spin model has a more complex solution at very low temperature as obtained by infinite step replica symmetry breaking [54].

The Thouless-Anderson-Palmer approach [60] based on the free energy landscape topology, and the Sompolinsky approach [25, 26] of spin glass dynamics assume two separate regimes, corresponding to the equilibrium regime and the nonergodic regime of quasi fluctuation-dissipation theorems, where dynamics in a single ergodic component is important in the former regime whereas slow dynamics across different local minima becomes important in the time scales of the latter regime [8, 44, 48].

When dynamics is dominated by activation processes in the free energy landscape with a broad distribution of barrier heights, the underlying configurational space with the activation transition times as a metric becomes ultrametric [61]. That is, the metastable spin configurations, with the hamming distance of activation barrier, or equivalently, logarithm of relaxation time, form the ultrametric space [62]. Considering a droplet of uniform spin configuration in a size L, the droplet model of Fisher and Huse [45] is based on the scaling assumption for the flipping free energy as L^x and the kinetic barrier against flipping of the droplet as L^y. Hamming distance d_H is then defined, to measure a hopping distance between two different spin configurations, as

$$d_H \propto \langle (\delta R)^2 \rangle$$

where δR represents random fluctuation in resistance R due to spin flip configurations and $\langle (\delta R)^2 \rangle$ tends to simulate a variance of a Gaussian distribution around zero [61].

Algebraic growth of inter-valley barrier height with increasing d_H leads to a logarithmic growth in time for $d_H(t)$, and this logarithmic growth of $\langle (\delta R)^2 \rangle$ in time brings about $1/f$ noise [61]. Higher than the second moment for $\langle (\delta R)^2 \rangle$ will be an implication for a non-Gaussian fluctuation. Once the droplet completes an infinite percolation network this droplet picture must be modified. The ultrametric dynamics as well as the droplet model leads to

the same $1/f$ fluctuation spectra of magnetization, corresponding to a linear response in a logarithmic time scale [63].

A local equilibrium state is defined such that a relative probability for a system to be in the states within a finite volume of the configurational space is given by Boltzmann distribution [10, 44]. That is, a state is represented by a probability distribution function $P(C)$ over the configurations C. Any local equilibrium state may thus be represented by a sum over pure equilibrium states, and thus pure states correspond to the extremal states of a convex set of equilibrium states [10]. Different boundary conditions yield different local equilibrium states, but intensive variables should not show fluctuations in the pure states showing a clustering behavior [10, 44].

A dynamical transition at $T_d > T_g$ is predicted in the discontinuous transition models as corresponding to the instability encountered with the mode coupling theory of glass transition [8, 9, 59].

A zero frequency mode at T_d is considered to be responsible for divergent relaxation time in glassy dynamics [9, 64, 65], and a speculation remains whether this T_d instability may be a mean filed artifact which can be removed by including activations over finite energy barriers [66, 67]. This instability is also reminiscent of a spinodal development of instability in the first order transitions [57].

A very large number of metastable states in proportion to $\exp(NC^*)$are involved in dynamic response to the instability but free energy remains to be in the paramagnetic phase in the region of $T_d > T > T_g$ [57].

As temperature is lowered further to T_g the number of metastable configurations would decrease, and the free energy is decreased. A true thermodynamic transition will then be reached when the metastable phase has free energy equal to that of the paramagnetic phase.

In mean field theories the metastable states get an infinite lifetime, and these mean field models of spin glass with a discontinuous transition (with respect to q_{EA} the Edwards-Anderson order parameter) would show a thermodynamic transition at T_g where the configurational entropy C^* collapses to zero with dynamics described by mode-coupling equations [57].

Statics and dynamics are not commuting in quantum mechanics, and the dynamical instability may survive with the quantum phase transition at zero temperature.

Non-dissipative quantum fluctuations can still generate disorders, driving discontinuous phase transition at $T_c > 0$ to a continuous phase transition at $T_c = 0$. Dynamical instability of mode-coupling theory may then be suppressed at $T = 0$ by quantum fluctuations [57].

Model systems without disorders are shown to be possible to exhibit spin glass dynamics due to a dynamic self generation of disorders [68].

Order parameter $Q_{ab}^{tt'} = \langle \sigma_a(t)\sigma_b(t') \rangle$ and response function $R(|t - t'|)$ for $a = b$ can be shown to be related to the susceptibility as [57]

$$\chi_0 = \frac{1}{k_B T}\widehat{R}_0$$

where $\widehat{R}_0$ is given from the following transforms

$$\widehat{R}_p = \frac{1}{M}\sum_{t=0}^{M-1} e^{i\omega_p t} R(t), \qquad \omega_p = \frac{2\pi}{M} p\,.$$

In the static approximation of Bray and Moore [69], considering only the zero frequency ($p = 0$) Matsubara mode, T_d and T_g coincide at $T = 0$ so that the transition may become continuous. That is, transition at $T = 0$ must be continuous since there is no room for metastable phase.

Although incorrect results of thermodynamic quantities such as finite entropy at $T = 0$ in the mean field glass of Sherrington-Kirkpatrick model and infinite entropy in the random orthogonal matrix model remain as serious defects of the static approximations, discontinuous transitions are well predicted to become continuous at $T = 0$ as shown schematically in Fig. 4 [57].

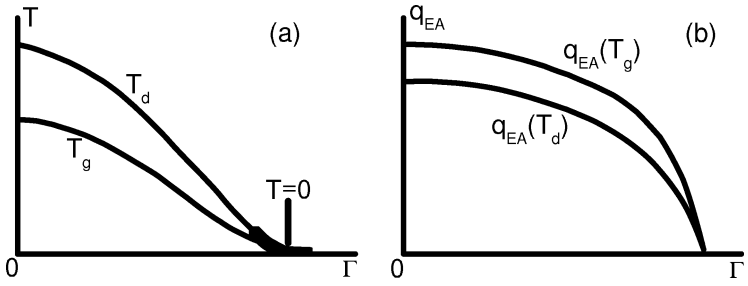

Fig. 4. Numerical studies of static (T_g) and dynamical (T_d) transitions of ROM model in the static approximation [57]. (**a**) Phase boundaries in temperature (T)-transverse field (Γ) plane, and (**b**) q_{EA} values along the phase boundary lines of $T_g(\Gamma)$ and $T_d(\Gamma)$

6 Quantum Phase Transition

Quantum phase transition was noted as an important problem in Fermi liquid metals where the divergent susceptibility may lead to an infinitely strong effective interaction between electrons [3].

This quantum critical point can be observed in the zero temperature continuous phase transition. As thermal fluctuations with increasing temperature can cause a phase transition from order to disorder, zero point quantum fluctuations tunable by an external control of pressure, field, etc. can cause a phase transition from ordered to disordered phase.

Critical divergence to infinity may well invalidate the Fermi liquid theory of metals, when metals turn into a non-Fermi liquid at the quantum critical point.

The standard ϕ^4 theory of critical region employs an effective dimensionality $d_{eff} = d+z$ where d is the space dimension and z the dynamic exponent to reflect a quantum mechanical mixing between statics and dynamics [70].

For systems of $d_{eff} > 4$, the upper critical dimension of the ϕ^4-model, the mean-field theory, that is, the Gaussian approximation should give the exact solutions. However, non-Gaussian localities of the quantum critical behaviors have been reported [71].

Coexistence of a long-range spatial ordering and local critical fluctuations is then expected to give novel anomalies as in the heavy fermion metals [72]. There are also quantum phase transitions without well-defined order parameter as in the disordered interacting electron system [13, 14]. Heisenberg quantum spin glass was studied as early as in 1975 [2], where quantum effects in the Sherrington-Kirkpatrick model spin glass were found to lower the transition temperature in quantum spin glass. Quantum fluctuations can indeed drive the spin glass transition down to absolute zero [73].

Replica symmetry breaking is expected to vanish in the limit $T_c \to 0$, and quantum spin glass should become most interesting. Critical behavior of a quantum spin glass will be same as that of a classical model in the phase transition at nonzero temperatures except renormalizations of such nonuniversal quantities as T_c by quantum effects.

Only at $T_c = 0$ by tuning quantum fluctuations of quantum tunneling between ground states, being equivalent to a disordering field, a genuine quantum phase transition of a different fixed point and different univerality class will be realized.

One-dimensional Ising spin glass (due to no frustration this model maps onto a random Ising ferromagnet) is ordered at $T = 0$, and requires a finite transverse field to go disordered, when a genuine quantum phase transition is introduced with the Griffiths phase of divergent paramagnetic susceptibilitiy ($\Gamma > \Gamma_c$) [74, 75, 76, 77]. Excitations in spin glass phase of a quantum Ising spin glass are known to conform with the droplet excitations of classical spin glass [78]. Continuous quantum phase transition at $T_c = 0$ is similar to those at $T_c \neq 0$ but with different critical exponents. The critical exponents are not controlled by quantum fluctuations in the quantum spin glass of $T_c \neq 0$.

This is because $k_B T \gg \hbar\Omega_c$, with $\Omega_c = 1/\tau \sim \xi^{-z} \to 0$, unless $T_c = 0$ of no thermal energy [74]. A spin glass system of $LiHo_xY_{1-x}F_4 (0.25 > x > 0.1)$ was shown to have $T_c \to 0$ in a transverse magnetic field [79].

Quantum system of d-dimension can be transformed to a $(d+1)$-dimensional classical problem. In fact, for uniform systems, quantum phase transitions are no longer different from showing classical universalities. However, for randomly quenched disorder systems the corresponding classical models become quite anisotropic, and a simple correspondence cannot be applied [80].

In the classical thermodynamic limit of infinite barrier height, nonergodicity sets in under thermal activation attempt, but the configurational energy barrier decreases in width with increasing system size so that quantum tunneling may be enhanced to give an ergodic, that is, replica-symmetric spin glass solutions [7, 74, 81, 82]. However, nonergodic solutions are also reported [83].

7 Quantum Spin Glass

We have two distinctive models of quantum spin glass:

1. vector spin glass [69] where quantum fluctuations are not tunable,
2. transverse Ising spin glass, which is a classical spin glass perturbed by tunable quantum fluctuations [84, 85, 86].

Statics of disorder-free H is quantum mechanically linked with Schroedinger dynamics in an imaginary time axis equivalent to another extra space dimension where the correlation length becomes proportional to inverse energy gap $1/\Delta E$. Randomly distributed quenched disorders implicate no correlation in space dimensions but time-independent perfect correlation in time dimension, and this extreme anisotropy is expected to give $\xi_\tau \sim (\Delta E)^{-z}$ with $z \neq 1$ [87]. This nontrivial extreme anisotropy may be more suscptible to the Griffiths phase in the quantum phase transition [87].

A good model of quantum spin glass is the transverse field Ising spin glass model [7, 84, 85, 86] defined by

$$\widetilde{H} = -\sum_{ij} J_{ij}\sigma_i^z\sigma_j^z - \Gamma\sum_i \sigma_i^x$$

where (i, j) is restricted to the nearest neighbor pairs, and quenched disorders $\{J_{ij}\}$ introduce frustration except for 1D system.

This quantum system $\widetilde{H}$ exhibits a 2nd order phase transition at $T = 0$ and $\Gamma = \Gamma_c$, characterized by [87]

$$\xi_\tau \sim |\Gamma - \Gamma_c|^{-\nu} \quad \text{and} \quad \Delta E \sim \omega \sim \xi_\tau^{-z}$$

For 1D system, with a broad distribution function for critical properties in logarithmic scales, a typical correlation length with critical exponent $\nu = 1$ becomes different from an average correlation length of critical exponent $\nu = 2$ [87].

It is the logarithm of excitation energy gap rather than the energy gap itself that maintains a scaling relation with the system size. Energy gap is thus observed to decrease with increasing system size as an exponential function instead of an algebraic dependence. This relation of $\langle \Delta E \rangle \sim \exp(-a\sqrt{L})$ gives $z = \infty$ since the inverse energy gap corresponds to the characteristic relaxation

time of quantum tunnelling fluctuations, equivalent to the activation kinetics in a classical spin glass [88, 89].

For 2D and 3D the numerical studies by quantum Monte Carlo simulations agree with the scaling theory predictions of droplet model, where no broadening of the probability distribution in logarithmic scales with increasing system size is confirmed, but $\chi_{nl}(\omega = 0)$ is found to diverge at $\Gamma = \Gamma_c$ and $T \to 0$ quite strongly [90, 91] in sharp contrast to the experimental observations with $LiHo_xY_{1-x}F_4$ [79].

Although quantum phase transition in the infinite-range model of a transverse Ising spin glass [92] gives a much weaker divergence in nonlinear susceptibiliy as compared with the short-range models, the contradiction still remains between theory of transverse Ising spin glass and experiment which yields the nonlinear susceptibility exponent $\gamma_{eff} \simeq 0$ at $T < 25\,\mathrm{mK}$ [79].

This SK model in a transverse field exhibits a continuous spin glass transition with mean field exponents [81, 82, 83, 84, 93].

Quantum Ising spin glass in 1D, due to no frustration entering the 1D random system, described by a random Ising spin chain in a transverse field

$$H = -\sum_{ij} J_{ij}\sigma_i^z\sigma_j^z - \sum_i \Gamma_i\sigma_i^x$$

where J_{ij} represents nearest neighbor coupling constraints and Γ_i the site-dependent field strength, gives more interesting exotic results [76]:
(1) exponential scaling of relaxation time with $\sqrt{L}$, equivalent to a dynamic scaling of $\tau \sim L^z$ with $z \to \infty$, where L represents system size,
(2) in the disorder phase of paramagnetic side, exponential decay of spin correlation function as $\exp(-x/\xi)$ at a large distance with $\langle\xi\rangle = A\delta^{-\nu}$, where $\delta = \langle \ln J_{ij}\rangle - \langle \ln \Gamma_i\rangle$ and $\nu = z$.

This dynamic scaling can be shown to correspond to the energy gap scaling with system size in the equivalent free fermion system conserving particle numbers by mapping transformations of Jordan-Wigner and Bogoliubov [77].

One-dimensional characterisitics of the random quantum models, with more distinctive effects from the Griffiths local criticality, was explored to reconfirm by numerical studies [77]:

(1) unconventional dynamic scaling of an infinite dynamical exponent,
(2) broad probability distribution, and thus difference between the average and the typical (most probable) value,
(3) divergent susceptibilitites inside the paramagnetic region as due to the rare clustering fluctuations of the quenched random variables, which are not found at all in the infinite-range model [74].

The $T = 0$ perspectives of quantum spin glass in realistic dimensions ($d = 2, 3$) mostly concern with a diluted dipolar Ising magnet $LiHo_x\ Y_{1-x}\ F_4$ ($T_{SG} \simeq 0.13\,\mathrm{K}$ at $x = 0.167$, at $x = 0.25\ T_c \to 0$)

$$\widetilde{H}_Q = -\sum_{i,j} J_{ij}\sigma_i^z\sigma_j^z - \Gamma\sum_i \sigma_i^x$$

which can be transformed to, in the critical region,

$$H_C = -\sum_{i,j,\tau} J_{ij} S_i(\tau) S_j(\tau) - \sum_{i,\tau} S_i(\tau) S_{i\tau}(\tau+1)$$

where σ_i's are Pauli spin matrices, S_i's are classical Ising spins, and the coupling in the extra dimension of imaginary time is ferromagnetic [7, 74, 94].

The rare fluctuations of the random distribution $\{J_{ij}\}$ are closely related to a perfect correlation of the J_{ij} random bonds in the extra time dimension.

Thermodynamic limit of a quantum model in simulations corresponds to a classical model of spatial dimension $L \to \infty$ while the infinity limit of the classical time dimension ($L_\tau \to \infty$) corresponds to the $T \to 0$ limit of the quantum model in the finite size scaling analysis [74].

Monte Carlo simulations of quantum Ising spin glass in 2D [90] and 3D [91] both show a finite temperature spin glass transition and a power law dynamic scaling with a finite z.

Rare fluctuations in 1D give a divergence of susceptibily in the paramagnetic phase to cause the Griffiths singularities. Rare clusters of strong bonds will be formed with probability of $P(L) \sim \exp(-aL^d)$, decreasing exponentially with volume L^d but the correlation length along the time-like axis increases exponentially as $\xi_\tau \sim \exp(bL^d)$ as given by the classical mapping of the original quantum system [74].

Simulation studies of 2D and 3D confirm the power law tails for the local susceptibility distributions [95, 96] as implied by the power law relationship between $P(L)$, that is, the local susceptibility and ξ_τ.

The non-universality in quantum spin glass models may be generic due to the rare-fluctuation dominant effects of Griffiths phase [74]. The rare fluctuations affect dynamics more directly than statics so that they may be more important in quantum systems [7, 74, 87, 97, 98]. For example, the point defects of rare fluctuation clusters in d-dimensional quantum systems are transformed as propagating in the time-like direction to the $(d+1)$-dimensional classical models, and thus act like the line defects which should give stronger perturbations than the same d-dimensional classical cases [74].

Acknowledgement

I am thankful to Korea Institute for Advanced Study in Seoul for their hospitality during my visit when this lecture note was prepared. I am also thankful to Dr. D.-H. Kim and Mr. S.-W. Yi who helped me with mathematical aspects and preparing the whole text in Springer Macro. Most of all I am grateful to Professor Bikas Chakrabarti and Dr. Arnab Das, who persuaded me to give this digressive lecture at a beginner's freedom.

Appendix

Quantum annealing and optimizations are the two main themes of the present workshop. Since the first observation of the spin glass phenomena [99], after more than 30 years of continuing great concerns from the core community of condensed matter physics, this spin glass physics is steering for a new exciting field of zero temperature physics, where quantum annealing and its application to optimization problems will be leading the central themes with the present workshop marking the epoch.

Classical spin glass is also far reaching to continue to create new complexities, such as chaotic size dependence, invariant metastates, etc. [10, 100].

Quantum annealing is a quantum mechanical way of annealing the system from the local minimum traps to the global absolutely lowest minimum.

Fine tuning of the quantum fluctuations, that is, quantum tunneling remains effective even at $T = 0$K when thermal annealing completely stops working. Although macroscopic quatum annealing appears to be extrmely rare, nature may have already hidden her success in quatum annealing and optimization with electrons in atoms and molecules, bosonic condensates, or even with black holes at quatum criticality.

References

1. K. H. Fischer and J. A. Hertz, *Spin Glasses*, Cambridge University Press (Cambridge, 1996). 101, 102, 103, 104, 105, 107, 110, 111, 112, 114, 116, 117, 127
2. K. H. Fischer, Phys. Rev. Lett. **34**, 1438 (1975). 101, 122
3. J. A. Hertz, Phys. Rev. B **14**, 1165 (1976). 101, 121
4. M. Mezard, G. Parasi, and M. Virasoro, *Spin Glasses Theory and Beyond* (World Scientific Lecture Notes in Physics, vol. 9), World Scientific (Singapore, 1987). 101, 103, 114, 116
5. A. P. Young (Ed.), *Spin Glasses and Random Fields* (World Scientific Series on Directions in Condensed Matter Physics, vol. 12), World Scientific (Singapore, 1998). 101, 127, 128, 129
6. M. Rubi and C. Perez-Vicente (Eds.), *Complex Behaviour of Glassy Systems* In: Lect. Notes Phys. **492** (1997). 101, 127, 128, 129
7. B. K. Chakrabarti, A. Dutta, and P. Sen, *Quantum Ising Phases and Transitions in Transverse Ising Models*. In: Lect. Notes Phys. **m41** (1996) 101, 103, 123, 125, 129
8. L. F. Cugliandolo, *Dynamics of Glassy Systems*, cond-mat/0210312 (Dec. 2002). 101, 107, 116, 117, 118, 119, 120
9. A. Crisanti and F. Ritort, *Violation of the Fluctuation-Dissipation Theorem in Glassy Systems : basic notions and the numerical evidence*, J. Phys. A **36**, R181–R290 (2003). 101, 107, 117, 118, 120
10. C. M. Newman and D. L. Stein, *Ordering and Broken Symmetry in Short-Ranged Spin Glasses*, J. Phys.: Condens. Matt. **15** R1319–R164 (2003). 101, 107, 116, 117, 120, 126
11. J. A. Mydosh, *Spin Glasses*, Taylor and Francis (London, 1993). 101, 102, 103, 104, 105, 107, 112, 114, 116, 1
12. V. Dotsenko, *An Introduction to the Theory of Spin Glasses and Neural Networks*, World Scientific (Singapore, 1994). 101, 103, 104, 112, 113, 114, 116

13. S. Sachdev, *Quantum Phase Transitions*, Cambridge University Press (New York, 1999). 101, 122, 128
14. M. A. Continentino, *Quantum Scaling in Many-Body Systems*, World-Scientific (Singapore, 2001). 101, 122, 128
15. P. Nordblad and P. Svendlindh, *Experiments on Spin Glasses* in [5] p. 1. See also [11]. 102, 104, 105, 106, 107, 117
16. P. Nordblad, P. Svendlindh, L. Lundgren, and L. Sandlund, Phys. Rev. B **19**, 645 (1986). 102
17. S. F. Edwards and P. W. Anderson, J. Phys. F **5**, 965 (1975). See also [1] and [11]. 103
18. G. Toulouse, Comm. Phys. **2**, 115 (1977). 103, 104
19. D. C. Mattis, Phys. Lett. A **56**, 421 (1976). 103
20. M. Plischke and B. Bergersen, *Equilibrium Statistical Physics*, World Scienctific (Singapore, 1989). 103, 104, 112, 114
21. D. Sherrington and S. Kirkpatrick, Phys. Rev. Lett. **35**, 1792 (1975). 104, 111, 114
22. J. R. L. de Almeida and D. J. Thouless, J. Phys. A **11**, 7384 (1985). 104, 107
23. G. Parisi, Phys. Lett. **73A**, 203 (1979). G. Parisi, J. Phys. A **13**, L115 (1980). G. Parisi, J. Phys. A **13**, 1101 (1980). G. Parisi, Phys. Rev. Lett. **43**, 1754 (1979). 104
24. A. P. Young and G. Katzgraber, Phys. Rev. Lett. **93**, 207203 (2004). 104
25. H. Sompolinsky and A. Zippelius, Phys. Rev. B **25**, 6860 (1982). 105, 119
26. H. Sompolinsky, Phys. Rev. Lett. **47**, 935 (1981). See also [1]. 105, 119
27. L. Levy, Phys. Rev. B **38**, 4963 (1987). 106
28. K. Gunnarson, P. Svedlindh, P. Nordblad, L. Lundgren, H. Aruga, and A. Ito, Phys. Rev. B **43**, 8199 (1991). 106
29. A. T. Ogielski, Phys. Rev. B **32**, 7384 (1985). K. Gunnarson, P. Svedlindh, P. Nordblad, L. Lundgren, H. Aruga, and A. Ito, Phys. Rev. Lett. **61**, 754 (1988). 106
30. W. L. McMillan, J. Phys. C **17**, 3179 (1984). A. J. Bray and M. A. Moore, Phys. Rev. Lett. **58**, 57 (1987). 107
31. J. Mattson, T. Jonsson, P. Nordblad, H. Aruga Katori, and A. Ito, Phys. Rev. Lett. **74**, 4305 (1995). 107
32. J. C. Lee, *Thermal Physics*, World Scientific (Singapore, 2002). M. E. J. Newman and G. T. Barkema, *Monte Carlo Methods in Statistical Physics*, Oxford University Press (Oxford, 1999). S. Jain, *Monte Carlo Simulation of Disordered Systems*, World Scientific (Singapore, 1998). R. E. Wilde and S. Singh, *Statistical Mechanics: Fundamentals and Modern Applications*, Wiley-Interscience (New York, 1998). G. Morandi, *Statistical Mechanics: An Intermediate Course*, World Scientific (Singapore, 1995). 107
33. L. E. Reichl, *A Modern Course in Statisical Physics*, University of Texas Press (Austin, 1980). C. Garrod, *Statistical Mechanics and Thermodynamics*, Oxford University Press (Oxford, 1995). 107, 108, 109
34. P. J. M. Bongaarts and Th. J. Siskens, Physica **68**, 315 (1973); ibid. **71**, 529 (1974). 109
35. C. A. Angell, *Entropy, Fragility, Landscapes, and the Glass Transition* in [6], p.1. 110, 118
36. I. M. Hodge, J. Non-Cryst. Sol. **131-133**, 435(1991); ibid. **169**, 211 (1994). 110
37. Scott Kirkpatrick and David Sherrington, Phys. Rev. B **17**, 4384 (1978). 111, 112, 114
38. G. Parisi, Phys. Lett. **73A**, 203 (1979); ibid. J. Phys. A: Math. Gen. **13**, 1101 (1980). 114

39. A. J. Bray and M. A. Moore, J. Phys. C **13**, L469 (1980). 116
40. G. Parisi, Phys. Rev. Lett. **50**, 1946 (1983). 116, 118
41. A. P. Young, Phys. Rev. Lett. **51**, 1206 (1983). 116
42. M. Mezard, G. Parisi, and M. A. Virasoro, J. Physique Lett. **46**, L-217 (1985). 116
43. M. Mezard, G. Parisi, N. Sourlas, G. Toulouse and M. Virasoro, J. Physique **45**, 843 (1984). M. Mezard, G. Parisi, N. Sourlas, G. Toulouse and M. Virasoro, Phys. Rev. Lett. **52**, 1156 (1984) 116
44. E. Marinari, G. Parisi, and J .J. Ruiz-Lorentzo, in [5], p.59. 116, 119, 120
45. D. S. Fisher and D. A. Huse, Phys. Rev. Lett. **56**, 1601 (1986). 117, 119, 129
46. P. W. Anderson, B. I. Halperin, and C. M. Varma, Phil. Mag. **25**, 1 (1972). S. K. Lyo, Phys. Rev. Lett. **48**, 688 (1982). 117
47. J.-P. Bouchaud, L. F. Cugliandolo, J. Kurchan, and M. Mezard, in [5], p.161. 117, 118
48. E. Vincent, J. Hammann, M. ocio, J.-P. Bouchaud, and L. F. Cugliandolo, in [6], p.184. 117, 119
49. R. G. Palmer, Adv. Phys. **31**, 669 (1982). 117
50. K. Binder, J. Baschnagel, W. Kob, K. Okun, W. Paul, K. Vollmayr, and M. Wolfgardt, in [5], p.22. 118
51. C. De Dominicis, I. Kondor, and T. Temesvari, in [5], p.119. 118, 128
52. K. Kawasaki, *Nonequilibrium and Phase Transition: Statistical Physics of Mesoscopic Scales* (translated into Korean by B. S. Kim and H. S. Lee), in Japanese (Asakura, Tokyo, 2000), and in Korean (Cheongmoon-Gak, Seoul, 2002). 118
53. D, J. Gross, I. Kanter, and H. Sompolinsky, Phys. Rev. Lett. **55**, 304 (1985). 118
54. E. Gardner, Nucl. Phys. B **257**, 747 (1985). T. R. Kirkpatrick, and D. Thirumalai, Phys. Rev. Lett. **58**, 2091 (1987). A. Crisanti, H. Horner, and H. J. Sommers, Z. Physik B **92**, 257 (1993) A. Crisanti and H. J. Sommers, Z. Physik B **87**, 341 (1992). L. F. Cugliandolo and J. Kurchan, Phys. Rev. Lett. **71**, 173 (1993). 118, 119
55. B. Derrida, Phys. Rev. B **24**, 2613 (1981). 118
56. E. Marinari, G. Parisi, and F. Ritort, J. Phys. A **27**, 7648 (1994). 118
57. F. Ritort, in *Complex Behaviour of Glassy Systems* (Springer Lecture Notes in Physics, **492** (1997), M. Rubi, C. Perez-Vincente (Eds.)) p. 125. See also K. Binder and A. P. Young, Rev. Mod. Phys. **58**, 801 (1986). 119, 120, 121
58. A. Crisanti and H. J. Sommers, Z. Physik B **87**, 341 (1992). 119
59. L. F. Cugliandolo and J. Kurchan, Phys. Rev. Lett. **71**, 173 (1993). A. Crisanti, H. Horner, and H. J. Sommers, Z. Physik B **92**, 257 (1993). 119, 120
60. D. J. Thouless, P. W. Anderson, and R. G. Palmer, Phil. Mag. **35**, 593 (1977). 119
61. M. B. Weissman, in [5], P.29. 119
62. A. T. Ogielski and D. L. Stein, Phys. Rev. Lett. **55**, 1634 (1985). 119
63. D. S. Fisher and D. A. Huse, J. Phys. A **20**, L1005 (1987). 120
64. F. Ritort, in [6], p.122. 120
65. C. de Dominicis and I. Kondor, Phys. Rev. B **27**, 606 (1983). See also [51]. 120
66. T. R. Kirkpatrick and D. Thirumlai, J. Phys. A **22**, L149 (1989). 120, 128
67. J. P. Bouchaud, L. Cugliandolo, J. Kurchan. and M. Mezard, Physica A **226**, 243 (1996). 120
68. J. P. Bouchaud and M. Mezard, J. Physique I **4**, 1109 (1994). E. Marinari, G. Parisi, and F. Ritort, J. Phys. A **27**, 7615 (1994). See also [66]. 120
69. A. J. Bray and M. A. Moore, J. Phys. C **13**, L655 (1980). 121, 123
70. A. J. Mills, Phys. Rev. B **48**, 7183 (1993). E. R. Duering, R. Schilling,and H. P. Wittman, Z. Phys. B **100**, 409 (1996). See also [13] and [14]. 122

71. A. Schroeder et. al. Nature **407**, 351 (2000). 122
72. Q. Si, J. Phys.: Condens. Matt. **15**, S2207 (2003). 122
73. R. N. Bhatt and P. A. Lee, Phys. Rev. Lett. **48**, 344 (1982). 122
74. R. N. Bhatt, in [5], p. 225. 122, 123, 124, 125
75. R. Shankar and G. Murthy, Phys. Rev. B **36**, 536 (1987). B. M. McCoy and T. T. Wu, Phys. Rev. B **176**, 631 (1968). B. M. McCoy, Phys. Rev. Lett. **23**, 383 (1969). 122
76. D. S. Fisher, Phys. Rev. Lett. **69**, 534 (1992). D. S. Fisher, Phys. Rev. B **51**, 6411 (1995). 122, 124
77. A. P. Young and H. Rieger, Phys. Rev. B **53**, 8486 (1996). 122, 124
78. M. J. Thill and D. A. Huse, Physica A **214**, 321 (1995). See also [45] 122, 129
79. W. Wu, B. Ellman, T. F. Rosenbaum, G. Aeppli, and D. H. Reich, Phys. Rev. Lett. **67**, 2076 (1991). W. Wu, D. Bitko, T. F. Rosenbaum, and G. Aeppli, Phys. Rev. Lett. **71**, 1919 (1993). 122, 124
80. M. Suzuki, Prog. Theo. Phys. **56**, 1454 (1976). M. Suzuki, in *Quantum Monte Carlo Methods* (Ed. M. Suzuki), Springer-Verlag (Heidelberg, 1986), p. 2. See also [7]. 122
81. P. Ray, B. K. Chakrabarti, and A. Chakrabarti, Phys. Rev. B **39**, 11828 (1989). 123, 124
82. D. Thirumalai, Q. Li, and T. R. Kirkpatrick, J. Phys. A **22**, 3339 (1989). 123, 124
83. Y. Y. Goldschmidt and P. Y. Lai, Phys. Rev. Lett. **64**, 2497 (1990). P. Y. Lai and Y. Y. Goldschmidt, Europhys. Lett. **13**, 289 (1990). 123, 124
84. B. K. Chakrabarti, Phys. Rev. B **24**, 4062, (1981). H. Ishii and T. Yamamoto, J. Phys. C **18**, 6225 (1985). 123, 124
85. P. Sen and B. K. Chakrabarti, Int. J. Mod. Phys. B **6**, 2439 (1992). See also [78] 123
86. H. Rieger, in *Annual Reviews of Computational Physics II* (Ed. D. Stauffer), World Scientific (Singapore, 1995), p. 925. 123
87. H. Rieger and A. P. Young, in [6], p. 256. 123, 125
88. D. S. Fisher, Phys. Rev. Lett. **69**, 534 (1992). D. D. Fisher, Phys. Rev. B **51**, 6411 (1995). 124
89. A. P. Young and H. Rieger, Phys. Rev. B. **53**, 8486 (1996). 124
90. H. Rieger and A. P. Young, Phys. Rev. Lett. **72**, 4141 (1994). 124, 125
91. M. Guo, R. N. Bhatt, and D. A. Huse, Phys. Rev. lett. **72**, 4137 (1994). 124, 125
92. J. Miller and D. Huse, Phys. Rev. Lett. **70**, 3147 (1993). 124
93. G. Buttner and K. Usadel, Phys. Rev. B **41**, 428 (1990). D.-H. Kim and J.-J. Kim, Phys. Rev.B **66**, 054432 (2002). 124
94. M. Guo, Ph.D. thesis, Princeton University (1995). 125
95. H. Rieger and A. P. Young, Phys. Rev. B **54**, 3328 (1996). 125
96. M. Guo, R. N. Bhatt and D. A. Huse, Phys. Rev. B **54**, 3336 (1996). 125
97. D. Dhar and M. Barma, J. Stat. Phys. **22**, 259 (1980). 125
98. M. Randeria, J. P. Sethna, and R. G. Palmer, Phys. Rev. Lett. **54**, 1321 (1985). 125
99. V. Cannella and J. A. Mydosh, Phys. Rev. B **6**, 4220 (1972). 126
100. D. L. Stein, "*Spin glasses: still complex after all these years?*" in *Quantum Decoherence and Entropy in Complex Systems*, H.-T. Elze (ed.), Springer (Berlin, 2003). 126

Decoherence and Quantum Couplings in a Noisy Environment

Andrew Fisher

Department of Physics and Astronomy, University College London, Gower St, London WC1E 6BT
andrew.fisher@ucl.ac.uk

In this chapter, I will review the established theory of quantum systems coupled to noisy condensed-phase environments, emphasising the central role played by the spectral functions of the environmental fluctuations. I will show how the application of the fluctuation-dissipation theorem to these functions leads to important connections between the coherent couplings and incoherent dynamics induced by the environment, and hence gives in-principle limits on the entangling power of quantum gates. I will give examples of this connection from condensed-matter and quantum-optical systems.

I will describe how such couplings may be expected to evolve under scaling transformations. I will also describe how to tailor response functions in such a way as to optimise the coherent evolution of the system, and describe a novel proposal to exploit local optical excitation to control the evolution of quantum states.

1 Qubits Coupled to a Bath

1.1 Quantum Operations

Conventionally in statistical mechanics we focus on the equilibrium properties of a small system coupled to a large bath with which it can exchange energy or particles. Now let us look instead at the dynamics in such a situation. If we make some general unitary operation $\hat{U}$ on the system and its environment, what is its effect on the system? First suppose that the overall density operator is initially a direct product $\hat{\rho}_S \otimes \hat{\rho}_E$. (This is a significant approximation–we'll come back to it later.) Let $\{|e_k\rangle\}$ be an orthonormal basis for the environment, and let $\hat{\rho}_E = |e_0\rangle\langle e_0|$ (i.e., suppose that the environment is in the pure state $|e_0\rangle$). This sounds like a further approximation, but in fact isn't; suppose we had an environmental density operator corresponding to the mixed state

$$\hat{\rho}_E = \sum_i p_i |\psi_i\rangle\langle\psi_i| \,, \tag{1}$$

A. Fisher: *Decoherence and Quantum Couplings in a Noisy Environment*, Lect. Notes Phys. **679**, 131–155 (2005)
www.springerlink.com

where the N states $\{\psi_i\}$ are not necessarily orthogonal but are normalized, and $\sum_i p_i = 1$. Then we can always introduce an additional 'far environment', F, with an orthonormal set of at least N states $\{|f_i\rangle\}$. The following pure state of the combined $E + F$ system,

$$|\Psi\rangle = \sum_i \sqrt{p_i}|\psi_i\rangle|f_i\rangle \ , \tag{2}$$

has the property that its reduced density matrix in the original environment is

$$\mathrm{Tr}_F[|\Psi\rangle\langle\Psi|] = \sum_{ij} \sqrt{p_i p_j}|\psi_i\rangle\langle\psi_j|\mathrm{Tr}_F[|f_i\rangle\langle f_j|] = \sum_i p_i|\psi_i\rangle\langle\psi_i| = \hat{\rho}_E \ , \tag{3}$$

and it is therefore indistinguishable (as far as any measurement within E only is concerned) from the original density matrix $\hat{\rho}_E$. This is referred to as a 'purification' of $\hat{\rho}_E$. For the moment we will suppose this has been done, and the original environment E replaced by a new, bigger, environment (which we will still, however label as E) in a pure state.

Now apply $\hat{U}$ to

$$\mathcal{E}(\hat{\rho}_S) = \mathrm{Tr}_E[\hat{U}(\hat{\rho}_S \otimes \hat{\rho}_E)\hat{U}^\dagger] \tag{4}$$

$$= \sum_k \langle e_k|\hat{U}(\hat{\rho}_S \otimes |e_0\rangle\langle e_0|)\hat{U}^\dagger|e_k\rangle \tag{5}$$

$$= \sum_k \hat{E}_k \hat{\rho}_S \hat{E}_k^\dagger \ , \tag{6}$$

where

$$E_k \equiv \langle e_k|\hat{U}|e_0\rangle \ . \tag{7}$$

Note that

$$\mathrm{Tr}_S[\mathcal{E}(\hat{\rho})] = \mathrm{Tr}_S\left[\sum_k E_k \hat{\rho} E_k^\dagger\right] = \mathrm{Tr}_S\left[\sum_k E_k^\dagger E_k \hat{\rho}\right] = 1 \tag{8}$$

for any $\hat{\rho}$, so it follows that

$$\sum_k E_k^\dagger E_k = \hat{1}_S \ . \tag{9}$$

What sort of thing is $\mathcal{E}$? It is more general than an ordinary operator, because it acts on density *operators* of the system, not on states of it. Hence it is called a **super-operator** [1] or a **quantum operation** [2].

The Requirements for a Quantum Operation

It is clear from the way $\mathcal{E}$ was introduced that any quantum operation ought generally to have certain properties.

(a) It should *preserve the normalization* of the state:

$$\mathrm{Tr}[\mathcal{E}(\hat{\rho})] = 1 \quad \text{if} \quad \mathrm{Tr}\hat{\rho} = 1 \,. \tag{10}$$

(b) It should be *linear*:

$$\mathcal{E}\left(\sum_i p_i \hat{\rho}_i\right) = \sum_i p_i \mathcal{E}(\hat{\rho}_i) \,. \tag{11}$$

(c) It is *completely positive*: if we choose any possible environment E and any possible density joint density matrix $\hat{\rho}$ of the system and environment, then the result of the composite operation $(\mathcal{I} \otimes \mathcal{E})\hat{\rho}$ is another positive operator. (This requirement includes, but is more general than, the requirement that $\mathcal{E}(\hat{\rho}_S)$ be positive for any system density matrix $\hat{\rho}_S$.)

Most generally, a quantum operation is simply *defined* as a map from density operators to other density operators satisfying these conditions.

The Kraus Representation Theorem

It turns out that any quantum operation satisfying the conditions in Sect. 1.1 can be expressed in the form

$$\mathcal{E}(\hat{\rho}) = \sum_k \hat{E}_k \hat{\rho} \hat{E}_k^\dagger \,, \tag{12}$$

with

$$\sum_k E_k^\dagger E_k = \hat{1} \,. \tag{13}$$

The formula (12) is known as the *Kraus representation* or *operator-sum representation* of the quantum operation; the operators $\{\hat{E}_k\}$ are known as the *Kraus operator*. For a proof see Sect. 3.3 of [1] or Sect. 8.2.4 of [2].

1.2 Examples

Unitary Evolution

Unitary evolution of the system by itself trivially has the form of a quantum operation:

$$\hat{\rho}_S \to \hat{U}_S \hat{\rho}_S \hat{U}_S^\dagger \,, \tag{14}$$

with

$$\hat{U}_S^\dagger \hat{U}_S = \hat{1}_S \,. \tag{15}$$

Probabilistic Unitary Evolution

Suppose our system remains isolated, but its Hamiltonian is uncertain because of some (classical) random process. The result is that different Hamiltonians may be applied with probabilities p_i; the resulting evolution is

$$\hat{\rho} \to \sum_i p_i \hat{U}_{Si} \hat{\rho}_S \hat{U}_{Si}^\dagger \,, \tag{16}$$

where $\hat{U}_{Si}$ is the unitary evolution associated with Hamiltonian i. This has the form of a quantum operation with Kraus operators $\sqrt{p_i}\hat{U}_{Si}$.

Von Neumann Measurements

Suppose we make a projective (von Neumann) measurement on our system. If the operator we measure is $\hat{O} = \sum_m o_m |m\rangle\langle m| \equiv \sum_m o_m \hat{P}_m$, then according to the standard von Neumann measurement postulate, result o_m is measured with probability $p_m = \langle m|\hat{\rho}_S|m\rangle = \mathrm{Tr}_S[\hat{P}_m\hat{\rho}_S]$. In this event the state of the system is replaced by $\hat{P}_m\hat{\rho}_S\hat{P}_m^\dagger/p_m$.

We can therefore regard the whole measurement process as that of replacing

$$\rho_S \to \sum_m p_m \frac{\hat{P}_m\hat{\rho}_S\hat{P}_m^\dagger}{p_m} = \sum_m \hat{P}_m\hat{\rho}_S\hat{P}_m^\dagger \,, \tag{17}$$

where by construction $\sum_m \hat{P}_m\hat{P}_m^\dagger = \sum_i \hat{P}_m = \hat{1}_S$. The von Neumann measurement is therefore a special case of a quantum operation in which the Kraus operators are the projection operators $\hat{P}_m$.

1.3 The Lindblad Equation

The theory of quantum operations supposes that things just 'happen' to the system's density matrix–we don't ask why, or how fast. Now let's start looking at the dynamics, but let's do so on a timescale δt that has to satisfy two conditions.

- δt should be small compared with the characteristic timescale of the system – so the system density matrix only evolves 'a little bit' in this time interval (i.e. $\delta t \ll \tau_S$).
- But δt should also be long compared with the time over which the environment 'forgets' its information about the system (i.e. $\delta t \gg \tau_E$).

Since we are beyond the timescale τ_E, we might hope that the evolution of the system will depend only on the present system density matrix, and not on anything that has happened in the past. In that case the evolution through time δt should be described by a quantum operation on the current system density matrix. Our presentation follows that of Preskill [1]; the idea is to

look for a suitable quantum operation such that $\hat{\rho}_S$ should be altered only to order δt:

$$\hat{\rho}_S(\delta t) = \mathcal{E}(\hat{\rho}_S(0)) = \sum_k \hat{E}_k \hat{\rho}_S(0) \hat{E}_k^\dagger = \hat{\rho}_S(0) + \mathrm{O}(\delta t) \; . \tag{18}$$

Thus it follows that one of the Kraus operators, $\hat{E}_0$ say, must be $\hat{1}_S + \mathrm{O}(\delta t)$, and the others must be $\mathrm{O}(\sqrt{\delta t})$. So, let's write

$$\hat{E}_0 = \hat{1}_S + \left(\hat{K} - \frac{\mathrm{i}}{\hbar} \hat{H} \right) \delta t, \tag{19}$$

$$\hat{E}_k = \sqrt{\delta t} \hat{L}_k, \quad k \geq 1 \; . \tag{20}$$

Here $\hat{K}$ and $\hat{H}$ are Hermitian operators, but are otherwise arbitrary at this stage; the operators $\hat{L}_k$ are also arbitrary and are known as **Lindblad operators** (note that they need be neither unitary nor Hermitian). However, the normalization condition on the Kraus operators requires

$$\sum_k \hat{E}_k^\dagger \hat{E}_k = \hat{1}_S \quad \Rightarrow \quad \hat{1}_S = \hat{1}_S + \left(2\hat{K} + \sum_k \hat{L}_k^\dagger \hat{L}_k \right) \delta t + \mathrm{O}(\delta t)^2 \; . \tag{21}$$

Hence

$$\hat{K} = -\frac{1}{2} \sum_k \hat{L}_k^\dagger \hat{L}_k \; , \tag{22}$$

and therefore

$$\begin{aligned} \hat{\rho}_S(\delta t) = & \left[\hat{1}_S + \delta t \left(\hat{K} - \frac{\mathrm{i}}{\hbar} \hat{H} \right) \right] \hat{\rho}(0) \left[\hat{1}_S + \delta t \left(\hat{K} + \frac{\mathrm{i}}{\hbar} \hat{H} \right) \right] \\ & + \delta t \sum_k \hat{L}_k \hat{\rho}(0) \hat{L}_k^\dagger \end{aligned} \tag{23}$$

$$\begin{aligned} = & \hat{\rho}_S(0) - \left\{ \frac{\mathrm{i}}{\hbar} [\hat{H}, \hat{\rho}_S(0)] + \sum_k \left[\hat{L}_k \hat{\rho}_S(0) \hat{L}_k^\dagger - \frac{1}{2} \{ \hat{\rho}_S(0), \hat{L}_k^\dagger \hat{L}_k \} \right] \right\} \delta t \\ & + \mathrm{O}(\delta t)^2 \; , \end{aligned} \tag{24}$$

where $\{\hat{A}, \hat{B}\}$ represents the anti-commutator $\hat{A}\hat{B} + \hat{B}\hat{A}$. Taking the limit $\delta t \to 0$ we obtain the **Lindblad master equation**:

$$\frac{\mathrm{d}\hat{\rho}_S}{\mathrm{d}t} = \frac{1}{\mathrm{i}\hbar} [\hat{H}, \hat{\rho}_S] + \sum_k \left[\hat{L}_k \hat{\rho}_S(0) \hat{L}_k^\dagger - \frac{1}{2} \{ \hat{\rho}_S(0), \hat{L}_k^\dagger \hat{L}_k \} \right] \; . \tag{25}$$

Note that:

- If there were no Lindblad operators (i.e., if there were only one Kraus operator in the decomposition (18), this formula would reduce to the quantum Liouville equation for a closed system:

$$\frac{\mathrm{d}\hat{\rho}_S}{\mathrm{d}t} = \frac{1}{\mathrm{i}\hbar}[\hat{H}, \hat{\rho}_S] \,. \tag{26}$$

We would then identify $\hat{H}$ as the Hamiltonian of the (closed) system.

- However, there is in general to reason to suppose that the operator $\hat{H}$ appearing in (25) is the Hamiltonian of the isolated system. Indeed, we shall see later that there are (potentially important) corrections to it that come from the interaction with the environment.
- Indeed, $\hat{H}$ is not even unique; the equation of motion remains invariant under the changes

$$\hat{L}_k \to \hat{L}_k + l_k \hat{1}_S, \qquad \hat{H} \to \hat{H} + \frac{1}{2\mathrm{i}} \sum_k (l_k^* \hat{L}_k - l_k \hat{L}_k^\dagger) + b\hat{1}_S \,, \tag{27}$$

where $\{l_k\}$ and b are arbitrary scalars. The equation of motion also remains invariant under an arbitrary unitary transformation of the Lindblad operators:

$$\hat{L}_k \to \sum_j u_{kj} \hat{L}_j \,. \tag{28}$$

- The right-hand side of equation (25) is a linear functional of $\hat{\rho}_S$; it defines the Liouvillian super-operator $\mathcal{L}$ through

$$\frac{\mathrm{d}\hat{\rho}_S}{\mathrm{d}t} = \mathcal{L}[\hat{\rho}_S] \,. \tag{29}$$

The formal solution to this can be written in the form of a time-evolution super-operator:

$$\hat{\rho}_S(t) = \mathcal{V}(T)\hat{\rho}_S(0) \equiv \hat{T}_{\leftarrow} \exp\left[\int_0^t \mathcal{L}(s)\mathrm{d}s\right] \hat{\rho}_S(0) \,. \tag{30}$$

Here $\hat{T}_{\leftarrow}$ is the same entity we previously called $\hat{T}$: the time-ordering operator that puts earliest times to the right and latest times to the left. Provided the Liouvillian is time-independent, this can be simplified to

$$\hat{\rho}_S(t) = \exp(\mathcal{L}t)\hat{\rho}_S(0) \,. \tag{31}$$

Note however that this is not a recipe for efficient practical calculations; if the dimension of the system's Hilbert space is N, a matrix representation for $\mathcal{L}$ would contain $N^4 = N^2 \times N^2$ elements; directly exponentiating it would therefore require $\mathrm{O}(N^{12})$ operations.

- The term involving the Lindblad operators on the RHS of equation (25) is known as the *dissipator*, written $\mathcal{D}[\hat{\rho}]$; thus we have

$$\mathcal{L}[\hat{\rho}_S] = \frac{1}{\mathrm{i}\hbar}[\hat{H}, \hat{\rho}_S] + \mathcal{D}[\hat{\rho}_S] \tag{32}$$

- This is all in the Schrödinger representation, where the wavefunction (or density matrix) is time-dependent but operators are not. An alternative way of representing the information is to transfer the time-dependence to the operators: we then require that the expectation value of any (system) operator $\hat{O}$ be the same in either picture.

$$\mathrm{Tr}_S[\hat{O}\hat{\rho}_S(t)] = \mathrm{Tr}_S[\hat{O}(\mathcal{V}\hat{\rho}_S(0))] = \mathrm{Tr}_S[(\mathcal{V}^\dagger(t)\hat{O})\hat{\rho}_S(0)] \equiv \mathrm{Tr}_S[\hat{O}_H(t)\hat{\rho}_S(0)] \,, \tag{33}$$

where $\mathcal{V}^\dagger(t) \equiv \hat{T}_{\rightarrow} \exp[\int_0^t \mathcal{L}^\dagger(s)\mathrm{d}s]$, and the operator $\hat{T}_{\rightarrow}$ orders in the opposite sense to normal (i.e. earliest times to the left). Note that $\hat{O}_H$ obeys the equation of motion

$$\frac{\mathrm{d}\hat{O}_H}{\mathrm{d}t} = \mathcal{V}^\dagger(t)\mathcal{L}^\dagger(t)\hat{O} \,. \tag{34}$$

In the case of a time-independent Liouvillian things simplify once again, and

$$\hat{O}_H(t) = \exp[\mathcal{L}^\dagger t]\hat{O}, \quad \frac{\mathrm{d}\hat{O}_H}{\mathrm{d}t} = \mathcal{L}^\dagger(t)\hat{O}_H(t) \,. \tag{35}$$

1.4 The Markovian Weak-Coupling Limit

We start by addressing in the simplest case, where the system is coupled weakly to the environment and so perturbation theory is applicable. We suppose that the Hilbert space of the system and the environment form a direct product.

The Redfield Equation

Write the Hamiltonian as

$$\hat{H} = \hat{H}_S + \hat{H}_E + \hat{H}_I \,, \tag{36}$$

where only $\hat{H}_I$ involves both the system and environment degrees of freedom. We work in the interation representation with $\hat{H}_I$ as the perturbation (so $\hat{H}_0 = \hat{H}_S + \hat{H}_E$ corresponds to uncoupled system and environment). So the equation of motion of the density matrix in the interaction representation is

$$\frac{\mathrm{d}\hat{\rho}(t)}{\mathrm{d}t} = \frac{1}{\mathrm{i}\hbar}[\hat{H}_I(t), \hat{\rho}(t)] \,. \tag{37}$$

(All expressions will be in the interaction representation until further notice.) This has formal solution

$$\hat{\rho}(t) = \hat{\rho}(0) + \frac{1}{\mathrm{i}\hbar}\int_0^t \mathrm{d}s\,[\hat{H}_I(s), \hat{\rho}(s)] \,, \tag{38}$$

which gives

$$\frac{\mathrm{d}\hat{\rho}(t)}{\mathrm{d}t} = \frac{1}{\mathrm{i}\hbar}[\hat{H}_I(t), \hat{\rho}(0)] - \frac{1}{\hbar^2}\int_0^t \mathrm{d}s\,[\hat{H}_I(t), [\hat{H}_I(s), \hat{\rho}(s)]]\,. \tag{39}$$

Tracing over the environment gives

$$\frac{\mathrm{d}\hat{\rho}_S(t)}{\mathrm{d}t} = \frac{1}{\mathrm{i}\hbar}\mathrm{Tr}_E[\hat{H}_I(t), \hat{\rho}(0)] - \frac{1}{\hbar^2}\int_0^t \mathrm{d}s\,\mathrm{Tr}_E[\hat{H}_I(t), [\hat{H}_I(s), \hat{\rho}(s)]]\,. \tag{40}$$

We now make

- **Assumption 1.** The first term on the RHS of (40) is zero. This is not really an assumption: we can always absorb terms into the system Hamiltonian $\hat{H}_S$ so as to ensure that the mean value of the interaction Hamiltonian, averaged over the density matrix of the environment, is zero: $\mathrm{Tr}_E[\hat{H}_I(t)\hat{\rho}(0)] = 0$.

More importantly, we also make

- **Assumption 2** (known as the Born Approximation in this literature). We suppose that the density matrix factors approximately at all times into $\hat{\rho}(t) = \hat{\rho}_S(t) \otimes \hat{\rho}_E$, where $\hat{\rho}_E$ is independent of time. This assumes weak system-environment coupling.

Assumptions 1 and 2 together enable us to write

$$\frac{\mathrm{d}\hat{\rho}_S(t)}{\mathrm{d}t} = -\frac{1}{\hbar^2}\int_0^t \mathrm{d}s\,\mathrm{Tr}_E[\hat{H}_I(t), [\hat{H}_I(s), \hat{\rho}_S(s) \otimes \hat{\rho}_E]]\,. \tag{41}$$

We now make

- **Assumption 3** (Markovian approximation, first part). We suppose that the timescales over which the 'memory' represented by the integral in equation (41) is important are sufficiently short that the system density matrix is hardly different from its current value, so we can replace $\hat{\rho}_S(s) \to \hat{\rho}_S(t)$.

Hence

$$\frac{\mathrm{d}\hat{\rho}_S(t)}{\mathrm{d}t} = -\frac{1}{\hbar^2}\int_0^t \mathrm{d}s\,\mathrm{Tr}_E[\hat{H}_I(t), [\hat{H}_I(s), \hat{\rho}_S(t) \otimes \hat{\rho}_E]]\,. \tag{42}$$

This is known as the **Redfield equation**. It is time-local (only involves $\hat{\rho}_S(t)$), but still contains an explicit reference to the 'starting time' at $t = 0$. This dependence on the past can be made explicit by substituting $s = t - s'$, in terms of which

$$\frac{\mathrm{d}\hat{\rho}_S(t)}{\mathrm{d}t} = -\frac{1}{\hbar^2}\int_0^t \mathrm{d}s'\,\mathrm{Tr}_E[\hat{H}_I(t), [\hat{H}_I(t-s'), \hat{\rho}_S(t) \otimes \hat{\rho}_E]]\,. \tag{43}$$

Now we make further

- **Assumption 4** (Markovian approximation, second part). We suppose that we can extend the integral on the RHS of equation (43) to infinity without significantly altering the results.

Thus we have

$$\frac{\mathrm{d}\hat{\rho}_S(t)}{\mathrm{d}t} = -\frac{1}{\hbar^2}\int_0^\infty \mathrm{d}s'\,\mathrm{Tr}_E[\hat{H}_I(t),[\hat{H}_I(t-s'),\hat{\rho}_S(t)\otimes\hat{\rho}_E]]\;. \tag{44}$$

This equation is fully Markovian in the sense that it depends only on the current density matrix $\hat{\rho}_S(t)$ and contains no explicit reference to any other time.

Assumptions 3 and 4 correspond to requiring that the time be large compared with the timescale of the environment's memory of what the system has done to it: $t \gg \tau_E$.

Correlation Functions

To see what we've done, it helps to write equation (44) in terms of the **correlation functions** of the environment. First decompose the interaction Hamiltonian into

$$\hat{H}_I(t) = \sum_\alpha \hat{A}_\alpha(t)\otimes\hat{B}_\alpha(t)\;, \tag{45}$$

where $\hat{A}$ is a system operator, and $\hat{B}$ is an environment operator. Note that, although it is not necessary for each individual $\hat{A}$ and $\hat{B}$ to be Hermitian, the Hermitian conjugate of each operator must also appear in the sum, so we can also write

$$\hat{H}_I(t) = \sum_\alpha \hat{A}^\dagger_\alpha(t)\otimes\hat{B}^\dagger_\alpha(t)\;, \tag{46}$$

Now define the correlation function

$$C_{\alpha\beta}(s) \equiv \mathrm{Tr}_E[\hat{B}^\dagger_\alpha(t)\hat{B}_\beta(t-s)\hat{\rho}_E] = \mathrm{Tr}_E[\hat{B}^\dagger_\alpha(s)\hat{B}_\beta(0)\hat{\rho}_E]\;, \tag{47}$$

where the second equality follows if the environment is stationary. (Note that, viewed as a matrix, C is Hermitian.) Now we can rewrite equation (44) as

$$\begin{aligned}\frac{\mathrm{d}\hat{\rho}_S(t)}{\mathrm{d}t} &= \frac{1}{\hbar^2}\int_0^\infty \mathrm{d}s'\,\mathrm{Tr}_E[\hat{H}_I(t-s')\hat{\rho}_S(t)\otimes\hat{\rho}_E\hat{H}_I(t)\\ &\quad - \hat{H}_I(t)\hat{H}_I(t-s')\hat{\rho}_S(t)\otimes\hat{\rho}_E] + \text{h.c.}\\ &= \frac{1}{\hbar^2}\int_0^\infty \mathrm{d}s'\sum_{\alpha\beta} C_{\alpha\beta}(s)[\hat{A}_\beta(t-s)\hat{\rho}_S(t)\hat{A}^\dagger_\alpha(t)\\ &\quad - \hat{A}^\dagger_\alpha(t)\hat{A}_\beta(t-s)\hat{\rho}_S(t)] + \text{h.c.}\end{aligned} \tag{48}$$

Now it's clear exactly which environmental timescales have to be short: the relevant τ_E is the time beyond which the correlation functions of the environmental operators that couple to the system decay.

To go further we need an explicit form for the time-dependence of the system operators $\hat{A}$. It turns out that different approximations are useful in the limit $\tau_S \ll \tau_R$ (good qubits) and $\tau_S \gg \tau_R$ (bad qubits).

1.5 Good Qubits – the Rotating Wave Approximation

If the system evolves very fast compared to any environmentally-induced relaxation, it makes sense to decompose the system operators into parts evolving with definite frequencies. Hence we write

$$\hat{A}_\alpha(t) = \sum_\omega \mathrm{e}^{-\mathrm{i}\omega t}\hat{A}_\alpha(\omega) \ , \tag{49}$$

where

$$\hat{A}_\alpha(\omega) = \sum_{\epsilon,\epsilon' \ \mathrm{s.t.}\ \epsilon'-\epsilon=\hbar\omega} \Pi(\epsilon)\hat{A}_\alpha\Pi(\epsilon') \ , \tag{50}$$

where $\Pi(\epsilon)$ projects onto the eigenstates of $\hat{H}_S$ having eigenvalue ϵ. A typical example would be for a spin-1/2 system in a magnetic field with Larmor frequency ω_0, where we could put

$$\sigma_x(t) = \mathrm{e}^{-\mathrm{i}\omega_0 t}\sigma_+ + \mathrm{e}^{\mathrm{i}\omega_0 t}\sigma_- \ . \tag{51}$$

So, now we have

$$\begin{aligned}\frac{\mathrm{d}\hat{\rho}_S(t)}{\mathrm{d}t} &= \frac{1}{\hbar^2}\sum_{\omega\omega'}\int_0^\infty \mathrm{d}s\mathrm{e}^{\mathrm{i}\omega s}\sum_{\alpha\beta} C_{\alpha\beta}(s)\mathrm{e}^{i(\omega'-\omega)t}[\hat{A}_\beta(\omega)\hat{\rho}_S(t)\hat{A}^\dagger_\alpha(\omega') \\ &\quad - \hat{A}^\dagger_\alpha(\omega')\hat{A}_\beta(\omega)\hat{\rho}_S(t)] + \mathrm{h.c.} \\ &= \frac{1}{\hbar^2}\sum_{\omega\omega'}\Gamma_{\alpha\beta}(\omega)\mathrm{e}^{i(\omega'-\omega)t}[\hat{A}_\beta(\omega)\hat{\rho}_S(t)\hat{A}^\dagger_\alpha(\omega') - \hat{A}^\dagger_\alpha(\omega')\hat{A}_\beta(\omega)\hat{\rho}_S(t)] \\ &\quad + \mathrm{h.c.} \ ,\end{aligned} \tag{52}$$

where

$$\Gamma_{\alpha\beta}(\omega) \equiv \int_0^\infty \mathrm{d}s\, \mathrm{e}^{\mathrm{i}\omega s}C_{\alpha\beta}(s) \tag{53}$$

is the *causal* (since it only involves $s > 0$) Fourier transform of the correlation function $C_{\alpha\beta}$. We now make

- **Approximation 5** (the Rotating Wave Approximation–RWA). This corresponds to saying that any term like $\mathrm{e}^{i(\omega-\omega')t}$ averages to zero on the timescales relevant to relaxation processes, so we only need to keep terms with $\omega = \omega'$.

This assumption simplifies our expression to

$$\frac{\mathrm{d}\hat{\rho}_S(t)}{\mathrm{d}t} = \frac{1}{\hbar^2}\sum_{\omega}\sum_{\alpha\beta}\Gamma_{\alpha\beta}(\omega)[\hat{A}_\beta(\omega)\hat{\rho}_S(t)\hat{A}^\dagger_\alpha(\omega) - \hat{A}^\dagger_\alpha(\omega)\hat{A}_\beta(\omega)\hat{\rho}_S(t)] + \text{h.c.} \tag{54}$$

Now we split up $\Gamma_{\alpha\beta}$ as

$$\Gamma_{\alpha\beta}(\omega) = \frac{1}{2}J_{\alpha\beta}(\omega) + \mathrm{i}S_{\alpha\beta}(\omega)\ , \tag{55}$$

where $J_{\alpha\beta}(\omega)$ is the power spectrum of the correlations (i.e. the full Fourier transform of the correlation functions)

$$J_{\alpha\beta}(\omega) = \Gamma_{\alpha\beta}(\omega) + \Gamma^*_{\beta\alpha}(\omega) = \int_{-\infty}^{\infty}\mathrm{d}s\,\mathrm{e}^{\mathrm{i}\omega s}C_{\alpha\beta}(s)\ , \tag{56}$$

and

$$S_{\alpha\beta}(\omega) = \frac{1}{2\mathrm{i}}[\Gamma_{\alpha\beta}(\omega) - \Gamma^*_{\beta\alpha}(\omega)]\ . \tag{57}$$

We then find

$$\frac{\mathrm{d}\hat{\rho}_S(t)}{\mathrm{d}t} = \frac{1}{\hbar^2}\sum_{\omega}\sum_{\alpha\beta}\Bigg\{-\mathrm{i}S_{\alpha\beta}(\omega)[\hat{A}^\dagger_\alpha(\omega)\hat{A}_\beta(\omega), \hat{\rho}_S(t)] + J_{\alpha\beta}(\omega)\left[\hat{A}_\beta(\omega)\hat{\rho}_S(t)\hat{A}^\dagger_\alpha(\omega) - \frac{1}{2}\{\hat{A}^\dagger_\alpha(\omega)\hat{A}_\beta(\omega), \hat{\rho}_S(t)\}\right]\Bigg\}\ . \tag{58}$$

This is almost of Lindblad form, with a Hamiltonian term

$$\hat{H}_{LS} = \frac{1}{\hbar^2}\sum_{\omega}\sum_{\alpha\beta}S_{\alpha\beta}(\omega)\hat{A}^\dagger_\alpha(\omega)\hat{A}_\beta(\omega)\ . \tag{59}$$

(The subscript LS shows that this Hamiltonian term plays a similar role to the Lamb shift in atomic physics – it modifies the Hamiltonian of the system as a result of the coupling from the bath. We shall return to the importance of this term in Sect. 1.10 below.) The dissipator is

$$\mathcal{D}(\hat{\rho}_s(t)) = \frac{1}{\hbar^2}\sum_{\omega}\sum_{\alpha\beta}J_{\alpha\beta}(\omega)\left[\hat{A}_\beta(\omega)\hat{\rho}_S(t)\hat{A}^\dagger_\alpha(\omega) - \frac{1}{2}\{\hat{A}^\dagger_\alpha(\omega)\hat{A}_\beta(\omega), \hat{\rho}_S(t)\}\right] \tag{60}$$

and may be put into conventional Lindblad form by diagonalising the matrix $J_{\alpha\beta}(\omega) = U\Lambda U^\dagger$ (where Λ is real and diagonal and U is unitary–recall J is Hermitian) for each response frequency ω. The result is that for each ω one obtains a set of Lindblad operators

$$\hat{L}_\mu = \sum_\beta(\Lambda_\mu)^{1/2}U_{\mu\beta}\hat{A}_\beta(\omega)\ . \tag{61}$$

1.6 The Quantum Optical Master Equation

A classic case where this approach is valid is for an atom (the system) coupled to electromagnetic field modes (the environment). In that case the environment is a set of harmonic oscillators:

$$\hat{H}_E = \sum_k \sum_\lambda \hbar\omega_k \hat{b}^\dagger_\lambda(k)\hat{b}_\lambda(k) \,, \tag{62}$$

where λ labels one of the two transverse polarizations for wavevector k and $\hat{b}_\lambda(k)$ is an annihilation operator. The interaction Hamiltonian is (in the electric dipole approximation)

$$-\hat{\mathbf{D}}\cdot\hat{\mathbf{E}} = -\mathrm{i}\hat{\mathbf{D}}\cdot\sum_k\sum_\lambda\sqrt{\frac{2\pi\hbar\omega_k}{V}}\mathbf{e}_\lambda(k)[\hat{b}_\lambda(k)-\hat{b}^\dagger_\lambda(k)] \,, \tag{63}$$

where V is a normalization volume for the field modes and $\mathbf{e}_\lambda$ is a unit polarization vector, We can decompose $\hat{\mathbf{D}}$ in the same manner as before:

$$\hat{\mathbf{D}}(t) = \sum_\omega \mathrm{e}^{-\mathrm{i}\omega t}\hat{A}(\omega) \,. \tag{64}$$

The spectral correlation tensor is now

$$\Gamma_{ij}(\omega) = \frac{1}{\hbar^2}\int_0^\infty \mathrm{d}s\,\mathrm{e}^{\mathrm{i}\omega s}\langle\hat{E}_i(t)\hat{E}_j(t-s)\rangle \,. \tag{65}$$

In thermal equilibrium (i.e. black-body radiation), we have

$$\Gamma_{ij}(\omega) = \delta_{ij}\left[\frac{1}{2}J(\omega)+\mathrm{i}S(\omega)\right] \,, \tag{66}$$

with

$$\begin{aligned} J(\omega) &= \frac{4\omega^3}{3\hbar c^3}[1+n(\omega)]; \\ S(\omega) &= \frac{2}{3\pi\hbar c^3}\mathcal{P}\left[\int_0^\infty \omega_k^3 \mathrm{d}\omega_k\left(\frac{1+n(\omega_k)}{\omega-\omega_k}+\frac{n(\omega_k)}{\omega+\omega_k}\right)\right] , \end{aligned} \tag{67}$$

where $\mathcal{P}$ stands for a Cauchy principal value. Hence the Lamb shift Hamiltonian becomes

$$\hat{H}_{LS} = \sum_\omega \hbar S(\omega)\hat{A}^\dagger(\omega)\hat{A}(\omega) \,, \tag{68}$$

and the dissipator is

$$\begin{aligned} \mathcal{D}(\hat{\rho}_S) = &\sum_{\omega>0}\frac{4\omega^3}{3\hbar c^3}[1+n(\omega)]\big(\hat{A}(\omega)\hat{\rho}_S\hat{A}^\dagger(\omega)-\frac{1}{2}\{\hat{A}^\dagger(\omega)\hat{A}(\omega),\hat{\rho}_S\}\big) \\ &+\sum_{\omega<0}\frac{4\omega^3}{3\hbar c^3}n(\omega)\big(\hat{A}^\dagger(\omega)\hat{\rho}_S\hat{A}(\omega)-\frac{1}{2}\{\hat{A}(\omega)\hat{A}^\dagger(\omega),\hat{\rho}_S\}\big) \,, \end{aligned} \tag{69}$$

Note that in both equations (68) and (69) the frequency sums go over the (usually discrete) energy response of the system.

For a two-level atom with Hamiltonian

$$\hat{H} = -\frac{\hbar\omega_0}{2}\sigma_z \tag{70}$$

(where ω_0 is the energy difference between the ground and excited states, and the minus sign gives us the usual convention that $|\uparrow\rangle = |0\rangle$ is the ground state and $|\downarrow\rangle = |1\rangle$ the excited state), and transition dipole $\mathbf{d}$, where we can write

$$\hat{\mathbf{D}}(t) = \mathbf{d}(\hat{\sigma}_+ \mathrm{e}^{-\mathrm{i}\omega_0 t} + \sigma_- \mathrm{e}^{+\mathrm{i}\omega_0 t}) \,, \tag{71}$$

we find that the dissipator contains two Lindblad operators:

$$\hat{L}_1 = |\mathbf{d}|\sqrt{\frac{4\omega_0^3}{3\hbar c^3}[1 + n(\omega_0)]}\hat{\sigma}_+; \quad \hat{L}_2 = |\mathbf{d}|\sqrt{\frac{4\omega_0^3}{3\hbar c^3}n(\omega_0)}\hat{\sigma}_- \,. \tag{72}$$

$\hat{L}_1$ produces decay from the excited state to the ground state, while $\hat{L}_2$ produces excitation. The rates of each process are precisely consistent with the values of the Einstein A and B coefficients.

To see how this affects the dynamics consider the limit $T \to 0$, where only emission and not absorption occurs. Then the one remaining Lindblad operator is

$$\hat{L}_1 = \sqrt{\Gamma}\begin{pmatrix} 0 & 1 \\ 0 & 0 \end{pmatrix} \quad \text{with} \quad \sqrt{\Gamma} = |\mathbf{d}|\sqrt{\frac{4\omega_0^3}{3\hbar c^3}} \,. \tag{73}$$

Thus

$$\frac{\partial}{\partial t}\begin{pmatrix} \rho_{00} & \rho_{01} \\ \rho_{10} & \rho_{11} \end{pmatrix} = \mathrm{i}\omega_0 \begin{pmatrix} 0 & \rho_{01} \\ -\rho_{10} & 0 \end{pmatrix} + \Gamma \begin{pmatrix} \rho_{11} & -\frac{1}{2}\rho_{01} \\ -\frac{1}{2}\rho_{10} & -\rho_{11} \end{pmatrix} \,. \tag{74}$$

The solutions are

$$\begin{aligned} \rho_{00}(t) &= \rho_{00}(0) + \rho_{11}(0)[1 - \exp(-\Gamma t)] \,; \\ \rho_{11}(t) &= \rho_{11}(0)\exp(-\Gamma t) \,; \\ \rho_{01}(t) &= \rho_{01}(0)\exp[(\mathrm{i}\omega_0 - \Gamma/2)t] \,; \\ \rho_{10}(t) &= \rho_{10}(0)\exp[(-\mathrm{i}\omega_0 - \Gamma/2)t] \,. \end{aligned} \tag{75}$$

Notice that the population in the excited state $|1\rangle$ decays exponentially with a time constant $T_1 = 1/\Gamma$, whereas the off-diagonal elements of the density matrix ('coherences') decay with a longer time constant $T_2 = 2/\Gamma$.

A very similar analysis can be made for the coupling to a phonon (rather than photon) bath in magnetic resonance experiments.

1.7 Bad Qubits–Quantum Brownian Motion

We now consider 'bad' qubits, where the system has very little chance to evolve before the interaction with the environment takes effect – in other words, where $\tau_S \gg \tau_R$.

First, we decompose the correlation functions in a different way to equation (55), as:

$$\begin{aligned} D_{\alpha\beta}(\tau) &= \mathrm{i}\langle[\hat{B}_\alpha(\tau), \hat{B}_\beta(0)]\rangle = \mathrm{i}\left(C_{\alpha\beta}(\tau)) - C_{\beta^\dagger\alpha^\dagger}(-\tau)\right) \\ &\qquad\qquad \text{(the 'dissipation kernel')}\,; \\ D^{(1)}_{\alpha\beta}(\tau) &= \langle\{\hat{B}_\alpha(\tau), \hat{B}_\beta(0)\}\rangle = \left(C_{\alpha\beta}(\tau)) + C_{\beta^\dagger\alpha^\dagger}(-\tau)\right) \\ &\qquad\qquad \text{(the 'noise kernel')}\,. \end{aligned} \tag{76}$$

Here $\alpha^\dagger$ is the index labelling those operators $\hat{A}$ and $\hat{B}$ which are the Hermitian conjugates of $\hat{A}_\alpha$ and $\hat{B}_\alpha$. Hence

$$C_{\alpha\beta}(\tau) = \frac{1}{2}[D^{(1)}_{\alpha\beta}(\tau) - \mathrm{i}D_{\alpha\beta}(\tau)]; \tag{77}$$

$$C_{\beta^\dagger\alpha^\dagger}(-\tau) = [C_{\alpha^\dagger\beta^\dagger}(\tau)]^* = \frac{1}{2}[D^{(1)}_{\alpha\beta}(\tau) + \mathrm{i}D_{\alpha\beta}(\tau)]\,. \tag{78}$$

Note that **if** the operators are Hermitian, then $\alpha^\dagger = \alpha$, and both D and $D^{(1)}$ are real:

$$\begin{aligned} D_{\alpha\beta} &= \mathrm{i}\left(C_{\alpha\beta}(\tau) - (C_{\alpha\beta}(\tau))^*\right) = -2\Im C_{\alpha\beta}(\tau); \\ D^{(1)}_{\alpha\beta}(\tau) &= (C_{\alpha\beta}(\tau)) + C_{\beta\alpha}(-\tau)) = 2\Re C_{\alpha\beta}(\tau)\,. \end{aligned} \tag{79}$$

Substituting in equation (44), we find

$$\begin{aligned} \frac{\mathrm{d}\hat{\rho}_S(t)}{\mathrm{d}t} &= \frac{1}{\hbar^2}\int_0^\infty \mathrm{d}s \sum_{\alpha\beta} C_{\alpha\beta}(s)[\hat{A}_\beta(t-s)\hat{\rho}_S(t)\hat{A}^\dagger_\alpha(t) \\ &\qquad -\hat{A}^\dagger_\alpha(t)\hat{A}_\beta(t-s)\hat{\rho}_S(t)+] + \text{h.c.} \\ &= \frac{1}{2\hbar^2}\int_0^\infty \mathrm{d}s \sum_{\alpha\beta}\Big[D^{(1)}_{\alpha\beta}(s)[\hat{A}^\dagger_\alpha(t), [\hat{\rho}_S(t), \hat{A}_\beta(t-s)]] \\ &\quad + \mathrm{i}D_{\alpha\beta}(s)[\hat{A}^\dagger_\alpha(t), \{\hat{\rho}_S(t), \hat{A}_\beta(t-s)\}]\Big]\,. \end{aligned} \tag{80}$$

In order to go from the first line to the second, we have grouped together the terms from operators $\alpha\beta$ with those in the Hermitian conjugate part from $\alpha^\dagger\beta^\dagger$.

Now, rather than make the decomposition (49) and use Approximation 5, we make instead

- **Approximation 5'**: since the system evolves very little during the time over which the environment influences it, we write

$$\hat{A}_\beta(t-s) \approx \hat{A}_\beta(t) - s\dot{\hat{A}}_\beta(t) \,, \tag{81}$$

where

$$\dot{\hat{A}}_\beta(t) = \frac{1}{\mathrm{i}\hbar}[\hat{A}_\beta(t), \hat{H}_S(t)] \tag{82}$$

(remember we are in the interaction representation).

Using this, we find

$$\begin{aligned}\frac{\mathrm{d}\hat{\rho}_S(t)}{\mathrm{d}t} = \frac{1}{2\hbar^2}\int_0^\infty \mathrm{d}s \sum_{\alpha\beta}\Big[& D^{(1)}_{\alpha\beta}(s)[\hat{A}^\dagger_\alpha(t), [\hat{\rho}_S(t), \hat{A}_\beta(t)]] \\ & + \mathrm{i}D_{\alpha\beta}(s)[\hat{A}^\dagger_\alpha(t), \{\hat{\rho}_S(t), \hat{A}_\beta(t)\}] \\ & - sD^{(1)}_{\alpha\beta}(s)[\hat{A}^\dagger_\alpha(t), [\hat{\rho}_S(t), \dot{\hat{A}}_\beta(t)]] \\ & - \mathrm{i}sD_{\alpha\beta}(s)[\hat{A}^\dagger_\alpha(t), \{\hat{\rho}_S(t), \dot{\hat{A}}_\beta(t)\}]\Big] \,. \end{aligned} \tag{83}$$

This gives us four integrals over s to perform.

1.8 Simplifications for a Harmonic Environment

To do this it's helpful to write the correlation functions in the following way. We suppose the environment is in thermal equilibrium: in that case the correlation functions obey the conditions

$$J_{\alpha\beta}(-\omega) = \mathrm{e}^{-\beta\hbar\omega}[J_{\alpha^\dagger\beta^\dagger}(\omega)]^* \,. \tag{84}$$

So, we lose no generality by writing

$$\begin{aligned} J_{\alpha\beta}(\omega) &= [n(|\omega|)+1]j_{\alpha\beta}(|\omega|) \qquad (\omega > 0) \\ &= n(|\omega|)[j_{\alpha^\dagger\beta^\dagger}(|\omega|)]^* \qquad (\omega < 0) \,, \end{aligned} \tag{85}$$

where $n(\omega)$ is the Bose occupation number

$$n(\omega) = \frac{1}{1-\exp(-\beta\hbar\omega)} \,, \tag{86}$$

which is real and satisfies

$$n(\omega) = \mathrm{e}^{-\beta\hbar\omega}[n(\omega)+1] \,. \tag{87}$$

The advantage of doing this is that in certain circumstances (notably when the environment is harmonic) the function $j(|\omega|)$ is temperature-independent, and all the temperature dependence is contained in the $n(|\omega|)$ factor. We

have already seen an example of this in Sect. 1.6, where $j(\omega) = 4\omega^3/3\hbar c^3$, but in fact it is generally true whenever the environment is harmonic and the coupling to the system is by some combination of the coordinates x_q of the different modes q:

$$\hat{B}_\alpha = \sum_q g_{\alpha q}\hat{x}_q \quad \Rightarrow \quad j_{\alpha\beta}(\omega) = \sum_q \frac{g^*_{\alpha q} g_{\beta q}}{2M_q\omega_q}\delta(\omega - \omega_q)\ . \tag{88}$$

Note that this also means that *at a particular temperature* and within these approximations, one can always find a linearly-coupled harmonic environment that mimics the effect of the actual environment via equations (85) and (88). However, if anharmonic terms are present this 'effective harmonic environment' will have a temperature-dependent spectral function.

Thus the dissipation kernel becomes

$$\begin{aligned} D_{\alpha\beta}(\tau) &= \imath[C_{\alpha\beta}(\tau) - C_{\beta^\dagger\alpha^\dagger}(-\tau)] \\ &= \mathrm{i}\int_{-\infty}^{\infty}\frac{\mathrm{d}\omega}{2\pi}\,(1 - \mathrm{e}^{-\beta\hbar\omega})J_{\alpha\beta}(\omega)\mathrm{e}^{-\mathrm{i}\omega\tau} = \mathrm{i}\int_{-\infty}^{\infty}\frac{\mathrm{d}\omega}{2\pi}\,\mathrm{sgn}(\omega)j_{\alpha\beta}(\omega)\mathrm{e}^{-\mathrm{i}\omega\tau} \\ &= 2\int_0^{\infty}\frac{\mathrm{d}\omega}{2\pi}\,[\Re(j_{\alpha\beta})\sin(\omega\tau) - \Im(j_{\alpha\beta})\cos(\omega\tau)]\ . \end{aligned} \tag{89}$$

Similarly, the noise kernel is

$$\begin{aligned} D^{(1)}_{\alpha\beta}(\tau) &= [C_{\alpha\beta}(\tau) + C_{\beta^\dagger\alpha^\dagger}(-\tau)] \\ &= \int_{-\infty}^{\infty}\frac{\mathrm{d}\omega}{2\pi}\,(1 + \mathrm{e}^{-\beta\hbar\omega})J_{\alpha\beta}(\omega)\mathrm{e}^{-\mathrm{i}\omega\tau} \\ &= \int_{-\infty}^{\infty}\frac{\mathrm{d}\omega}{2\pi}\,\mathrm{sgn}(\omega)\coth\left(\frac{\beta\hbar\omega}{2}\right)j_{\alpha\beta}(\omega)\mathrm{e}^{-\mathrm{i}\omega\tau} \\ &= 2\int_0^{\infty}\frac{\mathrm{d}\omega}{2\pi}\,\coth\left(\frac{\beta\hbar\omega}{2}\right)[\Re(j_{\alpha\beta})\cos(\omega\tau) - \Im(j_{\alpha\beta})\sin(\omega\tau)]\ . \end{aligned} \tag{90}$$

Note how, if j is temperature-independent, all the temperature-dependence is contained in the noise kernel $D^{(1)}$–hence the name.

Now back to those integrals. We can now do the time integrals using the result

$$\lim_{\epsilon\to 0^+}\int_0^{\infty}\mathrm{e}^{(\mathrm{i}\omega-\epsilon)\tau}\,\mathrm{d}\tau = \pi\delta(\omega) + \imath\mathcal{P}\left(\frac{1}{\omega}\right)\ , \tag{91}$$

from which we get

$$\int_0^{\infty}\cos(\omega\tau)\,\mathrm{d}\tau = \pi\delta(\omega); \tag{92}$$

$$\int_0^{\infty}\sin(\omega\tau)\,\mathrm{d}\tau = \mathcal{P}\left(\frac{1}{\omega}\right); \tag{93}$$

$$\int_0^{\infty}\tau\sin(\omega\tau)\,\mathrm{d}\tau = -\frac{\partial}{\partial\omega}\int_0^{\infty}\cos(\omega\tau)\,\mathrm{d}\tau = -\pi\delta'(\omega)\ . \tag{94}$$

If $j_{\alpha\beta}$ is real (as it is in all the examples we've seen so far), we get

$$\int_0^\infty \mathrm{d}s\, D^{(1)}_{\alpha\beta}(s) = -\pi \int_0^\infty \mathrm{d}\omega\, j_{\alpha\beta}(\omega) \coth\left(\frac{\beta\hbar\omega}{2}\right) \delta(\omega)$$
$$= \frac{\pi}{2} \lim_{\omega\to 0} j_{\alpha\beta}(\omega) \coth\left(\frac{\beta\hbar\omega}{2}\right); \tag{95}$$

$$\int_0^\infty \mathrm{d}s\, D_{\alpha\beta}(s) = 2\int_0^\infty \mathrm{d}\omega\, \frac{j_{\alpha\beta}(\omega)}{\omega}; \tag{96}$$

$$\int_0^\infty \mathrm{d}s\, sD_{\alpha\beta}(s) = -\pi \int_0^\infty j_{\alpha\beta}(\omega)\delta'(\omega) = \pi j'_{\alpha\beta}(0)\,. \tag{97}$$

1.9 Brownian Motion with Ohmic Dissipation

The values of all these integrals depend critically on what happens to $j_{\alpha\beta}$ in the limit $\omega \to 0$ (rather than as $\omega \to \omega_0$, as in the rotating wave approximation).

- If $j_{\alpha\beta} \sim \omega^p$ with $p < 1$, the integrals diverge. We shall see later that this is a symptom of the system's behaviour being qualitatively changed by its interaction with the environment; even the short-time propagation described by equation (81) is not a good approximation to the true evolution of the system.
- If $j_{\alpha\beta} \sim \omega^p$ with $p > 1$, the first and last integrals vanish.

Hence the critical case (where the integrals neither vanish nor diverge) is where $j_{\alpha\beta} \propto \omega$. This is known as **Ohmic dissipation**.

Assuming Ohmic dissipation, it is conventional to write

$$j_{\alpha\beta}(\omega) = \frac{2\eta_{\alpha\beta}\hbar}{\pi}\omega \quad \text{as} \quad \omega \to 0\,. \tag{98}$$

The parameter $\eta_{\alpha\beta}$ will turn out to be closely related to a damping rate or viscosity. We also assume that $j(\omega) \to 0$ for ω above some upper cutoff Ω; for example, we could have

$$j_{\alpha\beta}(\omega) = \frac{2\eta_{\alpha\beta}\hbar}{\pi}\omega\frac{\Omega^2}{\omega^2+\Omega^2}\,. \tag{99}$$

Thus

$$\int_0^\infty \mathrm{d}s\, D^{(1)}_{\alpha\beta}(s) = \frac{\pi}{2} \lim_{\omega\to 0} j_{\alpha\beta}(\omega) \coth\left(\frac{\beta\hbar\omega}{2}\right) = \frac{2\eta_{\alpha\beta}k_BT}{\hbar}\,; \tag{100}$$

$$\int_0^\infty \mathrm{d}s\, D_{\alpha\beta}(s) = 2\int_0^\infty \mathrm{d}\omega\, \frac{j_{\alpha\beta}(\omega)}{\omega}\,; \tag{101}$$

$$\int_0^\infty \mathrm{d}s\, sD(s) = -2\pi \int_0^\infty j_{\alpha\beta}(\omega)\delta'(\omega) = \pi j'_{\alpha\beta}(0) = 2\eta_{\alpha\beta}\hbar\,. \tag{102}$$

Finally, at high temperatures (i.e., such that $k_BT \gg \hbar\Omega$), we have

$$D^{(1)}_{\alpha\beta}(\tau) \approx 4\eta_{\alpha\beta}k_BT\Omega \mathrm{e}^{-\Omega\tau} \ , \tag{103}$$

so

$$\int_0^\infty \mathrm{d}s\, sD^{(1)}_{\alpha\beta}(s) = \frac{4\eta_{\alpha\beta}k_BT}{\Omega} \ . \tag{104}$$

Putting all this into (83), we get the following equation of motion in the interaction representation:

$$\begin{aligned}\frac{\mathrm{d}\hat{\rho}_S(t)}{\mathrm{d}t} = \frac{1}{2\hbar}\sum_{\alpha\beta}\Bigg[&\frac{2\eta_{\alpha\beta}k_BT}{\hbar}[\hat{A}^\dagger_\alpha(t),[\hat{\rho}_S(t),\hat{A}_\beta(t)]] \\ &- \frac{4\eta_{\alpha\beta}k_BT}{\Omega}[\hat{A}^\dagger_\alpha(t),[\hat{\rho}_S(t),\dot{\hat{A}}_\beta(t)]] \\ &+ \mathrm{i}\int_0^\infty \mathrm{d}\omega\, \frac{j_{\alpha\beta}(\omega)}{\omega}[\hat{A}^\dagger_\alpha(t),\{\hat{\rho}_S(t),\hat{A}_\beta(t)\}] \\ &- 2\eta_{\alpha\beta}\mathrm{i}[\hat{A}^\dagger_\alpha(t),\{\hat{\rho}_S(t),\dot{\hat{A}}_\beta(t)\}]\Bigg] \ . \end{aligned} \tag{105}$$

We can make several simplifications:

- The third term in fact represents a purely Hamiltonian evolution, because the $\alpha\beta$ and $\beta\alpha$ contributions can be combined to give

  $$\frac{1}{2}[\hat{A}^\dagger_\alpha(t),\{\hat{\rho}_S,\hat{A}_\beta\}] + \frac{1}{2}[\hat{A}_\beta(t),\{\hat{\rho}_S,\hat{A}^\dagger_\alpha\}] = \frac{1}{2}[\{\hat{A}^\dagger_\alpha,\hat{A}_\beta\},\hat{\rho}] \ , \tag{106}$$

  so this term looks like

  $$\frac{-\mathrm{i}}{\hbar}[\hat{H}_{\mathrm{eff}},\hat{\rho}] \quad \text{with} \quad \hat{H}_{\mathrm{eff}} = -\int_0^\infty \mathrm{d}\omega\, \frac{j_{\alpha\beta}(\omega)}{\omega}\{\hat{A}^\dagger_\alpha,\hat{A}_\beta\} \ . \tag{107}$$

  This term can be thought of as the energy contribution from all the normal modes of the environment relaxing to their new equilibrium positions as the system slowly evolves. It is sometimes absorbed into the definition of the system Hamiltonian, but its importance for us is once again that it can be non-local; it can couple different, spatially separated, parts of the 'system', and hence can generate coherent interactions among the qubits.
- Remembering that $p \sim m\omega_0 x$, where ω_0 is the system's intrinsic frequency scale, we see that the second term is of order ω_0/Ω times the first. Since, by assumption, $\omega_0 \ll \Omega$, we can neglect the second term.

This leaves us with the following master equation:

$$\begin{aligned}\frac{\mathrm{d}\hat{\rho}_S(t)}{\mathrm{d}t} = \frac{-\mathrm{i}}{\hbar}[\hat{H}_{\mathrm{eff}},\hat{\rho}] + \frac{1}{2\hbar}\sum_{\alpha\beta}\Bigg[&\frac{2\eta_{\alpha\beta}k_BT}{\hbar}[\hat{A}^\dagger_\alpha(t),[\hat{\rho}_S(t),\hat{A}_\beta(t)]] \\ &-2\mathrm{i}\eta_{\alpha\beta}[\hat{A}^\dagger_\alpha(t),\{\hat{\rho}_S(t),\dot{\hat{A}}_\beta(t)\}]\Bigg] \ . \end{aligned} \tag{108}$$

This is the general form of the Caldiera-Leggett master equation [3].

This can be further re-written if we notice that we can once again combine the $\alpha\beta$ and $\beta\alpha$ contributions, this time to the last term, to get

$$[\hat{A}_\alpha^\dagger, \{\hat{\rho}_S, \dot{\hat{A}}_\beta\}] = \frac{1}{2}[\{\hat{A}_\alpha^\dagger, \dot{\hat{A}}_\beta\}, \hat{\rho}_S] + \left(\hat{A}_\alpha^\dagger \hat{\rho}_S \dot{\hat{A}}_\beta - \frac{1}{2}\{\dot{\hat{A}}_\beta \hat{A}_\alpha^\dagger, \hat{\rho}_S\}\right) - \left(\dot{\hat{A}}_\beta \hat{\rho}_S \hat{A}_\alpha^\dagger - \frac{1}{2}\{\hat{A}_\alpha^\dagger \dot{\hat{A}}_\beta, \hat{\rho}_S\}\right) \quad (109)$$

Now let us simplify to the special case of a particle moving under a potential $V(x)$, so the system Hamiltonian is

$$\hat{H}_S = \frac{\hat{p}^2}{2m} + V(\hat{x}) \,, \quad (110)$$

interacting with a bath of harmonic oscillators with angular frequencies ω_q through the linear coupling

$$\hat{H}_I = -\hat{x}\hat{B} \quad \text{with} \quad \hat{B} = \sum_q g_q \hat{x}_q = \sum_q g_q \sqrt{\frac{\hbar}{2M_q\omega_q}}(\hat{b}_q + \hat{b}_q^\dagger) \,. \quad (111)$$

Hence the coupling is to a single environmental operator $\hat{B}$, and there is a single relevant correlation function, for which

$$j(\omega) = \sum_q \frac{\hbar |g_q|^2}{2M_q\omega_q}\delta(\omega - \omega_q) \,. \quad (112)$$

Then, coming back into the Schrödinger representation and looking at the full time dependence of the density matrix, we find that equation (108) becomes

$$\frac{\mathrm{d}\hat{\rho}_S(t)}{\mathrm{d}t} = -\frac{\mathrm{i}}{\hbar}[\hat{H}_{\text{eff}}, \hat{\rho}_S] - \frac{2\mathrm{i}\gamma}{\hbar}[\hat{x}(t), \{\hat{\rho}_S(t), \hat{p}(t)\}] + \frac{2m\gamma k_B T}{\hbar^2}[\hat{x}(t), [\hat{\rho}_S(t), \hat{x}(t)]] \quad (113)$$

This is the Caldeira-Legett master equation [3] for the density matrix of a particle diffusing under the influence of a harmonic bath.

1.10 The Fluctuation-Dissipation Theorem and the Link Between Coherent and Incoherent Evolution

In many circumstances, the qubits are localised objects (e.g. spins in bound states) and the only connection between them comes via the environment. This connection can, however, produce coherent dynamics, which (in a gate picture of quantum computation) can produce an entangling two-qubit gate, or (in a quantum annealing picture) can produce non-trivial quantum dynamics (such as the propagation of a domain wall). We should then regard the 'system' as consisting of the two qubits; the non-trivial coherent dynamics coupling them comes from the Lamb shift term in equation (59). Note in particular that

the part of $\hat{H}_{LS}$ that couples both qubits is proportional to those $S_{\alpha\beta}(\omega)$ for which one of the indices α and β comes from each qubit – it therefore depends on the extent of correlation between fluctuations at the two qubit sites.

However, even in the 'good-qubit' limit described by the rotating wave approximation, this coherent dynamics is inevitably accompanied by incoherent terms (corresponding to the dissiaptor in equation 60). Note that the incoherent dynamics depends on the full spectral functions $J_{\alpha\beta}(\omega)$, which are related to the $S_{\alpha\beta}$ by the Hilbert transform

$$S_{\alpha\beta}(\omega) = \frac{1}{\pi}\int_{-\infty}^{\infty} \frac{[J_{\alpha\beta}(\omega') + J^*_{\beta\alpha}(\omega')]}{\omega - \omega'} \mathrm{d}\omega' \ . \tag{114}$$

Hence, if we trivially extend the definition of the Lindblad operators (61) to arbitrary frequencies (not just the response frequencies of the system), we can express the effective ('Lamb-shift') Hamiltonian induced by the environmental coupling as

$$\hat{H}_{LS} = \sum_{\omega}\sum_{\mu}\int_{-\infty}^{\infty} \frac{\mathrm{d}\omega'}{2\pi} \frac{\left[\sum_{\mu} L^{\dagger}_{\mu,\omega'} L_{\mu,\omega'}\right]}{\omega - \omega'}. \tag{115}$$

This relation links the component of the effective Hamiltonian linking two states of the our particular system separated by frequency ω, to the Lindblad operators that would be appropriate for all possible different frequencies ω', provided that thw coupling to the environment is kept constant [4].

This relationship between the coherent and incoherent parts of the response is reminiscent of that embodied in the fluctuation-dissipation theorem between the real and imaginary parts of a dynamical susceptibility. Suppose that we take the same environment as before and couple it at $t = 0$, not to a quantum system, but to a time-dependent classical driving field:

$$\hat{H}_{1,\mathrm{class}} = f(t)\hat{B}_{\alpha}(t) \ . \tag{116}$$

Then, as is well known, to first order in f the corresponding change in the expectation value of $\hat{B}^{\dagger}_{\beta}(t)$ is

$$g(t) \equiv \delta\langle \hat{B}^{\dagger}_{\beta}(t)\rangle = \int_0^t \phi_{\beta\alpha}(t-t')f(t')\,\mathrm{d}t' \ , \tag{117}$$

where

$$\phi_{\beta\alpha}(\tau) = \mathrm{i}\langle[\hat{B}^{\dagger}_{\beta}(t), \hat{B}_{\alpha}(0)]\rangle \tag{118}$$

The corresponding response in the frequency domain involves the frequency-dependent susceptibility:

$$\widetilde{g}(\omega) = \chi_{\beta\alpha}(\omega)\widetilde{f}(\omega) \ , \tag{119}$$

where

$$\chi_{\beta\alpha}(\omega) = \int_{-\infty}^{\infty} \mathrm{d}\omega' \frac{(1 - \mathrm{e}^{-\beta\omega'}) J_{\beta\alpha}(\omega')}{\omega - \omega'} \,. \tag{120}$$

Note that, since both the applied field and the response are now real, classical quantities, and their Fourier transforms therefore contain both positive-frequency and negative-frequency parts, so does χ. The negative-frequency parts is suppressed by a factor $\mathrm{e}^{-\beta\omega}$. The real and imaginary parts of χ are connected by dispersion relations, and hence the dissipative (out-of-phase, hence imaginary) part of χ is directly connected to the fluctuation spectrum by

$$\Im(\chi_{\alpha\beta}(\omega)) + \Im(\chi_{\beta\alpha}(\omega)) = [J_{\alpha\beta}(\omega)n(\omega) + J_{\beta\alpha}(-\omega)n(-\omega)] \,. \tag{121}$$

In our case, where the environment is driven by *quantum-mechanical* systems, we have to distinguish between positive-frequency processes (environment transiently absorbs energy from system A or B) and negative-frequency (environment transiently gives out energy) processes. Both contribute to the effective Hamiltonian (59), but they correspond to different types of decoherence (i.e., to different Lindblad operators in the decomposition (25)).

1.11 Irreducible Decoherence and Decoherence-Free Subspaces

One elegant approach to designing quantum gates is to select states $|\psi\rangle$ to represent the quantum information which have the property that

$$\hat{A}_\alpha |\psi\rangle = 0 \quad \forall\alpha \,, \tag{122}$$

i.e. are annihilated by the interaction Hamiltonian with the bath. Such a set of states is known as a decoherence-free subspace [5, 6], and has the property that it states within it are not affected by the action of $\hat{H}_I$. Its evolution is 'decoherence-free'. However, it is apparent from equation (eq:lambshiftdft) that it is also entanglement-free: assuming (as we have all along) that the qubits are spatially separated, there is then no interaction in the system that can entangle one qubit with another.

Hence, the decoherence-free subspace does not give any absolute protection from decoherence during the operation of an entangling gate. The best it can do is to guide us in the choice of qubit states to eliminate the most important decohering interactions, while retaining enough coherent interaction to produce the desired qubit-qubit entanglement.

2 Scaling Transformations for Partially Coherent Dynamics

2.1 Scaling for Thermodynamic Properties

Scaling transformations for the description of equilibrium properties, especially in the context of critical phenomena, are well established (see, for

example, [7]). The essential idea is very simple to state: one looks for a new Hamiltonian $\hat{H}'$ that depends only on a reduced set of parameters $\{s'\}$ but which reproduces all the thermal averages of functions of $\{s'\}$ that are computed using the full Hamiltonian $\hat{H}$:

$$\begin{aligned}
&\hat{H} \to \hat{H}' \quad \text{s.t.} \quad \frac{1}{Z}\mathrm{Tr}_s[f(s')\exp(-\beta\hat{H})] = \frac{1}{Z'}\mathrm{Tr}_{s'}[f(s')\exp(-\beta\hat{H}')];\\
&Z = \mathrm{Tr}_s[\exp(-\beta\hat{H})];\\
&Z' = \mathrm{Tr}_{s'}[\exp(-\beta\hat{H}')];\\
&F = -\frac{1}{\beta}\log Z = \Delta F - \frac{1}{\beta}\log Z' \,. \qquad (123)
\end{aligned}$$

One then looks for fixed points of this scaling, which describe the long-wavelength thermodynamic properties of the system (the most important usually being the high-temperature, low-temperature and critical fixed points).

2.2 Scaling the Liouvillian

Suppose we now ask a different question: we start with a Liouvillian which generates the time evolution of a set of degrees of freedom s:

$$\rho_s(0) \to \rho_s(t) = \exp(\mathcal{L}t)\rho_s(0) \,. \qquad (124)$$

We now want to find a Liouvillian $\mathcal{L}'$ that reproduce as much as possible of the dynamics of some reduced set $\{s'\}$ of the variables.

$$\rho_{s'}(0) \to \rho_{s'}(t) = \exp[\mathcal{L}'t]\rho_{s'}(0) \,. \qquad (125)$$

Of course, if the original evolution $\mathcal{L}$ is purely Hamiltonian, i.e. if

$$\mathcal{L}[\rho] = \frac{1}{\mathrm{i}\hbar}[\hat{H}, \rho] \,, \qquad (126)$$

then we have already solved this problem (at least in the limit where the variables $\{s'\}$ are weakly coupled to the others); the solution is given by equation (48). How does this solution change if our starting dynamics is itself only partially coherent? We now want to find an $\mathcal{L}'$ generating an evolution such that

$$\rho_{s'}(t) = \exp[\mathcal{L}'t]\rho_{s'}(0) \qquad (127)$$

describes the same physics as

$$\rho_{s'}(t) = \mathrm{Tr}_s[\exp[\mathcal{L}t]\rho_{s'}(0)] \,. \qquad (128)$$

This is conveniently approached in the limit of the Time Convolutionless Projector Operator (TCL) method [8]. A full derivation will be presented elsewhere and here we only describe the main result: the analysis leading to equation (48) remains largely unaltered, but the correlation functions have

to be evaluated in the presence of the dissipation already present in the environment. An study of the dynamics of the 1D disordered Heisenberg and transverse-field Ising models by this approach is underway, and the results will be reported elsewhere.

3 Quantum Gates via Optical Excitation

To conclude this chapter, we briefly set out the principles of a novel approach to quantum information processing now being studied in a large project at our laboratory at University College London (UCL). In a sense it is intermediate between the conventional gate approach to quantum computing [2] and the quantum annealing ideas being discussed in this volume, since – while formally based on the a gate structure – it makes the maximum use of the intrinsic dynamics of a quantum system.

3.1 Advantages of Localised States

The advantages of well localised states for the transmission of quantum information can be seen from studying equation (115): if the environment has a discrete spectrum (as is generally the case when bound states are involved), the incoherent response occurs predominantly at a few isolated frequencies which one can tune to be some distance away from the frequencies at which the qubits themselves evolve, thereby suppressing the incoherent contributions to the dynamics. Indeed in such cases one can solve the time-evolution equations more rapidly, without making the rotating wave approximation, and can show that there are particular times when the environment is strictly decoupled from the system. The environment is therefore capable of inducing entangling interactions with very little decoherence of the qubits, provided the energy scales and operation times are suitably chosen.

3.2 The UCL Project

In a major experimental and theoretical project underway at UCL, we are working on realising a quantum gate whose principles are described in [9]. Simply stated, the idea is to take as qubits a set of electron spins bound at a random array of defects, for example donors in a semiconductor such as Si, and to switch exchange interactions between them by controlling optically the orbital state of one or more additional 'control electrons'. Although we cannot hope to control the locations of individual dopants precisely on the atomic scale, we can choose the overall dopant density so that the effective exchange interaction is close to zero when the system is in its ground state, but becomes appreciable (we estimate of order 10^{10} to 10^{11} Hz) when there is orbital excitation.

We have shown that, for spin-1/2 defects and a spin-1/2 control system, the parameters can in principle be chosen so that the qubits are returned to a pure state at the end of the gate operation, despite their correlation with the gate's operation during the process [10]. Although experimental work aimed at demonstration of the control of exchange couplings in our own system is still in progress, we were encouraged to see the observation of optically-induced entanglement in a related system (multiple spins in a semiconductor quantum well) [11].

4 Conclusions

The subjects of quantum annealing and more traditional gate-based quantum information processing are converging, and there is a need for a common set of theoretical tools to understand the evolution of quantum systems in noisy thermal environments. We have seen how the existing frameworks enable us to study the limits of both 'good' and 'bad' quantum evolution, and put quite general bounds on the relationship between entangling interactions and decohering ones. Finally we have seen that some of the new scaling ideas in this field will allow is to extract the long-distance, long-time response of interacting and disordered quantum systems.

Acknowledgement

I am grateful to Gabriel Aeppli, Sean Barrett, Iain Chapman, Tim Spiller, Phil Stamp and Marshall Stoneham for a number of discussions of the issues presented here. Parts of this work were supported by the IRC in Nanotechnology, by the IRC in Quantum Information Processing, and by the UK Research Councils Basic Technology project *Putting the Quantum into Information Processing*.

References

1. J. Preskill, available online at http://www.theory.caltech.edu/people/preskill/ph229/ (unpublished). 132, 133, 134
2. M.A. Nielsen and I.L. Chuang, *Quantum computation and quantum information* (Cambridge University Press, Cambridge, 2000). 132, 133, 153
3. A.O. Caldeira and A.J. Leggett, Phys. Rev. Lett. **46**, 211–214 (1981). 148, 149
4. A.J. Fisher, Phil. Trans. Roy. Soc. A **361**, 1441 (2003). 150
5. D.A. Lidar, I.L. Chuang, and K.B. Whaley, Phys. Rev. Lett. **81**, 2594 (1998). 151
6. D. Bacon, J. Kempe, D.A. Lidar, and K.B. Whaley, Phys. Rev. Lett. **85**, 1758 (2000). 151
7. J.J. Binney, N.J. Dowrick, A.J. Fisher, and M.E.J. Newman, *The theory of critical phenomena* (Oxford University Press, Oxford, 1992). 152

8. S. Chaturvedi and F. Sibata, Z. Phys. B **35**, 297 (1979). 152
9. A.M. Stoneham, A.J. Fisher, and P.T. Greenland, J. Phys.: Cond. Matt. **15**, L447 (2003). 153
10. R. Rodriquez, A.J. Fisher, P.T. Greenland, and A.M. Stoneham, J. Phys.: Cond. Matt. **16**, 2757 (2004). 154
11. J. Bao, A.V. Bragas, J.K. Furdyna, and R. Merlin, Nature Materials **2**, 175 (2003). 154

Part II

Quantum Annealing: Basics and Applications

Experiments on Quantum Annealing

Gabriel Aeppli[1] and Thomas F. Rosenbaum[2]

[1] London Centre for Nanotechnology and Dept. of Physics and Astronomy University College London, London WC1E 6BT UK
gabriel.aeppli@ucl.ac.uk
[2] James Franck Institute and Dept. of Physics University of Chicago Chicago, Illinois 60637 USA

1 Introduction

The standard deterministic, gate-based computation paradigms underlying modern digital computing are not those that nature uses to perform complex tasks such as finding the lowest energy states of spin glasses or proteins. Instead, for such complex problems, natural processes achieve their optima by trial and error, where the extent to which 'errors' are accepted is determined by the system temperature. Optima then follow by slow cooling from a high-temperature, annealed state. Nearly three decades ago, Kirkpatrick, Gelatt and Vecchi [1] suggested that for certain complex computational problems, including for example that of the travelling salesman, it may be more productive to simulate natural annealing and cooling on a computer, using standard Monte Carlo routines, rather than attempting to use classical mathematical algorithms to find solutions. The appeal of simulated annealing is not only that it can be applied to essentially any new optimization problem, but also that it provides a language, namely that of the thermodynamics of complex statistical mechanical systems, for describing why and how optima can be reached. Motivated by this early work, we asked[2] the question of whether quantum rather than thermal fluctuations could be used to relax a system of many interacting degrees of freedom. The reason why this seemed like a good question to ask is illustrated in Fig. 1 – quantum tunnelling makes transitions to regions of phase space possible that might be very difficult to access via classical, thermal barrier hopping.

To carry out meaningful tests of quantum annealing protocols in real system, it is necessary to do the following

1. Find a system with a complex free energy surface where quantum and thermal fluctuations can be tuned independently.
2. Establish that tunneling, rather than simply underlying thermal attempt frequencies, is being tuned.

G. Aeppli and T.F. Rosenbaum: *Experiments on Quantum Annealing*, Lect. Notes Phys. **679**, 159–169 (2005)
www.springerlink.com

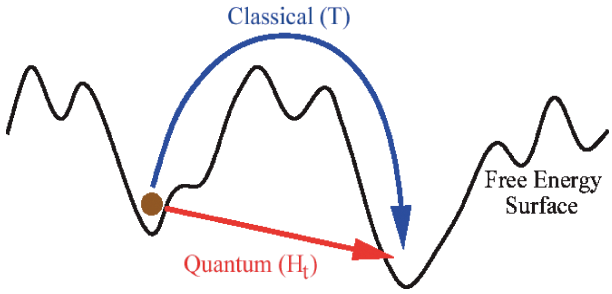

Fig. 1. Schematic objective function (or free energy surface) for an optimization problem as a function of a generalized configurational coordinate. From [2]

3. Try thermal and quantum annealing protocols to see if the results are different.

The rest of this book chapter is devoted to the three components of the experimental programme given above. We do not attempt to summarize the very interesting theoretical developments (from [3, 4, 5, 6, 7] among others) in this area which are described in great detail elsewhere in this volume.

2 System with a Complex Free Energy Surface and Tuneable Quantum Fluctuations

Ising models with random interactions between spins display the full panoply of complexity associated with spin glasses, and indeed hard optimization problems in general. Furthermore, in contrast to tunnelling quantum particles, for which it is somewhat impractical to tune quantum fluctuations in a fixed potential landscape as this would involve tuning their masses, an external transverse field represents a useable tuning parameter. The corresponding Hamiltonian is

$$\mathcal{H} = \sum_{i,j}^{N} J_{ij}\sigma_i^z\sigma_j^z + \Gamma_e \sum_{i}^{N} \sigma_i^x \tag{1}$$

where the σ's are Pauli spin matrices located at lattice sites i and j, the J_{ij}'s are longitudinal couplings, and Γ_e is an effective transverse field, perpendicular to the Ising axis. In the classical limit where $\Gamma_e = 0$, the commutator of $\mathcal{H}$ and σ vanishes, that any spin configuration is dynamically stable as long as there are no couplings to other degrees of freedom, such as phonons. As soon as Γ_e becomes non-zero, the commutator also becomes non-zero, with the result that Heisenberg's equation of motion,

$$\frac{d\sigma_i^z}{dt} = (2\pi h/i)\,[\mathcal{H}, \sigma_i^z] \tag{2}$$

becomes non-trivial.

A material which is a good realization of the transverse field Ising model is the transparent ferromagnet $LiHoF_4$ [8]. Figure 2 shows the underlying face-centered tetragonal crystal structure. The magnetism is derived from the incomplete 4f shells of the Ho^{3+} ions, and the primary interaction between the ions, with their large moments and tightly bound f electrons is the magnetic dipolar coupling. The crystal field imposes a strong Ising anisotropy, causing the spins to prefer an orientation along the crystal z(tetragonal)-axis. It is the fact that the dipolar interaction can be ferro- or antiferromagnetic, depending on the angle between the displacement vector separating the two spins and the Ising axis, that introduces frustration into the spin network upon dilution, and eventually leads [9, 10, 11, 12] to a spin glass rather than a ferromagnetic ground state as the Ho sites are partially populated by Y in the dilution series $LiHo_pY_{1-p}F_4$.

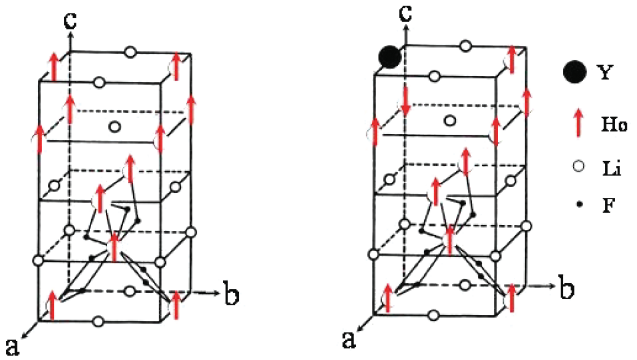

Fig. 2. Pure and Ho-site diluted (with Y) $Li(Ho, Y)F_4$, illustrating the mechanism by which dilution of magnetic Ho by non-magnetic Y first introduces defects into the underlying ferromagnetic state, and eventually cause ferromagnetism to be displaced entirely by spin glass behaviour

Figure 3 represents the phase diagram as a function of the transverse field and temperature [8]. There is a zero-field Curie temperature of $T_C = 1.53\,\mathrm{K}$, which is suppressed to zero at a quantum critical point occurring at $H_t = 50kOe$ (the laboratory field responsible for Γ_e in (1)). The dashed line in the figure is derived from mean field theory which takes account of only the electron spins, while the solid line includes the nuclear spins as well [8, 13]. The deviation of the solid from the dashed line below $T = 0.5\,\mathrm{K}$ is due to the cross-over from nuclear spins behaving as an incoherent bath for the electrons to forming composite nuclear-electronic objects, whose interacting z-components (i.e. along the Ising axis) are more stable with respect to the transverse field than those of the electronic moments by themselves.

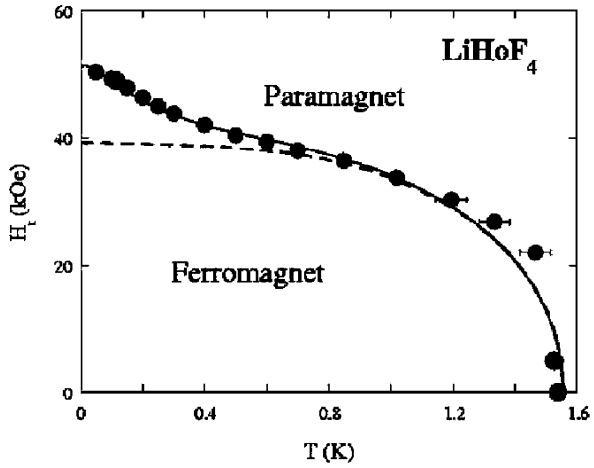

Fig. 3. Phase diagram as a function of laboratory transverse field H_t and temperature T from [8]

A quantum critical point at $T = 0$ is retained upon dilution of Ho with Y to create first disordered ferromagnets and then the spin glasses [11, 12], although the overall shape of the phase boundary is considerably altered, due probably in some measure to the fact that there is no longer an extended incoherent nuclear spin regime coexisting with electron spin ordering. Figure 4 shows the important phase diagram [2] for our present purposes, namely that for the disordered ferromagnet $LiHo_{0.44}Y_{0.56}F_4$. The zero-field Curie temperature is suppressed to a value given by the expected (according to mean field theory) occupancy fraction $p = 0.44$ of the rare earth sites multiplied by $T_C(p = 1) = 1.53\,\mathrm{K}$. The $T = 0$ quantum critical field H_C is also reduced substantially.

However, simple scaling of H_C with p at $T = 0$ is not expected to work because of the influence of the nuclear spin interactions as well as the fact that the effective transverse field Γ_e does not scale linearly with the external transverse field, although it can be calculated with high accuracy from the known crystal field Hamiltonian such that for low laboratory fields H_t, $\Gamma_e \sim H_t^2$ [2]. Figure 5 demonstrates [14] that even though there are long time relaxation phenomena associated with the glassy domain wall state labelled G in Fig. 4, the system at low temperatures displays conventional hysteresis as a function of small external longitudinal fields. What is very significant and interesting, though, is that the extent to which the loops are closed, magnified in the difference curves of Fig. 5b, is larger for the higher transverse fields closer to the quantum critical point. This means that the transverse field eases the motion of the walls over pinning centres, something we address more quantitatively in the next section.

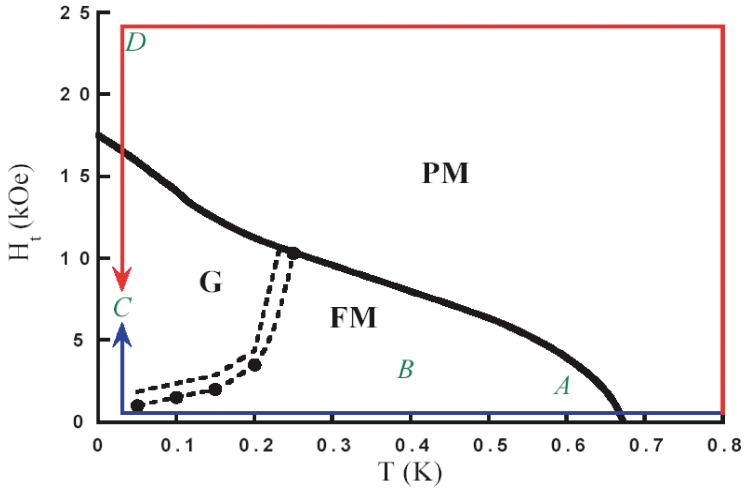

Fig. 4. Phase diagram for $LiHo_{0.44}Y_{0.56}F_4$ as a function of temperature T and an external (laboratory) transverse field H_t. The material behaves like a conventional ferromagnet in the region labelled FM, and shows slow relaxation in the glassy domain wall state labelled G. The lighter and the darker trajectories and points A, B, C and D refer to the data in Fig. 9 below. (From 2)

3 Demonstration of Domain Wall Tunnelling as the Dominant Mechanism for Low Temperature Magnetic Relaxation

We have measured the relaxation spectrum for the ordered state in $LiHo_{0.44}Y_{0.56}F_4$ using ac susceptometry. Figure 6 shows data obtained for a variety of fields for low temperature. From the semi-logarithmic plot, it is apparent that $\chi \sim \ln f$ over a range extending through several decades of f for the highest transverse field, $H_t = 9.6\,\mathrm{kG}$. The $\ln f$ dependence terminates at an upper cutoff f_o which we can use as a proxy for the entire dynamics of this ferromagnetic domain wall glass. One thing that is immediately clear is that raising H_t by less than a factor of two from 5.6 to 9.6 kG increases f_o by nearly two orders of magnitude, suggesting a very dramatic quantum-induced speedup of the spin dynamics. To see whether this speedup is associated with genuine quantum tunnelling or due to increase in the attempt frequency for thermal barrier hopping, we have made the Arrhenius plots of Fig. 7 which shows a clear cross-over from classical thermally activated behaviour at high T (low $1/T$) to a T-independent rate at low T. The latter is of course precisely what is expected for a quantum process, and indeed, its dependence on H_t and T can be modelled by an expression including the incoherent addition of thermal and quantum processes,

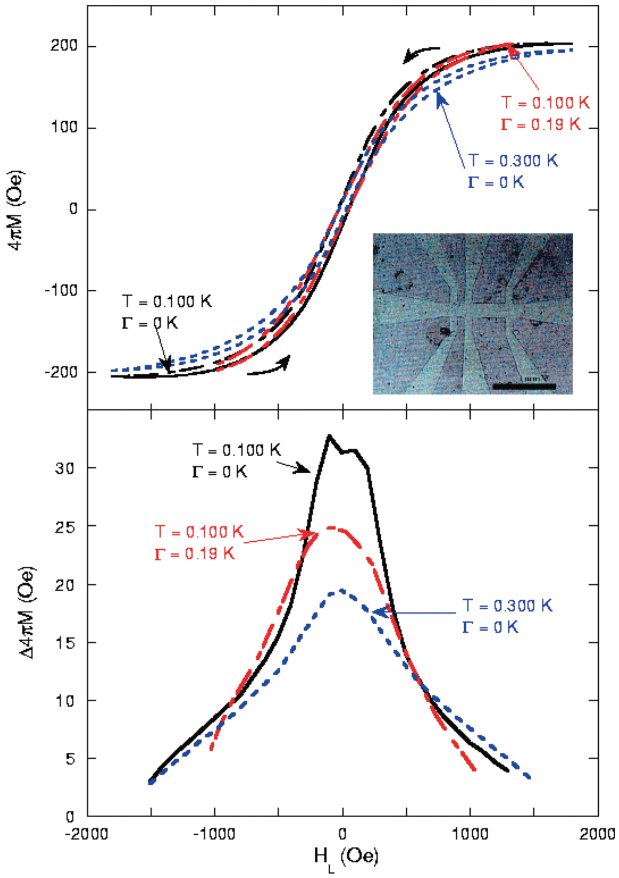

Fig. 5. Frame (**a**) shows hysteresis loops for $LiHo_{0.44}Y_{0.56}F_4$ (observed using InAs Hall bars depicted in inset) as a function of longitudinal fields for fixed temperatures and transverse fields as indicated. The lower frame (**b**) shows the difference curves between upward and downward longitudinal field sweeps, revealing that the degree of openness (amplitude of difference) can be reduced by either raising T for fixed Γ or raising Γ at fixed low T. (From 14)

$$f = F_0 \left[\exp\left(-\Delta_\Gamma / T\right) + \exp\left(-2w_0 \sqrt{\frac{2m_\Gamma}{\hbar^2} \Delta_\Gamma} \right) \right] .$$

The observation of the Arrhenius law at high temperatures allows the barrier height Δ_Γ to be fixed, while the barrier width w_0 can be set equal to the mean distance between Ho ions. Finally, the underlying attempt frequency F_0, due to an underlying (quantum) bath, is assumed to be the same for the Arrhenius and WKB processes. The low temperature speedup is then entirely accounted for the effective mass m_Γ of the tunnelling domain walls, which we can extract from the data in absolute units. The solid lines on the left

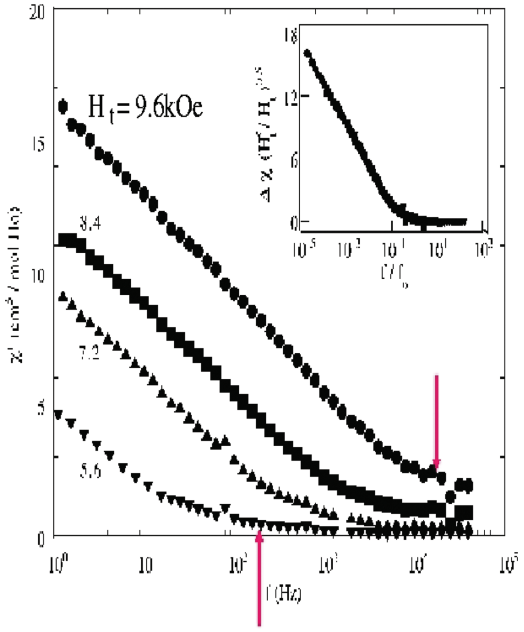

Fig. 6. Frequency (f)-dependence of the real part of the magnetic susceptibility for transverse fields indicated. Inset shows the magnetic susceptibility above the high-frequency residual, scaled by the square root of the critical field to the applied field, to be a universal function of the ratio of the measuring frequency to the cutoff frequency. (From 2)

hand of Fig. 7 correspond to the very simple model as just described, and Fig. 8 shows how m_Γ varies with the effective transverse field Γ_e. As Γ_e is increased, the walls become lighter, exactly as expected based on the theory of the transverse field Ising model. It thus seems that the highly ramified domain wall state in $LiHo_{0.44}Y_{0.56}F_4$ relaxes via quantum tunnelling of wall segments, which behave like simple quantum particles with tuneable masses! We are able to obtain a quantitative estimate of the area of the tunnelling segments simply by dividing the observed masses by those calculated for a one-dimensional model with the same average ferromagnetic coupling, and deduce that the tunnelling process involves a correlated flip of approximately 10 Ho moments.

4 Comparing Quantum and Thermal 'Computations'

We are now in the position to check whether quantum annealing is an interesting option for computation. The problem we pose is the optimal (lowest energy) placement of domain walls in the disordered ferromagnet $LiHo_{0.44}Y_{0.56}F_4$. The program for the computation consists of the schedule

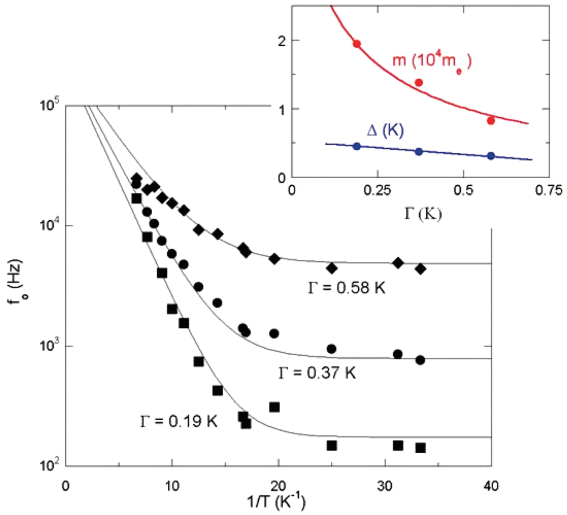

Fig. 7. The main frame shows how the cutoff frequency f_o for the ln f behaviour of χ depends on T and effective transverse field Γ_e, expressed in Kelvin and calculated from the known crystal field. The smaller right hand frame gives the effective domain wall mass and pinning barrier height extracted from the analysis described in text. (From 14)

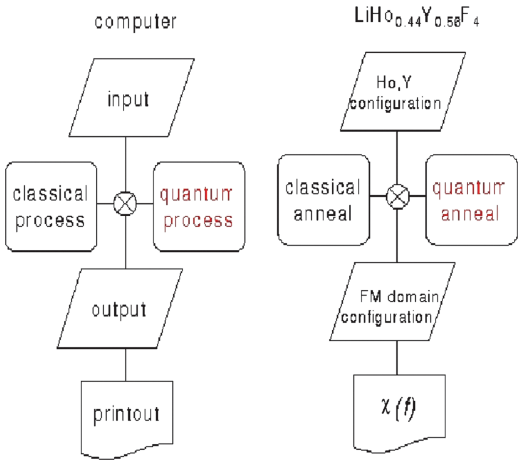

Fig. 8. Analogy between quantum computation and quantum/thermal annealing experiments on $LiHo_{0.44}Y_{0.56}F_4$

for thermal and quantum cooling steps, as illustrated by Fig. 8 which refers to the phase space trajectories in Fig. 3. For quantum and thermal computations, we enter the ordered phase by reducing H_t at fixed T or reducing T at fixed H_t, respectively. The read-out of the computation's outcome, i.e. the final state of the sample, is the bulk f-dependent susceptibility, and is displayed for the various points in phase space also marked in Fig. 3. Figure 9 shows the experimental results. We note that as one might hope for, what occurs above the quantum critical point at low T is independent of sample history. On the other hand, there are progressively more dramatic differences between quantum and thermal programs for phase space points in the ordered state. Most dramatic is the appearance of much faster(by a decade and half) dynamics for quantum rather than thermal cooling. What this means is that the state which is reached via the quantum 'computation' has landed the system in a different part of the free energy landscape, namely one where there is intrinsically more ability to tunnel in and out of minima – i.e. where pinning potentials are weaker. While we cannot make a rigorous statement that the energy of this state is lower because we have not examined heat release, the

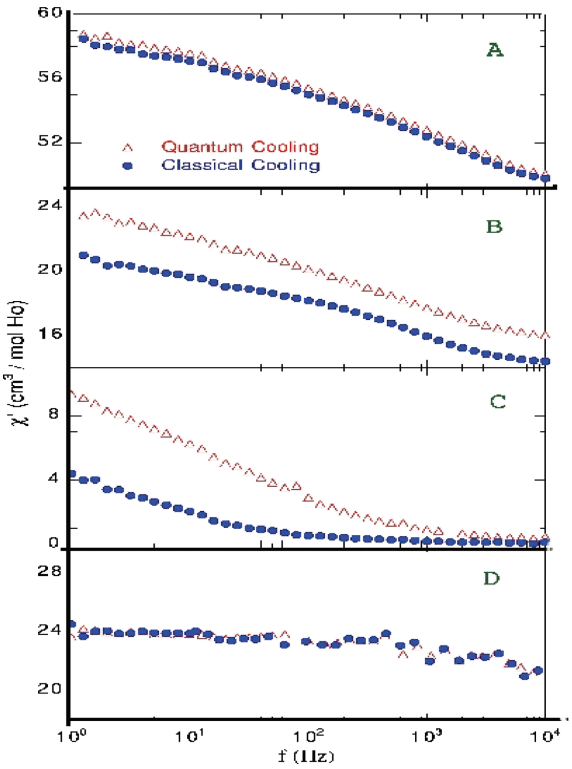

Fig. 9. Comparison between $\chi'(f)$ for thermal and quantum routes to states at conditions labelled by letters A-D in Fig. 3. (From 2)

odds are good that its entropy is higher. The other thing that can be said is that the quantum 'computation' reveals the logarithmic nature of $\chi'(f)$ much more clearly than the classical route, and so gives us much greater confidence in establishing the marginally stable nature of the ferromagnetic domain wall state of $LiHo_{0.44}Y_{0.56}F_4$.

5 Conclusions

We have tested the hypothesis of whether quantum annealing can lead to a different outcome in a highly complex optimization problem, namely that of domain wall placement in a disordered ferromagnet, than thermal annealing. The hypothesis was indeed verified by experiments, which now raises interesting questions for the future. Arguably the most fascinating concerns the relation of our results to conventional quantum computation and concepts such as entanglement [15]. We would argue, as sketched in Fig. 10, that quantum annealing actually entails many genuine quantum computations on scales of order the coherence volumes for the underlying domain wall tunnelling processes, but harnessed in parallel in an incoherent fashion over our $>$ mm scale sample to reveal something interesting about its preferred state.

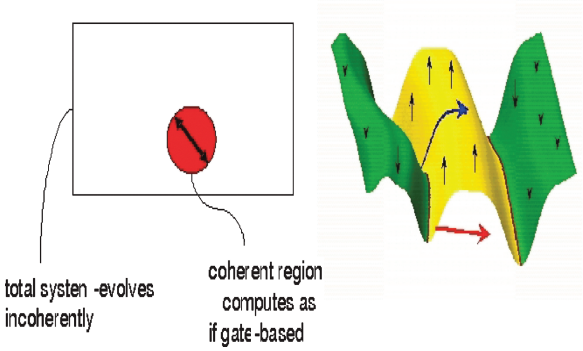

Fig. 10. Schematic of how quantum annealing can be considered an incoherent parallelization of smaller coherent quantum computations, exemplified by the tunnelling of domain walls illustrated at right (adapted from [14])

Acknowledgements

Work was supported by the NSF Materials Research Science and Engineering Center Grant No. DMR-0213745, a Wolfson Royal Society Research Merit Award and the Basic Technologies Programme of the UK Research Councils.

References

1. S. Kirkpatrick, C.D. Gelatt, Jr., M.P. Vecchi, Science **220**, 671 (1983). 159
2. J. Brooke, D. Bitko, T.F. Rosenbaum, G. Aeppli, Science **284**, 779 (1999). 159, 160, 162
3. G. Santoro, R. Martoňák, E. Tosatti, R. Car, Science **295**, 2427 (2002). 160
4. R. Martoňák, G. Santoro and E. Tosatti, arXiv:cond-mat/0402330(2004). 160
5. T. Kadowaki, H. Nishimori, Phys. Rev. E **58**, 5355 (1998). 160
6. Y. H. Lee and B. J. Berne, J. Phys. Chem A **104**, 86(2000). 160
7. A. Das, B. K. Chakrabarti, R. B. Stinchcombe, Phys. Rev. E **72**, 026701 (2005). 160
8. D. Bitko, T. F. Rosenbaum and G. Aeppli, Phys. Rev. Lett. **77** 940 (1996). 161, 162
9. D. H. Reich, T. F. Rosenbaum, G. Aeppli and H. J. Guggenheim, Phys. Rev. B **34** 4956 (1986). 161
10. D. H. Reich, B. Ellman, I. Yang, T. Rosenbaum, G. Aeppli and D. P. Belanger, Phys. Rev. B **42**, 4631 (1990). 161
11. W. Wu, B. Ellman, T. F. Rosenbaum, G. Aeppli and D. H. Reich, Phys. Rev. Lett. **67** 2076 (1991). 161, 162
12. W. Wu, D. Bitko, T. F. Rosenbaum and G. Aeppli, Phys. Rev. Lett **71** 1919 (1993). 161, 162
13. H. M. Ronnow, R. Parthasarathy, J. Jensen, G. Aeppli, T. F. Rosenbaum and D. F. McMorrow, Science **308**, 392 (2005). 161
14. J. Brooke, T. F. Rosenbaum and G. Aeppli, Nature **413** 610 (2001). 162
15. S. Ghosh, T. F. Rosenbaum, G. Aeppli and S. N. Coppersmith, Nature **425** 48 (2003). 168

Deterministic and Stochastic Quantum Annealing Approaches

Demian Battaglia[1], Lorenzo Stella[1], Osvaldo Zagordi[1], Giuseppe E. Santoro[1,2] and Erio Tosatti[1,2]

[1] SISSA [†] INFM Democritos, Via Beirut 2-4, Trieste, Italy
[2] ICTP, Trieste, Italy.
battagli@sissa.it

1 Introduction

The idea of quantum annealing (QA) is a late offspring of the celebrated *simulated thermal annealing* by Kirkpatrick et al. [1]. In simulated annealing, the problem of minimizing a certain cost (or energy) function in a large configuration space is tackled by the introduction of a fictitious temperature, which is slowly lowered in the course of a Monte Carlo or Molecular Dynamics simulation [1]. This device allows an exploration of the configuration space of the problem at hand, effectively avoiding trapping at unfavorable local minima through thermal hopping above energy barriers. It makes for a very robust and effective minimization tool, often much more effective than standard, gradient-based, minimization methods.

An elegant and fascinating alternative to such a classical simulated annealing (CA) consists in helping the system escape the local minima through *quantum mechanics*, by tunneling through the barriers rather than thermally overcoming them [2, 3]. Experimental evidence in disordered Ising ferromagnets subject to transverse magnetic fields showed that this strategy is not only feasible but presumably winning in certain cases [4]. These experimental results were confirmed by a Path-Integral Monte Carlo (PIMC) study of an Ising glass model, were the crucial role played by Landau-Zener tunneling events was also pointed out [5].

In essence, in quantum annealing one supplements the classical energy function – let us denote it by H_{cl} – with a suitable *time-dependent* quantum kinetic term, $H_{kin}(t)$, which is initially very large, for $t \leq 0$, then gradually reduced to zero in a time τ. For the Ising glass case, for instance, $H_{cl} =$

[†] This project was sponsored by MIUR through FIRB RBAU017S8R004, FIRB RBAU01LX5H, COFIN2003 and COFIN2004, and by INFM ("Iniziativa trasversale calcolo parallelo"). Early collaboration with Dr. Roman Martoňák and Prof. Roberto Car are gratefully acknowledged.

D. Battaglia et al.: *Deterministic and Stochastic Quantum Annealing Approaches*, Lect. Notes Phys. **679**, 171–206 (2005)
www.springerlink.com

$-\sum_{\langle ij \rangle} J_{ij}\sigma_i^z\sigma_j^z$ represents an Edward-Anderson disordered Ising model, while a very natural choice for H_{kin}, suggested by the experiment [4], is given by the transverse field term $H_{kin}(t) = -\Gamma(t)\sum_i \sigma_i^x$. At zero temperature, the quantum state of the system $|\Psi(t)\rangle$, initially prepared in the fully quantum ground state $|\Psi_0\rangle$ of $H(t=0) = H_{cl} + H_{kin}(0)$, evolves according to the Scrödinger equation

$$i\hbar\frac{d}{dt}|\Psi(t)\rangle = [H_{cl} + H_{kin}(t)]|\Psi(t)\rangle \ , \tag{1}$$

to reach a final state $|\Psi(t=\tau)\rangle$. A crucial basic question is then how the residual energy $\epsilon_{res}(\tau) = E_{fin}(\tau) - E_{opt}$, decreases for increasing τ. Here E_{opt} is the absolute minimum of H_{cl}, and $E_{fin}(\tau)$ is the average energy attained by the system after evolving for a time τ, so that

$$\epsilon_{res}(\tau) = E_{fin}(\tau) - E_{opt} = \frac{\langle\Psi(\tau)|(H_{cl} - E_{opt})|\Psi(\tau)\rangle}{\langle\Psi(\tau)|\Psi(\tau)\rangle} \ . \tag{2}$$

Generally speaking, this question has to do with the *adiabaticity* of the quantum evolution, i.e., whether the system is able, for sufficiently slow annealing (sufficiently long τ), to follow the instantaneous ground state of $H(t) = H_{cl} + H_{kin}(t)$, for a judiciously chosen $H_{kin}(t)$. (The fictitious kinetic energy $H_{kin}(t)$ can be chosen quite freely, with the only requirement of being reasonably easy to implement.) For this reason, this approach has also been called Quantum Adiabatic Evolution [6].

At the level of practical implementations on an ordinary (classical) computer, the task of following the time-dependent Schrödinger evolution in (1) is clearly feasible only for toy models with a sufficiently manageable Hilbert space [3, 6, 7]. Actual optimization problems of practical interest usually involve astronomically large Hilbert spaces, a fact that calls for alternative Quantum Monte Carlo (QMC) approaches. These QMC techniques, in turn, are usually suitable to using *imaginary time* quantum evolution, where the $i\hbar\partial_t$ in (1) is replaced by $-\hbar\partial_t$. One of the questions we have recently addressed, in the context of simplified problems [7], is whether an imaginary-time Schrödinger evolution changes the quantum adiabatic evolution approach in any essential way. The answer to this question appears to be that, as far as annealing is concerned, imaginary-time is essentially equivalent to real-time, and, as a matter of fact, can be quantitatively better [7].

A number of recent studies have applied Path-Integral Monte Carlo (PIMC) strategies to QA. A certain success has been obtained in a number of optimization problems, such as the folding of off-lattice polymer models [8, 9], the random Ising model ground state problem [5, 10] (see Sect. 4.2), and the Traveling Salesman Problem [11] (see Sect. 4.2). On the other hand, for the interesting case of Boolean Satisfiability – more precisely, a prototypical NP-complete problem such as 3-SAT – a recent study of our group shows that PIMC annealing performs definitely *worse* than simple CA [12] (see Sect. 4.2).

In view of these results, it is fair to stress that it is a priori not obvious or guaranteed that a QA approach should do better than, for instance, CA, on a given problem. Evidently, the comparative performance of QA and CA depends in detail on the energy landscape of the problem at hand, in particular on the nature and type of barriers separating the different local minima, a problem about which very little is known in many practical interesting cases [13]. That in turn depends crucially on the type and effectiveness of the kinetic energy chosen. Unfortunately, there is still no reliable theory predicting the performance of a QA algorithm, in particular correlating it with the energy landscape of the given optimization problem. Nevertheless, it is important to stress that QA is not a universal key to hard NP problems: indeed, one can think of trivial optimization problems, like the random Ising ferromagnet in one-dimension [7], where QA (as well as CA) will be by necessity slow.

In order to gain understanding on these problems, we have moved, more recently, one step back and concentrated attention on the simplest textbook problems where the energy landscape is well under control: essentially, one-dimensional potentials, starting from a double-well potential, the simplest form of barrier. On these well controlled landscapes we have carried out a detailed and exhaustive comparison between quantum adiabatic Schrödinger evolution, both in real and in imaginary time, and its classical deterministic counterpart, i.e., Fokker-Planck evolution [7]. This work will be illustrated in Sect. 2.1. On the same double well-potential, we have also studied [14] the performance of different stochastic approaches, both classical Monte Carlo and Path Integral Monte Carlo. Some of this work, which turns out to be quite instructive, is briefly presented in Sect. 4.4.

The rest of the Chapter is organized as follows: Sect. 2 illustrates the deterministic annealing approaches applied to toy problems, essentially the minimization of a function of a continuous coordinate. Section 3 discusses the crucial role played by disorder and the issue of Landau-Zener tunneling in QA. Section 4 introduces the Path-Integral Monte Carlo techniques, and illustrates some of the recent applications, notably on the random Ising model, on the Traveling Salesman Problem, and on Boolean Satisfiability problems. Section 5 discusses alternative approaches to optimization, including a discussion of Green's Function Monte Carlo QA, which seems to be a promising tool for future QA studies. Section 6, finally, contains a brief summary of the main points, and some concluding remarks.

2 Deterministic Approaches on the Continuum

Conceptually, one of the simplest problems to illustrate is that of finding the global minimum of an ordinary function of several continuum variables with many minima. Suppose the classical Hamiltonian H_{cl} mentioned in the introduction is just a potential energy $V(\mathbf{x})$, (with $\mathbf{x}$ a Cartesian vector of arbitrary dimension), of which we need to determine the absolute minimum

($\mathbf{x}_{opt}$, $E_{opt} = V(\mathbf{x}_{opt})$). Assume, generally, a situation in which a steepest-descent approach, i.e., the strategy of following the gradient of V, would lead to trapping into one of the many local minima of V, and would thus not work. Classically, as an obvious generalization of a steepest-descent approach, one could imagine of performing a stochastic (Markov) dynamics in x-space according to a Langevin's equation:

$$\dot{\mathbf{x}} = -\frac{1}{\eta(T)}\boldsymbol{\nabla} V(\mathbf{x}) + \xi(t) \; , \tag{3}$$

where the strength of the noise term ξ is controlled by the squared correlations $\overline{\xi_i(t)\xi_j(t')} = 2D(T)\delta_{ij}\delta(t-t')$, with $\bar{\xi} = 0$. Both $D(T)$ and $\eta(T)$ – with dimensions of a diffusion constant and of a friction coefficient and related, respectively, to fluctuations and dissipation in the system – are temperature dependent quantities which can be chosen, for the present optimization purpose, with a certain freedom. The only obvious constraint is in fact that the correct thermodynamical averages would be recovered from the Langevin dynamics only if $\eta(T)D(T) = k_B T$, an equality known as Einstein's relation [15]. Physically, $D(T)$ should be an increasing function of T, so as to lead to increasing random forces as T increases, with $D(T=0) = 0$, since noise is turned off at $T = 0$. Classical annealing can in principle be performed through this Langevin dynamics, by slowly decreasing the temperature $T(t)$ as a function of time, from some initially large value T_0 down to zero. Instead of working with the Langevin equation – a stochastic differential equation – one might equivalently address the problem by studying the probability density $P(\mathbf{x}, t)$ of finding a particle at position $\mathbf{x}$ at time t. The probability density is well known to obey a *deterministic* time-evolution equation given by the *Fokker-Planck* (FP) equation [15]:

$$\frac{\partial}{\partial t}P(\mathbf{x},t) \; = \; \frac{1}{\eta(T)}\,\mathrm{div}\,(P\boldsymbol{\nabla}V) \; + \; D(T)\nabla^2 P \; . \tag{4}$$

Here, the second term in the right-hand side represents the well known *diffusion term*, proportional to the diffusion coefficient $D(T)$, whereas the first term represents the effect of the *drift* force $-\boldsymbol{\nabla}V$, inversely proportional to the friction coefficient $\eta(T) = k_B T/D(T)$ [15]. Annealing can now be performed by keeping the system for a long enough equilibration time at a large temperature T_0, and then gradually decreasing T to zero as a function of time, $T(t)$, in a given annealing time τ. We can model this by assuming $T(t) = T_0\, f(t/\tau)$, where $f(y)$ is some assigned monotonically decreasing function for $y \in [0,1]$, with $f(y \leq 0) = 1$ and $f(1) = 0$. In this manner the diffusion constant D in (4) becomes a time-dependent quantity, $D_t = D(T(t))$. The FP equation should then be solved with an initial condition given by the equilibrium Boltzmann distribution at temperature $T(t=0) = T_0$, i.e., $P(\mathbf{x}, t=0) = e^{-V(\mathbf{x})/k_B T_0}$. The final average potential energy after annealing, in excess of the true minimum value, will then be simply given by:

$$\epsilon_{res}(\tau) = \int d\mathbf{x}\, V(\mathbf{x})\, P(\mathbf{x}, t=\tau) \;-\; E_{opt} \geq 0 \;, \tag{5}$$

where E_{opt} is the actual absolute minimum of the potential V.

In a completely analogous manner, we can conceive using Schrödinger's equation to perform a deterministic quantum annealing (QA) evolution of the system, by introducing quantum fluctuations through a standard kinetic term $H_{kin}(t) = -(\hbar^2/2m_t)\nabla^2$, with a fictitious time-dependent mass m_t. We are therefore led to studying the time-dependent Schrödinger problem:

$$\xi\hbar\frac{\partial}{\partial t}\psi(\mathbf{x}, t) = \left[-\Gamma(t)\nabla^2 + V(\mathbf{x})\right]\psi(\mathbf{x}, t) \;, \tag{6}$$

where $\xi = i$ for a *real-time* (RT) evolution, while $\xi = -1$ for an *imaginary-time* (IT) evolution. Here $\Gamma(t) = \hbar^2/2m_t$ will be our annealing parameter, playing the role that the temperature $T(t)$ had in classical annealing. Once again we may take $\Gamma(t)$ varying from some large value Γ_0 at $t \leq 0$ – corresponding to a small mass of the particle, hence to large quantum fluctuations – down to $\Gamma(t = \tau) = 0$, corresponding to a particle of infinite mass, hence without quantum fluctuations. Again, we can model this with $\Gamma(t) = \Gamma_0\, f(t/\tau)$, where f is a preassigned monotonically decreasing function. A convenient initial condition here will be $\psi(\mathbf{x}, t = 0) = \psi_0(\mathbf{x})$, where $\psi_0(\mathbf{x})$ is the *ground state* of the system at $t \leq 0$, corresponding to the large value $\Gamma(t) = \Gamma_0$ and hence to large quantum fluctuations. For such a large Γ, the ground state will be separated by a large energy gap from all excited states. The residual energy after annealing will be similarly given by (5), where now, however, the probability $P(\mathbf{x}, t = \tau)$ should be interpreted, quantum mechanically, as:

$$P(\mathbf{x}, t) = \frac{|\psi(\mathbf{x}, t)|^2}{\int d\mathbf{x}'\, |\psi(\mathbf{x}', t)|^2} \;.$$

In general, the residual energy will be different for a RT or an IT Schrödinger evolution. We will comment further on RT versus IT Schrödinger evolution later on.

In the remaining part of this section, we will present some of the results obtained along the previous lines on simple one-dimensional potential [7], starting with the simplest example of a problem with two minima separated by a barrier.

2.1 The Simplest Barrier: A Double-Well Potential

Consider, as a potential $V(\mathbf{x})$ to be optimized, a slightly generalized double-well potential in one-dimension

$$V_{\text{asym}}(x) = \begin{cases} V_0 \frac{(x^2 - a_+^2)^2}{a_+^4} + \delta x & \text{for } x \geq 0 \\ V_0 \frac{(x^2 - a_-^2)^2}{a_-^4} + \delta x & \text{for } x < 0 \end{cases} \;, \tag{7}$$

with, in general, $a_+ \neq a_-$, both positive, V_0, and δ real constants. (The discontinuity in the second derivative at the origin is of no consequence in our discussion.) In absence of the linear term ($\delta = 0$), the potential has two degenerate minima located at $x_- = -a_-$ and $x_+ = a_+$, separated by a barrier of height V_0. When a small linear term $\delta > 0$ is introduced , with $\delta a_\pm \ll V_0$, the two degenerate minima are split by a quantity $\Delta_V \approx \delta(a_+ + a_-)$, the minimum at $x \approx -a_-$ becoming slightly favored. For reasons that will be clear in a moment, it is useful to consider the situation, which we will refer to as "asymmetric double-well", in which the two wells possess definitely distinct *curvatures* at the minimum (i.e, their widths differ), realized by taking $a_+ \neq a_-$. (To lowest order in δ, we have: $V''(x = x_\pm) = 8V_0/a_\pm^2$.) In particular, we shall examine the case in which the metastable "valley" at x_+ is "wider" than the absolute minimum at x_-, which is realized by chosing $a_+ > a_-$. This will have a rather important effect on the quantum evolution, since, as we shall see, for intermediate values of the mass of the particle, the wavefunction of the system will be predominantly located on the metastable minimum. Obviously, if we set $a_+ = a_- = a$, and $\delta = 0$ we recover the standard double-well potential.

We now present the results obtained by the annealing schemes introduced in Sect. 2 above. The Fokker-Planck and the Schrödinger equation (both in RT and in IT) were integrated numerically using a fourth-order adaptive Runge-Kutta method, after discretizing the x variable in a sufficiently fine real space grid [7]. For the FP classical annealing, the results shown are obtained with a linear temperature schedule, $T(t) = T_0(1 - t/\tau)$, and a diffusion coefficient simply proportional to $T(t)$, $D_t = D_0(1 - t/\tau)$. (Consequently, the friction coefficient is kept constant in t, $\eta_t = k_B T(t)/D_t = k_B T_0/D_0$.) Similarly, for the Schrödinger quantum annealing we show results obtained with a coefficient of the Laplacian $\Gamma(t)$ vanishing linearly in a time τ, $\Gamma(t) = \Gamma_0(1 - t/\tau)$.

Figure 1 shows the results obtained for the final annealed probability distribution $P(x, t = \tau)$ at different values of τ, for both the Fokker-Planck (CA, panel (a)) and the Scrödinger imaginary-time case (IT, panel (b)), for an "asymmetric" double-well potential $V_{\text{asym}}(x)$, with $V_0 = 1$ (our unit of energy), $a_+ = 1.25, a_- = 0.75$, $\delta = 0.1$. Figure 1(c) summarizes the results obtained for the residual energy $\epsilon_{res}(\tau)$ in 5.

We notice immediately that QA wins over CA for large enough value of τ. The RT-QA, which behaves as its IT counterpart for a symmetric double-well ($a_+ = a_-$, see [7]), shows a slightly different behavior from IT-QA in the present asymmetric case (see below for comments). We discuss first the CA data (panel (a) and (c) of Figs. 1). Starting from an initially broad Boltzmann distribution at a high $T = T_0 = V_0$, $P(x, t = 0)$ (solid line), the system quickly sharpens the distribution $P(x, t)$ into two well-defined and quite narrow peaks located around the two minima $x_\pm$ of the potential. This agrees very well with what a CA for an harmonic potential would do [7]. If we denote by $p_\pm$ the integral of each of the two narrow peaks, with $p_- + p_+ = 1$, it is clear that the problem has effectively been reduced to a *discrete* two-level system

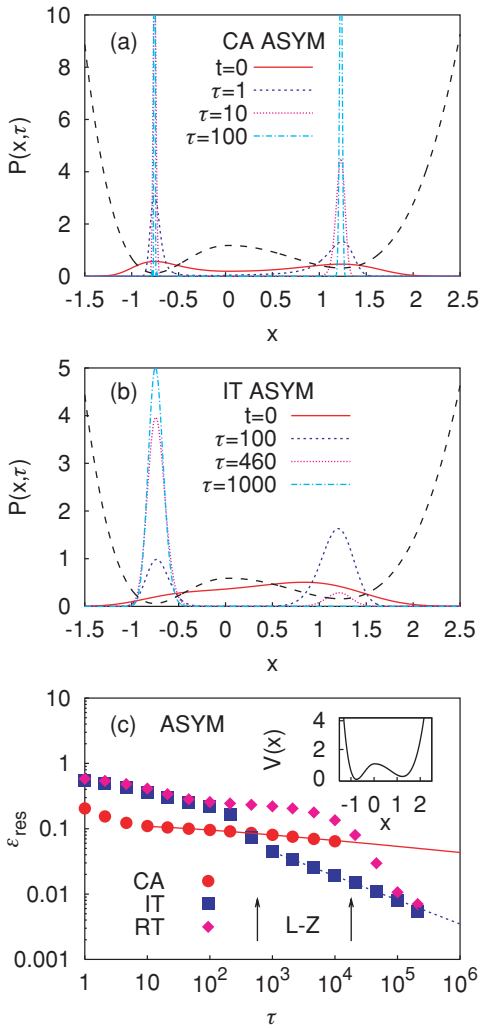

Fig. 1. (**a**,**b**): The annealed final probability distribution $P(x, t = \tau)$ at different values of the annealing time τ, for both the Fokker-Planck classical annealing (CA, panel (a)), and the Imaginary Time Schrödinger quantum annealing (IT-QA, panel (b)). (**c**) Final residual energy $\epsilon_{res}(\tau)$ versus annealing time τ for quantum annealing in Real Time (RT) and Imaginary Time (IT) compared to the Fokker-Planck classical annealing (CA). The solid line in (c) is a fit of the CA data (see text). The double well potential (dashed line in (a,b), inset of (c)) is here given by (7) with $a_+ = 1.25, a_- = 0.75$

problem. The time evolution of $p_{\pm}$, therefore, obeys a discrete Master equation which involves the thermal promotion of particles over the barrier V_0, of the form presented and discussed by Huse and Fisher in [16], where they show that, apart from logarithmic corrections, the leading behavior of the residual energy is of the form $\epsilon_{res} \sim \tau^{-\Delta_V/B}$, with the power-law exponent controlled by the ratio Δ_V/B between the energy splitting of the two minima Δ_V and the barrier $B = V_0 - V(x_+)$. As shown in Fig. 1(c) (solid lines through solid circles), the asymptotic behavior anticipated by Huse and Fisher fits nicely our CA residual energy data (solid circles), as long as the logarithmic corrections are accounted for in the fitting procedure [7]. Obviously, we can make the exponent as small as we wish by reducing the linear term coefficient δ, and hence the ratio Δ_V/B, leading to an exceedingly slow classical annealing.

The behavior of the QA evolution is remarkably different. Observe, as a first point, that the final annealed wavefunctions only slowly narrows around the minimum of the potential, although the residual energy asymptotics of QA is clearly winning. The asymptotic behavior of the QA residual energy is $\epsilon_{res}(\tau) \propto \tau^{-1/3}$, indicated by the dashed line in Fig. 1(c): this rather strange exponent turns out to be the appropriate one for the Schrödinger annealing with a linear schedule $\Gamma(t)$ within an harmonic potential (the lower minimum valley, see [7] for details). Going back to Fig. 1(b), the initial wavefunction squared $|\psi(x, t = 0)|^2$ corresponds to a quite small mass (a large $\Gamma_0 = 0.5$), and is broad and delocalized over both minima (solid line). As we start annealing, and if the annealing time τ is relatively short – that is, if $\tau < \tau_c$, with a characteristic time τ_c which depends on which kind of annealing, RT or IT, we perform – the final wavefunction becomes mostly concentrated on the *wrong minimum*, roughly corresponding to the ground state with a still relatively large $\Gamma_1 < \Gamma_0$ (see also Fig. 2 and accompaning discussion). The larger width of the wrong valley is crucial, giving a smaller quantum kinetic energy contribution, so that tunneling to the other (deeper) minimum does not yet occur. By increasing τ, there is a crossover: the system finally recognizes the presence of the other minimum, and effectively tunnels into it, with a residual energy that, as previously mentioned, decays asymptotically as $\epsilon_{res}(\tau) \propto \tau^{-1/3}$ (dashed line in Fig. 1(c)). There is a characteristic annealing time τ_c – different in the two Scrödinger cases, RT and IT – above which tunneling occurs, and this shows up as the clear crossover in the residual energy behavior of both IT and RT, shown in Fig. 1(c).

These findings can be quite easily rationalized by looking at the *instantaneous* (adiabatic) eigenvalues and eigenstates of the associated time-independent Schrödinger problem, which we show in Fig. 2(a,b). Looking at the instantaneous eigenvalues shown in Fig. 2(a) we note a clear avoided-crossing occurring at $\Gamma = \Gamma_{LZ} \approx 0.038$, corresponding to a resonance condition between the states in the two different valleys of the potential. For $\Gamma > \Gamma_{LZ}$ the ground state wavefunction is predominantly concentrated in the wider but metastable valley, while for $\Gamma < \Gamma_{LZ}$ it is mostly concentrated on the deeper and narrower global minimum valley. In the full time-dependent RT

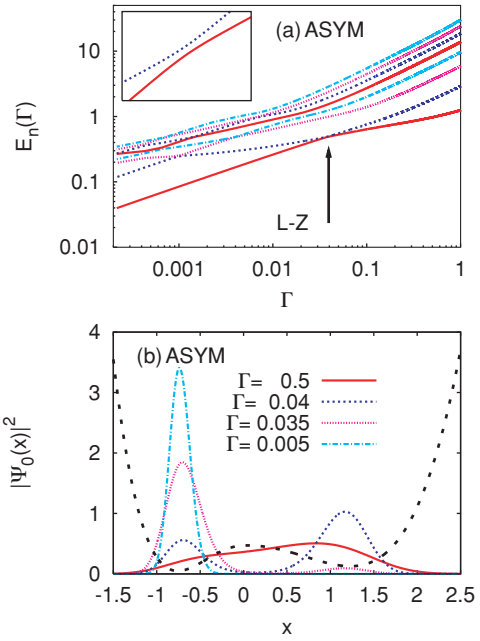

Fig. 2. Instantaneous eigenvalues (**a**) and ground state wavefunctions (**b**) of the Schrödinger problem $H\psi = E\psi$ for different values of Γ, for the potential in (7) with $a_+ = 1.25, a_- = 0.75$. Notice the clear Landau-Zener avoided crossing in (a), indicated by the arrow and magnified in the inset

evolution, transfer to the lower valley is a Landau-Zener problem [17, 18]: the characteristic time τ_c for the tunneling event is given by $\tau_{LZ} = \hbar\alpha\Gamma_0/2\pi\Delta^2$, where α is the relative slope of of the two crossing branches as a function of Γ, 2Δ is the gap at the avoided-crossing point, and Γ_0 is the initial value of the annealing parameter. (For the case shown in Fig. 2, we have $2\Delta = 0.0062$, $\alpha = 2.3$, hence $\tau_{LZ} \approx 18980$, see rightmost arrow in Fig. 1(c).) The Landau-Zener probability of jumping, during the evolution, from the ground state onto the "wrong" (excited) state upon fast approaching of the avoided level crossing is $P_{ex} = e^{-\tau/\tau_{LZ}}$, so that adiabaticity applies only if the annealing is slow enough, $\tau > \tau_{LZ}$. Notice that the gap 2Δ, and hence the probability of following adiabatically the ground state, can be made arbitrarily small by increasing the asymmetry of the two well, i.e., by making $a_+ \gg a_-$. The IT characteristic time is smaller, in the present case, than the RT one. This point is discussed in some detail in [7]. In a nutshell, the reason for this is the following. After the system has jumped into the excited state, which occurs with a probability $P_{ex} = e^{-\tau/\tau_{LZ}}$, the residual IT evolution will filter out the excited state; this relaxation towards the ground state is controlled by the annealing rate as well as by the average gap seen during the residual evolution. Numerically, the characteristic time τ_c seen during the IT evolution is of the order

of $\hbar/(2\Delta)$, see leftmost arrow in Fig. 1(c), rather than being proportional to $1/\Delta^2$ as τ_{LZ} would imply.

Obviously, instantaneous eigenvalues/eigenvectors can be studied for the Fokker-Planck equation as well; their properties, however, are remarkably different from the Landau-Zener scenario just described for the Schrödinger case. Figure 3(c) shows the first four low-lying eigenvalues of the FP equation as a function of T, while Fig. 3(a,b) show the corresponding eigenstates for two values of the temperature, $T/V_0 = 1$ and $T/V_0 = 0.1$ (the data refer to a

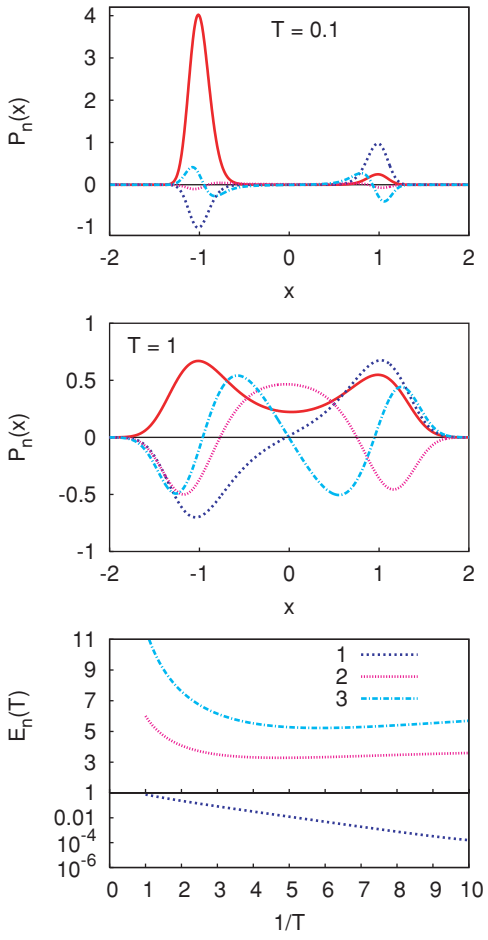

Fig. 3. Instantaneous eigenvalues of the Fokker-Planck equation (panel (**c**), the lowest eigenvalue $E_0 = 0$ is not shown) as a function of temperature T, and the corresponding eigenstates for two values of T (panels (**a**) and (**b**)). The potential here is symmetric, i.e., $V_{\rm asym}$ in 7 with $V_0 = 1$, $a_+ = a_- = 1$, $\delta = 0.1$. Similar results (not shown) are obtained for asymmetric choices of the double well potential

symmetric choice of the potential, $a_+ = a_- = 1$, but the asymmetric potential results, not shown, are virtually identical.) The lowest eigenvalue E_0 of the FP operator is identically 0 and the corresponding eigenvector [15] is the Boltzmann distribution $e^{-V(x)/k_BT}$, with roughly symmetric maxima on the two valleys. The first excited state corresponds to a function peaked on the two valley but with a node at the origin, and is separated from the ground state by an exponential small Arrhenius-like gap e^{-B/k_BT}. Higher excited states are separated by a very large gap, so that, effectively, only the two lowest lying states dominate the dynamics at small temperature. The reduction of a continuum double-well FP classical dynamics onto a discrete effective two-level system, previously noticed, is quite evident from this form of the spectrum. On the contrary, the true quantum case does not allow a discrete two-level system description to hold for small enough Γ. Indeed, when $\Gamma < \Gamma_{LZ}$ the tower of oscillator states within the valley at x_- is always very close in energy to the actual ground state, and the quantum annealing evolution reduces effectively to a particle in a single harmonic well. This explains the rather large width of the final distributions $P(x, \tau)$ observed in the quantum case.

Summarizing, we have found that QA and CA proceed in a remarkably different way. CA is sensitive to the height of the barrier, more precisely to the ratio Δ_V/B between the energy offset Δ_V of the two minima, and the barrier height B. On the contrary, QA crucially depends on the tunneling probability between the two valleys, which is reflected in a Landau-Zener (avoided crossing) gap: a wide tunneling barrier is obviously bad for QA.

2.2 Other Simple One-Dimensional Potentials with Many Minima

Moving on to multi-minima problems, we would like to mention one interesting one-dimensional potential (see [7] for details) which shows a remarkably different behaviour of CA and QA. The problem was proposed and solved, for CA, by Shinomoto and Kabashima in [19], and consists in a parabolically shaped washboard potential. This example will display a logarithmically slow classical annealing, showing that CA may run into trouble even in simple models with no complexity whatsoever, whereas quantum mechanics can do much better in this case. The problem consists in a wiggly one-dimensional potential with barriers of individual height $\approx B$ separating different local minima, regularly located a distance a apart one from each other, i.e., at positions $x_i = ai$, $i = 0, \pm 1, \pm 2, \ldots$. The ith-local minimum is at energy $\epsilon_i = ka^2i^2/2$, so that the resulting envelope is parabolic. By writing the appropriate Master equation governing the probability $P_i(t)$ that the particle is found in the ith-valley at time t, and taking the continuum limit $a \to 0$, Shinomoto and Kabashima [19] showed that the equation governing the evolution of $P(x, t)$ turns out to be a Fokker-Planck (FP) equation, (4), with an effective diffusion constant of the form

$$D_{\text{eff}}(T) = \gamma a^2 e^{-B/k_BT} \,, \tag{8}$$

$\eta(T) = k_B T / D_{\text{eff}}(T)$, and an effective drift potential $V(x) = kx^2/2$ given by the macroscopic parabolic envelope potential. This exponentially activated $D_{\text{eff}}(T)$ makes the annealing behavior of the $P(x,t)$ exceedingly slow. In fact, the surprising result of this exercise [19] is that the optimal annealing schedule $T(t)$ is *logarithmic* and the residual energy converges to 0 at best as $\epsilon_{res}(t) \sim \log(t)^{-1}$. The physical reason behind such a slow CA annealing is that the relaxation time $t_{\text{relax}} = k_B T/(2\gamma k a^2) e^{B/k_B T}$ for the system to termalize at any temperature T diverges exponentially at low T. As a result, the system will never be able to follow the decreasing T till the end of the annealing, by maintaining roughly the equilibrium value $\epsilon_{pot} = k_B T/2$. Indeed, if we assume for instance $T(t) = T_0(1 - t/\tau)$, the relaxation of the systems will cease to be effective – i.e., the system will fall *out of equilibrium* – at a time t^*, and temperature $T^* = T(t^*)$, at which $t_{\text{relax}} \approx \tau$, i.e., when $k_B T^* \approx B/\log \gamma\tau$. The residual energy at this point cannot be smaller then the equipartition value $k_B T^*/2$, hence $\epsilon_{res} \approx B/\log \gamma\tau$ as well. This freezing and falling out of equilibrium for classical systems with barriers seems to provide an ubiquitous source of logarithms in classical annealing [16].

The quantum mechanical approach to the same problem has been illustrated in [7]. In essence, starting from a tight-binding description in which the on-site energies ϵ_i are supplemented by a time-dependent nearest-neighbor hopping term which contains the inverse mass $\Gamma = \hbar^2/2m$ in the typical semi-classical (WKB) form $\sim e^{-\sqrt{V_h/\Gamma}}$ (V_h being an energy related to the details of the barrier), one can take, once again, the continuum limit $a \to 0$. The dynamics for the $\psi(x,t)$ reduces, in strict analogy with the classical case, to an effective Schrödinger equation for a particle moving in the parabolic envelop potential $V(x) = kx^2/2$, with an effective Laplacian coefficient $\Gamma_{\text{eff}}(t) \propto e^{-\sqrt{V_h/\Gamma(t)}}$, which plays here the role that the effective diffusion constant in 8 played in the FP case. Contrary to the classical case, however, where an exponentially activated behavior of the diffusion constant D_{eff} was *strongly detrimental* to the annealing (turning a power-law into a logarithm), here the exponential WKB-like behavior of Γ_{eff} *does no harm at all*: surprisingly, it improves the annealing. Indeed, as shown in [7], the power-law exponent Ω_{QA} determining the decrease of the residual energy for a particle in a harmonic well, $\epsilon_{res}(\tau) \propto \tau^{-\Omega_{QA}}$, increases as one switches-off the Laplacian coefficient more and more rapidly, tending to the value $\Omega_{QA} \to 1$ for an infinitely fast switching-off.

We believe that one of the important points that makes QA so different from CA in the present case is that the spectrum of the instantaneous eigenvalues of the quantum problem does not show any dangerous Landau-Zener avoided-crossing, and, correspondingly, the ground state wavefunction is always more peaked in the central valley (the minimum at $x_i = 0$) than elsewhere. As in the two-level case, a disorder in the width of the different valleys would drastically change this result.

3 Role of Disorder, and Landau-Zener Tunneling

Despite their disarming simplicity, the cases illustrated above turn out to be extremely informative in qualifying the profound difference of QA from CA, and their surprising consequences. Of course, the cases studied, although instructive, do not possess the real ingredient which makes annealing difficult, both in CA and QA, i.e., some form of disorder in the distribution of the minima. We argued [7], for instance, that even an irregular landscape with many minima, as the double-cosine potential $V(x) = V_1 \cos(2\pi x) + V_2 \cos(2\pi r x)$ (with r an irrational number) would already change drastically the behavior of QA (very likely, from a power-law to a logarithm). On quite general grounds, Anderson's localization [20] would predict that wavefunctions are localized for a genuinely disordered potential and for large enough mass (i.e., small enough kinetic energy bandwidth) in any $D > 2$ (this localization occurs for all values of the mass in $D = 1, 2$). Therefore, quantum annealing should always, via a cascade of Landau-Zener events [5], end up into some localized state which has, a priori, nothing to do with our search of the actual potential minimum.

A very simple illustration of the crucial role of disorder is given by the $D = 1$ disordered Ising ferromagnet :

$$H = -\sum_i J_i \sigma_i^z \sigma_j^z - \Gamma \sum_i \sigma_i^x \,, \tag{9}$$

where $J_i \geq 0$ are non-negative random variables in the interval $[0, 1]$, and Γ is the transverse field inducing quantum fluctuations. Obviously, the ground state is the ferromagnetic state with all spins aligned up (or down). However, arbitrarily weak values of the J_i can pin domain walls between up and down ferromagnetic regions, with a very small energy cost $2J_i$. For a finite system with periodic boundary conditions, domain walls appear in pairs, and separate sections of the system with alternating $\uparrow$ and $\downarrow$ ferromagnetic ground states. Given two domain walls, pinned at weak J_i points a distance $L \gg 1$ apart, healing the system via single spin flip moves requires flipping L spins, which can be a formidable barrier to tunnel through. The system will have a very slow annealing (quantum, as well as classical) while showing, at the same time, no complexity whatsoever: simple disorder is enough.

The simple case of a site-disordered Anderson model, where the goal is the trivial one of finding the minimal on-site energy ϵ_i, and the QA is carried by switching off, as a function of time, the nearest-neighbor hopping integral, illustrates very clearly the complications introduced by disorder. Figure 4 shows the instantaneous eigenvalues of a disordered three-dimensional Anderson model, on a lattice of size $10 \times 10 \times 10$, as a function of the nearest-neighbor hopping integral Γ. In the process of reducing Γ, the ground state encounters several "identity crisis" associated to tunneling from one region of the lattice to another. Some of these tunneling amplitudes can be tremendously small,

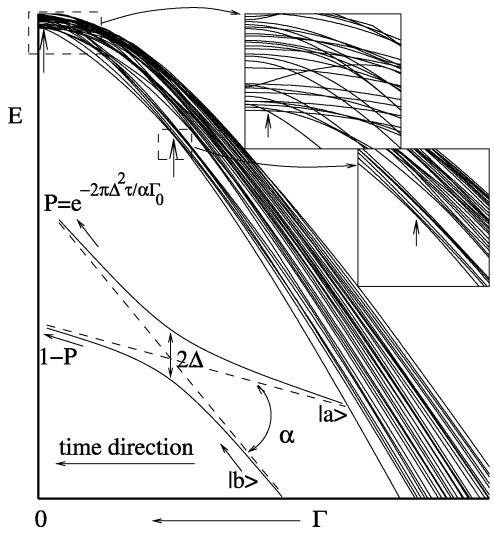

Fig. 4. Instantaneous low-lying eigenvalues of a three-dimensional disordered Anderson model, on a lattice of size $10 \times 10 \times 10$, as a function of the hopping integral Γ. Notice the Landau-Zener avoided crossings, particularly the one occurring at smaller Γ, which can have a tremendously small gap 2Δ. The inset shows a schematic of the Landau-Zener process

so that one has to wait for an astronomically large Landau-Zener characteristic time τ_{L-Z} (see Sect. 2.1) in order for the probability of "adiabatically following the Ground State" to be non-negligeable.

4 Path Integral Monte Carlo Quantum Annealing

In order to move from toy problems with a manageable Hilbert space to real optimization problems, stochastic approaches are mandatory. As discussed in the Introduction, imaginary-time stochastic approaches are perfectly suitable to the goal: there is no gain in doing, on a classical computer, a Schrödinger evolution in real time [7].

A very simple Quantum Monte Carlo approach, suitable to the proposed goal, is the Path-Integral Monte Carlo (PIMC) approach. We briefly sketch the idea of the approach with two introductory examples: the Ising case, as representative of discrete optimization problems, and the particle in a potential, as representative of continuum problems.

4.1 Path Integral Monte Carlo: Introduction

The first, crucial, observation is that PIMC is intended to simulate the *equilibrium* behaviour of a system at *finite temperature* T. Both these features are

potential limitations of the method. To clarify this point, consider, for instance, the Edward-Anderson Ising glass in a transverse field: $H = H_{cl} + H_{kin} = -\sum_{\langle ij \rangle} J_{ij}\sigma_i^z\sigma_j^z - \Gamma(t)\sum_i \sigma_i^x$. Strictly speaking, in the quantum annealing context, this is a *time-dependent* Hamiltonian, of which we would like to follow the low-lying states (ideally, the ground state) as a function of time, by turning off the transverse field $\Gamma(t)$. PIMC allows you to simulate the thermodynamics (at fixed strictly positive temperature T) for a fixed value of $\Gamma(t)$, by an approximate sampling of the quantum partition function

$$Z(T,\Gamma) = \mathrm{Tr} e^{-\beta(H_{cl}+H_{kin})} = \sum_{s^1} \langle s^1 | e^{-\beta(H_{cl}+H_{kin})} | s^1 \rangle \ , \tag{10}$$

where s^1 denotes a generic configuration of all the N spins. The idea behind the Path-Integral is to reduce 10 to a classical partition function which is than sampled in the usual way using, for instance, a Metropolis Monte Carlo. In order to do that, one needs to split the exponential of the Hamiltonian, appearing in 10, into products of exponentials. This is allowed by the Trotter theorem, stating that

$$e^{-\beta(H_{cl}+H_{kin})} = \lim_{P\to\infty} \left(e^{-\frac{\beta}{P}H_{cl}} e^{-\frac{\beta}{P}H_{kin}} \right)^P \ . \tag{11}$$

Using this relationship, and inserting identities between the various exponentials, we get:

$$Z(T,\Gamma) = \lim_{P\to\infty} \sum_{s^1 \ldots s^P} e^{-\frac{\beta}{P}\sum_{k=1}^P H_{cl}(s^k)} \langle s^1 | e^{-\frac{\beta}{P}H_{kin}} | s^2 \rangle \ldots \langle s^P | e^{-\frac{\beta}{P}H_{kin}} | s^1 \rangle \ . \tag{12}$$

The various configurations s^k ($k = 1 \cdots P$) are often referred to as *Trotter replicas* of the original configuration s^1. The next thing one needs to do, is to calculate explicitly the relevant exponential of the kinetic term, $\langle s^k | e^{-H_{kin}/PT} | s^{k+1} \rangle$, between two generic configurations. This is sometimes very easy to do – like in the Ising transverse field case, or in the Laplacian case (see below) – but can be also very difficult, for other choices of H_{kin} (see Sect. 4.2). In the Ising case, the problem factorizes into N indipendent sites, each of which involves a simple Pauli matrix expectation value, yielding:

$$\langle s^k | e^{-\frac{\beta}{P}H_{kin}} | s^{k+1} \rangle = C^N e^{\frac{\beta}{P}J^\perp \sum_i s_i^k s_i^{k+1}} \ , \tag{13}$$

where the transverse coupling $J^\perp$ is given by:

$$J^\perp = -\frac{P}{2\beta} \ln \left(\tanh \beta\Gamma/P \right) > 0 \tag{14}$$

(the constant C is not relevant for our discussion). This kinetic term has a very transparent interpretation: the $J^\perp$ gives a ferromagnetic Ising-like coupling between nearest-neighbor (k and $k+1$) Trotter replicas of the same spin.

In order to implement this approach numerically, a finite number of Trotter replicas P is mandatory. This leads to an approximation, the error of which is proportional to the square of the Trotter break-up time, $O((\beta/P)^2)$[21]. (Better Trotter break-ups, for given finite values of P, can lead to smaller errors, see Sect. 4.4, but we will concentrate here on the basic form proposed above.) For the full partition function we thus finally get, in the Ising case:

$$Z(T,\Gamma) \approx C^{NP} \sum_{s^1} \dots \sum_{s^P} e^{-\frac{\beta}{P} S_{D+1}} \tag{15}$$

$$S_{D+1} = -\sum_{k=1}^{P} \left(\sum_{\langle ij \rangle} J_{ij} s_i^k s_j^k + J^{\perp} \sum_i s_i^k s_i^{k+1} \right) \quad , \tag{16}$$

which represents the partition function of a classical $(D+1)$-dimensional anisotropic Ising system at temperature $P/\beta = PT$. The system has couplings J_{ij} along the original D-dimensional lattice bonds (same for all Trotter slices), and $J^{\perp}$ (same for all sites i) along the extra Trotter dimension where the system has a finite length P.

Similar expressions hold, for instance, for the problem of a particle in a potential $V(\mathbf{x})$, where $H_{cl} = V(\mathbf{x})$, $H_{kin} = -\Gamma\nabla^2$, and sums over configurations $\sum_{s^k}$ transform into integrals over the variables $\mathbf{x}^k$. Similarly, the kinetic term contribution

$$\langle \mathbf{x}^k | e^{-H_{kin}/PT} | \mathbf{x}^{k+1} \rangle = \left(\frac{K^{\perp}}{2\pi PT} \right)^{D/2} e^{-\frac{1}{PT}\frac{K^{\perp}}{2}(\mathbf{x}^k - \mathbf{x}^{k+1})^2} \quad , \tag{17}$$

where D is the dimension of the $\mathbf{x}$-space and $K^{\perp} = (PT)^2/(2\Gamma)$, admits a perfectly transparent interpretation: the transverse coupling $K^{\perp}$ between different Trotter replicas has the form of a *spring* coupling neighboring configurations $\mathbf{x}^k$ and $\mathbf{x}^{k+1}$.

In all cases, QA, in the present context, consists in externally controlling, during the PIMC dynamics, the value of the transverse field Γ – leaving T untouched –, in much the same way as one externally controls T in classical simulated annealing [1]. This approach, which we will refer to as PIMC-QA, does not lead, therefore, to the simulation of a true quantum mechanical annealing dynamics, of the type implied by 1, but only to a MC annealing dynamics. We now move on to describe some of the results obtained so far with this technique.

4.2 PIMC-QA Applied to Combinatorial Optimization Problems

In a quite general way, one could define a combinatorial optimization problem as the algorithmic task of minimizing any given *cost function* which depends on the configuration of variables assuming discrete values [22]. Further classifications are of course possible, but they somehow hide the fundamental

fact that it is straightforward to map such problems over the search for the ground state of some Hamiltonian depending on Potts (or Ising) spin degrees of freedom [23, 24]. This is the case, for instance, of the Traveling Salesman Problem [25, 26, 27, 28], Number Partitioning [31], Boolean Satisfiability [29, 30], Vertex Covering [32], Graph Coloring [33] and many others.

Random problem instances are of particular interest, because they can be investigated resorting to powerful techniques developed in the context of disordered statistical mechanics systems [34]. The physical approach to combinatorial optimization have often allowed the derivation of *phase diagrams*, telling us in which range of some control parameters hard instances are expected to be found [23, 24]. These analyses provide insight about the typical-case complexity of problem solving, in contrast with the more rigorous but less informative worst-case complexity theory, which constitutes one of the corner-stones of theoretical computer science [35]. The basic distinction between the **P** and **NP** complexity classes (that is, between problems for which a polynomial algorithm able to solve worst-case instances is or is not known) can sometimes be misleading. Easy instances of **NP**-complete problems (the hardest of all the **NP** problems, [36]) can easily be found (see e.g. [37]), while sometimes the optimization of instances of problems in **P** can take an exponential time using local search techniques (see e.g. [38]).

In the following, we shall briefly illustrate three specific problems which we have recently addressed using PIMC-Quantum Annealing.

Ising Spin Glass

Determining the ground state of a simple model like the Ising Spin Glass can be an extraordinarily difficult task.

To get the big picture, it is enough to think that the number of possible configurations of a very small 32×32 square lattice Ising model is of order 10^{308}, while the number of electrons in the universe is "just" of the order 10^{80}.[1] It can be rigorously shown that, in the 3D lattice and in the diluted case, the ground state determination belongs to the **NP-complete** complexity class [39], but here we shall report results on the simpler 2D lattice case, where E_{GS} can be calculated up to sufficiently large lattice sizes [40]. The Hamiltonian of an Ising spin glass has been already discussed in Sect. 4.1 and it is given by equation (9).

For a given 2D lattice size $L \times L$, (L up to 80) and for various quenched realizations of the random couplings J_{ij}, drawn from a flat distribution in the interval $(-2, 2)$, we carried out several repeated classical and quantum annealings (for more details, see [5, 10]). At the end of both QA and CA, the system remains generally trapped at energy $E_{final} = E_{GS} + \epsilon_{res}$ and the

[1] Other funny examples of this kind can be found in the appendices of D.J.C MacKay, *Information Theory, Inference and Learning Algorithms*, Cambridge University Press, Cambridge MA (2003).

efficiency of each protocol is monitored by considering the average residual energy $\epsilon_{res}(\tau)$ as a function of τ.

The annealing parameters T (CA) or Γ (QA) were decreased linearly from the initial value of $T_0 = 3$ or $\Gamma_0 = 2.5$ down to zero, with a total of τ MC steps per spin. In QA we used fixed values of $T_q = PT = 1, 1.5, 2$ at several P values and prepared the initial state (same for all replicas) by a classical pre-annealing stage. The computational cost scales linearly with P, but increasing P beyond a certain characteristic length (see inset in Fig. 5) does not produce any further improvement. The choice of $P = 20$ was found to be optimal. The moves proposed in both CA and QA are single-spin flip moves, but QA also attempts slightly more "global moves" by proposing a spin-flip for the spins $s_i^k, k = 1 \cdots P$ of all the Trotter replicas of a given site i. Figure 5 shows that QA is definitely superior to CA in the case of the Ising spin glass. This numerical evidence is in agreement with the experimental observation of significantly faster frequency-dependent relaxations during QA of the disordered magnet [4].

Traveling Salesman Problem

Given N cities and their tabulated inter-distances d_{ij}, TSP consists in finding the shortest path connecting them, visiting each city only once and returning to the starting point. An account of the vast literature about algorithms for

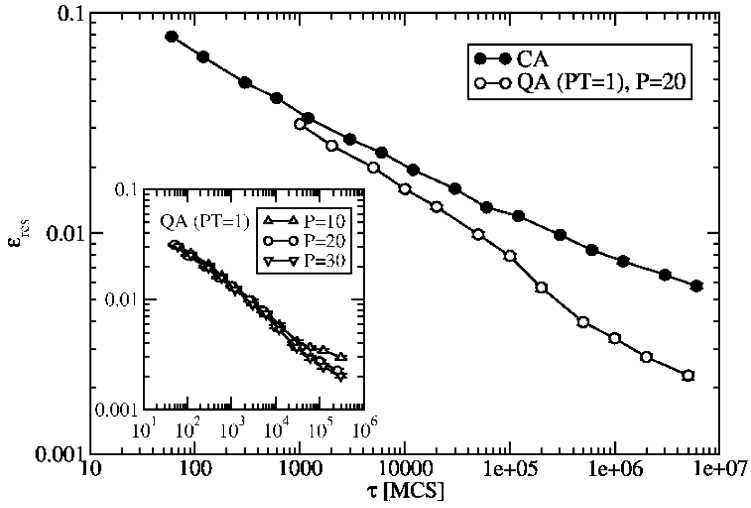

Fig. 5. Residual energy per site for an 80×80 disordered 2D Ising model after CA and QA. We show the QA data for the optimal value of $PT = 1$, with $T = 0.05$ and $P = 20$ Trotter replicas. The actual inverse annealing rate τ used in the QA has been rescaled (multiplied by P) for fair comparison with CA. Still, QA is faster than CA

TSP can be found e.g. in [41], while three classical papers analysing physics approaches to the problem are [26, 27, 28].

As a fist step to a QA optimization we have to chose a representation for the classical potential energy H_{pot} of a given configuration (in our case, the length of a tour), and, most crucially, a suitable source of quantum fluctuations H_{kin}. TSP can be mapped to a highly constrained Ising-like model – in a way similar to [25, 3] – in which each configuration of the system (a valid tour) is associated to a $N \times N$ 0/1-matrix $\hat{T}$. For every ordered sequence of cities, $\hat{T}_{i,j} = 1$ if the tour visits city i immediately after city j, and $\hat{T}_{i,j} = 0$ otherwise. For the *symmetric* TSP problem we want to consider (a TSP with symmetric distance matrix $d_{ij} = d_{ji}$), the directed tour represented by a $\hat{T}$, and the reversed tour, represented by the transposed matrix $\hat{T}^t$, have exactly the same length. It is then convenient to introduce the symmetric matrix $\hat{U} = \hat{T} + \hat{T}^t$ as representative of *undirected* tours. The length of a tour can now be written:

$$H_{pot}(\hat{U}) = \frac{1}{2} \sum_{(ij)} d_{ij} \hat{U}_{i,j} = \sum_{\langle ij \rangle} d_{ij} \hat{U}_{i,j} \ , \tag{18}$$

where $\langle ij \rangle$ signifies counting each link only once. H_{kin} should be chosen in order to induce fluctuations generating the important elementary "moves" of the problem. Deciding which configurations are to become direct neighbors of a given configuration is indeed a crucial step, because it determines the problem's effective landscape [42]. A very important move that is often used in heuristic TSP algorithms is the so-called *2-opt move*, which consists in eliminating two links in the current tour, $(c_1 \rightarrow c_2)$ and $(c_{1'} \rightarrow c_{2'})$, and rebuilding a new tour in which the connections are exchanged, $(c_1 \rightarrow c_{1'})$ and $(c_2 \rightarrow c_{2'})$ (see Fig. 6). Associating a spin variable $+1$ (-1) to each entry 1 (0), the whole 2-opt move, when working with $\hat{U}$ matrices, can be represented by just four spin-flip operators:

$$S^+_{\langle c_{1'}, c_1 \rangle} S^+_{\langle c_{2'}, c_2 \rangle} S^-_{\langle c_2, c_1 \rangle} S^-_{\langle c_{2'}, c_{1'} \rangle} \ ,$$

where, by definition, each $S^{\pm}_{\langle i,j \rangle}$ flips an Ising spin variable (defined as $S^z_{\langle i,j \rangle} = (2\hat{U}_{i,j} - 1) = \pm 1$) at position (i, j) and at the symmetric position (j, i), i.e., $S^{\pm}_{\langle i,j \rangle} = S^{\pm}_{i,j} S^{\pm}_{j,i}$. However, this kinetic Hamiltonian does not allow for an obvious Trotter discretization of the Path Integral (see discussion in Sect. 4), and the PIMC scheme cannot deal with it (for this purpose, Green's function MC methods, that do not use a Trotter break-up, should be more effective, see Sect. 5.1). We introduce then a drastic simplification to our kinetic energy term, replacing it altogether with a standard transverse Ising form, arriving finally at the Hamiltonian:

$$\tilde{H}_{TSP} = \sum_{\langle ij \rangle} d_{ij} \frac{\left(S^z_{\langle i,j \rangle} + 1 \right)}{2} - \Gamma(t) \sum_{\langle ij \rangle} [S^+_{\langle j,i \rangle} + H.c.] \ , \tag{19}$$

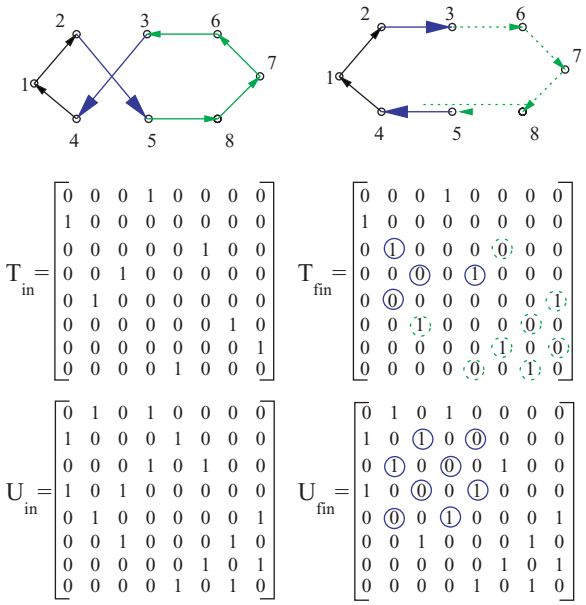

Fig. 6. *Left*: Representation of an 8-city tour, with the corresponding matrix $\hat{T}_{\text{in}}$ and $\hat{U}_{\text{in}} = \hat{T}_{\text{in}} + \hat{T}^t_{\text{in}}$. *Right*: The final tour obtained when a 2-opt move is performed, with a whole section reversed (*dotted line*). The matrices $\hat{T}_{\text{fin}}$ and $\hat{U}_{\text{fin}}$ are shown, the *circles* indicating the entries that have been switched ($0 \leftrightarrow 1$) by the 2-opt move. The *dotted circles* in $\hat{T}_{\text{fin}}$ are entries related to the trivial reversal of a section of the tour

This simplified form of kinetic energy no longer fulfills the constraint to take a valid tour to another valid tour, but this problem is avoided by proposing exclusively 2-opt moves in the MC algorithm [11].

We tested our QA algorithm against CA [11] on a standard benchmark TSP problem, namely the printed circuit board instance `pr1002` of the TSPLIB [43]. It is a structured TSP problem with $N = 1002$ cities whose optimal tour length L_{opt} is known exactly. For CA, we chose an optimal initial temperature T_0 by first performing several CA with various short cooling times τ and starting from sufficiently high temperatures. The point where the cooling curves for different τ's start to differ identifies an approximate "dynamical temperature" T_{dyn}. For `pr1002`, we obtained $T_{dyn} \sim 100$. As expected [41], the optimal T_0 for CA approximately coincides with T_{dyn}. Not surprisingly, for QA the same choice $PT \sim T_{dyn}$ yields the optimal results, together with the choice $\Gamma_0 = 300$. Figure 7 shows the results obtained [11] for the average percentage best-tour excess length $\epsilon_{exc}(\tau) = (\bar{L}_{best}(\tau) - L_{opt})/L_{opt}$, both with CA (filled squares) and with QA (open circles). As a reference, the best out of 1000 runs of the Lin-Kernighan algorithm (one of the standard local-search algorithms for TSP [41]) is also plotted (dashed line in Fig. 7). The results

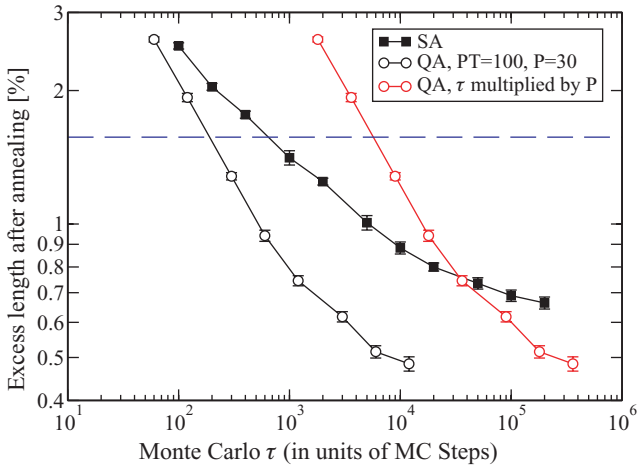

Fig. 7. Average residual excess length found after CA and QA for a total time τ (in MC steps), for the $N = 1002$ instance `pr1002` of the TSPLIB. The *dashed horizontal* line represents the best out of 1000 runs of the Lin-Kernighan algorithm (see text). QA is once again faster than CA

show that, once again, QA anneals more efficiently, even accounting for the extra factor P in the total CPU time (rightmost open circles), reducing the error at a much steeper rate than CA.

Random Boolean Satisfiability

In order to state the problem, consider a set of N boolean variables $z_1, \ldots, z_N$, where $z_i = 1$ or 0 ('True' or 'False'). Denoting by ζ_i the variable z_i or its negation $\bar{z}_i$, one then considers the disjunction (logical OR) of 3 variables $C = (\zeta_i \vee \zeta_j \vee \zeta_k)$, which is called a 3- *clause*. The random 3-SAT problem consists in deciding if the conjunction (logical AND) of M different clauses $C_1 \wedge C_2 \cdots \wedge C_M$ – each clause being formed by 3 variables extracted at random among the N variables, and appearing negated or directed with uniform probability – can be simultaneously satisfied by a truth value assignment $\{z_i\}$. If we associate an Ising spin variable $S_i = (-1)^{z_i}$ to each Boolean variable z_i, we can assign to any clause C_a involving three variables z_i, z_j, z_k an energy E_a given by:

$$E_a = \frac{(1 + J_{a,i} S_i)\,(1 + J_{a,j} S_j)\,(1 + J_{a,k} S_k)}{8}\,, \tag{20}$$

where the coupling $J_{a,i}$ assumes the value -1 if the variable z_i appears negated in clause a, $+1$ otherwise. Evidently, $E_a = 0$ if the corresponding clause is satisfied, $E_a = 1$ otherwise.

As in the case of TSP, archives of hard structured instances exist[44]. In addition, statistical mechanics techniques can be used to determine the

phase diagram of the Random 3-SAT problem [24, 29, 30]. The main parameter determining the hardness of a formula is the ratio $\alpha = M/N$ between the number, M, of clauses and the number, N, of variables. For $\alpha < \alpha_c \simeq 4.26$ it is typically possible to find satisfying assignments, but instances particularly hard to solve are expected to be found if $\alpha > \alpha_G \simeq 4.15$ [45]. It is expected that, due to the proliferation of an exponential number of metastable states acting as dynamical traps, local search gets trapped at an energy close to some finite threshold level, lower bounded by the so-called *Gardner energy* [46]. The trapping effect induced by the threshold states cannot be neglected when the instance-size is large ($N \geq 10000$) and large statistical fluctuations become sufficiently rare [45]. Smaller random formulas are, on the other hand, often easily solvable by classical simulated annealing and cannot be used as significant benchmarks.

We performed a first set of annealings over a single hard 3-SAT random instance with $N = 10^4$ and $\alpha = 4.24$ [12]. The kinetic term was given by a simple transverse field inducing single-spin-flip fluctuations, like in the Ising case, since no clever sets of moves are known for 3-SAT, unlike the TSP case [47]. Using an efficient *ad-hoc* algorithm (that will be shortly described in Sect. 5.2 and is presented in [45]), we verified that the chosen formula was actually satisfiable, as expected from theory for $\alpha < \alpha_c$. As in the case of the TSP optimization, we set both T_0 for CA and PT for QA equal to $T_{dyn} = 0.3$. The optimal field-ramp range was found to be between $\Gamma_0 = 0.7$ and $\Gamma_f \simeq 10^{-3}$.

A comparison between the performance of the optimal CA and the optimal QA at $P = 50$, both with and without global (i.e., all $s_i^k, k = 1 \cdots P$ are flipped) moves [12], is shown in Fig. 8. For each point, an average has been taken over 50 different realizations of the same experiment; in the case of QA, a second average was performed among the energies of the P replicas, which are in general different. It can be seen that the linear-schedule CA always performs better than the linear-schedule QA. No further improvement can be obtained for $P \geq 100$, see inset of Fig. 8 – a much larger value than in the case of the Ising Spin Glass and the TSP instance – but we chose $P = 50$ in order to extend as much as possible the simulation time. The asymptotic slope of the linear-schedule QA curves seems indeed to be definitely less steep than that of CA, independently of the number of replicas involved in the simulation and of the use of global moves.

4.3 PIMC-QA and 3-SAT: Lessons from a Hard Case

The substantial failure of PIMC-QA for the 3-SAT optimization calls for a deeper understanding of the peculiar way in which it explores the energy landscape of the problem. In the following subsections, we shall analyze in detail several features of the method.

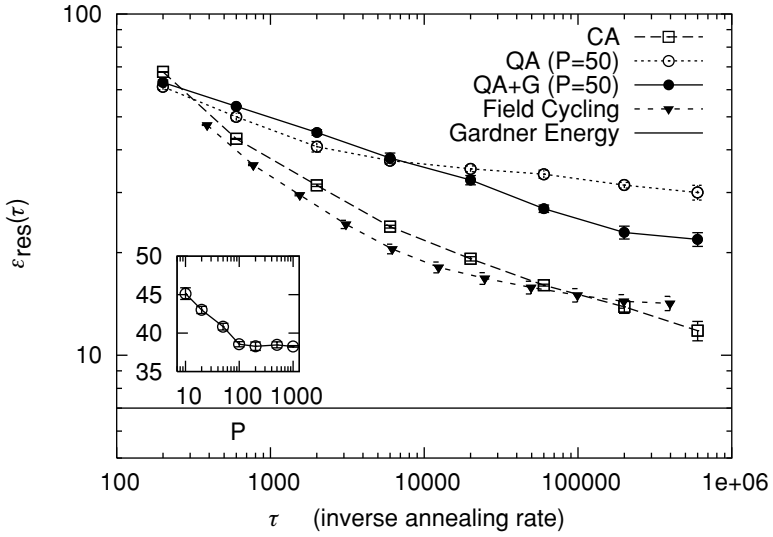

Fig. 8. Comparison between optimal linear-schedule Classical (CA) and Quantum Annealing (QA) for a 3-SAT problem with $N = 10^4$ and $\alpha = M/N = 4.24$. CA always performs better than QA simulated with $P = 50$ Trotter replicas. The average performance of linear QA is worse than that of CA, even if an improvement in the results can be obtained by introducing global moves (G) and by increasing P (in the inset the final average energy found by QA after 2000 iterations for increasing P is plotted and compared with the average result of a CA of the same length, dashed line). The solid triangles are the data obtained by the field-cycling QA hybrid strategy described in Sect. 4.3

Target Selection and Field-Cycling

We denote by $\langle\langle E\rangle\rangle$ the configuration energy averaged over different experiments *and* Trotter replicas (this is the energy reported everywhere in Fig. 8); the average among different experiments of the *best* replica energy will be, on the other hand, denoted by $\langle E\rangle$. In Fig. 9, the Monte Carlo "time" evolution profiles of $\langle\langle E\rangle\rangle$ and $\langle E\rangle$ are shown for a linear-schedule QA (2000 iterations long). The strength of the transverse field, and hence of the quantum coupling J_Γ given by (14) (see inset of Fig. 9), determines the relative importance of the classical and quantum terms in the Hamiltonian and its variation determines the transition between three regimes [12].

First ($\Gamma \approx \Gamma_0 \simeq 0.7$, $J_\Gamma \simeq 0$), the system is quenched at temperature T_q in presence of a strong external transverse field. The system enters an incoherent mixture of states, and, from the point of view of the PIMC simulation, when the coupling J_Γ is small, each replica behaves as if roughly independent from the others. After the abrupt out-of-equilibrium *quenching phase*, with increasing coupling strength, the fluctuations of the different replicas become correlated. Several spin flips that would have been unlikely in absence of the

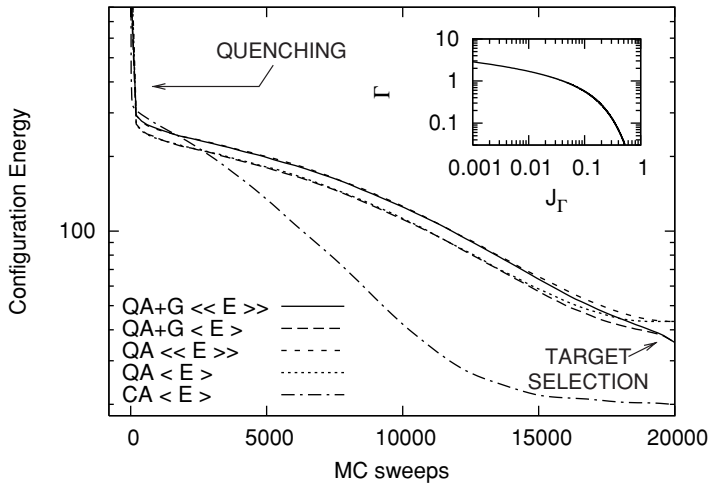

Fig. 9. Energy evolution during Quantum Annealing, compared to Simulated Annealing. The variation of the averages $\langle E \rangle$ (average best replica) and $\langle\langle E \rangle\rangle$ (average of the average replica) is shown as a function of the simulation time, for a set of experiments with $P = 50$ and 2000 annealing iterations. The inset shows the time-dependent value of the coupling J_Γ. Three different regimes can be distinguished, which will be called quenching, search (driven by quantum fluctuations) and target selection

the kinetic term can in this regime be accepted, and configurations generally not visited by typical CA trajectories are produced (*quantum search phase*). Finally, when the transverse field vanishes, quantum fluctuations are gradually switched off. and the system collapses completely into some selected target state. In this fundamentally classical regime, J_Γ becomes so strong that local spin flips can be accepted only at sites where the spins of two neighboring replicas are not aligned. If global moves are allowed, small-range classical oscillations induce a further energy reduction of quite small entity.

Considering this three-piece scenario (that will be confirmed by the autocorrelation and geometrical analysis of Sect. 4.3), the simulated QA could be described as a very basic kind of *evolutionary search* [48, 49]. The P replicas can be seen as a population of individuals, the spin configuration of each replica as its genotype, and the classical Hamiltonian (20) as a fitness function. Contiguous replicas can "mate", exchanging sequences of their genotype thanks to the duplicating action of the transverse coupling, that spreads around low-energy-inducing spin patterns (the so-called Holland *schemata* [50]). Suppose now that a new individual with exceptional fitness is generated when J_Γ is already considerably large. Its peculiar "genes" would be overwritten with high probability by the corresponding spin sequences in the most widespread configuration. The population must then collapse toward a group of "identical twins" and global moves cannot affect significantly this

picture, because they do not cure the problem of the lack of genetic diversity, which is constantly renewed by crossover, in standard evolutionary search.

However, in PIMC-QA, the mutation rate can be increased again by switching on the quantum fluctuations. In Fig. 10, we present the results of an experiment in which, after each linear descending ramp from $\Gamma_0 \simeq 0.7$ to $\Gamma_f \simeq 0.001$, the coupling is raised smoothly to the initial value J_{Γ_0} and then back again to J_{Γ_f} (for details of the schedule, see [12]). Many such field-cycles can be chained one after the other, slightly reducing the temperature T_q so as to avoid a complete re-initialization (related with memory effects [51]), and realizing thus a hybrid strategy (a linear-schedule CA, superposed with linear-schedule QA cycles over a shorter time-scale).

After each ascending ramp and a short transient phase, a new quantum search phase is initiated, starting from plateaus that lie at a distance progressively larger from the quenching level corresponding to the present temperature (see the arrows in Fig. 10). Over short time scales (number of MC iterations approximately smaller than 200000, when taking $P = 50$), this hybrid field-cycling strategy outperform the pure linear CA. Furthermore, a classical experiment with the same temperature schedule has been repeated in absence of the transverse magnetic field, with the same number of now completely decoupled Trotter replicas. We observed that $\langle\langle E\rangle\rangle_{\text{hybrid}}$ stays clearly below $\langle E\rangle_{\text{classical}}$, indicating that quantum effects give access to states that are hard to reach even by rare large classical fluctuations. One could say that quantum restarts are more effective than classical restarts [52], at least when short schedules are considered.

Longer field-cycling schedules are obtained by rescaling with a constant factor the duration of all the ramps in a shorter schedule. For larger total annealing times, the asymptotic slope of the field-cycling cooling curve saturates to a value remarkably similar to the other QA cases. If the reduction of temperature allows the system to explore the landscape at different length scales [51] and to find better target configurations, lower energy regions remain nevertheless fundamentally inaccessible.

Autocorrelation Analysis and Landscape Probing

Let us denote by $\{S_i(t)\}$ the instantaneous spin configuration of the sample 3-SAT formula at time t. An *autocorrelation function* $K(t,\tau)$ can be defined as:

$$K(t,\tau) = \left\langle \frac{1}{N}\sum_{i=1}^{N} S_i(t)S_i(t-\tau) \right\rangle , \tag{21}$$

where the average is performed over different dynamical realizations (and over replicas, in the quantum case). The autocorrelation function $K(t,\tau)$ allows us to visualize in a compact way the typical behavior of the overlap between two spin assignments at different evolution instants [12]. In Fig. 11 $K(t,\tau)$ is plotted as a function of the autocorrelation time τ for several fixed values t^*

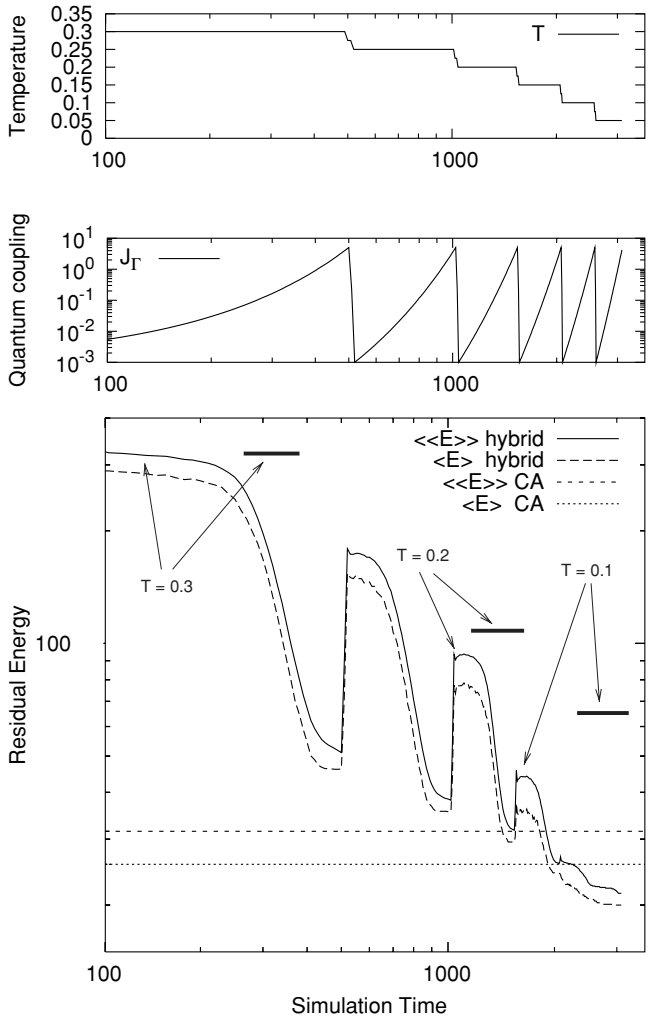

Fig. 10. Energy evolution during a field-cycling hybrid strategy. The strength of the transverse coupling J_Γ is varied cyclically between the values 0.001 and 5, by adjusting the value of the magnetic field. The effective temperature T_q is kept constant during each field ramp, but is reduced in a stepwise way among different ramps, from the initial value of 0.3 down to 0.05. Each ascending field-ramp unfreezes the system from a previously reached target state, and after a short transient regime, a new search phase is entered. The starting plateaus have energy values increasingly smaller than the quenching level at the new simulation temperature (the arrows in the graphs indicates the quenching level and the hybrid strategy plateau at a given value of the temperature). Each new target state has a better energy than the preceding one, and the final average energy is better than the value reachable by large classical fluctuations

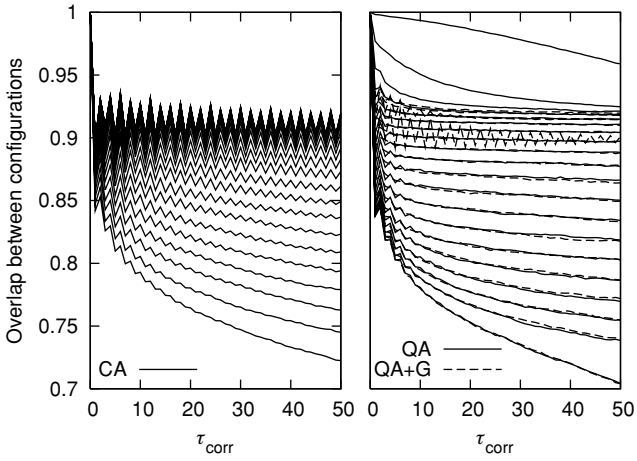

Fig. 11. Autocorrelation function $K(t,\tau)$ for CA (*Left*) and QA (*Right*). The different curves represent several fixed-simulation-time $t = t^*$ snapshots of the autocorrelation function, with t^* varying at fixed intervals between 200 and 2000, from bottom to top. For QA, both the results with (QA+G, *solid lines*) and without (QA, *dashed lines*) global moves (see text) are shown

of the simulation time t, for both the CA (Left panel) and QA (Right panel) dynamics. The results shown are averaged over 500 different runs, each consisting of 2000 annealing iterations (and over $P = 50$ replicas, in the case of QA). A $K(t^*,\tau)$ which decays fast with τ indicates that at time t^* the configuration is still rapidly evolving, and that at every time-step a large number of spins is being flipped; when a local stability is reached, on the other hand, $K(t^*,\tau)$ assumes a flat (or periodic) profile, indicating that the system has entered into some attracting configuration (or limit cycle). For CA, the self-overlap between $\{S_i(t^*)\}$ and $\{S_i(t^* - \tau)\}$ grows constantly with t^*, until when a periodic behavior of $K(t^*,\tau)$ gradually develops. In the final part of the classical relaxation, about 20% of the variables appear to be free to flip at each iteration, even if the average energy is no longer changing. The strongly regular oscillations of $K(t^*,\tau)$, as well as the non-vanishing asymptotic spin flip acceptance ratio, suggest that the system gets trapped into a very small portion of the phase space, and that a fraction of the variables is still allowed to fluctuate, but only cyclically repeating a limited amount of sequences of flips. The observation of the neighborhood geometry during the dynamics confirms this hypothesis. In Fig. 12 (dashed line), the fractions of downhill, flat and uphill directions (considering single spin-flip moves) are plotted against the energy of the visited configurations. One sees then that the number of downhill directions falls to zero when the lowest energies are approached (the number of remaining flat directions is compatible with the observed oscillation amplitude). For QA, the self-overlap increase becomes faster upon reducing

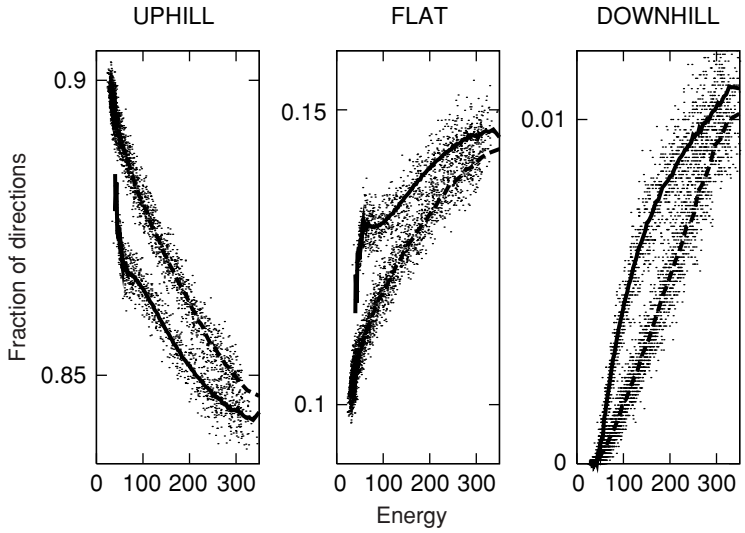

Fig. 12. The local geometry of the visited regions of the phase space is probed by counting the fraction of directions in which the energy variation is negative, null or positive. Although both CA (*dashed line*) and QA (*solid line*) get trapped in a local minimum, the quantum evolution tends to visit "valleys" that, at the same energies than CA, are more flat and with a larger number of downhill directions

the transverse magnetic field, because the pseudo-evolutionary replication of the "good" spin patterns, operated by the coupling in (14), has also a stabilizing effect on them. No trace of asymptotic periodic behavior is found, and all the replica configurations reach continuously a full overlap with a single final configuration. The introduction of global moves causes damped classical-like oscillations to set in, but target selection is not eliminated, as previously discussed. Figure 12 shows (solid line) that the target states are once again very close to local minima, with an extremely small number of downhill directions as in the CA case. Nevertheless, the phase space regions explored by the two algorithms are quite different. At the same value of the energy, the quantum system is visiting configurations with a significantly larger fraction of downhill and flat directions. One could say that the CA follows narrow canyons, while the QA prefers to explore the edges of mid-altitude plateaus. This phenomenon, which seems to be a genuinely quantum effect captured by the PIMC simulation, is strongly reminiscent of what happens in continuous space, where the choice of broader potential wells allows the system to reduce the kinetic contribution to the total energy. Furthermore, the various Trotter replicas differ in a number of spins comparable to the number of flat directions. All the configurations simultaneously taken by the quantum system belong then to a single broad landscape valley, which is nevertheless explored in all its wideness by the quantum system.

For vanishing field, the system "wants to become classical", and the number of uphill directions increases abruptly, approaching the classical curve. The dynamical collapse is then paralleled by a change in the local landscape topology. The poor performance of QA in the present 3-SAT case could be then explained by the existence of broad basins of attraction strewn with deceptive and highly attractive sinks, that, unlike the cleavages preferred from the very beginning by the CA, prevent access to lower energy sectors.

4.4 PIMC-QA of a Double-Well: Lessons from a Simple Case

We would like to finish our discussion about Path-Integral Monte Carlo based QA by mentioning recent results on a very simple case from which one can learn much about the limitations of the method [14]. Suppose we want to perform a QA optimization of the simple double-well potential which was investigated in Sect. 2.1 using PIMC. One is then lead to simulate the behaviour of a closed polymer made up of P Trotter replicas $\{x^k\}$ $(k = 1 \cdots P)$ of the original particle, held at temperature β/P and moving in the potential V_{asym} with a nearest-neighbor spring coupling, as shown in 17. One can actually be more sophysticated than that, and perform a higher order Trotter break-up, correct to $O(\beta/P)^4$ instead of $O(\beta/P)^2$, using, for instance, the Takahashi-Imada approximation [53]. Moreover, instead of performing single-bead moves, i.e., moves involving a single x^k at a time, one can reconstruct, during the move, entire sections of the polymer, using the *bisection* method [54]. We have applied this rather sophysticated PIMC to our double-well problem , working with a temperature $T = 0.03V_0$, a number of Trotter slices up to $P = 160$, and a bisection of level up to 4, i.e., involving up to 2^4+1 replicas x^k at each move. The initial temperature value of $\Gamma = \hbar^2/2m$ was taken to be $\Gamma_0 = 0.5$, and its value was reduced linearly to 0 in a certain total number τ of Monte Carlo moves. The results, shown in Fig. 13 by solid circles, are rather disappointing:

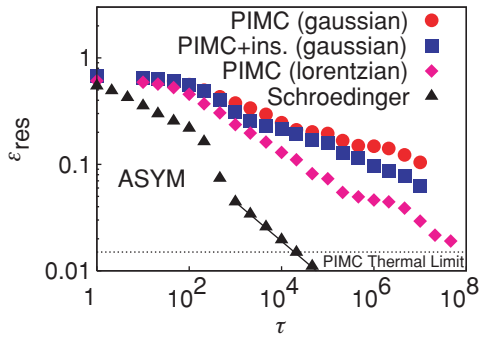

Fig. 13. Comparison between the Imaginary-Time Schrödinger annealing data of Fig. 1, solid triangles, and different types of PIMC-QA, on the double-well potential of Sect. 2.1

the data barely start to go below the level $\epsilon_{res} \approx 2\delta = 0.2$, which corresponds to the metastable minimum of the potential, for the largest values of τ simulated. This means that the system had no occasion, up to these values of τ, of realizing that there was another minimum available through tunneling. Moreover, the overall slope of the data is definitely less steep than what the direct Schrödinger annealing predicts, shown for comparison by solid triangles in Fig. 13. (The absolute values of τ are not comparable between the two sets of data, because they refer to different quantities: a Schrödinger dynamics versus a Monte Carlo dynamics.) The situation improves substantially (see solid squares in Fig. 13) if we propose, as candidate Monte Carlo moves, also the so-called *instanton moves*, i.e., basically classical trajectories that move from one minimum to the other (plus fluctuations) [55]. This is, however, not a fair game: we have substantially exploited a crucial information on the landscape which is generally *not available* for a complicated optimization problem!

One other lesson we can learn, in the present context, is the role of the kinetic energy operator H_{kin} on which the quantum fluctuations are based. Up to now, we were using as H_{kin} the usual non-relativistic kinetic energy $H_{kin} = p^2/2m$, and annealed the system by increasing the mass m of the particle. (The propagator of this kinetic term is just the Gaussian, as shown in 17.) Imagine now we pretend that the particle has a relativistic 'photon-like' dispersion:

$$H_{kin} = \Gamma|p| \quad \rightarrow \quad \langle \mathbf{x}^k | e^{-\frac{\beta}{P} H_{kin}} | \mathbf{x}^{k+1} \rangle = \frac{1}{\pi} \frac{\hbar\Gamma\beta/P}{(x^k - x^{k+1})^2 + (\hbar\Gamma\beta/P)^2} \ , \quad (22)$$

and that we anneal the system by reducing to 0 the velocity Γ of the dispersion. The bisection method can be generalized for this kind of kinetic energy, and the results obtained are shown by solid diamonds in Fig. 13. As one notices, the residual energy versus τ is now considerably lower than in the non-relativistic (Gaussian) case, and even levels-off, for large τ, to the thermal limit $k_B T/2 = 0.015$ set by our finite temperature T. This example shows the important role played by the choice of the kinetic energy H_{kin} (as well as the limitations imposed by the unavoidable finite temperature T).

Summarizing, PIMC-QA suffers evidently of a number of problems: *i*) It is only a fake Monte Carlo annealing dynamics, in principle not fully representative of the true imaginary-time Schrödinger dynamics; *ii*) The sampling of relevant "action" might be highly inefficient (recall the instanton problem above) and the cure for that might not be obvious at all; *iii*) The finite temperature T imposes a lower thermal limit for the residual energy $\epsilon_{res}(\tau)$ below which we can never possibly go; *iv*) The calculation of the propagator of $e^{-H_{kin}/PT}$ might be very difficult for a kinetic term which we would like to implement (see Sect. 2.1). These various problems clearly call for an alternative to PIMC in order to implement a stochastic QA approach: we believe that the usuful alternative is given by a Green's function Monte Carlo (GFMC) method.

5 Beyond Naive Local Search

Where simple local search strategies fail, other techniques have been or can be employed in order to improve the optimization performance. Here we shall briefly discuss the important feature of focusing, and the potential benefits of GFMC, as well as alternative message-passing approaches to the 3-SAT optimization.

5.1 Focusing in 3-SAT and GFMC Quantum Annealing

One of the most popular and most effective local search algorithms for satisfiability problems is WalkSAT [56]. This heuristic approach implements a feature – called *focusing* – which is common to other successful heuristics for SAT [57, 58]: the algorithm alternates "greedy moves" (i.e., steepest descent) with completely random bit flips, the latter, however, being only applied (focused) to variables appearing in *unsatisfied* clauses (according to the rule of thumb, "if it's not broken don't fix it"). The good results achieved by WalkSAT make the implementation of the focusing very appealing for other local search algorithms too, including more sophisticated QA approaches. This is where Green's Function Monte Carlo (GFMC) seems to be the appropriate method. As a further advantage, GFMC is free from most of the problems which plague PIMC (see discussion at the end of Sect. 4.1), and is therefore, in principle, a very promising tool for QA.

GFMC is a projection technique which implements in a stochastic way an imaginary time evolution of the type

$$|\psi(t+\Delta t)\rangle = e^{-\Delta t(H_{cl}+H_{kin}(t))}|\psi(t)\rangle \ , \tag{23}$$

or any other similar evolution which aims at filtering out the ground state of $H_{cl}+H_{kin}$ (hence, the method works intrinsically at $T=0$). This can be done without having to really calculate the exponential of the Hamiltonian, or having to use a Trotter break-up [59]. Moreover, the Hamiltonian itself does not really need to be an "Hermitean" operator for GFMC to be applicable: non-symmetric operators can be dealt with as well [60]. For a QA application, one has to perform many applications of 23 with a step-wise decreasing value of the coupling $\Gamma(t)$ appearing in $H_{kin}(t)$. One crucial ingredient of GFMC is, however, a reasonable *guiding function* which allows to perform the so-called *importance sampling* [59]: this is in principle the only big limitation of GFMC, but one can try to deal with this issue with a Variational Monte Carlo (VMC) approach.

Coming back to the issue of focusing in 3-SAT, we now show how to exploit the large freedom in the choice of H_{kin} to implement some form of focusing using GFMC. The crucial idea is that we do not want to turn a spin if it appears only in satisfied clauses. Denote by E_i the energy of a given spin, defined as the sum of the clause energies E_a, 20, for all the clauses in which

i appears: $E_i = \sum_{a|i\in a} E_a$. Hence E_i simply counts the number of UNSAT clauses in which i appears, and vanishes for bits appearing only in SAT clauses. Consider now, as a kinetic term inducing quantum fluctuations, a transverse field locally weighted with E_i:

$$H^{SAT}_{kyn,\mathrm{non-herm}} = -\Gamma \sum_{i=1}^{N} \sigma_i^x E_i \ , \tag{24}$$

which is intrinsically *non-Hermitean*, since E_i does not commute with σ_i^x. $H^{SAT}_{kinnon-herm}$ correctly implements the focusing strategy of leaving untouched the variables appearing only in SAT clauses (i.e., with $E_i = 0$). If we insist in using a Hermitean kinetic term, then a faithful focusing is in general impossible: the best we can do is to consider the symmetrized version of (24):

$$H^{(SAT)}_{kyn,\mathrm{herm}} = -\Gamma \sum_{i=1}^{N} (\sigma_i^x E_i + E_i \sigma_i^x) \ , \tag{25}$$

which still allows, via the second term, transitions were a spin flip leads to $E_i > 0$. Combinations of H_{kin} in Eqs. 24 and 25 are also possible. As for the guiding function [59], the simplest possible choice would be:

$$\psi(\mathbf{S}) = \exp\left\{ -\beta E^{(SAT)}_{pot}(\mathbf{S}) \right\} \ , \tag{26}$$

where β is a variational parameter, to be optimized at each value of the transverse field Γ. Research is currently in progress, in our group, on applications of GFMC as a QA tool for optimization.

5.2 Message-Passing Optimization

In recent years, the cavity-method analysis [61, 34] of constraint satisfaction problems like the random 3-SAT has allowed to derive a new class of *Survey-Propagation-based* algorithms [29, 30, 62, 45, 63], similar in spirit to the better known belief-propagation algorithm [64], but able to deal efficiently with the clustering scenario sketched in Sect. 4.2.

A graphical representation of a 3-SAT instance can be given, in which every variable is represented by a node of type A and each clause by a node of type B [65]. A variable node is connected to a clause node if the corresponding variable is involved in the corresponding clause. In such a way, tree-like bipartite graphs can be associated to every instance. Messages are exchanged between the nodes. Let $V(i)$ be the set of the clauses neighboring a variable i, $V(a)$ the set of variables neighboring a clause a and let $V(i) \setminus a$ and $V(a) \setminus i$ denote the two sets deprived, respectively, of the elements i and a. Every variable i sends a message $h_{i\to a}$ to a clause $a \in V(a)$ telling if and how much the clauses $b \in V(i) \setminus a$ are forcing it to orient itself in the positive or in the negative direction. On the other hand, if the tendencies of all the variables in $V(a) \setminus i$

are such that a would not be already satisfied by this partial assignment, a must send a message $u_{a\to i}$ to the only left variable i, telling: "Please, orient yourself in order to satisfy me!".

To every cluster of solutions corresponds univocally a single set of messages defined over all the edges of the bipartite graph associated to the instance [62]. Since many clusters are present, one can associate to every edge the probability distribution, called *survey*, of observing a specific value of the messages h's or u's. Such probability distributions can be computed in linear time thanks to a recursive self-consistent procedure, and this information can be exploited in order to determine an assignment for the most biased variables and simplify accordingly the original problem instance. The interested reader is referred to [45] for more details on the method.

Message-passing techniques are by far the most effective for the optimization of hard random SAT instances. In the hard SAT region, they allow the determination of an exponential number of complete solutions [63], but even in the UNSAT region they are able of retrieving assignments with an energy closer to the predicted ground state than to the Gardner energy, and, anyway, definitely below the lower bound for the glassy thresholds [45]. Such performance is inaccessible to classical local search techniques and even to specialized algorithms like WalkSAT or fRRT[56, 57]. Unfortunately, they cannot be applied to the optimization of structured instances associated to a non tree-like bipartite graph and the issue of devising new heuristic methods of universal application, like CA and QA, remains still an open problem of considerable practical relevance.

6 Summary and Conclusions

We have illustrated several applications of Quantum Annealing strategies to a range of problems going from textbook toy-models (displaying in a clear way the crucial differences between classical and quantum annealing), all the way to challenging hard optimization problems (Random Ising model, TSP, 3-SAT). The techniques used to implement QA are either deterministic Schrödinger's evolutions, for the toy models, or Path Integral Monte Carlo (PIMC) approaches, for the hard optimization problems.

As a way of summary, we would like to stress some of the major points touched upon:

1. *Is Quantum really better?* Although, in the examples illustrated, QA often wins over CA, sometimes it doesn't, and this results is *a priori* not guaranteed, the outcome of the battle being strongly related to the landscape of the problem one deals with (the negative result for the 3-SAT case is particularly instructive in this respect);
2. *Limitations of PIMC.* PIMC-QA suffers from several limitations (finite temperature T, sampling problems for the action, difficulties with the

Trotter break-up) which suggest investigating in the future other Quantum Monte Carlo approaches to QA, like Green's Function Monte Carlo.
3. *Role of kinetic energy.* The choice of the kinetic energy is clearly all important in QA: Sect. 4.4, illustrating the improvements in annealing a double-well potential upon using a relativistic kinetic energy, is particularly instructive.

In conclusion, it is quite clear that quantum annealing, although potentially useful and sometimes more convenient than classical annealing, is not capable, in general, of finding solutions of NP-complete problems in polynomial time. Nevertheless, understanding when and how quantum mechanics can quantitatively improve on the solution of hard optimization problems is still an open and timely issue.

References

1. S. Kirkpatrick, C.D. Gelatt, Jr., M.P. Vecchi, Science **220**, 671 (1983); 171, 186
2. A.B. Finnila, M.A. Gomez, C. Sebenik, C. Stenson, J.D. Doll, Chem. Phys. Lett. **219**, 343 (1994). 171
3. T. Kadowaki, H. Nishimori: Phys. Rev. E **58**, 5355 (1998). 171, 172, 189
4. J. Brooke, D. Bitko, T.F. Rosenbaum, G. Aeppli: Science **284**, 779 (1999). 171, 172, 188
5. G. Santoro, R. Martoňák, E. Tosatti, R. Car: Science **295**, 2427 (2002). 171, 172, 183, 187
6. E. Farhi, J. Goldstone, S. Gutmann, J. Lapan, A. Lundgren, D. Preda: Science **292**, 472 (2001). 172
7. L. Stella, G. E. Santoro, and E.Tosatti: to appear on Phys. Rev. B; preprint `cond-mat/0502129` 172, 173, 175, 176, 178, 179, 181, 182, 183, 184
8. Y.H. Lee, B.J. Berne: J. Phys. Chem. A **104**, 86 (2000). 172
9. Y.H. Lee, B.J. Berne: J. Phys. Chem. A **105**, 459 (2001). 172
10. R. Martoňák, G. Santoro, E. Tosatti: Phys. Rev. B **66**, 94203 (2002). 172, 187
11. R. Martoňák, G.E. Santoro, E. Tosatti: Phys. Rev. E **70**, 057701 (2004). 172, 190
12. D. Battaglia, G. Santoro, E. Tosatti: to appear on PRE; preprint *cond-mat/0502468*. 172, 192, 193, 195
13. P.F. Stadler and W. Schnabl: Phys. Lett. A **161**, 337 (1992). 173
14. L. Stella, G.E. Santoro, and E. Tosatti: in preparation. 173, 199
15. N.G. van Kampen: *Stochastic processes in physics and chemistry*, North-Holland, Amsterdam (1987). 174, 181
16. D.A. Huse, D.S. Fisher: Phys. Rev. Lett. **57**, 2203 (1986). 178, 182
17. L.D. Landau: Phys. Z. Sowjetunion **2**, 46 (1932). 179
18. C. Zener: Proc. Royal Soc. A **137**, 696 (1932). 179
19. S. Shinomoto and Y. Kabashima: J. Phys. A **24** L141 (1991); Y. Kabashima and S. Shinomoto: J. Phys. Soc. Japan **60** 3993 (1991). 181, 182
20. P.A. Lee and T.V. Ramakrishnan: Rev. Mod. Phys. **57**, 287 (1985). 183
21. M. Suzuki: Prog. Theor. Phys. **56**, 1454 (1976). 186
22. C.H. Papadimitriou: *Combinatorial Optimization: Algorithms and Complexity* (Dover, NY 1998). 186
23. H. Nishimori: *Statistical Physics of Spin Glasses and Information Processing* (Oxford University Press, 2001). 187

24. Special Issue on *NP-hardness and Phase transitions*, ed. by O. Dubois, R. Monasson, B. Selman and R. Zecchina, Theor. Comp. Sci. **265**, Issue: 1-2 (2001). 187, 192
25. J.J. Hopfield and D.W. Tank: Science **233**, 625 (1986). 187, 189
26. M. Mézard, G. Parisi: Europhys. Lett. **2**, 913 (1986) 187, 189
27. A.G. Percus, O.C. Martin: Jour. Stat. Phys. **94**, 739–758 (1999). 187, 189
28. D.S. Dean, D. Lancaster, S.N. Majumdar: J. Stat. Mech. L01001 (2005). 187, 189
29. M. Mézard, G. Parisi, R. Zecchina, Science 297, 812 (2002); 187, 192, 202
30. M. Mezard, R. Zecchina: Phys. Rev. E **66**, 56126 (2002). 187, 192, 202
31. S. Mertens: Phys. Rev. Lett. **81**, 4281- 4284 (1988). 187
32. M. Weigt, A.K. Hartmann: Phys. Rev. Lett. **84**, 6118 (2000) 187
33. A. Braunstein, R. Mulet, A. Pagnani, M. Weigt, R. Zecchina: Phys. Rev. E **68**, 036702 (2003) 187
34. G. Parisi, M. Mézard, M.Virasoro: *Spin Glass Theory and Beyond* (World Scientific, Singapore 1987). 187, 202
35. C. H. Papadimitriou, K. Steiglitz: *Combinatorial Optimization: Algorithms and Complexity* (Prentice-Hall, Englewood Cliffs, NJ, 1982). 187
36. M.R. Garey, D.S. Johnson: *Computers and Intractability* (Freeman, New York 1979). 187
37. D. Mitchell, B. Selman, H. Levesque: Hard and Easy Distribution of SAT Problems. In: *Proc. of the Tenth National Conference on Artificial Intelligence*, (AAAI-Press, 1992), p. 459. 187
38. M. Mezard, F. Ricci-Tersenghi, R. Zecchina: J. Stat. Phys **111**, 505 (2003). 187
39. F. Barahona: J. Phys. A **15**, 3241 (1982). 187
40. C. De Simone *et al.*: J. Stat. Phys. **80**, 487 (1995). 187
41. D.S. Johnson and L.A. McGeoch: In *Local Search in Combinatorial Optimization*, ed. E.H.L. Aarts and J.K. Lenstra (J. Wiley and Sons, London, 1997, pp. 215-310). 189, 190
42. P. F. Stadler: Towards a Theory of Landscapes. In: *Complex Systems and Binary Networks*, ed. by R. Lopez-Pena, R. Capovilla, R. Garca-Pelayo, H. Waelbroeck, and F. Zertuche (Springer Verlag, Berlin, New York 1995), pp. 77–163. 189
43. See `http://www.iwr.uni-heidelberg.de/groups/comopt/software/TSPLIB95` 190
44. See `http://www.intellektik.informatik.tu-darmstadt.de/SATLIB/` 191
45. D. Battaglia, M. Kolář, R. Zecchina: Phys. Rev. E **70**, 036107 (2004). 192, 202, 203
46. A. Montanari, G. Parisi, and F. Ricci-Tersenghi: J. Phys. A **37**, 2073 (2004). 192
47. Z. Michalewicz: *Genetic algorithms + data structures = evolution programs*, 3rd ed. (Springer-Verlag, Berlin 1996). 192
48. J.R. Koza: *Genetic Programming: On the Programming of Computers by Means of Natural Selection* (MIT Press, Cambridge MA, 1992). 194
49. J.H. Holland: Proc. Int. Un. Physiol. Soc. **3**, 330 (1962). 194
50. J.H. Holland: Processing and Processors for schemata. In: *Associative Information Processing* (American Elsevier, New York 1971). 194
51. J.P. Bouchaud, V. Dupuis, J. Hammann, E. Vincent: Phys. Rev. B **65**, 24439 (2001). 195
52. A. Montanari and R. Zecchina: Phys. Rev. Lett. **88**, 178701 (2002). 195
53. M. Takahashi and M. Imada: J. Phys. Soc. Jpn. **53**, 3765 (1984). 199
54. D. M. Ceperley: Rev. Mod. Phys. **67**, 275 (1995). 199
55. J.W. Negele and H. Orland: *Quantum Many-Particle Systems* (Addison-Wesley, 1988) 200
56. B. Selman, H. Kautz and B. Cohen: In: Proc. AAAI-94 (AAAI Press, Seattle WA 1994), pp. 337-343. 201, 203

57. S. Seitz, P. Orponen: An efficient local search method for random 3-satisfiability. In: *Proc. LICS'03 Workshop on Typical Case Complexity and Phase Transitions* (Ottawa, Canada, 2003); Electronic Notes in Discrete Mathematics Vol. 16 (Elsevier, Amsterdam, 2003). 201, 203
58. S. Boettcher, A. Percus: Phys. Rev. Lett. **86**, 5211 (2001). 201
59. N. Trivedi and D. M. Ceperley: Phys. Rev. B **41**, 4552 (1990). 201, 202
60. G. Santoro, S. Sorella, L. Guidoni, A. Parola, and E. Tosatti: Phys. Rev. Lett. **83**, 3065 (1999). 201
61. L. Onsager: J. Am. Chem. Soc. **58**, 1486 (1936). 202
62. A. Braunstein, M. Mézard, R. Zecchina: Survey propagation: an algorithm for satisfiability. To appear in *Random Structures and Algorithms*; preprint `cs.CC/0212002` 202, 203
63. D. Battaglia, A. Braunstein, J. Chavas, R. Zecchina: Source coding by efficient selection of ground states clusters, preprint `cond-mat/0412652`. 202, 203
64. J.S. Yedidia, W.T. Freeman and Y. Weiss: Generalized Belief Propagation. In: *Advances in Neural Information Processing Systems 13* (MIT press 2001), pp. 689–695. 202
65. F. R. Kschischang, B. J. Frey, and H.-A. Loeliger: IEEE Trans. Inf. Theory **47**, 498 (2002). 202

Simulated Quantum Annealing by the Real-time Evolution

Sei Suzuki[1,2] and Masato Okada[1,2]

[1] Graduate School of Frontier Sciences, University of Tokyo, Kashiwa 277-8561, Japan
[2] Brain Science Institute, RIKEN, Wako 351-0198, Japan
sei@mns.k.u-tokyo.ac.jp

1 Introduction

It has been revealed during the last few decades that approaches originating from the physics succeeds in solving combinatorial optimization problems[1]. The simulated thermal annealing method created such a close relation between physics and optimization problems. The quantum annealing method was born as an analogue of conventional thermal annealing[2, 3]. In spite of its origin, the mechanism and formulation of quantum annealing are fundamentally different from those of simulated thermal annealing. The former is based on the dynamics in quantum mechanics, while the latter is on the classical dynamics. Furthermore the quantum annealing is basically formulated for zero temperature in contrast to finite temperature simulation of thermal annealing. Because of these differences, the quantum annealing is expected as a novel efficient method for optimization problems. In practice, an experiment using spin-glass material has shown the superiority of the quantum annealing over the thermal annealing [4]. Simulations by means of the path-integral quantum Monte-Carlo have also shown that an optimization in the spin-glass model is achieved in a less time by the quantum annealing than by the thermal annealing [5]. However study on quantum annealing is insufficient for establishing this method as an effective optimization method. We focus in this paper on some basic features and a new method for implementation of the simulated quantum annealing.

A combinatorial optimization problem is a big subject relating with a variety of topics in sciences. It is classified mathematically into some classes according to the hardness. The class of easy problems is called P class. The problem in P class is a decision problem, whose solution is given by "Yes" or "No", and can be solved by deterministic processes in time of polynomial order of the problem size. The decision problem which can be solved by processes of the non-deterministic Turing machine in a polynomial time constructs the class NP. The NP class contains the P class by definition.

S. Suzuki and M. Okada: *Simulated Quantum Annealing by the Real-time Evolution*, Lect. Notes Phys. **679**, 207–238 (2005)
www.springerlink.com

The class of hardest decision problems is referred to as NP-hard class. The solution of an NP-hard problem derives the solution of any NP problem by a polynomial time of deterministic processes. In principle, the number of combinations in the combinatorial problem increases exponentially with increasing the problem size. No deterministic algorithm, by which an NP-hard problem is solved in a polynomial time of processes, has been discovered so far. Hence it takes exponentially long time to obtain the solution of NP-hard problems. It is an important work to find efficient algorithms, including deterministic polynomial-time algorithm if it exists, for NP-hard problems.

The combinatorial optimization problem can be formulated as the minimization problem of a cost function. One can first consider that the descending method may be valid for the minimization. However one of remarkable properties of the problem is that the cost function has a large number of local minima. Hence the ordinary descending method is useless. The simulated thermal annealing was proposed for the minimization of such complicated cost functions from the statistical mechanical standpoint. In terms of physics, the cost function is replaced by a classical Hamiltonian represented by randomly coupled Ising spin variables. Usually the classical Hamiltonian of the optimization problem is written as

$$\mathcal{H}_0 = -\sum_i J_i S_i^z - \sum_{ij} J_{ij} S_i^z S_j^z - \sum_{ijk} J_{ijk} S_i^z S_j^z S_k^z - \cdots, \tag{1}$$

where S_i^z is the Ising spin variable, and J_i, J_{ij}, J_{ijk}, $\cdots$ are disordered coupling constant. The minimization of the cost function corresponds to finding the ground state of the Hamiltonian (1). In order to obtain the ground state, the Boltzmann distribution at a finite temperature is considered in the simulated thermal annealing. It is supposed that the finite temperature distribution of Ising spin configuration is generated by means of the Metropolis Monte-Carlo algorithm[6]. If the temperature is fixed below the energy barrier between local minima, the distribution of thermal equilibrium is hard to obtain. This is because the distribution at a configuration corresponding to a local minimum is overestimated. On the other hand large thermal fluctuations overcome energy barriers if the temperature is sufficiently high. The distribution of equilibrium is easy to obtain in this case. The thermal annealing method produces the correct distribution at a low temperature through a dynamical process from high temperature to low temperature. A distribution at high temperature is changed gradually toward that at low temperature with lowering temperature. The annealing speed is crucial here. It has been known that the optimum annealing schedule is $T \propto 1/\ln t$[7]. Hence, if the temperature is lowered slower than the inverse of logarithm of the time, the ground state is obtained in the infinite time limit in principle.

In contrast to thermal fluctuations in the thermal annealing, quantum fluctuations are exploited in the quantum annealing[8]. Quantum fluctuations are induced by the transverse field for the Ising spin system. The transverse field plays the role similar to the temperature. The ground state of random

Ising models corresponding to the solution of optimization problems is typically characterized by the replica symmetry breaking[9]. Thermal fluctuations causes the restoration of replica symmetry. Quantum fluctuations also drives the state into a phase in which the replica symmetry is preserved. The temperature and transverse field are both parameters which control strength of fluctuations. It is remarkable here that the restoration of replica symmetry of the infinite-range random Ising (Sherrington-Kirkpatric[10]) model takes place at the infinitesimal transverse field, though it does at a finite temperature[11, 12]. Hence it is inferred that the random Ising system is more sensitive to quantum fluctuations than thermal fluctuations.

In the quantum annealing method, a quantum spin system composed of a random Ising Hamiltonian and the Zeeman energy accompanying transverse field is considered. The system with zero transverse field is identical to the classical system which is to be solved. If the transverse field is sufficiently large compared to the typical value of coupling constants in Ising Hamiltonian, all of the spins in the ground state are parallel with the transverse field. In the procedure of quantum annealing, the transverse field is decreased gradually toward zero field. The spin state changes dynamically with time according to the Schrödinger equation. If the change in the total Hamiltonian is sufficiently slow and the energy levels of ground and first excited states do not cross during the process, the spin state goes to the ground state of the classical Hamiltonian finally. It should be noted here that the dynamical process in the quantum annealing is governed by the Schrödinger equation in principle, different from the stochastic Markovian process in thermal annealing. Therefore we need not to be bound by the schedule of the thermal annealing. We mention the time schedule in the quantum annealing in detail in the next section.

Although any method provides the exact solution in the infinite time, we have to terminate the simulation in a finite time in actual. Then the obtained solution contains an error. The magnitude of the error for a wasted time indicates the efficiency of the used method. The residual energy is appropriate to the estimation of the error. It is defined by the energy difference between the obtained solution and the exact one. In case of the thermal annealing, the residual energy has been known to decrease with annealing time as[13, 14]

$$E_{\mathrm{res}}^{\mathrm{TA}} \sim \frac{A}{(\ln \tau)^{\zeta}}, \quad 1 \leq \zeta \leq 2 \tag{2}$$

for long annealing time, where $E_{\mathrm{res}}^{\mathrm{TA}}$ and τ stand for the residual energy and the annealing time respectively, and A is a constant. It has been shown by quantum Monte-Carlo calculation that the residual energy after quantum annealing is smaller than that after thermal annealing[5]. The authors of [5] have also predicted the asymptotic behavior of the residual energy similar to (2). However this prediction has not been confirmed, since the quantum Monte-Carlo method does not have accuracy enough. One of the purposes of this article is to clarify the asymptotic feature of the residual energy after the quantum annealing[15].

One of important aspects of the quantum annealing method is that this method provides a quantum algorithm for combinatorial optimization problems. Since Shor's discovery of quantum algorithm for factorization[16], quantum computation has attracted a lot of attentions in physics and computer science. Although there exists no rigorous proof that shows the NP-complete problem is reduced to a P problem, a numerical study for small-sized exact-cover problems using quantum annealing algorithm has suggested polynomial scaling of the process time by the problem size[17]. Furthermore, an elementary experiment of quantum computation using quantum annealing algorithm for a combinatorial optimization problem has been carried out[18, 19]. The quantum computation may open great possibilities for quantum annealing algorithm in the future.

Our interest in this paper lies in the use of quantum annealing method in the conventional computer. In order to explore fundamental features of quantum annealing algorithm and also to apply this algorithm to several problems, developments in simulations are demanded. The quantum Monte-Carlo method has been already applied for simulated quantum annealing[20, 21]. Large-sized problems can be handled by this method. However the dynamics of quantum annealing process is replaced in quantum Monte-Carlo by a stochastic dynamics. It is not clear whether the mechanism of quantum annealing method works correctly in stochastic dynamics. Other methods which involves real-time quantum dynamics are necessary for computation with strict grounds. In the present article, we propose application of the density matrix renormalization group method to simulated quantum annealing.

We organize this article as follows. In the next section, we formulate the quantum annealing method and explain the mechanism behind the algorithm. We review the theory on adiabatic evolution in the quantum mechanics in this section. The Sect. 3 is devoted to study on residual energy after quantum annealing. We discuss a new way of simulation for quantum annealing in Sect. 4. The article is concluded in Sect. 5.

2 Formulation and Mechanism of Quantum Annealing

2.1 Formulation of Quantum Annealing

The quantum annealing method brings about a solution of the classical problem through the dynamical process in quantum mechanics. Let us consider a classical Hamiltonian $\mathcal{H}_0$. We suppose that $\mathcal{H}_0$ has only diagonal elements for a basis. A typical example of $\mathcal{H}_0$ is an Ising Hamiltonian. The problem is to find the ground state of $\mathcal{H}_0$. For this classical problem, we introduce a quantum tunneling Hamiltonian $\mathcal{H}_T$. It is assumed that $\mathcal{H}_T$ has off-diagonal elements and the ground state of $\mathcal{H}_T$ is obtained easily. If $\mathcal{H}_0$ is an Ising Hamiltonian, $\mathcal{H}_T$ is introduced by an interaction between the spin and transverse magnetic field. Then we consider the following time-dependent Hamiltonian

composed of $\mathcal{H}_0$ and $\mathcal{H}_T$.

$$\mathcal{H}(t) = f(t)\mathcal{H}_T + g(t)\mathcal{H}_0 \ .$$

The time dependence of $\mathcal{H}(t)$ is represented by $f(t)$ and $g(t)$. These functions of time are monotonic and satisfy $f(0) \gg g(0)$, $f(t \to \infty) \to 0$, and $g(t \to \infty) \to 1$. The Hamiltonian $\mathcal{H}(t)$ is dominated by $\mathcal{H}_T$ at initial time ($t = 0$), while it becomes $\mathcal{H}_0$ at last. The change in $\mathcal{H}(t)$ is continuous.

The evolution of quantum state is essential in the quantum annealing method. According to the principle of the quantum mechanics, the real-time evolution of the state vector $|\Psi(t)\rangle$ is governed by the Schrödinger equation.

$$i\frac{d}{dt}|\Psi(t)\rangle = \mathcal{H}(t)|\Psi(t)\rangle \ . \tag{3}$$

We impose the initial condition given by

$$\mathcal{H}(0)|\Psi(0)\rangle = \epsilon_g(0)|\Psi(0)\rangle \ , \tag{4}$$

where $\epsilon_g(0)$ stands for the ground eigenenergy of the initial Hamiltonian $\mathcal{H}(0)$. Namely the initial state is assumed to be the ground state of the initial Hamiltonian.

The quantum annealing means gradual reduction of quantum fluctuations. Quantum fluctuations are represented by the tunneling Hamiltonian. The process of quantum annealing is realized by lowering the ratio of the tunneling Hamiltonian in the total Hamiltonian. If the change in Hamiltonian with time is sufficiently slow, the state initially at the ground state of the Hamiltonian evolves adiabatically. Then, when quantum fluctuations vanish after quantum annealing, the state becomes the approximate ground state of the classical Hamiltonian as far as the instantaneous ground state of $\mathcal{H}(t)$ does not degenerate at any time. This is an outline of the quantum annealing method.

If the instantaneous ground state happens to degenerate at a time, the state does not always evolve as the ground state. However the classical Hamiltonian of the problem is usually complicated. Hence we may suppose that the time-dependent Hamiltonian has no accidental symmetry which gives rise to degeneracy of the ground state.

The adiabatic evolution of the quantum state is influenced by the way of time-dependence of the Hamiltonian. Although there are many choices of $f(t)$ and $g(t)$, inappropriate choice causes unexpected non-adiabatic transitions to excited states. Kadowaki and Nishimori have studied several schedules for quantum annealing in literature[3], and found that the state does not converge on the true ground state for fast decaying $f(t)$ ($= 1/t$ for instance) when $g(t) = 1$. In the present article, we employ the following time-dependent Hamiltonian.

$$\mathcal{H}(t) = \left(1 - \frac{t}{\tau}\right)\mathcal{H}_T + \frac{t}{\tau}\mathcal{H}_0, \tag{5}$$

where τ is a parameter which stands for the annealing time. We define this Hamiltonian only in the time period from $t = 0$ to $t = \tau$. The Hamiltonian is identical with the tunneling Hamiltonian at the initial time, i.e., $\mathcal{H}(0) = \mathcal{H}_T$. It changes linearly in the time and becomes the classical Hamiltonian exactly at the final time, $\mathcal{H}(\tau) = \mathcal{H}_0$. Merits of this Hamiltonian lie in the following two facts. The first is that the initial state is exactly given by the ground state of $\mathcal{H}_T$. Construction of $\mathcal{H}_T$ whose ground state is obvious is usually easy. For precise calculations, it is necessary to give the initial state by the exact ground state. If the initial Hamiltonian contains both $\mathcal{H}_T$ and $\mathcal{H}_0$, it is difficult to obtain the exact ground state. The second is that the adiabatic theorem in the quantum mechanics guarantees the final state to converge on the exact ground state of the classical Hamiltonian for $\tau \to \infty$, if there is no degeneracy in the instantaneous ground state of the Hamiltonian at any time. We mention the adiabatic theorem in the next subsection in detail. For other schedule of quantum annealing, $f(t) = 1/t$ and $g(t) = 1$ for instance, there has been no proof that promises the convergence on the true solution.

We comment on the form of the Hamiltonian. The Hamiltonian (5) looks unphysical since the classical term grows from nothing with time. However the aim is in obtaining the ground state of the classical Hamiltonian as a result of quantum annealing. Therefore there is no physical need for the form of the Hamiltonian on the way to the final form.

2.2 Adiabatic Evolution of Quantum States

It has been known that the adiabatic theorem in the quantum mechanics accounts for the property of adiabatic evolution of quantum states when the change in the time-dependent Hamiltonian is sufficiently slow. We review the adiabatic theorem in the quantum mechanics in the next small section. On the other hand, the Landau-Zener theory has been known to describe the non-adiabatic transition when the change in the Hamiltonian is not sufficiently slow. We also review the Landau-Zener theory in the small section after the next one. The subsequent arguments follow [22] for the adiabatic theorem and [24] for the Landau-Zener theory.

Adiabatic Theorem

The adiabatic theorem in quantum mechanics accounts for the adiabatic time-evolution of quantum state. The deviation of an evolved state from the simultaneous eigenstate of the Hamiltonian is estimated, and the condition for adiabatic evolution is derived in the following.

We consider the time-dependent Hamiltonian,

$$\begin{aligned}\mathcal{H}_\tau(t) &= \left(1 - \frac{t}{\tau}\right)\mathcal{H}_A + \frac{t}{\tau}\mathcal{H}_B = (1-s)\,\mathcal{H}_A + s\mathcal{H}_B \\ &= \tilde{\mathcal{H}}(s)\ ,\end{aligned}$$

where τ is a parameter which means the time period of the evolution and $s = t/\tau$ is the dimensionless time. We assume that instantaneous eigenstates of the time-dependent Hamiltonian do not degenerate at any time. Denoting the state vector at the time s by $|\psi_\tau(s)\rangle$, we introduce the time-evolution operator.

$$|\psi_\tau(s)\rangle = U_\tau(s)|\psi_\tau(0)\rangle \ .$$

The Schrödinger equation is written in terms of the dimensionless time as

$$i\frac{d}{ds}|\psi_\tau(s)\rangle = \tau\tilde{\mathcal{H}}(s)|\psi_\tau(s)\rangle \ .$$

The equation of motion of $U_\tau(s)$ is given by

$$i\frac{d}{ds}U_\tau(s) = \tau\tilde{\mathcal{H}}(s)U_\tau(s) \ . \tag{6}$$

Next we introduce the projection operator, $P_j(s)$, of state vectors on instantaneous eigenstate of $\tilde{\mathcal{H}}(s)$. Writing the instantaneous eigenenergy of $\tilde{\mathcal{H}}(s)$ by $\varepsilon_j(s)$, the projection operator satisfies

$$\tilde{\mathcal{H}}(s)P_j(s)|\phi\rangle = \varepsilon_j(s)P_j(s)|\phi\rangle, \quad P_j(s)P_k(s) = \delta_{jk}P_j(s), \quad \sum_j P_j(s) = 1 \ ,$$

where $|\phi\rangle$ is an arbitrary state and δ_{jk} is the Kronecker's delta. The Hamiltonian is written in terms of the projection operator by

$$\tilde{\mathcal{H}}(s) = \sum_j \varepsilon_j(s)P_j(s) \ . \tag{7}$$

We define the axis-rotation operator $A(s)$ by

$$P_j(s) = A(s)P_j(0)A^\dagger(s) \ . \tag{8}$$

The axis-rotation operator rotates the axis of the projection space from that of the initial time to that of the time s. $A(s)$ is a unitary operator which satisfies $A(s)A^\dagger(s) = A^\dagger(s)A(s) = 1$. Using the axis-rotation operator, we moreover define an hermite operator $K(s)$

$$i\frac{d}{ds}A(s) = K(s)A(s), \quad -i\frac{d}{ds}A^\dagger(s) = A^\dagger(s)K(s) \ . \tag{9}$$

The equation of motion of $P_j(s)$ is written in terms of $K(s)$ by

$$\frac{d}{ds}P_j(s) = -i\left[K(s), P_j(s)\right] \ . \tag{10}$$

This equation is the condition of necessity and sufficiency of (8). The reason is shown as follows.

proof of necessity
We assume $P_j(s) = A(s)P_j(0)A^\dagger(s)$.

$$\begin{aligned}\frac{d}{ds}P_j(s) &= \frac{d}{ds}\left(A(s)P_j(0)A^\dagger(s)\right)\\ &= \frac{dA(s)}{ds}P_j(0)A^\dagger(s) + A(s)P_j(0)\frac{dA^\dagger(s)}{ds}\\ &= -i\left[K(s), P_j(s)\right] \ .\end{aligned}$$

proof of sufficiency
We assume $\frac{d}{ds}P_j(s) = -i\left[K(s), P_j(s)\right]$.

$$\begin{aligned}&\frac{d}{ds}\left(A^\dagger(s)P_j(s)A(s)\right)\\ &= \frac{dA^\dagger(s)}{ds}P_j(s)A(s) + A^\dagger(s)\frac{dP_j(s)}{ds}A(s) + A^\dagger(s)P_j(s)\frac{dA(s)}{ds}\\ &= iA^\dagger(s)\Big(K(s)P_j(s) - [K(s), P_j(s)] - P_j(s)K(s)\Big)A(s)\\ &= 0 \ .\end{aligned}$$

Since $A(0) = A^\dagger(0) = 1$, we obtain

$$A^\dagger(s)P_j(s)A(s) = A^\dagger(0)P_j(0)A(0) = P_j(0) \ .$$

This yields

$$P_j(s) = A(s)P_j(0)A^\dagger(s) \ .$$

There is an ambiguity in the equation of motion of $P_j(s)$, since the right hand side of (10) is not affected by a transformation of $K(s) \to K(s) + \sum_k P_k(s)\mathcal{O}_k(s)P_k(s)$ for an arbitrary hermite operator $\mathcal{O}_j(s)$. This ambiguity comes from the fact that the diagonal elements of $K(s)$ is not determined by the series of (8), (9), and (10). In order to settle the diagonal element, we impose the following condition.

$$P_j(s)K(s)P_j(s) = 0 \quad (j = 1, 2, \cdots) \ . \tag{11}$$

Now we introduce the axis-rotation representation of operators by

$$\tilde{\mathcal{H}}^A(s) = A^\dagger(s)\tilde{\mathcal{H}}(s)A(s) = \sum_j \varepsilon_j(s)A^\dagger(s)P_j(s)A(s) = \sum_j \varepsilon_j(s)P_j(0) \tag{12}$$

$$U_\tau^A(s) = A^\dagger(s)U_\tau(s)$$

$U_\tau^A(s)$ obeys the following equation of motion.

$$\begin{aligned}i\frac{d}{ds}U_\tau^A(s) &= i\frac{dA^\dagger(s)}{ds}U_\tau(s) + iA^\dagger(s)\frac{dU_\tau(s)}{ds}\\ &= \left(\tau\tilde{\mathcal{H}}^A(s) - K^A(s)\right)U_\tau^A(s) \ ,\end{aligned}$$

where (9) and (6) are used for arrangements. Since $\tilde{\mathcal{H}}^A(s)$ and $K^A(s)$ are independent of τ, the first term dominates the right hand side of the above equation in infinite limit of τ. Namely the equation of $U_\tau^A(s)$ for $\tau \to \infty$ should be

$$i\frac{d}{ds}U_\tau^A(s) \cong \tau\tilde{\mathcal{H}}^A(s)U_\tau^A(s) \; .$$

We consider an operator $V_\tau^A(s)$ which obeys

$$i\frac{d}{ds}V_\tau^A(s) = \tau\tilde{\mathcal{H}}^A(s)V_\tau^A(s) \; .$$

The operator $V_\tau^A(s)$ is expanded using the projection operator at the initial time as

$$V_\tau^A(s) = \sum_j \eta_{\tau j}(s)P_j(0) \; .$$

By substitution of (12) in the equation of $V_\tau^A(s)$, it is found that coefficients of expansion satisfy

$$i\frac{d}{ds}\eta_{\tau j}(s) = \tau\varepsilon_j(s)\eta_{\tau j}(s) \; .$$

Integration of this equation yields

$$\eta_{\tau j}(s) = \exp\left[-i\tau\phi_j(s)\right], \quad \phi_j(s) \equiv \int_0^s d\sigma\varepsilon_j(\sigma) \; .$$

Hence we obtain

$$V_\tau^A(s) = \sum_j e^{-i\tau\phi_j(s)}P_j(0) \; .$$

Comparing the equations of $U_\tau^A(s)$ and $V_\tau^A(s)$, it is conjectured that $U_\tau^A(s) \cong V_\tau^A(s)$, i.e., $U_\tau(s) \cong A(s)V_\tau^A(s)$ for $\tau \to \infty$.

We define an operator corresponding to the overlap between $U_\tau^A(s)$ and $V_\tau^A(s)$ by

$$W(s) = V_\tau^{A\dagger}(s)U_\tau^A(s) = V_\tau^{A\dagger}(s)A^\dagger(s)U_\tau(s) \; .$$

The equation of motion of $W(s)$ is given by

$$\begin{aligned} i\frac{d}{ds}W(s) &= i\frac{d}{ds}V_\tau^{A\dagger}(s)U_\tau^A(s) + iV_\tau^{A\dagger}(s)\frac{d}{ds}U_\tau^A(s) \\ &= -V_\tau^{A\dagger}(s)K^A(s)U_\tau^A(s) \\ &= -\sum_{jk} e^{i\tau(\phi_j(s)-\phi_k(s))}P_j(0)K^A(s)P_k(0)W(s) \\ &= -\sum_{jk} e^{i\tau(\phi_j(s)-\phi_k(s))}K_{jk}^A(s)W(s) \; , \end{aligned}$$

where the matrix element of $K^A(s)$ is defined by

$$K^A_{jk}(s) = P_j(0)K^A(s)P_k(0) = P_j(0)A^\dagger(s)K(s)A(s)P_k(0)$$
$$= A^\dagger(s)P_j(s)K(s)P_k(s)A(s)\ .$$

The diagonal element of $K^A(s)$ vanishes because of the condition (11) imposed on $K(s)$. We define an integral,

$$F_{\tau jk}(s) = \int_0^s d\sigma e^{i\tau(\phi_j(\sigma)-\phi_k(\sigma))}K^A_{jk}(\sigma) \tag{13}$$
$$= \frac{1}{i\tau}\left[e^{i\tau(\phi_j(\sigma)-\phi_k(\sigma))}\frac{K^A_{jk}(\sigma)}{\varepsilon_j(\sigma)-\varepsilon_k(\sigma)}\Big|_0^s \right.$$
$$\left. - \int_0^s d\sigma e^{i\tau(\phi_j(\sigma)-\phi_k(\sigma))}\frac{d}{d\sigma}\left[\frac{K^A_{jk}(\sigma)}{\varepsilon_j(\sigma)-\varepsilon_k(\sigma)}\right]\right],$$

where we note that $\frac{d}{d\sigma}(\phi_j(\sigma)-\phi_k(\sigma)) = \varepsilon_j(\sigma)-\varepsilon_k(\sigma)$. Same as $K^A(s)$, $F_\tau(s)$ has no non-zero diagonal element. For off-diagonal elements, the second term is negligible. This is because $\phi_j(\sigma)-\phi_k(\sigma)$ is a monotonic function of σ and thus the integrand highly oscillates for τ much larger than inverse of the minimum of $\varepsilon_j(s)-\varepsilon_k(s)$. The first term has a finite upper bound, since the eigenenergies of states j and k differ from each other. Hence we find that $F_{\tau jk}(s)$ takes a value of the order of $1/\tau$ for large τ,

$$F_{\tau jk}(s) \cong O\left(\frac{1}{\tau}\right)\ . \tag{14}$$

Now the equation of $W(s)$ is arranged in an integral equation.

$$W(s) = 1 + i\sum_{jk}\int_0^s d\sigma e^{i\tau(\phi_j(\sigma)-\phi_k(\sigma))}K^A_{jk}(\sigma)W(\sigma)$$

Taking (13) into account, this equation is expanded perturbatively as follows.

$$W(s) = 1 + i\sum_{jk}F_{\tau jk}(s) + \frac{i^2}{2!}\left(\sum_{jk}F_{\tau jk}(s)\right)^2 + \cdots$$

Due to (14), we obtain an approximation formula of $W(s)$ for infinite τ up to the order of $1/\tau$.

$$W(s) \cong 1 + i\sum_{jk}F_{\tau jk} \cong 1 + O\left(\frac{1}{\tau}\right)\ . \tag{15}$$

Thus time-evolution operator is written as

$$U_\tau(s) \sim A(s)V^A_\tau(s)\left(1 + i\sum_{j,k}F_{\tau jk}(s)\right)\ .$$

The deviation of an evolved state from the eigenstate is estimated as follows. We assume that the initial state is the ground eigenstate of the initial Hamiltonian. We denote the instantaneous eigenstate of the time-dependent Hamiltonian by $|n(s)\rangle$. The eigenstate at a time $t = \tau s$ is related to that at the time $t = 0$ by $|n(s)\rangle = A(s)V_\tau^A(s)|n(0)\rangle$. The initial state is written as $|\psi_\tau(0)\rangle = |0(0)\rangle$. Then the deviation of the state at the time t from the instantaneous eigenstate is represented by

$$\begin{aligned}\eta &= \sum_{n\neq 0} |\langle n(s)|U_\tau(s)|0(0)\rangle|^2 \\ &= \sum_{n\neq 0} \langle 0(0)|U_\tau^\dagger(s)A(s)V_\tau^A(s)|n(0)\rangle\langle n(0)|V_\tau^{A\dagger}(s)A^\dagger(s)U_\tau(s)|0(0)\rangle \\ &= \sum_{n\neq 0} \langle 0(0)|W^\dagger(s)|n(0)\rangle\langle n(0)|W(s)|0(0)\rangle \ . \end{aligned} \tag{16}$$

Substituting (15), η is written as

$$\eta \cong \sum_{n\neq 0} \langle 0(0)|F_{\tau 0n}^*(s)|n(0)\rangle\langle n(0)|F_{\tau n0}(s)|0(0)\rangle \ .$$

Here we recall the definition of F_τ, i.e., (13). Substituting the definition of K^A and taking (8) and (9) into account, $F_{\tau n0}$ is written as follows.

$$\begin{aligned}&\langle n(0)|F_{\tau n0}(s)|0(0)\rangle \\ &= \langle n(0)| \int_0^s ds' e^{i\tau \int_0^{s'} ds_0(\varepsilon_n(s_0)-\varepsilon_0(s_0))} P_n(0)A^\dagger(s')K(s')A(s')P_0(0)|0(0)\rangle \\ &= \int_0^s ds' e^{i\tau \int_0^{s'} ds_0(\varepsilon_n(s_0)-\varepsilon_0(s_0))} \langle n(0)|A^\dagger(s')i\sum_j \frac{dP_j(s')}{ds'}P_j(s')A(s')|0(0)\rangle \\ &= i\int_0^s ds' e^{i\tau \int_0^{s'} ds_0(\varepsilon_n(s_0)-\varepsilon_0(s_0))} \langle n(0)|A^\dagger(s')\sum_j \frac{dP_j(s')}{ds'}A(s')P_j(0)|0(0)\rangle \\ &= i\int_0^s ds' e^{i\tau \int_0^{s'} ds_0(\varepsilon_n(s_0)-\varepsilon_0(s_0))} \langle n(0)|A^\dagger(s')\frac{dP_0(s')}{ds'}A(s')|0(0)\rangle \end{aligned} \tag{17}$$

where we used a relation between $K(s)$ and $P_j(s)$ which is derived by (10) and (11).

$$i\sum_j \frac{dP_j(s)}{ds}P_j(s) = \sum_j \big(K(s)P_j(s)^2 - P_j(s)K(s)P_j(s)\big) = K(s) \ . \tag{18}$$

In order to arrange the matrix element of F_τ further, it is convenient to utilize a similar equation.

$$-i\sum_j P_j(s)\frac{dP_j(s)}{ds} = -\sum_j \big(P_j(s)K(s)P_j(s) - P_j(s)^2K(s)\big) = K(s) \tag{19}$$

These equations lead to

$$P_j(s)K(s)P_k(s) = i\sum_l P_j(s)\frac{dP_l(s)}{ds}P_l(s)P_k(s) = iP_j(s)\frac{dP_k(s)}{ds}P_k(s) \tag{20}$$

$$= -i\sum_l P_j(s)P_l(s)\frac{dP_l(s)}{ds}P_k(s) = -iP_j(s)\frac{dP_j(s)}{ds}P_k(s)\ . \tag{21}$$

Hence we obtain

$$P_j(s)\frac{dP_k(s)}{ds}P_k(s) = -P_j(s)\frac{dP_j(s)}{ds}P_k(s)\ .$$

By the way, the Hamiltonian is given in terms of the projection operator by (7). Then the derivative of the Hamiltonian is written as

$$\frac{dH(s)}{ds} = \sum_j \varepsilon_j(s)\left(\frac{dP_j(s)}{ds}P_j(s) + P_j(s)\frac{dP_j(s)}{ds}\right) + \sum_j \frac{d\varepsilon_j(s)}{ds}P_j(s)\ ,$$

where we note that $P_j(s) = P_j(s)^2$. Using (20) and (21), the equation for the matrix element of the derivative of the Hamiltonian is obtained as follows.

$$\begin{aligned}
P_j(s)\frac{dH(s)}{ds}P_k(s) &= \sum_l \varepsilon_l(s)P_j(s)\left(\frac{dP_l(s)}{ds}P_l(s) + P_l(s)\frac{dP_l(s)}{ds}\right)P_k(s) \\
&\quad + \sum_l \frac{\varepsilon_l(s)}{ds}P_j(s)P_l(s)P_k(s) \\
&= \varepsilon_k(s)P_j(s)\frac{dP_k}{ds}P_k(s) + \varepsilon_j(s)P_j(s)\frac{dP_j(s)}{ds}P_k(s) \\
&\quad + \delta_{jk}\frac{d\varepsilon_j(s)}{ds} \\
&= (\varepsilon_k(s) - \varepsilon_j(s))P_j(s)\frac{dP_k(s)}{ds}P_k(s) + \delta_{jk}\frac{d\varepsilon_j(s)}{ds}\ .
\end{aligned}$$

From this equation, the matrix element in the right hand side of (17) is written as

$$\begin{aligned}
\Gamma_{n0}(s) &= \left\langle n(0)|A^\dagger(s)\frac{dP_0(s)}{ds}A(s)|0(0)\right\rangle = \left\langle n(s)|P_n(s)\frac{dP_0(s)}{ds}P_0(s)|0(s)\right\rangle \\
&= \left\langle n(s)|\left(\frac{-1}{\varepsilon_n(s)-\varepsilon_0(s)}P_n(s)\frac{d\mathcal{H}(s)}{ds}P_0(s) - \delta_{n0}\frac{d\varepsilon_0(s)}{ds}P_0(s)\right)|0(s)\right\rangle \\
&= \frac{-1}{\varepsilon_n(s)-\varepsilon_0(s)}\left\langle n(s)|\frac{d\mathcal{H}(s)}{ds}|0(s)\right\rangle\ ,
\end{aligned}$$

Defining $\omega_{n0}(s) = \varepsilon_n(s) - \varepsilon_0(s)$, (17) is reduced to

$$\langle n(0)|F_{\tau n0}(s)|0(0)\rangle = \int_0^s ds' e^{i\tau\int_0^{s'} ds_0\omega_{n0}(s_0)}\frac{-1}{\omega_{n0}(s')}\left\langle n(s')\left|\frac{d\mathcal{H}(s')}{ds'}\right|0(s')\right\rangle\ .$$

If $\omega_{n0}(s)$ and the matrix element of $d\mathcal{H}(s)/ds$ do not depend on the time, the above integration is carried out and yields

$$|\langle n(0)|F_{\tau n0}(s)|0(0)\rangle|^2 = \frac{1}{\tau^2}\frac{1}{\omega_{n0}^4}\left|\langle n(s)|\frac{d\mathcal{H}(s)}{ds}|0(s)\rangle\right|^2 2\left(1-\cos\omega_{n0}\tau s\right) \ .$$

When $\omega_{n0}(s)$ and the matrix element of $d\mathcal{H}(s)/ds$ varies with time, the integral is estimated by the minimum of $\omega_{n0}(s)$ and the maximum of the matrix element as far as the variation is moderate.

$$|\langle n(0)|F_{\tau n0}(s)|0(0)\rangle|^2 \lesssim \frac{1}{\tau^2}\frac{1}{\min[\omega_{n0}(s)]^4}\max\left[\left|\langle n(s)|\frac{d\mathcal{H}(s)}{ds}|0(s)\rangle\right|\right]^2 \ .$$

This formula provides the transition probability from the ground state to an excited state resulting from the time-evolution. This is derived using the adiabatic approximation represented by (15). As far as the value of right hand side is much smaller than the unity, the result is consistent with the adiabatic approximation. Namely the criterion on the validity of adiabatic approximation is given by the smallness of transition probability from the ground state to the first excited state. It is represented by

$$\tau \gg \frac{\max\left[\left|\langle 1(s)|\frac{d\mathcal{H}(s)}{ds}|0(s)\rangle\right|\right]}{\min\left[\omega_{10}(s)\right]^2} \ . \tag{22}$$

Landau-Zener Theory

Two energy levels moving with time are considered in the Landau-Zener theory. These levels, separated widely at first, approach each other with time and part away again at last. When the levels are separated sufficiently, each energy eigenstate preserves an individual character. On the other hand, these characters mixes due to an interaction between two states when the energy levels are close to each other. If the interaction is absent, the energy levels degenerate at crossing point. However the level crossing is avoided in the presence of the interaction. Figure 1 shows the energy levels considered in the Landau-Zener theory. We consider the time-evolution of quantum state in this model. We suppose the energy levels are widely separated initially and the initial state is the ground state. If the change in the Hamiltonian is slow, the state evolves adiabatically during the entire time. However, if the change is not slow, a non-adiabatic transition takes place when the energy levels become close. The Landau-Zener theory derives the probability of non-adiabatic transition from the ground state to the excited state.

We consider the following non-interacting time-dependent Hamiltonian.

$$\mathcal{H}_0(t) = \varepsilon_1(t)|1(t)\rangle\langle 1(t)| + \varepsilon_2(t)|2(t)\rangle\langle 2(t)| \ ,$$

where $\varepsilon_j(t)$ and $|j(t)\rangle$ $(j=1,2)$ denote the instantaneous eigenenergy and eigenstate respectively. We impose the condition for eigenenergies.

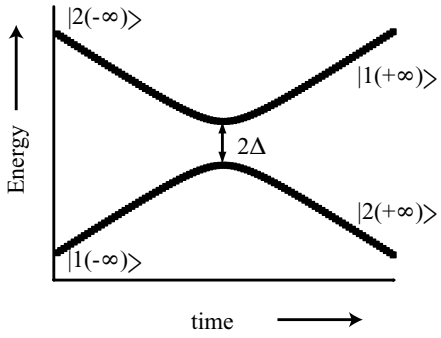

Fig. 1. Energy levels of the Landau-Zener Hamiltonian

$$\varepsilon_1(t) - \varepsilon_2(t) = \alpha t \ ,$$

namely linear time-dependence of energy level spacing is assumed. α stands for the gradient of the level spacing with respective to the time. We assume α positive. Mixing between two states is introduced by the following Hamiltonian.

$$\mathcal{H}_{int} = \Delta \left(|1(t)\rangle\langle 2(t)| + |2(t)\rangle\langle 1(t)| \right) \ .$$

We assume that Δ has no time-dependence. The total Hamiltonian is given by

$$\mathcal{H}(t) = \mathcal{H}_0(t) + \mathcal{H}_{int} \ . \tag{23}$$

In this Hamiltonian, the level-cross avoiding takes place at $t = 0$, and the energy gap shows the minimum value given by 2Δ at the same time. We depict the eigenenergies of the Landau-Zener Hamiltonian (23) in Fig. 1.

We solve the Schrödinger equation for the Hamiltonian (23). We express the state vector as

$$|\psi(t)\rangle = \tilde{C}_1(t)|1(t)\rangle + \tilde{C}_2(t)|2(t)\rangle$$

The Schrödinger equation (3) gives a series of equations for $\tilde{C}_1(t)$ and $\tilde{C}_2(t)$.

$$i\frac{d}{dt}\tilde{C}_1(t) = \varepsilon_1(t)\tilde{C}_1(t) + \Delta\tilde{C}_2(t)$$
$$i\frac{d}{dt}\tilde{C}_2(t) = \varepsilon_2(t)\tilde{C}_2(t) + \Delta\tilde{C}_1(t)$$

The following transformation is introduced.

$$\tilde{C}_1(t) = C_1(t)e^{-i\int_{-\infty}^{t} dt'\varepsilon_1(t')}, \quad \tilde{C}_2(t) = C_2(t)e^{-i\int_{-\infty}^{t} dt'\varepsilon_2(t')} \ .$$

The series of equations are simplified as follows.

$$i\frac{d}{dt}C_1(t) = \Delta C_2(t)e^{i\int_{-\infty}^{t} dt'(\varepsilon_1(t')-\varepsilon_2(t'))}, \tag{24}$$

$$i\frac{d}{dt}C_2(t) = \Delta C_1(t)e^{-i\int_{-\infty}^{t} dt'(\varepsilon_1(t')-\varepsilon_2(t'))}. \tag{25}$$

Now as the boundary condition, we assume the state is at $|1(t)\rangle$ when $t = -\infty$. This is, in other words, written by

$$|C_1(-\infty)| = 1, \quad C_2(-\infty) = 0\,,$$

where we note the normalization condition $|C_1(t)|^2+|C_2(t)|^2 = 1$. Eliminating $C_1(t)$ in (24) and (25), an equation of $C_2(t)$ is obtained.

$$\frac{d^2}{dt^2}C_2(t) + i(\varepsilon_1(t) - \varepsilon_2(t))\frac{d}{dt}C_2(t) + \Delta^2 C_2(t) = 0\,,$$

where we took $d\Delta/dt = 0$ into account. We here introduce a transformation.

$$C_2(t) = \exp\left[-\frac{i}{2}\int_{\infty}^{t} dt'(\varepsilon_1(t') - \varepsilon_2(t'))\right] U(t)\,.$$

Derivatives of $C_2(t)$ are expressed by $U(t)$ as follows.

$$\frac{d}{dt}C_2(t) = e^{-\frac{i}{2}\int_{\infty}^{t} dt'(\varepsilon_1(t')-\varepsilon_2(t'))}\left[-\frac{i}{2}(\varepsilon_1(t) - \varepsilon_2(t))U(t) + \frac{d}{dt}U(t)\right] \tag{26}$$

$$\begin{aligned}\frac{d^2}{dt^2}C_2(t) = e^{-\frac{i}{2}\int_{\infty}^{t} dt'(\varepsilon_1(t')-\varepsilon_2(t'))}\Bigg[&\left(-\frac{i}{2}\alpha - \frac{\alpha^2 t^2}{4}\right)U(t)\\ &-i(\varepsilon_1(t) - \varepsilon_2(t))\frac{d}{dt}U(t) + \frac{d^2}{dt^2}U(t)\Bigg]\end{aligned} \tag{27}$$

Substitution of (26) and (27) yields an equation of $U(t)$.

$$\frac{d^2}{dt^2}U(t) + \left(\Delta^2 - \frac{i}{2}\alpha + \frac{\alpha^2}{4}t^2\right)U(t) = 0\,.$$

Performing the variable transformation,

$$z = e^{-\frac{\pi}{4}i}\alpha^{\frac{1}{2}}t\,, \tag{28}$$

we obtain

$$\frac{d^2}{dz^2}\tilde{U}(z) + \left(n + \frac{1}{2} - \frac{1}{4}z^2\right)\tilde{U}(z) = 0, \tag{29}$$

where we denote $U(t) = U(e^{\frac{\pi}{4}i}\alpha^{-\frac{1}{2}}z)$ by $\tilde{U}(z)$, and define $n = i\Delta^2/\alpha$. This equation is known as the Weber's differential equation. The boundary condition for $\tilde{U}(z)$ is $\tilde{U}(z = Re^{\frac{3}{4}\pi i}) = 0$ for $\alpha > 0$ when $R = \infty$. The Weber functions $D_{-n-1}(-iz)$, the particular solution of Weber's equation, vanishes

for $z = Re^{\frac{1}{4}\pi i}$ and $z = Re^{\frac{3}{4}\pi i}$ with $R = \infty$. This is suitable for the present boundary condition. Hence the solution including the normalization factor A is written as

$$\tilde{U}(z) = AD_{-n-1}(-iz)$$

We remark that the axis in z plane which corresponds to t-axis is along $e^{\frac{3}{4}\pi i}$ $(t < 0)$ or $e^{-\frac{1}{4}\pi i}$ $(t > 0)$.

The normalization factor is determined by the asymptotic value of $C_1(-\infty)$. We first write down the asymptotic expansion of $D_{-n-1}(iz)$ along $e^{-\frac{1}{4}\pi i}$.

$$D_{-n-1}(iRe^{-\frac{1}{4}\pi i}) \cong e^{-\frac{\pi}{4}(n+1)i} e^{-iR^2/4} R^{-n-1} \ .$$

Then the derivative is written as

$$\frac{d}{dR} D_{-n-1}(iRe^{-\frac{1}{4}\pi i}) \cong e^{-\frac{\pi}{4}(n+1)i} \left(-\frac{iR}{2}\right) e^{-iR^2/4} R^{-n-1} \ ,$$

where terms of higher order in $1/R$ are neglected. From (24), the asymptotic form of $C_1(t)$ for $t \to -\infty$ is obtained as follows.

$$\begin{aligned} C_1(t) &= \frac{i}{\Delta} e^{i\int_{-\infty}^{t} dt'(\varepsilon_1(t') - \varepsilon_2(t'))} \frac{d}{dt} C_2(t) = \frac{1}{\Delta}\left(\frac{1}{2}\alpha t U(t) + i\frac{d}{dt}U(t)\right) \\ &= \frac{1}{\Delta} A \left(-\frac{1}{2}\alpha^{\frac{1}{2}} R D_{-n-1}(iRe^{-\frac{\pi}{4}i}) - i\alpha^{\frac{1}{2}} \frac{d}{dR} D_{-n-1}(ie^{-R\frac{\pi}{4}i})\right) \\ &\cong \frac{-1}{\Delta} A\sqrt{\alpha} e^{-\frac{\pi}{4}(n+1)i} e^{-iR^2/4} R^{-n} \end{aligned}$$

where t relates with R by $\sqrt{\alpha}t = -\sqrt{|\alpha|}|t| = -R$. The boundary condition of $C_1(t)$ yields

$$1 = |C_1(-\infty)| = \frac{\sqrt{\alpha}}{\Delta} |A_+| e^{-\frac{\pi}{4}(i\frac{\Delta^2}{\alpha})i} = \frac{\sqrt{\alpha}}{\Delta} |A_+| e^{\frac{\pi}{4}\frac{\Delta^2}{\alpha}} \ ,$$

where we substituted $n = i\Delta^2/\alpha$. Hence we obtain

$$|A| = \gamma^{1/2} e^{-\pi\gamma/4} \ ,$$

where we defined $\gamma = \Delta^2/|\alpha|$.

Now we examine the value of the solution in infinite limit of t. We first note that $t \to \infty$ corresponds to $z = Re^{-\frac{1}{4}\pi i}$ with $R \to \infty$.

$$\begin{aligned} \lim_{t\to\infty} e^{\frac{i}{2}\int_{-\infty}^{t} dt'(\varepsilon_1(t') - \varepsilon_2(t'))} C_2(t) &= \lim_{t\to\infty} U(t) = \lim_{t\to\infty} \tilde{U}(e^{-\frac{1}{4}\pi i}\alpha^{\frac{1}{2}} t) \\ &= \gamma^{1/2} e^{-\pi\gamma/4} \lim_{R\to\infty} D_{-n-1}(iRe^{\frac{3}{4}\pi i}) \end{aligned}$$

The asymptotic expansion of $D_\lambda(z)$ for infinite z along the axes $ie^{\frac{3}{4}\pi i} = e^{-\frac{3}{4}\pi i}$ tells

$$\lim_{R\to\infty} D_{-n-1}(iRe^{\frac{3}{4}\pi i}) \cong e^{-iR^2/4}e^{\frac{3}{4}\pi(n+1)i}R^{-n-1} + \frac{\sqrt{2\pi}}{\Gamma(n+1)}e^{iR^2/4}e^{\frac{\pi}{4}ni}R^n,$$

Since n is a pure imaginary number, the first term in right hand sides is negligible. Substituting $n = i\gamma$, we obtain

$$\begin{aligned}|C_2(+\infty)|^2 &= \gamma e^{-\pi\gamma/2}\frac{2\pi}{|\Gamma(i\gamma+1)|^2}e^{-\frac{\pi}{2}\gamma} \\ &= \frac{2\pi\gamma e^{-\pi\gamma}}{\gamma^2|\Gamma(i\gamma)|^2} = 1 - e^{-2\pi\gamma}\ ,\end{aligned}$$

where we used the identity on the gamma function, $|\Gamma(ix)|^{-2} = \frac{x}{2\pi}(e^{\pi x} - e^{-\pi x})$.

The initial condition is $|C_1(-\infty)|^2 = 1$. The adiabatic evolution corresponds to the motion from $|1(-\infty)\rangle$ to $|2(+\infty)\rangle$. The probability of adiabatic evolution is given by $P_{\rm ad} = |C_2(+\infty)|^2$. On the other hand, the non-adiabatic transition takes place during the evolution from $|1(-\infty)\rangle$ to $|1(+\infty)\rangle$. Its probability is given by $P_{\rm non-ad} = |C_1(+\infty)|^2 = 1 - |C_2(+\infty)|^2$. Thus we obtain

$$P_{\rm non-ad} = e^{-2\pi\gamma}, \tag{30}$$

$$\gamma = \frac{\Delta^2}{|\alpha|} = \frac{\Delta^2}{|\frac{d}{dt}(\varepsilon_1(t) - \varepsilon_2(t))|}\ . \tag{31}$$

3 Residual Energies

We investigate the residual energy after quantum annealing. The residual energy is defined by the energy difference between the solution obtained by a method and the exact one. It is significant to study problems whose exact solution is available, in order to reveal properties of the method. After an explanation on problems and the way of simulations, we first show results of numerical simulations for small-sized problems. Then we discuss the property of the residual energy after slow quantum annealing analytically.

3.1 Simulations for Small-Sized Problems

Way of Simulations

In order to carry out simulated quantum annealing, we need to pursue the real-time evolution of quantum states. The way of numerical calculation for a dynamical process in quantum mechanics has not been developed sufficiently so far, when the size of the problem is large. The difficulty lies in exponential increase in the number of bases with the size. We then study only small-sized problems, for which the number of bases is up to thousands. The real-time evolution of states is computed using Runge-Kutta algorithm.

Let us denote a basis by $|n\rangle$. Supposing that M is the number of bases, n runs from 1 to M. We assume that $|n\rangle$ is the eigenstate of a classical Hamiltonian $\mathcal{H}_0$.

$$\mathcal{H}_0|n\rangle = \epsilon_n|n\rangle \ ,$$

where ϵ_n is the eigenenergy of $\mathcal{H}_0$. A tunneling Hamiltonian $\mathcal{H}_T$ has off-diagonal elements with respect to the basis $|n\rangle$. We denote the matrix element by

$$\langle m|\mathcal{H}_T|n\rangle = H_{Tmn} \ .$$

The time-dependent Hamiltonian is composed of $\mathcal{H}_0$ and $\mathcal{H}_T$ and given by (5). The state vector is expanded by the basis $|n\rangle$.

$$|\Psi(t)\rangle = \sum_{n=1}^{M} C_n(t)|n\rangle \ .$$

The equation of motion of $C_n(t)$ is derived from the Schrödinger equation (3) as

$$i\frac{d}{dt}C_m(t) = \sum_{n=1}^{M}\left(\left(1-\frac{t}{\tau}\right)H_{Tmn} + \frac{t}{\tau}\delta_{mn}\varepsilon_m\right)C_n(t) \ .$$

Note that $C_n(t)$ is a complex number. Denoting the real and imaginary parts of $C_n(t)$ by $C_n^{re}(t)$ and $C_n^{im}(t)$ respectively, $C_n(t) = C_n^{re}(t) + iC_n^{im}(t)$, we obtain a series of equations for real functions of time.

$$-\frac{d}{dt}C_m^{im}(t) = \sum_{n=1}^{M}\left(\left(1-\frac{t}{\tau}\right)H_{Tmn} + \frac{t}{\tau}\delta_{mn}\varepsilon_m\right)C_n^{re}(t), \tag{32}$$

$$\frac{d}{dt}C_m^{re}(t) = \sum_{n=1}^{M}\left(\left(1-\frac{t}{\tau}\right)H_{Tmn} + \frac{t}{\tau}\delta_{mn}\varepsilon_m\right)C_n^{im}(t). \tag{33}$$

By the procedure of the quantum annealing method, the initial condition for the state vector is specified by the ground state of $\mathcal{H}_T$. The series of equations (32) and (33) is solved numerically using fourth order Runge-Kutta algorithm.

The residual energy is defined by the difference between the energy expectation value of the final state and the ground eigenenergy of the classical Hamiltonian.

$$\begin{aligned} E_{\rm res} &= \langle\Psi(\tau)|\mathcal{H}_0|\Psi(\tau)\rangle - E_g \\ &= \sum_{n=1}^{M}\varepsilon_n|C_n(\tau)|^2 - E_g, \end{aligned} \tag{34}$$

where E_g is given by the lowest energy in ε_n $(n = 1, 2, \ldots, M)$. It is not hard to obtain E_g in the models studied in this section.

Model

We study two models which stand for optimization problems. The first is the tight-binding model. We consider a single particle in the one-dimensional lattice. The particle feels a potential energy at each lattice point. The potential energies are different at different lattice points. The classical Hamiltonian is given by

$$\mathcal{H}_0 = \sum_{j=1}^{M} V_j |j\rangle\langle j| \,, \tag{35}$$

where $|j\rangle$ denotes the single particle state at site j, and V_j is the potential energy on the same site. The tunneling Hamiltonian is given by hopping between nearest neighbor sites. It is written as

$$\mathcal{H}_T = -\alpha \sum_{j=1}^{M-1} \left(|j\rangle\langle j+1| + |j+1\rangle\langle j| \right), \tag{36}$$

where α indicates the strength of tunneling. The initial state, namely the ground state of $\mathcal{H}_T$, is given by

$$|\Psi(0)\rangle = \sum_{j=1}^{M} |j\rangle \,.$$

The second model is the random Ising model. The classical Hamiltonian of the random Ising model is written as

$$\mathcal{H}_0 = -\sum_{<i,j>} J_{ij} S_i^z S_j^z - h \sum_i S_i^z, \tag{37}$$

where S_i^z is the z-component of the spin operator. The geometry of the system is assumed to be two-dimensional simple square lattice. The coupling constant J_{ij} takes the value of $+1$ or -1. We assume the nearest neighbor interaction. A longitudinal magnetic field is taken into account to remove trivial degeneracy of the ground state. The tunneling Hamiltonian in the present system is brought by the interaction with transverse magnetic field. It is written as

$$\mathcal{H}_T = -\alpha \sum_i S_i^x, \tag{38}$$

where S_i^x denotes the x-component of the spin operator. α is a parameter which determines the strength of the transverse field. All spins are aligned along x-direction in the ground state of $\mathcal{H}_T$. This state determines the initial condition of the state vector. It is expressed by

$$|\Psi(0)\rangle = \bigotimes_i \left[\frac{|\uparrow\rangle_i + |\downarrow\rangle_i}{\sqrt{2}} \right] \,, \tag{39}$$

where $|\uparrow\rangle_i$ and $|\downarrow\rangle_i$ indicate the eigenstate of S_i^z with eigenvalues $\frac{1}{2}$ and $-\frac{1}{2}$ respectively.

Results of Simulations

We first studied the two-site tight-binding model as the simplest case, namely $M = 2$ in eqs.(35) and (36). The potential energies on the sites $j = 1$ and $j = 2$ are set as $V_1 = \frac{1}{2}$ and $V_2 = \frac{1-\delta}{2}$ with $\delta = 0.05191685$. These values are not essential in the result. Since V_2 is smaller than V_1, the wave function initially being the symmetric state between two sites should result in the localized state at the site 2 after slow quantum annealing. Figure 2(a) shows the time-evolution of the probability of finding the particle in the site 2, $P_2(t) = |\langle 2|\Psi(t)\rangle|^2$, for the annealing time $\tau = 10000$. Because the initial state is the symmetric state, the probability is equal to 0.5 at $t = 0$. $P_2(t)$ increases with time and reaches almost unity at $t = \tau$ finally. We performed the simulation for several values of the tunneling strength α. For a fixed t, $P_2(t)$ becomes larger for smaller α. This is because the component of the tunneling Hamiltonian in the total Hamiltonian becomes smaller and thus the total Hamiltonian gets closer to the classical Hamiltonian for smaller α. Figure 2(b) shows the annealing-time dependence of the residual energy. The residual energy decreases with increasing the annealing time. It is remarkable that the curve in the figure is almost straight in long τ region. Since the scales of both axes are logarithmic, the straight line means that the residual energy decreases by $\tau^{-\zeta}$ for long τ. By an estimation of the gradient, we obtain $\zeta \sim 2$.

We have carried out the simulation for larger systems of tight-binding model. We show results on the system with twenty sites ($M = 20$) in Fig. 3. The potential energies on the sites are randomly generated and shown in Fig. 3(a). The potential energy on the site 17 is the lowest. Hence the ground energy is given by V_{17}. The change of the residual energy with annealing time

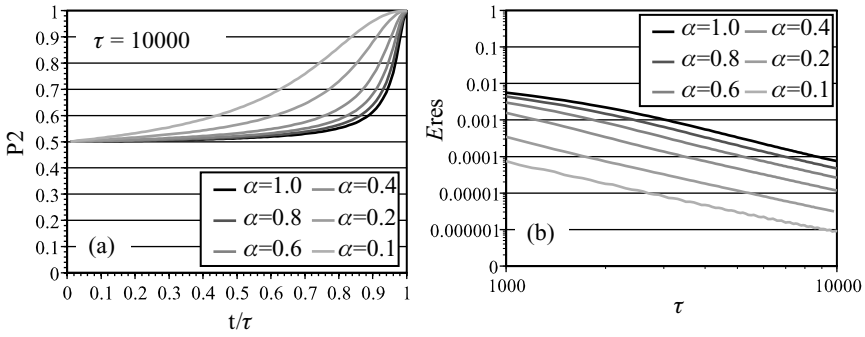

Fig. 2. Results of simulations for the two-site tight-binding model. The potentials on the sites are $V_1 = \frac{1}{2}$ and $V_2 = \frac{1-\delta}{2}$ with a positive δ less than 1. Simulations are performed for several values of α. Figure (a) shows the time-evolution of the probability that the particle is found at the site 2. Figure (b) shows the annealing-time dependence of the residual energy. Both axes in Fig. (b) are in logarithmic scale

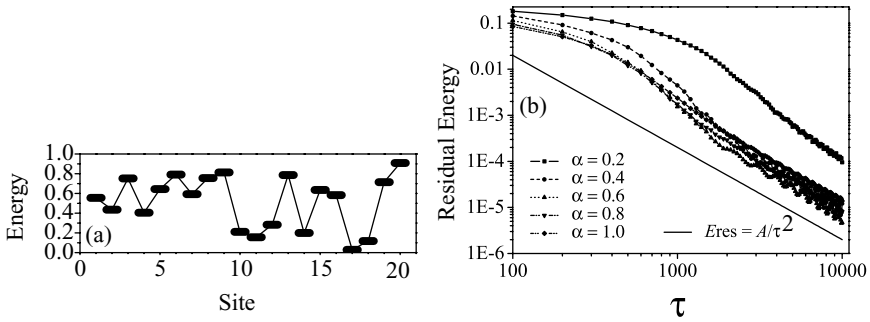

Fig. 3. Results of simulations for multi-site tight-binding model. We studied the system composed of twenty sites. Figure (**a**) shows the potential energy on each site. These energies are generated randomly between 0 and 1. Figure (**b**) shows the annealing-time dependence of the residual energy. A straight line stands for a function proportional to $1/\tau^2$. Comparing curves of the residual energy with the straight line, we find the residual energy decreases almost as $1/\tau^2$ for long τ

is shown in Fig. 3(b). Simulations have been performed for several values of α. Large α lifts energy gap above the instantaneous ground eigenstate of $\mathcal{H}(t)$ for $t \neq \tau$. Since large energy gap is appropriate for the adiabatic evolution, large α is preferable to quantum annealing. On the other hand, small α makes the change in $\mathcal{H}(t)$ with time slow and slow change is preferable for the adiabatic evolution. Therefore there is an optimum value in α. In Fig. 3(b), $\alpha = 0.6$ seems optimum, because the residual energy for $\alpha = 0.6$ is the lowest in long τ region. We see that curve is almost straight for long τ, neglecting small oscillations. A function proportional to $1/\tau^2$ is also plotted in the figure. Comparing results of simulation with the line of $1/\tau^2$, we find the residual energy decreases as $1/\tau^2$ for long τ.

We show results on the random Ising model in Fig. 4. Different from tight-binding model, the random Ising model is a many-body problem. Hence the hardness of this problem is qualitatively different from previous two problems. We studied the 3×3 two-dimensional simple square lattice. The value of coupling constant J_{ij}, chosen from $+1$ and -1, is depicted in Fig. 4(a). Figure 4(b) shows the annealing-time dependence of the residual energy for several α's. A line of a function proportional to $1/\tau^2$ is also shown for comparison. In spite of the qualitative difference in problems, results of simulations on the random Ising model is quite similar to those on the tight-binding model. First we see that there is an optimum α which lowers the residual energy. Next, it is clear that the curve of the residual energy becomes almost straight for long τ. Therefore the residual energy decreases with the annealing time as $1/\tau^{\zeta}$. The exponent is estimated at $\zeta \sim 2$ from the comparison with the straight line in the same figure.

Results for different models studied here show that the residual energy decreases with the annealing time as

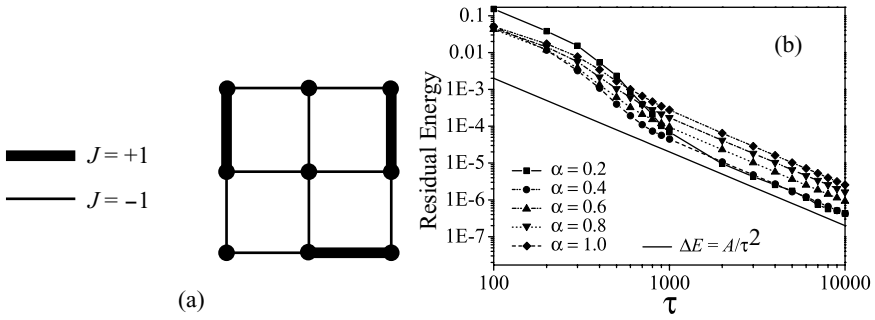

Fig. 4. Results of simulations for the random Ising model. We studied two-dimensional simple square lattice composed of nine sites. Figure (**a**) shows the value of coupling constant J_{ij}. Figure (**b**) shows the annealing-time dependence of the residual energy for several strength of transverse field. A function proportional to $1/\tau^2$ is also shown. It is clearly seen that the residual energy behaves as $1/\tau^2$ for long τ

$$E_{\text{res}} \propto \frac{1}{\tau^2} \tag{40}$$

for long τ limit. It is remarkable that this property is independent of the model. We naturally infer that the power law of the residual energy with respect to the annealing time is a universal feature in the quantum annealing method.

3.2 Analytic Considerations

The asymptotic behavior of the solution on the annealing time should be characterized by the adiabatic theorem in the quantum mechanics for infinite annealing time limit, since the solution by quantum annealing method is brought by the adiabatic evolution of quantum state. We derive a feature on residual energy on the ground of the adiabatic theorem.

Let us denote the eigenstate and eigenenergy of the classical Hamiltonian $\mathcal{H}_0$ by $|n(1)\rangle$ and $\varepsilon_n(1)$, where $n = 0$ indicates the ground level, $n = 1$ the first excited level, and so on. Moreover, we denote the final state $|\Psi(\tau)\rangle$ after the time-evolution by $|\Psi_\tau(1)\rangle$. These notations are consistent with those in Sect. 2.2. Then the residual energy, (34), is represented by

$$\begin{aligned} E_{\text{res}} &= \langle\Psi_\tau(1)|\mathcal{H}_0|\Psi_\tau(1)\rangle - \varepsilon_0(1) \\ &= \sum_{n\geq 0} \varepsilon_n(1) \left|\langle n(1)|\Psi_\tau(1)\rangle\right|^2 - \varepsilon_0(1) \sum_{n\geq 0} \left|\langle n(1)|\Psi_\tau(1)\rangle\right|^2 \\ &= \sum_{n\geq 1} \left(\varepsilon_n(1) - \varepsilon_0(1)\right) \left|\langle n(1)|\Psi_\tau(1)\rangle\right|^2 . \end{aligned}$$

Using the notation in Sect.2.2 (see (16)), we obtain for $n \neq 0$

$$\begin{aligned}\left|\langle n(1)|\Psi_\tau(1)\rangle\right|^2 &= \langle 0(0)|W^\dagger(1)|n(0)\rangle\langle n(0)|W(1)|0(0)\rangle \\ &= \langle 0(0)|F^*_{\tau 0n}(1)|n(0)\rangle\langle n(0)|F_{\tau n0}(1)|0(0)\rangle\ ,\end{aligned}$$

where we substituted (15), namely the perturbation formula up to $1/\tau$, for $W(s)$. Hence the residual energy is written as

$$E_{\rm res} = \sum_{n\geq 1}\left(\varepsilon_n(1)-\varepsilon_0(1)\right)\left|\langle n(0)|F_{\tau n0}(1)|0(0)\rangle\right|^2 .$$

$F_{\tau n0}(1)$ is of the order of $1/\tau$ for long τ. Then each term in the right hand side of above equation is of the order of $1/\tau^2$. Since the first excited state makes the largest contribution to the summation, we may neglect contribution from higher excited states. Thus it is shown that the residual energy is of the order of $1/\tau^2$.

$$E_{\rm res} \sim \left(\varepsilon_1(1)-\varepsilon_0(1)\right) O\left(\frac{1}{\tau^2}\right). \tag{41}$$

We consider varying τ with other parameters fixed. It follows from (41) that the residual energy decreases by $1/\tau^2$ for long limit of τ, since the term of $1/\tau^2$ dominates the residual energy. This behavior of the residual energy is nothing but the result of numerical simulations previously. The power law of the residual energy for long annealing time is a universal feature which has the ground in the adiabatic theorem in the quantum mechanics.

3.3 Discussion

It is significant to clarify when the residual energy obeys the power law. Since the power law originates in the adiabatic theorem in the quantum mechanics, the condition for the power law corresponds to the criterion for the adiabatic theorem. We have shown that the criterion for the adiabatic theorem is given by (22). Therefore the condition for the power law is also given by

$$\tau \gg \tau_C, \quad \tau_C = \frac{\max\left[\left|\langle 1(s)|\frac{d\tilde{\mathcal{H}}(s)}{ds}|0(s)\rangle\right|\right]}{\min\left[\varepsilon_1(s)-\varepsilon_0(s)\right]^2}, \tag{42}$$

where we denote the time-dependent Hamiltonian $\mathcal{H}(t)$ ((5)) by $\tilde{\mathcal{H}}(s)$ using normalized time $s = t/\tau$. $|n(s)\rangle$ and $\varepsilon_n(s)$ represent the instantaneous eigenstate and eigenenergy of $\mathcal{H}(t) = \tilde{\mathcal{H}}(s)$. The adiabatic theorem accounts for the property of the state after a successful adiabatic evolution. Hence the observed power law implies that the adiabatic evolution results almost in success. The characteristic annealing time τ_C indicates hardness of the adiabatic evolution or efficiency of the quantum annealing method. A long annealing time is needed for a long τ_C.

It is natural to ask how the residual energy is scaled by τ around $\tau \sim \tau_C$. The Landau-Zener theory is validated in this region of τ. To see this, we consider the following time-dependent Hamiltonian.

$$\mathcal{H}_{LZ}(t) = -\left(\frac{1}{2} - \frac{t}{\tau}\right) hS^z - \alpha S^x \ . \tag{43}$$

We define this Hamiltonian for the time period $0 \leq t \leq \tau$. The Hamiltonian (43) differs from the general form of the time-dependent Hamiltonian defined by (5) for quantum annealing. However it is instructive to investigate the time-evolution of quantum state for this Hamiltonian. The eigenenergies of $\mathcal{H}_{LZ}$ is shown in Fig. 5(a). Since the system represented by the Hamiltonian (43) consists of a single spin, only two levels specify the system. We denote the instantaneous eigenenergies of $\mathcal{H}_{LZ}(t)$ by $\varepsilon_0(t/\tau)$ and $\varepsilon_1(t/\tau)$.

The Landau-Zener theory is applicable to the Hamiltonian (43). We suppose that the initial state at $t = 0$ is the ground state of $\mathcal{H}_{LZ}(0)$, same as the quantum annealing method. Applying the Landau-Zener formula, (30) and (31), the probability of the non-adiabatic transition from the ground state to the excited state is given by

$$P_1 = \exp\left[-\frac{2\pi\alpha^2\tau}{h}\right] \ . \tag{44}$$

This formula immediately leads to the following expression of the residual energy.

$$\begin{aligned} E_{\text{res}} &= \varepsilon_1(1)P_1 + \varepsilon_0(1)P_0 - \varepsilon_0(1) = (\varepsilon_1(1) - \varepsilon_0(1))\, P_1 \\ &= (\varepsilon_1(1) - \varepsilon_0(1)) \exp\left[-\frac{\pi}{2}\frac{\tau}{\tau_C}\right], \end{aligned} \tag{45}$$

$$\tau_C = \frac{h}{4\alpha^2} \tag{46}$$

where P_0 denotes the probability of finding the ground state of $\mathcal{H}(\tau)$ in the finial state and it satisfies $P_0 + P_1 = 1$ due to the conservation of the probability. τ_C indicates the characteristic time for the adiabatic evolution of the present model. The definition by (42) yields the above expression of τ_C. The exponential behavior of (45) is in contrast to the power law behavior, (41), from the adiabatic theorem. In order to see the change between these two characters, we performed a numerical simulation on the time-evolution of quantum state using the method described in Sect. 3.1. Figure 5(b) shows the result on residual energy. Dots combined by line are obtained from time-evolution of the state. The analytic results from the Landau-Zener theory and the adiabatic theorem, (45) and (41), are also shown for comparison. The residual energy manifests different features in two regimes governed by the Landau-Zener theory and the adiabatic theorem. Since the present model is well described by the Landau-Zener theory, the residual energy is well fitted by (45) for around $\tau \sim \tau_C$. We note that $\tau_C = 25$ is given from parameters used for numerical calculation. On the other hand, the residual energy decreases by $1/\tau^2$ basically for $\tau \gg \tau_C$. It is remarkable that the change between two features is drastic.

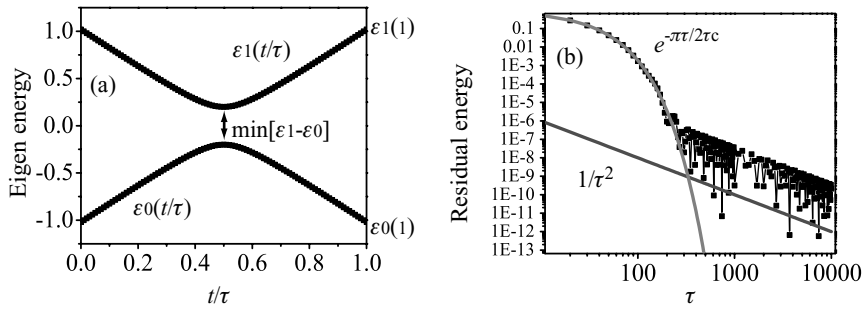

Fig. 5. (**a**) Instantaneous eigenenergies of the time-dependent Hamiltonian (43), and (**b**) residual energy after time-evolution. Parameters in the Hamiltonian is settled as $h = 4$ and $\alpha = 0.2$

We ask ourselves how the residual energy behaves in large-sized problems. It is expected in large-sized problems that level-cross avoidings take place sequentially and the characteristic time τ_C becomes small. Nevertheless, the adiabatic theorem is validated for $\tau \gg \tau_C$. Hence the power law should be observed for long τ limit. On the other hand, multiple non-adiabatic transitions should be taken into account for $\tau \sim \tau_C$. Santoro et al. have predicted the logarithmic behavior, $E_{\rm res} \sim A/(\ln \tau)^6$, on the basis of a cascade of Landau-Zener non-adiabatic transitions[5]. If this is true, a transition between logarithmic law and power law may be observed. By now the logarithmic behavior of the residual energy has not been confirmed numerically. Methods of simulation for large-sized problems is needed to reveal the behavior of the residual energy for $\tau \sim \tau_C$.

4 A method of Simulation for Large-Sized Problems

For an application of the quantum annealing method, numerical simulation for large-sized problems is indispensable. To implement the simulated quantum annealing, we have to realize the time-evolution of quantum spin states. Numerical simulations on dynamics of quantum systems involve difficulties in the capacity of memory in computers, since the quantity of information needed to represent a quantum state increases exponentially with the size of the problem. The quantum Monte-Carlo method provides a possibility of simulating dynamical processes of a quantum system. In the quantum Monte-Carlo method, a D-dimensional quantum system in a finite temperature is mapped into a classical system of $(D+1)$-dimension. The Markovian Monte-Carlo process is substituted for the dynamical process of the classical system. Therefore the dynamics produced in the quantum Monte-Carlo method is different from the real-time dynamics in the quantum mechanics. Nevertheless the quantum Monte-Carlo method sometimes succeeds in obtaining a good

solution. We however propose in this article another method of simulation using the density matrix renormalization group (DMRG) technique. DMRG method has been developed recently for use in simulating the real-time dynamics of quantum system at zero temperature[25]. The use of DMRG enables us to carry out quantum annealing by real-time evolution for large systems. We explain the method in next subsection and present some results of simulations after that. The applicability of DMRG for models including long-range interaction is discussed at last.

4.1 Real-Time Evolution by Means of DMRG

We consider the time-evolution of a quantum state $|\Psi(t)\rangle$. We denote the Hamiltonian of the system by $\mathcal{H}(t)$. We assume that the Hamiltonian varies with time. The time-evolution of the state is governed by the Schrödinger equation. In particular, an evolution during a short time Δt is written using the time-evolution operator $e^{-i\mathcal{H}(t)\Delta t}$ as

$$|\Psi(t+\Delta t)\rangle \cong e^{-i\mathcal{H}(t)\Delta t}|\Psi(t)\rangle \ .$$

If we consider a time period from $t=0$ to $t=\tau$, the final state is given by

$$|\Psi(\tau)\rangle \cong e^{-i\mathcal{H}((N_t-1)\Delta t)\Delta t}\cdots e^{-i\mathcal{H}(\Delta t)\Delta t}e^{-i\mathcal{H}(0)\Delta t}|\Psi(0)\rangle, \tag{47}$$

where the Trotter number N_t satisfies $N_t\Delta t=\tau$. Subsequently we are concerned with a single time-evolution operator.

We assume a spin system whose Hamiltonian consists of pair interactions in addition to on-site spin-field interactions. The total time-dependent Hamiltonian is divided into pair Hamiltonians.

$$\mathcal{H}(t)=\mathcal{H}_1(t)+\mathcal{H}_2(t)+\cdots \ .$$

We suppose here that $\mathcal{H}_j(t)$ contains only one pair interaction term and spin-field terms. Denoting the number of pairs by M, the total Hamiltonian is expressed by M pair Hamiltonians. The time-evolution operator is decomposed symmetrically into products of time-evolution operators with respect to pair Hamiltonians[26].

$$\begin{aligned} &e^{-i\mathcal{H}(t)\Delta t} \cong \\ &e^{-i\mathcal{H}_1(t)\frac{\Delta t}{2}}\cdots e^{-i\mathcal{H}_{M-1}(t)\frac{\Delta t}{2}}e^{-i\mathcal{H}_M(t)\Delta t}e^{-i\mathcal{H}_{M-1}(t)\frac{\Delta t}{2}}\cdots e^{-i\mathcal{H}_1(t)\frac{\Delta t}{2}} . \end{aligned} \tag{48}$$

We consider the one-dimensional lattice with nearest neighbor interaction for simplicity. We pay attention to a site j and $j+1$. In DMRG method, the one-dimensional lattice is divided into four blocks. Two blocks consist of single site, j or $j+1$. The other two blocks, named left and right blocks, contain remaining spins. The state vector is represented using bases of four blocks by

$$|\phi\rangle = \sum_{a,b,k,l} \phi_{a,b,k,l}|a\rangle_L|k\rangle_j|l\rangle_{j+1}|b\rangle_R \ ,$$

where $|a\rangle_L$ and $|b\rangle_R$ are the basis of left and right blocks, while $|k\rangle_j$ and $|l\rangle_{j+1}$ are the basis of the j and $j+1$ sites respectively. We suppose that $e^{-i\mathcal{H}_j(t)\Delta t}$ contains the spin operators of site j and $j+1$. Denoting the matrix element of $e^{-i\mathcal{H}_j(t)\Delta t}$ by $\left[e^{-i\mathcal{H}_j(t)\Delta t}\right]_{kl;k'l'}$, we obtain

$$e^{-i\mathcal{H}_j(t)\Delta t}|\phi\rangle = \sum_{a,b,k,l} \tilde{\phi}_{a,b,k,l}|a\rangle_L|k\rangle_j|l\rangle_{j+1}|b\rangle_R \ ,$$

where

$$\tilde{\phi}_{a,b,k,l} = \sum_{k',l'} \left[e^{-i\mathcal{H}_j(t)\Delta t}\right]_{kl;k'l'} \phi_{a,b,k',l'} \ .$$

We define the density matrix by

$$\rho_{ak;a'k'} = \sum_{b,l} \tilde{\phi}_{a,b,k,l}\tilde{\phi}^*_{a',b,k',l} \ .$$

The density matrix is diagonalized as follow.

$$\rho_{ak;a'k'} = \sum_{\lambda} u_{ak,\lambda} d_\lambda (u^\dagger)_{\lambda,a'k'} \ ,$$

where $u_{ak,\lambda}$ is a unitary matrix and d_λ is the eigenvalue of the density matrix. The basis of the left block and the site j is represented by the eigenstate of the density matrix.

$$|a\rangle_L|k\rangle_j = \sum_{a'} (u^\dagger)_{a',ak}|a'\rangle \ .$$

We employ $|a\rangle = |a\rangle_{L'}$ as the basis of the new left block composed of the old left block and the site j. The right block is divided into one spin of the left side and new right block. Then the basis of old right block is written using new bases as

$$|b\rangle_R = \sum_{l,b'} v_{b,lb'}|l\rangle_{j+2}|b'\rangle_{R'} \ ,$$

where $v_{b,lb'}$ is a unitary matrix which diagonalizes the density matrix with respect to the site $(j+2)$ and the right block R'. $v_{b,lb'}$ is supposed to have been obtained in the previous left-ward sweep. We remark that the number of spins in $|b'\rangle_{R'}$ in the right hand side is less than that in $|b\rangle_R$ in the left hand side by one. Using the new bases, $|a\rangle_{L'}$, $|k\rangle_{j+1}$, $|l\rangle_{j+2}$, and $|b\rangle_{R'}$, we express the state vector as

$$\begin{aligned}
&\sum_{a,b,k,l} \tilde{\phi}_{a,b,k,l}|a\rangle_L|k\rangle_j|l\rangle_{j+1}|b\rangle_R \\
&= \sum_{a,b,k,l} \tilde{\phi}_{a,b,k,l} \sum_{a',b',l'} (u^\dagger)_{a',ak} v_{b,l'b'}|a'\rangle_{L'}|l\rangle_{j+1}|l'\rangle_{j+2}|b'\rangle_{R'} \\
&= \sum_{a,b,k,l} \phi'_{a,b,k,l}|a\rangle_{L'}|k\rangle_{j+1}|l\rangle_{j+2}|b\rangle_{R'} \ ,
\end{aligned}$$

$$\phi'_{a,b,k,l} = \sum_{a',b',k'} \tilde{\phi}_{a',b',k',k} (u^\dagger)_{a,a'k'} v_{b',lb} \ .$$

The norm of the state vector is written in terms of the eigenvalue of the density matrix.

$$\sum_{a,b,k,l} \phi_{a,b,k,l} \phi^*_{a,b,k,l} = \sum_a d_a \ .$$

The eigenvalue d_a is a positive number. If d_a is negligibly small, the norm of the state vector is not affected by the absence of the state $|a\rangle_{L'}$. The procedure of density matrix renormalization is to remove bases with small eigenvalue so as to preserve the norm[27]. As far as the number of dominant eigenvalues is kept small, it is allowed to keep the number of bases to a certain small number. Thus we transform the basis and move to next operation of $e^{-\mathcal{H}_{j+1}(t)\Delta t}$. The operation of one time-evolution operator (48) is accomplished by the rightward sweep followed by the left-ward sweep.

4.2 Results of Simulation

For a pilot study of quantum annealing using DMRG, we consider the one-dimensional random Ising model with periodic boundary condition. The classical Hamiltonian is given by

$$\mathcal{H}_0 = -\sum_{j=1}^{N-1} J_{jj+1} S^z_j S^z_{j+1} - J_{N1} S^z_N S^z_1 - h \sum_{j=1}^{N} S^z_j \ .$$

The coupling constant J_{jj+1} is randomly generated. The spin on the site N interacts with the spin on the site 1. We decide the sign of the coupling constant J_{N1} so as to induce a frustration into the system. If the magnetic field is absent, namely $h = 0$, the ground states are degenerated. Their spin configurations are determined by the sign of the coupling constant, except that the pair with the weakest coupling constant is devoted to unfavorable configuration. However, in the presence of the magnetic field, the state which lowers the interaction energy the most can raise the potential energy due to the magnetic field. To search the ground state which is favorable to both interaction and potential energies is a non-trivial problem.

The time-dependent Hamiltonian for quantum annealing is given by

$$\mathcal{H}(t) = \left(1 - \frac{t}{\tau}\right)(-\alpha) \sum_{j=1}^{N} S^x_j + \frac{t}{\tau} \mathcal{H}_0 \ . \tag{49}$$

We performed numerical simulation of quantum annealing using DMRG for several sizes. We have confirmed that the solution obtained after quantum annealing using DMRG converges to the exact solution for systems with spins less than $N = 32$. The DMRG method for real-time evolution involves two parameters. The one is the width of time step Δt. The final state expressed by

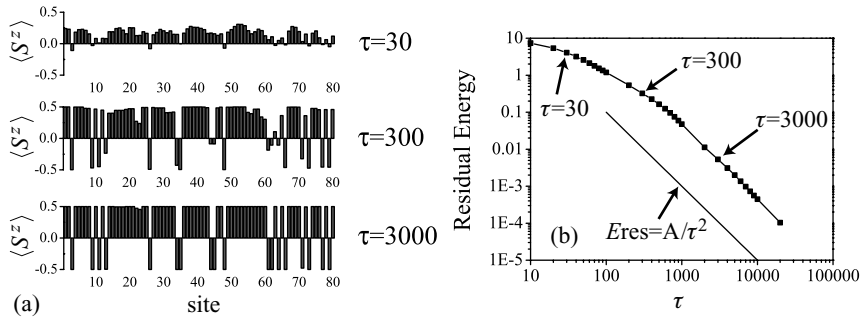

Fig. 6. Results of simulated quantum annealing using DMRG for one-dimensional random Ising model with periodic boundary condition. The width of time slice and the number of bases kept in density matrix renormalization are settled as $\Delta t = 0.2$ and $m = 22$. The longitudinal and transverse fields are set to $h = 0.1$ and $\alpha = 1$ respectively. Figure (**a**) shows the expectation value of spin at each site for annealing time $\tau = 30$, 300, and 3000. Figure (**b**) shows the residual energy vs annealing time

(47) contains an error of the order of $N_t \frac{d\mathcal{H}(t)}{dt} \Delta t^2 \sim \Delta t$ for the time-dependent Hamiltonian given by (49). Although we have tested several Δt's from 0.2 to 0.05, even $\Delta t = 0.2$ seems to produce accurate results. The other parameter is the number of bases kept by the density matrix renormalization. For the model studied here, if we keep $m = 22$ bases, the 23rd eigenvalue of the density matrix is about 10^{-15}. Hence it is expected that the $m = 22$ bases are sufficient for precise calculations. Indeed, we have observed no meaningful difference in results for $m = 16$, 22, and 40.

Figures 6 shows results of simulated quantum annealing using DMRG. The system with $N = 80$ spins was studied. We gave parameters for DMRG as $\Delta t = 0.2$ and $m = 22$. The longitudinal and transverse field was settled as $h = 0.1$ and $\alpha = 1.0$ respectively. Figure 6(a) shows the expectation value of each spin in the final state for annealing time $\tau = 30$, 300, and 3000. It is clear that the spin state approaches a unique classical state from a quantum superposition of classical states with increasing τ. For this system with 80 spins, the exact ground state is not available by means of the examination of all configurations. However it is reasonable to think the asymptotic classical state obtained by quantum annealing to be the true solution. Figure 6(b) shows the annealing time dependence of the residual energy. We substituted the energy of the asymptotic classical state obtained by quantum annealing for the true ground energy. The residual energy decreases as $1/\tau^2$ for long τ. We emphasize that the system size is much larger than those studied in previous section. This result strongly supports the result in the previous section that the residual energy for long τ obeys the power law. However the result is insufficient to clarify the scaling behavior of residual energy for $\tau \sim 100$. Further study is needed to reveal the feature in the Landau-Zener regime.

4.3 Comments

It has been known that the DMRG method is not usually appropriate for study of models including long-range interactions. Systems in high-dimension or those with periodic boundary condition are reduced to one-dimensional models including long-range interactions. The cause of failure in DMRG calculation comes from the existence of exchange interactions. The DMRG yields correct results for models with small or no exchange interaction even if long-range interactions are present. Now we consider the time-dependent Hamiltonian given by (5). Typically, the classical Hamiltonian is expressed by Ising spin operators, while the tunneling Hamiltonian is given by on-site potentials due to transverse fields. Fortunately the total Hamiltonian contains no exchange interaction. Hence it is probable that the quantum annealing using DMRG succeeds in producing a correct result even for models with long-range interactions. Furthermore we have applied this method to one-dimensional model with periodic boundary condition and obtained correct results. Success for a model with periodic boundary is one of the evidences which indicate simulated quantum annealing with DMRG is applicable to models with long-range interactions. Thus we expect that the use of DMRG creates possible new algorithm to hard combinatorial optimization problems.

5 Conclusion

The quantum annealing method provides a new quantum algorithm for combinatorial optimization problems represented by random Ising models. The problem is to obtain the ground state of a random Ising model, and the solution is given by a certain classical spin configuration. The quantum annealing method extracts a classical state from a quantum superposition of classical states. The process of quantum annealing is realized in principle by the real-time adiabatic evolution from the quantum ground state to the classical ground state. We reviewed theories on the adiabatic evolution in quantum mechanics.

Since the quantum annealing method is a fresh algorithm, properties on this method has not been revealed sufficiently. The residual energy is known as an important quantity which tells the efficiency of the method used. We investigated the annealing-time dependence of the residual energy, and obtained that the residual energy decreases as square inverse of the annealing time τ,

$$E_{\mathrm{res}}^{\mathrm{QA}} \sim \frac{A}{\tau^2} \,,$$

for long annealing-time limit. This result is in contrast to the logarithmic behavior, (2), in thermal annealing. Therefore the convergence of the solution to the exact one by the quantum annealing is qualitatively faster than that by the thermal annealing.

Special methods are required for simulation of quantum annealing in conventional computers. Direct simulations are limited to small-sized problems because of exponential increases in the number of bases. The quantum Monte-Carlo method has been applied to quantum annealing. Although it utilizes Markovian Monte-Carlo process instead of real-time evolution, it sometimes succeeds in obtaining the ground state. However there is no guarantee on the adiabatic evolution in the Monte-Carlo process, and moreover quantum Monte-Carlo method involves small thermal fluctuations. As a new method of simulation which overcomes problems in quantum Monte-Carlo technique, we proposed use of the density matrix renormalization group (DMRG) method for quantum annealing. Results of simulation on one-dimensional random Ising model with periodic boundary condition show success of quantum annealing, though DMRG is known to be inappropriate to periodic systems. The successful performance for periodic systems in addition to the absence of exchange interactions in the model intended for quantum annealing suggest applicability of DMRG to models including long-range interactions. We expect the simulated quantum annealing using DMRG provides a powerful method for optimization problems.

Acknowledgement

S.S. thanks N. Shibata for fruitful discussions. The present work is supported by a Grant-in-Aid for Scientific Research (Grant No.14084212 and 16500093) by the Ministry of Education, Culture, Sports, Science and Technology of Japan.

References

1. S. Kirkpatrick, C. D. Gelett, and M. P. Vecchi, Science **220**, 671 (1983). 207
2. A. B. Finnila, M. A. Gomez, C. Sebenik, C. Stenson, and J. D. Doll, Chem. Phys. Lett. **219**, 343 (1994). 207
3. T. Kadowaki and H. Nishimori, Phys. Rev. E **58**, 5355 (1998). 207, 211
4. J. Brooke, D. Bitko, T. F. Rosenbaum, and G. Aeppli, Science **284**, 779 (1999). 207
5. G. E. Santoro, R. Martoňák, E. Tosatti, and R. Car, Science **295**, 2427 (2002). 207, 209, 231
6. N. Metropolis, A. W. Rosenbluth, M. N. Rosenbluth, A. H. Teller, and E. Teller, J. Chem. Phys. **21**, 1087 (1953). 208
7. S. Geman and D. Geman, IEEE Trans. Pattern. Anal. Mach. Intell. **6**, 721 (1984). 208
8. T. Sato, N. Hatano, M. Suzuki, and H. Takayama, (unpublished). 208
9. J. R. L. de Almeida and D. J. Thouless, J. Phys. A **11**, 983 (1978). 209
10. D. Sherrington and S. Kirkpatrick, Phys. Rev. Lett. **35**, 1792 (1975). 209
11. T. Yokota, Phys. Lett. A **125**, 482 (1087). 209
12. P. Ray, B. K. Chakrabarti, and A. Chakrabarti, Phys. Rev. B **39**, 11828 (1989). 209
13. D. A. Huse and D. S. Fisher, Phys. Rev. Lett. **57**, 2203 (1986). 209

14. S. Shinomoto and Y. Kabashima, J. Phys. **A 24**, L141 (1991). 209
15. S. Suzuki and M. Okada, J. Phys. Soc. Jpn. (in press); cond-mat/0502203. 209
16. P. W. Shor, in Proceeding of the 35th Annual Symposium on Foundation of Computer Science, IEEE Computer Society Press, Los Alamitos, CA, 124 (1994). 210
17. E. Farhi, J. Goldstone, S. Gutmann, J. Lapan, A. Lundgren, and D. Preda, Science **292**, 472 (2001). 210
18. T. Hogg, Phys. Rev. A **67**, 22314 (2003). 210
19. M. Steffen, W. van Dam, T. Hogg, G. Breyta, and I. Chuang, Phys. Rev. Lett. **90**, 67903 (2003). 210
20. T. Kadowaki, Thesis, quant-ph/0205020. 210
21. R. Martoňák, G. E. Santoro, and E. Tosatti, Phys. Rev. B **66**, 94203 (2002). 210
22. A. Messiah, *Quantum Mechanics*, Vol. 2 (North-Holland, Amsterdam, 1962). 212
23. L. D. Landau and E. M. Lifshitz, *Quantum Mechanics : non-relativistic theory*, 2nd ed. (Pergamon Press, Oxford, 1965).
24. C. Zener, Proc. Roy. Soc. London Ser. A **137**, 696 (1932). 212
25. S. R. White and A. E. Feiguin, Phys. Rev. Lett. **93**, 076401 (2004). 232
26. M. Suzuki, J. Math. Phys. **26**, 601 (1985). 232
27. S. R. White, Phys. Rev. Lett. **69**, 2863 (1992). 234

Quantum Annealing of a $\pm J$ Spin Glass and a Kinetically Constrained System

Arnab Das and Bikas K. Chakrabarti

Theoretical Condensed Matter Physics Division and Center for Applied Mathematics and Computational Science, Saha Institute of Nuclear Physics 1/AF, Bidhannagar, Kolkata-700064, India
arnab.das@saha.ac.in
bikask.chakrabarti@saha.ac.in

1 Introduction

Thermal annealing [1] is known to be a very general and useful method for obtaining approximate solutions of multi-variable optimization problems. Such a problem consists of the minimization of a multi-variable function (cost-function) with respect to its variables (sometimes obeying a given set of constraints). The cost-function landscape are often very rugged, consisting of local minima surrounded by high cost-barriers. In such cases optimization using iterative minimization heuristics can fail miserably by getting trapped into an arbitrarily shallow minimum. In thermal annealing a fictitious thermal fluctuation is introduced into the minimization dynamics to generate possibility of going uphill. This enables the system to get out of the shallow traps and explore the landscape more widely to find out a reasonably deep minimum for settling down. The thermal fluctuation is eventually, but slowly, reduced to zero and one ends up, to a good approximation, with a globally optimized solution.

Quantum annealing is essentially a similar method, where the fluctuations employed for the annealing are quantum (rather than thermal) in nature [2, 3]. In this method one maps the multi-variable cost function to a (classical) Hamiltonian $\mathcal{H}$, and the independent variables, to the degrees of freedom (involved in $\mathcal{H}$). One can represent $\mathcal{H}$ by a hermitian matrix; the eigenstates of $\mathcal{H}$ (basis states) will represent different classical configurations (different sets of values of the independent variables) and the eigenvalues corrosponding to them, the values of the cost function for respective configurations. As such, all the terms (corrosponding to interactions between different degrees of freedom) in $\mathcal{H}$ are mutually commuting since the degrees of freedom are all classical. Quantum fluctuation is introduced by adding to the Hamiltonian, a suitable kinetic term $\mathcal{H}'(t)$ that does not commute with $\mathcal{H}$. This non-commuting term $\mathcal{H}'(t)$ introduces tunnelling probabilities between the eigenstates of $\mathcal{H}$. The

A. Das and B.K. Chakrabarti: *Quantum Annealing of a Spin Glass and a Kinetically Constrained System*, Lect. Notes Phys. **679**, 239–257 (2005)
www.springerlink.com

ground state of the total Hamiltonian $(\mathcal{H}'(t)+\mathcal{H})$ is thus a superposition of the eigenstates of $\mathcal{H}$. The introduction of such a quantum tunnelling is supposed to make the energy barriers in the landscape transparent to the system. This allows transitions between different configurations classically trapped between even infinite barriers, if the barriers are narrow enough. In other words, it is expected that application of a quantum tunnelling term will make the free energy landscape completely ergodic, i.e., the system will consequently be able to visit any configuration with finite probability [4]. Finally, of course, the quantum tunnelling term is to be tuned to zero following some annealing schedule to get back the classical Hamiltonian.

According to adiabatic theorem of quantum mechanics, in such a quantum mechanical evolution, if the initial state of the sytem is the ground state of the total Hamiltonian, then for a slow enough annealing schedule, the system will continue to be in the ground state of the evolving Hamiltonian, and in the limit $t \to \infty$, the system will be found in the ground state of $\mathcal{H}$ (which is the solution to the optimization problem). Thus in principle, a sufficiently slow adiabtic evolution for any $\mathcal{H}$, can always end up with the solution of the corrosponding classical problem, no matter how hard it may be. But if the problem is NP-hard, then whether such an adiabatic evolution can actually solve the problem in polynomeal time (i.e., the evolution time that guarantees the attainment of the ground state, is bounded by some polynomeal in the system size N) is still an open question. Some positive indications in this direction have been found from the study of time-dependent Schrödinger Equation for small systems [5, 6]. However, the cpu time for following exact Schrödinger evolution in a classical computer is clearly much greater than that required for solving the original (classical) problem itself, since at the early stage of the annealing when the non-commuting term $\mathcal{H}'$ is very high, the ground state of the system will be a superposition, where all the basis states (classical configurations) contribute substancially. Hence at each step of evolution one has to evaluate all possible classical configurations at this stage of annealing.

One can in any case, use quantum Monte Carlo methods to simulate such quantum evolutions in order to anneal systems representing hard optimization problems. Such Monte Carlo quantum annealing methods at finite temperature have been reported to work much better than thermal annealing in some cases[7]. It has been argued that when the barriers are very high but narrow enough, quantum annealing would be the better choice, since the probability of quantum tunnelling across a barrier increases with the decrease of barrier width, while the thermal transition probability in such a case has no such dependence on barrier width [4]. This is however, not the case in general [8]. Actually, quantum and thermal fluctuations are inherently different in nature (as reflected in the functional forms of the transition probabilities in respective cases), giving rise to non-trivial differences in their effectiveness in performing annealing. In fact, unlike the classical glasses below glass transition point,

quantum spin glasses (transverse Ising spin glasses in particular) may remain ergodic even in the glass phase (for low enough tunnelling fields [4, 10, 9]).

In this article we discuss quantum annealing of two different kinds of glassy systems, namely a $\pm J$ infinite range Ising spin glass and a kinetically constrained system in one dimension, using zero temperature quantum Monte Carlo methods.

2 Quantum Annealing of $\pm J$ Ising Spin Glass at Infinite Dimension

In this section we discuss the annealing (relaxation) behaviour of a $\pm J$ infinite range Ising system at zero temperature. The Monte Carlo method used here, samples the ground state of a given quntum Hamiltonian for a given set of values of its parameters (tunnelling field, etc). We start with a high value of the quantum tunnelling term and decrease it to zero very slowly during the simulation. Thus the Monte Carlo method effectively simulates the zero temperature adiabatic evolution of the system (so far ground state expectation values are concerned). Here our aim is to study the nature of such evolution in the system during annealing (rather than formulating an efficient algorithm for finding the ground state of the system).

2.1 Model

Let us consider an infinite range Ising spin system whose Hamiltonian is

$$\mathcal{H} = -\sum_{i,j(>i)}^{N} J_{ij}\sigma_i^z\sigma_j^z \ ,$$

where σ_i^z is the z-component of Pauli spin, representing a classical Ising spin at site i and J_{ij}'s are random variables taking up values either $+1$ or -1 with equal probabilities. The above Hamiltonian describes a cluster of N Ising spins, each connected to all others through exchange interactions of equal strength ($J = 1$) but random signs. Clearly, the eigenstates of $\mathcal{H}$ (the basis states) are the direct-products of the eigenstates of σ_i^z's. Each basis state represents a distinct spin configuration of the system.

For such a system, finding the ground state spin configuration for any arbitrary given realization of interactions (the set of J_{ij}'s), is known to be an NP-hard problem [11]. In thermodynamic limit the system becomes a non-ergodic spin glass below some spin glass temperature T_G. To perform zero temperature quantum annealing of this $\pm J$ Ising system, we need to introduce quantum fluctuations into the system. This is done by adding a transverse field term $\mathcal{H}' = \Omega(t)\sum_{i=1}^{N}\sigma_i^x$ where σ_i^x's are x-components of Pauli spins which introduces probability of tunnelling between the basis states (classical

configurations), and $\Omega(t)$ is the strength of the transverse field. The total Hamiltonian is thus given by

$$\mathcal{H}_{tot} = \mathcal{H} + \mathcal{H}'(t) = -\sum_{i,j(>i)}^{N} J_{ij}\sigma_i^z\sigma_j^z - \Omega(t)\sum_{i=1}^{N}\sigma_i^x \ . \tag{1}$$

We start with a high enough value of Ω initially (at $t = 0$) and sample the ground state of $\mathcal{H}_{tot}$ using a zero temperature quantum Monte Carlo algorithm (discussed below). During sampling, we reduce the strength $\Omega(t)$ of the transverse field very slowly following a linear annealing schedule. At the end of the simulation $\Omega(t)$ becomes zero, and we are left with the classical Hamiltonian $\mathcal{H}$. The simulated system is finally found to be in an optimized eigenstate of $\mathcal{H}$, occationally mixed (in a very small percentage) with few other energetically close basis states.

2.2 The Zero Temperature Quantum Monte Carlo Method Used

To simulate the ground state of $\mathcal{H}_{tot}$, we use a zero-temperature quantum Monte Carlo technique [12]. In this method one makes a linear transformation of the form

$$\mathcal{T} = C\mathcal{I} - \mathcal{H}_{tot} \ , \tag{2}$$

where C is a suitable real constant and $\mathcal{I}$ is the identity operator, such that the matrix representation of $\mathcal{T}$ in the eigen-basis of $\mathcal{H}$ is non-negative and irreducible (if such a transformation could not be done for an $\mathcal{H}_{tot}$, then this method would not be applicable for it). One can then consider $\mathcal{T}$ to be the transfer-matrix of a uniform chain (with Periodic Boundary Condition (PBC)) of classical plackets, where each placket is nothing but a classical cluster of N mutually interacting Ising spins represented by $\mathcal{H}$.

Now the key point is that one can simulate the chain of classical plackets using the elements of its transfer-matrix $\mathcal{T}$ and in this simulation the equilibrium average of any observable (say, energy) related to a single placket is approximately equal to the expectation value of the observable over the dominant eigenstate of $\mathcal{T}$. The dominant eigenstate of $\mathcal{T}$ in turn, is the ground state of $\mathcal{H}_{tot}$ (due to the form of the linear transformation between them). Thus we actually simulate the ground state properties of $\mathcal{H}_{tot}$ by simulating the chain. In the next section we establish the scheme in details.

Simulation of a Chain of Classical Plackets Using Transfer-Matrix

In this subsection we demonstrate that the equilibrium averages for a single member of a uniform classical chain (with PBC) is approximately equal to the respective averages (expectation values) over the dominant eigenstate of the transfer-matrix of the chain. Let us consider a uniform chain of L identical classical spin clusters (or may be any localized discrete degrees of freedom in

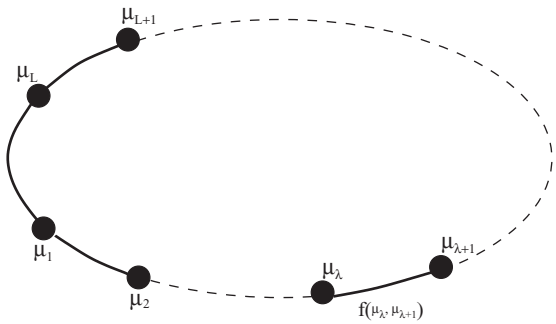

Fig. 1. The figure shows the uniform chain of plackets (with periodic boundary condition) used to simulate the ground state of $\mathcal{H}_{tot}$ (1). A placket (*solid circle*) in the chain is basically the cluster of N Ising spins with a given realization of J_{ij}'s, represented by $\mathcal{H}$ in (1). The interactions $f(\mu_\lambda, \mu_{\lambda+1})$ between any two nearest-neighbour-plackets are determined by the relation $\mathcal{T}_{\mu_\lambda \mu_{\lambda+1}} = e^{-\beta f(\mu_\lambda, \mu_{\lambda+1})}$, where $\mathcal{T}$ is obtained from $\mathcal{H}_{tot}$ by the linear transformation (8). If the dimension of each placket is d, then the dimension of the resulting chain is $d+1$

general) μ_i's, as shown in Fig. 1. Each of the μ_i's can be in, say, p different states. One may note here, that if each placket μ is a spin cluster embedded in dimension d, then the chain is actually a $d+1$-dimensional object. Since the chain is uniform, its Hamiltonian will be of the form

$$\mathcal{H}_{d+1} = \sum_{\lambda=1}^{L} f(\mu_\lambda, \mu_{\lambda+1}) \ ,$$

where $f(\mu_\lambda, \mu_{\lambda+1})$ is a $p \times p$ matrix whose elements are the possible contributions to the Hamiltonian from a pair of neighbouring spins, as each of them takes up p different values independently. The partition function of the chain is thus given by

$$\begin{aligned} Z &= \sum_{\mu_1=1}^{p} \cdots \sum_{\mu_L=1}^{p} \exp\left[-\beta \sum_{\lambda=1}^{L} f(\mu_\lambda, \mu_{\lambda+1})\right] \\ &= \sum_{\mu_1=1}^{p} \cdots \sum_{\mu_L=1}^{p} e^{-\beta f(\mu_1,\mu_2)} \times e^{-\beta f(\mu_2,\mu_3)} \times \cdots \times e^{-\beta f(\mu_L,\mu_1)} \\ &= \sum_{\mu_1=1}^{p} \cdots \sum_{\mu_L=1}^{p} \mathcal{T}_{\mu_1\mu_2} \times \mathcal{T}_{\mu_2\mu_3} \times \cdots \times \mathcal{T}_{\mu_L\mu_1} \ , \end{aligned}$$

where $\mathcal{T}_{\mu_\lambda \mu_{\lambda+1}} = e^{-\beta f(\mu_\lambda, \mu_{\lambda+1})}$, β being the temperature inverse. Again, since each of μ_λ and $\mu_{\lambda+1}$ can take up p independent values (i.e., can be in p independent states), $\mathcal{T}_{\mu_\lambda \mu_{\lambda+1}}$ defines a $p \times p$ matrix $\mathcal{T}$. Hence summing over all the indices from μ_2 to μ_L and recalling the rule of matrix multiplication one gets

$$Z = \sum_{\mu_1=1}^{p} (\mathcal{T}^L)_{\mu_1\mu_1} = Trace(\mathcal{T}^L) \ .$$

The matrix $\mathcal{T}$ is a transfer-matrix for the chain. If the matrix $\mathcal{T}$ is symmetric then (it is not the necessary but the sufficient condition) one can write

$$Z = \sum_{r=1}^{p} (\theta_r)^L \ ,$$

where θ_r are the eigenvalues of $\mathcal{T}$ ordered by the index r, so that $|\theta_i| \geq |\theta_j|$ if $i < j$. Here a few points are to be noted. Since all the elements of $\mathcal{T}$ are strictly positive at any finite β, the matrix $\mathcal{T}$ is both non-negative and primitive (i.e., there exists some finite n, such that $\mathcal{T}^n$ is strictly positive). Then according to Perron-Frobenius theorem (see [13]) the dominant eigenvalue θ_1 is strictly positive and non-degenerate. Thus

$$\begin{aligned} Z &= (\theta_1)^L + \sum_{r=2}^{p} \left(\frac{\theta_r}{\theta_1}\right)^L \\ &\approx (\theta_1)^L \end{aligned}$$

Here, the leading order error is $(\theta_2/\theta_1)^L$ and since θ_1 is non-degenerate,

$$\lim_{L\to\infty} \left(\frac{\theta_i}{\theta_1}\right)^L = 0 \tag{3}$$

for any $i \neq 1$.

Now, to see how one can simulate the chain using $\mathcal{T}$, one has to note that the probability that the chain be in a given state A, in which $\mu_1 = \mu_1(A), \mu_2 = \mu_2(A) \cdots$ etc, is

$$\begin{aligned} P(A) &= \left(e^{-\beta f[\mu_1(A),\mu_2(A)]} \times \cdots \times e^{-\beta f[\mu_L(A),\mu_1(A)]}\right)/Z \\ &= \left(\mathcal{T}_{\mu_1(A)\mu_2(A)} \times \cdots \times \mathcal{T}_{\mu_L(A)\mu_1(A)}\right)/Z \end{aligned} \tag{4}$$

Thus using the conditions of detailed balance, one obtains transition probability from a state A to another state B given by

$$P(A \to B) = \frac{\mathcal{T}_{\mu_1(B)\mu_2(B)} \times \cdots \times \mathcal{T}_{\mu_L(B)\mu_1(B)}}{\mathcal{T}_{\mu_1(A)\mu_2(A)} \times \cdots \times \mathcal{T}_{\mu_L(A)\mu_1(A)}} \ . \tag{5}$$

Thus if $\mathcal{T}$ is given, we can simulate the equilibrium properties (thermal average) of any physical quantity related to a placket μ in the chain. To obtain that, we require to know the probabilites for the placket μ to be in its different possible states when the chain is in equilibrium. Let $P(\mu = k)$ denotes the probability that the placket is found in its k-th state when the chain is at thermal equilibrium (at a given β). If the k-th state is represented by a column vector $|k\rangle$, then these column vectors satisfy the matrix relation

$$\langle i|\mathcal{T}|j\rangle = \mathcal{T}_{ij} \ ,$$

where $\langle i|$ is the transpose of $|i\rangle$ and the sequence of matrices implies the proper multiplications between them.

On the other hand, if $|E_1\rangle$ be the dominant (normalized) eigenvector of $\mathcal{T}$ corrosponding to the dominant eigenvalue θ_1, and if $\mathcal{T}$ is hermitian then one can expand $|E_1\rangle$ linearly in terms of the basis vectors as

$$|E_1\rangle = \sum_{k=1}^{p} \gamma_1^k |k\rangle \ , \tag{6}$$

where γ_k^1 is the amplitude of the basis state $|k\rangle$ in $|E_1\rangle$. Thus in the sampling of $|E_1\rangle$ using the basis states $|k\rangle$'s, the probability of occurance of the state $|k\rangle$ will be $|\gamma_k^1|^2$. Now, one can show that

$$P(\mu = k) = |\gamma_k^1|^2 + \mathcal{O}\left[(\theta_2/\theta_1)^L\right] \ . \tag{7}$$

The above equation says that one can sample the dominant eigenstate $|E_1\rangle$ of the matrix $\mathcal{T}$ just by sampling its basis states (classical configurations of a placket in the chain) according to the probability of their occurance in the simulation of the placket at equilibrium in the chain (using the elements of $\mathcal{T}$ itself, as prescribed in (5)).

To prove equation (7), we take any placket in the chain and call it μ_1. Probability that μ_1 is found in the state $|k\rangle$ is

$$\begin{aligned} P(\mu_1 = k) &= \frac{1}{Z}\left[\sum_{\mu_2}\sum_{\mu_3}\cdots\sum_{\mu_L} \mathcal{T}_{\mu_1\mu_2}\mathcal{T}_{\mu_2\mu_3}\cdots\mathcal{T}_{\mu_L\mu_1}\right]_{\mu_1=k} \\ &= \frac{1}{Z}\,(\mathcal{T})^L_{kk} = \frac{\langle k|(\mathcal{T})^L|k\rangle}{trace\{(\mathcal{T})^L\}} \ . \end{aligned} \tag{8}$$

Above, we have summed up the probabilities of all the configurations of the chain, in which $\mu_1 = k$. Now let $|\theta_i\rangle$ $(i = 1, 2, \cdots p)$ denote the normalized eigenvector of $\mathcal{T}$ corrosponding to the eigenvalue θ_i. Then one may have a linear transformation between $|\theta_i\rangle$'s and $|k\rangle$ of the form

$$|\theta_i\rangle = \sum_k \gamma_k^i |\mu_k\rangle$$

and the reverse transformation

$$|k\rangle = \sum_i (\gamma^\dagger)_i^k |\theta_i\rangle = \sum_i \gamma_k^{i*} |\theta_i\rangle \ ,$$

γ being an unitary matrix. Hence

$$\begin{aligned} \mathcal{T}^L|k\rangle &= \sum_i \gamma_k^{i*}\theta_i^L|\theta_i\rangle \\ \Rightarrow \langle k|\mathcal{T}^L|k\rangle &= \sum_i |\gamma_k^i|^2\theta_i^L \ , \end{aligned}$$

using ortho-normality of $|\theta_i\rangle$'s. Thus, from equation (8) we get

$$\begin{aligned} & P(\mu_1 = k) \\ = & \frac{\langle k|\mathcal{T}^L|k\rangle}{trace\{\mathcal{T}^L\}} \\ = & \frac{\sum_i |\gamma_k^i|^2 \theta_i^L}{\sum_i \theta_i^L} \\ = & \frac{\sum_i |\gamma_k^i|^2 (\theta_i/\theta_1)^L}{1 + \sum_{i\neq 1} (\theta_i/\theta_1)^L} \\ \approx & |\gamma_k^1|^2 + \mathcal{O}[(\theta_2/\theta_1)^L] \ , \end{aligned}$$

which proves equation (7).

Thus one can in fact simulate the dominant eigenstate of any given suitable (hermitian, non-negative and primitive) $N \times N$ matrix upto a good approximation using the above results. One has to define a uniform chain (with PBC) of classical plackets, each having N possible configurations. The i-th state of a placket corrosponds to the i-th vector of the basis in which the given matrix is represented. One then views the given matrix as the transfer-matrix for a placket in the chain, and simulate the chain using its elements (as prescribed in (5)). At equilibrium, the probability of getting a placket in its i-th state is equal to the modulus square of the weight of the i-th basis vector in the representation of the dominant eigenstate of the given matrix (upto an error of the form discussed above).

Implementation of the Monte Carlo

We now illustrate the implementation of the above Monte Carlo scheme by employing it to simulate the ground state of $\mathcal{H}_{tot}$ given in (1). Here basis vectors $|k\rangle$'s are the eigenvectors of $\mathcal{H}$, and a classical placket is the cluster of N Ising spins with exchange interaction described by $\mathcal{H}$. Now we make a linear transformation of the form given in (2), with $C = N(N-1)/2$. The resulting $\mathcal{T}$ matrix is clearly non-negative (since none of its diagonal element are all smaller than $N(N-1)/2$ and off-diagonal elements are either 0 or $\Omega(t)$, which we always take to be positive.). Since $\mathcal{H}_{tot}$ connects a basis state to all other basis states that can be obtained by a single spin flip from it, there is no closed subspace for $\mathcal{H}_{tot}$. Thus $\mathcal{T}$ is also irreducible. It can be shown that for a non-negative irreducible matrix, all the results of Perron-Frobenius theorem we have used here, holds good [13]. Besides, $\mathcal{T}$ is of course hermitian. Hence we can take $\mathcal{T}$ as a transfer-matrix for the chain. It corrosponds to some interaction $f(\mu_\lambda, \mu_{\lambda+1})$ between two neighbouring (μ_λ and $\mu_{\lambda+1}$) and some inverse temperature β (not explicitly important here), given by

$$\mathcal{T}(\mu_\lambda, \mu_{\lambda+1}) = e^{-\beta f(\mu_\lambda, \mu_{\lambda+1})} \ .$$

To simulate the ground state of $\mathcal{H}_{tot}$ at a given Ω for a particular realization of J_{ij}'s, we construct a uniform chain of L plackets with PBC. Each placket is a cluster of N classical Ising spins (described by cooperative term of $\mathcal{H}_{tot}$) connected through the given particular realization of J_{ij}'s (see 1). We start with an arbitrary spin configuration (same for all plackets) and a given value of Ω. In one Monte Carlo step we randomly visit L plackets. At each such visit we make an allowed move (a move whose probability is not trivially zero), such that the chain goes from a state A, say, to a new state, say B. The probability of acceptance of the move is nothing but the transition probablity $P(A \rightarrow B)$ calculated following (5) (using the elements of $\mathcal{T}$). While sampling, one can easily avoid moves whose probabilities are trivially zero (due to the sparsity of the matrix $\mathcal{T}$) by constructing a more restricted Markov process to do the sampling [12].

For doing quantum annealing of the same system, we start with a high enough value of Ω and reduce it very slowly with time t (Monte Carlo step) following a linear schedule. During visiting different plackets in a given Monte Carlo step, Ω is however held fixed. The linear schedule is specified by $\Omega(t = 0) = \Omega_{in}$ and The total number of Monte Carlo steps executed; Ω_{in} is linearly reduced to zero with t within 95% of the total Monte Carlo steps.

2.3 Results and Discussions

We have studied the relaxation behaviour of several random J_{ij} samples with $N = 30$ for linear annealing schedule (we start with an initial transverse field Ω_{in} and reduce it linearly with Monte Carlo step, so that it becomes zero before last few, 5%, steps. We observe that for an annealing of $\sim 10^7$ Monte Carlo steps, the system reaches the true ground state (determined by an extensive search method) in almost every case, for a suitably large initial transverse field Ω_{in}. We calculate the average exchange energy of the chain (over L plackets) in each Monte Carlo step, and average that over a few ~ 500 Monte Carlo steps. The exchange energy (as given by $\mathcal{H}$ of (1)) is not linear in N and we have to scale it by a factor $N^{3/2}$ to obtain the intensive energy density. In thermodynamic limit, this intensive energy density approaches the value -0.7633[11] (our finite size results shows some fluctuations about that). In Fig. 2 the relaxation behaviour of three typical random realizations (R1, R2 and R3) during their annealing are shown. We found that for doing annealing of a given sample within a given number of steps, there is a suitable range of Ω_{in}. If Ω_{in} falls below the range, then the transition probabilities are too low to be able to anneal the system within the given time. On the other hand, if Ω_{in} is above the range, then the rate of change of $\Omega(t)$ is not slow enough to ensure the convergence to the ground state finally (i.e., the evolution in no more adiabatic). In Fig. 2, the values of respective Ω_{in}'s belong to the lower end of the respective ranges. The ranges are generally wide enough, and one can find a Ω_{in} within the range, just by a few trials.

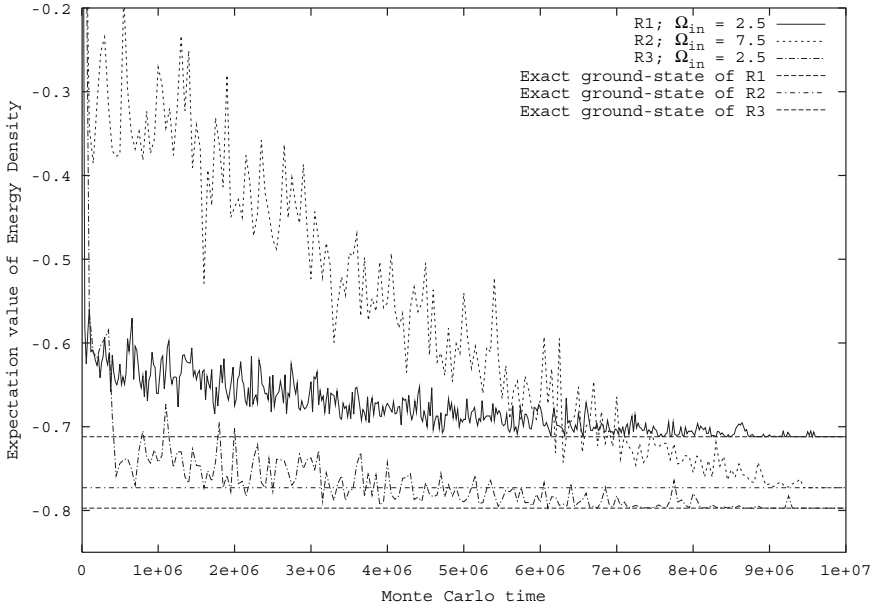

Fig. 2. In the figure, annealing behaviour of three different randomly generated realizations (R1, R2 and R3) of J_{ij}'s are shown for $N = 30$. In Each case the system goes to the exact ground state (shown by respective horizontal lines) at the end of the annealing. In each case the annealing time is 10^7 Monte Carlo steps, number of plackets in the chain is $L = 600$, and each Monte Carlo step consists of visiting L plackets randomly and making a random spin-flip trial there. In each case, the initial transverse field (Ω_{in}) has been reduced to zero following a linear schedule, within the Monte Carlo steps. The initial transverse field Ω_{in} is chosen to be just sufficient for reaching the ground state finally, within the given Monte Carlo steps

The relaxation behaviour is found to be typically "linear" in the sense that the long-time averages decrease linearly with time (see lower part of Fig. 3). The relaxation observed in shorter time scale of course shows fluctuations around that linear behaviour (shown in the upper part of Fig. 3). This linear nature of relaxation is typically seen independent of the details of the particular realizations. The slope of the linear fit of course depends on the the annealing time, Ω_{in}, and also on the system size, (not discussed here).

3 Quantum Annealing in a Kinetically Constrained System

Here we demonstrate the effectiveness of quantum annealing in the context of a certain generalized Kinetically Constrained Systems (KCS) [14]. KCS's are simple model systems having trivial ground state structures and static

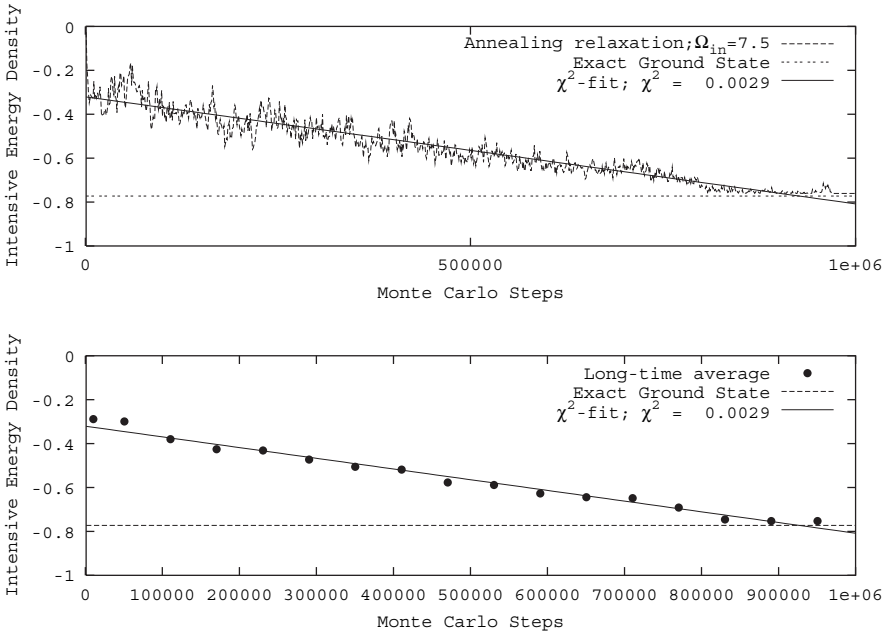

Fig. 3. In this figure the annealing relaxation ($N = 30$, $L = 600$ and $\Omega_{in} = 7.5$) for a particular realization is shown. The upper frame shows the relaxation of intensive energy density with time, when averaged over small ($\sim$500) Monte Carlo steps. The lower frame shows the same relaxation, when the averaging is done over a much larger number of ($\sim 10^4$) Monte Carlo steps. A linear χ^2-fit for the longer time average is shown in the lower part of the figure

properties, but a complex relaxation behaviour due to some explicit constraints introduced in the dynamics of the system [14]. These systems are very important in understanding how much of the slow and complex relaxation behaviour of a glass can be attributed to its constrained dynamics alone, leaving aside any complexity of its energy landscape structure. In KCS's one can view the constraints to be represented by infinitely high energy barriers appearing dynamically. To study annealing, we generalize such models by allowing the height of such kinetically occurring barriers to be finite but large.

Here we study quantum annealing in the context of a kinetically constrained system, which can be represented by a generalized version of East model [15] (a one dimensional KCS). We also compare the results with that of thermal annealing done in the same system. The original East model is basically a one-dimensional chain of non-interacting classical Ising ('up-down') spins in a longitudinal field h, say, in downward direction. The ground state of such a system is trivially given by all spins down. A kinetic constraint is introduced in the model by putting the restriction that the i-th spin cannot flip if the $(i-1)$-th spin is down. Such a kinetic constraint essentially changes

the topology of the configuration space, since the shortest path between any two configurations differing by one or more forbidden flips, is increased in a complicated manner owing to the blockage of the 'straight' path consisting of direct flips of the dissimilar spins. Further, the constraint becomes more limiting as more spins turn down, as happens in the late approach to equilibrium. As a result, the relaxation processes have to follow more complex and lengthier paths, giving rise to exponentially large timescale ($\sim e^{1/T^2}$, where T is the temperature) [15].

3.1 Model

Our model [16] is a chain of asymmetric double-wells (each with infinite boundary walls), with a particle localized within each of them. The asymmetry is due to an energy difference of $2h$ between the two wells of a double well. The particle in one of the two (asymmetric) well can change its location to the other well stochastically, either due to the thermal fluctuation or due to quantum fluctuation present in the system. The generalized kinetic constraint is introduced by assuming that if the particle in the $(i-1)$-th double-well resides in the lower one of the two wells, then there appears a barrier of height χ and width a between the two wells of the i-th double-well. In such a situation the particle in the i-th double-well has to cross the barrier in order to change its location from one well to the other (Fig. 4(b)). On the other hand, if the particle of the $(i-1)$-th is in its upper well, there is no such barrier to cross for (Fig. 4(a)). Following the approximate mapping done in case of symmetric double-well [10], this model can be approximately represented by

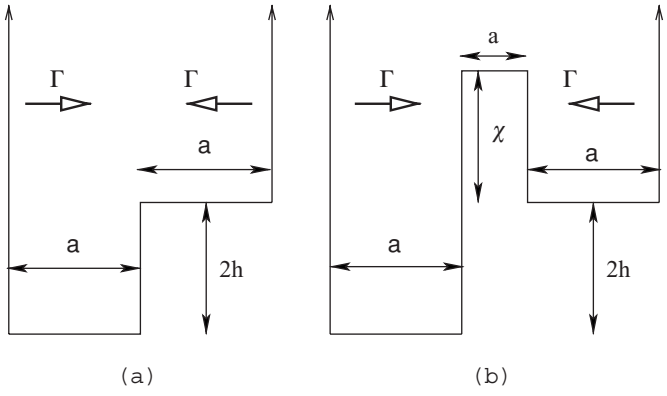

Fig. 4. Potential energy wells for the spin at site i, when $(i-1)$-th spin is (a) up and (**b**) down, with the external field h in the downward direction and barrier height χ very large and the width a small. For the classical generalized East model, flipping across the barrier in (b) is a thermal jump (at any finite T). In the quantum model considered here, probability for crossing the barrier in (b) is due to quantum tunnelling through it at a finite Γ

a generalized version of East model, where each Ising spin is in a local longitudinal field h in downward direction. The spin at the i-th site sees a barrier of height χ and width a between its two energy states when the $(i-1)$-th spin is down (Fig. 4(b)), where as no such barrier occurs for the i-th spin when the $(i-1)$-th spin in up (Fig. 4(a)). This kinetic constraint is same in both cases irrespective of whether the dynamics is classical or quantum.

When dynamics of the particle is due to quantum fluctuations, the tunnelling probabilities come from the following semi-classical picture of scattering of a particle in a double-well with infinitely remote outer boundaries ($a \to \infty$ in Fig. 4). If a particle is put in one of the wells of such a double-well with some kinetic energy (actually the expectation value) Γ, then it will eventually be scattered by the separator (a barrier or step) between the two wells. In such a scattering, there is a finite probability P that the particle manages to go to the other well. We calculate P from the simple picture of scatterings of a particle by one dimensional potentials as prescribed below. In thermal case we take simple Boltzmann probabilities for crossing the same barriers. The minimum of the energy of the Ising chain (equivalent to the potential energy of the chain of the double-wells) trivially corresponds to the state with all the spins down, i.e., aligned along the longitudinal field h (where all the particles are in their respective lower wells). To reach the ground state in quantum case, we start with a very large initial value of Γ and then reduce it following an exponential schedule given by $\Gamma = \Gamma_0 \exp(-t/\tau_Q)$. Here t denotes the time, and τ_Q sets the effective time scale of annealing. At zero temperature the slow spin flip dynamics occurs only due to the tunnelling (kinetic energy) term Γ, and hence the system ceases to have any relaxation dynamics in the limit $\Gamma \to 0$. It may be mentioned here that in absence of any analytical expression for the tunnelling probability in asymmetric case of the type discussed here (see e.g., [17]), we employ the asymmetric barrier tunnelling probabilities available [18]. Similarly, in thermal case, we start with a high initial temperature T_0 and reduce it eventually following an exponentially decreasing temperature schedule given by $T = T_0 \exp(-t/\tau_C)$; τ_C being the time constant for the thermal annealing schedule. Here, when $(i-1)$-th spin is down, the flipping probability for the i-th spin ($\sim \exp(-\chi/T)$). Otherwise, it flips with probability $P = 1$ if it were in the up state, and with Boltzmann probability $P = \exp(-h/T)$ if it were in the down state.

3.2 Simulation and Results

We have employed [16] the quantum transmission (flipping) probabilities (cf. [18]) from a very elementary scattering picture which is qualitatively adequate, though not strictly valid for the asymmetric double-well (shown in Fig. 4(b)) because the states within it are bound by its finite width a. Following are the flipping probabilities (P) for the i-th spin in different possible situations used in our Monte Carlo simulation:

I. If the $(i-1)$-th spin is up and the i-th spin is also up then $P = 1$.

II. If the $(i-1)$-th spin is up and the i-th spin is down then (a) $P = 0$ for $\Gamma < 2h$ and (b)$P = min\{1, 4[\Gamma(\Gamma - 2h)]^{1/2}/(\sqrt{\Gamma} + \sqrt{\Gamma - 2h})^2\}$ for $\Gamma \geq 2h$.

III. If the $(i-1)$-th spin is down and the i-th spin is up then $P = min\{1, 4[\Gamma(\Gamma + 2h)]^{1/2} /((\sqrt{\Gamma} + \sqrt{\Gamma + 2h})^2 + g^2)\}$.

IV. If the $(i-1)$-th spin is down and the i-th spin is down then (a) $P = 0$ for $\Gamma < 2h$, and (b) $P = min\{1, 4[\Gamma(\Gamma - 2h)]^{1/2}/((\sqrt{\Gamma} + \sqrt{\Gamma - 2h})^2 + g^2)\}$ for $\Gamma \geq 2h$ (h and Γ denoting the magnitudes only).

Here $g = \chi a$, χ and a being respectively the height and width of the barrier representing the kinetic constraint. The above expressions for P are actually the transmission coefficients in respective cases of one-dimensional scattering across asymmetric barrier or step (according to the form of the potential encountered in passing from one well to the other, see e.g., [18]). Application of the above scattering picture, even for the double-wells in Fig. 4b (which our simulation is based on) as discussed before, is of course an approximation. It may be noted that our flipping probabilities used here do not satisfy the condition of detailed balance, though the evolution matrix has got the required stochastic structure.

In our simulation [16], we take N Ising spins ($\sigma_i = \pm 1, \quad i = 1, \ldots, N$) on a linear chain with PBC. The initial spin configuration is taken to be random such that magnetization $m = (1/N)\sum_i \sigma_i$ is practically negligible ($m_i \approx 0$). We then start with a tunnelling field Γ_0 and follow the zero temperature (semi-classical) Monte Carlo scheme as mentioned above, using the spin flip probabilities P's appropriate for the four cases I-IV. Each complete run over the entire lattice is taken as one time unit and as time progresses, Γ is decreased from its initial value Γ_0 according to $\Gamma = \Gamma_0 e^{-t/\tau_Q}$. The results are shown in Fig. 5. It shows that for $N = 50000$ $g = 100$ and $\Gamma_0 = 100$ the system freezes before reaching the ground state ($m_f = 1$) for low values of τ_Q; say for $\tau_Q = 2000$. For a somewhat greater value, e.g., $\tau_Q = 5000$, the system is completely annealed to the ground state within about 4×10^4 time steps. However, for a much greater τ_Q, like $\tau_Q = 20000$, the system of course anneals completely but consumes more time unnecessarily. These generic features remain the same for other higher values of g. We have also studied the dependence of annealing behaviour with the parameter g, which is actually a measure of how impenetrable is the infinite barrier representing the kinetic constraint. Computations were carried out to locate, for a given value of g, the minimum value of τ_Q for which the system just anneals up to $m_f = 0.8$ (complete annealing requires prohibitively longer computer time for this comparative study).

We call this minimum value $(\tau_Q)_{min}$. A bisection scheme was used to locate $(\tau_Q)_{min}$ for different values of g starting for the same initial configuration. The inset in Fig. 5 shows that $(\tau_Q)_{min}$ increases fairly sharply with g (an empirical analysis shows $(\tau_Q)_{min} \sim g^{1.67}$, for $g \leq 1000$. This variation with g depends on the specific functional forms of P occurring in the quantum case. In contrast

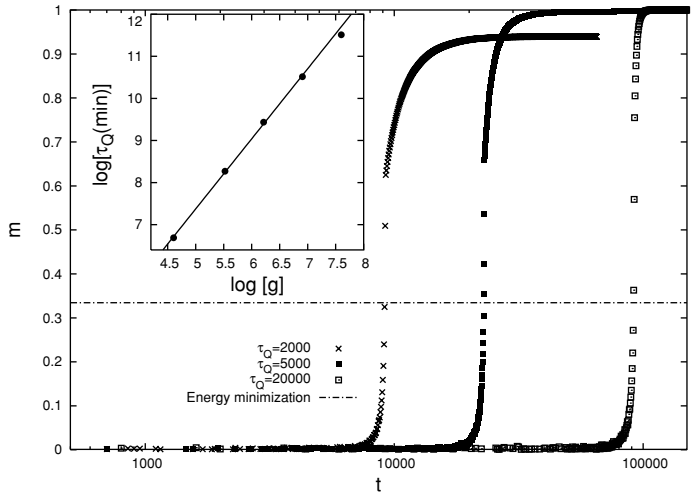

Fig. 5. Quantum annealing ($T = 0$) for $g = 100$, $\Gamma_0 = 100$ and $h = 1$ is shown for different values of τ_Q, for a chain of 5×10^4 spins (m averaged over the same set of 10 initial configurations for each τ_Q). The horizontal (*dashed*) line indicates the average (over the same set $\mathcal{C}$) value of m that could be reached from the initial configurations by simply minimizing the energy following the downhill principle (a single step is enough to get there). In the inset, variation of $\log[(\tau_Q)_{min}]$ with $\log[g]$ is shown (by the points) for one given configuration. The error in $(\tau_Q)_{min}$ is typically less than 0.5% in each case. The continuous line in the inset shows a fit of the data by the continuous line $(\tau_Q)_{min} \sim g^{\kappa}$; $\kappa \approx 1.67$ (obtained by linear least-square fitting)

to this, in classical case, $(\tau_C)_{min}$ grows exponentially with the barrier height χ and is independent of the barrier width a. However, for even higher values of g, the slope is expected to decrease, and finally in the asymptotic limit $g \to \infty$, the relaxation behaviour should converge to that of one with an unsurpassed kinetic constraint (like the classical East model). This asymptotic convergence could not however be explored, since the required computational time becomes prohibitively long as g is increased further.

We compare the results of thermal and quantum annealing (Fig. 6) for the same order of initial value and time constant for Γ and T (barrier height χ is taken to be 1000 in both the cases while g was taken to be 100 in the quantum annealing case, or equivalently the barrier width a is taken to be of the order of 0.1). We observe that to achieve a similar degree of annealing (attaining a certain final magnetization m_f), starting from the same disordered configuration, one typically requires much smaller τ_Q compared to τ_C; typically, $\tau_C \sim 10^3 \times \tau_Q$ for equivalent annealing (for similar optimal values of final order $m_f \sim 0.92$). For annealing with final order $m_f \sim 1$, we find $\tau_C \sim 10^4 \times \tau_Q$. This comparison of course depends on the barrier characteristics (value of g) as shown in the inset of Fig. 5.

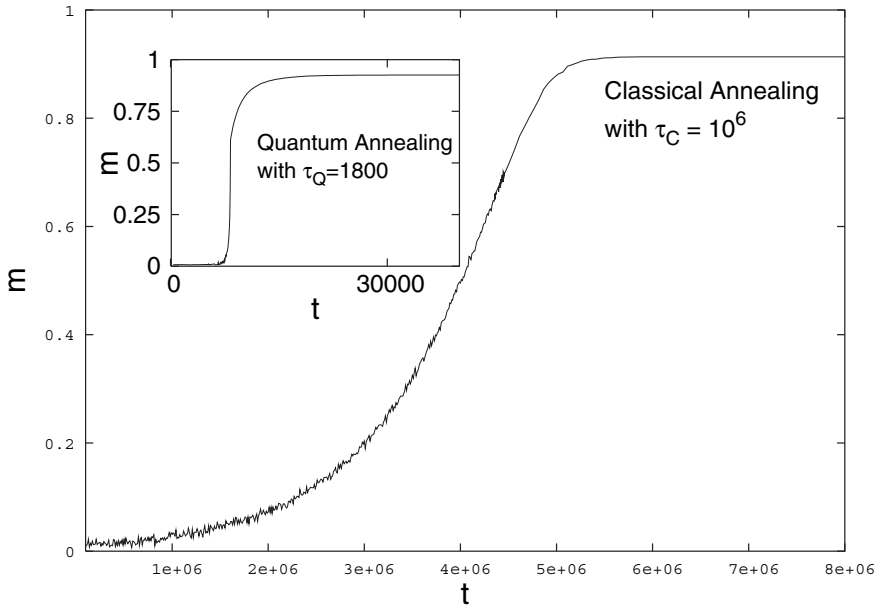

Fig. 6. Comparison between classical and quantum annealing for a chain of 5×10^4 spins (for the same initial disordered configuration with $m_i \sim 10^{-3}$). We show the results for $\tau_Q = 1.8 \times 10^2$ (for quantum) and $\tau_C = 10^6$ (for classical) with $h = 1$; a lower τ_C would not produce substantial annealing. Starting from the same initial values $\Gamma_0 = T_0 = 100$, (and $g = 100$ in the quantum case) we observe that classical annealing requires about 10^7 steps, whereas quantum annealing takes about 10^4 steps for achieving the same final order $m_f \sim 0.92$

3.3 Summary and Discussion

In this chapter, first we have discussed a zero temperature quantum Monte Carlo method using transfer-matrix, and the results of its application to the annealing of an infinite range $\pm J$ Ising system. Since at each instance the Monte Carlo tries to sample the ground state of the system and there is no temperature, for slow enough annealing schedule, the long-time averages calculated by this method are expected to be close to those of the true adiabatic quantum evolution. The quantum Monte Carlo method applied here is quite easy to implement and generally applicable. The only criteria is that the Hamiltonian should be irreducible and there should exist a suitable linear transformation to make the matrix non-negative. If the matrix is reducible and one can identify the individual irreducible blocks in its block-diagonal form, then one can apply the method for each block (using the corrosponding subset of basis) separately. One may note that the meeting of the condition of Perron-Frobenius theorem assures the complete lifting of the degeneracy of the ground state of the Hamiltonian (dominant eigenstate of its linear transform).

This is in fact a necessary condition for the quantum tunnelling term (generating the off-diagonal elements of the Hamiltonian) to assure convergence to the global ground state at the end of the annealing (otherwise one may end up with the lowest energy state within one of the subspaces which are not connected by the tunnelling probabilities, depending on the initial state).

The relaxation behaviour of different random samples to their respective ground states are studied. The long-time average of the intensive energy is found to relax linearly with time (rather than logerithmic [7]). The slope of the linear relaxation depends on the annealing schedule and also on the system size (to be discussed else where).

Next we have discussed the annealing of a generalized kinetically constrained chain of N double-wells with a particle in each, starting from a disordered state (with negligible initial order), to its (external field induced) fully ordered ground state. In our model kinetic constraints are represented by barriers of finite height and width. We have shown that for certain barrier characteristics, namely very high but thin barriers quantum annealing can be far superior to its thermal counter part in reaching the ground state. In this study we have put the barrier features (the height and the width) by hand and see how the difference between the classical and the quantum annealing depends on them.

The noise necessary for the annealing are introduced by temperature T in thermal case and by a quantum mechanical kinetic energy term Γ in quantum case. The introduced noise, is reduced following an exponential schedule in both the cases: $T = T_0 e^{-t/\tau_C}$, $\Gamma = \Gamma_0 e^{-t/\tau_Q}$, with $T_0 \approx \Gamma_0$. For our simulation for the quantum case, we have taken the tunnelling probabilities P (for cases I-IV) and employed them in a semi-classical fashion for the one dimensional spin chain considered. We observe that for similar achievement in final order ($m_f \simeq 0.92$ starting from $m_i = 10^{-3}$), $\tau_C \sim 10^3 \tau_Q$ for $N = 5 \times 10^4$. For even larger order ($m_f \sim 1$), quantum annealing works even better ($\tau_C \sim 10^3 \tau_Q$, for the same value of N). These comparison are for $g = 10^2$ and $\chi = 10^3$ for the constraint barriers.

In this picture, we considered the collective dynamics of a many particle system, where each one is confined in a (field) induced asymmetric double-well potential for which we considered only the low lying two states (the wave packet localized in one well or the other), representing the two states (up and down) of an Ising spin discussed above. The tunnelling of the wave packet from one well to the other was taken into account by employing a scattering picture and we used the tunnelling probabilities as the flip probabilities for the quantum Ising spins. As such, the reported simulation for the one dimensional quantum generalized East model is a semi-classical one.

Here a few words regarding the absence of detailed balance in our flipping probabilities will be in order. Detailed balance (e.g., using rates which are ratios of Boltzmann probabilities) is indeed the simplest way of ensuring the approach of a non-equilibrium system to the simplest types of steady state (e.g., the thermal equilibrium state' corresponding to a canonical ensemble).

But the study of the approach of non-equilibrium systems to steady states typically (and necessarily, in the case of non-product states) involves a more general set of dynamic rules, captured for example by an evolution operator involving a (typically non-hermitian) Hamiltonian which has the usual stochastic structure which ensures conservation of probability, and ensures eigenvalues, one of which is zero, having non-negative real parts. Tunneling is one among many possible processes (usually captured by transition rates in a master equation) which can satisfy these requirements, and is clearly more appropriate than e.g., Arrhenius rates in a quantum system at zero temperature.

It may be noted that, because of the absence of inter-spin interaction, the dimensionality actually plays no role in this model except for the fact that the kinetic constraints on any spin depend only on the left nearest neighbor (directedness in one dimension). Hence the semi-classical one dimensional simulation, instead of a proper quantum Monte Carlo simulation (equivalent to a higher dimensional classical one [10]), is quite appropriate here. Additionally, even for interacting (finite range) one dimensional system order is always completely destroyed at any finite temperature ($T = 0$ is the critical point). Thus it is difficult to reach the ground state efficiently by employing thermal annealing in such systems in presence of competing interactions [10]. However, quantum critical points in such systems exists at finite value of the tunnelling (disordering) field Γ, and one can utilize the order below the critical point while annealing, and reach the ground state more efficiently.

Acknowledgement

We are grateful to Robin B. Stinchcombe for the collaboration in the study on annealing in quantum East model [16] presented here.

References

1. S. Kirkpatrick, C.D. Gelatt, Jr., M.P. Vecchi, Science **220**, 671 (1983) 239
2. T. Kadowaki and H. Nishimori, Phys. Rev. E **58** 5355 (1998) 239
3. J. Brook, D. Bitko, T.F. Rosenbaum and G. Aeppli, Science **284** 779 (1999) 239
4. P. Ray, B.K. Chakrabarti and A. Chakrabarti, Phys. Rev. B **39** 11828 (1989) 240, 241
5. E. Farhi, J. Goldstone, S. Gutmann, J. Lapan, A. Lundgren, and D. Preda, Science **292**, 472 (2001) 240
6. S. Suzuki and M. Okada, *Simulated Quantum Annealing by the Real-time Evolution*. In: Lect. Notes Phys. **679** (2005) pp. 207–238 240
7. G.E. Santoro, R. Martonak, E. Tosatti and R. Car, Science 295, 2427 (2002); R. Martonak, G.E. Santoro and E. Tosatti Phys. Rev. E **70**, 057701 (2004) 240, 255
8. D. Battaglia, L. Stella, O. Zagordi, G.E. Santro and E. Tosatti, *Deterministic and Stochastic Quantum Annealing Approches*. In: Lect. Notes Phys. **679** (2005) pp. 171–206 240

9. D.-H. Kim and J.-J. Kim, Phys. Rev. B **66** 054432 (2002); see however, D. Thirumalai, Q. Li and T.R. Kirkpatrick, J. Phys. A **22** 3339 (1989); see also J.-J. Kim *Ergodicity, Replica Symmetry, Spin Glass and Quantum Phase Transition*. In: Lect. Notes Phys. **679** (2005), pp. 101–129 241
10. B.K. Chakrabarti, A. Dutta, P. Sen: *Quantum Ising Phases and Transitions in Transverse Ising Models*. In: Lect. Notes Phys. **M41** (1996); see also B.K Chakrabarti and A. Das, *Transverse Ising Model, Glass and Quantum Annealing*. In: Lect. Notes Phys. **679** (2005) pp. 3–38 241, 250, 256
11. M. Mezard, G. Parisi and M.A. Virasoro, *Spin Glass Theory And Beyond* (World Scientific, Singapore, 1987) 241, 247
12. J.P. Neirotti and M.J. de Oliveira, Phys. Rev. B **53**, 668 (1996); M.J. de Oliveira and J.R.N. Chiappin Physica A **307** (1997) 242, 247
13. E. Seneta *Non-negative Matrices and Markov Chains (2nd Ed.)* (Springer-Verlag, New York, 1981) 244, 246
14. G.H. Fredrickson and H.C. Andersen, Phys. Rev. Lett. **53** 1224 (1984); G.H. Fredrickson and H.C. Andersen, J. Chem. Phys. **83** 5822 (1985) 248, 249
15. J. Jackle and S. Eisinger, Z. Phys. B **84** 115 (1991); M.A. Munoz, A. Gabrielli, H. Inaoka and L. Peitronero, Phys. Rev. E **57** 4354 (1998); P. Sollich, M.R. Evans, Phys. Rev. Lett. **83** 3238, F. Ritort and P. Sollich, Adv. Phys., **52** 219 (2003) 249, 250
16. A. Das, B.K. Chakrabarti and R.B. Stinchcombe, Phys. Rev. E **72**, 026701 (2005). 250, 251, 252, 256
17. J.G. Cordes and A.K. Das, Superlatt. Microstr., **29** 121 (2001), R. Koc, D. Haydargil, arXiv:quant-ph/0410067 v1 (2004) 251
18. B.K. Chakrabarti and A. Das, *Transverse Ising Model, Glass and Quantum Annealing*. In: Lect. Notes Phys. **679** (2005) pp. 3–38 251, 252

Quantum Spin Glasses Quantum Annealing, and Probabilistic Information Processing

Jun-Ichi Inoue

Graduate School of Information Science and Technology, Hokkaido University, N13-W8, Kita-ku, Sapporo 060-8628, Japan
jinoue@cb4.so-net.ne.jp

1 Introduction

Recently, problems of information processing were investigated from the statistical mechanical point of view [1]. Among them, image restoration (see [2, 3, 4] and references therein) and error-correcting codes [5] are most suitable subjects. In the field of error-correcting codes, Sourlas [5] showed that the convolution codes can be constructed by an infinite range spin-glass Hamiltonian and the decoded message should correspond to the zero temperature spin configuration of the Hamiltonian. Ruján [6] suggested that the error of each bit can be suppressed if one uses finite temperature equilibrium states (sign of the local magnetization) as the decoding result, what we call the *MPM* (*maximizer of posterior marginal*) estimate, instead of zero temperature spin configurations, and this optimality of the retrieval quality at a specific decoding temperature (this temperature is well known as the *Nishimori temperature* in the field of spin glasses) is proved by Nishimori [7].

The next remarkable progress in this direction was made by Nishimori and Wong [8]. They succeeded in giving a new procedure in order to compare the performance of the zero temperature decoding (statisticians call this strategy the *MAP* (*maximum a posteriori*) estimation) with that of the finite temperature decoding, the MPM estimation. They introduced an infinite range model of spin glasses such as the Sherrington–Kirkpatrick (SK) model [9] as an exactly solvable example. Kabashima and Saad [10] succeeded in constructing more practical codes, namely, low density parity check (LDPC) codes by using the spin-glass model with finite connectivities. In these decoding processes, one of the most important problems is how one obtains minimum energy states of the effective Hamiltonian as quickly as possible. Geman and Geman [11] used simulated annealing [12] in the context of image restoration to obtain good recovery of the original image from its corrupted version. Recently, Tanaka and Horiguchi [13, 2] introduced a quantum fluctuation, instead of the thermal one, into the mean-field annealing algorithm and

J.-I. Inoue: *Quantum Spin Glasses Quantum Annealing,and Probabilistic Information Processing*, Lect. Notes Phys. **679**, 259–297 (2005)
www.springerlink.com

showed that the performance of the image recovery is improved by controlling the quantum fluctuation appropriately during its annealing process. The attempt to use the quantum fluctuation to search the lowest energy states in the context of annealings by Markov chain Monte Carlo methods, what we call *quantum annealing*, is originally introduced in [14, 15] and its application to the combinatorial optimization problems including the ground state search for several spin-glass models was done by Kadowaki and Nishimori [16] and Santoro et al. [17]. However, these results are restricted to the research aided by computer simulations, although there exist some extensive studies on the Landou–Zener model for the single spin problems [18, 19, 20].

Recently, the averaged case performance of both the MPM and MAP estimations for image restoration with quantum fluctuation was investigated by the present author [21] for the mean-field model. He also used the quantum Monte Carlo method to evaluate the performance for two-dimensional pictures and found that the quantum fluctuation suppresses the error due to failing to set the hyperparameters effectively; however, the best possible value of the bit-error rate does not increase by the quantum fluctuation. In this result the quantum and thermal fluctuations are combined in the MPM estimation (the effective temperature is unity). Therefore, it is important for us to revisit this problem and investigate to what extent the MPM estimation, which is based on pure quantum fluctuation and without any thermal one, works effectively.

In this chapter, we make this point clear and show that the best possible performance obtained by the MPM estimation, which is purely induced by quantum fluctuations, is exactly the same as the results by the thermal MPM estimation. The Nishimori–Wong condition [7, 8] for the quantum fluctuation, on which the best possible performance is achieved, is also discussed. Moreover, we extend the Sourlas codes [5] by means of the spin-glass model with p-spin interaction in a transverse field [22, 23] and discuss the tolerance of the error-less (or quite low-error) state to the quantum uncertainties in the prior distribution. In the last section of this chapter, we check the performance of the MAP and MPM image restorations predicted by the analysis of the mean-field infinite range model by using the quantum Markov chain Monte Carlo method [24] and the quantum annealing [14, 15, 16, 17].

This chapter is organized as follows. In Sects. 2 and 3, we introduce our model system for image restoration and error-correcting codes. We also explain the relation between Bayesian inference and statistical mechanics. In Sect. 4, we investigate the performance of the MAP and MPM estimations for these two problems by using the analysis of the infinite range model. In Sect. 5, we carry out the quantum Markov chain Monte Carlo method and the quantum annealing to check the results we obtained from the analysis of the infinite range models. In the final section we give the summary.

2 Bayesian Statistics and Information Processing

In the field of signal processing or information science, we need to estimate the original message which is sent via email or fax. Usually, these massages are degraded by some noise and we should retrieve the original messages, and if possible, we send these messages not only as sequence of information bits but also as some redundant information such as *parity check*. In such problems, noise channels or statistical properties of the original message are specified by some appropriate probabilistic models. In this section, we explain the general definitions of our problems and how these problems link to statistical physics.

2.1 General Definition of the Model System

Let us suppose that the original information is represented by a configuration of Ising spins $\{\xi\} \equiv (\xi_1, \xi_2, \ldots, \xi_N)$ $(\xi_i = \pm 1, i = 1, \ldots, N)$ with probability $P(\{\xi\})$. Of course, if each message/pixel ξ_i is generated from independent identical distribution (i.i.d.), the probability of the configuration $\{\xi\}$ is written by the product of the probability $P(\xi_i)$, namely, $P(\{\xi\}) = \prod_{i=1}^{N} P(\xi_i)$.

These messages/pixels $\{\xi\}$ are sent through the noisy channel by not only the form $\{\xi_{i1} \cdots \xi_{ip}\} \equiv \{J^0_{i1\cdots ip}\}$ for appropriately chosen set of indexes $\{i1, \ldots, ip\}$ (what we call *parity check* in the context of error-correcting codes) but also the sequence of the original messages/pixels itself $\{\xi\}$. Therefore, the outputs of the noisy channel are exchange interactions $\{J_{i1\cdots ip}\}$ and fields $\{\tau_i\}$.

In the field of information theory, the noisy channel is specified by the conditional probability such as $P(\{\tau\}|\{\xi\})$ or $P(\{J\}|\{J^0\})$. If each message/pixel ξ_i and parity check $J^0_{i1\cdot ip}$ are affected by the channel noise independently, the probability $P(\{\tau\}|\{\xi\})$ or $P(\{J\}|\{J^0\})$, namely, the probabilities of output sequences $\{\tau\} \equiv (\tau_1, \ldots, \tau_2)$ or $\{J\} \equiv (J_{11\cdots 1p}, \ldots, J_{N1\cdots Np})$ for given input sequences $\{\xi\} = (\xi_1, \ldots, \xi_N)$ or $\{J^0\} = (J^0_{11\cdots 1p}, \ldots, J^0_{N1\cdots Np})$ are written as

$$P(\{\tau\}|\{\xi\}) = \prod_{i=1}^{N} P(\tau_i|\xi_i), \qquad P(\{J\}|\{J^0\}) = \prod_{i=1}^{N} P(J_{i1\cdots ip}|J^0_{i1\cdots ip}) \,, \tag{1}$$

respectively.

In this chapter, we use the following two kinds of the noisy channel. The first one is referred to as *binary symmetric channel* (BSC). In this channel, each message/pixel ξ_i and parity check $J_{i1\cdots jp}$ change their sign with probabilities p_τ and p_r, respectively. By introducing the parameters $\beta_\tau \equiv (1/2)\log(1 - p_\tau/p_\tau), \beta_r \equiv (1/2)\log(1 - p_r/p_r)$, the conditional probabilities (1) are given by

$$P(\{\tau\}|\{\xi\}) = \frac{\exp(\beta_\tau \sum_i \tau_i \xi_i)}{[2\cosh\beta_\tau]^N},\ P(\{J\}|\{J^0\}) = \frac{\exp(\beta_r \sum_{i1\cdots ip} J_{i1\cdots ip} J^0_{i1\cdots ip})}{[2\cosh\beta_r]^{N_B}} \tag{2}$$

where we defined $N \equiv \sum_i 1, N_B \equiv \sum_{i1\cdots ip} 1$.

Thus, the probability of the output sequences $\{J\}, \{\tau\}$ provided that the corresponding input sequence of the original messages/pixels is $\{\xi\}$ is obtained by $\sum_{\{J_0\}} P(\{J\}|\{J^0\})P(\{J^0\}|\{\xi\})P(\{\tau\}|\{\xi\})$, that is to say,

$$P(\{J\},\{\tau\}|\{\xi\}) = \frac{\exp\left(\beta_r \sum_{i1,\ldots,ip} J_{i1\cdots ip}\, \xi_{i1}\cdots\xi_{ip} + \beta_\tau \sum_i \tau_i \xi_i\right)}{(2\cosh\beta_r)^{N_{\mathrm{B}}} (2\cosh\beta_\tau)^N} \tag{3}$$

where we used the following condition:

$$P(\{J^0\}|\{\xi\}) = \prod_{i=1}^{N} \delta_{J^0_{i1\cdots ip}, \xi_{i1}\cdots\xi_{ip}}\ . \tag{4}$$

The second type of the noisy channel is called the *Gaussian channel* (GC). The above BSC (3) is simply extended to the GC as follows:

$$\begin{aligned} &P(\{J\},\{\tau\}|\{\xi\}) \\ &= \frac{\exp\left(-\frac{1}{2J^2}\sum_{i1,\ldots,ip}(J_{i1\cdots ip} - J_0\xi_{i1}\cdots\xi_{ip})^2 - \frac{1}{2a^2}\sum_i(\tau_i - a_0\xi_i)^2\right)}{(\sqrt{2\pi}J)^{N_{\mathrm{B}}}(\sqrt{2\pi}a)^N}\ . \end{aligned} \tag{5}$$

We should notice that these two channels can be treated within the single form:

$$\begin{aligned} P(\{J\},\{\tau\}|\{\xi\}) = &\prod_{i1\cdots ip} F_r(J_{i1\cdots ip}) \prod_i F_\tau(\tau_i) \\ &\times \exp\left(\beta_r \sum_{i1\cdots ip} J_{i1\cdots ip}\, \xi_{i1}\cdots\xi_{ip} + \beta_\tau \sum_i \tau_i \xi_i\right) \end{aligned} \tag{6}$$

with

$$F_r(J_{i1\ldots ip}) = \frac{\sum_{j=\pm1}\delta(J_{i1\cdots ip} - j)}{2\cosh\beta_r}, \qquad F_\tau(\tau_i) = \frac{\sum_{j=\pm1}\delta(\tau_i - j)}{2\cosh\beta_\tau} \tag{7}$$

for the BSC and

$$F_r(J_{i1\cdots ip}) = \frac{\exp\left[-\frac{1}{2J^2}(J^2_{i1\cdots ip} + J_0^2)\right]}{\sqrt{2\pi J^2}}, \qquad F_\tau(\tau_i) = \frac{\exp\left[-\frac{1}{2a^2}(\tau_i^2 + a_0^2)\right]}{\sqrt{2\pi a^2}} \tag{8}$$

for the GC. Therefore, it must be noted that there exist relations between the parameters for both channels as

$$\beta_r = \frac{J_0}{J^2}, \qquad \beta_\tau = \frac{a_0}{a^2}\ . \tag{9}$$

The main purpose of signal processing we are dealing with in this chapter is to estimate the original sequence of messages/pixels $\{\xi\}$ from the outputs $\{J\}, \{\tau\}$ of the noisy channel. With this aim, it might be convenient for us to construct the probability of the estimate $\{\sigma\}$ for the sequence of the original messages/pixels $\{\xi\}$ provided that the outputs of the noisy channel are $\{J\}$ and $\{\tau\}$.

From the Bayes formula, the probability $P(\{\sigma\}|\{J\},\{\tau\})$ is written in terms of the so-called *likelihood* $P(\{J\},\{\tau\}|\{\sigma\})$ and the *prior* $P_m(\{\sigma\})$ as follows:

$$P(\{\sigma\}|\{J\},\{\tau\}) = \frac{P(\{J\},\{\tau\}|\{\sigma\})P_m(\{\sigma\})}{\sum_{\{\sigma\}} P(\{J\},\{\tau\}|\{\sigma\})P_m(\{\sigma\})} \,. \tag{10}$$

As the likelihood has a meaning of the probabilistic model of the noisy channel, we might choose it naturally as

$$P(\{J\},\{\tau\}|\{\sigma\}) = \frac{\exp\left(\beta_J \sum_{i1\cdots ip} J_{i1\cdots ip}\,\sigma_{i1}\cdots\sigma_{ip} + h\sum_i \tau_i\sigma_i\right)}{(2\cosh\beta_J)^{N_{\rm B}}(2\cosh h)^N} \tag{11}$$

for the BSC and

$$P(\{J\},\{\tau\}|\{\sigma\}) = \frac{\exp\left(-\frac{\beta_J}{2}\sum_{i1\cdots ip}(J_{i1\cdots ip} - \sigma_{i1}\cdots\sigma_{ip})^2 - h\sum_i(\tau_i-\sigma_i)^2\right)}{(2\pi/\beta_J)^{N_{\rm B}/2}(\pi/h)^{N/2}} \tag{12}$$

for the GC. Therefore, what we call the *posterior* $P(\{\sigma\}|\{J\},\{\tau\})$ which is defined by (10) is rewritten in terms of the above likelihood as

$$P(\{\sigma\}|\{J\},\{\tau\}) = \frac{\mathrm{e}^{-\beta\mathcal{H}_{\rm eff}}}{\sum_{\{\sigma\}}\mathrm{e}^{-\beta\mathcal{H}_{\rm eff}}} \tag{13}$$

where we defined the inverse temperature $\beta = 1/T$ and set $T = 1$. The effective Hamiltonian $\mathcal{H}_{\rm eff}$ is also defined by

$$\mathcal{H}_{\rm eff} = -\beta_J \sum_{i1\cdots ip} J_{i1\cdots jp}\,\sigma_{i1}\cdots\sigma_{ip} - h\sum_i \tau_i\sigma_i - \log P_m(\{\sigma\}) \tag{14}$$

for the BSC and

$$\mathcal{H}_{\rm eff} = -\frac{\beta_J}{2}\sum_{i1\cdots ip}(J_{i1\cdots ip} - \sigma_{i1}\cdots\sigma_{ip})^2 - h\sum_i(\tau_i-\sigma_i)^2 - \log P_m(\{\sigma\}) \tag{15}$$

for the GC.

2.2 MAP Estimation and Simulated Annealing

As we mentioned, the posterior $P(\{\sigma\}|\{J\},\{\tau\})$ is a useful quantity in order to determine the estimate $\{\sigma\}$ of the sequence of the original messages/pixels.

We might choose $\{\sigma\}$ as the estimate of the original message/pixel sequence, which maximizes the posterior for a given set of the output sequences $\{J\}, \{\tau\}$. Apparently, this estimate $\{\sigma\}$ corresponds to the ground state of the effective Hamiltonian $\mathcal{H}_{\rm eff}$. In the context of the Bayesian statistics, this type of estimate $\{\sigma\}$ is referred to as *maximum a posteriori* (MAP) estimate.

From the view point of important sampling from the posterior as the Gibbs distribution (Gibbs sampling), such a MAP estimate is obtained by controlling the temperature T as $T \to 0$ during the Markov chain Monte Carlo steps. This kind of optimization method is well known and widely used as *simulated annealing* (SA) [11, 12]. The optimal scheduling of the temperature T is $T(t) = c/\log(1+t)$, which was proved by using mathematically rigorous arguments [11].

2.3 MPM Estimation and a Link to Statistical Mechanics

From the posterior $P(\{\sigma\}|\{J\}, \{\tau\})$, we can attempt to make another kind of estimation. For this estimation, we construct the following marginal distribution for each pixel σ_i:

$$P(\sigma_i|\{J\}, \{\tau\}) = \sum_{\{\sigma\} \neq \sigma_i} P(\{\sigma\}|\{J\}, \{\tau\}) \, . \tag{16}$$

Then, we might choose the sign of the difference between $P(1|\{J\}, \{\tau\})$ and $P(-1|\{J\}, \{\tau\})$ as the estimate of the ith message/pixel; to put it in another way,

$$\mathrm{sgn}\left[\sum_{\sigma_i} \sigma_i P(\sigma_i|\{J\}, \{\tau\})\right] = \mathrm{sgn}\left(\frac{\sum_{\{\sigma\}} \sigma_i \, \mathrm{e}^{-\mathcal{H}_{\rm eff}}}{\sum_{\{\sigma\}} \mathrm{e}^{-\mathcal{H}_{\rm eff}}}\right) \equiv \mathrm{sgn}(\langle \sigma_i \rangle_1) \tag{17}$$

where we defined the bracket $\langle \cdots \rangle_\beta$ as

$$\langle \cdots \rangle_\beta \equiv \frac{\sum_{\{\sigma\}} (\cdots) \, \mathrm{e}^{-\beta \mathcal{H}_{\rm eff}}}{\sum_{\{\sigma\}} \mathrm{e}^{-\beta \mathcal{H}_{\rm eff}}} \, . \tag{18}$$

Therefore, the above estimate has a link to statistical mechanics through the local magnetization $\langle \sigma_i \rangle_1$ for the spin system that is described by $\mathcal{H}_{\rm eff}$ at temperature $T = 1$. This estimate $\mathrm{sgn}(\langle \sigma_i \rangle_1)$ is referred to as *maximizer of posterior marginal* (MPM) *estimate* or *finite temperature* (FT) *estimate* [6]. It is well known that this estimate minimizes the following *bit-error rate*:

$$p_b^{(\mathrm{MPM})} = P_b^{(1)}(\beta_J, h : P_m) = \frac{1}{2}\left[1 - R^{(1)}(\beta_J, h : P_m)\right] \tag{19}$$

with the overlap between the original message/pixel ξ_i and its MPM estimate $\mathrm{sgn}(\langle \sigma_i \rangle)$:

$$R^{(1)}(\beta_J, h : P_m) = \sum_{\{\xi, J, \tau\}} P(\{J\}, \{\tau\}, \{\xi\})\, \xi_i \operatorname{sgn}(\langle \sigma_i \rangle_1) \ . \tag{20}$$

Obviously, the bit-error rate for the MAP estimate is given by

$$p_b^{(\mathrm{MAP})} = \lim_{\beta \to \infty} P^{(\beta)}(\beta_J, h : P_m) = \frac{1}{2}\left[1 - \lim_{\beta \to \infty} R^{(\beta)}(\beta_J, h : P_m)\right] \tag{21}$$

with

$$R^{(\beta)}(\beta_J, h : P_m) = \sum_{\{\xi, J, \tau\}} P(\{J\}, \{\tau\}, \{\xi\})\, \xi_i \operatorname{sgn}(\langle \sigma_i \rangle_\beta) \ . \tag{22}$$

In the next section, we compare $p_b^{(\mathrm{MPM})}$ with $p_b^{(\mathrm{MAP})}$ by using the replica method and show that the former is smaller than the latter.

2.4 The Priors and Corresponding Spin Systems

In the previous two subsections, we have shown the relation between the Bayesian inference of the original messages/pixels under some noises and statistical physics [1]. However, we have not yet mentioned about the choice of the prior distribution $P_m(\{\sigma\})$ in the effective Hamiltonian $\mathcal{H}_{\mathrm{eff}}$. In the framework of the Bayesian statistics, the choice of the prior is arbitrary; however, the quality of the estimation for a given problem strongly depends on the choice.

Image Restoration and Random Field Ising Model

In image restoration, we might have an assumption that in the real world two-dimensional pictures, the nearest neighboring sites should be inclined to be the same values; in other words, we assume that the real picture should be locally smooth (see Fig. 1). Taking this smoothness into account, then, it seems reasonable to choose the prior for image restoration as

$$P_m(\{\sigma\}) = \frac{\exp\left(\beta_m \sum \langle ij \rangle \sigma_i \sigma_j\right)}{Z(\beta_m)}, \qquad Z(\beta_m) = \sum_{\{\sigma\}} \exp\left(\beta_m \sum_{\langle ij \rangle} \sigma_i \sigma_j\right) \ . \tag{23}$$

In conventional image restoration, we do not send any parity check and only available information is the degraded sequence of the pixels $\{\tau\}$. Thus, we set $\beta_J = 0$ for this problem. Then, we obtain the effective Hamiltonian for image restoration as

$$\mathcal{H}_{\mathrm{eff}} = -\beta_m \sum_{\langle ij \rangle} \sigma_i \sigma_j - h \sum_i \tau_i \sigma_i \ . \tag{24}$$

This Hamiltonian is identical to that of the *random field Ising model* in which the random field on each cite corresponds to each degraded pixel τ_i.

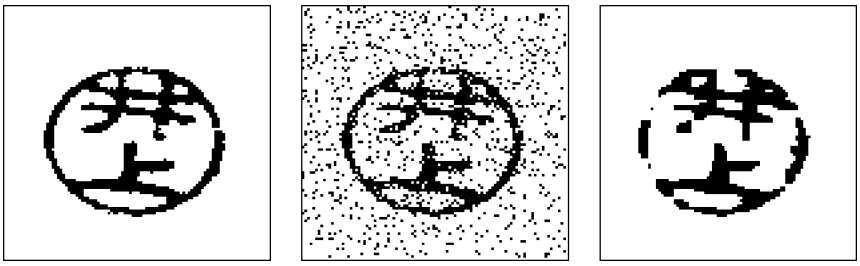

Fig. 1. A typical example of image data retrieval. From the left to the right, the original $\{\xi\}$, degraded $\{\tau\}$, and the recovering $\{\sigma\}$ images. The above restored image was obtained by quantum annealing. The detailed account of this method will be explained and discussed in last part of this chapter

Error-Correcting Codes and Spin Glasses with p-Body Interaction

In error-correcting codes, we usually use so-called *uniform distribution* because we do not have any idea about the properties of the original message sequence $\{\xi\}$ as we assumed smoothness for images. Thus, we set the prior as $P_m(\{\sigma\}) = 2^{-N}$ and substitute $-\log P_m(\{\sigma\}) = N \log 2 = \text{const.}$ into $\mathcal{H}_{\text{eff}}$ (usually, we neglect the constant term).

In this case, we do not use any a priori information to estimate the original message; however, in error-correcting codes, we compensate this lack of information with extra redundant information as a form of $\xi_{i1} \cdots \xi_{ip}$, besides the original message sequence $\{\xi\}$. In information theory, it is well known that we can decode the original message $\{\xi\}$ without any error when the transmission rate R, which is defined by $R = N/N_{\text{B}}$ (N is the original message length and N_{B} is the redundant message length), is smaller than the channel capacity C (see for example [26]). The channel capacity is given by $C = 1 + p \log_2 p + (1-p) \log_2 (1-p)$ for the BSC and $p = (1/2) \log_2 (1 + J_0^2/J^2)$ for the GC. As we will mention in the next section, when we send ${}_N C_r$ combinations of p bits among the original images $\{\xi\}$, as products $\xi_{i1} \cdots \xi_{ip}$, errorless decoding might be achieved in the limit of $p \to \infty$. We call this type of code *Sourlas codes* [5]. For there Sourlas codes, we obtain the following effective Hamiltonian:

$$\mathcal{H}_{\text{eff}} = -\beta_J \sum_{i1 \cdots ip} J_{i1 \cdots ip} \, \sigma_{i1} \cdots \sigma_{ip} - h \sum_i \tau_i \sigma_i \ . \tag{25}$$

It is clear that this Hamiltonian is identical to that of the *Ising spin glass model with p-body interaction* under some random fields on cites.

3 Quantum Version of the Model

In the previous sections, we explained the relation between the Bayesian statistics and statistical mechanics. We found that there exists an effective

Hamiltonian for each problem of image restoration and error-correcting codes. In order to extend the model systems to their quantum version, we add the transverse field term $-\Gamma \sum_i \sigma_i^x$ into the effective Hamiltonian [22]. In this expression, $\{\sigma^x\}$ means the x-component of the Pauli matrix and Γ controls the strength of *quantum fluctuation*. Each term $\Gamma\sigma_i^x$ appearing in the sum might be understood as tunneling probability between the states $\sigma_i^z = +1$ and $\sigma_i^z = -1$ intuitively. As a result, the quantum version of image restoration is reduced to that of statistical mechanics for the following effective Hamiltonian:

$$\mathcal{H}_{\text{eff}}^{\text{Quantum}} = -\beta_m \sum_{\langle ij \rangle} \sigma_i^z \sigma_j^z - h \sum_i \tau_i \sigma_i^z - \Gamma \sum_i \sigma_i^x \ . \tag{26}$$

We also obtain the quantum version of the effective Hamiltonian for error-correcting codes as

$$\mathcal{H}_{\text{eff}}^{\text{Quantum}} = -\beta_J \sum_{i1\cdots ip} J_{i1\cdots ip}\, \sigma_{i1}^z \cdots \sigma_{ip}^z - h \sum_i \tau_i \sigma_i^z - \Gamma \sum_i \sigma_i^x \ . \tag{27}$$

We should keep in mind that in the context of the MAP estimation, it might be useful for us to control the strength of quantum fluctuation, namely, the amplitude of the transverse field Γ as $\Gamma \to 0$ during the quantum Markov chain Monte Carlo steps. If this annealing process of Γ is slow enough, at the end $\Gamma = 0$, we might obtain the ground states of the classical spin systems described by the Hamiltonian

$$\mathcal{H}_{\text{eff}}^{\text{classical}} = -\beta_m \sum_{\langle ij \rangle} \sigma_i^z \sigma_j^z - h \sum_i \tau_i \sigma_i^z \tag{28}$$

for image restoration and

$$\mathcal{H}_{\text{eff}}^{\text{classical}} = -\beta_J \sum_{i1\cdots ip} J_{i1\cdots ip}\, \sigma_{i1}^z \cdots \sigma_{ip}^z - h \sum_i \tau_i \sigma_i^z \ . \tag{29}$$

for error-correcting codes. This is an essential idea of the *quantum annealing*. Unfortunately, up to now, there are no mathematically rigorous arguments for the optimal scheduling of $\Gamma(t)$ corresponding to Geman and Geman's proofs [11] for the simulated annealing [12]. We will revisit this problem in the last section. In this chapter, we investigate its averaged case performance by the analysis of the infinite range model and by carrying out quantum Markov chain Monte Carlo simulations.

4 Analysis of the Infinite Range Model

In the previous section, we completely defined our two problems of information processing, that is to say, image restoration and error-correcting codes as the

problems of statistical mechanics of random spin systems in a transverse field. We found that there exist two possible candidates to determine the original sequence of the messages/pixels. The first one is the MAP estimation and the estimate is regarded as ground states of the effective Hamiltonian that is defined as a minus of logarithm of the posterior distribution. As we mentioned, to carry out the optimization of the Hamiltonian, both the simulated annealing and the quantum annealing are applicable. In order to construct the quantum annealing, we should add the transverse field to the effective Hamiltonian and control the amplitude of the field Γ during the quantum Markov chain Monte Carlo steps. Therefore, the possible extension of the classical spin systems to the corresponding quantum spin systems in terms of the transverse field is an essential idea of our work.

Besides the MAP estimate as a solution of the optimization problems, the MPM estimate, which is given by the sign of the local magnetization of the spin system, is also available. This estimate is well known as the estimate that minimizes the bit-error rate. Performances of both the MAP and MPM estimations are evaluated through this bit-error rate.

In order to evaluate the performance, we first attempt to calculate the bit-error rate analytically by using the mean-field infinite range model. As the most famous example of the solvable model, the Sherrington–Kirkpatrick model [9] in spin glasses, we also introduce the solvable models for both image restoration and error-correcting codes. In this section, according to the previous work by the present author [21], we first investigate the performance of image restoration.

It is important to bear in mind that in our Hamiltonian, there exist two types of terms, namely, $\mathcal{A}_0 = -\mathcal{H}_{\rm eff}^{\rm classical}$ and $\mathcal{A}_1 = -\Gamma \sum_i \sigma_i^x$, and they do not commute with each other. Therefore, it is impossible to calculate the partition function directly. Then, we use the *Suzuki–Trotter* (ST) *decomposition* [24, 25]

$$Z_{\rm eff} = \lim_{M\to\infty} \mathrm{tr} \left(\mathrm{e}^{\frac{\mathcal{A}_0}{M}} \mathrm{e}^{\frac{\mathcal{A}_1}{M}} \right)^M \tag{30}$$

to cast the problem into an equivalent classical spin system. In the following, we calculate the macroscopic behavior of the model system with the assistance of the ST formula [24, 25] and replica method [9] for the data $\{\xi, J, \tau\}$ average $[\cdots]_{\rm data}$:

$$[\log Z_{\rm eff}]_{\rm data} = \lim_{n\to 0} \frac{[Z_{\rm eff}^n]_{\rm data} - 1}{n} \tag{31}$$

of the infinite range model.

4.1 Image Restoration

In order to analyze the performance of the MAP and MPM estimations in image restoration, we suppose that the original image is generated by the next probability distribution,

$$P(\{\xi\}) = \frac{\exp\left(\frac{\beta_s}{N}\sum_{ij}\xi_i\xi_j\right)}{Z(\beta_s)}, \qquad Z(\beta_s) = \sum_{\{\xi\}}\exp\left(\frac{\beta_s}{N}\sum_{ij}\xi_i\xi_j\right), \tag{32}$$

namely, the Gibbs distribution of the ferromagnetic Ising model at the temperature $T_s = \beta_s^{-1}$. For this original image and under the Gaussian channel, the macroscopic properties of the system such as the bit-error rate are derived from the data-averaged free energy $[\log Z_{\rm eff}]_{\rm data}$. Using the ST formula and the replica method, we write down the replicated partition function as

$$\begin{aligned}
[Z_{\rm eff}^n]_{\rm data} = \sum_{\{\xi\}}\int_{-\infty}^{\infty}\prod_{ij}\frac{{\rm d}J_{ij}}{\sqrt{2\pi J^2/N}}\exp\left(-\frac{N}{2J^2}\sum_{ij}\left(J_{ij}-\frac{J_0}{N}\xi_i\xi_j\right)^2\right) \\
\times\int_{-\infty}^{\infty}\prod_{i}\frac{{\rm d}\tau_i}{\sqrt{2\pi}a}\exp\left(-\frac{1}{2a^2}\sum_{i}(\tau_i - a_0\xi_i)^2\right) \\
\times\frac{\exp\left(\beta_s/N\right)\sum_{ij}\xi_i\xi_j\Big)}{Z(\beta_s)} \\
\times{\rm tr}_{\{\sigma\}}\prod_{\alpha=1}^{n}\prod_{K=1}^{M}\exp\left[\frac{\beta_J}{M}\sum_{ij}J_{ij}\sigma_{iK}^{\alpha}\sigma_{jK}^{\alpha}+\frac{\beta_m}{MN}\sum_{ij}\sigma_{iK}^{\alpha}\sigma_{jK}^{\alpha}\right. \\
\left.+\frac{h}{M}\sum_{i}\tau_i\sigma_{iK}^{\alpha}+B\sum_{i}\sigma_{iK}^{\alpha}\sigma_{i,K+1}^{\alpha}\right]
\end{aligned} \tag{33}$$

where $[\cdots]_{\rm data}$ means the average over the quenched randomness, namely, over the joint probability $P(\{J\},\{\tau\},\{\xi\})$. We should keep in mind that these quantities $\{\xi\}$ and $\{J\},\{\tau\}$ mean the data we send to the receiver and the outputs of the channel the receiver obtain, respectively. Therefore, by calculating these averages $[\cdots]_{\rm data}$, we can evaluate the *data-averaged case performance* of image restoration [21]. We also defined the partition function $Z(\beta_s)$ for the original images and B as $Z(\beta_s) \equiv \sum_{\{\xi\}}\exp\Big(\beta_s/N\Big)\sum_{ij}\xi_i\xi_j\Big), B \equiv (1/2)\log\coth(\Gamma/M)$. The standard replica calculation leads to the following expressions of the free energy density:

$$[\log Z_{\rm eff}]_{\rm data} = \frac{[Z_{\rm eff}^n]_{\rm data}-1}{nN} = -\frac{f_0^{\rm RS}}{n} - f^{\rm RS} \tag{34}$$

$$f_0^{\rm RS} = \frac{1}{2}\beta_s m_0^2 - \log 2\cosh(\beta_s m_0) \tag{35}$$

$$\begin{aligned}
f^{\rm RS} = -\frac{(\beta_J J)^2}{2}Q^2 + \frac{(\beta_J J)^2}{2}S^2 + \frac{\beta_m}{2}m^2 + \frac{\beta_J J_0}{2}t^2 \\
-\sum_{\xi}\mathcal{M}(\xi)\int_{-\infty}^{\infty}{\rm D}u\log\int_{-\infty}^{\infty}{\rm D}w\,2\cosh\sqrt{\Phi^2+\Gamma^2}
\end{aligned} \tag{36}$$

and the saddle point equations with respect to the order parameters.

$$S[\langle\sigma_{iK}^{\alpha}\rangle]_{\rm data} = m = \sum_{\xi}\mathcal{M}(\xi)\int_{-\infty}^{\infty}{\rm D}u\int_{-\infty}^{\infty}{\rm D}\omega\,\left(\frac{\Phi\sinh\Xi}{\Xi\Omega}\right) \tag{37}$$

$$[\xi_i\langle\sigma_{iK}^{\alpha}\rangle]_{\rm data} = t = \sum_{\xi}\xi\mathcal{M}(\xi)\int_{-\infty}^{\infty}{\rm D}u\int_{-\infty}^{\infty}{\rm D}\omega\,\left(\frac{\Phi\sinh\Xi}{\Xi\Omega}\right) \tag{38}$$

$$[\langle(\sigma_{iK}^{\alpha})^2\rangle]_{\rm data} = Q = \sum_{\xi}\mathcal{M}(\xi)\int_{-\infty}^{\infty}{\rm D}u\left[\int_{-\infty}^{\infty}{\rm D}\omega\,\left(\frac{\Phi\sinh\Xi}{\Xi\Omega}\right)\right]^2 \tag{39}$$

$$\begin{aligned}&[\langle\sigma_{iK}^{\alpha}\sigma_{iL}^{\alpha}\rangle]_{\rm data} = S\\ &= \sum_{\xi}\mathcal{M}(\xi)\int_{-\infty}^{\infty}\frac{{\rm D}u}{\Omega}\int_{-\infty}^{\infty}\left[\left(\frac{\Phi}{\Xi}\right)^2\cosh\Xi + \Gamma^2\left(\frac{\sinh\Xi}{\Xi^3}\right)\right]\end{aligned} \tag{40}$$

with $[\xi_i]_{\rm data} = m_0 = \tanh(\beta_s m_0)$ and $\mathcal{M}(\xi) = {\rm e}^{\beta_s m_0\xi}/2\cosh(\beta_s m_0)$, where we used the replica symmetric and the static approximation, that is,

$$t_K = t, \qquad S_{\alpha}(KL) = \begin{cases} S & (K\neq L)\\ 1 & (K=L)\end{cases}, \qquad Q_{\alpha\beta} = Q \tag{41}$$

and $\langle\cdots\rangle$ denotes the average over the posterior distribution and Φ, y, and Ω are defined as

$$\Phi \equiv u\sqrt{(ah)^2 + (J\beta_J)^2 Q} + J\beta_J\omega\sqrt{S-Q} + (a_0 h + J_0\beta_J t)\xi + \beta_m m \tag{42}$$

$$\Xi \equiv \sqrt{\Phi^2+\Gamma^2}, \qquad \Omega \equiv \int_{-\infty}^{\infty}{\rm D}\omega\,\cosh\Xi\,. \tag{43}$$

Then, the overlap R which is a measure of retrieval quality is calculated explicitly as

$$[\xi_i\,{\rm sgn}(\langle\sigma_{iK}^{\alpha}\rangle)]_{\rm data} = R = \sum_{\xi}\xi\mathcal{M}(\xi)\int_{-\infty}^{\infty}{\rm D}u\int_{-\infty}^{\infty}{\rm D}w\,{\rm sgn}(\Phi)\,; \tag{44}$$

then, of course, the bit-error rate is given by $p_b = (1-R)/2$.

4.2 Image Restoration at Finite Temperature

We first investigate the image restoration without the parity check term $\beta_J = 0$. For this case, the saddle point equations lead to the following much simpler coupled equations:

$$m_0 = \tanh(\beta_s m_0), \qquad m = \sum_{\xi}\mathcal{M}(\xi)\int_{-\infty}^{\infty}{\rm D}u\,\frac{\Phi_0\,\tanh\sqrt{\Phi_0^2+\Gamma^2}}{\sqrt{\Phi_0^2+\Gamma^2}} \tag{45}$$

with $\Phi_0 \equiv m\beta_m + a_0 h\xi + ahu$. Then, the overlap R is also reduced to

$$R = \sum_{\xi} \xi \mathcal{M}(\xi) \int_{-\infty}^{\infty} \mathrm{D}u \, \mathrm{sgn}(\Phi_0) = 1 - 2p_b \tag{46}$$

where R depends on Γ through m. In Fig. 2 (left), for the case of no parity check $\beta_J = 0$, we plot the bit-error rate p_b as a function of $T_m = \beta_m^{-1}$. We choose the temperature of the original image $T_s^{-1} = \beta_s = 0.9$ and noise rate $\beta_\tau = a_0/a^2 = 1$. We keep the ratio h/β_m to its optimal value $\beta_\tau/\beta_s = 0.9$ and investigate the T_m-dependence of p_b. Then, the parameter T_m has the meaning of temperature for the simulated annealing. Obviously, $p_b^{(\mathrm{MAP})} = \lim_{T_m \to 0} p_b$ and p_b at $T_m = T_s$ is the lowest value of $p_b^{(\mathrm{MPM})}$ for $\Gamma = 0$.

Let us stress again that in practice, the infinite range model is not useful for realistic two-dimensional image restoration because all pixels are neighbor of each other. In order to restore these two-dimensional images, we should use the prior $P(\{\xi\})$ for two dimensions. In fact, let us think about the overlap r between an original pixel ξ_i and the corresponding degraded pixel τ_i, namely,

$$r = [\xi_i \tau_i]_{\mathrm{data}} = \frac{\sum_{\tau,\xi} \mathrm{e}^{\beta_\tau \xi\tau + \beta_s m_0 \xi}(\xi\tau)}{4\cosh(\beta_\tau)\cosh(\beta_s m_0)} = \tanh(\beta_\tau) \, . \tag{47}$$

From this relation, the error probability p_τ is given as $p_\tau = (1-r)/2 = 1/(1+\mathrm{e}^{2\beta_\tau}) = 0.119 < p_b^{(\mathrm{MPM})}$ for $\beta_\tau = 1$, and unfortunately, the restored image becomes much worse than the degraded one (see Fig. 2 (left)). This is because any spacial structure is ignored in this artificial model. This result might be understood as a situation in which we try to restore the finite-dimensional

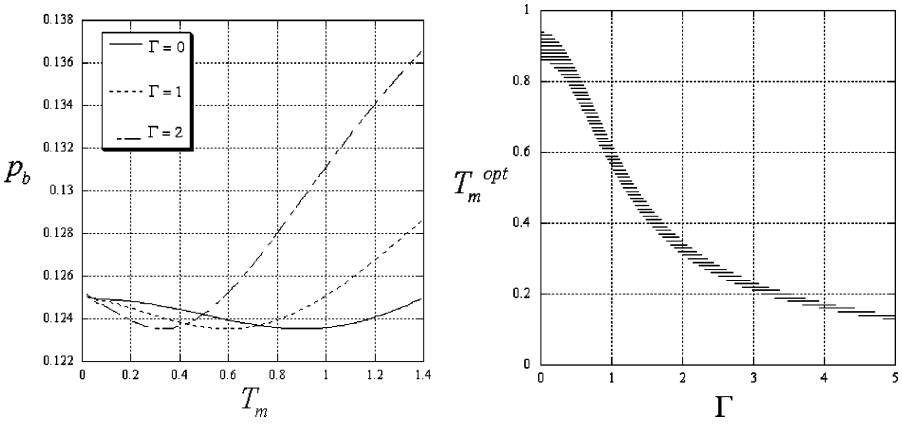

Fig. 2. The bit-error rate $p_b = (1-R)/2$ without exchange term ($\beta_J = 0$) as a function of temperature $T_m = \beta_m^{-1}$ (*left*). Keeping the ratio to $h/\beta_m = \beta_\tau/\beta_s = a_0/a^2\beta_s = 0.9$ (we set $a_0 = a = 1$), we change the value of T_m. For the case of $\Gamma = 0$, p_b takes its minimum at $T_m = T_s = 0.9$. For finite Γ, the optimal temperature T_m is not T_s; however, the minimum of p_b does not change. The *right panel* shows the optimal temperature T_m^{opt} as a function of Γ

image with some structures by using the infinite range prior without any structure (namely, the correlation length between pixels is also infinite). However, the infinite range model is useful to predict the qualitative behavior of macroscopic quantities such as bit-error rate and we can grasp the details of its hyperparameters' (namely, T_m, h, or Γ) dependence and can also compare the MAP with the MPM estimations. This is a reason why we introduce this model to the analysis of image restoration problems. Of course, if we use two-dimensional structural priors, both the MAP estimation via simulated and quantum annealing and the MPM estimation by using thermal and quantum fluctuations work well for realistic two-dimensional image restoration. In the next section, we will revisit this problem and find it. It is also important for us to bear in mind that the quality of restoration depends on the macroscopic properties of the original image.

In our choice of the original image, its macroscopic qualities are determined by the temperature T_s and magnetization m_0 as a solution of $m_0 = \tanh(\beta_s m_0)$. Although we chose the temperature $T_s = 0.9$ in Fig. 2 (left), it is important to check the retrieval quality for different temperatures T_s. In Fig. 3 (right), we plot the bit-error rate for the case of $T_s = 0.7$. From this panel, we find $p_b < p_\tau$ and the MPM estimation improves the quality of the restoration.

For $\Gamma > 0$, the optimal temperature which gives the minimum of p_b is not T_s. In the right panel of Fig. 2, we plot the $T_m^{\rm opt}$ as a function of Γ. In Fig. 3 (left), we plot the bit-error rate as a function of Γ for $T_m = T_s = 0.9$ setting the ratio to its optimal value $h/\beta_m = \beta_\tau/\beta_s = 0.9$. From this figure, we find that the MPM optimal estimate no longer exists by adding the transverse field $\Gamma > 0$ and the bit-error rate p_b increases as the amplitude of the transverse field Γ becomes much stronger.

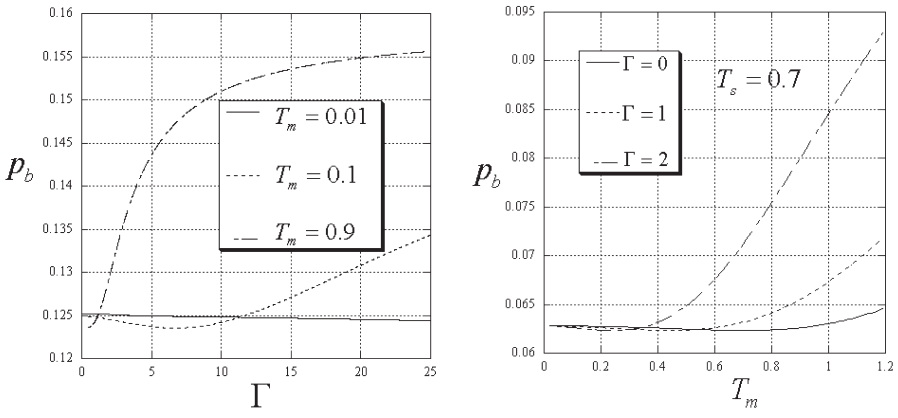

Fig. 3. The bit-error rate p_b is drawn for $T_m = 0.01, 0.1$ and $T_m = 0.9$ as a function of Γ (*left*). The right panel is the same type of the plot as the right panel in Fig. 2 for the case of $T_s = 0.7$

On the other hand, when we set the temperature $T_m = 0.01$, the Γ-dependence of the bit-error rate is almost flat (see Fig. 3 (right)). We should notice that p_b at $\Gamma = 0$ for $T_m = 0$ corresponds to the performance of the MAP estimation by quantum annealing. We discuss the performance of the quantum annealing in the last part of this subsection.

We next consider the performance for the MAP and MPM estimations with the parity check term ($\beta_J \neq 0$). We plot the result in Fig. 4. As we mentioned before, the two-body parity check term works very well to decrease the bit-error rate p_b. However, in this case, there does not exist the optimal β_J which minimizes the bit-error rate for any finite values of Γ. As we see in the left panel of Fig. 4, for a small value of β_J, the restoration by a finite Γ is superior to that in the absence of the transverse field ($\Gamma = 0$).

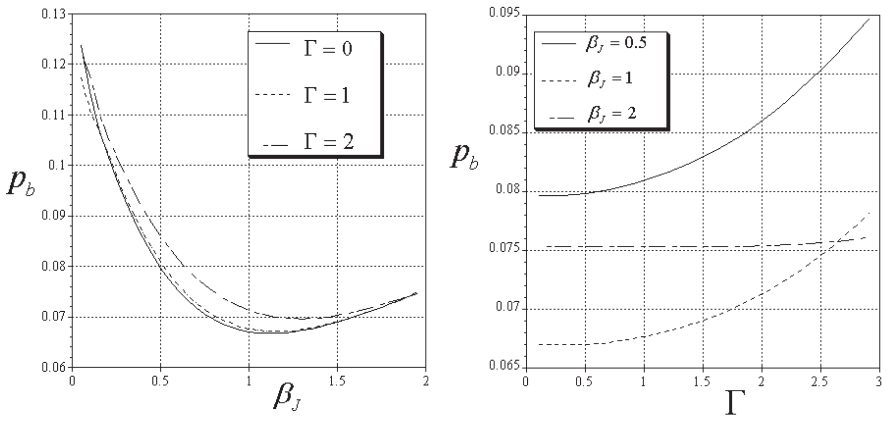

Fig. 4. The bit-error rate p_b as a function of β_J for $\Gamma = 0, 1, 2$ keeping the ratio constant $h/\beta_m = \beta_\tau/\beta_s$ (*left*). In the right panel, p_b is plotted as a function of Γ for the case of $\beta_J = 0.5, 1, 2.0$

Hyperparameter Estimation

In this subsection, we evaluated the performance of the MAP and MPM estimations in image restoration through the bit-error rate. In these results, we found that the macroscopic parameters β_m, h, and Γ-dependence of the bit-error rate have important information to retrieve the original image. However, from the definition, (44),(46), as the bit-error rate contains the original image $\{\xi\}$, it is impossible for us to use p_b as a cost function to determine the best choice of these parameters. In statistics, we usually use the *marginal likelihood* [27] which is defined by the logarithm of the normalization constant of $\mathrm{tr}_{\{\sigma\}} P(\{\sigma\}|\{\tau\}) P_m(\{\sigma\})$, that is,

$$K(\beta_m, h, \Gamma : \{\tau\}) \equiv \log Z_{\text{Pos.}} - \log Z_{\text{Pri.}} - \log Z_{\text{L}} \tag{48}$$

where $Z_{\text{Pos.}}, Z_{\text{Pri}}$ and Z_{L} are the normalization constants for the posterior, the prior and the likelihood, respectively, and which are given by

$$Z_{\text{Pos.}} = \text{tr}_{\{\sigma\}} \exp\left(\beta_m \sum_{ij} \sigma_i^z \sigma_j^z + h \sum_i \tau_i \sigma_i^z + \Gamma \sum_i \sigma_i^x\right) \tag{49}$$

$$Z_{\text{Pri.}} = \text{tr}_{\{\sigma\}} \exp\left(\beta_m \sum_{ij} \sigma_i^z \sigma_j^z + \Gamma \sum_i \sigma_i^x\right), Z_{\text{L}} = \text{tr}_{\{\tau\}} \exp\left(h \sum_i \tau_i \sigma_i^z\right), \tag{50}$$

respectively. For simplicity, let us concentrate ourselves on the case of no parity check $\beta_J = 0$.

It must be noted that the marginal likelihood (48) is constructed by using the observables $\{\tau\}$ and does not contain the original image $\{\xi\}$ at all. Therefore, in practice, the marginal likelihood has a lot of information to determine the macroscopic parameters, what we call *hyperparameters*, before we calculate the MAP the MPM estimates.

In the infinite range model, it is possible for us to derive the data-averaged marginal likelihood per pixel $K(\beta_J, h, \Gamma) = [K(\beta_J, h, \Gamma : \{\tau\})]_{\text{data}}/N$ explicitly. Here we first investigate the hyperparameter dependence of the marginal likelihood. $\log Z_{\text{Pri}}$ and $[\log Z_{\text{L}}]_{\text{data}} = [\log \int_{-\infty}^{\infty} \prod_i \text{d}\tau_i F_\tau(\tau_i) \text{e}^{h\tau_i \sigma_i^z}]_{\text{data}}$ per pixel can be calculated as

$$\frac{\log Z_{\text{Pri}}}{N} = -\frac{\beta_m m_1^2}{2} + \log 2 \cosh \sqrt{(\beta_m m_1)^2 + \Gamma^2} \tag{51}$$

$$\frac{[\log Z_{\text{L}}]_{\text{data}}}{N} = -\frac{h^2}{2}\left[\left(\frac{a_0}{ah}\right)^2 - a^2\right] \tag{52}$$

and the data average of the first term on the right-hand side of (48) is identical to the free energy density for $\beta_J = 0$. Thus, we obtain the data-averaged marginal likelihood as

$$K(\beta_m, h, \Gamma) = -\frac{\beta_m m^2}{2} + \sum_\xi \mathcal{M}(\xi) \int_{-\infty}^{\infty} \text{D}u \log 2 \cosh \sqrt{\Phi_0^2 + \Gamma^2}$$
$$+ \frac{\beta_m m_1^2}{2} - \log 2 \cosh \sqrt{(\beta_m m_1)^2 + \Gamma^2} + \frac{h^2}{2}\left[\left(\frac{a_0}{ah}\right)^2 - a^2\right] \tag{53}$$

where m_1, m mean the magnetizations of the prior and the posterior, and they are given by

$$m_1 = \frac{\beta_m m_1 \tanh \sqrt{(\beta_m m_1)^2 + \Gamma^2}}{\sqrt{(\beta_m m_1)^2 + \Gamma^2}} \tag{54}$$

and (45), respectively. In Fig. 5 (left), we plot $K(\beta_m, h, \Gamma)$. In this figure, we set $T_s = 0.9, \beta_\tau = 1$. We found that the data-averaged marginal likelihood

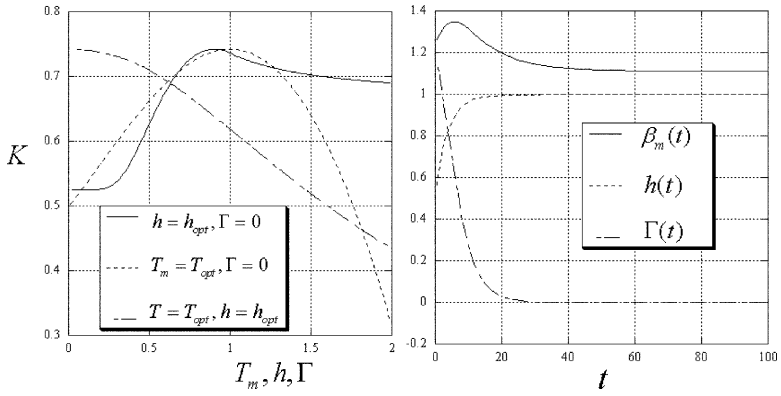

Fig. 5. The data-averaged marginal as a function of hyperparameters β_m, h, and Γ (left). The right panel shows the time development of the hyperparameters, β_m, h, and Γ via the gradient descent of the marginal likelihood. We set the time constants $c_{\beta_m} = c_h = c_\Gamma = 1$ and the values of true hyperparameters as $T_s = \beta_s^{-1} = 0.9$, $\beta_\tau = 1$

takes its maximum at $T_m = T_s, h = \beta_\tau$, and $\Gamma = 0$. This result might be naturally understood because the performance of both the MAP and MPM estimations should be the best for setting the probabilistic models of the noise channel and the distribution of the original image to the corresponding true probabilities. Therefore, it might seem that the transverse field Γ has no meaning for restoration. However, when we attempt to maximize the marginal likelihood via gradient descent, we need to solve the following coupled equations,

$$c_{\beta_m}\frac{\mathrm{d}\beta_m}{\mathrm{d}t} = \frac{\partial K}{\partial \beta_m} = \left\langle \sum_{ij}\sigma_i^z\sigma_j^z \right\rangle_{\text{Pos.}} - \left\langle \sum_{ij}\sigma_i^z\sigma_j^z \right\rangle_{\text{Pri.}} \tag{55}$$

$$c_h\frac{\mathrm{d}h}{\mathrm{d}t} = \frac{\partial K}{\partial h} = \left\langle \sum_{i}\tau_i\sigma_i^z \right\rangle_{\text{Pos.}} - \left\langle \sum_{i}\tau_i\sigma_i^z \right\rangle_{\text{Pri.}} - \left\langle \sum_{i}\tau_i\sigma_i^z \right\rangle_{\text{L}} \tag{56}$$

$$c_\Gamma\frac{\mathrm{d}\Gamma}{\mathrm{d}t} = \frac{\partial K}{\partial \Gamma} = \left\langle \sum_{i}\sigma_i^x \right\rangle_{\text{Pos.}} - \left\langle \sum_{i}\sigma_i^x \right\rangle_{\text{Pri.}} \tag{57}$$

with the definitions of the brackets

$$\langle\cdots\rangle_{\text{Pos.}} = \frac{\mathrm{tr}_{\{\sigma\}}(\cdots)\exp\left(\beta_m\sum_{ij}\sigma_i^z\sigma_j^z + h\sum_i\tau_i\sigma_i^z + \Gamma\sum_i\sigma_i^x\right)}{\mathrm{tr}_{\{\sigma\}}\exp\left(\beta_m\sum_{ij}\sigma_i^z\sigma_j^z + h\sum_i\tau_i\sigma_i^z + \Gamma\sum_i\sigma_i^x\right)} \tag{58}$$

$$\langle\cdots\rangle_{\text{Pri.}} = \frac{\mathrm{tr}_{\{\sigma\}}(\cdots)\exp\left(\beta_m\sum_{ij}\sigma_i^z\sigma_j^z + \Gamma\sum_i\sigma_i^x\right)}{\mathrm{tr}_{\{\sigma\}}\exp\left(\beta_m\sum_{ij}\sigma_i^z\sigma_j^z + \Gamma\sum_i\sigma_i^x\right)},$$

$$\langle \cdots \rangle_{\rm L} = \frac{{\rm tr}_{\{\tau\}}(\cdots)\exp(h\sum_i \tau_i \sigma_i^x)}{{\rm tr}_{\{\tau\}}\exp(h\sum_i \tau_i \sigma_i^x)} \tag{59}$$

and the time constants c_{β_m}, c_h, and c_Γ. Thus, when we solve the above equations, we need to evaluate these expectations for every time steps by using the quantum Markov chain Monte Carlo method. It is obvious that it takes quite long time to obtain the solutions. From the reasons mentioned above, it is convenient for us to suppress the error of hyperparameter estimation by introducing the transverse field. From Figs. 2, and 3, we actually find these desirable properties.

Incidentally, for the infinite range model, we derive these coupled equations explicitly. The results are given by

$$\begin{aligned} c_{\beta_m}\frac{{\rm d}\beta_m}{{\rm d}t} &= \frac{m_1^2 - m^2}{2} - \frac{\beta_m m_1^2 \tanh\sqrt{(\beta_m m_1)^2 + \Gamma^2}}{\sqrt{(\beta_m m_1)^2 + \Gamma^2}} \\ &\quad + m\sum_\xi \mathcal{M}(\xi)\int_{-\infty}^{\infty} {\rm D}u\, \frac{\Phi_0 \tanh\sqrt{\Phi_0^2 + \Gamma^2}}{\sqrt{\Phi_0^2 + \Gamma^2}} \end{aligned} \tag{60}$$

$$c_h\frac{{\rm d}h}{{\rm d}t} = -a^2 h + \sum_\xi \mathcal{M}(\xi)\int_{-\infty}^{\infty} {\rm D}u\, \frac{\Phi_0(a_0\xi + au)\tanh\sqrt{\Phi_0^2 + \Gamma^2}}{\sqrt{\Phi_0^2 + \Gamma^2}} \tag{61}$$

$$c_\Gamma\frac{{\rm d}\Gamma}{{\rm d}t} = -\frac{\Gamma\tanh\sqrt{(\beta_m m_1)^2 + \Gamma^2}}{\sqrt{(\beta_m m_1)^2 + \Gamma^2}} + \Gamma\sum_\xi \mathcal{M}(\xi)\int_{-\infty}^{\infty} {\rm D}u\, \frac{\tanh\sqrt{\Phi_0^2 + \Gamma^2}}{\sqrt{\Phi_0^2 + \Gamma^2}} \tag{62}$$

where m_1 and m satisfy (45) and (54). We plot the results by solving the differential equations with respect to the hyperparameters, namely, (60),(61),(62), numerically in Fig. 5. We find that each hyperparameter converges to its optimal value.

4.3 Image Restoration Driven by Pure Quantum Fluctuation

In the above discussion, we investigated mainly the MPM estimation at the finite temperature $T_m > 0$ according to reference [21]. However, it is worthwhile for us to check the limit $\beta_m \to \infty$, keeping the *effective amplitude of the transverse field* $\Gamma_{\rm eff} = \Gamma/\beta_m$ finite. In this limit, we investigate pure effect of the quantum fluctuation without any thermal one. To evaluate the performances of the MAP and MPM estimations for this zero temperature case, we set $\Phi_0 = \beta_m(m + h_* a_0\xi + h_* a u) = \beta_m\phi_0$, where h_* is its optimal value $h_* = \beta_s/\beta_\tau$, and consider the asymptotic form of the saddle point equations with respect to m and m_1 in the limit of $\beta_m \to \infty$. We easily find

$$m_1 = \sqrt{1 - \Gamma_{\rm eff}^2}, \quad m = \sum_\xi \mathcal{M}(\xi)\int_{-\infty}^{\infty} \frac{\phi_0 {\rm D}u}{\sqrt{\phi_0^2 + \Gamma_{\rm eff}^2}} \tag{63}$$

and the time evolution of $\Gamma_{\rm eff}$ as

$$c_{\Gamma_{\rm eff}} \frac{{\rm d}\Gamma_{\rm eff}}{{\rm d}t} = -\frac{\Gamma_{\rm eff}}{\sqrt{m_1^2 + \Gamma_{\rm eff}^2}} + \sum_{\xi} \mathcal{M}(\xi) \int_{-\infty}^{\infty} \frac{\Gamma_{\rm eff} {\rm D}u}{\sqrt{\phi_0^2 + \Gamma_{\rm eff}^2}} \tag{64}$$

where $c_{\Gamma_{\rm eff}} = \beta_m c_\Gamma$. The bit-error rate is given by $p_b = (1 - m_0)/2 + \sum_\xi \mathcal{M}(\xi)\xi H(u_*)$, where $u_* = (a_0 h_* \xi + m)/a h_*$. We fist plot the $\Gamma_{\rm eff}$-dependence of the bit-error rate at $T_m = 0$ in Fig. 6. In this figure, the value at $\Gamma_{\rm eff} = 0$ corresponds to the quantum MAP estimation which might be realized by the quantum annealing. From this figure, we find that the performance of the quantum MPM estimation is superior to the MAP estimation and there exists some finite value of the amplitude Γ at which the bit-error rate takes its minimum. In the same figure, we also plot the T_m-dependence of the bit-error rate for $\Gamma = 0$. We find that, for both the quantum and thermal cases, the best possible values of both the MAP and MPM estimations are exactly the same. In Fig. 6 (right), we plot the time development of the effective amplitude of the transverse field and the resultant bit-error rate. From this figure, we notice that at the beginning of the gradient descent the bit-error rate decreases but as Γ decreases to zero, the error converges to the best possible value for the quantum MAP estimation. The speed of the convergence is exponentially fast. Actually, in the asymptotic limit $t \to \infty, \Gamma_{\rm eff} \to 0$, Eq. (64) is solved as $\Gamma_{\rm eff} = \Gamma_{\rm eff}(0)\, {\rm e}^{-\theta_{\Gamma_{\rm eff}} t}$, where $\theta_{\Gamma_{\rm eff}} \equiv (1/c_{\Gamma_{\rm eff}})(1 - \sum_\xi \mathcal{M}(\xi) \int_{-\infty}^{\infty} {\rm D}u/|\phi_0|)$. However, this fact does not mean that it is possible for us to decrease the effective amplitude of the transverse field to zero by using exponentially fast scheduling to realize the best possible performance of the quantum MAP estimation. This is because the time unit t appearing in (64) does not correspond to the quantum Monte Carlo step

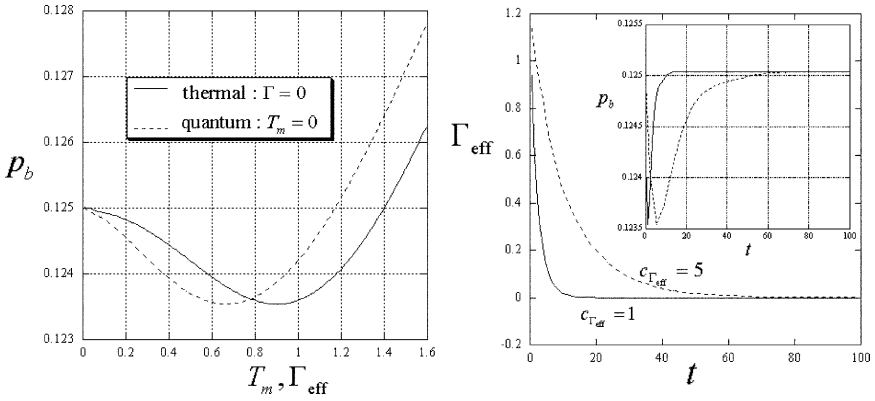

Fig. 6. The bit-error rate for the quantum ($T_m = 0$) and thermal (classical) ($\Gamma = 0$) estimations (left). The right panel shows the time development of the effective amplitude of the transverse field $\Gamma_{\rm eff} = \Gamma/\beta_m$. The inset means the time dependence of the bit-error rate

and the dynamics (64) requires the (equilibrium) magnetization $m(\Gamma_{\rm eff})$ at each time step in the differential equation. As result, we need the information about m near $\Gamma_{\rm eff} \to 0$, namely, the asymptotic form $m(t \to \infty, \Gamma_{\rm eff} \to 0)$, to discuss the annealing schedule to obtain the MAP estimation. Although we assume that in each time step in (64), the system obeys the equilibrium condition : $m = \sum_\xi \mathcal{M}(\xi) \int_{-\infty}^{\infty} \phi_0 {\rm D}u / \sqrt{\phi_0^2 + \Gamma_{\rm eff}^2}$, we need the dynamics of m to discuss the optimal annealing scheduling about $\Gamma_{\rm eff}$. This point will be discussed in the last section by means of the quantum Markov chain Monte Carlo method.

The Nishimori–Wong Condition on the Effective Transverse Field

From Fig. 6 (left), we found that the lowest value of the bit-error rate is the same for both the thermal and quantum MPM estimations. In the thermal MPM estimation, Nishimori and Wong [8] found the condition under which the best performance is obtained, namely, what we call the *Nishimori–Wong condition*. They showed that the condition $(m/m_0) = (h/\beta_\tau)(\beta_s/\beta_m)$ should hold in order to obtain the lowest value of the bit-error rate. When we set the hyperparameter h to its true value $h = \beta_\tau$, the condition is reduced to the simple form $T_m^{\rm opt} = T_s$. Therefore, it is important for us to derive the same kind of condition which gives the best performance of the quantum MPM estimation. Here we derive the condition and show that the lowest values of p_b for the thermal and quantum MPM estimations are exactly the same.

We first evaluate the condition $(\partial p_b / \partial \Gamma_{\rm eff}) = 0$ for $p_b = (1 - m_0)/2 + \sum_\xi \xi \mathcal{M}(\xi) H(u_*)$. After some simple algebra, we obtain

$$m(\Gamma_{\rm eff}^{\rm opt}) \sum_\xi \xi \mathcal{M}(\xi) \exp\left[-\frac{\{a_0 h_* \xi + m(\Gamma_{\rm eff}^{\rm opt})\}^2}{2a^2 h_*^2} \right] = 0 \,. \tag{65}$$

Taking into account that $m(\Gamma_{\rm eff}) \neq 0$ is needed for meaningful image restorations, the Nishimori–Wong condition for the quantum MPM estimation is written as

$$\frac{m_0(\beta_s)}{m(\Gamma_{\rm eff}^{\rm opt})} = \frac{a_0}{a^2 h_* \beta_s} \,. \tag{66}$$

As we chose $h_* = \beta_\tau / \beta_s, \beta_\tau = a_0 / a^2$, this condition is simply rewritten as $m_0(\beta_s) = m(\Gamma_{\rm eff})$.

Let us summarize the Nishimori–Wong condition for the MPM estimation:

$$\begin{aligned} &\text{Thermal:} \quad T_m^{\rm opt} = T_s \quad \text{(Reference [8])} \\ &\text{Quantum:} \quad m_0(\beta_s) = \sum_\xi \mathcal{M}(\xi) \int_{-\infty}^{\infty} \frac{\phi_0 {\rm D}u}{\sqrt{\phi_0^2 + (\Gamma_{\rm eff}^{\rm opt})^2}} \,. \end{aligned}$$

In Fig. 7, we plot the temperature of the original image T_s-dependence of the optimal temperature $T_m^{\rm opt}$ and the optimal amplitude of the transverse field

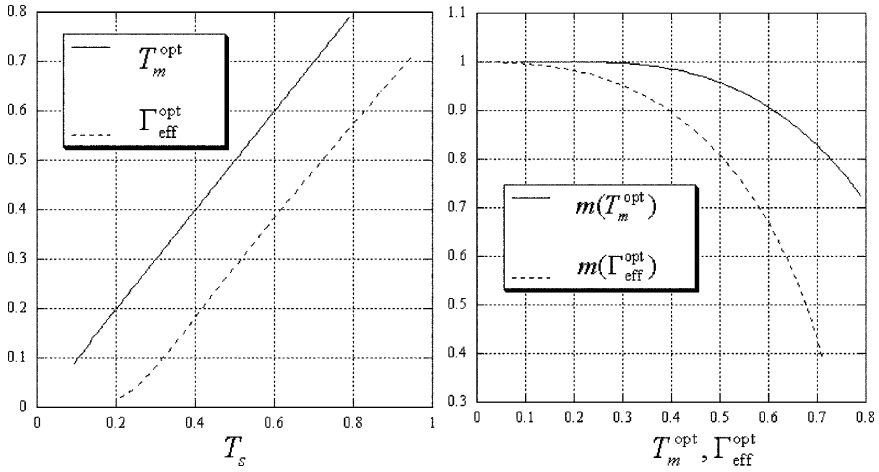

Fig. 7. The optimal temperature $T_m^{\rm opt}$ and the optimal transverse field $\Gamma_{\rm eff}^{\rm opt}$ as a function of the temperature T_s of the original image (*left*), respectively. The optimal temperature for the thermal MPM estimation $T_m^{\rm opt}$ is simply given by $T_m^{\rm opt} = T_s$ (Nishimori temperature). The *right panel* shows the magnetizations $m(T_m^{\rm opt})$ and $m(\Gamma_{\rm eff}^{\rm opt})$

$\Gamma_{\rm eff}^{\rm opt}$. In the right panel of this figure, the magnetizations $m(T_m^{\rm opt})$ and $m(\Gamma_{\rm eff}^{\rm opt})$ are plotted. The effective amplitude of the transverse field $\Gamma_{\rm eff}$ at which the bit-error rate takes its minimum in Fig. 6 is consistent with $\Gamma_{\rm eff}^{\rm opt}(T_s = 0.9) \simeq 0.66$ as shown in Fig. 7 (left).

From these results, it is shown that the lowest values of the bit-error rate for both the thermal and quantum MPM estimations are exactly the same and the value is given by

$$p_b = \frac{1 - m_0}{2} + \sum_{\xi} \xi \mathcal{M}(\xi) H\left(\frac{a_0 h_* \xi + m_0}{a h_*}\right) . \tag{67}$$

Therefore, we conclude that it is possible for us to construct the MPM estimation purely induced by the quantum fluctuation (without any thermal fluctuation) and the best possible performance is exactly the same as that of the thermal MPM estimation.

4.4 Error-Correcting Codes

In this subsection, we investigate the performance of the decoding in the so-called Sourlas codes [5], in which uncertainties in the prior are introduced as the quantum transverse field. Although we usually choose the prior in the Sourlas codes as $P(\{\sigma\}) = 2^{-N}$ (the uniform prior), here we use $P(\{\sigma\}) = \prod_i {\rm e}^{-\Gamma \hat{\sigma}_i^x}$. Then, the effective Hamiltonian of the extended Sourlas codes leads to

$$\mathcal{H}_{\rm eff} = -\beta_J \sum_{i1,\ldots,ip} J_{i1\cdots ip}\, \sigma_{i1}^z \sigma_{i2}^z \cdots \sigma_{ip}^z - h \sum_i \tau_i \sigma_i^z - \Gamma \sum_i \sigma_i^x \,. \tag{68}$$

Hereafter, we call this type of error-correcting codes *quantum Sourlas codes*. We first derive the Γ-dependence of the bit-error rate for a given p. Then, the channel noise is specified by the next output distribution:

$$P(\{J\},\{\tau\}|\{\xi\}) = \frac{\exp\left(-\frac{N^{p-1}}{J^2 p!}\sum_{i1,\ldots,ip}\left(J_{i1\cdots ip} - \frac{J_0 p!}{N^{p-1}}\xi_{i1}\cdots\xi_{ip}\right)^2 - \frac{1}{2\tau^2}(\tau_i - a_0\xi_i)^2\right)}{(J^2\pi p!/N^{p-1})^{1/2}\sqrt{2\pi}a} \,. \tag{69}$$

For simplicity, we treat the case in which the original message sequence $\{\xi\}$ is generated by the following uniform distribution $P(\{\xi\}) = 2^{-N}$. Then, the moment of the effective partition function $Z_{\rm eff}$ leads to

$$Z_{\rm eff}^n = \exp\left[\frac{\beta_J}{M}\sum_{i1,\ldots,ip}\sum_{\alpha=1}^{n}\sum_{t=1}^{M} J_{i1\cdots ip}\,\sigma_{i1}^\alpha(t)\sigma_{i2}^\alpha(t)\cdots\sigma_{ip}^\alpha(t) + \frac{h}{M}\sum_i\sum_{\alpha=1}^{n}\sum_{t=1}^{M}\tau_i\sigma_i^\alpha(t) + B\sum_i\sum_{t=1}^{M}\sigma_i(t)\sigma_i(t+1)\right] \tag{70}$$

where α and t mean the indexes of the replica number and the Trotter slice, respectively. We set $B \equiv (1/2)\log\coth(\Gamma/M)$ and used the gauge transform $J_{i1\cdots ip} \to J_{i1\cdots ip}\,\xi_{i1}\cdots\xi_{ip}, \sigma_{ip} \to \xi_{ip}\sigma_{ip}^z$. After averaging $Z_{\rm eff}^n$ over the quenched randomness $[\cdots]_{\rm data}$, namely, over the joint distribution $P(\{J\},\{\tau\},\{\xi\})$, we obtain the following data-averaged effective partition function:

$$[Z_{\rm eff}^n]_{\rm data} = \prod_{tt'}\prod_{\alpha\beta}\int_{-\infty}^{\infty}{\rm d}Q_{\alpha\beta}(t,t')\int_{-\infty}^{\infty}{\rm d}\lambda_{\alpha\beta}(t,t')\int_{-\infty}^{\infty}{\rm d}m_\alpha(t)\int_{-\infty}^{\infty}{\rm d}\hat{m}_\alpha(t) \times \exp\left[-Nf(m,\hat{m},\boldsymbol{Q},\boldsymbol{\lambda})\right] \tag{71}$$

with

$$\begin{aligned} f(m,\hat{m},\boldsymbol{Q},\boldsymbol{\lambda}) = &-\frac{\beta_J J_0}{M}\sum_{t,\alpha} m_\alpha^p(t) - \frac{h\tau_0}{M}\sum_{t,\alpha} m_\alpha(t) \\ &- \frac{(\beta_J J)^2}{4M^2}\sum_{tt',\alpha\beta} Q_{\alpha\beta}^p(t,t') - \frac{(h\tau)^2}{2M^2}\sum_{tt',\alpha\beta} Q_{\alpha\beta}(t,t') \\ &+ \frac{1}{M}\sum_{t,\alpha}\hat{m}_\alpha(t)m_\alpha(t) + \frac{1}{M^2}\sum_{tt',\alpha\beta}\lambda_{\alpha\beta}(t,t')Q_{\alpha\beta}(t,t') \\ &- \frac{1}{M}\sum_{t,\alpha}\hat{m}_\alpha(t)\sigma^\alpha(t) - \frac{1}{M^2}\sum_{tt',\alpha\beta}\lambda_{\alpha\beta}(t,t')\sigma^\alpha(t)\sigma^\beta(t') \\ &- B\sum_t\sigma(t)\sigma(t+1) \end{aligned} \tag{72}$$

where we labeled each Trotter slice by index t. Using the replica symmetric and static approximations, namely,

$$m_\alpha(t) = m, \qquad \hat{m}_\alpha(t) = \hat{m} \tag{73}$$

$$Q_{\alpha\beta}(t,t') = \begin{cases} \chi \ (\alpha = \beta) \\ q \ (\alpha \neq \beta) \end{cases}, \qquad \lambda_{\alpha\beta}(t,t') = \begin{cases} \lambda_1 \ (\alpha = \beta) \\ \lambda_2 \ (\alpha \neq \beta) \end{cases}, \tag{74}$$

we obtain the free energy density f^{RS} :

$$\begin{aligned} \beta_J f^{\mathrm{RS}}(m,\chi,q) = (p-1)\beta_J J_0 m^p + \frac{1}{4}(p-1)(\beta_J J)^2(\chi^p - q^p) \\ - \int_{-\infty}^{\infty} \mathrm{D}w \log \int_{-\infty}^{\infty} \mathrm{D}z \, 2\cosh \Xi \end{aligned} \tag{75}$$

where we used the saddle point equations with respect to $\hat{m}, \lambda_1, \lambda_2$, namely, $\hat{m} = p\beta_J J_0 m^{p-1} + a_0 h$ and $\lambda_1 = \frac{p}{2}(\beta_J J)^2 \chi^{p-1} + (ah)^2, \lambda_2 = \frac{p}{2}(\beta_J J)^2 q^{p-1} + (ah)^2$. Then, the saddle point equations are derived as follows:

$$m = \int_{-\infty}^{\infty} \mathrm{D}\omega \int_{-\infty}^{\infty} \mathrm{D}z \left(\frac{\Phi \sinh \Xi}{\Xi \Omega} \right) \tag{76}$$

$$\chi = \int_{-\infty}^{\infty} \frac{\mathrm{D}\omega}{\Omega} \int_{-\infty}^{\infty} Dz \left[\left(\frac{\Phi}{\Xi} \right)^2 \cosh \Xi + \Gamma^2 \left(\frac{\sinh \Xi}{\Xi^3} \right) \right] \tag{77}$$

$$q = \int_{-\infty}^{\infty} \mathrm{D}\omega \left[\int_{-\infty}^{\infty} \mathrm{D}z \left(\frac{\Phi \sinh \Xi}{\Xi \Omega} \right) \right]^2 \tag{78}$$

where we defined

$$\begin{aligned} \Phi = \omega \sqrt{\frac{p}{2}(\beta_J J)^2 q^{p-1} + (ah)^2} + z \sqrt{\frac{p}{2}(\beta_J J)^2 (\chi^{p-1} - q^{p-1})} \\ + p\beta_J J_0 m^{p-1} + a_0 h \end{aligned} \tag{79}$$

and $\Xi = \sqrt{\Phi^2 + \Gamma^2}$, $\Omega = \int_{-\infty}^{\infty} \mathrm{D}z \cosh \Xi$. The resultant overlap leads to

$$R = \int_{-\infty}^{\infty} \mathrm{D}\omega \int_{-\infty}^{\infty} \mathrm{D}z \, \mathrm{sgn}(\Phi) = 1 - 2 \int_{-\infty}^{\infty} \mathrm{D}w \, H(-z_p^*) \tag{80}$$

where we defined z_p^* by

$$z_p^* = -\frac{(p\beta_J J_0 m^{p-1} + a_0 h) + w\sqrt{\frac{p}{2}(\beta_J J)^2 q^{p-1} + (ah)^2}}{\sqrt{\frac{p}{2}(\beta_J J)^2 (\chi^{p-1} - q^{p-1})}} \tag{81}$$

and the error function $H(x)$ defined as $H(x) = \int_x^{\infty} \mathrm{D}z$. Thus, the bit-error rate for the problem of error-correcting codes is given by $p_b = (1-R)/2 = \int_{-\infty}^{\infty} \mathrm{D}w \, H(-z_p^*)$, where the above bit-error rate p_b depends on Γ through the order parameters χ, q, and m.

4.5 Analysis for Finite p

We first evaluate the performance of the quantum Sourlas codes for the case of finite p by solving the saddle point equations numerically.

4.5.1 Absence of the External Field $h = 0$

In FIG. 8 (left), we first plot the Γ-dependence of the bit-error rate p_b for the case of $p = 2$ without magnetic field $h = 0$. In this plot, we choose $J = J_0 = 1$ and set $\beta_J = 1$. It must be noted that J_0/J corresponds to the signal to noise ratio (SN ratio). From this figure, we find that the bit-error rate gradually approaches to the random guess limit $p_b = 0.5$ as Γ increases. This transition is regarded as a second-order phase transition between the ferromagnetic and paramagnetic phases. We plot the Γ-dependence of the order parameters m, χ and q in the right panel of Fig. 8. We should notice that in the classical limit $\Gamma \to 0$, the order parameter χ should take the value 1 and both magnetization m and spin glass order parameter q continuously become zero at the transition point. Therefore, for the case of $p = 2$, the increase of the quantum fluctuation breaks the error-less state gradually. On the other hand, in Fig. 9, we plot the Γ-dependence of the bit-error rate p_b for the case of $p = 3$. In this figure, we find that the bit-error rate suddenly increases to 0.5 at the transition point $\Gamma = \Gamma_c$ and the quality of the message retrieval becomes the same as the random guess. This first-order phase transition from the ferromagnetic error-less phase to the paramagnetic random guess phase is observed in the right panel of Fig. 9.

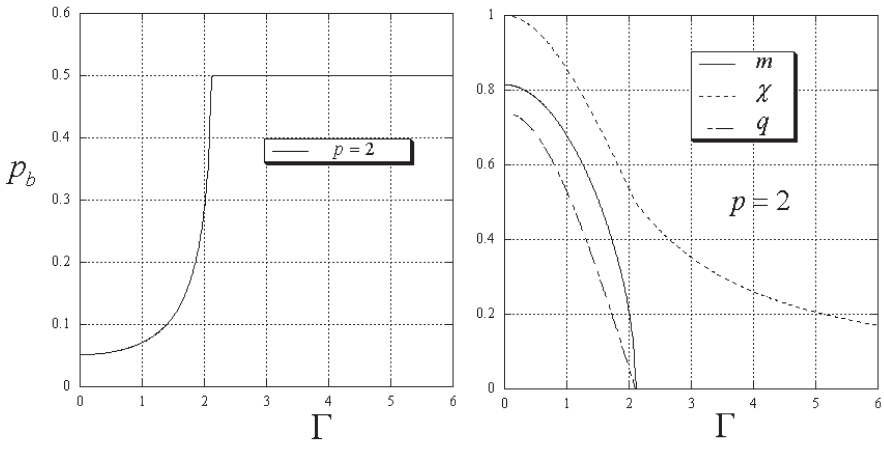

Fig. 8. The Γ-dependence of the bit error-rate p_b for the case of $p = 2$ without magnetic field $h = 0$ (*left*) and order parameters m, χ and q as a function of Γ (*right*). We set $\beta_J = 1, J = J_0 = 1$

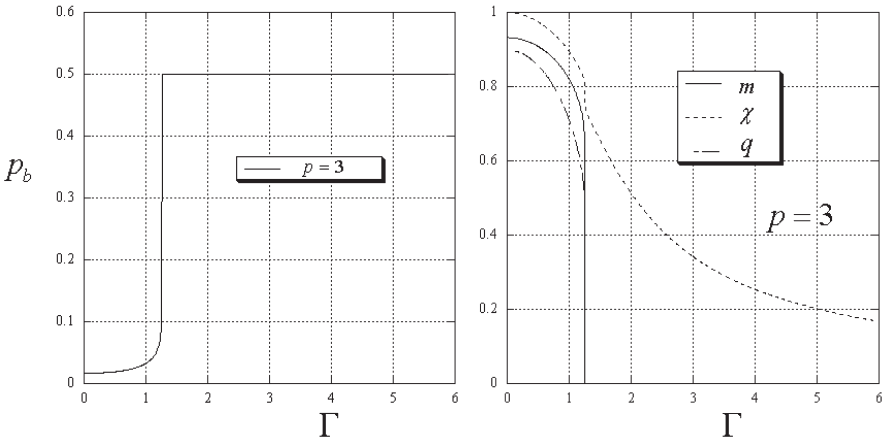

Fig. 9. The Γ-dependence of the bit error-rate p_b for the case of $p = 3$ without magnetic field $h = 0$ (*left*) and order parameters m, χ and q as a function of Γ (*right*). We set $\beta_J = 1, J = J_0 = 1$, and $a_0 = a1$

We find that the system undergoes the first-order phase transition for $p \geq 3$. In FIG. 10, we plot the Γ-dependence of the bit-error rate for $p = 2, 3, \ldots, 6$ and $p = 12$. From this figure, we find that the transition for $p \geq 3$ is first-order and the bit-error rate changes its state from the ferromagnetic almost perfect information retrieval phase to the paramagnetic random guess phase at $\Gamma = \Gamma_c$. The tolerance to the quantum fluctuation increases as the number of degrees p of the interaction increases.

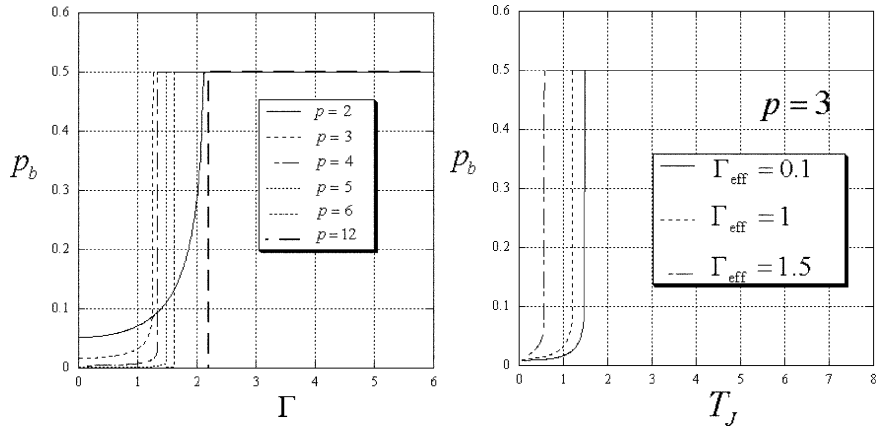

Fig. 10. The Γ-dependence of the bit error-rate p_b for $p = 2, \ldots, 6$ and $p = 12$ without magnetic field $h = 0$ (*left*). We set $\beta_J = 1, J = J_0 = 1$. The right panel shows the $T_J = \beta_J^{-1}$ dependence of the bit-error rate for keeping the ratio $\Gamma/\beta_J \equiv \Gamma_{\text{eff}}$ to the values $\Gamma_{\text{eff}} = 0.1, 1$, and 1.5

Presence of the external field $h \neq 0$

We next consider the case of $h \neq 0$. This means that we send not only the parity check $\{J_{i1\cdots ip}\}$ but also bit sequence $\{\xi\}$ itself. We plot the bit-error rate as a function of Γ in Fig. 11. From this figure, we find that the bit-error rate gradually goes to some finite value which is below the random guess limit. The right panel of this figure that in this case there is no sharp phase transition induced by the quantum fluctuation. In Fig. 12, we plot the bit-error rate and corresponding order parameters as a function of Γ. This figure that the the bit-error rate suddenly increases at some critical length of the transverse field Γ_c. As we add the external field h, this is not a ferro-paramagnetic phase transition; however, there exist two stable states, namely good retrieval phase and poor retrieval phase. In Fig. 13, we plot the Γ-dependence of the bit-error rate for $p = 3, \ldots, 6$ and $p = 12$ (left) and for $p = 6$ and $\beta_J = 0.2, \ldots, 12$ (right). From the right panel, interesting properties are observed. For small Γ, the bit-error rate becomes small as we increase p. On the other hand, for large Γ, the bit-error rate becomes large as p increases. Moreover, the bit-error rate for $p = 6$ takes its maximum at some finite value of Γ.

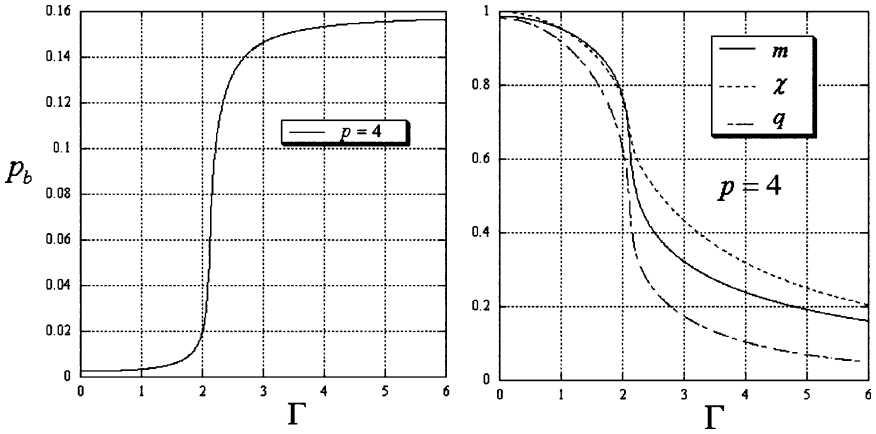

Fig. 11. The Γ-dependence of the bit error-rate p_b for the case of $p = 4$ with magnetic field $h = 1$ (*left*) and order parameters m, χ, and q as a function of Γ (*right*). We set $\beta_J = 1, J = J_0 = 1$, and $a_0 = a = 1$

4.6 Phase Diagrams for $p \to \infty$ and Replica Symmetry Breaking

In this subsection, we investigate properties of the quantum Sourlas codes in the limit of $p \to \infty$. In this limit, we easily obtain several phase boundaries analytically and draw the phase diagrams.

First of all, we consider the simplest case, namely, the case of $J_0 = 0, h = 0$. For this choice of parameters, the ferromagnetic phase does not appear and

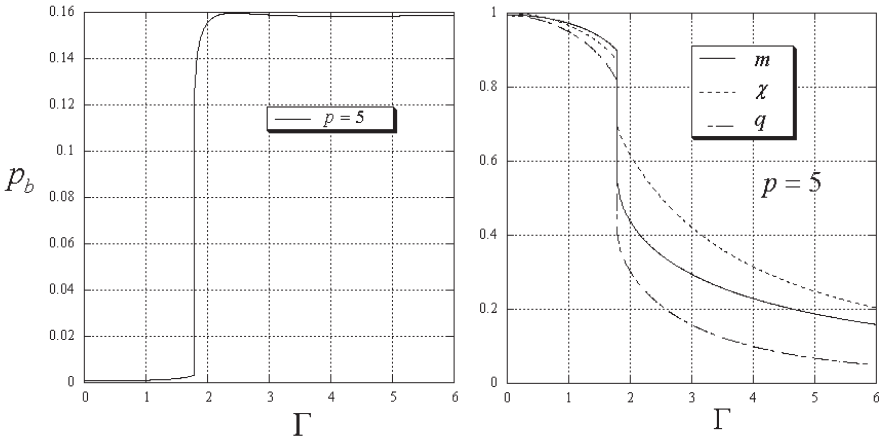

Fig. 12. The Γ-dependence of the bit error-rate p_b for the case of $p = 5$ with magnetic field $h = 1$ (*left*) and order parameters m, χ, and q as a function of Γ (*right*). We set $\beta_J = 1, J = J_0 = 1$, and $a_0 = a = 1$

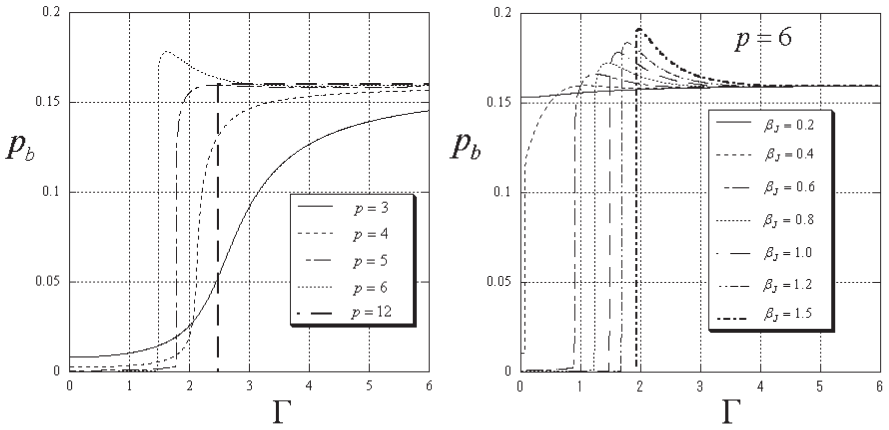

Fig. 13. The Γ-dependence of the bit-error rate for $p = 3, \ldots, 6$ and 12 (*left*). For $p = 6$, the Γ-dependences of the bit-error rate for $\beta_J = 0.2, \ldots, 1.2$ are shown in the *right panel*

possible phases are paramagnetic phase and spin-glass phase. The free energy density we evaluate is now rewritten as

$$f^{\mathrm{RS}} = -\frac{1}{4}(p-1)\beta_J J^2(q^p - \chi^p) - T_J \int_{-\infty}^{\infty} Dw \log \int_{-\infty}^{\infty} Dz 2\cosh \beta_J \sqrt{\phi_0^2 + \Gamma_{\mathrm{eff}}^2} \tag{82}$$

with $\phi_0 = w\sqrt{pJ^2q^{p-1}/2} + z\sqrt{pJ^2(\chi^{p-1} - q^{p-1})/2}$, where we defined $\Gamma_{\mathrm{eff}} = \Gamma/\beta_J$. In the paramagnetic phase, there is no spin-glass ordering, namely, $q = 0$. Thus, the free energy density in the paramagnetic phase leads to

$$f_{\rm para}^{\rm RS} = \frac{J^2\beta_J}{4}(p-1)\chi^p - T_J \log \int_{-\infty}^{\infty} {\rm D}z 2\cosh\beta_J\sqrt{\Gamma_{\rm eff}^2 + \frac{p}{2}J^2\chi^{p-1}z^2}\ . \quad (83)$$

The saddle point equation with respect to χ is given by

$$\chi = \frac{\int_{-\infty}^{\infty}{\rm D}z\left\{\left(\frac{\phi_{00}}{\Gamma_{\rm eff}^2+\phi_{00}}\right)\cosh\beta_J\sqrt{\Gamma_{\rm eff}^2+\phi_{00}} + \Gamma_{\rm eff}^2 T_J\frac{\sinh\beta_J\sqrt{\Gamma_{\rm eff}^2+\phi_{00}}}{\sqrt{\Gamma_{\rm eff}^2+\phi_{00}}^3}\right\}}{\int_{-\infty}^{\infty}{\rm D}z\cosh\beta_J\sqrt{\Gamma_{\rm eff}^2+\phi_{00}^2}} \quad (84)$$

with $\phi_{00} = pJ^2\chi^{p-1}z^2/2$. In the limit of $p\to\infty$, there are two possible solutions of χ, that is $\chi^p = 1$ and $\chi^p = 0$. The former is explicitly given from (84) as $\chi \simeq 1 - 4\Gamma_{\rm eff}^2 T_J^2/p^2J$. Then, we obtain the free energy density for this solution as $f_{\rm I} = -J^2/4T_J - T_J\log 2$ by substituting this χ into (83) and evaluating the integral with respect to z at the saddle point in the limit of $p\to\infty$. Let us call this phase *PI*. The latter solution is explicitly evaluated as $\chi = (T_J/\Gamma_{\rm eff})\tanh(\Gamma_{\rm eff}/T_J)$ $(<1;$ thus, $\chi^p = 0)$ and the corresponding free energy density leads to $f_{\rm II} = -T_J\log 2 - T_J\log\cosh(\Gamma_{\rm eff}/T_J)$. We call this phase PII.

Here we should not overlook the entropy in *PI*, namely, $S = -(\partial f_{\rm I}/\partial T) = -J^2/4T_J^2 + \log 2$. Obviously, S becomes negative for $T < (J/2\sqrt{\log 2})^{-1}$ and in this region, the replica symmetry of the order parameters might be broken. Therefore, in this low temperature region, we should construct the replica symmetry breaking (RSB) solution. To obtain the RSB solution, we break the symmetry of the matrices $\boldsymbol{q}$ and $\boldsymbol{\lambda}$ as

$$q_{l\delta,l'\delta'} = \begin{cases} q_0 & (l = l') \\ q_1 & (l \neq l') \end{cases}, \qquad \lambda_{l\delta,l'\delta'} = \begin{cases} \hat{\lambda}_0 & (l = l') \\ \hat{\lambda}_1 & (l \neq l') \end{cases} \quad (85)$$

for $l = 1,\ldots,n/x$, $\delta = 1,\ldots,x$. Then, we obtain the free energy density for one-step RSB solution as

$$\begin{aligned} f^{\rm 1RSB} = {} & (p-1)J_0m^p + \frac{\beta_J J^2}{4}[xq_1^p + (1-x)q_0^p] + \frac{\beta_J J^2}{4}(p-1)\chi^p \\ & - \frac{\beta_J}{2}[xq_1\hat{\lambda}_1 + (1-x)q_0\hat{\lambda}_0] \\ & - \frac{T_J}{x}\int_{-\infty}^{\infty}{\rm D}w\log\int_{-\infty}^{\infty}{\rm D}z\left(\int_{-\infty}^{\infty}{\rm D}y 2\cosh\beta_J\sqrt{\hat{\phi}^2+\Gamma_{\rm eff}^2}\right)^x \end{aligned} \quad (86)$$

with $\hat{\phi} = w\sqrt{\hat{\lambda}_1} + z\sqrt{\hat{\lambda}_0 - \hat{\lambda}_1} + y\sqrt{pJ^2\chi^{p-1}/2 - \hat{\lambda}_0} + p\beta_J J_0 m^{p-1} + a_0 h$. By taking $(\partial f^{\rm 1RSB}/\partial q_0) = (\partial f^{\rm 1RSB}/\partial q_1) = 0$, we obtain $\hat{\lambda}_1 = pJ^2q_1^{p-1}/2$, $\hat{\lambda}_0 = pJ^2q_0^{p-1}/2$.

Here we set the parameters J_0, h again to $J_0 = h = 0$. At low temperature, we naturally assume $q_1 < 0$ $(\hat{\lambda}_1 = 0)$, $q_0 = 1$ $(\hat{\lambda}_0 = pJ^2/2)$, and $\chi = 1$. Substituting these conditions into (86) and evaluating the integral with respect to y at the saddle point in the limit of $p\to\infty$, we obtain the free energy density in

this phase, which will be referred to as SGI, as $f_{\rm SGI} = -\beta_J J^2 x/4 - \log 2/(\beta_J x)$. Substituting the solution of $(\partial f_{\rm SGI}/\partial x) = 0$, namely, $x = 2\sqrt{\log 2}/(JT_J)$ into $f_{\rm SG}$, we obtain the free energy density which specifies SGI as $f_{\rm SGI} = -J\sqrt{\log 2}$.

Let us summarize

$$\text{PI (para)}: \quad f_{\rm I} = -\frac{J^2}{4T_J} - T_J \log 2 \quad (\chi = 1, q = 0)$$

$$\text{PII (para)}: \quad f_{\rm II} = -T_J \log 2 - T_J \log\cosh\left(\frac{\Gamma_{\rm eff}}{T_J}\right) \quad (\chi^p = q = 0)$$

$$\text{SGI (spin glass)}: \quad f_{\rm SGI} = -J\sqrt{\log 2} \quad (\chi = q = 1)\ .$$

We illustrate the phase diagram in Fig. 14 (left).

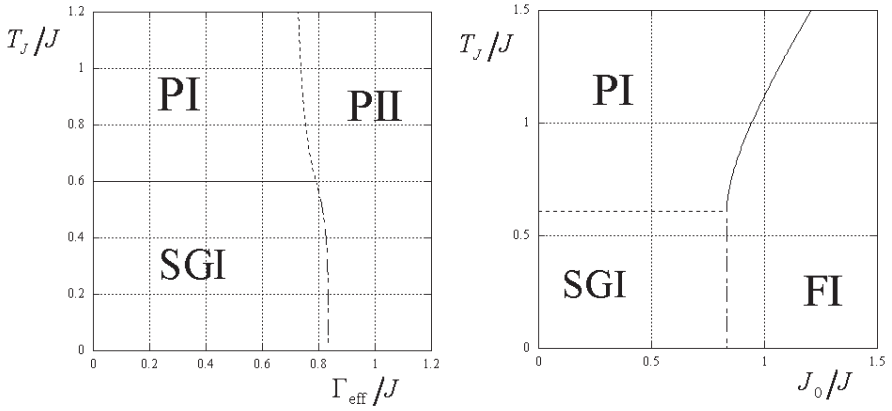

Fig. 14. The phase diagrams in the limit of $p \to \infty$. In the case of $J_0 = 0$, there exist three phases, namely, *PI*, *PII*, and *SGI*. Below the critical point $(T_J/J)_c = (1/2J\sqrt{\log 2})$, the replica symmetry is broken (the *left panel*). The *right panel* shows that the critical SN ratio $(J_0/J)_c$, above which (labeled *FI* in the panel) decoding without errors is achieved, is given by $\sqrt{\log 2}$

As the phase transitions between two arbitrary phases among the three phases *PI, PII, SGI* are all first order, each phase boundary is obtained by balancing the free energy density. Namely, $\Gamma_{\rm eff} = T_J \cosh^{-1}(e^{J^2/4T_J^2})$ $(T_J > T_c)$ for *PI–PII*, $\Gamma_{\rm eff} = T_J \cosh^{-1}(e^{J\sqrt{\log 2}/T_J}/2)$ $(T_J < T_c)$ for *PII–SGI*, and $T_J = J/2\sqrt{\log 2} = T_c$ for *SGI–PI*.

We next consider the case of $J_0 \neq 0$. This case is much more important in the context of error-correcting codes. For the case the of absence of the external field $h = 0$, the phase transition between the error-less phase and the random guess phase is specified as the ferro-paramagnetic (or spin-glass) phase transition. From the reasons we mentioned above, our main purpose here is to determine the transition point $(J_0/J)_c$ below which the ferromagnetic phase is stable. The critical SN ratio $(J_0/J)_c$ is important because as we mentioned

Au: Please check whether the edit mode here retains the intended sense.

before, the error-less decoding is possible when the channel capacity C and the transmission rate R satisfy the inequality $R \leq C$. The channel capacity for the Gaussian channel we are dealing with is given by $C = (1/2)\log_2(1 + J_0^2/J^2)$ with $J_0 = J_0 p!/N^{p-1}, J = J^2 p!/2N^{p-1}$, that is, $C \simeq J_0^2 p!/(J^2 N^{p-1}\log 2)$ in the limit of $N \to \infty$ for a given p. On the other hand, the transmission rate R is given as $R = N/N_{\rm B} = N/{}_N C_p \simeq p!/N^{p-1}$. Therefore, the error-less decoding is possible when the inequality

$$\frac{R}{C} = \left(\frac{J}{J_0}\right)^2 \log 2 \leq 1 \tag{87}$$

holds and the question now arises, namely, is it important to ask whether the above inequality is satisfied or not at the critical point $(J/J_0)_c$? In the following, we make this point clear.

We start from the saddle point equations which are derived from the free energy density of the one-step RSB (86). These equations are given explicitly as

$$\begin{aligned}
m &= \int_{-\infty}^{\infty} {\rm D}w \frac{\int_{-\infty}^{\infty} {\rm D}z \left(\int_{-\infty}^{\infty} {\rm D}y 2\cosh\beta_J \hat{\Xi}\right)^{x-1} \int_{-\infty}^{\infty} {\rm D}y \left(\frac{\hat{\phi}}{\hat{\Xi}}\right) 2\sinh\beta_J \hat{\Xi}}{\int_{-\infty}^{\infty} {\rm D}z \left(\int_{-\infty}^{\infty} {\rm D}y 2\cosh\beta_J \hat{\Xi}\right)^{x}} \\
q_0 &= \int_{-\infty}^{\infty} {\rm D}w \frac{\int_{-\infty}^{\infty} {\rm D}z \left(\int_{-\infty}^{\infty} {\rm D}y 2\cosh\beta_J \hat{\Xi}\right)^{x-2} \left(\int_{-\infty}^{\infty} {\rm D}y \left(\frac{\hat{\phi}}{\hat{\Xi}}\right) 2\sinh\beta_J \hat{\Xi}\right)^2}{\int_{-\infty}^{\infty} {\rm D} \left(\int_{-\infty}^{\infty} {\rm D}y 2\cosh\beta_J \hat{\Xi}\right)^{x}} \\
q_1 &= \int_{-\infty}^{\infty} {\rm D}w \left\{ \frac{\int_{-\infty}^{\infty} {\rm D}z \left(\int_{-\infty}^{\infty} {\rm D}y \left(\frac{\hat{\phi}}{\hat{\Xi}}\right) 2\sinh\beta_J \hat{\Xi}\right)^{x}}{\int_{-\infty}^{\infty} {\rm D}z \left(\int_{-\infty}^{\infty} {\rm D}y 2\cosh\beta_J \hat{\Xi}\right)^{x}} \right\}^2
\end{aligned} \tag{88}$$

$$\begin{aligned}
\chi &= \int_{-\infty}^{\infty} {\rm D}w \frac{\int_{-\infty}^{\infty} {\rm D}z \left(\int_{-\infty}^{\infty} {\rm D}y 2\cosh\beta_J \hat{\Xi}\right)^{x-1} \int_{-\infty}^{\infty} {\rm D}y \left(\frac{\hat{\phi}}{\hat{\Xi}}\right)^2 2\sinh\beta_J \hat{\Xi}}{\int_{-\infty}^{\infty} {\rm D}z \left(\int_{-\infty}^{\infty} {\rm D}y 2\cosh\beta_J \hat{\Xi}\right)^{x}} \\
&+ \Gamma_{\rm eff}^2 T_J \int_{-\infty}^{\infty} {\rm D}w \frac{\int_{-\infty}^{\infty} {\rm D}z \left(\int_{-\infty}^{\infty} {\rm D}y 2\cosh\beta_J \hat{\Xi}\right)^{x-1} \int_{-\infty}^{\infty} {\rm D}y \left(\frac{2\sinh\beta_J \hat{\Xi}}{\hat{\Xi}^3}\right)}{\int_{-\infty}^{\infty} {\rm D}z \left(\int_{-\infty}^{\infty} {\rm D}y 2\cosh\beta_J \hat{\Xi}\right)^{x}}
\end{aligned} \tag{89}$$

with

$$\hat{\phi} = Jw\sqrt{\frac{p}{2}q_1^{p-1}} + Jz\sqrt{\frac{p}{2}(q_0^{p-1} - q_1^{p-1})} + Jy\sqrt{\frac{p}{2}(\chi^{p-1} - q_0^{p-1})} + pJ_0 m^{p-1} \tag{90}$$

and $\hat{\Xi} = \sqrt{\hat{\phi}^2 + \Gamma_{\rm eff}^2}$. When the number of products p of the estimate of the original bits is extremely large and $J/J_0, m$ is positive, $\hat{\phi} = pJ_0 m^{p-1}$ and

the solutions of the above saddle point equations lead to $m = q_0 = q_1 = 1$ and $\chi = 1$. Thus, the system is in the ferromagnetic phase and the replica symmetry is not broken ($q_0 = q_1$). Substituting the replica symmetric solution $m = q = 1$ into (75) and evaluating the integral with respect to w at the saddle point in the limit of $p \to \infty$, we obtain the free energy density in this phase (let us call this *FI*) as $f_{\rm FI} = -J_0$. We should notice that this free energy density does not depend on the effective amplitude of the transverse field $\Gamma_{\rm eff}$ at all. From the argument of the $J_0 = 0$ case, the phase specified $\chi = 1, T_J < T_c = (2\sqrt{\log 2})$ is the spin-glass phase. Therefore, the condition (87) is satisfied and the ferromagnetic error-less phase exists for $(J_0/J) \geq (J_0/J)_c = \sqrt{\log 2}$, where (J_0/J) is determined by balancing the free energy densities $f_{\rm FI} = f_{\rm SGI}$. As a result, we conclude that the error-less decoding is achieved if the SN ratio (J_0/J) is greater than the critical value $(J_0/J)_c = \sqrt{\log 2}$ and the condition is independent of $\Gamma_{\rm eff}$. To put it into other words, Shannon's bound is not violated by the quantum uncertainties in the prior distribution in the limit of $p \to \infty$.

The details of the analysis, including the numerical RSB solutions for finite p, will be reported in the conference and in the forthcoming article [28].

5 Quantum Markov Chain Monte Carlo Simulation

In the previous section, we investigated the performance of the MAP and MPM estimations for the problems of image restoration and error-correcting codes by using analysis of the mean-field infinite range model. In the Sourlas codes, the infinite range model is naturally accepted because we do not have to consider any structure in the bit sequence $\{\xi\}$, and in that sense, the range of interactions in the parity check $\{\xi_{i1} \cdots \xi_{ip}\}$ is infinite.

On the other hand, in image restoration, there should exist some geometrical structures in each pair in the sequence of the original images $\{\xi\}$. Then, we should introduce an appropriate two-dimensional lattice on which each pixel is located. Therefore, in this section, we carry out computer simulations for the two-dimensional model system to investigate the qualities of the MAP and MPM image restorations quantitatively.

5.1 Quantum Markov Chain Monte Carlo Method

Let us remind the readers that our effective Hamiltonian for image restoration is described by $\mathcal{H}_{\rm eff} = -\beta_m \sum_{\langle ij \rangle} \sigma_i^z \sigma_j^z - h \sum_i \tau_i \sigma_i^z - \Gamma \sum_i \sigma_i^x$. In this section, we suppose that each pixel σ_i^z is located on the two-dimensional square lattice. To evaluate the expectation value of an arbitrary quantity A in the quantum spin system

$$\langle A \rangle = \frac{{\rm tr}_{\{\sigma\}} A \, {\rm e}^{-\beta \mathcal{H}_{\rm eff}}}{{\rm tr}_{\{\sigma\}} \, {\rm e}^{-\beta \mathcal{H}_{\rm eff}}} \ , \tag{91}$$

we use the following ST formula [24] to carry out the above trace in practice as

$$\exp(-\beta\mathcal{H}_{\rm eff}) = \lim_{M\to\infty}\left(\mathrm{e}^{\frac{\mathcal{A}}{M}}\mathrm{e}^{\frac{\mathcal{B}}{M}}\right) \tag{92}$$

where we defined

$$\mathcal{A} = \beta(\beta_m\sum_{\langle ij\rangle}\sigma_i^z\sigma_j^z + h\sum_i\tau_i\sigma_i^z) = -\beta\mathcal{H}_{\rm eff}^{\rm classical}, \qquad \mathcal{B} = \beta\Gamma\sum_i\sigma_i^x\ . \tag{93}$$

We should keep in mind that these two terms $\mathcal{A}$ and $\mathcal{B}$ are easily diagonalized.

Then, by inserting the complete set $\sum_{\{\sigma_{jk}\}}|\{\sigma_{jk}\}\rangle\langle\{\sigma_{jk}\}| = 1$, the partition function Z_M for a fixed Trotter size M leads to

$$\begin{aligned} Z_M = \mathrm{tr}_{\{\sigma\}}\left(\mathrm{e}^{\frac{\mathcal{A}}{M}}\mathrm{e}^{\frac{\mathcal{B}}{M}}\right) = \sum_{\{\sigma_{jk}=\pm1\}}&\langle\{\sigma_{j1}\}|\mathrm{e}^{\frac{\mathcal{A}}{M}}|\{\sigma'_{j1}\}\rangle\langle\{\sigma'_{j1}\}|\mathrm{e}^{\frac{\mathcal{B}}{M}}|\{\sigma_{j2}\}\\ &\times\ \cdots\times\langle\{\sigma_{jM}\}|\mathrm{e}^{\frac{\mathcal{A}}{M}}|\{\sigma'_{jM}\}\ \rangle\langle\{\sigma'_{jM}\}|\mathrm{e}^{\frac{\mathcal{B}}{M}}|\{\sigma_{j1}\}\rangle \end{aligned} \tag{94}$$

where $|\{\sigma_{jk}\}\rangle$ is the Mth product of eigenvectors $\{\sigma\}$ and is explicitly given by $|\{\sigma_{jk}\}\rangle = |\sigma_{j1}\rangle\otimes|\sigma_{j2}\rangle\otimes\cdots\otimes|\sigma_{jM}\rangle$.

By taking the limit of $M\to\infty$, we obtain the *effective partition function* $Z_{\rm eff}$ of the quantum spin system with $B = (1/2)\log\coth(\beta\Gamma/M)$ as follows:

$$\begin{aligned} &Z_{\rm eff} \equiv \lim_{M\to\infty} Z_M\\ &= \lim_{M\to\infty}(a_M)^N\sum_{\{\sigma_{jk}\}=\pm1}\exp\left(\frac{\beta\beta_m}{M}\sum_{ij,k}\sigma_i^k\sigma_j^k + \frac{\beta h}{M}\sum_{i,k}\tau_i\sigma_i^k + B\sum_{i,k}\sigma_i^k\sigma_i^{k+1}\right)\\ &= \lim_{M\to\infty}(a_M)^N\\ &\quad\times\sum_{\{\sigma_{jk}=\pm1\}}\exp\left[\beta_{\rm eff}\left\{\beta_m\sum_{ij,k}\sigma_i^k\sigma_j^k + h\sum_{i,k}\tau_i\sigma_i^k + B_M\sum_{i,k}\sigma_i^k\sigma_i^{k+1}\right\}\right] \end{aligned} \tag{95}$$

where we defined a_M and B_M as $a_M \equiv \{(1/2)\sinh(2\beta_{\rm eff}\Gamma)\}^{1/2}$, $B_M \equiv (1/2\beta_{\rm eff})\log\coth(\beta_{\rm eff}\Gamma)$, respectively, and introduced the *effective inverse temperature* $\beta_{\rm eff} = \beta/M$. Thus, this is the partition function of a $(d+1)$-dimensional classical system at the effective temperature $T_{\rm eff} = \beta_{\rm eff}^{-1}$.

Let us think about the limit of $\Gamma\to 0$ in this expression. Then, the coupling constant of the last term appearing in the argument of the exponential becomes strong. As a result, copies of the original system, which are described by $\mathcal{H}_{\rm eff}^{\rm classical}$ and located in the Trotter direction labeled as k, have almost the same spin configurations. Thus, the partition function is now reduced to that of the classical system at the temperature $T = \beta^{-1}$.

We should not overlook that when we describe the same quantum system at $T = 0$ of the effective Hamiltonian $\mathcal{H}_{\rm eff}^{\rm Quantum}$ by the analysis of

the Schrödinger equation $i\hbar(\partial|\psi(t)\rangle/\partial t) = \mathcal{H}(t)|\psi(t)\rangle$ for the time-dependent Hamiltonian $\mathcal{H}(t) = -\beta_m \sum_{\langle ij\rangle} \sigma_i^z \sigma_j^z - h\sum_i \tau_i \sigma_i^z - \Gamma(t)\sum_i \sigma_i^x$, the inverse temperature β does not appear in the above expression. Therefore, we cannot use β in the quantum Monte Carlo method to simulate the quantum system at $T = 0$.

To realize the equilibrium state at the ground state $T = 0$ for a finite amplitude of the quantum fluctuation $\Gamma \neq 0$, we take the limit $\beta \to \infty, M \to \infty$ keeping the effective inverse temperature $\beta_{\text{eff}} = \mathcal{O}(1)$. Namely, the effective parameters to simulate the pure quantum system by the quantum Monte Carlo method are β_{eff} and M, instead of β and M. This choice is quite essential especially in the procedure of quantum annealing [16] because the quantum annealing searches the globally minimum energy states by using only the quantum fluctuation without any thermal fluctuation. Therefore, if we set the effective inverse temperature β_{eff} as of order 1 object in the limit of $M \to \infty$ (we can take into account the quantum effect correctly in this limit) and $\beta \to \infty$ (the thermal fluctuation is completely suppressed in this limit), we simulate the quantum spin system at the ground state $T = 0$.

5.2 Quantum Annealing and Simulated Annealing

According to the argument in the previous subsection, we construct the quantum annealing algorithm to obtain the globally minimum energy states of our effective Hamiltonian $\mathcal{H}_{\text{eff}}^{\text{classical}}$. To realize the algorithm, we control the amplitude of the transverse field as

$$\text{Quantum Annealing (QA):} \quad \Gamma \to 0 \quad \text{for } \beta_{\text{eff}} = 1,\ M \to \infty.$$

We should notice that the simulated annealing (thermal annealing) is achieved by controlling the parameter β as

$$\text{Simulated Annealing (SA):} \quad \beta \to \infty \quad \text{for finite } M \text{ and } \Gamma = 0.$$

As we mentioned, the scheduling of $T(t)$ and $\Gamma(t)$ might be essential in the simulated annealing and the quantum annealing. Although we know the optimal temperature scheduling $T(t) \sim (\log t)^{-1}$, we have not yet obtained any mathematically rigorous arguments for $\Gamma(t)$ as in the simulated annealing. Therefore, in this section, we use the same scheduling for $\Gamma(t)$ as that of the simulated annealing, namely, $T(t) = \Gamma(t)$. The justification of identification of $\Gamma(t)$ and $T(t)$ comes from the results we obtained in the previous section, that is, the shape of the bit-error rate at $T = 0$ as a function of Γ is almost the same as the bit-error rate for the thermal one. Thus, we assume that Γ and T might have the same kind of role to generate the equilibrium states for given Γ and T. However, the mathematical arguments on the scheduling of Γ are quite important and should be made clear in near future.

5.3 Application to Image Restoration

We investigate the MAP and MPM estimations by the quantum Monte Carlo method and the quantum annealing for the two-dimensional pictures which are generated by the Gibbs distribution $P(\{\xi\}) = \exp\Big(\beta_s \sum_{\langle ij\rangle} \xi_i \xi_j / Z(\beta_s)\Big)$. It must be noted that the above sum $\sum_{\langle ij\rangle}(\cdots)$ should be carried out for the nearest neighboring pixels located on the two-dimensional square lattice. A typical snapshot from this distribution is shown in Fig. 16.

Thermal MPM Estimation Versus Quantum MPM Estimation

Before we investigate the performance of the simulated annealing and the quantum annealing, as a simple check for our simulations, we demonstrate the thermal MPM estimation for the degraded image with $p_\tau = 0.1$ of the original image generated at $T_s = 2.15$ by using the thermal and quantum Markov chain Monte Carlo methods. We show the result of the T_m-dependence of the bit-error rate in Fig. 15. We carried out 30 independent runs for the system size 100×100. We set $h/\beta_m = T_s\beta_\tau = (T_s/2)\log(1-p_\tau/p_\tau)$. From this figure, we find that the best performance is achieved around the temperature $T_m = T_s = 2.15$. In Fig. 16, we show the original, degraded, and restored images. From this figure, we found that the restored image at relatively low temperature $T_m = 0.6$ is pained in even for the local structure of the original

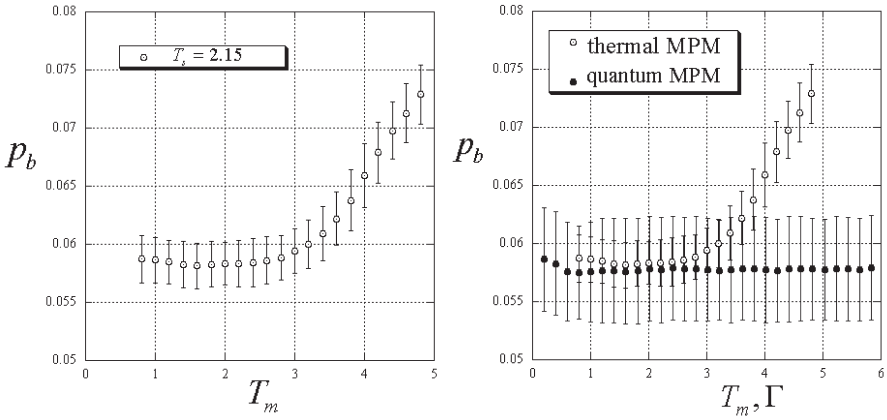

Fig. 15. The bit-error rate p_b for the thermal MPM estimation as a function of the temperature T_m (*left*). The plots were obtained from 30 independent runs for the system size 100×100. We set the temperature of the original image $T_s = 2.15$ and the noise rate $p_\tau = 0.1$. The right panel shows the bit-error rate for the quantum MPM estimation for the system size 50×50, and the Trotter number $M = 200$ for the same noise level $p_\tau = 0.1$ as shown in the left panel. The error-bars are obtained from 50-independent runs

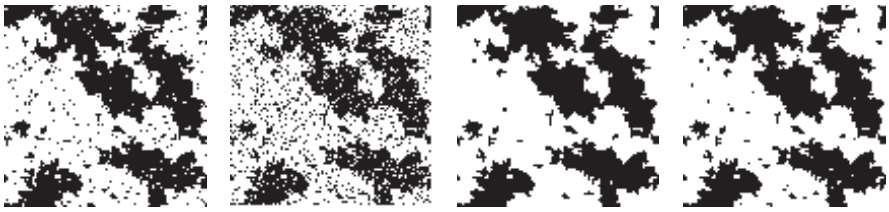

Fig. 16. From the left to the right, original, degraded ($p_\tau = 1$), and restored pictures at $T_m = 0.6$ and $T_m = T_s = 2.15$ are displayed

images. On the other hand, at the optimal temperature $T_m = 2.15$, the local structures of the original image are also restored.

We next investigate the quantum MPM estimation. In Fig. 15, we plot the bit-error rate for the quantum MPM estimation of the original image generated by the Gibbs distribution for the two-dimensional ferromagnetic Ising model. We control the effective transverse field $\Gamma_{\rm eff}$ on the condition that the inverse temperature β is equal to $\beta = \beta_{\rm eff} M$, namely, the effective inverse temperature $\beta_{\rm eff} = 1$. The hyperparameter $\beta_m^{-1} = T_m$ and h are fixed to their optimal values $T_m = T_s = 2.15$ and $h = \beta_\tau = (1/2)\log(1 - p_\tau/p_\tau)$. To draw this figure, we carry out 50 independent runs for the system size 50×50 for the Trotter size $M = 200$. The Monte Carlo step (MCS) needed to obtain the equilibrium state is chosen as $t^{'} = Mt$, where $t = 10^5$ is the MCS for the thermal MPM estimation. One Monte Carlo step in the calculation the quantum MPM estimate takes M times evaluations of spin flips than the calculation of the thermal MPM estimate. Thus, we provide a reasonable definition of the time $t^{'}$ of which the quantity is plotted and compared as a function as $t^{'} = t$ (thermal) and $t^{'} = Mt$ (quantum).

From this figure, we find that the lowest values of the bit-error rate for the quantum and thermal MPM estimations are almost the same as our analysis of the mean-field infinite range model predicted; however, the Γ-dependence of the bit-error rate is almost flat. We display several typical examples of restored images by the thermal and quantum MPM estimations in Fig. 17. From

Fig. 17. From the *left* to the *right*, the 50×50 original image generated at $T_s = 2.15$, degraded images ($p_\tau = 0.1$), and the restored image by the thermal MPM estimation, and the restored image by the quantum MPM estimation. Each bit-error rate is $p_b = 0.06120$ for the thermal MPM at $T_m = T_s = 2.15$ and $p_b = 0.06040$ for the quantum MPM estimation with $\Gamma = 0.8$ (at the nearest point from the solution of $m_0 = m(\Gamma)$), respectively

this figure, we find that the performance of the quantum MPM estimation is slightly superior to the thermal MPM.

Simulated Annealing Versus Quantum Annealing

In last part of this section, we investigate how effectively the quantum tunneling process possibly leads to the global minimum of the effective Hamiltonian for the image restoration problem in comparison to the temperature-driven process used in the simulated annealing. It is important for us to bear in mind that the observables we should check in the problem of image restoration are not only the energy on time E but also the bit-error rate p_b. As we mentioned, the globally minimum energy state of the classical Hamiltonian does not always minimize the bit-error rate. Therefore, from the view point of image restoration, the dynamics of the bit-error rate is also a relevant quantity, although, to evaluate the performance of the annealing procedure, the energy on time is a much more important measure. In this chapter, we investigate both of these two measures.

In our simulations discussed below, we choose the temperature and the amplitude of transverse scheduling as $\Gamma(t) = T(t) = 3/\sqrt{t}$ according to Kadowaki and Nishimori [16]. To suppress the thermal and quantum fluctuations at the final stage of the annealing procedure, we set $\Gamma = T = 0$ in the last 10% of the MCS.

In Fig. 18, we plot the time development of the bit-error rate and the energy on time, namely, $E_t = -\beta_m \sum_{\langle ij \rangle} \sigma_i^z \sigma_j^z - h \sum_i \tau_i \sigma_i^z$, where we defined

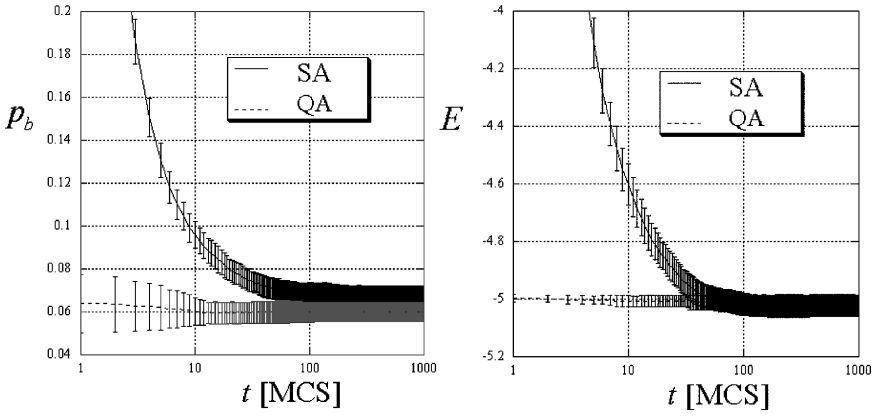

Fig. 18. The time dependence of the bit-error rate for the simulated annealing (SA) and the quantum annealing (QA). The MCS $t^{'}$ for the quantum annealing is defined by $t^{'} = Mt$ for the MCS, where t is the MCS for the SA. The right panel indicates the dynamical process of the energy function by the SA and the QA. We carried out this simulation for the system size 50×50 with the Trotter size $M = 200$. The noise rate is $p_\tau = 0.1$. The error bars are calculated by 50 independent runs

$\sigma_i^z = (1/M)\sum_k \sigma_i^k$ for the quantum annealing. As the MCS $t^{'}$ for the quantum annealing is defined by $t^{'} = Mt$ for the MCS, where t is the MCS for the SA, we should not overlook that the initial behavior of the first Mth MCS in the quantum annealing is not shown in this figure. We carried out this simulation for the system size 50×50 with the Trotter size $M = 200$. The noise rate is $p_\tau = 0.1$. We set $\beta_m^{-1} = T_s = 2.15$ and $h = (1/2)\log(1 - p_\tau/p_\tau) = 1.1$. From this figure, we find that the mean value of the bit-error rate calculated by the quantum annealing is smaller than that of the simulated annealing. However, the energy on time of the simulated annealing is slightly lower than that of the quantum annealing. Although this result is not enough to decide which annealing is superior, the simulated annealing with temperature scheduling $T(t) = 3/\sqrt{t}$ seems to be much more effective than the quantum annealing with the same scheduling of the amplitude of the transverse field for finding the minimum energy state. Of course, we should check more carefully to choose the optimal or much more effective scheduling of Γ. This might be one of the important future problems. In Fig. 19, we display the resultant restored images by the simulated annealing and the quantum annealing. For this typical example, the performance of the quantum annealing restoration measured by the bit-error rate is better than that of the simulated annealing. The difference of the correct pixels is estimated as $\Delta n = 50 \times 50 \times \Delta p_b = 2,500 \times 0.0084 = 21$ (pixels), where $\Delta p_b = p_b(\mathrm{SA}) - p_b(\mathrm{QA})$. From the reasons we mentioned above, the MAP estimate obtained by the quantum annealing is not a correct MAP estimate; however, the quality of the restoration is really fine.

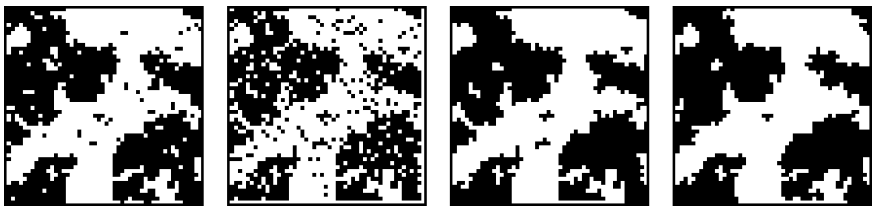

Fig. 19. From the left to the right, the original image ($T_s = 2.15$), degraded image ($p_\tau = 0.1$), and typical restored images by the simulated annealing and the quantum annealing. The resultant bit-error rates are $p_b = 0.066400$ for the SA and $p_b = 0.058000$ for the QA

6 Summary

In this chapter, we investigated the role of the quantum fluctuation introduced by means of the transverse field extensively. From the analysis of the infinite range model, we showed that the performances of the quantum MAP and MPM estimations are exactly the same as those of the thermal one. We derived

the Nishimori–Wong condition on the effective amplitude of the transverse field and this information might be useful to determine the optimal amplitude of the transverse field for given degraded image data. We also investigated the tolerance of the Sourlas codes to the quantum uncertainties in the prior distribution and discussed the condition on which the error-less ferromagnetic phase exists. We found that Shannon's bound is not violated by the quantum fluctuation in the limit of $p \to \infty$. The analytic results of the image restoration were checked by the quantum Markov chain Monte Carlo method. The results supported the analysis of the infinite range model finely.

I hope that the present work provides some useful information for deep understanding of the optimization method based on the quantum fluctuation which is essentially a different mechanism from the thermal hill-climbing.

Acknowledgements

The author thanks Bikas K. Chakrabarti and Dr. Arnab Das for organizing the workshop *Quantum Annealing and Other Optimization Methods*. He also acknowledges Saha Institute of Nuclear Physics (SINP) for the kind hospitality during his stay in Kolkata.

References

1. H. Nishimori: *Statistical Physics of Spin Glasses and Information Processing An Introduction* (Oxford University Press, Oxford 2001) 259, 265
2. K. Tanaka: J. Phys. A: Math. Gen. **35**, R81 (2002) 259
3. G. Winkler: *Image analysis, Random fields, and Markov Chain Monte Carlo Methods: A Mathematical Introduction* (Springer, Berlin Heidelberg New York 2002) 259
4. J.M. Pryce, A.D. Bruce: J. Phys. A: Math. Gen. **28**, 511 (1995) 259
5. N. Sourlas: Nature **339**, 693 (1989) 259, 260, 266, 279
6. P. Ruján: Phys. Rev. Lett. **70**, 2968 (1993) 259, 264
7. H. Nishimori: J. Phys. Soc. Japan **62**, 2973 (1993) 259, 260
8. H. Nishimori, K.Y.M. Wong: Phys. Rev. E **60**, 132 (1999) 259, 260, 278
9. D. Sherrington, S. Kirkpatrick: Phys. Rev. Lett. **35**, 1792 (1975) 259, 268
10. Y. Kabashima, D. Saad: Europhys. Lett. **45**, 98 (1999) 259
11. S. Geman, D. Geman: IEEE Trans. Pattern Anal. Math. Intell. **6-6**, 721 (1984) 259, 264, 267
12. S. Kirkpatrick, C.D. Gelatt Jr., M.P. Vecchi: Science **220**, 671 (1983) 259, 264, 267
13. K. Tanaka, T. Horiguchi: IEICE **J80-A-12**, 2217 (1997) (in Japanese) 259
14. P. Amara, D. Hsu, J.E. Straub: J. Phys. Chem. **97**, 6715 (1993) 260
15. A.B. Finnila, M.A. Gomez, C. Sebenik, C. Stenson, J.D. Doll: Chem. Phys. Lett. **219**, 343 (1994) 260
16. T. Kadowaki, H. Nishimori: Phys. Rev. E **58**, 5355 (1998) 260, 291, 294
17. E. Santoro, R. Martonak, E. Tosatti, R. Car: Science **295**, 2427 (2002) 260
18. C. Zener: Proc. R. Soc. London, Ser. A **137**, 696 (1932) 260
19. S. Miyashita: J. Phys. Soc. Japan **64**, 3207 (1995) 260

20. S. Miyashita: J. Phys. Soc. Japan **65**, 2734 (1996) 260
21. J. Inoue: Phys. Rev. E **63**, 046114 (2001) 260, 268, 269, 276
22. B.K. Chakrabarti, A. Dutta, P. Sen: *Quantum Ising Phases ans Transitons in Transverse Ising Models*, (Springer, Berlin Heidelberg New York 1995) 260, 267
23. Y.Y. Goldshmidt: Phys. Rev. B **41**, 4858 (1990) 260
24. M. Suzuki: Prog. Theor. Phys. **58**, 1151 (1977) 260, 268, 290
25. H.F. Trotter: Proc. Am. Math. Soc. **10**, 545 (1959) 268
26. R.B. Ash, *Information Theory* (Dover, New York 1965) 266
27. J. Inoue, K. Tanaka: Phys. Rev. E **65**, 016125 (2002) 273
28. J. Inoue, *APS March Meeting in Los Angels 2005*, in preparation 289

Part III

Other Optimizations

Combinatorial Optimization and the Physics of Disordered Systems

Heiko Rieger

Theoretische Physik, Universität des Saarlandes, 66041 Saarbrücken, Germany
h.rieger@mx.uni-saarland.de

1 Introduction

The purpose of this chapter of this monograph is to confront the reader with a number of optimization algorithms that are *exact* and *polynomial* in time and which have interesting applications in the physics of disordered systems. These are solid materials which contain a substantial degree of quenched disorder, have been an experimental and a theoretical challenge for physicists for many decades. The different thermodynamic phases emerging in random magnets, the aging properties and memory effects of spin glasses, the disorder induced conductor-to-insulator transition in electronic or bosonic systems, the collective behaviour of magnetic flux lines in amorphous high temperature superconductors, and the roughening transition of a disordered charge density wave systems are only a few examples for these fascinating phenomena that occur due to the presence of quenched disorder.

Analytic studies of models for these systems are usually based on perturbation theories valid for weak disorder, on phenomenological scaling pictures or on mean-field approximations. Therefore the demand for efficient numerical techniques that allow the investigation of the model Hamiltonians of disordered systems has always been high. Three facts make life difficult here: 1) The regime, where disorder effects are most clearly seen, are at low temperatures – and are even best visible at zero temperature; 2) the presence of disorder slows the dynamics of theses systems down, they become *glassy*, such that for instance conventional Monte-Carlo or molecular dynamics simulations encounter enormous equilibration problems; 3) any numerical computation of disordered systems has to incorporate an extensive disorder average.

In recent years more and more model systems with quenched disorder were found that can be investigated numerically 1) at zero temperature, 2) without equilibration problems, 3) extremely fast, in polynomial time (for a review on these developments see [1, 2] and [3] for an introduction to the non-expert). This *is* indeed progress, which became possible by the application of *exact* combinatorial optimisation algorithms developed by mathematicians

H. Rieger: *Combinatorial Optimization and the Physics of Disordered Systems*, Lect. Notes Phys. **679**, 301–324 (2005)
www.springerlink.com

and computer scientists over the last few decades. This gift is not for free: first a mapping of the problem of finding the *exact* ground state of the model Hamiltonian under consideration onto a standard combinatorial optimisation problem has to be found. If one is lucky, this problem falls into the class of P-problems, for which polynomial algorithms exist. If not, the intellectual challenge for the theoretical physicist remains to reformulate the model Hamiltonian in such a way that its universality class is not changed but a mapping on a P-problem becomes feasible.

Here we review some of the most fruitful applications of polynomial algorithms from the realm of combinatorial optimisation to various problems in the statistical physics of disordered systems. The next section presents the application of Dijkstras algorithm for finding shortest paths in weighted networks to the model of a non-directed polymer in a disordered environment with isotropical correlations. Then, in the 3rd and 4th section, we discuss minimum cost flow problems on weighted graphs and its solution via the successive shortest path algorithm and apply it to the roughness properties and the entanglement transition of elastic lines in a disordered environment and to the loop percolation transition in a vortex glass model. In the 5th section we focus on the minimum cut – maximum flow problem and discuss among its many applications the roughening transition of elastic media in a disordered environment. A discussion closes this paper in the 6th section.

2 Polymers in a Disordered Environment and Dijkstras Algorithm

A well studied model of a single elastic line [4], like an individual polymer or a single magnetic flux line in a type-II superconductor, in a disordered environment is the following: If one excludes overhangs (and by this also self-overlaps) of the elastic lines one can parametrise its configuration by the longitudinal coordinate z. The line configuration can then be described by the transverse coordinate $\mathbf{r}(z)$ as a function of z. The presence of disorder is usually modelled by a random potential energy $V(\mathbf{r}, z)$ and the ground state configuration of the line is highly non-trivial due to the competition between the elastic energy, that tends to straighten the line, and the random energy, that tries to bend the line into positions of favourable energy:

$$\mathcal{H}_{\rm single-line} = \mathcal{H}_{\rm elastic} + \mathcal{H}_{\rm random} = \int_0^H dz \left\{ \frac{\gamma}{2} \left[\frac{d\mathbf{r}}{dz} \right]^2 + V[\mathbf{r}(z), z] \right\} , \quad (1)$$

where H is the longitudinal length (not the proper length) of the line. The random potential energy is a Gaussian variable with prescribed mean and correlations $\langle\langle V[\mathbf{r}, z] V[\mathbf{r}', z']\rangle\rangle = g(\mathbf{R} - \mathbf{R}')$, where $\mathbf{R} = (\mathbf{r}, z)$ and $\langle\langle \cdots \rangle\rangle$ denotes the average over the disorder.

A lattice version of this continuum model is the *directed* polymer model: The lines correspond to directed paths on a hyper-cubic lattice that start at a specific lattice site, say $(0, 0, \ldots, 0)$ and proceed only in the $(1, 1, \ldots, 1)$ direction along the bonds. The energy contribution for a path passing bond $\mathbf{i}$ of the lattice is a *positive* random variable $e_{\mathbf{i}}$ and the total energy of a path $\mathcal{P}$ is simply

$$\mathcal{H}^{\text{lattice}}_{\text{single-line}} = \sum_{\mathbf{i}\in\mathcal{P}} e_{\mathbf{i}} = \sum_{\mathbf{i}} e_{\mathbf{i}} n_{\mathbf{i}} \ , \tag{2}$$

where $n_{\mathbf{i}} = 1$ if the path passes bond $\mathbf{i}$ (i.e. $\mathbf{i} \in \mathcal{P}$) and $n_{\mathbf{i}} = 0$ otherwise.

We are interested in isotropically correlated disorder and consider the problem on a *non-directed* (square) lattice (i.e. paths can pass any bond in both directions) in order not too exclude overhangs right from the beginning. In case of uncorrelated disorder overhangs were shown to be irrelevant [6], but for isotropically correlated disorder this is not clear. We define the latter to decay algebraically with the spatial distance of the bonds

$$\langle\langle e_{\mathbf{i}} - e_{\mathbf{j}}\rangle\rangle = |\mathbf{R}_{\mathbf{i}} - \mathbf{R}_{\mathbf{j}}|^{2\alpha-1} \ , \tag{3}$$

where $\mathbf{R}_{\mathbf{i}}$ spatial position of bond $\mathbf{i}$, and we generate correlated random numbers using a well-established numerical procedure [5].

We calculate the exact ground states of the Hamiltonian (2) or optimal paths using Dijkstras algorithm (note that all energies $e_{\mathbf{i}}$ are positive). This simple polynomial algorithm works as follows: Let $V = \{1, \ldots, L^d\}$ be the set of lattice sites and $A = \{(i, j)|i, j \in V \text{ nearest neighbors}\}$ the set of bonds. The algorithm increases successively a subset S of sites for which the optimal path starting at the fixed site s are known. Obviously initially $S := \{s\}$. We denote the energy of the optimal path starting at s and terminating at i with $E(i)$ and since all optimal paths can be constructed via a predecessor list, we keep track of this list, too, via an array $pred(i)$, denoting the predecessor site of site i in a shortest path from s to i:

algorithm Dijkstra
begin
  $S := \{s\}$; $\overline{S} := V \backslash \{s\}$;
  $E(s) := 0$, $pred(s) := 0$;
  while $|S| < |V|$ **do**
  begin
    choose $(i, j) : E(j) := \min_{k,m}\{E(k) + e_{(k,m)}|k \in S, m \in \overline{S}, (k, m) \in A\}$;
    $\overline{S} := \overline{S} \backslash \{j\}$; $S := S \cup \{j\}$;
    $pred(j) := i$;
  end
end

In Fig. 1 we show examples of the set $\{i\}$ of lattice sites that are end-points of optimal paths starting from a fixed initial site and having a total energy

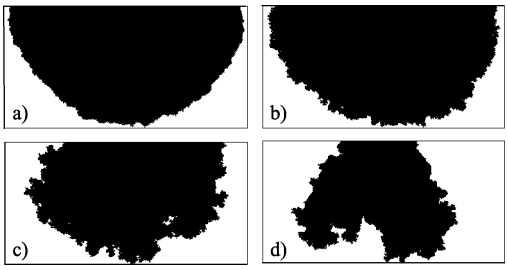

Fig. 1. Example for the growth front of the non-directed polymer for uncorrelated disorder (**a** and **b**) and correlated disorder (**c** and **d**; $\alpha = 0.4$). The black pixels indicate the lattice sites of the (*square*) lattice are connected via optimal paths to the offspring (*centre* of the *top line*) with energy less than a given value

$E(i)$ less than a given value $E_{\max}$. For uncorrelated disorder the surface of this set is roughly a semi-circle, whereas for strongly correlated disorder the surface becomes topologically more complicated.

The universal properties of the optimal paths are typically described the scaling of two characteristic quantities: The average transverse fluctuations $\langle\langle \mathbf{r}^2 \rangle\rangle \propto H^{\nu}$ and the energy fluctuations $\langle\langle E^2 \rangle\rangle \propto H^{\omega}$, where H is the longitudinal distance between starting point and end point of the paths. By computing the optimal paths for several thousands of samples for a given disorder correlation exponent α and for a given longitudinal distances H and fitting the resulting data for transverse and energy fluctuations to the expected power laws we can extract the exponents ν and ω (the details of these computations can be found in [7]). The resulting estimates in 2d are shown in Fig. 2 [7]. Although the number of overhangs in the optimal paths we computed in the non-directed case increased with α (i.e. increasing correlations)

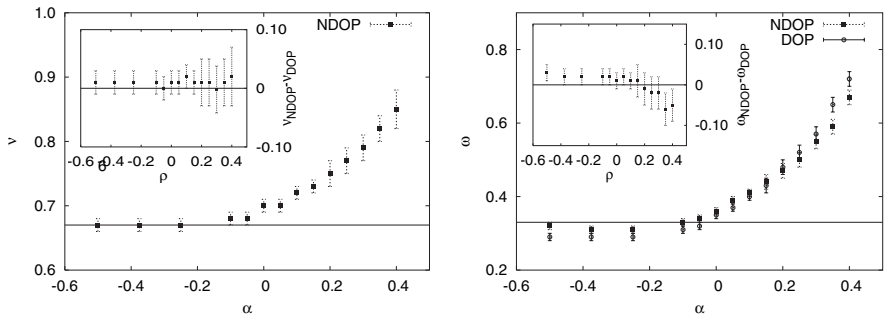

Fig. 2. Numerical estimate of the roughness exponent ν (*left*) and energy fluctuation exponent ω (*right*) for as a function of the correlation exponent α. The straight lines are at exactly know values $\nu = 2/3$ and $\omega = 1/3$ for uncorrelated disorder. Around $\alpha = 0$ the correlations of the disorder become relevant. The insets show the difference of our estimates between the directed and non-directed case

the fraction of bonds contributing to overhangs scaled to zero for all values of α we considered. Hence overhangs appear to be irrelevant also in the presence of correlated disorder.

3 Interacting Elastic Lines in a Disordered Environment

When one puts interacting elastic lines together into a finite system with a given density of lines they will show interesting collective behaviour. Examples are the entanglement of magnetic flux lines in high-T_c superconductors in the mixed phase [8] or the entanglement of polymers in materials like rubber [9]. The degree of entanglement of the lines usually manifests itself in various measurable properties like stiffness or shear modulus in the case of polymers and in transport or dynamical properties for magnetic flux lines in superconductors. A theoretical description of these line systems can be based on the single-line Hamiltonian (1) plus an appropriate line interaction term:

$$\mathcal{H}_{\text{many-lines}} = \sum_{i=1}^{N} \mathcal{H}^{(i)}_{\text{single-line}} + \sum_{i<j} \int_0^L dz \int_0^L dz' \, V_{\text{int}}[\mathbf{R}_i(z) - \mathbf{R}_j(z')] \; , \quad (4)$$

where $\mathbf{R}_i(z) = (\mathbf{r}_i(z), z)$ is the spatial position of the infinitesimal line segment dz of the i-th line. If the interactions $V_{\text{int}}[\mathbf{R}_i(z) - \mathbf{R}_j(z')]$ are short ranged (i.e. in case of flux lines the screening length small compared to the average line distance) or just hard core repulsive, and the random, δ-correlated disorder potential $V_r[\mathbf{r}_i(z), z]$ in (1) is strong compared to the elastic energy ($\propto \gamma$) this continuum model reduces to a lattice model reminiscent of the single-line lattice model (2):

$$\mathcal{H}^{\text{lattice}}_{\text{many-lines}} = \sum_{\mathbf{i}} e_{\mathbf{i}} n_{\mathbf{i}} \; , \quad (5)$$

where $n_{\mathbf{i}} = 1$ if a line passes bond $\mathbf{i}$ and $n_{\mathbf{i}} = 0$ otherwise and the *positive* random variable $e_{\mathbf{i}}$ is the energy cost for a line segment to occupy bond $\mathbf{i}$. The hard core constraint is thus enforced on the bonds but for the sake of an easier formal description we allow the lines to touch in isolated points, the lattice sites. The lines live on the bonds of a simple cubic lattice with a lateral width L and a longitudinal height H ($L \times L \times H$ sites) with free boundary conditions in all directions. Each line starts and ends at an arbitrary position on the bottom respective top planes. The number N of lines threading the sample is fixed by a prescribed density $\rho = N/L^2$. For a single line $N = 1$, one recovers the non-directed polymer model (2). The random bond energies are uniformly distributed over the interval $[0, 1]$.

Note that the allowed configurations of the bond variables $n_{\mathbf{i}}$ are only those that be identified with lines threading the samples (or loops inside the sample, which, however, cost energy and therefore do not occur in the ground state), which means that the number of occupied bonds connected to a lattice

site that lies neither on the top nor on the bottom plane has always to be even. If we connect all sites on the top to an extra site, called the source, an all sites on the bottom to another extra site, called the targe, than the latter statement remains true also for the top an bottom plane. We can now say that N lines start at the source node and terminate at the target node, or, in network flow jargon: The feasible configurations of the variables $n_{\mathbf{i}}$ constitute a flow with zero excess on all lattice sites and an excess $+N$ and $-N$ for the source and target node, respectively.

Thus the determination of the ground state configuration of the N-line problem with the Hamiltonian (5) is a minimum-cost-flow-problem, which can be solved with a successive shortest path algorithm [1, 2, 3]. In essence one starts with the zero flow $n_{\mathbf{i}} = 0$, corresponding to zero lines in the system, and sends successively one unit of flow from the source to the target, corresponding to adding one line after the other to the system. This has to happen with the minimal energy, i.e. along optimal paths, which are calculated using Dijkstras algorithm that we encountered already in the single line problem discussed in the last section. However, when trying to add a line to a system with a number, say M, of lines already present, the existing line configuration sometimes must be changed to minimise the total energy for $M+1$ line solution. That becomes feasible by allowing flow to be sent *backwards* on already occupied bonds. By this operation one *gains* energy (whereas occupying an empty bond $\mathbf{i}$ always costs energy $e_{\mathbf{i}} \geq 0$), which means one has to operate on a network that has to be adapted to the existing flow configuration and has negative energies on all occupied bonds. Unfortunately Dijkstras algorithm works only for positive bond energies, and one has either to use a slower (label-correcting) algorithm to find the optimal paths in a graph with negative edge costs [3] or one has to use the concept of node potentials, by which one can make all energies in the adapted network non-negative without changing the actual shortest paths. This procedure is described in full detail in [3], and an example for a ground state configuration of a 3d system is shown in Fig. 3.

3.1 Roughening in 2d

The first quantity we are interested in is the disorder averaged line roughness [10]. The mean square displacement of a single line with index i in one sample is defined as

$$w_i^2 = \overline{r^2}_i - \overline{r}_i^2 \tag{6}$$

with $\overline{r^n}_i = H^{-1} \sum_{z=1}^{H} r_i^n(z)$ for $n = 1, 2$. The mean square displacement of all lines in one sample is $\bar{w}^2 = \frac{1}{N} \sum_{i=1}^{N} w_i^2$ and the roughness w is defined as the square root of the disorder averaged sample mean square displacement $w = \sqrt{\langle \bar{w}^2 \rangle}$.

The roughness of a one line system ($N = 1$) scales as $w \sim H^{\zeta}$ in the limit of infinite transverse system size. In 2d the value of the roughness exponent is $\zeta = 2/3$ [11], whereas in 3d it is close to $\zeta = 5/8$ [12, 13]. In the case of a

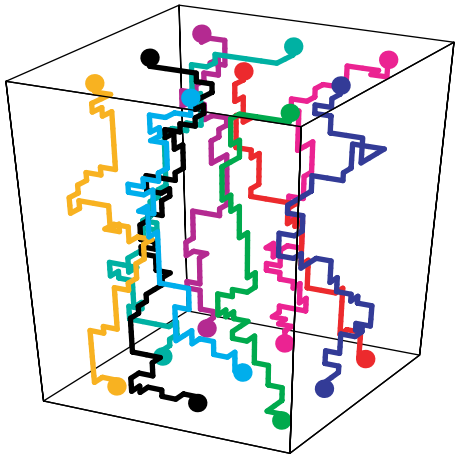

Fig. 3. Ground state configuration in 3d of a N-line system with $N = 9$ defined by (5). The entry/exit points are fixed in a regular 3×3 array for better visibility

non-vanishing line density one expects to observe this single line behavior as long as the transverse fluctuations of the individual lines are smaller than the average line-to-line distance a, which is given by the line density $\rho = 1/a$ in 2d. This means that we expect $w \sim H^{\zeta}$ for $H \ll a^{1/\zeta}$.

Once the transverse fluctuations of the individual lines have reached the size of average line-to-line distance one expects a collective behavior of the lines that restricts the individual line roughness due to the presence of the others. If the line system behaves like an elastic medium the roughness in the collective regime is expected to behave like $w \sim \ln L$ [14]. Hence, for fixed line density ρ we expect the following scaling form

$$w \approx a \ln(L) \cdot g_{2d}(H/(a \ln L)^{1/\zeta}) \,, \tag{7}$$

where $g_{2d}(x)$ is a scaling function with the asymptotic behavior $g_{2d}(x) \propto x^{\zeta}$ for $x \ll 1$, corresponding to the single-line behavior, and $g_{2d}(x) = const.$ for $x \gg 1$, corresponding to the collective regime. Note that we have assumed that the line density enters this form only via a rescaling of the lateral length scales.

We computed the ground states of a large number of disorder realizations (up to 10^3) for various values of L, H and ρ and produced scaling plots for fixed line density ρ according to the suggested size scaling form (7). We found a good data collapse for all values of ρ that we checked ($\rho = 0.05,\ldots,0.5$). In Fig. 4 we show the data collapse for $\rho = 0.05$. This particular value results in the best data collapse for the achieveable system sizes.

We estimated the saturation roughness $w_{\mathrm{sat}} = \lim_{H\to\infty} w(H)$ from the flat tail of the roughness curves $w(H)$ and show them in Fig. 4 as a function of L for several values of the line-density ρ. The data can be fitted to the

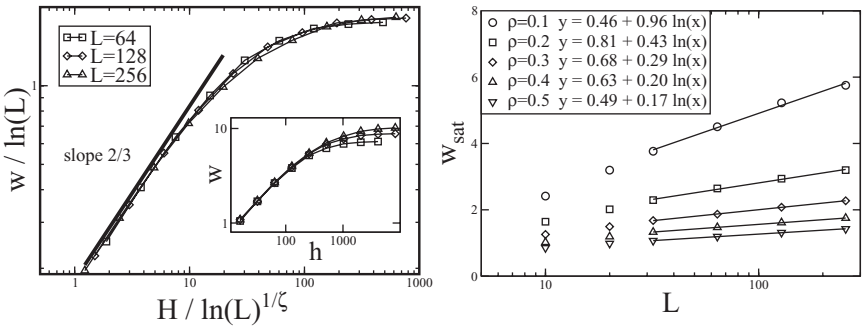

Fig. 4. *Left:* Scaling plot of the roughness in 2d according to the finite size scaling form (7). The line density is $\rho = 0.05$, the roughness exponent is $\zeta = 2/3$. *Right:* Saturation roughness as a function of the system width with fits of the form $y = A + B\,ln(L)$

form $y = A + B\ln(L)$ again reflecting the collective super-rough scaling of the roughness in 2d. The slope B of the data sets decreases as ρ increases while the constant part A does not vary much. This leads to the strengthening of finite size effects with increasing ρ.

The crossover from single-line to multi-line scaling takes place when $H^{\zeta} \sim a$, where a is the average line-to-line distance $a = 1/\rho$ in 2d. For fixed but large lateral system size L the scaling form (7) predicts

$$w \approx a \cdot \tilde{g}_{2d}(H/a^{1/\zeta}) \tag{8}$$

where the scaling function $\tilde{g}_{2d}(x)$ has the asymptotic behavior $\tilde{g}_{2d}(x) \sim x^{\zeta}$ for $x \ll 1$ and $\tilde{g}_{2d}(x) \sim const.$ for $x \gg 1$. Figure 5 shows the corresponding data collapse of the roughness data that we computed. Note that the height has been also rescaled with a factor of $1 - 1/a$ to account for the limit $\rho \to 1$.

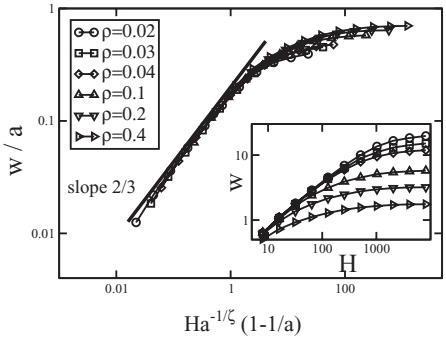

Fig. 5. Scaling plot for the roughness in 2d according to the scaling form (8). The system size is fixed at $L = 256$

3.2 Roughening in 3d

In this section we present our numerical results and the corresponding scaling laws obtained for the 3d case. If the observations we made in the last section could be carried over to the 3d case, one would expect 2 regimes: One for small heights H, in which the transverse fluctuations of the lines are still much smaller than the average line-to-line distance $a = 1/\rho^{1/2}$ in 3d; and one for large H, in which the line roughness is restricted due to collective effects. *Only in the case* our line system would also for 3d fall into the same universality class as a 3d elastic medium (this is, as we have shown the case in 2d), one would expect $w_{\mathrm{sat}} \propto \sqrt{\ln L}$ [16, 17].

However, surprisingly we find i) three regimes instead of two (cf. the data shown in Fig. 6), and ii) $w_{\mathrm{sat}} \propto L$, i.e. the size of the transverse fluctuations is not restricted by the presence of a large number of other lines but only by the lateral system size. Apparently in 3d the lines become transparent to each other, and the wandering of any line to the transverse direction does not induce collective behavior.

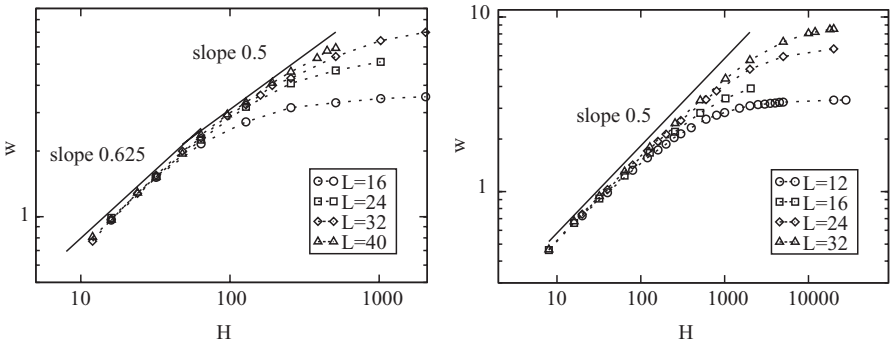

Fig. 6. Data for the roughness w as a function of the height H for different transverse system sizes L and two densities: $\rho = 0.005$ (*top*) and $\rho = 0.4$ (*bottom*). In the low density limit (*top*) the crossover from single line to collective behavior is visible – indicated by the two straight lines with slope 0.625, the sinle line roughness exponent, and 0.5, respectively. In the high density limit the crossover from collective line behavior (indicated by the straight line with slope 0.5) to the saturation regime is visible. The data points are averaged over 100–1000 samples

The three regimes that we find can be characterized as follows: 1) A single line regime for $H \ll a^{1/\zeta}$ in which the roughness behaves as in the the one-line case: $w \propto H^{\zeta}$. 2) An intermediate regime for $a^{1/\zeta} \ll H \ll L^2$ in which the roughness increases as $H^{1/2}$, which is identical to the behavior of random walks. Between the two regimes one can see a cross-over that can be shown to be related to the entropic repulsion of the lines. Recall that this leads in 2d asymptotically to collective effects, but here the consequences are different.

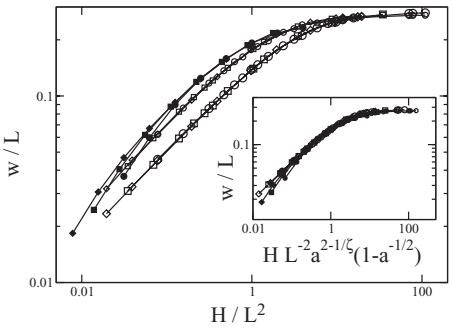

Fig. 7. Scaling plot of the roughness in 3d according to the finite size scaling form (9) for different line densities $\rho = 0.1$ (*filled symbols*), 0.2 (*bold*) and 0.4 (*empty*) for system sizes $L = 16$ (*ovals*), 24 (*squares*) and 32 (*diamonds*). The inset shows data collapse according to the scaling form (12)

3) The saturation regime for $H \gg L^2$ in which the roughness saturates at the lateral system size: $w \approx L$. In the following we support this central result with the data we obtained from our ground state calculations for the 3d system and derive the appropriate scaling forms for the different regimes.

In Fig. 7 we show our results for the roughness in 3d in the crossover region from the intermediate or multi-line regime to the saturation regime. We show data for three different line density values, but we have also data for other values, and they all fit well into the scenario that we propose now). The finite size scaling plots yield an excellent data collapse using the scaling form:

$$w = L \cdot g_{3d}^{(a)}(H/L^2) \quad . \tag{9}$$

The scaling function $g_{3d}^{(a)}(x)$, which still depends on a, or the line density $\rho = 1/a^2$, has the following asymptotic behavior: $g_{3d}^{(a)}(x) \propto x^{1/2}$ for $x \to 0$ and $g_{3d}^{(a)}(x) = const.$ for $x \to \infty$.

The first crucial observation here – and the essential difference to the 2d case – is that in the limit $L \to \infty$ the roughness is not significantly restricted by the presence of the other lines but approaches a value proportional to the lateral system size. Actually, as we see from the plot of the saturation roughness as a function of L shown in Fig. 8 that $w_{\rm sat} = \lim_{H\to\infty} w(L,a) = 0.28 \cdot L + c_a$, where c_a is a small constant that varies only slightly with a. This variation with a is a boundary effect: The free boundary conditions act effectively in a repulsive way on the lines that competes with the steric inter-line repulsion. Therefore systems with a lower line density show smaller transverse line fluctuations than those with a higher density.

The second crucial observation is that the roughness of the lines in the intermediate regime grows like $H^{1/2}$, i.e. they have a roughness exponent that is smaller than the single line value of $\zeta = 0.625$ and is identical to the value for simple random walks. Although the actual line configuration is constructed

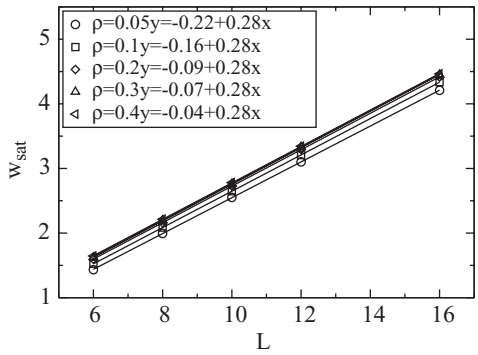

Fig. 8. Saturation roughness as a function of the system width with linear fits to the data points

in a highly non-trivial manner via a global criterion, namely the computation of the global N-line ground state, their universal geometric properties appear to be similar to that of random walks.

The density dependence of the scaling functions $g_{3d}^{(a)}(x)$ can be worked out by matching it with the scaling form for the single- to multi-line regime. Here the relevant length scale in the H-direction is $a^{1/\zeta}$, and in analogy to the 2d case we expect for $L \gg a$ the L-independent scaling form

$$w = a \cdot \tilde{g}_{3d}(H/a^{1/\zeta}) \tag{10}$$

with the asymptotics $\tilde{g}_{3d}(x) = x^{\zeta}$ for $x \ll 1$ and $\tilde{g}_{3d}(x) = x^{1/2}$ for $x \gg 1$. In Fig. 9 we show the corresponding scaling plot for the data that we obtained from our calculations. Hence we get the expected single line behavior $w \sim H^{\zeta}$ when $H \ll a^{1/\zeta}$, and we obtain

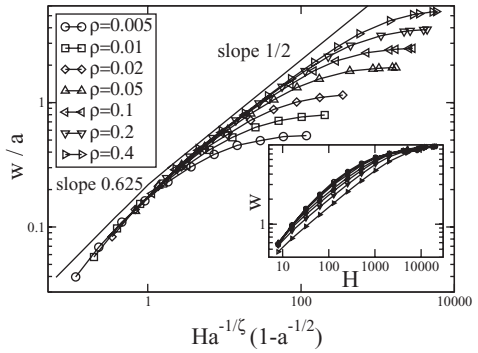

Fig. 9. Scaling plot for the roughness in 3d in the crossover region from single to multi-line behavior. The system size is $L = 32$. The inset shows the original, unscaled data

$$w = a^{1-(1/2\zeta)} H^{1/2} \quad \text{for} \quad w \ll L \quad \text{and} \quad H \gg a^{1/\zeta} \ . \tag{11}$$

From this the natural scaling variable for the crossover region from the intermediate regime (where w should be described by (11)) to the saturation regime (where w should be proportional to L according to (9)) appears to be $a^{1-(1/2\zeta)} H^{1/2}/L$ or $H/a^{1/\zeta-2}L^2$, which implies that (9) can be rewritten as

$$w = L \cdot g_{3d}(H/a^{1/\zeta-2}L^2) \quad \text{for} \quad H \gg a^{1/\zeta} \ . \tag{12}$$

with $g_{3d}(x) = x^{1/2}$ for $x \to 0$ and $g_{3d}(x) = 0.28$ for $x \to \infty$ (see the inset in Fig. 7). As in 2d, for high line densities $\rho > 0.1$ ($a \leq 3$) one has to take into account the limiting case $\rho = 1$ where lines fill all parallel lattice bonds resulting zero roughness. This limit can be incorporated into (12) by rescaling H by $1/(1-\rho)$.

At this point we would like to stress that the random walk like scaling is *not* related to the actual distance at which the lines touch or cross each other (and are in some cases continued randomly). Both in 2d and in 3d the typical length scale s between two consecutive intersection points on one line is much larger then the length scale ξ for the crossover from single line to collective behavior and its divergence with the line average distance a is much stronger. This can be seen in Fig. 10, where we show scaling plots for the average length of line segments s between two crossings, from which one concludes that s scales with a as $a^{2.6}$ in 2d (compared to $a^{1.5}$ for the crossover lenght scale ξ) and $a^{3.2}$ in 3d (compared to $a^{1.6}$ for ξ). This also demonstrates that the lines do *not* behave like independent random walkers in 3d but reflect the effect of a steric repulsion that tends to avoid random crossings between them (visible in 2d and in 3d).

3.3 Entanglement Transition

The main result of the roughness calculations for the 3d system is that the lines with only hard core repulsion can transverse the whole system, in marked

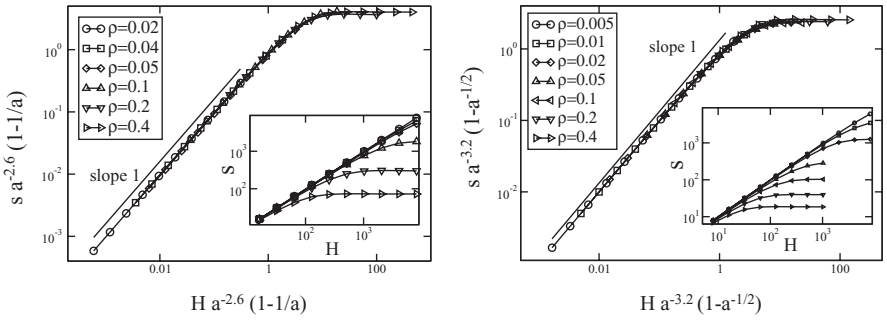

Fig. 10. Scaling plots for the length of line segments s between two crossings (**a**) in 2d, the system size is $L = 256$ and (**b**) in 3d, the system size is $L = 32$. The insets show the original, unscaled data

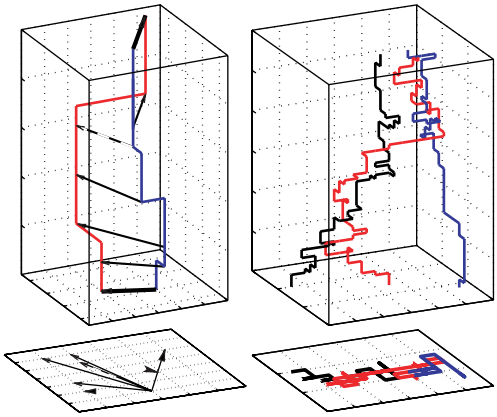

Fig. 11. Definition of the winding angle of two flux lines. Right part, *top*: A configuration of three lines that are entangled. Right part, *bottom*: The projection of the line configuration on the basal plane, defining a connected cluster

difference to the 2d case. Consequently one expects the lines to be topologically entangled, which we study in this section.

We compute the winding angle of all line pairs as indicated in Fig. 11 (c.f. [19]). For each z-coordinate the vector connecting the two lines is projected onto that basal plane (Fig. 11). $z = 0$ gives the reference line with respect to which the consecutive vectors for increasing z-coordinate have an angle $\phi(z)$. If the two lines intersect we neglect the intersection point and interpolate between the last and the next point in such a way that the global winding angle is minimised. We define two lines to be *entangled* when $\phi(z) > 2\pi$. This choice is one that measures entanglement from the topological perspective [20], and comes from the requirement that an entangled pair of lines can not be separated by a suitable linear transformation in the basal plane (i.e. the lines almost always would cut each other, if one were shifted). The precise definition of entanglement is not of major relevance, and the one used is useful since it is the computationally easiest.

Sets or *bundles* of pairwise entangled lines are formed so that a line belongs to a bundle if it is entangled at least with one other line in the set. The topological multi-line-entanglement could be characterised by other measures as well; the universal properties of the transition will not depend on these. These line bundles are spaghetti-like – i.e. topologically complicated and knotted sets of one-dimensional objects. To study the size distribution of these objects we project these bundles on the basal plane, as indicated in Fig. 3, where a bundle projects onto a connected cluster. The probability for two lines to be entangled increases with increasing system height. Consequently one would expect that the bundle size increases with H, and therefore also their projections, the clusters. This scenario is exemplified in Fig. 12, for the

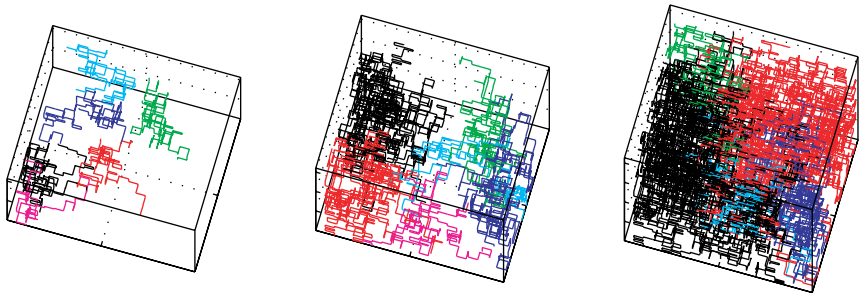

Fig. 12. Line configurations for different heights H (from left to right: $H = 64$, 96, 128), the lateral size $L = 20$, the line density is $\rho = 0.3$. Only the largest line bundles are shown, indicated by a varying grey scale. Black denotes the largest cluster, which eventually percolates

largest height the largest cluster spans from one side of the system to the other, i.e. it *percolates*.

Hence, for a given line density ρ we expect that for system heights larger than a critical value H_c an system spanning large entangled bundle occurs, containing an infinite number of lines in the limit $L \to \infty$. We will call this an *entanglement transition* occurring at a finite system height H_c. In the projection plane this appears like a percolation transition and in the following we will investigate its universal properties.

The numerical data we present have been obtained by averaging over upto 10^3 realizations of the random potentials e_i in (5) and the statistical error resulting from this finite sample average is in all cases smaller than the symbol size. We studied different line densities between $\rho = 0.1$ and $\rho = 0.5$, but present for brevity only data for $\rho = 0.3$. In Fig. 13 we show the probability $P_{\rm perc}$ of the clusters, formed by the entangled bundles in the projection plane, to percolate as a function of the height H of the system. The curves for different lateral system sizes L intersect at H_c, which gives our estimate for $H_c(\rho = 0.3) = 134$. The inset shows a scaling plot according to

$$P_{\rm perc} = p(L^{1/\nu}\delta) \tag{13}$$

with $\delta = (H - H_c)/H_c$ the reduced distance from the critical height and $\nu = 4/3$ the correlation length exponent. The finite size corrections for smaller system sizes than those shown are large, but could be incorporated in the scaling plot by using an L-dependent shift $H_c(L)$ that converges to H_c for larger L.

$\nu = 4/3$ is the exponent of conventional bond percolation in two dimensions. Thus we are led to the conclusion that the entanglement transition belongs to the same universality class as conventional $2d$ percolation. We checked other quantities to confirm this result The cluster size distribution $P(n)$ at $H = H_c$ approaches $P(n) \propto n^{-\tau}$ with $\tau = 187/91 \approx 2.055$ in the limit $L \to \infty$. The mass (i.e. number of entangled lines) of the percolating

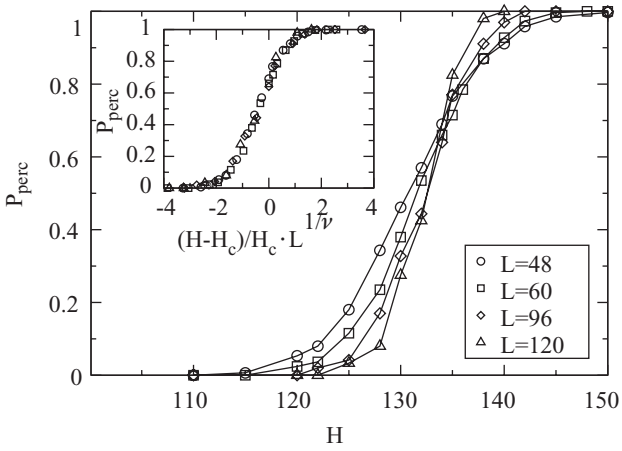

Fig. 13. Percolation probability for different lateral system sizes L as a function of the system height H, the line density is $\rho = 0.3$. Inset: Scaling plot of the data with $H_c = 134$ and $\nu = 4/3$

bundle at H_c fits well to $M \propto L^{d_f}$ with $d_f = 91/48 \approx 1.896$. Both exponents, the cluster distribution exponent τ and the fractal dimension d_f are identical to those for conventional bond percolation and one can also use the order parameter exponent, $\beta = 5/36$, to fit the data reasonably well. Details of these computations can be found in [21].

4 Disorder Induced Loop Percolation in Vortex Glasses

Another application of the successive shortest path algorithm for minimum-cost-flow-problem is finding the ground state of the Hamiltonian

$$H = \sum_{\mathbf{i}} (n_{\mathbf{i}} - b_{\mathbf{i}})^2 \qquad \text{with the constraint} \quad \forall k : \sum_{l \text{ n.n. of } k} n_{(kl)} = 0 \,, \qquad (14)$$

where the integer variables $n_{\mathbf{i}}$ live on the bonds $\mathbf{i}$ of a d-dimensional hypercubic lattice and $b_{\mathbf{i}} \in [-2\sigma, 2\sigma]$ are real valued quenched random variables with $\sigma \geq 0$ setting the strength of the disorder. The constraint $\sum_{l \text{ n.n. of } k} n_{(kl)} = 0$ means that at all lattice sites k the incoming flow has to balance the outgoing flow, i.e. the flow $\{n_{\mathbf{i}}\}$ is divergenceless. The physical motivation of studying models these kind of models is the following:

In 2d the Hamiltonian (14) occurs for instance in the context of the solid-on-solid (SOS) model on a disordered substrate [22]. The SOS representation of a 2d surface is defined by integer height variables u_k for each lattice site k of a square lattice. The disordered substrate is modelled via random offsets $d_k \in [0, 1]$ for each lattice site, such that the total height at lattice site k is $h_k = u_k + d_k$. The the total energy of the surface is

$$\mathcal{H}_{\rm SOS} = \sum_{(kl)} (h_k - h_l)^2 = \sum_{(\tilde{kl})} (n_{(\tilde{kl})} - b_{(\tilde{kl})})^2 \tag{15}$$

where the first sum runs over all nearest neighbor pairs (kl) of the square lattice and the second sum runs over all bonds $(\tilde{kl})$ of the *dual* lattice (being a square lattice, too), which connect the centers of the elementary plaquettes of the original lattice. A dual bond $(\tilde{kl})$ therefore crosses perpendicularly a bond (kl) connecting neighbors k and l on the original lattice. We define $n_{(\tilde{kl})} = n_k - n_l$ and $d_{(\tilde{kl})} = d_l - d_k$ if l is either the right or the upper neighbor of k (i.e. for $k = (x, y)$ either $l = (x+1, y)$ or $l = (x, y+1)$ and $n_{(\tilde{kl})} = n_l - n_k$ and $d_{(\tilde{kl})} = d_k - d_l$ if l is either the left or the lower neighbor of k (i.e. for $k = (x, y)$ either $l = (x-1, y)$ or $l = (x, y-1)$. In this way the sum over all four dual bond variables attached to one site of the dual lattice corresponds to the sum of original height variables around an elementary plaquettes in the original lattice: $(n_{(x,y)} - n_{(x,y+1)}) + (n_{(x,y+1)} - n_{(x+1,y+1)}) + (n_{(x+1,y+1)} - n_{(x+1,y)}) + (n_{(x+1,y)} - n_{(x,y)}) = 0$, which implies that the flow $\{n_{(\tilde{kl})}\}$ is divergence free as inferred in (14).

In 3d the Hamiltonian (14) is the strong screening limit of the vortex glass model for disordered superconductors [23, 24]

$$\mathcal{H}_{\rm VG} = \sum_{i,j} (n_i - b_i) G_\lambda(\mathbf{r}_i - \mathbf{r}_j)(n_j - b_j) \; , \tag{16}$$

where the integer vortex variables n_i live on the bonds of a simple cubic lattice and have to fulfill the constraint in (14) since they represent magnetic vortex lines that are divergence free. The real valued quenched random variables $b_i \in [-2\sigma, 2\sigma]$ are derived from the lattice curl of a random vector potential ($\sigma \geq 0$ being the strength of the disorder). The 3d vector $\mathbf{r}_i$ denotes the spatial positions of bond i in the lattice and the sum runs over all bond pairs of the lattice (not only nearest neighbors). The lattice propagator $G_\lambda(\mathbf{r})$ has the asymptotic form $G_\lambda(\mathbf{r}) \propto \exp(-|\mathbf{r}|/\lambda)/|\mathbf{r}|$, where λ is the screening length. In the strong screening limit $\lambda \to 0$ only the on-site repulsion survives [23] and gets

$$\mathcal{H}_{\rm VG}^{\lambda \to 0} = \sum_i (n_i - b_i)^2 \tag{17}$$

which is the Hamiltonian (14) in 3d that we intend to discuss here.

The ground state of (14) can again be computed within polynomial time by a successive shortest path algorithm [3]. As for the N-line problem one starts with a configuration $\{n_{\mathbf{i}}\}$ that optimizes the Hamiltonian in (14) but does not, in general, fulfill the mass balance constraint given in (14). In the N-line problem that was simply the zero-flow $n_{\mathbf{i}} = 0$, which does not fulfill the requirement that the source and the target have excess $+N$ and $-N$, respectively. Here we start with $n_{\mathbf{i}}$ the closest integer to the real number $b_{\mathbf{i}}$ for each bond $\mathbf{i}$. Since this solution violates the mass-balance constraint one

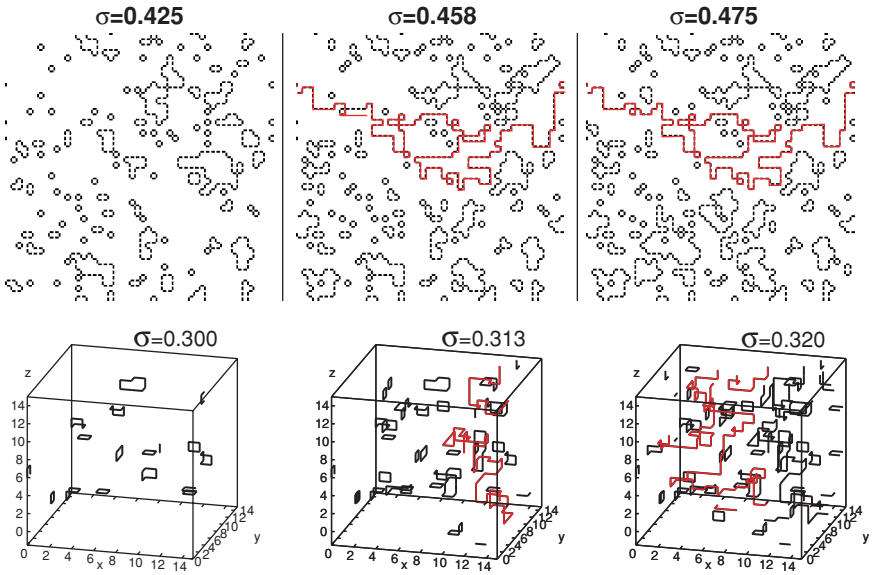

Fig. 14. Examples of ground state configurations of the Hamiltonian (14) for varying disorder strengths σ (for particular disorder realizations). *Top*: $2d$, $L = 50$, the critical disorder strength is $\sigma_c \approx 0.46$; *Bottom*: $3d$, $L = 16$, the critical disorder strength is $\sigma_c \approx 0.31$. The occupied bonds ($n_i \neq 0$) are marked black, the percolating loop is marked by light grey

successively sends flow from nodes that have an excess flow to nodes that have a deficit along optimal paths that are again found using node potentials (to make all costs non-negative) and Disjkstras algorithm. The details of this algorithm can be found in [1, 2, 3].

Figure 14 shows three typical ground state configurations for different strength of the disorder σ in 2d and in 3d. For small σ only small isolated loops occur, whereas for larger σ one finds loops that extend through the whole system, they percolate. A finite size scaling study of the underlying percolation transition yields a novel universality class with numerically estimated critical exponents (see Fig. 15) $\nu = 3.3 \pm 0.3$, $\beta = 1.8 \pm 0.4$ and $\tau = 2.45 \pm 0.05$ in $2d$, and $\nu = 1.05 \pm 0.05$, $\beta = 1.4 \pm 0.1$ and $\tau = 2.85 \pm 0.05$ in $3d$. Details of these calculations can be found in [25].

5 Elastic Manifolds in a Disordered Environment and a Periodic Potential

A system of strongly interacting (classical) particles or other objects, like magnetic flux lines in a type-II superconductor (as we discussed in Sect. 3 and for which the starting Hamiltonian would given by (4)), or a charge density

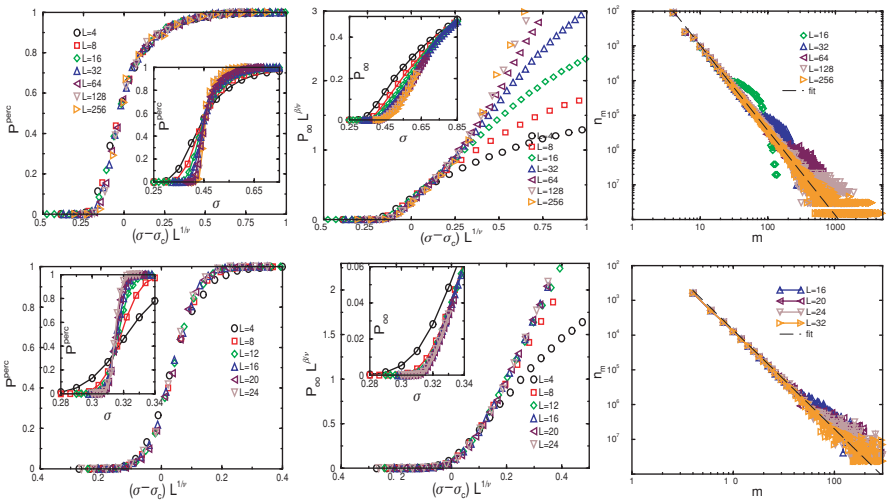

Fig. 15. Finite size scaling analysis for the model (14) in $2d$ (*top*) and $3d$ (*bottom*). Plot of the percolation probability P^{perc} (*left*) and of the probability P_∞ for a bond belonging to a percolating loop (*middle*). For $2d$ the best data collapse is obtained for $\nu = 3.3$, $\beta = 1.8$, for $3d$ its is $\nu = 1.05$, $\beta = 1.4$. The insets shows the raw data. (*Right*) Plot of the average number n_m of loops of mass m per lattice bond at $\sigma_c = 0.458$ in $2d$ and at $\sigma_c = 0.3129$ in $3d$, respectively. The straight line represents $n_m \propto m^\tau$, with $\tau = 2.45$ in $2d$ and $\tau = 2.85$ in $3d$

wave system in a solid, will order at low temperatures into a regular arrangement a lattice (crystal lattice or flux line lattice). Fluctuations either induced by thermal noise (temperature) or by disorder (impurities, pinning centers) induce deviations of the individual particles from their equilibrium positions. As long as these fluctuations are not too strong an expansion of the potential energy around these equilibrium configuration might be appropriate. An expansion up to 2nd order is called the elastic description or elastic approximation, which in a coarse grained form (where the individual particles that undergo displacements from their equilibrium positions do not occur any more and are replaced by a continuum field $\phi(\mathbf{r})$ reads then

$$\mathcal{H}_{\rm manifold} = \mathcal{H}_{\rm elastic} + \mathcal{H}_{\rm random} = \int d^d\mathbf{r}\ \frac{\gamma}{2}|\nabla\phi(\mathbf{r})|^2 + V(\phi(\mathbf{r}),\mathbf{r})\ . \qquad (18)$$

The random potential energy is a delta-correlated Gaussian variable with mean zero, $\langle\langle V(\phi,\mathbf{r})V(\phi',\mathbf{r}')\rangle\rangle = D^2\delta(\phi-\phi')\delta\mathbf{r}-\mathbf{r}')$. The integration extends over the whole space that paramterizes the manifold, for instance $d = 1$ for an elastic line in a random potential, $d = 2$ for an interface or a surface in a disordered environment etc. Note that for $d = 1$ one recovers the single line Hamiltonian (1). The many-line Hamiltonian (4) also allows such an elastic description in the limit, in which the interactions are strong and the the

random potential is weak compared to the elastic energy. In this limit the lines will only deviate moderately from a regular, translationally invariant configuration (the Abrikosov flux line lattice). This case is called an elastic periodic medium and one has to modify the ϕ-part of the disorder correlator such that the Hamiltonian has the correct translational symmetry [26].

The presence of a periodic background potential, like a crystal potential, has a smoothening effect on the elastic manifold and tends to locck it into one of its minma. The competition between the random potential, that roughens the manifold, and such a periodic potential might lead to a roughening transition [27, 28]. In $2d$ this is actually not the case [29], but in $3d$ there is as we will see. We consider a lattice version of the Hamiltonian

$$\mathcal{H} = \mathcal{H}_{\text{manifold}} + H_{\text{periodic}} \quad \text{with} \quad H_{\text{periodic}} = \int d^d\mathbf{r}\, V_{\text{periodic}}(\phi(\mathbf{r}))\ , \tag{19}$$

where $V_{\text{periodic}}(\phi) = -\cos\phi$ represents the periodic potential.

We introduce a discrete solid-on-solid (SOS) type interface model for the elastic manifold whose continuum Hamiltonian is given in (19). Locally the EM remains flat in one of periodic potential minima at $\phi = 2\pi h$ with integer h. Due to fluctuations, some regions might shift to a different minimum with another value of h to create a step (or domain wall) separating domains. To minimize the cost of the elastic and periodic potential energy in (19), the domain-wall width must be finite, say ξ_o. Therefore, if one neglects fluctuations in length scales less than ξ_o, the continuous displacement field $\phi(\mathbf{r})$ can be replaced by the integer height variable $\{h_{\mathbf{x}}\}$ representing a $(3+1)d$ SOS interface on a simple cubic lattice with sites $\mathbf{x} \in \{1, \ldots, L\}^3$. The lattice constant is of order ξ_o and set to unity. The energy of the interface is given by the Hamiltonian

$$\mathcal{H} = \sum_{\langle \mathbf{x},\mathbf{y}\rangle} J_{(h_{\mathbf{x}},\mathbf{x});(h_{\mathbf{y}},\mathbf{y})}|h_{\mathbf{x}} - h_{\mathbf{y}}| - \sum_{\mathbf{x}} V_R(h_{\mathbf{x}},\mathbf{x})\ , \tag{20}$$

where the first sum is over nearest neighbour site pairs. After the coarse graining, the step energy $J > 0$ as well as the random pinning potential energy V_R becomes a quenched random variable distributed independently and randomly. Note a periodic elastic medium has the same Hamiltonian as in (20) with random but periodic J and V_R in h with periodicity p [30]. In this sense, the elastic manifold emerges as in the limit $p \to \infty$ of the periodic elastic medium.

To find the ground state, one maps the 3D SOS model onto a ferromagnetic random bond Ising model in $(3+1)d$ hyper-cubic lattice with anti-periodic boundary conditions in the extra dimension [31] (for the 3 space direction one uses periodic boundary conditions instead). The anti-periodic boundary conditions force a domain wall into the ground state configuration of the $(3+1)d$ ferromagnet. Note that bubbles are *not* present in the ground state. A domain wall may contain an overhang which is unphysical in the interface interpretation. Fortunately, one can forbid overhangs in the Ising model representation

using a technique described in [31]. If the longitudinal and transversal bond strengths are assigned with $J/2$ and $V_R/2$ occurring in (20), respectively, this domain wall of the ferromagnet becomes equivalent to the ground state configuration of (20) for the interface with the same energy. The domain wall with the lowest energy is then determined exactly by using a combinatorial optimisation algorithm, a so-called max-flow/min-cost algorithm [1, 2, 3].

For completeness we briefly sketch how solve the task of finding the minimal energy configuration for an interface in a $d+1$ dimensional random bond ferromagnet $H = \sum_{\langle ij \rangle} J_{ij}\sigma_i\sigma_j$ in which we fix all spins in the lower (upper) plane, i.e. all σ_i with $i = (x_1 1, \ldots, x_d, y)$ and $y = 1$ ($y = H$), to be $\sigma_i = +1(-1)$. First one maps it onto a flow problem in a capacitated network. We introduce two extra sites, a source node s, which we connect to all spins of the hyperplane $y = 1$ with bonds $J_{s,(x_1,\ldots,x_d,y=1)} = J_\infty$, and a sink node t, which we connect to all spins of the hyperplane $y = H$ with bonds $J_{s,(x_1,\ldots,x_d,y=H)} = J_\infty$. We choose $J_\infty = 2\sum_{(ij)} J_{ij}$, i.e. strong enough that the interface cannot pass through a bond involving one of the two extra sites. Now we enforce the aforementioned boundary conditions for the spins in the upper and the lower plane by simply fixing $\sigma_s = +1$ and $\sigma_t = -1$. The graph underlying the capacitated network we have to consider is now defined by the set of vertices (or nodes) $N = \{1, \ldots, H \cdot L^d\} \cup \{s, t\}$ and the set of edges (or arcs) connecting them $A = \{(i, j)|i, j \in N,\ J_{ij} > 0\}$.

The capacities u_{ij} of the arcs (i, j) is given by the bond strength J_{ij}. For any spin configuration $\sigma = (\sigma_1, \ldots, \sigma_N)$ we define now $S = \{i \in N|\sigma_i = +1\}$ and $\overline{S} = \{i \in N|\sigma_i = -1\} = N\backslash S$. Obviously $\sigma_s \in S$ and $\sigma_t \in \overline{S}$. The knowledge of S is sufficient to determine the energy of any spin configuration via $H(S) = -C + 2\sum_{(i,j)\in(S,\overline{S})} J_{ij}$ where $(S, \overline{S}) = \{(i, j)|i \in S, j \in \overline{S}\}$. The constant $C = \sum_{(i,j)\in A} J_{ij}$ is irrelevant, i.e. independent of S. Note that $(S, \overline{S})$ is the set of edges (or arcs) connecting S with $\overline{S}$, this means it cuts N in two disjoint sets. Since $s \in S$ and $t \in \overline{S}$, this is a so called s-t-cut-set, abbreviated $[S, \overline{S}]$. Thus the problem of finding the ground state configuration of an interface in the random bond ferromagnet can be reformulated as a **minimum cut** problem

$$\min_{S\subset N}\{H'(S)\} = \min_{[S,\overline{S}]} \sum_{(i,j)\in(S,\overline{S})} J_{ij}\ . \tag{21}$$

in the above defined capacitated network (with $H' = (H + C)/2$). It does not come as a surprise that this minimum cut is *identical* with the interface between the $(\sigma_i = +1)$-domain and the $(\sigma_i = -1)$-domain that has the lowest energy. Actually any s-t-cut-set defines such an interface, some of them might consist of many components, which is of course energetically unfavourable.

A flow in the network G is a set of nonnegative numbers x_{ij} subject to a capacity constraint and a mass balance constraint for each arc

$$0 \leq x_{ij} \leq u_{ij} \quad \text{and} \quad \sum_{\{j|(i,j)\in A\}} x_{ij} - \sum_{\{j|(j,i)\in A\}} x_{ji} = \begin{cases} -v & \text{for } i = s \\ +v & \text{for } i = t \\ 0 & \text{else} \end{cases} \tag{22}$$

This means that at each node everything that goes in has to go out, too, with the only exception being the source and the sink. What actually flows from s to t is v, the value of the flow. The **maximum flow problem** for the capacitated network G is simply to find the flow $\mathbf{x}$ that has the maximum value v under the constraint (22).

Let $\mathbf{x}$ be a flow, v its value and $[S, \overline{S}]$ an s-t-cut. Then, by adding the mass balances for all nodes in S we have $v = \sum_{(i,j)\in(S,\overline{S})} x_{ij} - \sum_{(i,j)\in(\overline{S},S)} x_{ji}$ and since $x_{ij} \leq u_{ij}$ and $x_{ji} \geq 0$ the following inequality holds: $v \leq \sum_{(i,j)\in(S,\overline{S})} u_{ij} = u[S, \overline{S}]$ Thus the value of any flow $\mathbf{x}$ is less or equal to the capacity of any cut in the network. If we discover a flow $\mathbf{x}$ whose value equals to the capacity of some cut $[S, \overline{S}]$, then $\mathbf{x}$ is a maximum flow and the cut is a minimum cut. The following implementation of the augmenting path algorithm constructs a flow whose value is equal to the capacity of a s-t-cut it defines simultaneously. Thus it will solve the maximum flow problem (and, of course, the minimum cut problem).

Given a flow $\mathbf{x}$, the residual capacity r_{ij} of any arc $(i, j) \in A$ is the maximum additional flow that can be sent from node i to node j using the arcs (i, j) and (j, i). The residual capacity has two components: 1) $u_{ij} - x_{ij}$, the unused capacity of arc (i, j), 2) x_{ji} the current flow on arc (j, i), which we can cancel to increase the flow from node i to j $r_{ij} = u_{ij} - x_{ij} + x_{ji}$. The residual network $G(\mathbf{x})$ with respect to the flow $\mathbf{x}$ consists of the arcs with *positive* residual capacities. An augmenting path is a directed path from the node s to the node t in the residual network. The *capacity of an augmenting path* is the minimum residual capacity of any arc in this path.

Obviously, whenever there is an augmenting path in the residual network $G(\mathbf{x})$ the flow $\mathbf{x}$ is not optimal. This motivates the following generic augmenting path algorithm:

algorithm Ford-Fulkerson
begin
  Initially set $x_{ij} := 0, x_{ji} := 0$ for all $(i, j) \in A$;
  do
    construct residual network R with capacities r_{ij};
    if there is an augmenting path from s to t in G' **then**
    begin
      Let $r_{\min}$ the minimum capacity of r along this path;
      Increase the flow in N along the path by a value of $r_{\min}$;
    end
  until no such path from s to t in G' is found;

This algorithm is polynomial in the number of lattice sites if the distribution of capacities is discrete (binary for instance). In the general case it has to be improved, and there are indeed more efficient algorithms to solve this problem in polynomial time [1, 2, 3]. We stop the description of these algorithms and focus on the results we obtained by applying them to the particular elastic manifold model we are interested here:

We performed the ground state calculation for the Hamiltonian (20) on $L^3 \times H$ hyper-cubic lattices for $L \leq 32$. H, the size in the extra direction, is taken to be larger than the interface width. We present the results for an exponential distribution for $J > 0$, $P(J) = e^{-J/J_0}/J_0$ and uniform distribution for $0 \leq V_R \leq V_{max}$. The disorder strength is controlled with the parameter $\Delta \equiv V_{max}/J_0$. Other distributions studied include (bimodal, bimodal) and (uniform, uniform) distributions for (J, V_R), and gave identical estimates for the critical exponents.

The order parameter that provides the information about the suspected roughening transition is the magnetisation-like quantity $m \equiv \langle|\langle e^{i\pi h_{\mathbf{x}}}\rangle_o|\rangle$, which is non-zero in the flat phase and vanishes in the rough phase. The critical point Δ_c can be determined from the finite-size-scaling property of the order parameter:

$$m(L, \varepsilon) = L^{-\beta/\nu} \mathcal{F}(\varepsilon L^{1/\nu}) \quad , \tag{23}$$

where $\varepsilon \equiv \Delta - \Delta_c$, and β (ν) is the order parameter (correlation length) exponent. The scaling function $\mathcal{F}(x)$ has a limiting behaviour $\mathcal{F}(x \to 0) =$ const. so that the order parameter decays algebraically with L as $m \sim L^{-\beta/\nu}$ at the critical point. It also behaves as $\mathcal{F}(x \to -\infty) \sim |x|^\beta$ so that $m \sim |\varepsilon|^\beta$ for $\Delta < \Delta_c$ in the infinite system size limit.

Consider the effective exponent $[\beta/\nu](L) = -\log(m(2L)/m(L))/\log 2$. It converges to the value of β/ν at the critical point and deviates from it otherwise as L increases. We estimate the critical threshold as the optimal value of Δ at which the effective exponent approaches a nontrivial value. The plot for this effective exponent is shown in Fig. 16. One can see that there is a downward and upward curvature for $\Delta < 4.20$ and $\Delta > 4.30$, respectively. From this behaviour we estimate that $\Delta_c = 4.25 \pm 0.05$ and $\beta/\nu = 0.07 \pm 0.03$.

Note that the effective exponent varies with L even at the estimated critical point, which implies that corrections to scaling are not negligible for system sizes up to $L = 32$. For that reason our numerical results for Δ_c and β/ν have rather large error bars, and one may need larger system sizes for better precision. The exponents β and ν could also be obtained from the scaling analysis using (23). We fix the values of Δ_c and β/ν to the values obtained before and vary ν to have an optimal data collapse. We obtain $\nu = 1.4 \pm 0.2$ and the corresponding scaling plot is shown in Fig. 16. The order-parameter scaling property shows that the roughening phase transition is a *continuous* transition, though the exponent $\beta \simeq 0.1$ is very small, as opposed to the results of the Gaussian variational study [27] predicting a first order transition.

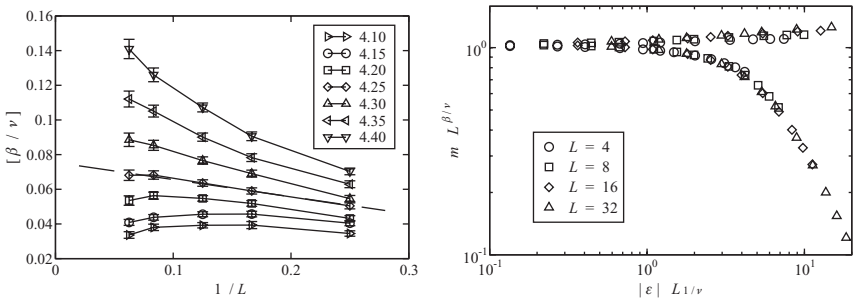

Fig. 16. *Left:* The effective exponent $[\beta/\nu](L)$ for different values of Δ as a function of $1/L$. The broken line is a guide for the eyes that separates the curves with a downward bending ($\Delta < \Delta_c$) from those with an upward bending ($\Delta > \Delta_c$). *Right:* Scaling plot of $mL^{\beta/\nu}$ vs. $|\varepsilon|L^{1/\nu}$ with $\varepsilon = \Delta - 4.25$, $\beta/\nu = 0.07$, and $\nu = 1.4$

6 Summary

To conclude we discussed several applications of polynomial combinatorial optimisation algorithms to the numerical investigation of ground state properties of disordered systems. We did not touch the application of matching algorithms, with which one can compute the ground states of spin glass models on planar graphs (e.g. in $2d$ with free boundary conditions [32, 33] and to study $2d$ disordered elastic media [34]. We also did not discuss the optimisation of sub-modular function, which is useful in the context of the $q \to \infty$ limit of the $2d$ random bond Potts model [35]. Together with the example we presented in this paper we learn that there are plenty of interesting problems in the realm of the theory of disordered that can be effectively studied with *polynomial* algorithms. There is another plentitude of problems that are currently investigated with *non-polynomial* combinatorial optimisation algorithms (like the notorious $3d$ spin glass problem [3]) as well as with quantum annealing algorithms.

References

1. H. Rieger, Lecture Notes in Physics **501** (ed. J. Kertesz and I. Kondor), pp. 122–158 (Springer Verlag, Berlin-Heidelberg-New York, 1998). 301, 306, 317, 320, 322
2. M. Alava, P. Duxbury, C. Moukarzel and H. Rieger, Phase Transition and Critical Phenomena, Vol. **18** (ed. C. Domb and J. L. Lebowitz), pp. 141–317, (Academic Press, Cambridge, 2000). 301, 306, 317, 320, 322
3. A. Hartmann and H. Rieger, *Optimization in Physics* (Wiley VCH, Darmstadt, 2002). 301, 306, 316, 317, 320, 322, 323
4. T. Halpin-Healy and Y.-C. Zhang, Phys. Rep. **254**, 215 (1995). 302
5. C.-K. Peng, S. Havlin, M. Schwartz and H.E. Stanley, Phys. Rev. A **44**, 2239 (1991); N.-N. Pang, Y.-K. Yu and T. Halpin-Healy, Phys. Rev. E **52**, 3224 (1995). 303

6. M. Marsili and Y.-C. Zhang, Phys. Rev. E **57**, 4814 (1998); N. Schwartz, A.L. Nazaryev and S. Havlin, Phys. Rev. E **58**, 7642 (1998). 303
7. R. Schorr and H. Rieger, Europ. Phys. J. **33**, 347 (2003). 304
8. For a review see G. Blatter et al., Rev. Mod. Phys. **66**, 1125 (1994). 305
9. M. Doi and S.F. Edwards, *The theory of Polymer Dynamics*, (Oxford University Press, Oxford, 1986). 305
10. V. Petäjä, D.-S. Lee, H. Rieger, and M. Alava. J. Stat. Mech. P10010 (2004). 306
11. D.A. Huse and C.L. Henley, Phys. Rev. Lett. **54**, 2708 (1985); M. Kardar, Phys. Rev. Lett. **55**, 2924(C) (1985); D.A. Huse, C.L. Henley and D.S. Fisher, Phys. Rev. Lett. **55**, 2924 (1985). 306
12. B.M. Forrest and L.H. Tang, Phys. Rev. Lett. **64**, 1405 (1990); J.M. Kim, M.A. Moore, A.J. Bray, Phys. Rev. A **44**, 2345 (1991). 306
13. A.-L. Barabasi and H.E. Stanley, *Fractal Concepts in Surface Growth* (Cambridge University Press, Cambridge, 1995). 306
14. J. Toner and D.P. DiVicenzo, Phys, Rev. B **41**, 632 (1990); T. Hwa and D.S. Fisher, Phys. Rev. Lett. **72**, 2466 (1994). 307
15. C. Zeng, A. Alan Middleton, and Y. Shapir, Phys. Rev. Lett. **77**, 3204 (1996); S. Bogner, T. Emig and T. Nattermann, Phys. Rev. **63** 174501 (2001).
16. T. Giamarchi and P. Le Doussal, Phys. Rev. B **52**, 1242 (1995). 309
17. D. McNamara and A. Alan Middleton, Phys. Rev. B **60** 10062 (1999). 309
18. V. Petäjä, M. Alava, and H. Rieger, Int. J. Mod. Phys. C 12, 421 (2001).
19. B. Drossel and M. Kardar, Phys. Rev. E **53**, 5861 (1996). 313
20. R. Bikbov and S. Nechaev, Phys. Rev. Lett. **87**, 150602 (2001). 313
21. V. Petäjä, M. Alava, and H. Rieger, cond-mat/0302509. 315
22. H. Rieger and U. Blasum, Phys. Rev. B **55** 7394R (1997); F. Pfeiffer and H. Rieger, J. Phys. A **33**, 2489 (2000). 315
23. H.S. Bokil and A.P. Young, Phys. Rev. Lett. **74**, 3021 (1995). 316
24. J. Kisker and H. Rieger, Phys. Rev. B **58**, R8873 (1998); F. Pfeiffer and H. Rieger, Phys. Rev. B **60**, 6304 (1999). 316
25. F.O. Pfeiffer and H. Rieger, J. Phys. C **14**, 2361 (2002); F.O. Pfeiffer and H. Rieger, Phys. Rev. E **67**, 056113 (2003). 317
26. T. Nattermann, Phys. Rev. Lett. **64**, 2454 (1990); T. Giarmachi and P. Le Doussal, Phys. Rev. Lett. **72**, 1530 (1994); and Phys. Rev. B **52**, 1242 (1995). 319
27. J.-P. Bouchaud and A. Georges, Phys. Rev. Lett. **68**, 3908 (1992). 319, 322
28. T. Emig and T. Nattermann, Phys. Rev. Lett. **79**, 5090 (1997); Eur. J. Phys. B **8**, 525 (1999). 319
29. E.T. Seppälä, M.J. Alava, and P.M. Duxbury, Phys. Rev. E **63**, 036126 (2001). 319
30. J.D. Noh and H. Rieger, Phys. Rev. Lett. **87**, 176102 (2001); Phys. Rev. E **66**, 036117 (2002). 319
31. A.A. Middleton, Phys. Rev. E **52**, R3337 (1995). 319, 320
32. N. Kawashima and H. Rieger, Europhys. Lett. **39**, 85 (1997). 323
33. A.K. Hartmann, A.P. Young, Phys. Rev. B **66**, 094419 (2002); A.K. Hartmann, A.J. Bray, A.C. Carter, M.A. Moore, A.P. Young, Phys. Rev. B **66**, 224401 (2002). 323
34. A.A. Middleton, Phys. Rev. B **61**, 14787 (2000). 323
35. R. Juhasz, H. Rieger, F. Iglóoi, Phys. Rev. E **64**, 056122 (2001); J-Ch. Angles d'Auriac, F. Iglói, Phys. Rev. Lett. **90**, 190601 (2003). 323

Dynamical Frustration in ANNNI Model and Annealing

Parongama Sen and Pratap K. Das

Department of Physics, University of Calcutta, 92 Acharya Prafulla Chandra Road, Kolkata 700009, India
psphy@caluniv.ac.in

1 Introduction

Simulated annealing is usually applied to systems with frustration, like spin glasses and optimisation problems, where the energy landscape is complex with many spurious minima. There are certain other systems, however, which have very simple energy landscape picture and ground states, but still the system fails to reach its ground state during a energy-lowering dynamical process. This situation corresponds to "dynamical frustration". We have specifically considered the case of the axial next nearest neighbour (ANNNI) chain, where such a situation is encountered. In Sect. II, we elaborate the notion of dynamic frustration with examples and in Sect. III, the dynamics in ANNNI model is discussed in detail. The results of application of the classical and quantum annealing are discussed in Sects. IV and V. Summary and some concluding comments are given in the last section.

2 Dynamic Frustration in Ising Models

Quenching dynamics in magnetic systems has been a topic of intense research over the last few decades. In quenching dynamics, the system has a disordered initial configuration corresponding to a high temperature. As the temperature is suddenly decreased quite a few interesting phenomena take place like domain growth [1, 2], persistence [3, 4, 5, 6] etc.

The Ising model maybe regarded as the simplest model describing magnetic properties of many real systems and it shows a rich dynamical behaviour with respect to the above phenomena. The dynamics of Ising models has been extensively studied in lattices of different dimensions as well as on graphs and networks.

In dynamical studies, the system is allowed to evolve from the initial configuration following a certain prescription and the commonly used dynamical

P. Sen and P.K. Das: *Dynamical Frustration in ANNNI Model and Annealing*, Lect. Notes Phys. **679**, 325–337 (2005)
www.springerlink.com

rule at zero temperature is the Glauber dynamics, i.e., a spin is chosen randomly and flipped if it makes the energy lesser, not flipped if energy increases and flipped with probability 1/2 if there is no energy change.

The zero temperature deterministic dynamics in Ising models can be visualised as the motion of interfaces and the domains grow in size as the interfaces annihilate on approaching each other (Fig. 1). In one dimension, a zero temperature quench of the Ising model ultimately leads to the equilibrium configuration, i.e., all spins point up (or down).

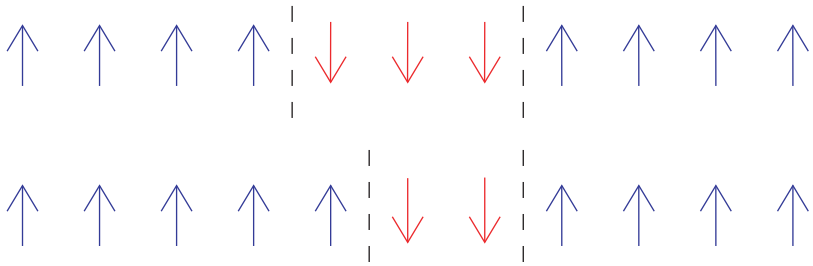

Fig. 1. Domain coarsening in one dimensional Ising model: the spin at the boundary of the left domain wall flips making the two domain walls move closer (*Top*: earlier picture, *bottom*: later picture)

In two or higher dimensions, however, the system does not always reach equilibrium [7, 8, 9, 10, 11, 12]. Such a situation corresponds to dynamical frustration when the system gets frozen in a metastable state which does not correspond to the ground state. For example, in the two dimensional lattice (Fig. 2), the dynamics stops at a higher energy when the domain walls are straight and appear without any corner. The system thus acquires a "striped phase", where the number of stripes is an even number. In dimensions higher than two, there maybe other kind of frozen states in which the system gets locked.

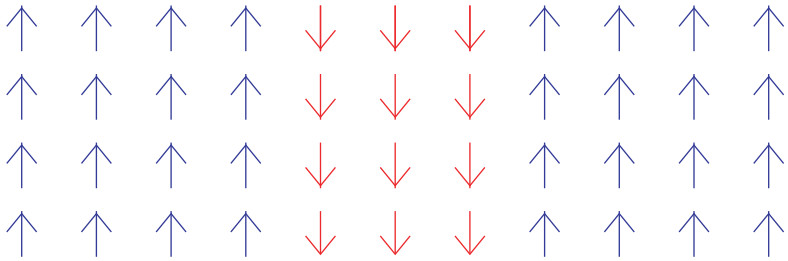

Fig. 2. Striped phase in two dimensional Ising model under zero temperature quenching dynamics – the domain walls are straight and no spin flips can occur

This kind of freezing or blocking is also encountered in ferromagnetic Ising models on random graphs and small world networks where there are finite number of random long range bonds. In the random graph, any two spins are connected with a finite probability while in the small world network, random long range connections occur in addition to nearest neighbour links. In these cases, the domain walls may get pinned resulting in a frozen state [13, 14, 15, 16, 17]. Recently, freezing has been observed on scale-free networks also, where, although the system is locked in an excited state, the dynamics continues indefinitely [18].

In the above examples of freezing in Ising models on finite dimensional lattices, graphs and networks, a few things are to be noted

(a) The ground state is simple in all the cases
(b) There is no frustration arising out of the interactions in the system.

In addition, power law scalings with time (e.g., domain size $\sim t^{1/z}$) exist for the finite dimensional lattices [19] but in the case of networks or random graphs, one has an exponential relaxation behaviour consistent with the mean field nature of these systems [20, 21, 22, 23].

3 Dynamics in ANNNI Chain

We will now discuss the dynamics in the axial next nearest neighbour Ising (ANNNI) model [24] in which there is frustration but no randomness or disorder. The ANNNI model in one dimension is described by the Hamiltonian

$$H = -J_1 \Sigma S_i S_{i+1} + J_2 \Sigma S_i S_{i+2} \ . \tag{1}$$

The ground state of this model is well-known: it is ferromagnetic for $\kappa = J_2/J_1 < 0.5$; antiphase for $\kappa = J_2/J_1 > 0.5$ and highly frustrated for $J_2/J_1 = 0.5$. All configurations having domains of size ≥ 2 are ground states at the point $\kappa = 0.5$, which we call the fully frustrated point.

The dynamics of the ANNNI chain has quite a few interesting behaviour [25, 26]. When zero temperature quenching dynamics is considered, $\kappa = 1.0$ emerges as a dynamical transition point. For $\kappa < 1$, there is no conventional domain coarsening or persistence behaviour. Here, all domains of size 1 immediately vanish but domains of size two are stable such that two domain walls cannot approach each other and annihilate (Fig. 3).

Unlike in the Ising model in $d = 2$, here the domain walls are not pinned but can move around keeping their number fixed. The energy of the system is constant as spin flips occur with zero energy cost. The system thus wanders in a subspace of iso-energy metastable states forever. As a result, the model also does not show a power-law decay in the persistence probability. Interestingly, there is no special effect of the $\kappa = 0.5$ point (which dictates the static behaviour) on the dynamics.

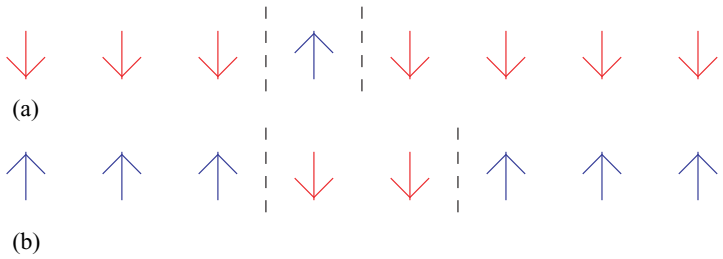

Fig. 3. Dynamics in ANNNI chain for $\kappa < 1$: All domains of size 1 are unstable and they immediately vanish (**a**). The system is left with domains of size $\geq$2. A domain of size two, as shown in (**b**), is energetically stable as the spins within the domain satisfy the antiferromagnetic ordering with their second neighbours and energy contribution from first neighbours is zero. As a result, two domain walls have to maintain a minimum distance and cannot approach each other and annihilate

As the domain walls continue moving in the system, the number of spin flips at any time becomes a constant in time. This constant is independent of the value of κ. That is expected as this quantity is proportional to the number of domain walls. The average number of domain walls remaining in the system (per spin) turns out to be close to 0.28 [26].

The residual energy E_r, defined as the excess energy over the ground state energy shows an interesting behaviour with κ (Fig. 4). At small values of κ the large number of domain walls makes the residual energy large. As κ is increased, E_r becomes lesser and at $\kappa = 0.5$ it is zero. This is not surprising however; the configurations with domain sizes $\geq$2 are nothing but the degenerate ground states of the $\kappa = 0.5$ point. The residual energy decreases as $\kappa = 0.5$ is approached from both sides.

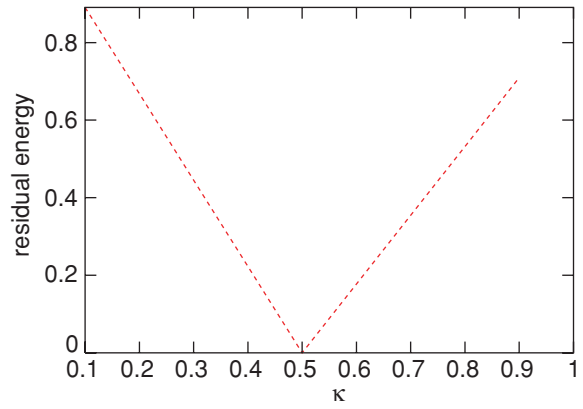

Fig. 4. Constant residual energy of the ANNNI model with zero temperature dynamics for $\kappa < 1$

For the sake of completeness, it should be mentioned that the ANNNI model shows conventional relaxation behaviour for $\kappa > 1$ although with a dynamic exponent different from that of the nearest neighbour Ising model.

Since the conventional dynamics does not bring the system to the ground state, one has to employ some other method to do this. Simulated annealing for the Ising model on random graphs has been attempted to "melt" the system with success [13]. For small world networks, freezing can be got rid off by letting more number of edges in the system also [27]. We discuss in the next two section the result of applying different annealing schedules to the ANNNI model for various values of $\kappa < 1$.

4 Classical Annealing (CA)

We have adopted two different schemes for applying classical or thermal annealing.

Scheme A

This is the conventional scheme where one starts with a finite temperature $T = T_0$ and slowly reduces it according to a linear schedule, such that, at the t-th iteration step,

$$T = T_0(1 - t/\tau) \,, \tag{2}$$

where τ is the total number of Monte Carlo steps (MCS). The final temperature (at $t = \tau$) is zero for any starting value of T.

Since for all non-zero temperature, the ANNNI model is in a paramagnetic state, one may start with a random initial configuration corresponding to T_0.

We have calculated the residual energy and the order parameter as functions of τ; the former is expected to approach zero and the latter should increase towards unity with larger values of τ.

In Fig. 5, we show the behaviour of E_r against τ for different κ values. These simulations have been done for a system of 100 spins keeping $T_0 = 10$. The number of configurations n over which averaging has been done decreases with τ; starting with $n = 1000$ for smaller values of τ, it is decreased to $n = 100$ for very large τ values. While for $\kappa = 0.2$, we find a stretched exponential decay, the nature of the curves changes to a power law decay for higher values of κ. Close to 0.5 it has a very slow decay. Corresponding to a power law fit $E_r \sim \tau^{-\alpha}$, α is very small here, e.g., for $\kappa = 0.4$, $\alpha = 0.08 \pm 0.01$, and for $\kappa = 0.6$, $\alpha = 0.03 \pm 0.01$. The slowing down of the decay pattern of E_r seems to depend on the closeness to $\kappa = 0.5$ as well as on the nature of the ground state. For the various values of κ for which the annealing scheme has been employed, the slowest decay is observed at $\kappa = 0.6$, when the system is close to $\kappa = 0.5$ and the ground state is also antiphase. The power law remains valid for $\kappa > 0.5$ with an increasing value of α.

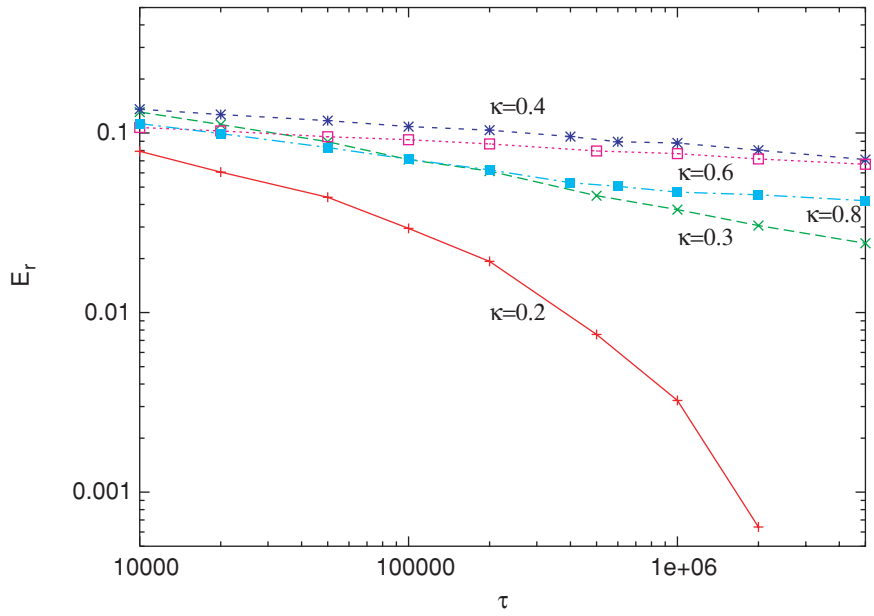

Fig. 5. Residual Energy vs. MCS τ in the ANNNI model for different values of $\kappa < 1.0$. The decay is slow close to $\kappa = 0.5$. $T_0 = 10$ here

We have also checked the efficiency of this scheme for different values of T_0. Note that the decrease in T is made with a slope equal to T_0/τ (2), so we compare the results for different T_0's by plotting E_r against τ/T_0. For $\kappa = 0.4$ or 0.6, E_r is independent of T_0 (as long as T_0 is not very small compared to 1) while for $\kappa = 0.2$, lowering T_0 makes the decay faster at large τ. However, when T_0 is made smaller than unity the decay does not become faster any more. This plot (Fig. 6) also shows that for κ close to 0.5, the power law behaviour is actually valid over a large range of τ which is not so apparent from Fig. 5.

Thus E_r depends strongly on κ: not only does the functional form change from a stretched exponential to power law, there is also a non-universal exponent α which depends on the value of κ. The role of $\kappa = 0.5$ is felt clearly as the annealing is least effective close to this point.

While estimating the order parameter (OP), it should be noted that for $\kappa < 0.5$, the order parameter is just the magnetisation while for $\kappa > 0.5$, it is the average of the four sublattice magnetisations defined as

$$m_\alpha = \Sigma_{j=0}^{L/4-1} S_{\alpha+4j}; \quad \alpha = 1, 2, 3, 4 \tag{3}$$

as in [26]. In Fig. 7, we plot the behaviour of the OP with τ for different values of κ. The behaviour of the order parameter is also κ dependent. The variations with τ are not smooth: the reason is that decreasing energy is not

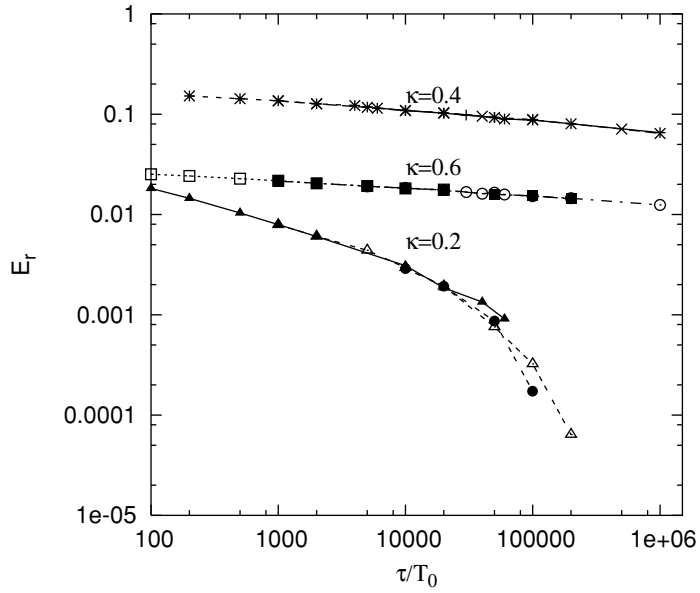

Fig. 6. The residual energy vs the number of MCS (τ) for different starting values of T_0. The scaled data shows a good collapse for $T_0 \geq 1$ for $\kappa = 0.4, 0.6$. For $\kappa = 0.2$, the decay is fastest for $T_0 = 1$ (*filled circles*). The data for $\kappa = 0.6$ and 0.2 have been shifted for clarity

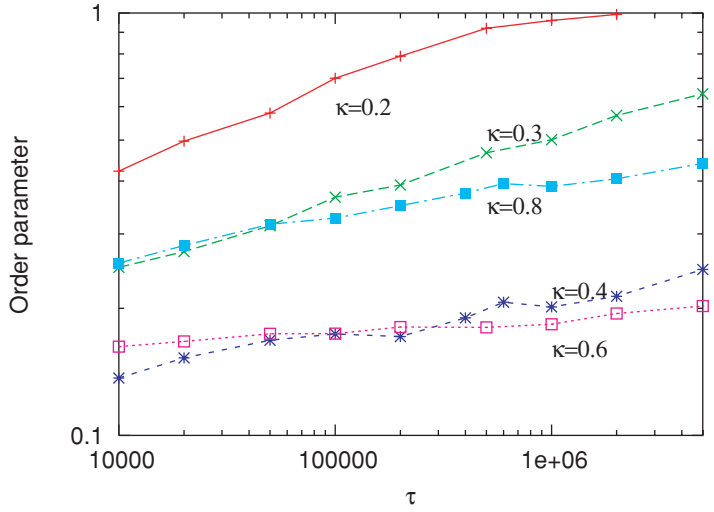

Fig. 7. Order parameter vs. MCS τ in the ANNNI model for different values of $\kappa < 1.0$. The growth is slow close to $\kappa = 0.5$

necessarily equivalent to increasing the order parameter. However it seems to have a rough power law increase for all values of κ (Fig. 7). As expected, the growth of the order parameter is slowest at $\kappa = 0.6$.

Thus we find that this annealing schedule is not very effective near $\kappa = 0.5$ but works well for small values of κ. It is not possible to detect whether there is a value of κ for which the behaviour of the residual energy changes from stretched exponential to power law from the present numerical study.

Scheme B

In this scheme, we first let the system evolve from a random configuration (corresponding to a high temperature) using the zero temperature dynamics and then, after a few steps, apply scheme A. The difference here is, we let the system reach one of the metastable states under zero temperature dynamics, heat it to a finite temperature T_0 which is then gradually decreased.

In the ANNNI chain, for the first 100 iterations, the temperature is kept zero such that when re-heated, the system is in one of the metastable iso-energy states. We find that this scheme accelerates the decay of the residual energy remarkably for small values of κ (e.g., $\kappa = 0.2$) at large τ. However, for higher values, e.g., $\kappa = 0.3, 0.4, 0.6$, for which scheme A gave a power law decay of E_r, the results are identical to that of scheme A. Thus near the $\kappa = 0.5$ point, this scheme is also seen to fail to bring the system to its static ground state.

This scheme is highly appropriate for cases where the system has a fractional probability to end up in a metastable or frozen state not corresponding to the ground state. Here it is not possible to predict whether a random initial configuration will reach the ground state under zero temperature dynamics or not. A good example is the two dimensional Ising model as it reaches a frozen state in about 30% cases. It is useless to apply scheme A here because 70% of the cases do not require any annealing at all. Therefore in order to see whether CA is useful, it should be better to apply scheme A to an initial configuration of frozen state which can be assumed to have evolved from a perfectly random initial state with zero temperature Glauber dynamics. Thus effectively it has undergone a period of cooling at zero temperature and when scheme A is now applied to it, it is equivalent to scheme B.

We have performed some simulation on a square lattice of size $L = 40$, where the number of stripes s is equal to 2 or 4. In each case, we find that the behaviour of both the residual energy and the magnetisation is exponential which means that the scheme works very well in this case. In Fig. 8, we show the variation of the residual energy and magnetisation for $s = 2$. The exponential relaxation is easily understood, as the thermal perturbation breaks the structure of the domain walls and the system is then again free to evolve dynamically. The results are identical for $s = 2$ and 4 at large τ. It may be mentioned here that for a value of the stripe number s comparable to L, the situation is very similar to the ANNNI model (as stripe sizes have to be ≥ 2) and then the exponential behaviour may no longer be present. However, the

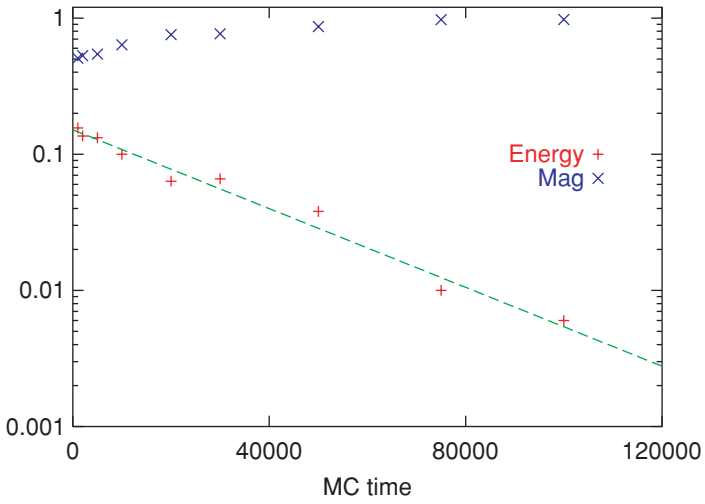

Fig. 8. Order parameter (magnetisation) and residual energy versus MC time τ in the 2-*d* Ising model under scheme B. The value of T_0 is 1 here. The *dashed line* has slope equal to 3.33×10^{-5} in the log-linear plot

probability of a large value of s is small and so, we have not considered values of $s > 4$.

5 Quantum Annealing (QA)

Although the classical annealing methods work quite well for the ANNNI model for small κ, we find that close to the $\kappa = 0.5$ point, it leads to very slow relaxation. In several situations, quantum annealing is far more efficient in decreasing the energy of the system [28, 29] and we therefore apply this method in the ANNNI model. Here instead of thermal fluctuation, quantum fluctuation is considered to induce tunnelling to enable the system reach the ground state for $\kappa < 1$.

The Hamiltonian for the quantum ANNNI chain is :

$$H = -J_1 \Sigma S_i S_{i+1} + J_2 \Sigma S_i S_{i+2} - \Gamma \Sigma S_i \tag{4}$$

This can be mapped to a 2-dimensional classical model [30, 31] using the Suzuki-Trotter formula:

$$H = -J_1 \Sigma S_{\alpha,i} S_{\alpha,i+1} + J_2 \Sigma S_{\alpha,i} S_{\alpha,i+2} - J_p \Sigma S_{\alpha,i} S_{\alpha+1,i} \tag{5}$$

where

$$J_p = -PT/2 \ln(\tanh(\Gamma/PT))$$

and α denotes the αth row in the Trotter direction. Subsequently, one can use a linear schedule for the transverse field as in [29] and find out the results for E_r and the order parameter. However, it is not possible to make Γ equal to zero in the last step as that would make J_p infinite.

We would first show some curious features of the results on applying this method to the ANNNI model and then try to justify the results.

The Suzuki-Trotter mapping is exact for $P \to \infty$ but it can be a good approximation if $PT \geq 1$. One needs to find out an optimum value of PT for which E_r does not change with P. We therefore fix PT and find out E_r for different values of P following [29]. We first fix $PT = 1$. For small κ, e.g., for $\kappa = 0.1$, the scheme indeed makes E_r go down with τ quite efficiently. However, the value of E_r for the same τ and different values of P shows that E_r actually increases with P. Thus results for any finite P may not be reliable. Even increasing PT to 2, we find that this behaviour persists. The reason for this maybe that the Suzuki-Trotter mapping works with a non-zero temperature for which the system is disordered and is always at a high energy state compared to the perfectly ordered state and therefore E_r does not go to zero for large τ and P. These results are shown in Fig. 9.

In case of a value of κ close to 0.5, e.g., $\kappa = 0.4$, we find that E_r remains virtually a constant for all P values when $PT = 1$ which apparently implies that $PT = 1$ is a good optimum value. However, E_r actually remains a

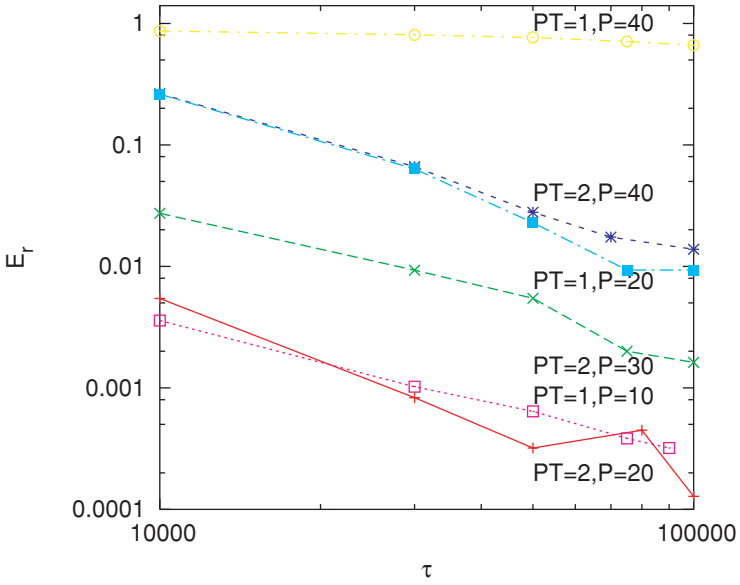

Fig. 9. The quantum annealing scheme does not appear to work well for the ANNNI chain. For example at $\kappa = 0.1$, an optimum value of PT is difficult to find out as E_r increases with P where PT is fixed at 1 or 2 at any value of τ

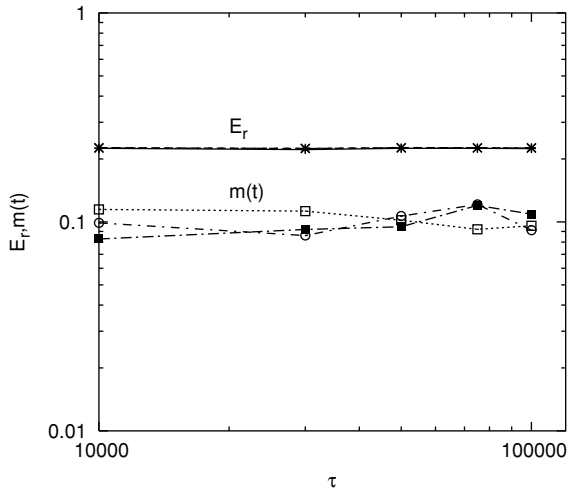

Fig. 10. The variation of residual energy and order parameter for $\kappa = 0.4$ against τ are shown for 3 different values of P. E_r actually remains constant with τ and P while the OP ($m(t)$) seems to fluctuate around a constant value

constant for all τ values as well showing that it does not relax at all. Thus here too the quantum annealing method will not work well. The reason is again because a non-zero temperature of the system has been used. However, the manifestation of this non-zero temperature is different for small and higher values of κ.

On hindsight, it may appear that quantum annealing is a redundant exercise in this case. However, it is interesting to find out how the redundancy makes itself known for different values of κ in different ways.

6 Summary and Conclusions

In summary, we have shown that in systems with dynamic frustration, simulated annealing can be applied which gives results according to the nature of the system. For the ANNNI model, which has a competing interaction leading to frustration, (but well defined ground states with trivial degeneracy for $\kappa \neq 0.5$) classical annealing seems to work well for values of κ close to $\kappa = 0$.

We have applied a different scheme of thermal annealing where the system is heated after an initial period of cooling. The results remain same in case of the ANNNI model when the frustration parameter is appreciable. But this method is useful in case of some other models where the conventional scheme is not very handy, e.g., the two dimensional Ising model. The better effectiveness of the annealing scheme for the two dimensional model in comparison to the ANNNI model may be attributed to the fact that there is no frustration in the

former. The frustration present in the ANNNI model especially near $\kappa = 0.5$ makes it unresponsive to the thermal annealing while the unfrustrated two dimensional Ising model responds fast to the thermal fluctuation.

In case of the ANNNI model, it is also interesting to note that while in the dynamical studies it was shown that the $\kappa = 0.5$ point hardly has any role to play, and dynamical quantities like persistent probability, number of spins flipped at any time etc. were κ independent, things become strongly κ dependent under any annealing schedule with non-universal exponents governing the power law decays. The effect of $\kappa = 0.5$ is also felt as the annealing fails to make any impact close to it.

The application of a quantum annealing method with non-zero temperature also fails to "melt" the system to its ground states and its effect is differently manifested for small and large values of κs.

In fact we find that much is left to be done for a successful annealing programme near $\kappa = 0.5$, e.g., one may attempt a zero-temperature quantum annealing schedule.

Even for the classical annealing case, the change in behaviour of the residual energy as κ is varied requires to be studied more intricately and possibly for larger syatem sizes. Our present study may act as a guideline for such future research work.

Lastly, we note that the variations of the residual energy does not follow a Huse-Fisher [32] type scaling in any parameter range for the ANNNI model.

Acknowledgements

We are grateful to Arnab Das and Subinay Dasgupta for very valuable discussions. P. K. Das acknowledges support from CSIR grants no. 9/28(608)/2003-EMR-I.

References

1. J. D. Gunton, M. San Miguel and P. S. Sahni, *Phase Transitions and critical phenomena*, Vol 8, eds. C. Domb and J. L. Lebowitz (Academic Press, London, 1984). 325
2. A. J. Bray, Adv. Phys. **43** 357 (1994) and the references therein. 325
3. For a review, see S. N. Majumdar, Curr. Sci. **77** 370 (1999). 325
4. B. Derrida, A. J. Bray and C. Godreche, J. Phys. A **27** L357 (1994) 325
5. D. Stauffer, J. Phys. A **27** 5029 (1994). 325
6. P. L. Krapivsky, E. Ben-Naim and S. Redner, Phys. Rev. E **50** 2474 (1994). 325
7. V. Spirin, P. L. Krapivsky and S. Redner, Phys. Rev. E **63** 036118 (2001); Phys. Rev. E **65** 016119 (2002). 326
8. P. Sundaramurthy and D. L. Stein, cond-mat/0411286. 326
9. C. Godreche and J. M. Luck, cond-mat/0412077. 326
10. C. M. Newman and D. L. Stein, Phys. Rev. Lett. **82** 3944 (1999). 326

11. S. Jain, Phys. Rev.E **60** R2445 (1999). 326
12. P. M. Gleiser, F. A. Tamarit, S. A. Cannas and M. A. Montemurro, Phys. Rev. B **68** 134401 (2003). 326
13. P. Svenson, Phys. Rev. E **64** 036122 (2001). 327, 329
14. O. Haggstrom, Physica A **310** 275 (2002). 327
15. D. Boyer and O. Miramontes, Phys. Rev. E **67** R035102 (2003). 327
16. P. Svenson and D. A. Johnson, Phys. Rev. E **65** 036105 (2002). 327
17. J. Y. Zhu and H. Zhu, Phys. Rev. E **67** 026125 (2003). 327
18. D. Jeong, M. Y. Choi and H. Park, cond-mat/0501099. 327
19. The persistence probability in case of four dimensional lattice, however, does not show a power law decay due to blocking (D. Stauffer, Int. J. Mod. Phys. C **8** 361 (1997)). 327
20. N. R. da Silva and J. M. Silva, Phys. Lett. A **135** 373 (1989). 327
21. C. P. Herrero, Phys. Rev. E **65** 066110 (2002). 327
22. H. Hong, B. J. Kim and M. Y Choi, Phys. Rev. E **66** 011107 (2002). 327
23. J. V. Lopes et al., cond-mat/0402138. 327
24. W. Selke, Phys. Rep. **170** 213 (1988). 327
25. S. Redner and P. L. Krapivsky, J. Phys. A **31** 9229 (1998) 327
26. P. Sen and S. Dasgupta, J. Phys. A **37** 11949 (2004) 327, 328, 330
27. P. K. Das and P. Sen, cond-mat/0503138. 329
28. T. Kadawoki and H. Nishimori, Phys. Rev. E **58** 5355 (1998). 333
29. G. E. Santoro, R. Martonak, E. Tosatti and R. Car, Science **295** 2427 (2002). 333, 334
30. M. Suzuki, Prog. Theor. Phys. **56** 1454 (1976). 333
31. B. K. Chakrabarti, A. Dutta and P. Sen, *Quantum Ising Phases and Transitions in Transverse Ising models*. In: Lect. Notes Phys. **M41**, (1996). 333
32. D. A. Huse and D. S. Fisher, Phys. Rev. Lett. **57** 2203 (1986). 336

Exploring Complex Landscapes with Classical Monte Carlo

Victor Martín-Mayor

[1] Departamento de Física Teórica I, Facultad de Ciencias Físicas, Universidad Complutense, 28040 Madrid, Spain
[2] Instituto de Biocomputación y Física de Sistemas Complejos (BIFI), Corona de Aragón 42, Zaragoza 50009, Spain
victor@lattice.fis.ucm.es

1 Introduction

Nowadays, the annealing concept is useful in (at least) two different fields, namely Physics and Optimization. The annealing strategy was well known in a physical context when Kirkpatrick, Gellat and Vecchi [1] generalized it to complex Optimization problems. A familiar example (for a physicist) is that of crystal growth: the more slowly you cool a liquid, the better crystal you will obtain when temperature drops beyond the melting point.[1] One could say that Nature is trying to solve an Optimization problem: the variables to play with are the atomic positions, while the cost function to be minimized is the potential energy. The configuration that minimizes the cost function is the perfect crystal, and a slow annealing schedule allows Nature to find good crystals.

The annealing strategy can be mimicked by researchers with the help of a computer. The physical *dynamics at a given temperature* is represented by a Monte Carlo Markovian random walk in configuration space,[3, 4] while the slow quench is reproduced by changing accordingly in the computer the parameter playing the role of the physical temperature. This combination yields a powerful optimization method that can be used when trying to minimize a physical potential energy,[2] or a more general cost function [1].

When one tries to reproduce in the computer a *physical* annealing process, it turns out that the accessible timescales do not match with experiments. For a spin system, the typical annealing experiment last at least some seconds (see

[1] By a better crystal we mean one with less defects (such as vacants, interstitials, dislocations, etc., see for instance Kittel[2]) and composed of larger grains. Ideally it would be a monocrystal.
[2] At finite temperature the problem is minimizing the free energy, while at zero temperature one wants to minimize the internal energy.

V. Martín-Mayor: *Exploring Complex Landscapes with Classical Monte Carlo*, Lect. Notes Phys. **679**, 339–372 (2005)
www.springerlink.com

e.g. [5]). In spite of the accessibility of dedicated computers,[8] this timescale is larger by five orders of magnitude than the simulations you may do[6, 7] for a small system of 2×10^5 degrees of freedom (a 60^3 lattice). For the simulation of a liquid, you are restricted to some 10^4 particles, whose evolution may be followed for microseconds [9]. The unpleasant conclusion is that, if your experimentalist friend cannot optimize it by means of an annealing experiment, you will not do any better with a computer (at least doing what Nature does). Of course you may try tricks. A very successful one is to use artificial Monte Carlo dynamics, such as the cluster methods,[10, 4] which attempt global changes of configuration variables not occurring in physical systems. These methods are tremendously successful, but also highly problem-specific: you need to find the *right* global changes. Another possibility is to use a quantum dynamics (experimentally or simulating it in a classical computer; in both cases it is a heavy task), that exploits the parallel computing possibilities offered by quantum time evolution [11]. This promising alternative is illustrated in several contributions in this volume.

Here, we will illustrate two of those Optimization problems that Nature seems unable to solve by means of (classical) annealing, namely spin-glasses [12, 13, 14, 15, 16] and supercooled glass-forming liquids [18, 19]. For both kind of systems we have reasonably realistic three-dimensional models, as well as Mean-Field models [14, 20, 21] (the p-spin Sherrintong-Kirkpatrick models, see Sect. 3). The infinite dimensional Mean-Field models offer clear advantages: they can be solved analytically and these solutions yield nice physical pictures. Unfortunately, it is by no means obvious that the Mean-Field solutions bear any resemblance to the three dimensional systems that they aim to represent [24, 25]. Surprisingly enough, experiments have not yet settled this controversy [15, 24, 25]. In the case of spin-glasses, the reason is clear: the Mean-Field solution tell us about equilibrium properties, while no experiment has reached thermal equilibrium for a spin-glass below its glass temperature. The situation is somehow better for supercooled liquids. In that case, the Mean-Field solution contains also *dynamical* information (actually, it is in this way that the correspondence with liquids is established[20]). Important features of the Mean-Field solution are not present in liquids, but Mean-Field is still considered an useful approximation.

Yet, when one wants to extract information from the three dimensional systems, a numerical study of three dimensional models is still the main choice. For a restricted family of models of glass-forming liquids, modified classical Monte Carlo dynamics [22, 23] are quite (even too much[3]) effective. In the spin-glass case, parallel tempering,[26] a sophisticated version of classical annealing, has shown some limited success in three dimensions [27]. Things look better in two dimensions, where no ordered low-temperature phase exists for

[3] In the sense that the unwanted absolute minimum of the free energy, the crystalline phase, appears even if one is interested in the metastable supercooled liquid.

temperature $T > 0$. Effective ground-state (i.e. $T = 0$) search algorithms are known (see H. Rieger in this volume), as well as an efficient cluster method for $T > 0$ [28]. Furthermore, quantum annealing has been shown to be superior to classical annealing in the ground-state search in 2D [29]. However,[30] a similar procedure performs *worse* than classical annealing in the study of a Mean-Field Sherrintong-Kirkpatrick model appropriated for glass-forming liquids. A rather important open question is whether quantum annealing could be useful in the study of three-dimensional hard optimization problems, such as those posed by spin-glasses and glass-forming liquids. Clues for the answer should be looked for in other contributions to this volume.

The layout of the rest of this note is as follows. In Sect. 2 we shall recall some of the most general features of an out-equilibrium glass. Then we shall specialize to glass-forming liquids. In Sect. 3 we collect some ideas from the Sherrington-Kirkpatrick model, in particular the relationship between the glass transition and the topological features of the energy landscape. In Sect. 4 we shall comment on numerical attempts to give flesh to some of the Mean Field concepts in three dimensions. In Sect. 5 we shall describe our proposal to use high-frequency X-ray and neutron scattering data to study the energy landscape. In Sect. 6 we elaborate on the use of modified Monte Carlo moves (the *swap*) to deal with this problem. The last part of this note, Sects. 7 deals with our investigations of *rejuvenation* and *memory*, two features of out-of-equilibrium spin-glasses that, one would say, preclude the use of (classical) annealing strategies.

2 Aging

Aging is found in many complex systems out of equilibrium, like supercooled liquids,[18, 19] polymers,[31] colloids,[32] or spin-glasses,[33] and understanding it is a necessary step toward a unified description of such systems [17, 34]. Aging is nicely demonstrated, for instance, in measures of the thermoremanent magnetization in spin-glasses (see e.g. [35]): in the presence of a magnetic field, cool an spin-glass from room temperature to the working temperature, T, below its glass-temperature; hold the magnetic field for a while (the time elapsed will be called t_w hereafter), then switch-off the field and record the time-decay of the magnetization $M_{t_w}(t)$. Not only this decay is very slow but, even for the longest t_w tried up to now, $M_{t_w}(t)$ strongly depends on t_w (the larger t_w is, the slower decays $M_{t_w}(t)$). Similar results are found in most aging systems. After a short transient since preparation, a state is reached in which one-time observables (e.g. energy, enthalpy) vary extremely slowly, while two-time quantities (correlations, susceptibilities) strongly depend on the *age*, t_w, of the system as well as on frequency ω (or the measurement time t).

Despite recent efforts, our knowledge of aging of real materials is scant in the theoretically important regime of large t_w and small frequency, where

universal features should show up [17]. Two issues still open are the scaling of correlations and the behavior of the fluctuation-dissipation ratio. The two problems are briefly described below. Still more complex situations, such as the behavior of aging systems under temperature changes, will be addressed in Sect. 7.

2.1 Time Sectors

To illustrate the two times scaling of correlations, let us address quantitatively the time-decay of $M_{t_w}(t)$ or equivalently, given the Fluctuation-Dissipation Theorem,[17] the time-dependent spin-spin correlation function[4] in the absence of a magnetic field:

$$C(t, t_w) = \frac{1}{N} \sum_i \langle \sigma_i(t + t_w)\, \sigma_i(t) \rangle \ , \tag{1}$$

(the reader will find often in the literature that $C(t, t+t_w)$ is named $C(t, t_w)$). Now, it seems to be a fact of general validity in out-equilibrium dynamics [17] that $C(t, t_w)$ behaves differently in different *time-sectors*. Loosing generality[5] for the sake of clarity, this amounts to say that it can be decomposed as

$$C(t, t + t_w) = \sum_i f_i \left(\frac{(t + t_w)^{1-\mu_i} - t_w^{1-\mu_i}}{1 - \mu} \right) \ . \tag{2}$$

Here, f_i are smooth, decreasing functions that tend to zero at infinity, and such that $f_i(0)$ is of order one. It follows that if $t \ll t_w^{\mu_i}$ the i=th time sector contributes the constant value $f_i(0)$ to $C(t, t_w)$, while for $t \gg t_w^{\mu_i}$ it contributes nothing. In other words, the i=th time sector is active only for $t \sim t_w^{\mu_i}$ (notice that the different time sectors get neatly separated only in the limit of very large t_w).

Not much is known about the exponents μ_i defining the different time sectors. With the popular parametrization in (2),[17, 35] one has $0 \leq \mu_i \leq 1$. For the simple case of the coarsening-dynamics (domain-growth) of an ordered ferromagnet,[41] only two time sectors are needed for a complete description: $\mu_1 = 0$ describing the stationary, t_w independent dynamics found at small t, and $\mu_2 = 1$ describing the *full-aging* situation where the correlation-function depends on the ratio t/t_w. Also the spin-glass dynamics has been experimentally claimed[35] to be ruled only by two time sectors: $\mu_1 = 0$ and $\mu_2 = 0.97$. The second time sector is slightly but clearly different from the full-aging t/t_w behavior ($\mu = 1$) and is thus named sub-aging. However, a very recent experiment[39] seems to indicate that the sub-aging behavior is just an artifact of the finite-time needed to cool the system down to the

[4] Actually, in the aging regime they are related by a very smooth function [36, 37, 38].

[5] The here presented formulation cannot describe logarithmic domain-growth, for instance. See in [17] the general framework.

working temperature (a limitation not suffered of in numerical simulations). Using their fastest cooling protocol, Rodriguez et al.[39] have found a clear full-aging behavior $\mu_2 = 0.999$. Furthermore, the role of the stationary time-sector ($\mu_1 = 0$) to describe the data is far less critical than previously[35] thought. The results by Rodriguez et al.[39] have not being universally accepted, and there still is an ongoing controversy regarding the presence of full-aging in spin-glasses (See [6, 7, 40]). For colloids, both *superaging*[42] ($\mu > 1$) and full aging[43] has been reported. Polymers show rather *subaging*[31, 44] ($\mu < 1$), as has also been observed numerically in simple liquids [45]. However, the values quoted often correspond to different time regimes, and the regime where $t_w \to \infty$ with t/t_w fixed has not been carefully studied (except for spin glasses). For example in glycerol [46] full aging has not been seen either close to the glass temperature, T_g (almost at equilibrium) or at lower temperatures T. In both regimes the explored frequencies were much larger than $1/t_w$.

2.2 The Fluctuation-Dissipation Ratio

Consider observables A and B (B couples to an external field h). One example will be given in Sect. 6. The susceptibility χ is the time integral of the linear response:

$$R(t_w, t + t_w) \equiv \left. \frac{\delta \langle A(t + tw) \rangle}{\delta h(t_w)} \right|_{h=0} , \tag{3}$$

while the correlation function is

$$C(t_w, t + t_w) \equiv \langle A(t + t_w) B(t_w) \rangle \ . \tag{4}$$

In the simplest instance of (2), both $R(t_w, t + t_w)$ and $C(t_w, t + t_w)$ are expected to be of the form [17]

$$C(t_w, t_w + t) = C_{\rm st}(t) + C_{\rm ag} \left(\frac{g(t_w + t)}{g(t_w)} \right) \ . \tag{5}$$

The stationary part $C_{\rm st}(t)$ is the $\mu = 0$ sector, while $g(t)$ is a monotonic function acting as an "effective" correlation time, and $C_{\rm ag}$ describes the aging of the system [35].

Aging is also characterized by a non-trivial behavior of the fluctuation-dissipation ratio (FDR), namely

$$X(t_w, t + t_w) = \frac{T R(t_w, t + t_w)}{dC(t_w, t_w + t)/dt_w} \ . \tag{6}$$

The fluctuation-dissipation theorem (FDT) states that $X = 1$ in thermodynamic equilibrium, but this need not be so during aging, and *FDT violations* (i.e. $X \neq 1$) are observed. Experiments [47, 48], mean-field results [36] and simulations [38, 49, 50] suggest that the FDR depends on time only through the correlation function:

$$X = X[C(t_w, t_w + t)] \ . \tag{7}$$

In structural glasses, in which we concentrate from now on, simulations also show that at fixed t_w, X takes essentially two values: $X(C) = 1$ for C greater than some $q_{\rm EA}(T)$ (called Edwards-Anderson parameter) and $X(C) = x(t_w) < 1$ for $C < q_{\rm EA}(T)$. Since T/X can be interpreted as an effective temperature $T_{\rm eff}$,[36] it seems that FDT violations in structural glasses can be characterized by a single time-dependent

$$T_{\rm eff}(t_w) \equiv T/x(t_w) \ , \tag{8}$$

related to the slowest degrees of freedom. This lacks experimental confirmation. (Note that other definitions of effective temperatures have been explored [46, 51]). Also open is the issue of the behavior of $T_{\rm eff}(t_w)$ as $t_w \to \infty$, of great theoretical interest because it is related to the possible *thermodynamic* meaning of $T_{\rm eff}$ [36].

3 Pictures from the Sherrington-Kirkpatrick Model

The Sherrington-Kirkpatric model is a Mean-Field version of the Edwards-Anderson model. The variables of the Edwards-Anderson model are spins ($\sigma_i = \pm 1$, $i = 1, 2 \ldots N$) placed in the nodes of a regular lattice. The Edwards-Anderson Hamiltonian couples only nearest neighbor spins, and is itself a random quantity:

$$H = - \sum_{<i,j>} J_{ij} \sigma_i, \sigma_j \ . \tag{9}$$

The couplings J_{ij} are independent random variables extracted from a Gaussian distribution of mean $\overline{J_{ij}} = 0$ and variance $\overline{J_{ij}^2} = J^2$ (it is customary to measure temperatures in units of J). Note that we represent the Boltzman thermal average as $\langle \ldots \rangle$ while the average over the couplings is given by an overline. All important quantities are obtained in this order: first, you obtain the thermal averages over the spins for a fixed coupling distribution, and later you average the results over the couplings. For instance, the free energy is

$$\mathcal{F} = -T \ \overline{\log \left[\sum_{\sigma_1 = \pm 1} \ldots \sum_{\sigma_N = \pm 1} \mathrm{e}^{-H_J/T} \right]} \tag{10}$$

In the standard jargon, one says that the J_{ij} are quenched random variables.

The Sherrignton-Kirkpatrick model is a Mean-Field version of the model (9) in the sense that all spins interact with each other, but their coupling is small:

$$H = - \sum_{i \neq j} J_{ij} \sigma_i \sigma_j \ , \quad \overline{J_{ij}^2} = \frac{J^2}{N} \ . \tag{11}$$

The Sherrington-Kirkpatrick model can be solved analytically,[14] and this solution yields a rich picture for the spin-glass phase. However, here we will not be concerned with it. We are rather interested in the properties of a generalization of the Sherrington-Kirkpatrick model, the so-called p-spin model, where we admit p-body interactions:[6]

$$H = - \sum_{i_1<i_2<\ldots<i_p} J_{i_1,i_2,\ldots,i_p} \sigma_{i_1} \sigma_{i_2} \ldots \sigma_{i_p} \,, \tag{12}$$

with $\overline{J^2_{i_1,i_2,\ldots,i_p}} = J^2/N^{p-1}$. The p-spin model is a kind of Mean-Field model for supercooled liquids [20].

At first-sight, one is puzzled by this connection: a liquid is not made of spins, and there is nothing in liquid physics [52] that could play the role of the quenched couplings. However, when one tries to find closed equations for the evolution of the correlation functions and the linear responses, recall (3), for the model (12), you find that the standard Mode-Coupling approximation that you make for supercooled liquids,[53] is *exact* in this case. Since the Mode-Coupling approximation is, in general, somehow uncontrolled, it is very interesing to have a model at hand where it can be used with full confidence. We give here a very sketchy description of the main results of this analysis, referring to the lectures notes by Cugliandolo [21] for details and further references.

In a nutshell, below the so called Mode-Coupling temperature, $T_{\rm mc}$, a divorce is found between the statical and dynamical properties of model (12). Indeed, the free energy is an analytical function of temperature down to the critical temperature, $T_{\rm c} < T_{\rm mc}$. However, if one follows the (Langevin) dynamics of an initially disordered system, in the large N limit its energy density cannot go below the so-called threshold energy, $\mathcal{E}_{\rm th}$, at any temperature. The threshold energy is *not* the ground-state energy, but the equilibrium energy at temperature $T_{\rm mc}$. In fact, for $T < T_{\rm mc}$ the equilibrium energy density verifies $\mathcal{E}(T) < \mathcal{E}_{\rm th}$. Classical annealing [1] is useless for model (12). Therefore, for $T < T_{\rm mc}$ the system is eternally out of equilibrium and a non-trivial Fluctuation-Dissipation ratio, (6), is to be expected. As for thermodynamic properties, a funny continuous transition is found at $T_{\rm c}$, where the susceptibilities are continuous, but the order parameter (defined below) has a discontinuous jump. A geometrical description of this puzzling behaviour is provided by the TAP free energy [54].

3.1 The TAP Free Energy

Since model (12) is of Mean-Field nature, it can be solved (for a fixed realization of the random couplings $J_{i_1,i_2,\ldots,i_p}$) by minimizing a free-energy function

[6] It is sometimes useful to relax the constraint $\sigma_i = \pm 1$. One rather considers a *spherical model* where the constraint relaxes to $\sum_{i=1}^{N} \sigma_i^2 = N$ (see [21] for details).

that depends in the average magnetization of each spin. Hence we introduce the variational parameters:

$$m_i = \langle \sigma_i \rangle \,, \tag{13}$$

$$q_{\mathrm{EA}} = \frac{1}{N} \sum_{i=1}^{N} m_i^2 \ . \tag{14}$$

The Edwards-Anderson parameter, $0 \leq q_{\mathrm{EA}} \leq 1$ plays the role of an order parameter. The values of the m_i are obtained by minimizing the TAP free-energy:

$$\begin{aligned} F^{\mathrm{TAP}} = & \sum_{i=1}^{N} \frac{1+m_i}{2} \log\left[\frac{1+m_i}{2}\right] + \frac{1-m_i}{2} \log\left[\frac{1-m_i}{2}\right] \\ & - \sum_{i_1<i_2<\ldots<i_p} J_{i_1,i_2,\ldots,i_p} m_{i_1} m_{i_2} \ldots m_{i_p} \\ & - 2N \left[1 - q_{\mathrm{EA}}^p - p(q_{\mathrm{EA}}^{p-1} - q_{\mathrm{EA}}^p)\right] \end{aligned} \tag{15}$$

The first term approximates the entropy of the spins, the second their energy while the third is the Onsager back-reaction term.

3.2 The TAP States

The TAP state at temperature T, for a given J realization, are the stationary points of F^{TAP}:[7]

$$0 = \frac{\partial F^{\mathrm{TAP}}}{\partial m_i} \ . \tag{16}$$

We name all the magnetizations for a generic state by $\boldsymbol{m}$. States are classified according to their *index*, that is the number of negative eigenvalues of the Hessian matrix, $\partial^2 F^{\mathrm{TAP}}/\partial m_i \partial m_j$, at the TAP states (states with zero index are minima).

The difference with a standard Mean-Field calculation is in that one cannot directly identify the free-energy with the minimum of F^{TAP}: there could be so many states of high free energy that their contribution becomes relevant. Indeed,[55] the free energy should be obtained by summing the contributions of all states, $\mathrm{e}^{-\beta \mathcal{F}_J} = \sum_\alpha e^{-\beta F^{\mathrm{TAP}}(\boldsymbol{m}_\alpha)}$. Now, specially at low temperatures, the number of states with free-energy density $f = F^{\mathrm{TAP}}/N$ is $\mathrm{e}^{N \Sigma_J(\beta,f)}$. We call $\Sigma_J(\beta, f)$ the complexity and, since it is self-averaging, we will drop the J subindex.

The free energy

$$\mathrm{e}^{-\beta \mathcal{F}} = \int \mathrm{d}f \, \mathrm{e}^{-N[\beta f - \Sigma(\beta,f)]} \ , \tag{17}$$

[7] Finding TAP states is a non trivial numerical task.

can be calculated using a saddle point method [56]:

$$\mathcal{F} = N[f^* - \Sigma(\beta, f^*)], \quad \beta = \left.\frac{\partial \Sigma(\beta, f)}{\partial f}\right|_{f^*} \tag{18}$$

This is a sketch of the situation as temperature varies:

- For $T > T_{\rm mc}$, $\Sigma(\beta, f^*) = 0$ and f^* is the free-energy of the paramagnetic state. More than one solution exist for the TAP equations (16). But solutions other than the paramagnetic one are metastable states that play no role in thermodynamics.
- For $T_{\rm c} < T \leq T_{\rm mc}$, $\Sigma(\beta, f^*) > 0$. The states that dominate the thermodynamics have larger free-energy than the paramagnetic state, but there are so many of them that their contribution is relevant. Nevertheless, $[f^* - \Sigma(\beta, f^*)]$ is the analityc continuation of the free-energy of the paramagnetic states.
- For $T < T_{\rm c}$, we have again $\Sigma(\beta, f^*) = 0$. The number of states is subexponential. The phase transition at $T_{\rm c}$ is identified with the thermodynamic glass transition.

3.3 Dynamics and TAP States

One may further refinate the concept of complexity, by considering the number of states with index 0 (minima), $e^{N\Sigma_0(\beta,f)}$, with index 1 (saddles with one unstable direction), $e^{N\Sigma_1(\beta,f)}$, etc.

One has above $T_{\rm mc}$,

$$\Sigma_0 = \Sigma_1 = \Sigma_2 = \dots \ .$$

Yet, below $T_{\rm mc}$ they may be ordered as

$$\Sigma_0 > \Sigma_1 > \Sigma_2 > \dots \ .$$

In other words, above $T_{\rm mc}$ the typical TAP state is a saddle of $F^{\rm TAP}$, while below $T_{\rm mc}$ they are minima.

The situation[57] is depicted in Fig. 1. Below $T_{\rm mc}$ the equilibrium TAP states are minima, separated from each other and from other metastable states by free-energy barriers of order N. Those barriers cannot be overcome by a local Langevin dynamics. Precisely at $T_{\rm mc}$ the threshold states become relevant. The spectra of eigenvalues for the Hessian of $F^{\rm TAP}$ touches zero, which means that there are flat-directions (escaping from the threshold state along a flat direction does not cost you free energy). Unfortunately, those flat directions only connect threshold states. For $T < T_{\rm mc}$, the dynamics get trapped by the threshold states, as it is not able to overcome the free energy barriers of order N separating them from the stable minima.

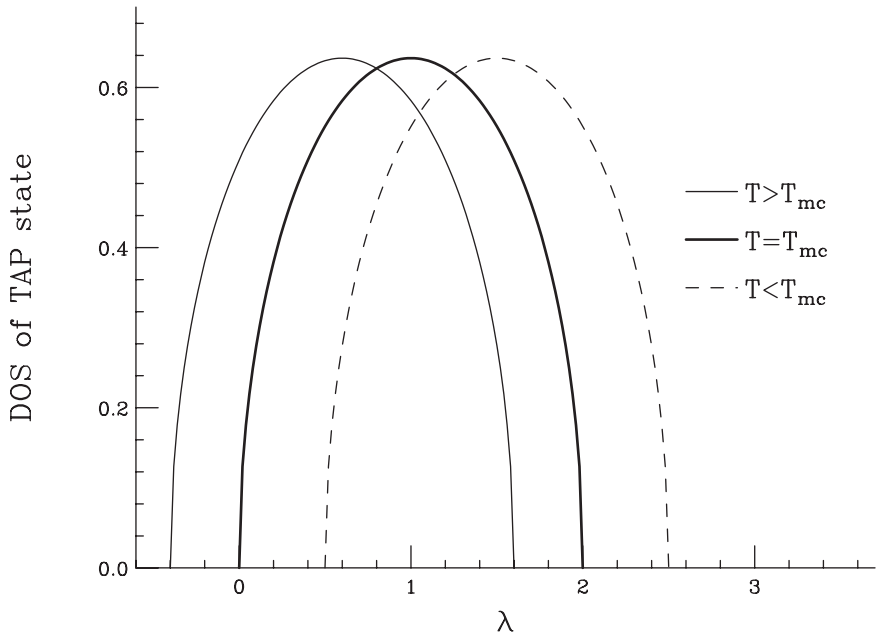

Fig. 1. Typical densities of eigenvalues for the Hessian of the TAP free energy evaluated at TAP states, above, just at, and below the Mode-Coupling temperature. Above $T_{\rm mc}$ the typical TAP state is unstable. At $T_{\rm mc}$ the TAP states are marginally stable, as the spectra touch zero. The dynamically unaccesible equilibrium states below $T_{\rm mc}$ are stable minima

4 Inherent Structures

When one tries to interpretate the Mean Field picture in 3D, difficulties are encountered. The free energy is not a function, but a functional. It is not obvious how to generalize the TAP states, obtained findinf the stationary point of a function, see (16), to a finite dimension.

In the context of the physics of liquids, an operational alternative has been proposed, namely to consider the potential energy landscape [58]. We denote the potential energy $U(\{\boldsymbol{r}_i\})$, which is a function (not a functional!) of particle positions. The potential energy per particle is named u. The basic objects are named *inherent-structures* and are defined in the context of a numerical simulation. The procedure is quite simple: from your instantaneous liquid configuration $\boldsymbol{r}_i$, $i = 1, \ldots N$, you obtain a minimum of the potential energy using conjugate-gradient or any other local minimization algorithm. The reached minimum is named an inherent-structure (IS), the corresponding potential energy density being $e_{\rm IS}$.

In the bottom part of Fig. 2 we show an example of the procedure. The $e_{\rm IS}$ is a well defined function of T: the larger the system is, the smaller the

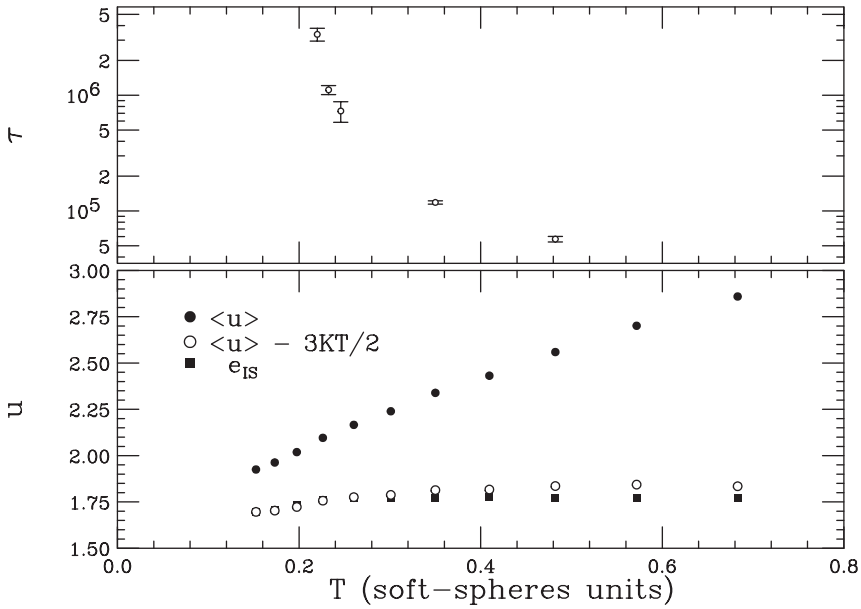

Fig. 2. *Top*: autocorrelation time (in Monte Carlo steps) for the soft-sphere system described in Sect. versus temperature. For this system, $T_{\rm mc} = 0.226$. *Bottom*: For the same system of top panel, average potential energy density versus temperature, as obtained in a numerical annealing. We also plot the corresponding energy for inherent structures (*black squares*), as well as the potential energy density minus the harmonic contribution to be expected for vibrations around frozen atomic positions (*open circles*)

fluctuations you find for $e_{\rm IS}$. At high-temperatures, you find $e_{\rm IS} = e_{\rm th}$, independently of T. If one tries to consider the system as a solid (i.e. the energy should have an harmonic contribution, $\frac{3}{2}k_{\rm B}T$, plus the energy corresponding to the equilibrium position of the atoms, $e_{\rm IS}$), the results are disappointing. You find that $\langle u \rangle$ is larger than $e_{\rm IS} + \frac{3}{2}k_{\rm B}T$. Yet, when the temperature decreases and approaches $T_{\rm mc}$, you start finding IS with $e_{\rm IS} < e$th while the difference $\langle u \rangle - e_{\rm IS} - \frac{3}{2}k_{\rm B}T$ shrinks. The system starts to behave as a collection of atoms vibrating around the equilibrium positions determined by the IS (i.e. like an amorphous solid or a very viscous liquid). As you may check in the top part of Fig. 2, as this process progress, the relaxation time increases quite significantly. Although it is finite at $T_{\rm mc}$, which in 3D corresponds to a crossover temperature rather than to a dynamical critical temperature, it increases beyond what is measurable in present day computers. Similarly, experiments cannot measure relaxation times longer than hours [18].

Note that the configuration space is partitioned in basins of attraction [58], each basin corresponding to a IS. Assuming that the dynamics in each bassin is made of harmonic vibrations, you may easily calculate the entropy for every

IS, using standard formulae for solids [2]. You simply need to diagonalize the Hessian of the potential energy function at the IS. Furthermore, you know the equilibrium entropy of the liquid (in the limit $T \to \infty$ it is the entropy of an ideal gas, and you may reach finite T integrating the specific heat). The difference between the total entropy and the entropy of a single IS is the 3D quantity corresponding to the Mean-Field complexity, Σ.

5 The Physics of Vibrations and the Landscape

The potential energy landscape paradigm is very appealing, but its implications for experiments are not immediately obvious. We outline here a proposal [59] to relate it to scattering experiments.

Glasses[18, 19] are amorphous solids, in the sense that they display elastic behaviour. In crystals, elasticity is associated with phonons, quantized sound-wave excitations. Phonon-like excitations exist also in glasses at very high frequencies (THz), and they remarkably persist into the supercooled liquid [61].

Vibrational excitations of glasses in the THz region, and the related vibrational density of states (VDOS), play a crucial role in their thermodynamic properties [60]. Recent results suggest that the VDOS is determined by the properties of the potential energy landscape [58] (PEL). Indeed, the VDOS and the dynamic structure factor can be qualitatively reproduced from the (harmonic) vibrational spectrum obtained from the diagonalization of the Hessian matrix of the potential energy evaluated at the IS of a Lennard-Jones system [62]. The same numerical procedure led to quantitative agreement with inelastic X-ray scattering experiments in amorphous silica [63].

The high-frequency (0.1–10 THz) excitations have been experimentally shown to have linear dispersion relations [61, 64, 65, 66, 67, 68, 69] in the mesoscopic momentum region ($\sim$ 1–10 nm^{-1}). Although clearly not plane waves, they are highly reminiscent of phonons because they propagate with the speed of sound and because the VDOS, $g(\omega)$, is Debye-like ($g(\omega) \propto \omega^2$) at low enough frequency. These excitations have in fact been dubbed *high-frequency sound* and a coherent theoretical picture of their properties was obtained [70, 71, 72, 73] using Euclidean Random Matrix Theory [74] (ERMT).

However, there is more to the low frequency VDOS of glasses than the Debye law. A characteristic feature is that the VDOS departs from the Debye form, displaying an excess of states, which has been named *Boson peak* (BP). As observed in many materials, [61, 64, 65, 66, 67, 68, 69] the BP is in a region of frequencies where the dispersion relation for phonons is still linear ($\omega \sim$ a few THz). Our preferred definition of the BP is that of the authors that extract $g(\omega)$ from their neutron scattering data and look for a peak in $g(\omega)/\omega^2$.

The origin of the Boson peak can be understood if we consider the ensemble of generalized inherent structures (GIS): for each equilibrium configuration the associated GIS is the nearest stationary point of the Hamiltonian. If we

start from an equilibrium liquid configuration at low temperature, the GIS is a local minimum, and it coincides with the more frequently used IS (i.e. the nearest minimum of the potential energy). On the contrary, if we start from high temperature, the GISs are saddle points (recall Sect. 3.3). In the GIS ensemble there is a sharp phase transition separating these two regimes. It takes place in glass-forming liquids [75, 76, 77] at $T_{\rm mc}$. Above $T_{\rm mc}$ liquid diffusion is no longer ruled by rare *activated* jumps between ISs but by the motion along the unstable directions of saddles. Phonons are present in the spectrum of the VDOS in the low temperature phase (IS dominated) but are absent in the saddle phase.

The key point, following both from analytic computations in soluble models [57] and simulations,[75, 76, 77] is that the minima obtained starting from configurations below $T_{\rm mc}$ and the saddles obtained starting above $T_{\rm mc}$ join smoothly at $T_{\rm mc}$. Thus we can study GIS as a single ensemble, parametrized by the initial temperature or the final energy. We expect that the GIS ensemble belong to a large universality class.

This transition from the phonon phase to the saddle phase is a quite general phenomenon that it is not restricted to glasses. It has been studied in the framework of the Euclidean Random Matrix Theory (ERMT) [74], showing [70] that close to this transition, a BP is present in the *phonon* phase, whose position shifts to lower frequencies on approaching the transition point, while its height grows without bound. The BP actually signals a crossover at frequency $\omega_{\rm BP}$ between a (phonon dominated) ω^2 scaling of $g(\omega)$ to an ω^γ scaling ($\gamma < 2$) that is present at the phase transition point. More precisely, at frequencies small respect to the Debye frequency, the VDOS should satisfy the scaling law

$$g(\omega, \Delta) = \omega^\gamma h(\omega \Delta^{-\rho}) \ , \tag{19}$$

where Δ is the distance from the critical point and depends on the actual laboratory control parameter (pressure, temperature, etc.) Actually, Δ will be proportional to the difference between the system's $e_{\rm IS}$ and the energy of the IS at the mode-coupling temperature, $e_{\rm IS}(T_{\rm mc})$. The scaling function $h(x)$ is such that $h(x) \sim x^{2-\gamma}$ for $x \ll 1$ and $h(x) \sim$ constant for $x \gg 1$. This scaling law implies that

$$\omega_{\rm BP} \propto \Delta^\rho, \qquad \frac{g(\omega_{\rm BP})}{\omega_{\rm BP}^2} \propto \Delta^{-\beta}, \tag{20}$$

where $\beta = \rho(2 - \gamma)$. Under the resummation of a given class of diagrams, ERMT predicts [70] that $\rho = 1$, $\gamma = 3/2$ and $\beta = 1/2$. Of course the actual (universal) values of these critical exponents in three dimension may differ slightly from the values found in this approximation.

Since we know that $e_{\rm IS}$ decreases slowly with time after a quench,[79] the above results enable us to make predictions about the *ageing* of the VDOS, and in particular of the BP. With increasing time the system moves farther from the critical point, and thus the BP should decrease in height and shift to

higher frequencies. Moreover, at a given frequency (below the asymptotic $\omega_{\rm BP}$) $g(\omega)$ should decrease, since it will be of order ω^γ at short times and of order ω^2 at very long times. Similarly, one should expect a cooling rate dependence of the shape of the BP: the slower the cooling, the lower the asymptotic $e_{\rm IS}$ and thus a larger $\omega_{\rm BP}$ and less pronounced BP.

6 Swap Monte Carlo for Glass-Forming Liquids

The swap algorithm, [22, 80, 23] is an artificial modification of the standard Monte Carlo dynamics, that has been made to work for a binary mixture of particles, interacting though a soft sphere potential.[8]

We have simulated [80] this model using a *non-local Metropolis Monte Carlo* algorithm (hereafter SMC) which adds swap moves (with probability p) to standard *local Monte Carlo* (LMC). The LMC movement proposal consists in shifting the position of one particle by an small amount. A Metropolis test decides wether the proposal is accepted or rejected. The *swap proposal* consists in that particles of different type, choosen at random, interchange their positions. Again, the swap proposal is submitted to a Metropolis test.

Although swap acceptance is very low ($\approx 3\times 10^{-3}$) the equilibration time is considerably shortened; e.g. at $0.89\,\{T_{\rm MC}\}$ extrapolations estimate it [80] to be three orders of magnitude larger for LMC than for SMC (note that other non-local algorithms have proved useful in simulations of bidimensional models for structural glasses [82]). We used the following protocol: Starting from a random configuration, a system of $N = 2048$ particles was instantaneously quenched to the final temperature T, and let evolve for t_w steps. This preparation was done with the SMC algorithm with $p = 0.1$, which gives the faster equilibration for this system size. After t_w, the correlation and response functions in the presence of an external field h were computed, mostly in SMC runs with $p = 0.1$, but also in LMC and SMC runs with different p in order to assess the dependence of the results on the dynamics.

To check for the Fluctuation-Dissipation ratio, (6), we need to choose observables A and B. Due to the swap moves, particle diffusion is not a convenient observable. Instead, we divided the simulation box in N_c cubic subcells and considered the quantity

$$A(t) = \frac{1}{N}\sum_{\alpha=1}^{N_c} \epsilon_\alpha n_\alpha(t), \tag{21}$$

[8] The model [81] consists in a 50% mixture of particles of type A and B of equal mass, interacting though a pair potential $V_{\alpha\beta}(r) = \epsilon[(\sigma_\alpha+\sigma_\beta)/r]^{12} + C_{\alpha\beta}$ where $\alpha,\beta = A, B$. Calling σ_0 to our unit length, we impose a cutoff at $r_c = \sqrt{3}\sigma_0$. $C_{\alpha\beta}$ is chosen to ensure continuity of the potential at the cut-off. We take $\sigma_B = 1.2\sigma_A$, with $(2\sigma_A)^3 + 2(\sigma_A+\sigma_B)^3 + (2\sigma_B)^3 = 4\sigma_0^3$. The diameter ratio $\sigma_B = 1.2\sigma_A$ strongly inhibits crystallization. We simulate at constant volume, with particle density fixed to σ_0^{-3} .

where $\epsilon_\alpha = \pm 1$ randomly and n_α is the occupation number of subcell α. The side of the subcells was about $0.35\,\sigma_{AA}$ so that essentially $n_\alpha = 0, 1$. Note that swap moves do not change $A(t)$. To measure response, a term $\lambda N A$ was added to the Hamiltonian, with $\lambda \equiv h k_B T$ (h is dimensionless). We considered the correlation $C(t_w, t_w + t) \equiv \overline{\langle N A(t_w) A(t_w + t)\rangle}$, where $\overline{\langle \ldots \rangle}$ means average over both thermal histories and the ϵ_α, together with the integrated response $k_B T \chi(t_w, t_w + t) \equiv \overline{\langle A(t_w + t)\rangle / h}$ [9].

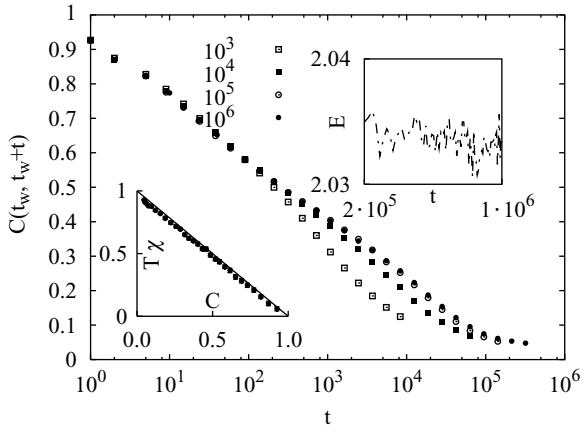

Fig. 3. Correlation function $C(t_w, t_w + t)$ vs. t for $T = 0.89 T_{MC}$ at $t_w = 10^3, 10^4, 10^5, 10^6$ (24 samples). *Bottom, left*: integrated response $T\chi$ vs. correlation function C at $t_w = 10^6$. *Top, right*: Energy per particle E vs. t during a SMC quench with $p = 0.1$. Error bars are of the order of point size

With SMC we can equilibrate the system down to $T = 0.89\,T_{\rm MC}$. The correlation $C(t_w, t_w + t)$ shows aging up to $t_w = 10^5$, but does not change between $t_w = 10^5$ and 10^6, which is approximately the region where the energy reaches a stationary value (Fig. 3). We conservatively estimate the autocorrelation time as the time τ needed for C to reach the asymptotic value N/N_c (~ 0.04), obtaining $\tau = 2 \times 10^5$, much smaller than 10^6 (the total lenght of the simulation). Hence we claim that the system has equilibrated. This is further confirmed by the fact that the FDT holds (see Fig. 3, bottom-left part). Indeed, if we plot the integrated response function (multiplied by temperature) versus the correlation function for the same t and t_w, a straight line of slope -1 is found, meaning that $X = 1$. In contrast, well below $0.89\,T_{MC}$ the system is out of equilibrium up to $t_w = 2 \times 10^7$ (our largest observational time).

[9] The center of mass (CM) was constrained to be fixed in order to avoid a spurious fast decay of the correlation due to random fluctuations of the CM position.

6.1 Time-Sectors Out of Equilibium

The swap also allows to addres the issue of the scaling of the correlation during aging. We consider an example for temperature $T = 0.53\,T_{\rm MC}$ (in general far below T_g, e.g. for glycerol this corresponds to $T \sim 140\,{\rm K}$, while $T_g \sim 190\,{\rm K}$). With SMC we find (Fig. 4) that the correlations for $t_w = 5 \times 10^5$, 5×10^6 can be made to collapse by plotting them as a function of t/t_w^μ with $\mu = 1.05(6)$, compatible with full aging. The collapse applies to the aging part ($C_{\rm ag}$, 5), which dominates the correlation for $t/t_w > 0.1$ ($\omega t_w < 10$), as has also been observed in spin glasses [39, 6]. The two shortest t_w's (inset) can instead be scaled with $\mu \sim 0.85$. The same value (within errors) was found in molecular dynamics simulations of the Lennard-Jones binary mixture,[45] so we argue that the accelerated dynamics does not affect the scaling. If one insists on scaling all curves, it can be done reasonably well using $\mu \sim 0.9$, though this is likely an artifact of mixing two different regimes. The relevant point is that $\mu \sim 1$ is seen clearly only for $t_w \gg 1$ and in the $t \sim t_w$ region.

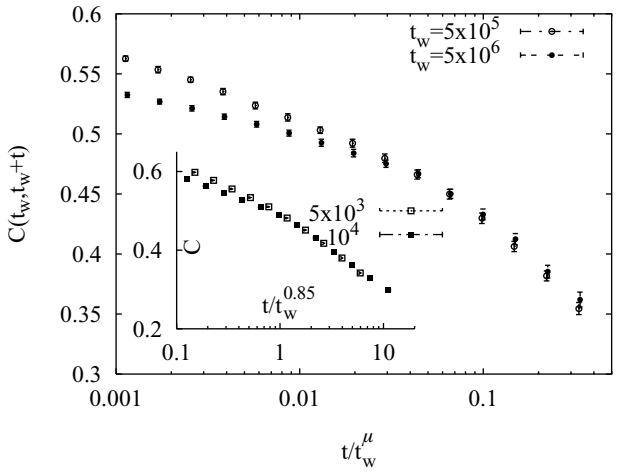

Fig. 4. C vs. t/t_w^μ, $\mu = 1.05(6)$, for $t_w = 5 \times 10^5, 5 \times 10^6$ at $T = 0.53\,T_{\rm MC}$ from SMC runs (24 samples). Inset: C vs. $t/t_w^{0.85}$ for $t_w = 5 \times 10^3, 10^4$ (48 samples)

6.2 The Fluctuation-Dissipation Ratio

An important result is that although the susceptibility and correlation are affected by the choice of dynamics, the FDR is not. The typical fluctuation-dissipation plot is shown in the inset of Fig. 5. Note that at short times (i.e. correlations close to one) we have an straight line of slope -1 (equilibrium). Only at later times, when the correlation function becomes small enough, the

curve departs from the equilibrium straigh-line. It is from the slope of this second step that one obtains

$$\frac{T_{\rm eff}}{T} = \frac{1}{X} \ .$$

In fact, Fig. 5 shows the ratio at $T = 0.89\,T_{MC}$ during aging and up to equilibration for both SMC and LMC algorithms, obtained measuring the FDR in simulations that used configurations taken along the SMC quench as a starting point.

Coming back to the comparison of LMC and SMC, note in Fig. 5 how, after a short transient ($\sim 10^4$ steps), the FDRs become indistinguishable within errors. At $T = 0.53\,T_{MC}$ and with LMC, we can reach the region of FDT violations only for $t_w = 10^4$, so we look at the FDR at fixed t_w for LMC and SMC with $p = 0.1$ and 0.3, obtaining a good agreement (Fig. 5, inset).

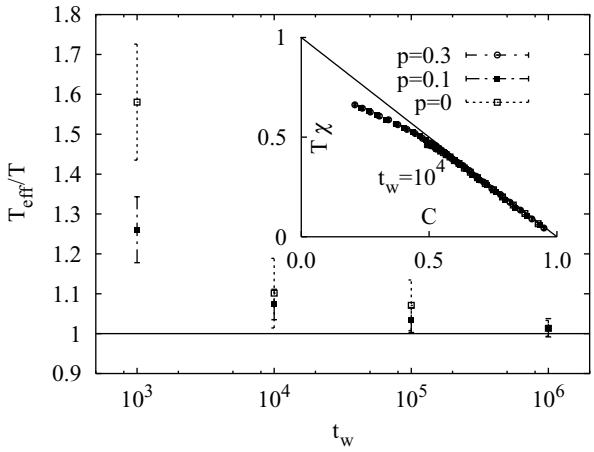

Fig. 5. $T_{\rm eff}/T$ vs. t_w for SMC and LMC runs at $T = 0.89\,T_{MC}$ (16 samples), obtained by a linear fit of the points of the parametric $T\chi$ vs. C plots deviating from the FDT line. Errors were estimated with the jacknife method. Inset: $T\chi$ vs.C for $t_w = 10^4$ at $T = 0.53\,T_{\rm MC}$ for $p = 0$ (LMC) and $p = 0.1, 0.3$ (SMC), $N = 20000$ (8 samples)

6.3 The FDR and the Potential-Energy Landscape

We consider[80] now the FDR for large times at $T = 0.53\,T_{MC}$. In Fig. 6 we plot $T_{\rm eff}$ at $t_w = 5 \times 10^3$, 10^4, 5×10^5 and 5×10^6 as a function of the instantaneous inherent structure (IS) energy $E_{\rm IS}(t_w)$. We also plot $T_{\rm eff}$ computed according to the IS approach,[50] $T_{\rm eff}^{-1} = \partial\Sigma/\partial f$, where $\Sigma(f)$ is the logarithm of the number of IS with free-energy f, and $\partial\Sigma/\partial f$ is obtained as

in [50]. Previously to swap dynamics, this idea (which makes no prediction about the $t_w \to \infty$ limit of $T_{\rm eff}$) was confirmed only in the very early aging regime by molecular dynamic simulations [50]. Our results show a reasonable agreement even at quite large times.

The limiting value of $T_{\rm eff}$ as $t_w \to \infty$ is of great theoretical interest. If the system eventually equilibrates, then $T_{\rm eff} \to T$, as we have found for $T = 0.89\, T_{\rm MC}$. Approaches that consider aging a result of critical slowing down due to the proximity of a critical point which is never reached (beacuse it is located at $T = 0$,[83], or because of the impossibility to establish a *liquid* long range order [84]) predict this to be the case for all temperatures. A different view relates the asymptotic value of the FDR to a thermodynamic transition described by replica symmetry breaking [85]. Above the transition, $X(C)$ is predicted[34] to reach slowly the equilibrium value 1 (so $T_{\rm eff} \to T$) while below the FDR should remain non trivial and

$T_{\rm eff}$ tend for $t_w \to \infty$ to a constant larger than T, since the system never equilibrates. In this scenario the asymptotic FDR is claimed to classify complex systems in universality classes [17, 85]. A third possibility is that FDT violations are due to nucleation and slow growth of the crystal phase,[86] in which case at long times one expects the coarsening regime to be reached, and so $T_{\rm eff} \to \infty$.

Our results for $0.53\, T_{MC}$ do not seem to support this last possibility. The data are instead compatible with the presence of a thermodynamic replica symmetry breaking (RSB) transition,[85] since FDR does not seem to change between $t_w = 5 \times 10^5$ and $t_w = 5 \times 10^6$ (E_{IS} are respectively 1.691 and 1.671). Note that this is the same regime where the system displays full aging. It cannot be excluded that $T_{\rm eff} \to T$, but it looks less likely if we note that extrapolating $E_{\rm IS}(t_w)$ to $t_w \to \infty$ with a power-law gives an asymptotic $E_{\rm IS} = 1.642$. We just observe that, at the qualitative level, the fact that the measured $T_{\rm eff}/T$ in Fig. 6 levels off at a value greater than 1 in the late aging regime supports the phase-transition scenario.

7 Rejuvenation and Memory in Spin-Glasses

Memory and *rejuvenation* [87, 88] are sophisticated manifestations of aging in experiments where the temperature is not kept constant. They are rather less understood than the previously considered problems ones. We therefore will be more descriptive in style, presenting recent results [7].

Rejuvenation arises when changing temperature from T_1 to T_2 (T_1 and T_2 smaller than the critical temperature, $T_{\rm c}$) a system that has spent some time at T_1, so that the a.c. suceptibility, $\chi(\omega, t_w)$ barely depends on t_w. Just after the $T_1 \to T_2$ change, aging restarts. The imaginary part of the susceptibility suddenly grows then relax. The t_w dependency of $\chi''(\omega, t_w)$ gets stronger, as for a *younger* system. Rejuvenation means that the relaxation of $\chi''(\omega, t_w)$ is very similar to the one of a system just quenched from $T > T_{\rm c}$ to T_2.

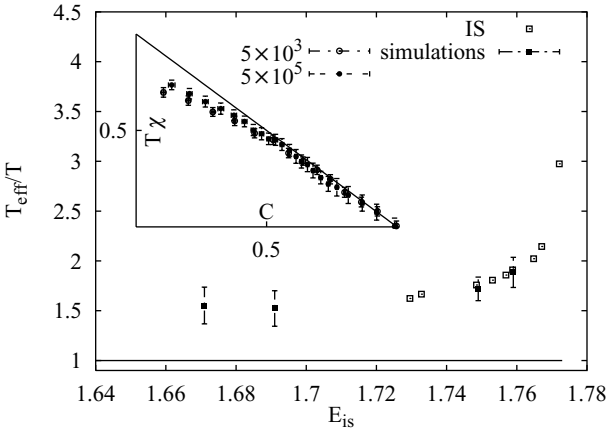

Fig. 6. $T_{\rm eff}/T$ for $T = 0.53T_{MC}$ vs. the the istantaneous IS energy $E_{IS}(t_w)$ measured in SMC runs. $E_{is}(t_w)$ is found by energy minimization starting from 50 instantaneous configurations within a small time window ($\ll t_w$) around t_w. We also show the $T_{\rm eff}$ predicted by the IS approach [50]. Inset: the $T\chi$ vs.C plot for two different t_w

Sometimes it is said that the relaxation is identical to the one of a system instantaneously quenched to T_2 from infinite temperature (in Sect. 7.3, below, we elaborate on the different meaning of *instantaneous temperature quench* in a experiment and in a computer simulation). If the susceptibility just after the quench to T_2 rises *above* the final value it had at T_1, one speaks of [89]. On the other hand, when the system is put back at temperature T_1, $\chi''(\omega, t_w)$ continue its relaxation where it left it just before the temperature change (*memory effect*). These effects can also be observed in the real part of the susceptibility (see e.g. Fig. 1 of [90]), although rejuvenation is very diminished as compared with the imaginary part. With the sophisticated *dip-experiment* temperature-change protocol,[87] memory and rejuvenation are truly spectacular.

Memory and rejuvenation have been found in systems quite different from spin-glasses (see, however, [91]). Examples are structural glasses [92], polymers (PMMA [94, 95]), and systems not particularly glassy (or not widely recognized as such), like colossal magnetoresistance oxides [96]. Moreover, a disordered ferromagnetic alloy,[93] becoming spin-glass at lower temperatures, has shown rejuvenation and memory, through the dip-experiment protocol (although in this case memory could be easily erased by lowering the temperature). Nevertheless, spin-glasses display the quantitatively stronger effects.

The above definitions for memory and rejuvenation need qualification. Under very small temperature changes [97] (say $\frac{T_1 - T2}{T_1} < 5 \times 10^{-3}$) the behavior of the spin-glass is rather smooth. On the other hand, sharp memory and rejuvenation can be observed [98] for $\frac{T_1 - T2}{T_1} \sim 0.07$. The crossover from small to drastic effects is rationalized using *effective isothermal waiting times* [97, 5].

Consider the simplest temperature change protocol: a system is aged for time t_w at temperature T_1, then its temperature is suddenly shifted from T_1 to T_2. After the shift, the zero-field cooled magnetization (ZFC) is measured.[10] The effective time, $t_{T_2}^{\mathrm{eff,shift}}$, is the age of the isothermally aged system at temperature T_2, whose ZFC magnetization[11] is most similar to the one of the temperature-shifted system (the two relaxations are not identical[97]). Rejuvenation arises when $t_{T_2}^{\mathrm{eff,shift}}/t_w$ is below experimental resolution.

Similarly, one can define [5] an effective time for the temperature cycle protocol $T_1 \to T_2 \to T_1$:[12] one keeps the system a time t_w at T_1, then shifts the temperature to T_2, waits a time $t_2 \sim 20t_w$, shifts back the temperature to T_1, switches on a magnetic field and then records the ZFC magnetization. The effective time $t_{T_1}^{\mathrm{eff,cycle}}$ is obtained by looking to the system aged at temperature T_1 for a time $t_w + t_{T_1}^{\mathrm{eff,cycle}}$ whose ZFC magnetization is most similar to the one of the temperature-cycled system. One has memory, as we defined it above, when $t_{T_1}^{\mathrm{eff,cycle}}/t_2$ gets below experimental resolution. In a large variety of spin-glasses experiments find[5, 40] for $T_1 > T_2$

$$\frac{t_{T_1}^{\mathrm{eff,cycle}}}{t_w} = \exp\left[-\frac{T_1 - T_2}{x_0 T_2}\right], \tag{22}$$

with[13]

$$x_0 \sim 10^{-2}\,. \tag{23}$$

Memory and rejuvenation can be recovered in the dynamics of abstract energy landcsape models [99]. However, one wants to reproduce these phenomena in the Langevin dynamics for the standard spin-glass model, the Edwards-Anderson (EA) model, (9). This dynamics for the EA model can only be investigated by Monte Carlo simulation. Yet, difficulties have arisen in numerical investigation of memory and rejuvenation [89, 101, 102, 103, 104]. Furthermore, the progress achieved regards only temperature-shift and temperature-cycle experiments.

Experiments where $(T_2 - T_1)/T_1$ is very small can be accounted for by the *cumulative aging* scenario,[97, 5] consisting in the three following hypothesis:

(a) Aging is ruled by the growth of a coherence length,[105] signaling the building of a spin-glass order. For isothermal aging, this length is named $\xi_T(t)$, t being the total time spent in the glass phase. This isothermal

[10] You cool the spin-glass below T_c for time t_w, then switch-on the magnetic field. The magnetization, that in the presence of the field grows with time, is named zero field cooled magnetization.

[11] That is, one ages the system at T_2 for time $t_{T_2}^{\mathrm{eff,shift}}$, then switches on the magnetic field and records the growing magnetization.

[12] We somehow simplify the protocol description, for details see [5].

[13] The actual value of x_0 depends both on T_1 and on the anisotropy of the microscopic spin-spin interaction (the more Heisenberg-like the interaction is, the smaller x_0 becomes [5]).

growth-law has been studied in experiments [5] and simulations,[108, 109] although the measured $\xi_T(t)$ grows by an small factor in both cases. Numerically, a power law

$$\xi_T(t) = A_T t^{z(T)}, \quad z(T) = z_c \frac{T}{T_c} , \tag{24}$$

fairly fits the data. However, more complicated rules has been used [97, 5, 98, 40].

(b) The coherence-length always grows with time. It behaves continuously upon temperature changes.

(c) Effective times follow from the *isothermal* growth of the coherence length. Consider a temperature shift after aging for time t_w at T_1. One has

$$\xi_{T_1}(t_w) = \xi_{T_2}(t_{T_2}^{\mathrm{eff,shift}}) . \tag{25}$$

A time t after the shift, the coherence length is

$$\xi^{\mathrm{shift}}(t) = \xi_{T_2}(t + t_{T_2}^{\mathrm{eff,shift}}) xs . \tag{26}$$

Similar reasoning is used in the analysis of more complicated temperature-change protocols.

Equation (25) is used in an indirect way, both in the analysis of simulations [104, 89] and experiments [97, 5, 98]. Relations such as (24), obtained in a different experiment, are used to convert the measured effective times into length-scales and viceversa. It is difficult to find in the literature *direct* data on the behavior of the coherence length upon temperature changes. A nice exception are the simulations of [101] where (26) was directly checked. Those simulation spanned 10^5 Monte Carlo steps (MCS). For comparison with experiments, recall that 1 MCS $\sim$ 1 picosecond.

Memory and rejuvenation appear as hardly compatible with the cumulative aging. Experiments show[97] that $\xi_{T_1}(t_w) < \xi_{T_2}(t_{T_2}^{\mathrm{eff,shift}})$ when the measured effective times are converted in length-scales, both for $T_2 > T_1$ and $T_1 < T_2$, in contradiction with (25).

Two theoretical scenarios are currently being considered to account for memory and rejuvenation. Rejuvenation was interpreted in terms of temperature chaos,[132] namely extreme sensitivity of *equilibrium* states in the glass phase to small temperature changes. An overlap-length, $l_0(T_1, T_2)$, is postulated to exist. Features at scale smaller than l_0 are unaffected by a temperature change $T_1 \to T_2$ while at larger scales the system is completely reorganized. Rejuvenation is then attributed to large length scales and strong rejuvenation requires small l_0. The ghost-domain scenario (see [98] for a recent account) allows to reproduce memory in the chaos scenario. The other scenario [100] is closer in spirit to cumulative aging. Rejuvenation after a negative temperature shift would arise from the so-called fast modes involving length-scales smaller than $\xi_{T_1}(t_w)$, that were equilibrated at T_1 but fall out of equilibrium

at T_2. Memory would arise from time and length scales separation: back to temperature T_1, fast modes re-equilibrate very fast so that aging continues from the previous T_1 state.

However, when it comes to actual calculations, it turns out that no convincing memory and rejuvenation has been found in computer simulations of $3D$ spin-glass models, either with a two-temperatures [101, 103, 89, 104] or with a dip-experiment protocol [102]. When the behavior of the coherence length is followed for times up to 10^5 MCS,[101] (25) and (26) are fulfilled even for $\frac{T_1-T_2}{T_2} \approx \pm 0.33$. Consistently with this finding, when the temperature cycle protocol is analyzed in the EA model,[104, 106] the x_0 in (22) turns out to be of order 1 rather than of order 10^{-2} . Should x_0 not decrease significantly for larger times, the whole low-temperature phase of the EA model could be accounted for by cumulative aging (i.e. the low-temperature phase would not be a spin-glass phase).

This contradiction with experiments is puzzling. It could be indicating that the EA model lacks some crucial ingredient [102]. A more conservative possibility is that memory and rejuvenation involve time and length scales unaccessible to present-day simulations. Indeed, experiments are performed on a time-scale which is about 10^8 times longer than typical simulations. Yet, experimentally,[5] there are around $\sim 10^5$ spins in a coherent cluster (hence $\xi_T(t_w) \sim 40$ lattice spacings), while simulations achieve (see below) $\xi_T(t_w) \sim 10$ lattice spacings. Some hope arrives from simulations [103] of the temperature cycle protocol for the 4D EA model, taht yielded strong rejuvenation (as defined in [89]). Yet, results in full agreement with cumulative aging, (25), were reported for $\frac{T_1-T_2}{T_2} \approx \pm 0.125$ (the simulation time was smaller than 10^4 MCS). In the Migdal-Kadanof lattice,[107] where rather larger times can be simulated, rejuvenation was found for $\frac{T_1-T_2}{T_1} \sim 0.1$, suggesting that x_0 in (22), does depends on the age of the system. Furthermore, the extremelly long 3D simulations of [7] that we recall below, performed with a dedicated computer,[8] have shown clear deviations from the cumulative aging in the EA model.

7.1 The Simulations

In [7], the EA model was considered in a (hyper) cubic lattice in 3D and 4D. The random couplings are $J = \pm 1$ with 50% probability. The system evolved using a sequential, local heat-bath dynamics. Our time-unit (1 MCS $\sim$ 1 picosecond) is a full-lattice update. For the spin-glass we studied lattice-size $L = 60$ in 3D (mostly in SUE), and $L = 20$ for 4D (on PC clusters) with some tests in $L = 30$ finding no differences. The number of disorder realizations vary within 16 and 240. Errors were estimated from sample-tosample fluctuations. Although most of the considered magnitudes are *self-averaging* (i.e. their sample-to-sample fluctuations depends on the number of spins as $N^{-1/2}$), errors are not negligible, specially at long times.

In the following, we will call a *direct-quench* to the procedure of placing a fully disordered system (infinite temperature) instantaneously at the working temperature. This corresponds to an infinite quenching-rate.

The Fluctuation-Dissipation Theorem (FDT) relates the autocorrelation function in zero magnetic field

$$C(t_w, t_w + t_0) = \frac{1}{V} \sum_i \langle \sigma_i(t_w) \sigma_i(t_w + t_0) \rangle \tag{27}$$

to the real part of the susceptibility: $\chi(\omega = 2\pi/t_0, t_w) \approx [1 - C(t_w, t_w + t_0,)]/T$. Yet, as we saw in Sects. 2 and 6, off-equilibrium, FDT needs to be generalized replacing T by $T/X[C]$ Hence, one assumes [101, 102, 103, 107] to be in pseudo-equilibrium regime ($\omega t_w \gg 1$ thus $X[C] = 1$), which is not always true [7].

We also obtain *spatial* information from the correlation function of the overlap field, $q_i(t) = \sigma_i^{(1)}(t)\sigma_i^{(2)}(t)$, built from two independently evolving systems with the same couplings, at the same temperature:

$$C_4(r, t_w) = \frac{1}{V} \sum_i \langle q_i(t_w) q_{i+r}(t_w) \rangle \ . \tag{28}$$

7.2 Strong Rejuvenation

In Fig. 7 is shown the time-evolution of the naive $\chi(\omega, t_w)$ (*i.e.* $[1 - C(t_w, t_w + t_0)]/T$) for the EA model in 3D (top) and 4D (bottom) for a (double) temperature cycle: $T_1 \to T_2 \to T_1 \to T_2$ ($T_1 = 0.9T_c$, $T_2 = 0.4T_c$). In 3D the system spends $t_s = 2 \times 10^8$ MCS at each temperature (1000 times longer than previous works), while in 4D $t_s = 10^6$ MCS. The results of a reference run, with temperature fixed to T_1, are also shown (continuous line). When the temperature drops to T_2, $\chi(\omega, t_w)$ increases over the reference curve and starts a new relaxation (*strong rejuvenation* [89]). When temperature is back to T_1, $\chi(\omega, t_w)$ catches the reference run almost instantaneously (*memory*). We call $t_{\rm rej}$ to the time that the rejuvenated $\chi(\omega, t_w)$ is above the reference run (see insets in Fig. 7), that is found to grow consistently with t_0 (much faster in 4D). It is then conceivable that an effect of macroscopic time-duration could be observed (experiments explore $t_0 \sim 10^{13}$ MCS). However, specially in $3D$, $t_{\rm rej} < t_0$. This implies that this strong rejuvenation is confined to the regime $\omega t_w < 1$, which is out of reach for measurements of the a.c. susceptibility (note that strong rejuvenation is not always observed experimentally in the real part of the susceptibility [90]).

In agreement [103], the relaxing curve after the temperature drop is independent of t_s on the explored range ($t_s = 10^6, 2 \times 10^7$ and 2×10^8 MCS in $D = 3$). Also shown in Fig. 7 is the relaxation of $\chi(\omega, t_w)$ for a direct-quench to T_2 (dashed-line). Such a infinitely-fast temperature drop is not realistic (see Sect. 7.3). Anyhow, the relaxation is not identical to the one after the

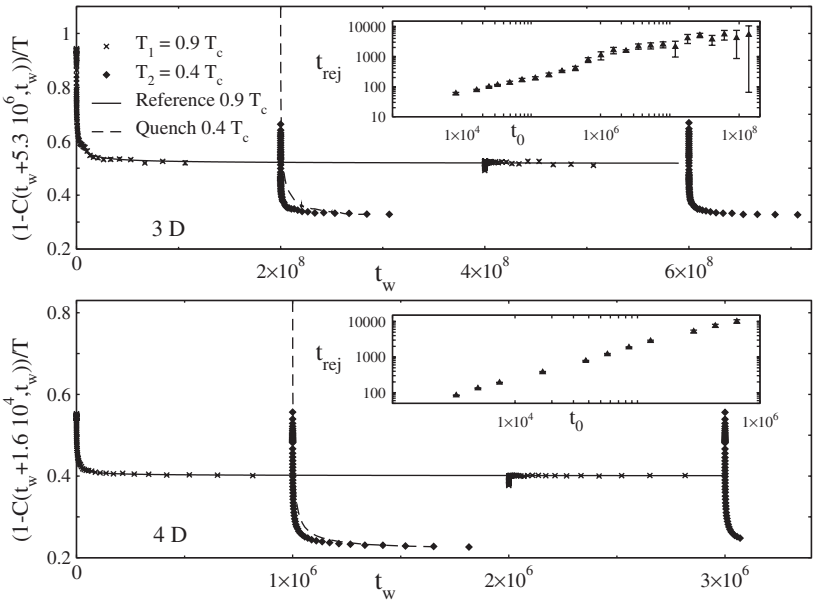

Fig. 7. *Top*: Naive $\chi(\omega = 2\pi/t_0, t_w)$, $t_0 = 5.3 \times 10^6$ for the 3D EA model vs. time. The T-cycle is $T_1 \to T_2 \to T_1 \to T_2$, each step lasting $t_s = 2 \times 10^8$. The full line is a reference run at $0.9T_c$. The inset shows the rejuvenation time (see text) vs. t_0. The dashed line is a direct-quench to T_2. *Bottom*: as top part for D = 4, $t_0 = 1.6 \times 10^4$ and $t_s = 10^6$

temperature shift, but the two become very similar (in $D = 3$, this happens for $t_w \sim 4t_0$). This is in marked contrast with previous simulations where $t_s \sim 10^4$ and $t_0 = 64$ [89]. For such a short times, one needs $t_w \sim 500t_0$ for the two relaxation curves to approach each other.

7.3 Comparison with *Experimental* Direct-Quench

In view of (22) and (23), and the large temperature drop that we are studying, one would expect a perfect rejuvenation effect. However, Fig. 7 show that the relaxation after the first step at $0.9T_c$ considerably differs from the direct-quench (although this difference is smaller than for shorter simulations [101, 89]). This seems in plain contradiction with experiments (see e.g. Fig. 4 of [98]). Yet, upon reflection, one realizes that the experimental direct-quench bears little resemblance with the simulational one. In fact, the experimental sample that is "instantaneously" quenched to 0.4 T_c, expends at least 10 seconds ($\sim 10^{13}$ MCS!) in the spin-glass phase.

In order to make a fair comparison with experiments, one should study the relaxation after a "soft" quench (Fig. 8) from high-temperature to the working temperature below the glass transition. Yet, the fastest quenching rate that

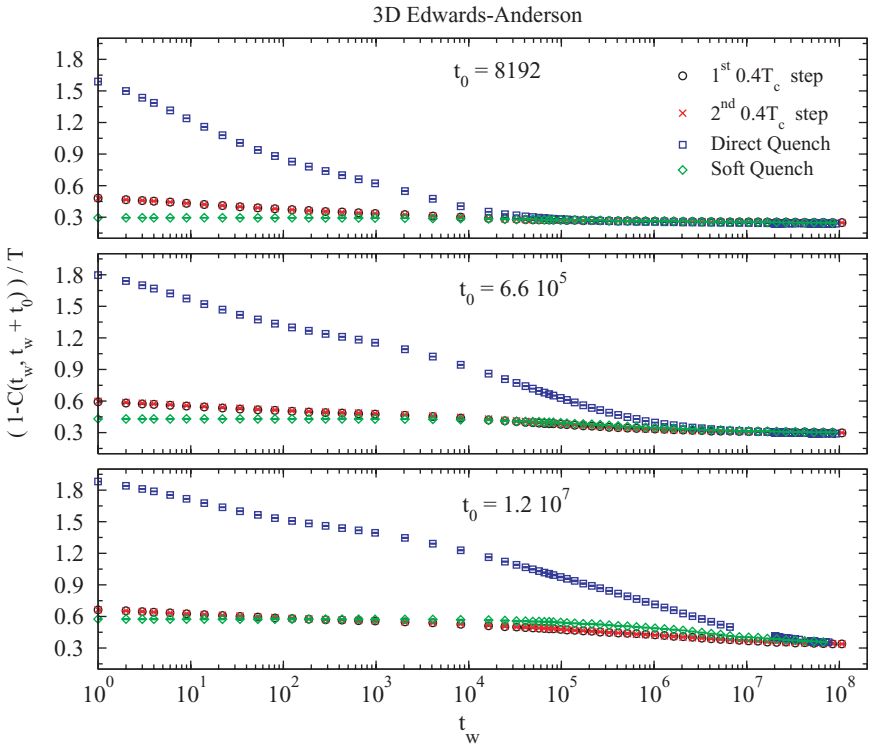

Fig. 8. Naive $\chi(\omega = 2\pi/t_0, t_w)$ of the 3D EA model vs. time, at temperature $T_2 = 0.4T_c$, for several values of t_0 and thermal histories. In all cases, t_w is measured from the time of the (last) instantaneous quench to T_2. *Squares* correspond to the instantaneous drop from infinite temperature to T_2. *Circles* correspond to the system that has spent $t_s = 2\times10^8$ MCS at $T_1 = 0.9T_c$, then suffers an instantaneous quench to T_2. *Crosses* correspond to the system that has been a time t_s at T_1, then time t_s at T_2, then time t_s at T_1 and finally suffers the instantaneous quench to T_2. *Diamonds* correspond to a gradual drop from $9T_c$ to T_2 in 20000 MCS (we incremented $1/T$ in $0.113/T_c$ every 10^3 steps, the system spending 1.2×10^4 MCS in the spin-glass phase)

can be achieved in experiments is far too slow to be reproduced in present-day computers. To achieve a very slow temperature drop from high temperature to working temperature, it is useful to consider Fig. 7 in a different way. One realizes that the system that has spent $t_s = 2\times10^8$ MCS at $0.9T_c$, then suffers an instantaneous temperature drop to $0.4T_c$ is a better approximation to the experimental direct-quench to $0.4T_c$. In fact, the system spends quite a long time close to the critical temperature, where the time evolution –recall (24)– is faster. When looking to the double temperature cycle in Fig. 7, one needs to compare the relaxation in the first and in the second steps at $0.4T_c$, the first corresponding to the *reference* direct-quench, the second being looked at as

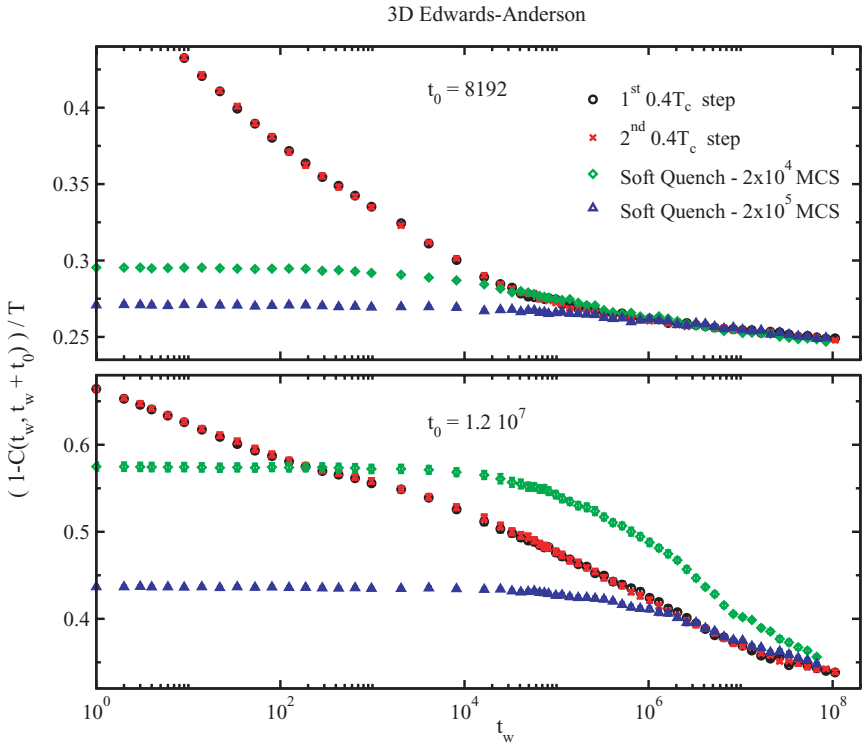

Fig. 9. Close-up to the *top* and *bottom* panels of Fig. 8, excluding the data for the instantaneous drop from infinite temperature to $T_2 = 0.4T_c$. We also include data (*triangles*) for a still slower drop from $9T_c$ to T_2 in 200000 MCS (we incremented $1/T$ in $0.113/T_c$ every 10^4 steps, so that the system spends 1.2×10^5 MCS in the spin-glass phase)

the *temperature-cycled* system. This comparison is shown in Fig. 8, together with the relaxation after a *soft-quench*.

The frequencies shown in Fig. 8 span three orders of magnitude. In all cases, the relaxation for the softly-quenched system,[14] that has spent 1.2×10^4 MCS in the spin-glass phase, is much closer to the one of the cycled-system than the one of infinite quenching rate. Furthermore, the relaxations for the first and the second steps at $0.4T_c$ are identical, up to our statistical accuracy (see Fig. 9). This you may wish to call *perfect rejuvenation*.

In Fig. 9 we perform a detailed comparison between the soft-quench (with two quenching rates) and the two-steps protocol. To have a feeling of the frequency dependence, we show the smallest and the largest frequencies in Fig. 8. For very short times, in the two-steps protocols we find a quick decay

[14] Soft-quench in this context actually means not infinite quenching rate, but dramatically faster than in experiments.

of the susceptibility due to the sharp temperature drop. On the other hand, the softly-quenched system shows a basically constant behavior (the slower the quench, the lower the intial plateau is). When time becomes of the order of the total time spent in the spin-glass phase during the soft-quench, the susceptibility starts to decay and becomes very similar to the two-steps protocol. At $t_0 = 8192$, the two soft-quenches catch the relaxation of the two-step protocol and become identical. At the smallest frequency, the fastest quench approaches but does not catch the two-steps relaxation. On the other hand, for the smallest quenching rate, the relaxation curve becomes identical to the one of the two-steps protocol for $t_w \stackrel{>}{\sim} t_0$, which corresponds to the experimentally accessible time range.

7.4 The Coherence-Length

The coherence-length may play a crucial role [100] in this physics, and should be followed in detail during temperature changes. This was done previously in [101], for times up to 10^5 MCS. Results in agreement with (26) were reported. A much longer simulation [7] in 3D show qualitatively different results.

The coherence-length may be obtained from $C_4(r, t_w)$ (which *is* self-averaging for not very large r). The resulting curve has been fitted to [108]

$$C_4(r, t_w) = \frac{A}{r^\alpha} \exp\left[- \left(\frac{r}{\xi(t_w)} \right)^\beta \right] . \tag{29}$$

In 3D, we find fair fits in the range $2 < r < 20$, fixing $\alpha = 0.65$ and $\beta = 1.7$ for all times and temperatures. The constant behavior of α does not agree with the results for the 4D model with Gaussian couplings [103]. To estimate errors in the three parameters fit (29) is very difficult. To have a feeling of their magnitude, let us report that $\alpha = 0.7$ yields good fits as well, with a 10% increased ξ estimate.

See in Fig. 10 (top), $\xi(t_w)$ for a direct-quench to $T_2 = 0.4 T_c$ and for a thermal cycle $T_1 \to T_2 \to T_1$ with $T_1 = 0.9 T_c$ and $t_s = 2 \times 10^7$. A power law with exponent ~ 0.144 fits nicely $\xi_{T_1}(t_w)$ for $t_w < t_s$, while the exponent for the direct-quench to T_2 is ~ 0.065 (full-lines in Fig. 10-top). During the T_2-step, ξ grows over the T_1 value, and it is larger than for the direct-quench to T_2. However, ξ decreases when the system is back to T_1 . Memory is striking: data for the second T_1 step, if translated back t_s MCS, are on top of the fit (obtained for $t_w < t_s$!). Let us stress two points regarding this result:

(a) The coherence-length can *decrease* upon temperature changes, violating cumulative-aging, (26), and in contradiction with the time and length scales separation scenario [100, 133]. However, the effect is not symmetrical for negative and positive temperature shifts, as it was inferred experimentally from effective-time measurements [97].

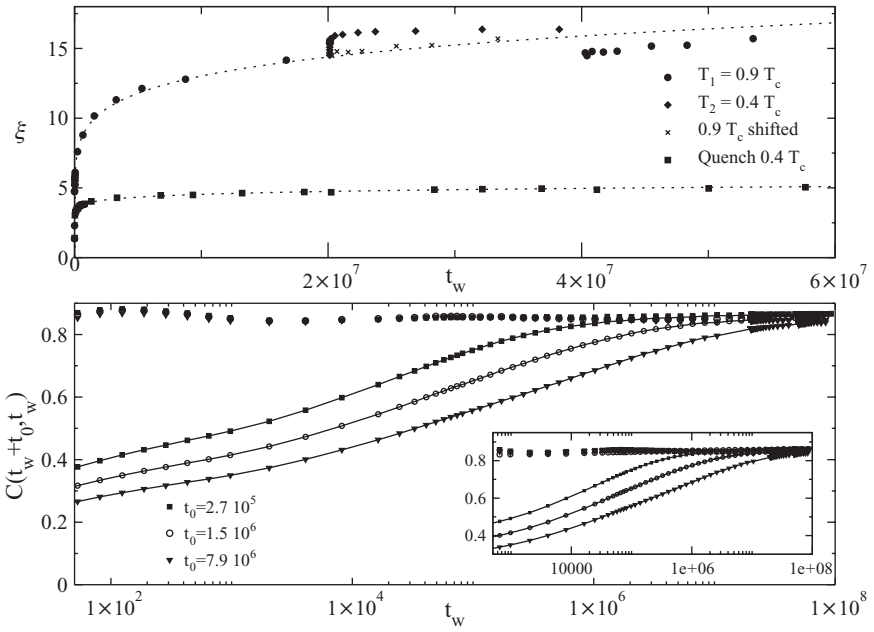

Fig. 10. Coherence-length vs. time, for the 3D EA model (*top*) and the diluted-ferromagnet (*bottom*). The thermal history has been a T-cycle $T_1 \to T_2 \to T_1$, being $t_s = 2 \times 10^7$ for the EA model and $t_s = 10^5$ for the Ising-diluted model.(*Crosses:* second T_1-step data, translated back in time t_s ; *Dotted lines:* fits to $\xi(t_w) = At_w^x$ for $t_w < t_s$). *Bottom*: Correlation functions of the direct-quench to T_2 of the top part for three different t_0 vs. t_w with (points) and without (lines) the correcting $(\xi(t+t_w)/\xi(t_w))^{3/2}$ factor. Notice that most of the t_w evolution can be absorbed by this factor. *Inset:* same as main plot for the step at T_2 of the thermal-cycle in the top part

(b) The effective time for the temperature cycle is compatible with zero (within our accuracy). This implies that, for $t_s \sim 10^7$, x_0 in (22) is *not* of order one, as it was found[104] for $t_s \sim 10^4$.

A rather crucial feature of aging [17] is that two time-scales, t_0 and t_w, are involved. One would like to relate the *one* time quantity $\xi_T(t_w)$, to the *two* times correlation function. A crude estimate for $t_0 \gg t_w$ is

$$C(t_w, t_w + t_0) \propto \frac{\xi^{D/2}(t_w)}{\xi^{D/2}(t_w + t_0)} \,, \tag{30}$$

i.e. the coherent cluster that at time $t_w + t_0$ has linear size $\xi(t_w + t_0)$, at time t_w was composed of mutually incoherent clusters of linear size $\xi(t_w)$.

Indeed, (Fig. 10, bottom), the factor $\xi^{3/2}(t_w + t_0)/\xi^{3/2}(t_w)$ absorbs almost all the t_w and t_0 dependency of $C(t_w, t_w + t_0)$, both for a direct-quench to T_2 and for the T_2 part of the thermal cycle. Note that even the constant value

for $C(t_w, t_w + t_0)\xi^{3/2}(t_w + t_0)/\xi^{3/2}(t_w)$ is equal for the direct-quench and for the thermal cycle. Also at T_1, $C(t_w, t_w + t_0)\xi^{3/2}(t_w + t_0)/\xi^{3/2}(t_w)$ is constant within a band of width 5% of its mean-value [131]. In spite of the crudeness of the argument leading to (30) and the uncertainty in the determination of ξ, the results are surprisingly clear.

Thus, memory and rejuvenation are driven by the rate-growth of $\xi_T(t_w)$ rather than by its value or by the short-distance behavior of $C_4(r, t_w)$ [100, 103]. In our simulation, rejuvenation is due to a *growth* of ξ upon cooling (probably, because of a sudden fall into a nearby energy minima), provoking a change in the evolution of $C(t_w, t_w + t_0)$. When temperature is shifted back to T_1, ξ_{T1} continues its growth as if it had never being at T_2 with analogous consequences for the correlation-function (memory). This implies a non monotonic behavior of $\xi_T(t)$, in contradiction with cumulative-aging, (25) and (26).

8 Conclusions

The aim of this contribution to this volume on Quantum Annealing, is to propose difficult problems that cannot be solved using classical annealing, namely the behaviour of glass-forming liquids and of spin-glasses. In both cases, the important low energy structures are not reachable even on experimental time scales, let alone computer simulations. The alternative of using artificial (classical) Monte Carlo moves, not present in physical systems, has been made to work only for a restricted family of models for glass-forming liquids. Both spin-glasses and glass-forming liquids, in low temperature experiments, are out of thermodynamic equilibrium and *age*.

In the case of glass-forming liquids, we have a well developed conceptual framework. The framework is inheritated from infinite-dimensional Mean-Field calculations. In spite of the difficulties, the potential energy landscape paradigm allows to give flesh to the Mean-Field concepts in 3D. The implications of this paradigm for scattering experiments can be worked out. These implications are expressed as scaling laws for the universal spectral feature known as the Boson Peak. The potential energy landscape paradigm allows as well to quantitatively describe aging at long times, and temperatures well below the experimental glass transition.

The study of aging for spin glasses, is less developed. The properties of memory and rejuvenation were not reproduced in most numerical simulations. The question arises of wether our microscopic 3D models are sensible or not. A simulation longer by a factor of 1000, has shown more optimistic results. Although the behaviour of the Edwards-Anderson model investigated in this timescale is still not exactly as in experiments, memory and rejuvenation are observed. The issue of the correctness of the Edwards-Anderson model is still open, but we are closer to a positive answer.

Acknowledgements

I am deeply indebted with the people with whom I collaborated on the problems here described: A. Cruz, S. Ciliberti, L.A. Fernandez, T.S. Grigera, S. Jimenez, G. Parisi, S. Perez-Gaviro, J.J. Ruiz-Lorenzo, A. Tarancon, P. Verrocchio. Much was also learnt from discussions with A. Cavagna, B. Coluzzi, I. Giardina, E. Marinari, A. Maiorano, A. Pagnani, O. Pilla, F. Ricci-Tersenghi, and G. Ruocco.

This work has been financially supported by MEC (Spain) though research contracts BFM2003-08532 and FIS2004-05073-C04.

References

1. S. Kirkpatrick, C.D. Gellatt, Jr., M.P. Vecchi, Science **20,** 671 (1983).
2. C. Kittel, *Introduction to Solid State Physics,* John Wiley & Sons; 8 edition (2004). 339, 345
3. See e.g. M.E.J. Newman, G.T. Barkema, M. Newman, *Monte Carlo Methods in Statistical Physics,* Oxford University Press (1999); D.P. Landau and K. Binder, *A Guide to Monte Carlo Simulations in Statistical Physics,* Cambridge University Press (2000). 339, 350
4. A.D. Sokal, in *Functional Integration: Basics and Applications* (1996 Cargèse summer school), ed. C. DeWitt-Morette, P. Cartier and A. Folacci (Plenum, New York, 1997). 339
5. F. Bert, V. Dupuis, E. Vincent, J. Hammann and J.-P. Bouchaud, Phys. Rev. Lett. **92,** 167203 (2004). 339, 340
6. S. Jiménez, V. Martín-Mayor, G. Parisi and A. Tarancón, J. Phys. A **36,** 10755 (2003). 340, 357, 358, 359, 360
7. S. Jimenez, V. Martin-Mayor, S. Perez-Gaviro, cond-mat/0406365 and in preparation. 340, 343, 354
8. A. Cruz, J. Pech, A. Tarancón, P. Téllez, C.L. Ullod and C. Ungil, Comput. Phys. Commun. **133,** 165 (2001). 340, 343, 356, 360, 361, 365
9. See e.g. J.Horbach, W. Kob and K. Binder, *J. Phys. Chem. B* **103,** 4104–4108 (1999) 340, 360
10. R.H. Swendsen and J.-S. Wang, Phys. Rev. Lett. **58,** 86 (1987). 340
11. M. Nielsen, I.L. Chaung, *Quantum Computation and Quantum Information,* Cambridge University Press (2000). 340
12. J.A. Mydosh, *Spin Glasses: an Experimental Introduction* (Taylor and Francis, London 1993). 340
13. K. Binder and A.P. Young, Rev. Mod. Phys. **58**, 801 (1986); K.H. Fisher and J.A. Hertz, *Spin Glasses* (Cambridge University Press, Cambridge U.K. 1991) 340
14. M. Mézard, G. Parisi and M.A. Virasoro, *Spin Glass Theory and Beyond* (World Scientific, Singapore 1987); 340
15. E. Marinari, G. Parisi, F. Ricci-Tersenghi, J.J. Ruiz-Lorenzo and F. Zuliani, J. Stat. Phys. **98**, 973 (2000). 340, 345
16. *Spin Glasses and Random Fields*, edited by A.P. Young. World Scientific (Singapore, 1997). 340

17. J.P. Bouchaud, L. Cugliandolo, J. Kurchan and M. Mézard, in [16]; J.J. Ruiz-Lorenzo, *Advances in Condensed Matter and Statistical Mechanics*, Ed. E. Korutcheva, R. Cuerno, Nova Science Publishers (2004). 340, 369
18. C.A. Angell, Science **267,** 1924–1935 (1995). 341, 342, 343, 356, 366
19. P.G. DeBenedetti and F.H. Stillinger, Nature **410,** 259–267 (2001). 340, 341, 349, 350
20. T.R. Kirkpatrick and D. Thirumalai, Phys. Rev. Lett. **58,** 2091 (1987) and Phys. Rev. B **36,** 5388 (1987); T.R. Kirkpatrick, D. Thirumalai and P.G. Wolynes, Phys. Rev. A **40,** 1045 (1989). 340, 341, 350
21. L. Cugliandolo, *Dynamics of glassy systems,* Lecture notes, Les Houches, July 2002, cond-mat/0210312. 340, 345
22. T.S. Grigera and G. Parisi, Phys. Rev. E **63,** 045102(R) (2001). 340, 345
23. L.A. Fernández, V. Martín-Mayor and P. Verrocchio, in preparation. 340, 352
24. W.L. McMillan, J. Phys. C **17**, 3179 (1984). A.J. Bray and M.A. Moore, in *Heidelberg Colloquium on Glassy Dynamics*, edited by J.L. Van Hemmen and I. Morgenstern (Springer Verlag, Heidelberg, 1986), p. 121. D.S. Fisher and D.A. Huse, Phys. Rev. Lett. **56**, 1601 (1986); Phys. Rev. B **38**, 386 (1988). 340, 352
25. M. Palassini and A.P. Young, Phys. Rev. Lett. **85**, 3017 (2000). 340
26. M. Tesi, E. Janse van Resburg, E. Orlandini and S.G. Whillington, J. Stat. Phys. **82**, 155 (1996); K. Hukushima and K. Nemoto, J. Phys. Soc. Jpn. 65, 1604 (1996). 340
27. H.G. Ballesteros, A. Cruz, L.A. Fernandez, V. Martin-Mayor, J. Pech, J.J. Ruiz-Lorenzo, A. Tarancon, P. Tellez, C.L. Ullod and C. Ungil, Phys. Rev. B **62,** 14237 (2000). 340
28. J. Houdayer, Eur. Phys. Jour. B **22,** 479 (2001). 340
29. G.E. Santoro, R. Martonak, E. Tosatti and R. Car, Science **295,** 2427 (2002). 341
30. See D.A. Battagglia, G.E. Santoro and E. Tosatti, cond-mat/0502468. Actually, in this paper the 3-SAT problem is studied. This model is a close relative of the $p = 3$ Sherrington-Kirkpatrick model. 341
31. L.C.E. Struick, *Physical aging in amorphous polymers and others materials*, (Elsevier, Houston, 1978). 341
32. D. Bonn, H. Tanaka, G. Wegdam, H. Kellay, and J. Meunier, Europhys. Lett. **45,** 52 (1998). 341, 343
33. R.V. Chamberlin, M. Hardiman and R. Orbach, J. Appl. Phys. **52,** 1771 (1983); L. Lundgren, P. Svelindh, P. Norblad and O. Beckman, Phys. Rev. Lett. **51,** 911 (1983) and J. Appl. Phys. **57,** 3371 (1985). 341
34. J. Kurchan, Comptes Rendus de Physique de l'Academie des Sciences **IV,** 239 (2001). 341, 356
35. E. Vincent, J. Hamman, M. Ocio, J.P. Bouchaud and L.F. Cugliandolo in *Complex behaviour of glassy systems,* ed. M. Rubi, Springer-Verlag Lecture Notes in Physics **492,** 184 (1997) (cond-mat/96072224). 341, 342, 343
36. L.F. Cugliandolo and J. Kurchan, Phys. Rev. Lett. **71,** 173 (1993); L.F. Cugliandolo, J. Kurchan and L. Peliti, Phys. Rev. E **55,** 3898 (1997). 342, 343, 344
37. S. Franz, M. Mézard, G. Parisi, L. Peliti, Phys. Rev. Lett. **81**, 1758 (1998); J. Stat. Phys. **97**, 459 (1999). 342
38. E. Marinari, G. Parisi, F. Ricci-Tersenghi and J.J. Ruiz-Lorenzo, J. Phys. A **31**, 2611 (1998); S. Franz and H. Rieger, J. Stat. Phys. **79**, 749 (1995). 342, 343
39. G.F. Rodriguez, G.G. Kenning and R. Orbach, Phys. Rev. Lett. **91,** 037203 (2003). 342, 343, 354
40. V. Dupuis, F. Bert, J.-P. Bouchaud, J. Hammann, F. Ladieu, D. Parker and E. Vincent, cond-mat/0406721. 343, 358, 359

41. A.J. Bray, Adv. Phys. **43,** 357 (1994). 342
42. J.-P. Bouchaud in: *Soft and Fragile Matter: Nonequilibrium Dynamics, Metastability and Flow,* edited by M.E. Cates and M.R. Evans (IOP publishing, Bristol, 2000). 343
43. B. Abou, D. Bonn, and J. Meunier, Phys. Rev. E, **64** 021510 (2001); A. Knaebel, M. Bellor, J.-P. Munch, V. Viasnoff, F. Lequeux, and J.L. Harden, Europhys. Lett. **52**, 73 (2000). 343
44. L. Buisson, L. Bellon, and S. Ciliberto, J. Phys: Cond. Matt. **15**, S1163 (2003). 343
45. W. Kob and J.-L. Barrat, Phys. Rev. Lett. **78**, 4581 (1997). 343, 354
46. R.L. Leheny and S.R. Nagel, Phys. Rev. B **57,** 5154 (1998). 343, 344
47. T.S. Grigera and N.E. Israeloff, Phys. Rev. Lett. **83,** 5038 (1999). 343
48. L. Bellon, S. Ciliberto, and C. Laroche, Europhys. Lett. **53**, 511 (2001); L. Bellon and S. Ciliberto, Physica D **168,** 325 (2002); D. Hérisson and M. Ocio, Phys. Rev. Lett. **88,** 257202 (2002); L. Buisson, S. Ciliberto, and A. Garcimartín, Europhys. Lett. **63,** 603 (2003). 343
49. G. Parisi, Phys. Rev. Lett. **79,** 3660 (1997); J.L. Barrat and W. Kob, Europhys. Lett. 46, 637 (1999); R. Di Leonardo, L. Angelani, G. Parisi, and G. Ruocco. Phys. Rev. Lett. 84, 6054 (2000). 343
50. F. Sciortino and P. Tartaglia, Phys. Rev. Lett. **86,** 107 (2001). 343, 355, 356, 357
51. A.Q. Tool, J. Am. Ceram. Soc. **29,** 240 (1946); O.S. Narayanaswamy, *ibid.* **54,** 491 (1971); C.T. Moyniham, *ibid.* **59,** 12 (1976); **59,** 16 (1976). 344
52. See e.g. J.P. Hansen and I.R. McDonald, *Theory of Simple Liquids,* Academic Press (San DIego, 1986). 345
53. W. Götze, L. Sjögren, Rep. Prog. Phys. **55,** 241 (1992). 345
54. D.J. Thouless, P.W. Anderson and R.G. Palmer, Phil. Mag. **35,** 593 (1977). 345
55. C. de Dominicis and A.P. Young, J. Phys. A **16,** 2063 (1983). 346
56. R. Monasson, Phys. REv. Lett. **75,** 2847 (1995). 347
57. Cavagna, A., Giardina, I., Parisi, G., Role of saddles in mean-field dynamics above the glass transition *J. Phys. A: Math. Gen.* **34,** 5317–5326 (2001) 347, 351
58. F.H. Stillinger, Science **267,** 1935–1939 (1995). 348, 349, 350
59. T.S. Grigera, V. Martin-Mayor, G. Parisi and P. Verrocchio, Nature **422,** 289 (2003) 350
60. W.A. Phillips, U. Buchenau, N. Nücher, A.-J. Dianoux, and W. Petry, Phys. Rev. Lett. **63,** 2381–2384 (1989). 350
61. F. Sette, M.H. Krisch, C. Masciovecchio, G. Ruocco and G. Monaco, Science **280,** 1550–1555 (1998). 350
62. G. Ruocco et al., Phys. Rev. Lett. **84,** 5788–5791 (2000). 350
63. O. Pilla et al., preprint condmat/0209519 350
64. C. Masciovecchio et al., Phys. Rev. Lett. **76,** 3356–3359 (1996). 350
65. A. Matic et al., Europhys. Lett. **54,** 77–83 (2001). 350
66. C. Masciovecchio et al., Phys. Rev. B **55,** 8049–8051 (1997). 350
67. P. Benassi et al., Phys. Rev. Lett. **77,** 3835–3838 (1996). 350
68. D. Fioretto et al., Phys. Rev. E **59,** 4470–4475 (1999). 350
69. O. Pilla et al., Phys. Rev. Lett. **85,** 2136–2139 (2000). 350
70. T.S. Grigera, V. Martín-Mayor, G., Parisi, and P. Verrocchio, J. Phys.: Condens. Matter **14,** 2167–2179 (2002). 350, 351
71. V. Martín-Mayor, M. Mèzard, G., Parisi, and P. Verrocchio, J. Chem. Phys. **114,** 8068–8081 (2001). 350
72. T.S. Grigera, V. Martín-Mayor, G. Parisi, and P. Verrocchio, Phys. Rev. Lett. **87,** 085502-1–085502-4 (2001). 350

73. S. Ciliberti, T.S. Grigera, V. Martin-Mayor, G. Parisi and P. Verrocchio, J. Chem. Phys. **119,** 8577 (2003) 350
74. M. Mèzard, G. Parisi, G., and A. Zee, Nuc. Phys. B **559,** 689–701 (1999). 350, 351
75. L. Angelani, R. Di Leonardo, G. Ruocco, A. Scala, and F. Sciortino, Phys. Rev. Lett. **85,** 5356–5359 (2000). 351
76. K. Broderix, K. Bhattacharya, A. Cavagna, A. Zippelius, and I. Giardina, Phys. Rev. Lett. **85,** 5360–5363 (2000). 351
77. T.S. Grigera, A. Cavagna, I, Giardina, I., and G. Parisi, Phys. Rev. Lett. **88,** 055502-1–055502-4 (2002). 351
78. W. Kob and H.C. Andersen, Phys. Rev. E **51,** 4626–6241 (1995).
79. W. Kob, F. Sciortino, and P. Tartaglia, Europhys. Lett. **49,** 590–596 (2000). 351
80. T.S. Grigera, V. Martin-Mayor, G. Parisi, and P. Verrocchio, Phys. Rev. B **70,** 014202 (2004). 352, 355
81. B. Bernu, J.-P. Hansen, Y. Hiwatari, and G. Pastore, Phys. Rev. A **36,** 4891–4903 (1987). 352
82. L. Santen and W. Krauth, Nature **405**, 550 (2000). 352
83. L. Berthier and J.P. Garrahan J. Chem. Phys. **119**, 4367 (2003); S. Whitelam, L. Berthier, and J.P. Garraham, Phys. Rev. Lett. **92,** 185705 (2004). 356
84. D. Kivelson, S.A. Kivelson, X. Zhao, Z. Nussinov, and G. Tarjus, Physica A **219**, 27 (1995). 356
85. M. Mézard and G. Parisi, Phys. Rev. Lett. **82,** 747 (1998); B. Coluzzi, G. Parisi, and P. Verrocchio, Phys. Rev. Lett. **84,** 306 (2000). 356
86. A. Cavagna, I. Giardina, and T.S. Grigera, J. Chem. Phys. **118,** 6974 (2003). 356
87. K. Jonason, K. Jonason, E. Vincent, J. Hammann, J.P. Bouchaud, and P. Nordblad, Phys. Rev. Lett. **81,** 3243 (1998). 356, 357
88. L. Lundgren, P. Svendlinsh, O. Beckman, Journal of Magn. Magn. Mat. **31-34,** 1349 (1983); T. Jonsson, K. Jonason, P. Jönsson, and P. Nordblad, Phys. Rev. B **59,** 8770(1999); J. Hammann, E. Vincent, V. Dupuis, M. Alba, M. Ocio and J.-P. Bouchaud, J. Phys. Soc. Jpn. **69,** (2000) Suppl. A, 206-211. 356
89. H. Takayama and K. Hukushima, J. Phys. Soc. Jpn. **71,** 3003 (2002). 357, 358, 359, 360, 361, 362
90. S. Miyashita, E. Vincent, Eur. Phys. J. B **22,** 203 (2001). 357, 361
91. P.E. Jönsson, H. Yoshino, H. Mamiya and H. Takayama, preprint cond-mat/0405276. 357
92. H. Yardimci, R.L. Leheny, Europhys. Lett. **62,** 203 (2003). 357
93. E. Vincent, V. Dupuis, M. Alba, J. Hammann, J.-P. Bouchaud, Europhys. Lett **50,** 674 (2000). 357
94. L. Bellon, S. Ciliberto, C. Laroche, Eur. Phys. J. B **25,** 223 (2002). 357
95. K. Fukao and A. Sakamoto, cond-mat/0410602. 357
96. P. Levy, F. Parisi, L. Granja, E. Indelicato and G. Polla, Phys. Rev. Lett. **89,** 137001 (2002). 357
97. P.E. Jönson, H. Yoshino and P. Nordblad, Phys. Rev. Lett. **89,** 97201 (2002). 357, 358, 359, 365
98. P.E. Jönsson, R. Mathieu, P. Nordblad, H. Yoshino, H. Aruga Katori and A. Ito, Phys. Rev. B **70,** 174402 (2004). 357, 359, 362
99. J.-P. Bouchaud and D.S. Dean, J. Phys. I (France) **5,** 265 (1995); M. Sales, J.-P. Bouchaud and F. Ritort, J. Phys. A: Math. Gen. **36,** 665 (2003); M. Sasaki, V. Dupuis, J.-P. Bouchaud and E. Vincent, Eur. Phys. J. B **29,** 469 (2002). 358
100. J.P. Bouchaud, *Soft and Fragile matter*, Eds: M.E. Cates, M.R. Evans (Institute of Physics Publishing, 2000). 359, 365, 367
101. T. Komori, H, Yoshino, H. Takayama, J. Phys. Soc. Jpn. **69,** Suppl., 228 (2000). 358, 359, 360, 361, 362, 365

102. M. Picco, F. Ricci-Tersenghi, F. Ritort, Phys. Rev. B **63**, 174412 (2001). 358, 360, 361
103. L. Berthier, J.-P. Bouchaud, Phys. Rev. B **66**, 054404 (2002). 358, 360, 361, 365, 367
104. A. Maiorano, E. Marinari and F. Ricci-Tersenghi, cond-mat/0409577. 358, 359, 360, 366
105. See L.W. Bernardi, H. Yoshino, K. Hukushima, H. Takayama, A. Tobo and A. Ito, Phys. Rev. Lett. **86,** 720 (2001),. 358
106. F. Ricci-Tersenghi, private communication. 360
107. M. Sasaki, O.C. Martin, Phys. Rev. Lett. **91,** 097201 (2003). 360, 361
108. E. Marinari, G. Parisi, F. Ricci-Tersenghi and J.J. Ruiz-Lorenzo, J. Phys. A **33**,2373 (2000). 359, 365
109. T. Komori, H. Yoshino and H. Takayama, J. Phys. Soc. Jpn. **68,** 3387 (1999). 359
110. H.G. Ballesteros, L.A. Fernández, V. Martín-Mayor, A. Muoz Sudupe, G. Parisi and J.J. Ruiz-Lorenzo, Phys. Rev. B, **58** 2740 (1998).
111. J.P. Bouchaud, *Soft and Fragile matter*, Eds: M.E. Cates, M.R. Evans (Institute of Physics Publishing, 2000).
112. T. Komori, H, Yoshino, H. Takayama, J. Phys. Soc. Jpn. **69,** Suppl., 228 (2000).
113. L. Berthier, J.-P. Bouchaud, Phys. Rev. B **66**, 054404 (2002).
114. A. Maiorano, E. Marinari and F. Ricci-Tersenghi, cond-mat/0409577.
115. See L.W. Bernardi, H. Yoshino, K. Hukushima, H. Takayama, A. Tobo and A. Ito, Phys. Rev. Lett. **86,** 720 (2001),.
116. F. Ricci-Tersenghi, private communication.
117. M. Sasaki, O.C. Martin, Phys. Rev. Lett. **91,** 097201 (2003).
118. E. Marinari, G. Parisi, F. Ricci-Tersenghi and J.J. Ruiz-Lorenzo, J. Phys. A **33**,2373 (2000).
119. T. Komori, H. Yoshino and H. Takayama, J. Phys. Soc. Jpn. **68,** 3387 (1999).
120. H.G. Ballesteros, L.A. Fernández, V. Martín-Mayor, A. Muoz Sudupe, G. Parisi and J.J. Ruiz-Lorenzo, Phys. Rev. B, **58** 2740 (1998).
121. J.P. Bouchaud, *Soft and Fragile matter*, Eds: M.E. Cates, M.R. Evans (Institute of Physics Publishing, 2000).
122. T. Komori, H, Yoshino, H. Takayama, J. Phys. Soc. Jpn. **69,** Suppl., 228 (2000).
123. L. Berthier, J.-P. Bouchaud, Phys. Rev. B **66**, 054404 (2002).
124. A. Maiorano, E. Marinari and F. Ricci-Tersenghi, cond-mat/0409577.
125. See L.W. Bernardi, H. Yoshino, K. Hukushima, H. Takayama, A. Tobo and A. Ito, Phys. Rev. Lett. **86,** 720 (2001),.
126. F. Ricci-Tersenghi, private communication.
127. M. Sasaki, O.C. Martin, Phys. Rev. Lett. **91,** 097201 (2003).
128. E. Marinari, G. Parisi, F. Ricci-Tersenghi and J.J. Ruiz-Lorenzo, J. Phys. A **33**, 2373 (2000).
129. T. Komori, H. Yoshino and H. Takayama, J. Phys. Soc. Jpn. **68,** 3387 (1999).
130. H.G. Ballesteros, L.A. Fernández, V. Martín-Mayor, A. Muoz Sudupe, G. Parisi and J.J. Ruiz-Lorenzo, Phys. Rev. B, **58** 2740 (1998).
131. S. Jiménez, Ph.D. Thesis, U. Zaragoza, January 2005. 367
132. A.J. Bray, M.A. Moore, Phys. Rev. Lett. **58**, 57 (1987) 359
133. Parametrizations of $C_4(r,t)$ different from (29) can be found, where ξ does not decrease (J.P. Bouchaud and L. Berthier, private communication). 365

Index

Lecture Notes in Physics

For information about earlier volumes
please contact your bookseller or Springer
LNP Online archive: springerlink.com

Vol.632: A. M. Greco (Ed.), Direct and Inverse Methods in Nonlinear Evolution Equations

Vol.633: H.-T. Elze (Ed.), Decoherence and Entropy in Complex Systems, Based on Selected Lectures from DICE 2002

Vol.634: R. Haberlandt, D. Michel, A. Pöppl, R. Stannarius (Eds.), Molecules in Interaction with Surfaces and Interfaces

Vol.635: D. Alloin, W. Gieren (Eds.), Stellar Candles for the Extragalactic Distance Scale

Vol.636: R. Livi, A. Vulpiani (Eds.), The Kolmogorov Legacy in Physics, A Century of Turbulence and Complexity

Vol.637: I. Müller, P. Strehlow, Rubber and Rubber Balloons, Paradigms of Thermodynamics

Vol.638: Y. Kosmann-Schwarzbach, B. Grammaticos, K. M. Tamizhmani (Eds.), Integrability of Nonlinear Systems

Vol.639: G. Ripka, Dual Superconductor Models of Color Confinement

Vol.640: M. Karttunen, I. Vattulainen, A. Lukkarinen (Eds.), Novel Methods in Soft Matter Simulations

Vol.641: A. Lalazissis, P. Ring, D. Vretenar (Eds.), Extended Density Functionals in Nuclear Structure Physics

Vol.642: W. Hergert, A. Ernst, M. Däne (Eds.), Computational Materials Science

Vol.643: F. Strocchi, Symmetry Breaking

Vol.644: B. Grammaticos, Y. Kosmann-Schwarzbach, T. Tamizhmani (Eds.) Discrete Integrable Systems

Vol.645: U. Schollwöck, J. Richter, D. J. J. Farnell, R. F. Bishop (Eds.), Quantum Magnetism

Vol.646: N. Bretón, J. L. Cervantes-Cota, M. Salgado (Eds.), The Early Universe and Observational Cosmology

Vol.647: D. Blaschke, M. A. Ivanov, T. Mannel (Eds.), Heavy Quark Physics

Vol.648: S. G. Karshenboim, E. Peik (Eds.), Astrophysics, Clocks and Fundamental Constants

Vol.649: M. Paris, J. Rehacek (Eds.), Quantum State Estimation

Vol.650: E. Ben-Naim, H. Frauenfelder, Z. Toroczkai (Eds.), Complex Networks

Vol.651: J. S. Al-Khalili, E. Roeckl (Eds.), The Euroschool Lectures of Physics with Exotic Beams, Vol.I

Vol.652: J. Arias, M. Lozano (Eds.), Exotic Nuclear Physics

Vol.653: E. Papantonoupoulos (Ed.), The Physics of the Early Universe

Vol.654: G. Cassinelli, A. Levrero, E. de Vito, P. J. Lahti (Eds.), Theory and Appplication to the Galileo Group

Vol.655: M. Shillor, M. Sofonea, J. J. Telega, Models and Analysis of Quasistatic Contact

Vol.656: K. Scherer, H. Fichtner, B. Heber, U. Mall (Eds.), Space Weather

Vol.657: J. Gemmer, M. Michel, G. Mahler (Eds.), Quantum Thermodynamics

Vol.658: K. Busch, A. Powell, C. Röthig, G. Schön, J. Weissmüller (Eds.), Functional Nanostructures

Vol.659: E. Bick, F. D. Steffen (Eds.), Topology and Geometry in Physics

Vol.660: A. N. Gorban, I. V. Karlin, Invariant Manifolds for Physical and Chemical Kinetics

Vol.661: N. Akhmediev, A. Ankiewicz (Eds.) Dissipative Solitons

Vol.662: U. Carow-Watamura, Y. Maeda, S. Watamura (Eds.), Quantum Field Theory and Noncommutative Geometry

Vol.663: A. Kalloniatis, D. Leinweber, A. Williams (Eds.), Lattice Hadron Physics

Vol.664: R. Wielebinski, R. Beck (Eds.), Cosmic Magnetic Fields

Vol.665: V. Martinez (Ed.), Data Analysis in Cosmology

Vol.666: D. Britz, Digital Simulation in Electrochemistry

Vol.667: W. D. Heiss (Ed.), Quantum Dots: a Doorway to Nanoscale Physics

Vol.668: H. Ocampo, S. Paycha, A. Vargas (Eds.), Geometric and Topological Methods for Quantum Field Theory

Vol.669: G. Amelino-Camelia, J. Kowalski-Glikman (Eds.), Planck Scale Effects in Astrophysics and Cosmology

Vol.670: A. Dinklage, G. Marx, T. Klinger, L. Schweikhard (Eds.), Plasma Physics

Vol.671: J.-R. Chazottes, B. Fernandez (Eds.), Dynamics of Coupled Map Lattices and of Related Spatially Extended Systems

Vol.672: R. Kh. Zeytounian, Topics in Hyposonic Flow Theory

Vol.673: C. Bona, C. Palenzula-Luque, Elements of Numerical Relativity

Vol.674: A. G. Hunt, Percolation Theory for Flow in Porous Media

Vol.675: M. Kröger, Models for Polymeric and Anisotropic Liquids

Vol.676: I. Galanakis, P. H. Dederichs (Eds.), Halfmetallic Alloys

Vol.678: M. Donath, W. Nolting (Eds.), Local-Moment Ferromagnets

Vol.679: A. Das, B. K. Chakrabarti (Eds.), Quantum Annealing and Related Optimization Methods